

# **Effect of Doping on Nickel Metal-Based Chalcogenide Nanomaterials for Electrochemical Water Splitting**

**THESIS**

Submitted in partial fulfillment  
of the requirements for the degree of

*Doctor of Philosophy*

by

**Divya Rathore**

2018PHXF0435P

Under the Supervision of

**Dr. Surojit Pande**



**BIRLA INSTITUTE OF TECHNOLOGY AND  
SCIENCE PILANI, PILANI CAMPUS (RAJASTHAN),**

**INDIA**

**2024**

**BIRLA INSTITUTE OF TECHNOLOGY AND  
SCIENCE, PILANI**

**CERTIFICATE**

This is to certify that the thesis entitled “**Effect of Doping on Nickel Metal-Based Chalcogenides Nanomaterials for Electrochemical Water Splitting**” submitted by **Ms. Divya Rathore** ID No. **2018PHXF0435P** for an award of Ph.D. of the institute embodies original work done by her under our supervision.

Signature of the Supervisor

**Dr. Surojit Pande**

Professor

Department of Chemistry

Birla Institute of Technology and Science

Pilani, Pilani Campus, Rajasthan

**Date:** / /2024

# ***Dedicated***

***To Almighty for showering the grace***

***To My Parents and Teachers who gave me a luminous path  
and motivation***

***To those who believe in hard work and never give upon  
their dreams***

## *Acknowledgements*

---

The completion of this thesis owes its success to the unwavering guidance and support of several individuals, and I wish to express my heartfelt gratitude to each one of them.

Foremost, I extend my sincere thanks to my research supervisor Dr. Surojit Pande, for entrusting me with the opportunity to be part of their esteemed research team. I am particularly grateful to Dr. Mrinmoyee Basu for her encouragement during challenging times, valuable insights, suggestions, and motivational influence on enhancing my research skills. Their consistent guidance, trust, inspiration, and constructive feedback were instrumental throughout my Ph.D. journey. Without their unconditional support, this thesis would have remained an unattainable dream. The weekly presentations on the progress of our work significantly improved my presentation and writing abilities. I am indebted to both of them for the countless lab sessions, support in experiments, enlightening discussions, and care that facilitated my overall progress. I extend my gratitude to the Vice-Chancellors, Directors, Deans, and Associate Deans of Birla Institute of Technology and Science (BITS) Pilani, as well as the Heads of the Department of Chemistry, for providing the necessary facilities and a conducive environment for my doctoral studies.

I am sincerely thankful to the faculty members of the Department of Chemistry for their cooperation and affection. Special appreciation goes to the members of the Doctoral Advisory Committee, including Prof. Saumi Ray and Dr. Bibhas Sarkar, whose valuable suggestions played a crucial role in refining my thesis.

My thanks also go to the office and lab staff, including Mr. C. P. Soni, Mrs. Pushpalata, Mr. Suresh Saini, Mr. Nandlal Saini, and Mr. Ashok Sharma, for their indispensable assistance during lab experiments. I appreciate the support received from the office staff of AUGSD, AGSRD, and the library, whose secretarial aid was invaluable throughout my Ph.D. tenure. Additionally, I express my thanks to the central instrument facilities at BITS-Pilani and the Department of Physics for providing access to the XRD instrument.

I consider myself fortunate to have been surrounded by supportive seniors, including Dr. Pragati Fageria, Dr. Chavi Mahala, Dr. Jagrity Chaudhary and Dr. Mamta devi Sharma, whose unwavering support, care, and guidance was crucial during challenging times. I am also grateful for the camaraderie of fellow Ph.D. candidates, including Dr. Roshan Nazir, Mr. Prashant, Ms. Aastha, Ms. Anakshi, Ms. Prekshi, Ms. Ritu, and Ms. Rajrani as well as friends and batchmates who were a constant source of support and companionship. I am grateful for the roommate Ms.



## *Acknowledgements*

---

Pavitra, and Ms. Manisha for their continuous love and support. I extend my gratitude to my friends and batchmates Mr. Mahesh, Mr. Sumit, Ms. Neha, Ms. Gurpreet, Ms. Sonam, Mr. Rishi, Ms. Tina, Ms. Radha, Mr. Anukaran, Mr. Ram Prasad, Ms. Pragya, Ms. Vishakha, Ms. Aarzo, Ms. Aishwarya, Mr. Ajeet, Ms. Sakshi and Mr. Pramod for their constant support and love.

My most profound appreciation goes to my family, without whom my journey as a person and scholar would have been impossible. I am profoundly grateful to my father, Mr. Ladu Singh, for being a constant source of inspiration and to my mother, Mrs. Vinod Kanwar, for her unconditional support and confidence. I convey my regards to my father-in-law, Mr. Ratan Singh Shekhawat, and mother-in-law, Mrs. Kailash Kanwar, for their endless support and love. Special thanks to Chamandeep, Monika, Manvendra, and Nikita for their unwavering love and strong support. I extend my gratitude to my husband, Major Monu Singh Shekhawat, for his encouragement and unwavering support, without which this success would not have been possible. Lastly, I thank the almighty for granting me the health and strength to face each day with faith and optimism. My sincere thanks also go to BITS Pilani, Rajasthan, for providing the necessary infrastructure and the research fellowship.

Thanks to All!

*Date: / /2024*

*Place: Pilani, India*

*Divya Rathore*

# Table of Contents

---

<b>Contents</b>	<b>Page No.</b>
<i>Certificate</i>	i
<i>Dedication</i>	ii
<i>Acknowledgments</i>	iii
<i>Table of Contents</i>	v
<i>Abstract</i>	xi
<i>List of Abbreviations</i>	xii
<i>List of Symbols</i>	xiv
<i>List of Tables</i>	xv
<i>List of Schemes</i>	xvii
<i>List of Figures</i>	xviii

---

<b>Chapter 1</b>	<b>Introduction</b>	<b>1-55</b>
<b>1.1</b>	<b>Nanoscience and Nanotechnology: Historical Background</b>	1-2
<b>1.2</b>	<b>Nanomaterials: Brief Overview</b>	3-6
1.2.1	Uniqueness of Nanomaterials	3
1.2.2	Dimensionality of Nanomaterials	4-5
1.2.3	Synthetic Approaches of Nanomaterials	5-6
<b>1.3</b>	<b>Application of Nanomaterials in Energy Conversion</b>	6-21
1.3.1	Methods of water splitting	7-15
1.3.1.1	Thermal water splitting	7
1.3.1.2	Photoelectrochemical water splitting	7-8
1.3.1.3	Biological water splitting	9
1.3.1.4	Photocatalytic water splitting	10-11
1.3.1.5	Electrochemical water splitting	11-15
1.3.2	The mechanism of water splitting reaction	16-21
1.3.2.1	Hydrogen evolution reaction (HER)	16-19
1.3.2.2	Oxygen evolution reaction	19-21
<b>1.4</b>	<b>Evaluation parameters of water splitting reaction</b>	22-29
1.4.1	overpotential	22-23

# Table of Contents

---

1.4.2	Electrochemical active surface area (ECSA)	24
1.4.3	Tafel slope	24-26
1.4.4	Faradaic efficiency	26-27
1.4.5	Electrochemical stability	27-28
1.4.6	Impedance	28-29
<b>1.5</b>	<b>Transition metal chalcogenides as an important candidate for water-splitting</b>	29-31
<b>1.6</b>	<b>Important strategies to enhance electrocatalytic activity</b>	32
1.6.1	Morphology	32-35
1.6.1.1	1D nanomaterial	32-33
1.6.1.2	2D nanomaterial	33-34
1.6.1.3	3D nanomaterial	35
1.6.2	Structure	35-37
1.6.2.1	Phase Change	35-36
1.6.2.2	High index crystal phase	36
1.6.2.3	Amorphous structure	36-37
1.6.3	Electronic structure	37-41
1.6.3.1	Chemical doping	37
1.6.3.1.1	Anion doping	38-39
1.6.3.1.2	Cation doping	39-40
1.6.3.2	Heterostructure formation	40-41
<b>1.7</b>	<b>Doping of transition metal ions in Nickel-based electrocatalyst</b>	41
<b>1.8</b>	<b>Synthetic approaches for the development of doped nanomaterials</b>	41-44
1.8.1	Hydrothermal route	41-42
1.8.2	Electrodeposition method	42-43
1.8.3	Microwave assisted method	43
1.8.4	Wet chemical method	43-44
<b>1.9</b>	<b>Gaps in existing research</b>	44-45
<b>1.10</b>	<b>Thesis objective and outline</b>	45-46
<b>1.11</b>	<b>References</b>	46-55

---

# Table of Contents

---

<b>Chapter 2</b>	<b>Materials, Methods, and Instrumentation</b>	<b>56-72</b>
<b>2.1</b>	<b>Used Chemicals</b>	56-57
<b>2.2</b>	<b>Used Materials</b>	57
2.2.1	Carbon cloth	57
<b>2.3</b>	<b>Methods</b>	57-59
2.3.1	Synthesis Method	57-58
2.3.2	Sample Preparation Method for Analysis	58-59
<b>2.4</b>	<b>Instrumentation</b>	59-66
2.4.1	List of Instruments	59-60
2.4.2	Powder X-ray Diffraction (PXRD)	60-62
2.4.3	X-ray Photoelectron Spectroscopy	62
2.4.4	Electron Microscopy	63-64
2.4.5	Fourier Transform Infrared (FTIR) Spectroscopy	64
2.4.6	Raman spectroscopy	64-65
2.4.7	BET analysis	65
2.4.8	ICP-AES analysis	65-66
<b>2.5</b>	<b>Techniques for electrochemical Application</b>	66-68
2.5.1	Voltammetry Techniques	66-67
2.5.2	Amperometry Techniques	67-68
2.5.3	Electrochemical Impedance Spectroscopy	68
2.5.4	Faradaic efficiency	68
2.5.5	Rate constant	68
<b>2.6</b>	<b>Electrochemical Cell to perform the Water-Splitting</b>	68-70
<b>2.7</b>	<b>References</b>	70-73
<b>Chapter 3</b>	<b>Ni/Ni(OH)<sub>2</sub>/NiOOH Nanoworms on Carbon Cloth for Electrochemical Hydrogen Evolution</b>	<b>74-106</b>
<b>3.1</b>	<b>Introduction</b>	76-78
<b>3.2</b>	<b>Experimental Section</b>	78-81
3.2.1	Synthesis of Ni/Ni(OH) <sub>2</sub> /NiOOH	78-79

---

# Table of Contents

---

3.2.2	Synthesis of Ni(OH) <sub>2</sub> /NiOOH	79
3.2.3	Synthesis of Ni/Ni(OH) <sub>2</sub>	79-80
3.2.4	Electrochemical measurement	80-81
<b>3.3</b>	<b>Results and Discussion</b>	81-100
3.3.1	Synthesis and structural analysis of electrodeposited sample	81-85
3.3.2	FESEM, TEM, and EDS analysis of electrodeposited sample	85-88
3.3.3	Mechanism of formation of the Ni/Ni(OH) <sub>2</sub> /NiOOH heterostructure	88-89
3.3.4	Electrochemical HER activity	90-98
3.3.5	OER activity	98-99
3.3.6	Comparative Study	99-100
<b>3.4</b>	<b>Conclusion</b>	100-101
<b>3.5</b>	<b>References</b>	101-106

---

<b>Chapter 4</b>	<b>Bifunctional Tungsten-doped Ni(OH)<sub>2</sub>/NiOOH Nanosheets for Overall Water Splitting in Alkaline Medium</b>	<b>107-148</b>
------------------	---	----------------

---

<b>4.1</b>	<b>Introduction</b>	109-111
<b>4.2</b>	<b>Experimental Section</b>	111-114
4.2.1	Synthesis of Ni(OH) <sub>2</sub> /NiOOH nanosheets	111
4.2.2	Synthesis of W doped Ni(OH) <sub>2</sub> /NiOOH	112
4.2.3	Electrochemical measurement	113
4.2.4	Preparation of standard electrocatalyst	113
4.2.5	Computational methods	113-114
4.3	<b>Results and Discussion</b>	114-143
4.3.1	Material synthesis and Characterization	114-116
4.3.2	XPS analysis	116-119
4.3.3	FESEM, EDS, ICP-AES and TEM analysis	120-123
4.3.4	Electrochemical Activity	124-141
4.4	DFT Study	142-143
<b>4.4</b>	<b>Conclusion</b>	143-144
<b>4.5</b>	<b>References</b>	144-148

---

# Table of Contents

---

<b>Chapter 5</b>	<b>Co-Doped Ni<sub>9</sub>S<sub>8</sub> Nanostructures for Electrocatalytic Water-Splitting in a Wide pH Region</b>	<b>149-198</b>
5.1	<b>Introduction</b>	151-154
5.2	<b>Experimental Section</b>	154-157
5.2.1	Synthesis of Ni <sub>9</sub> S <sub>8</sub>	154
5.2.2	Synthesis of Co doped Ni <sub>9</sub> S <sub>8</sub>	155
5.2.3	Electrochemical measurement	155-156
5.2.4	Computational study	156-157
5.3	<b>Results and Discussions</b>	157-190
5.3.1	Structural analysis	157-163
5.3.2	Morphological analysis	164-166
5.3.3	Electrochemical Activity	167-181
5.3.4	Overall water splitting	181-182
5.3.5	Theoretical calculation	182-190
<b>5.4</b>	<b>Conclusion</b>	191
<b>5.5</b>	<b>References</b>	191-198
<b>Chapter 6</b>	<b>Ce-Doped Ni<sub>0.85</sub>Se 2D Nanosheets Developed on Carbon Cloth for Electrochemical Water-Splitting</b>	<b>199-234</b>
<b>6.1</b>	<b>Introduction</b>	201-203
<b>6.2</b>	<b>Experimental Section</b>	203-205
6.2.1	Synthesis of Ni <sub>0.85</sub> Se	203
6.2.2	Synthesis of Ce doped Ni <sub>0.85</sub> Se	204
6.2.3	Electrochemical study	205
<b>6.3</b>	<b>Result and Discussion</b>	205-230
6.3.1	Mechanism of formation	205-206
6.3.2	XRD, Raman, BET and XPS study	206-213
6.3.3	Morphological study	213-217
6.3.4	Electrocatalytic Study	217-226
6.3.5	Two electrode system	227-229
<b>6.4</b>	<b>Conclusion</b>	229-230
<b>6.5</b>	<b>References</b>	230-234

---

# Table of Contents

---

<b>Chapter 7</b>	<b>Fe-Doped NiCo<sub>2</sub>Se<sub>4</sub> Nanorod Arrays as Electrocatalysts for Overall Electrochemical Water-Splitting</b>	<b>235-287</b>
<b>7.1</b>	<b>Introduction</b>	237-239
<b>7.2</b>	<b>Experimental Section</b>	240-243
7.2.1	Synthesis of NiCo <sub>2</sub> Se <sub>4</sub>	240
7.2.2	Synthesis of Fe doped NiCo <sub>2</sub> Se <sub>4</sub>	240-241
7.2.3	Electrochemical study	241-242
7.2.4	Computational methodology	242-243
<b>7.3</b>	<b>Results and Discussions</b>	243-279
7.3.1	PXRD and XPS study	243-249
7.3.2	Morphological study	249-253
7.3.3	Electrochemical Activity	254-268
7.3.4	Two electrodes	268-271
7.3.5	Structural properties using theoretical study	272-273
7.3.6	Electronic properties	274-277
7.3.7	Gibbs Free energy calculation	278-279
<b>7.4</b>	<b>Conclusion</b>	279-280
<b>7.5</b>	<b>References</b>	280-287
<b>Chapter 8</b>	<b>Summary, conclusion, and Future Scope of Study</b>	<b>288-291</b>
	<b>Appendices</b>	<b>A1-A4</b>
[A-1]	List of Publications	
[A-2]	List of Poster Presented in Conferences	
[A-3]	Brief Biography of the Candidate	
[A-4]	Brief Biography of the Supervisor	

---

# ***Abstract***

---

The thesis entitled “Effect of Doping on Nickel Metal-Based Chalcogenides Nanomaterials for Electrochemical Water Splitting” describes the development of different nanostructures of the Ni-based chalcogenides materials and their application in the electrochemical water-splitting (EC) reaction for the generation of hydrogen ( $H_2$ ) and oxygen ( $O_2$ ). The first chapter of the thesis gives an insight into nanoscience and nanotechnology, a brief literature overview about the nanomaterials, their synthetic approaches, and their application in electrochemical fields. This chapter provides a detailed discussion of the different pathways for water-splitting. This chapter also delivers an overview of electrocatalyst fundamentals, keyfeatures of an electrode, and various strategies for the enhancing efficiency of an electrocatalyst. Chapter two illustrates synthesis methodology, calculation methods, chemicals, and instrumentation techniques that are used to carry out thesis work. Chapters three to seven deal with the development of efficient Ni-based nanostructures for electrochemical water-splitting reaction. In chapter three, Ni/Ni(OH)<sub>2</sub>/NiOOH nano worm heterostructure deposited on carbon cloth is applied for electrochemical HER reaction. In further chapters, doping strategy is chosen as an important strategy to improve electrochemical activity and stability in Ni based chalcogenides. The dopant amount is optimized with ratio variation and developed optimized electrocatalyst is characterized with various techniques. Chapter four describes the development of W<sup>6+</sup> doped Ni(OH)<sub>2</sub>/NiOOH nanosheets which enhances the EC activity by synergistic effect. In chapter five, Ni<sub>9</sub>S<sub>8</sub> nanostructure is doped with Co<sup>2+</sup> cation to generate lattice distortion and change in electronic environment which leads to enhancement in EC activity of Ni<sub>9</sub>S<sub>8</sub> in the corrosive environment. In chapter six, the Ce<sup>4+</sup> doped Ni<sub>0.85</sub>Se nanosheets is applied for EC water splitting. The optimized Ce<sub>0.1</sub>Ni<sub>0.85</sub>Se electrocatalyst shows comparable activities to the noble catalyst in two-electrode system. In chapter seven, thin nanorods of Fe-doped NiCo<sub>2</sub>Se<sub>4</sub> on CC are developed. The multi-metallic selenides show improved electrochemical activity with presence of different metal ions. The role of metal ions in electrochemical activity is proved with thiocyanate study. Finally, the last chapter summarizes the main results obtained from the study of different electrodes for EC water-splitting. Additionally, this chapter also provides directions for future studies using efficient electrodes which may find practical applicability.

***Keywords:*** Nickel-based electrodes, Nanosheets, Heterostructure, Electrochemicalwater-splitting, Corrosive environment, Nanorods.



## *List of Abbreviations*

---

AM	Air Mass
AU	Arbitrary Unit
atm	Atmosphere
BE	Binding energy
CB	Conduction band
CC	Carbon Cloth
CV	Cyclic Voltammetry
D	Dimension
eV	Electron Volt
$E_g$	Band gap
$E_F$	Fermi level
EC	Electrochemical
ECSA	Electrochemical surface area
EDS	Energy dispersive spectroscopy
EIS	Electrochemical impedance spectra
FTIR	Fourier transform Infrared spectroscopy
FESEM	Field emission scanning electron microscopy
HRTEM	High-resolution transmission electron microscopy
HOMO	Highest occupied molecular orbital
h	Hour
HER	Hydrogen evolution reaction
ICP-AES	Induced couple plasma atomic emission spectroscopy
KJ	Kilo Joule
LUMO	Lowest unoccupied molecular orbital
LSV	Linear sweep voltametry
ms	Milliseconds
mA	Milliampere
$\mu\text{M}$	Micrometer
MO	Molecular orbital
mW	Milliwatt
NHE	Normal hydrogen electrode
NP	Nanoparticle

## *List of Abbreviations*

---

NWs	Nanowires
ns	Nanosecond
nm	Nanometer
NIR	Near Infra-red
OER	Oxygen evolution reaction
PV	Photovoltaic
PEC	Photoelectrochemical
PEIS	Photoelectrochemical impedance spectra
PC	Photocatalytic
PVEC	Photovoltaic electrochemical
PXRD	Powder X-ray Diffraction
QSE	Quantum size effect
QDs	Quantum dots
Rs	Solution resistance
Rct	Charge transfer resistance
SCE	Saturated calomel electrode
XPS	X-ray photoelectron spectroscopy
SPR	Surface plasmon resonance
Sec	Seconds
TW	Terra Watt
UV	Ultraviolet
VB	Valance band
XPS	X-ray photoelectron spectroscopy

## *List of Symbols*

---

$\text{\AA}$	Angstrom
$\alpha$	Alpha
$\alpha^{-1}$	absorption coefficient
$k$	Boltzmann constant
$\chi$	Chi
$\Delta$	Delta
$\eta$	Eta
$\epsilon_0$	Epsilon
$^{\circ}\text{C}$	Degree Celsius
$\lambda$	Lambda
$\mu$	mu
$\nu$	Nu
$h$	Plank constant
$\Phi$	Phi
$\pi$	pi
$c$	Velocity of light
$\tau$	tau
$\theta$	Theta (diffraction angle)

# *List of Tables*

<i>S. No.</i>	<i>Caption</i>	<i>Page No.</i>
2.1	List of the chemicals used in this thesis work with their purchasing company.	56-57
3.1	All the electrochemical parameters for Ni/Ni(OH) <sub>2</sub> /NiOOH, Ni(OH) <sub>2</sub> /NiOOH, and Pt/C electrocatalyst.	94
3.2	A comparative study of all the electrochemical parameters with the as developed electrocatalysts.	100
4.1	XPS binding energy values of Ni(OH) <sub>2</sub> / NiOOH, W <sub>0.1</sub> Ni(OH) <sub>2</sub> /NiOOH, W <sub>0.2</sub> Ni(OH) <sub>2</sub> /NiOOH, and W <sub>0.06</sub> Ni(OH) <sub>2</sub> /NiOOH.	119
4.2	ICP-AES analysis of W <sub>0.1</sub> Ni(OH) <sub>2</sub> /NiOOH, W <sub>0.2</sub> Ni(OH) <sub>2</sub> /NiOOH, and W <sub>0.06</sub> Ni(OH) <sub>2</sub> /NiOOH.	122
4.3	All the electrochemical HER parameters for Ni(OH) <sub>2</sub> /NiOOH, W <sub>0.1</sub> Ni(OH) <sub>2</sub> /NiOOH, W <sub>0.2</sub> Ni(OH) <sub>2</sub> /NiOOH, W <sub>0.06</sub> Ni(OH) <sub>2</sub> /NiOOH, and Pt/C electrocatalysts.	128
4.4	All the electrochemical OER parameters for Ni(OH) <sub>2</sub> /NiOOH, W <sub>0.1</sub> Ni(OH) <sub>2</sub> /NiOOH, W <sub>0.2</sub> Ni(OH) <sub>2</sub> /NiOOH, W <sub>0.06</sub> Ni(OH) <sub>2</sub> /NiOOH, and RuO <sub>2</sub> electrocatalysts.	134
4.5	All the electrochemical OER parameters for Ni(OH) <sub>2</sub> /NiOOH, W <sub>0.1</sub> Ni(OH) <sub>2</sub> /NiOOH, W <sub>0.2</sub> Ni(OH) <sub>2</sub> /NiOOH, W <sub>0.06</sub> Ni(OH) <sub>2</sub> /NiOOH, and RuO <sub>2</sub> electrocatalysts.	141
5.1	Comparative table for XPS binding energy values.	162
5.2	ICP-AES data for Co <sub>0.05</sub> Ni <sub>8.95</sub> S <sub>8</sub>	165
5.3	All the electrochemical HER parameters for Ni <sub>9</sub> S <sub>8</sub> , Co <sub>0.1</sub> Ni <sub>8.9</sub> S <sub>8</sub> , Co <sub>0.05</sub> Ni <sub>8.95</sub> S <sub>8</sub> , Co <sub>0.03</sub> Ni <sub>8.97</sub> S <sub>8</sub> , and 5% Pt-C deposited on carbon cloth.	170
5.4	A comparative HER study of all the electrochemical parameters with the electrocatalyst.	173
5.5	All the electrochemical OER parameters for Ni <sub>9</sub> S <sub>8</sub> , Co <sub>0.1</sub> Ni <sub>8.9</sub> S <sub>8</sub> , Co <sub>0.05</sub> Ni <sub>8.95</sub> S <sub>8</sub> ,	176

## *List of Tables*

---

$\text{Co}_{0.03}\text{Ni}_{8.97}\text{S}_8$ , and commercial  $\text{RuO}_2$ .

5.6	A comparative OER study of all the electrochemical parameters with the electrocatalyst.	181
6.1	ICP-AES data of $\text{Ni}_{0.85}\text{Se}$ and $\text{Ce}_{0.1}\text{Ni}_{0.85}\text{Se}$ .	215
6.2	A comparative study of all the electrochemical parameters with the electrocatalyst.	219
6.3	All the electrochemical HER parameters for $\text{Ni}_{0.85}\text{Se}$ , $\text{Ce}_{0.05}\text{Ni}_{0.85}\text{Se}$ , $\text{Ce}_{0.1}\text{Ni}_{0.85}\text{Se}$ , $\text{Ce}_{0.2}\text{Ni}_{0.85}\text{Se}$ , and 5% Pt-C deposited on carbon cloth.	220
6.4	All the electrochemical OER parameters for $\text{Ni}_{0.85}\text{Se}$ , $\text{Ce}_{0.05}\text{Ni}_{0.85}\text{Se}$ , $\text{Ce}_{0.1}\text{Ni}_{0.85}\text{Se}$ , $\text{Ce}_{0.2}\text{Ni}_{0.85}\text{Se}$ , and commercial $\text{RuO}_2$ deposited on carbon cloth.	225
6.5	Comparative table for XPS binding energy values.	228
7.1	XPS binding energy value for bare and doped $\text{NiCo}_2\text{Se}_4$ .	249
7.2	ICP-AES data for undoped and doped $\text{NiCo}_2\text{Se}_4$ .	252
7.3	All the electrochemical HER parameters for $\text{NiCo}_2\text{Se}_4$ , Fe-doped $\text{NiCo}_2\text{Se}_4$ , and 5% Pt-C were deposited on carbon cloth.	257
7.4	All the Electrochemical Parameters for OER Using $\text{NiCo}_2\text{Se}_4$ , $\text{Fe}_{0.1}\text{NiCo}_{1.9}\text{Se}_4$ , $\text{Fe}_{0.2}\text{NiCo}_{1.8}\text{Se}_4$ , $\text{Fe}_{0.4}\text{NiCo}_{1.6}\text{Se}_4$ , and $\text{RuO}_2$ Electrocatalysts.	263
7.5	A comparative electrochemical study of all the electrochemical parameters with the electrocatalyst.	268
8.1	Comparative table for HER, OER data and cell potential, and stability for all the developed electrodes.	290

## *List of Scheme*

---

<i>S. No.</i>	<i>Caption</i>	<i>Page No.</i>
3.1	Schematic illustration for the synthesis of Ni/Ni(OH) <sub>2</sub> /NiOOH on carbon cloth via electrodeposition.	79
4.1	Schematic illustration for the synthesis of Ni(OH) <sub>2</sub> /NiOOH and W <sub>0.1</sub> Ni(OH) <sub>2</sub> /NiOOH on carbon cloth.	112
5.1	Schematic representation for the synthesis of Co doped Ni <sub>9</sub> S <sub>8</sub> on CC surface.	155
6.1	Diagram representation for the synthesis of Ce doped Ni <sub>0.85</sub> Se on CC surface.	204
7.1	Schematic representation for the development of Fe doped NiCo <sub>2</sub> Se <sub>4</sub> .	241

# *List of Figures*

<i>S. No.</i>	<i>Caption</i>	<i>Page No.</i>
1.1	Representation of application of nanomaterials in the field of electrochemistry.	2
1.2	Discretization of electronic energy levels with size variation (quantum size effect).	4
1.3	Schematic illustration of 0D, 1D, 2D, and 3D nanostructures.	5
1.4	Top-down and bottom-up approaches for the synthesis of nanomaterials.	6
1.5	A schematic diagram of the PEC cell.	9
1.6	A schematic representation of the photocatalytic cell.	11
1.7	Schematic representation of electrochemical cell reactions.	14
1.8	Schematic representation of PV-EC cell.	15
1.9	Schematic representation of HER mechanism in an alkaline medium.	17
1.10	Volcano plot of exchange current density ( $j_0$ ) as a function of DFT-calculated Gibbs free energy ( $\Delta G_H^*$ ) of adsorbed atomic hydrogen on pure metals.	19
1.11	Schematic mechanism of OER in alkaline medium	20
1.12	schematic representation of OER in an alkaline medium through AEM and LOM pathways.	21
1.13	Diagrammatic scheme of parameters for evaluation of electrochemical reaction.	22
1.14	Impedance plot of one of the developed samples showing semicircle. The Inset of Figure 1.14 is the Randles circuit.	29
1.15	Schematic presentation of transition metal chalcogenides in various fields	31
1.16	FESEM image representing 1D nanostructure of (a) $\text{NiCo}_2\text{Se}_4$ (b) P doped $\text{NiCo}_2\text{Se}_4$ (c) $(\text{NiCo})_{0.85}\text{Se}$ .	33
1.17	FESEM image of (a) Ni-doped ultrathin $\text{CoS}_2$ , (b) Mesoporous Co-doped $\text{NiSe}_2$ nanosheets, (c) Fe-doped $\text{Ni}(\text{OH})_2/\text{NiOOH}$ nanoflower.	34
1.18	3D nanostructure of (a) $\text{NiCoS}/\text{NiCoP}$ electrode (b) $\text{NiCo}_2\text{O}_4$ octahedron.	35
2.1	Schematic representation of three-electrode system for electrochemical water splitting.	69

## *List of Figures*

2.2	Schematic representation of two electrode systems for electrochemical water splitting.	70
3.1	(a) PXRD analysis and (b) FESEM image of Ni/Ni(OH) <sub>2</sub> .	80
3.2	PXRD pattern of (a) fresh (b) 2-day (c) 7-day Ni/Ni(OH) <sub>2</sub> /NiOOH heterostructure.	82
3.2	(a) TGA analysis, (b) FTIR spectra, (c) Raman analysis of Ni/Ni(OH) <sub>2</sub> /NiOOH heterostructure.	83
3.4	XPS analysis of Ni/Ni(OH) <sub>2</sub> /NiOOH heterostructure (a) survey spectrum, (b) and (c) deconvoluted spectra of Ni(0), Ni(OH) <sub>2</sub> , and NiOOH, and (d) deconvoluted spectra of O 1s.	85
3.5	FESEM images of Ni/Ni(OH) <sub>2</sub> /NiOOH heterostructure at different magnifications, (a) low, (b) medium, (c and d) high.	86
3.6	(a) EDS spectra (b) Line mapping analysis of Ni/Ni(OH) <sub>2</sub> /NiOOH heterostructure.	87
3.7	(a) TEM and (b) HRTEM image of Ni/Ni(OH) <sub>2</sub> /NiOOH heterostructure. The inset of figure (a) exhibits the distribution of nano worms. HRTEM for d-spacing calculation (c) and SAED (d) for Ni/Ni(OH) <sub>2</sub> /NiOOH heterostructure.	88
3.8	Digital pictures of electrodeposited Ni/Ni(OH) <sub>2</sub> /NiOOH before and after drying on CC.	89
3.9	Polarization curve at (a) low scale and (b) large scale using Ni/Ni(OH) <sub>2</sub> /NiOOH, Ni(OH) <sub>2</sub> /NiOOH, Ni/Ni(OH) <sub>2</sub> , and Pt/C samples. A plot between potential required to produce 50 mA/cm <sup>2</sup> current density and onset potential (V) vs. RHE (c) and histogram plot of current density obtained at -0.2 V vs. RHE (d) for all the developed Ni(OH) <sub>2</sub> /NiOOH, Ni/Ni(OH) <sub>2</sub> /NiOOH, Ni/Ni(OH) <sub>2</sub> and Pt/C (5%) on carbon cloth.	91
3.10	(a) Comparative polarization curve of Ni/Ni(OH) <sub>2</sub> /NiOOH, Ni-2d, and Ni-7d samples. (b) LSV of Ni/Ni(OH) <sub>2</sub> /NiOOH electrocatalyst via 10 min, 20 min, and 30 min electrodeposition. (c and d) FESEM of 10- and 30-min deposited sample.	92
3.11	Cyclic voltammetry curves of (a) electrodeposited Ni/Ni(OH) <sub>2</sub> /NiOOH, (b) Ni(OH) <sub>2</sub> /NiOOH recorded in 1 M KOH recorded with different scan rates, (c) capacitive current at 0.925 (V vs. RHE) as a function of scan rate for Ni/Ni(OH) <sub>2</sub> /NiOOH and Ni(OH) <sub>2</sub> /NiOOH.	93
3.12	(a) Tafel plot and (b) Nyquist plots of Ni/Ni(OH) <sub>2</sub> /NiOOH, Ni(OH) <sub>2</sub> /NiOOH, and Ni/Ni(OH) <sub>2</sub> electrocatalysts. Inset of figure b represents equivalent circuit of Ni/Ni(OH) <sub>2</sub> /NiOOH heterostructure.	96



## List of Figures

3.13	(a) Polarization curves of Ni/Ni(OH) <sub>2</sub> /NiOOH electrocatalyst for initial, 100 cycles, and after 1000 cycles. (b) Amperometric data recorded at a fixed potential. (c) PXRD and (d) FESEM analyses of Ni/Ni(OH) <sub>2</sub> /NiOOH heterostructure after electrocatalysis.	97
3.14	(a) EDS mapping analysis of post electrolysis. (b) Hydrogen gas evolution of Ni/Ni(OH) <sub>2</sub> /NiOOH electrode under applied potential of -0.225 V vs. RHE.	98
3.15	Polarization OER curve (b) Tafel slope of Ni/Ni(OH) <sub>2</sub> /NiOOH, Ni(OH) <sub>2</sub> /NiOOH, Ni/Ni(OH) <sub>2</sub> , and RuO <sub>2</sub> samples.	99
4.1	(a) PXRD pattern of Ni(OH) <sub>2</sub> /NiOOH and W <sub>0.1</sub> Ni(OH) <sub>2</sub> /NiOOH materials. JCPDS values for Ni(OH) <sub>2</sub> and NiOOH are shown at the bottom of the graph (b) PXRD analysis of W <sub>0.1</sub> Ni(OH) <sub>2</sub> /NiOOH, W <sub>0.2</sub> Ni(OH) <sub>2</sub> /NiOOH, and W <sub>0.06</sub> Ni(OH) <sub>2</sub> /NiOOH. (c) W-H plot.	115
4.2	Raman spectrum of Ni(OH) <sub>2</sub> /NiOOH, W <sub>0.1</sub> Ni(OH) <sub>2</sub> /NiOOH, W <sub>0.2</sub> Ni(OH) <sub>2</sub> /NiOOH, and W <sub>0.06</sub> Ni(OH) <sub>2</sub> /NiOOH materials.	116
4.3	XPS analysis of Ni(OH) <sub>2</sub> /NiOOH (a) survey spectrum, (b) deconvoluted spectra of Ni 2p and (c) deconvoluted spectra of O 1s.	117
4.4	XPS analysis of W <sub>0.1</sub> Ni(OH) <sub>2</sub> /NiOOH (a) survey spectrum, (b) deconvoluted spectra of Ni 2p, (c) high-resolution spectra of W 4f, and (d) deconvoluted spectra of O 1s.	118
4.5	FESEM images of (a) Ni(OH) <sub>2</sub> /NiOOH. The inset of figure 4.5 a shows the uniform coverage of carbon cloth surface with Ni(OH) <sub>2</sub> /NiOOH. (b) W <sub>0.1</sub> Ni(OH) <sub>2</sub> /NiOOH (with inset of CC surface) (c) W <sub>0.2</sub> Ni(OH) <sub>2</sub> /NiOOH (d) W <sub>0.06</sub> Ni(OH) <sub>2</sub> /NiOOH.	120
4.6	Elemental composition and EDS mapping showing the distribution of Ni and O on the carbon cloth in Ni(OH) <sub>2</sub> /NiOOH.	121
4.7	Elemental composition and EDS mapping showing the distribution of W, Ni and O on the carbon cloth in W <sub>0.1</sub> Ni(OH) <sub>2</sub> /NiOOH.	121
4.8	(a and b) TEM and (c) HRTEM image (d) SAED pattern of Ni(OH) <sub>2</sub> /NiOOH.	122
4.9	(a and b) TEM and (c) HRTEM image (d) SAED pattern of W <sub>0.1</sub> Ni(OH) <sub>2</sub> /NiOOH.	123
4.10	Polarization HER curve at (a) low scale and (b) high scale. (c) Plot between potential required to produce 100 mA/cm <sup>2</sup> current density and onset potential (V) vs. RHE (d) Histogram plot of current density obtained at -0.3 V vs. RHE of Ni(OH) <sub>2</sub> /NiOOH, W <sub>0.1</sub> Ni(OH) <sub>2</sub> /NiOOH, W <sub>0.2</sub> Ni(OH) <sub>2</sub> /NiOOH, W <sub>0.06</sub> Ni(OH) <sub>2</sub> /NiOOH, and Pt/C samples.	125

# List of Figures

4.11	Cyclic voltammetry curves of (a) Ni(OH) <sub>2</sub> /NiOOH (b) W <sub>0.1</sub> Ni(OH) <sub>2</sub> /NiOOH (c) W <sub>0.2</sub> Ni(OH) <sub>2</sub> /NiOOH (d) W <sub>0.06</sub> Ni(OH) <sub>2</sub> /NiOOH recorded in 1 M KOH recorded with different scan rates, (e) capacitive current at 0.925 (V vs. RHE) as a function of scan rate for all the samples.	127
4.12	(a) Tafel plot and (b) Nyquist plots of Ni(OH) <sub>2</sub> /NiOOH, W <sub>0.1</sub> Ni(OH) <sub>2</sub> /NiOOH, W <sub>0.2</sub> Ni(OH) <sub>2</sub> /NiOOH, and W <sub>0.06</sub> Ni(OH) <sub>2</sub> /NiOOH materials. The inset of Figure (b) shows the corresponding equivalent circuit. (c) Polarization HER curve of W <sub>0.1</sub> Ni(OH) <sub>2</sub> /NiOOH electrocatalyst for initial and after 1000 cycles. (d) Chronoamperometric data was recorded for 120 hours at a fixed potential for HER. All the data are recorded using a 1.0 M KOH solution.	131
4.13	Polarization OER curve at (a) low scale and (b) high scale. (c) The plot of current density obtained at 1.8 V vs. RHE and onset potential (V) vs. RHE (d) histogram plot of current density obtained at 1.65 V vs. RHE of Ni(OH) <sub>2</sub> /NiOOH, W <sub>0.1</sub> Ni(OH) <sub>2</sub> /NiOOH, W <sub>0.2</sub> Ni(OH) <sub>2</sub> /NiOOH, W <sub>0.06</sub> Ni(OH) <sub>2</sub> /NiOOH, and RuO <sub>2</sub> samples.	133
4.14	CV analysis of of Ni(OH) <sub>2</sub> /NiOOH, W <sub>0.1</sub> Ni(OH) <sub>2</sub> /NiOOH, W <sub>0.2</sub> Ni(OH) <sub>2</sub> /NiOOH, and W <sub>0.06</sub> Ni(OH) <sub>2</sub> /NiOOH electrocatalysts.	135
4.15	(a) Tafel plot, and (b) Nyquist plots of Ni(OH) <sub>2</sub> /NiOOH, W <sub>0.1</sub> Ni(OH) <sub>2</sub> /NiOOH, W <sub>0.2</sub> Ni(OH) <sub>2</sub> /NiOOH, and W <sub>0.06</sub> Ni(OH) <sub>2</sub> /NiOOH electrocatalysts. The corresponding equivalent circuit is shown in the inset of Figure (b). (c) Polarization OER curve of W <sub>0.1</sub> Ni(OH) <sub>2</sub> /NiOOH electrocatalyst for initial, and after 1000 cycles. (d) Chronoamperometric data were recorded for 120 hours at a fixed potential for OER. All the data are recorded using a 1.0 M KOH solution.	137
4.16	(a) Two electrode system activity with W <sub>0.1</sub> Ni(OH) <sub>2</sub> /NiOOH (+)    W <sub>0.1</sub> Ni(OH) <sub>2</sub> /NiOOH (-) cell (b) chronoamperometric stability of 12 hours in 1 M KOH. Inset in Figure a is digital image of W <sub>0.1</sub> Ni(OH) <sub>2</sub> /NiOOH (+)    W <sub>0.1</sub> Ni(OH) <sub>2</sub> /NiOOH (-) cell.	138
4.17	(a) FESEM analysis (b) EDS spectra of W <sub>0.1</sub> Ni(OH) <sub>2</sub> /NiOOH post electrolysis.	139
4.18	XPS of W <sub>0.1</sub> Ni(OH) <sub>2</sub> /NiOOH after OER electrolysis (a) survey spectrum, (b) deconvoluted spectra of Ni 2p and (c) deconvoluted spectra of O 1s (d) deconvoluted spectra of W.	140
4.19	H adsorption on the NiOOH surface. (a) β-NiOOH (015) surface; (b) W doped β-NiOOH (015) surface; (c-d) H adsorbed (indicated by dotted line) at a surface Ni of β -NiOOH (015) and W doped β-NiOOH (015) surface. The Ni atoms are in blue, W in gray, O in red, and H in white.	142
4.20	Density of states projected on the d-band for the surface Ni site. a) β-NiOOH (015) surface; b) W doped β-NiOOH (015) surface. The d band centres (in eV) are indicated with respect to the Fermi level (E <sub>F</sub> ).	143

# List of Figures

---

5.1	(a) PXRD (b) FESEM, (c) EDS analysis of Ni(OH) <sub>2</sub> .	154
5.2	(a) XRD of Ni <sub>9</sub> S <sub>8</sub> , stacked with JCPDF 22-1193 and (b) XRD analysis of Co <sub>0.1</sub> Ni <sub>8.9</sub> S <sub>8</sub> , Co <sub>0.05</sub> Ni <sub>8.95</sub> S <sub>8</sub> and Co <sub>0.03</sub> Ni <sub>8.97</sub> S <sub>8</sub> .	158
5.3	(a) low scan rate XRD profile of Ni <sub>9</sub> S <sub>8</sub> and Co <sub>0.05</sub> Ni <sub>8.95</sub> S <sub>8</sub> with peak shifting. (b) Williamson-Hall plot of Ni <sub>9</sub> S <sub>8</sub> and Co <sub>0.05</sub> Ni <sub>8.95</sub> S <sub>8</sub> .	159
5.4	(a) Raman analysis of Ni <sub>9</sub> S <sub>8</sub> and Co <sub>0.05</sub> Ni <sub>8.95</sub> S <sub>8</sub> (b and c) BET adsorption isotherm and surface area of Co <sub>0.05</sub> Ni <sub>8.95</sub> S <sub>8</sub> .	160
5.5	XPS analysis of Ni <sub>9</sub> S <sub>8</sub> (a) survey spectrum, (b) deconvoluted spectra of Ni 2p and (c) deconvoluted spectra of S 2p.	161
5.6	XPS analysis of Co <sub>0.05</sub> Ni <sub>8.95</sub> S <sub>8</sub> (a) survey spectrum, (b) deconvoluted spectra of Ni 2p, (c) deconvoluted spectra of S 2p, and (d) high-resolution spectra of Co 2p.	163
5.7	FESEM images of (a) Ni <sub>9</sub> S <sub>8</sub> (b) Co <sub>0.05</sub> Ni <sub>8.95</sub> S <sub>8</sub> (c) Co <sub>0.1</sub> Ni <sub>8.9</sub> S <sub>8</sub> and (d) Co <sub>0.03</sub> Ni <sub>8.97</sub> S <sub>8</sub> samples. Inset of b represent low magnification image of Co <sub>0.05</sub> Ni <sub>8.95</sub> S <sub>8</sub> catalyst.	164
5.8	Elemental composition and EDS mapping showing the distribution of Ni and S on the carbon cloth for Ni <sub>9</sub> S <sub>8</sub> sample.	165
5.9	Elemental composition and EDS mapping showing the distribution of Co, Ni and S on the carbon cloth for Co <sub>0.05</sub> Ni <sub>8.95</sub> S <sub>8</sub> sample.	165
5.10	(a) TEM and (b) HRTEM image of bare Ni <sub>9</sub> S <sub>8</sub> (c) TEM and (d) HRTEM image of Co <sub>0.05</sub> Ni <sub>8.95</sub> S <sub>8</sub> .	166
5.11	Polarization HER curve at (a) low scale and (b) Co <sub>0.05</sub> Ni <sub>8.95</sub> S <sub>8</sub> , Co <sub>0.1</sub> Ni <sub>8.9</sub> S <sub>8</sub> and Co <sub>0.03</sub> Ni <sub>8.97</sub> S <sub>8</sub> (c) comparative HER of Co <sub>9</sub> S <sub>8</sub> and Co <sub>0.05</sub> Ni <sub>8.95</sub> S <sub>8</sub> (c) Plot between potential required to produce 50 mA/cm <sup>2</sup> current density and onset potential (V) vs. RHE (d) Histogram plot of current density obtained at -0.4 V vs. RHE of Ni <sub>9</sub> S <sub>8</sub> , Co <sub>0.1</sub> Ni <sub>8.9</sub> S <sub>8</sub> , Co <sub>0.05</sub> Ni <sub>8.95</sub> S <sub>8</sub> , Co <sub>0.03</sub> Ni <sub>8.97</sub> S <sub>8</sub> , and Pt/C samples.	167
5.12	(a) Comparative LSV of Co <sub>0.05</sub> Ni <sub>8.95</sub> S <sub>8</sub> working under different pH medium. (b) Histogram of onset potential to generate 10 mA/cm <sup>2</sup> current density in different pH medium.	168
5.13	(a) Tafel plot and (b) Nyquist plots of materials. Tafel slope of Ni <sub>9</sub> S <sub>8</sub> , Co <sub>0.1</sub> Ni <sub>8.9</sub> S <sub>8</sub> , Co <sub>0.05</sub> Ni <sub>8.95</sub> S <sub>8</sub> , Co <sub>0.03</sub> Ni <sub>8.97</sub> S <sub>8</sub> , and Pt/C is included in Fig. (a). The inset of Fig. (b) shows the corresponding equivalent circuit. (c) Polarization HER curve of Co <sub>0.05</sub> Ni <sub>8.95</sub> S <sub>8</sub> electrocatalyst for initial, and after 1000 cycles. (d) Chronoamperometric data was recorded for 60 hours at a fixed potential for HER.	172

# List of Figures

5.14	Polarization OER curve at (a) low scale and (b) comparative (c) Plot between potential required to produce 100 mA/cm <sup>2</sup> current density and onset potential (V) vs. RHE (d) Histogram plot of current density obtained at 1.65 V vs. RHE of Ni <sub>9</sub> S <sub>8</sub> , Co <sub>0.1</sub> Ni <sub>8.9</sub> S <sub>8</sub> , Co <sub>0.05</sub> Ni <sub>8.95</sub> S <sub>8</sub> , Co <sub>0.03</sub> Ni <sub>8.97</sub> S <sub>8</sub> , and RuO <sub>2</sub> samples.	174
5.15	Comparative pH study for OER of Co <sub>0.05</sub> Ni <sub>8.95</sub> S <sub>8</sub>	175
5.16	Cyclic voltammetry curves of Co <sub>0.05</sub> Ni <sub>8.95</sub> S <sub>8</sub> at different scan rate (a) (b) (c) (d) capacitive current at 1.125 (V vs. RHE) as a function of scan rate for ECSA calculation (e).	176
5.17	CV analysis of all the developed electrocatalysts in a particular potential window.	177
5.18	(a) Tafel plot for OER and (b) Nyquist plots of materials. Tafel slope of Ni <sub>9</sub> S <sub>8</sub> , Co <sub>0.1</sub> Ni <sub>8.9</sub> S <sub>8</sub> , Co <sub>0.05</sub> Ni <sub>8.95</sub> S <sub>8</sub> , and Co <sub>0.03</sub> Ni <sub>8.97</sub> S <sub>8</sub> , is included in Fig. (a). The inset of Fig. (b) shows the corresponding equivalent circuit. (c) Polarization OER curve of Co <sub>0.05</sub> Ni <sub>8.95</sub> S <sub>8</sub> electrocatalyst for initial, and after 1000 cycles. (d) Chronoamperometric data for 80 hours at a fixed negative potential.	178
5.19	(a) FESEM image (b) EDS of Co <sub>0.05</sub> Ni <sub>8.95</sub> S <sub>8</sub> after electrocatalysis.	179
5.20	PXRD of Co <sub>0.05</sub> Ni <sub>8.95</sub> S <sub>8</sub> after electrocatalysis.	179
5.21	XPS analysis of Co <sub>0.05</sub> Ni <sub>8.95</sub> S <sub>8</sub> after OER electrocatalysis.	180
5.22	(a) LSV and (b) 24 hours stability test of constructed two electrode system of Co <sub>0.05</sub> Ni <sub>8.95</sub> S <sub>8</sub> (+)    Co <sub>0.05</sub> Ni <sub>8.95</sub> S <sub>8</sub> (-).	182
5.23	Optimized geometry of pristine Ni <sub>9</sub> S <sub>8</sub> as obtained from GGA-PBE level of theory. Red and yellow colours represent Ni and S atoms respectively.	183
5.24	Optimized geometries of Co - doped Ni <sub>9</sub> S <sub>8</sub> system for (a) 0.5%, (b) 0.75%, (c) 3% and (d) 6% doping of Co as obtained from GGA-PBE level of theory. Red, yellow, and blue colors represent Ni, S, and Co atoms respectively.	184
5.25	Electronic band structures (a) pristine Ni <sub>9</sub> S <sub>8</sub> and (b) doped Co <sub>0.05</sub> Ni <sub>8.95</sub> S <sub>8</sub> systems along with the high-symmetry points Y→Γ→T→Γ→Z→S as obtained from the GGA+Udd level of theory. The indirect bandgap of pristine Ni <sub>9</sub> S <sub>8</sub> and the Fermi energy level (EF) are marked with the red arrow and black dashed line respectively.	185
5.26	Left panel shows (A) TDOS and (a) PDOS spectra for pristine Ni <sub>9</sub> S <sub>8</sub> compounds. Right panel shows (B) TDOS and (b) PDOS spectra for the doped Co <sub>0.05</sub> Ni <sub>8.95</sub> S <sub>8</sub> system as obtained from the GGA+Udd level of theory. The van-Hove singularity and the Fermi energy level (EF) are marked with a black circle and black dashed line respectively.	187

## *List of Figures*

5.27	The Gibbs free energy versus (A) hydrogen, (B) oxygen coverage, and the exchange current density as a function of Gibbs free energy for (a) HER, (b) OER activities of Co - doped Ni <sub>9</sub> S <sub>8</sub> systems as obtained from GGA+Udd level of theory.	189
5.28	The energy barriers for the Volmer-Heyrovsky, Volmer-Tafel reaction pathways for (a) HER and (b) OER activities of Co - doped Ni <sub>9</sub> S <sub>8</sub> systems as obtained from the NEB method. [“M” is the metal center or catalyst surface].	190
6.1	(a) XRD analysis of pristine and Ce doped Ni <sub>0.85</sub> Se catalysts (b) low scan XRD of pristine and Ce doped Ni <sub>0.85</sub> Se catalysts.	207
6.2	Raman analysis of Ni <sub>0.85</sub> Se, and Ce <sub>0.1</sub> Ni <sub>0.85</sub> Se.	208
6.3	(a) BET adsorption-desorption isotherm (b) BJH plot of Ce doped Ni <sub>0.85</sub> Se	209
6.4	XPS analysis of pristine Ni <sub>0.85</sub> Se (a) Ni 2p (b) Se 3d, and (c) survey spectrum.	210
6.5	XPS analysis of Ce <sub>0.1</sub> Ni <sub>0.85</sub> Se (a) deconvoluted spectra of Ni 2p, (b) deconvoluted spectra of Se 3d, (c) high-resolution spectra of Ce 3d, and (d) high-resolution spectra of Co 2p survey spectrum.	211
6.6	Depth XPS analysis of pristine Ni <sub>0.85</sub> Se (a) Ni 2p and (b) Se 3d.	212
6.7	Depth XPS analysis of pristine Ce <sub>0.1</sub> Ni <sub>0.85</sub> Se (a) Ni 2p (b) Se 3d and (c) Ce 3d.	212
6.8	FESEM images of Ni <sub>0.85</sub> Se catalyst at various magnifications (a and b) Ce <sub>0.1</sub> Ni <sub>0.85</sub> Se catalyst at various magnifications, (c and d).	214
6.9	EDS analysis of Ni <sub>0.85</sub> Se.	215
6.10	EDS analysis of Ce <sub>0.1</sub> Ni <sub>0.85</sub> Se.	215
6.11	(a) TEM, (b) HRTEM (c) SAED analysis of Ni <sub>0.85</sub> Se.	216
6.12	(a) TEM images, (b) HRTEM, (c) SAED analysis of Ce <sub>0.1</sub> Ni <sub>0.85</sub> Se.	216
6.13	(a) Linear sweep voltammetry of blank CC, Ni <sub>0.85</sub> Se, Ce <sub>0.1</sub> Ni <sub>0.85</sub> Se, and 5% Pt/C for HER, (b) histogram plot at -0.4 V vs. RHE, (c) comparative HER of other doped samples.	218
6.14	(a) Tafel slope, and (b) impedance of Ni <sub>0.85</sub> Se, Ce <sub>0.1</sub> Ni <sub>0.85</sub> Se, and 5% Pt/C. The inset of Figure b represents an equivalent circuit for impedance (c) 1000 cycle stability (d) chronoamperometric stability for 48 hours.	222
6.15	(a) CV analysis for Ni <sub>0.85</sub> Se (b) CV analysis of Ce doped Ni <sub>0.85</sub> Se (c) ECSA analysis of Bare and doped samples.	223

## *List of Figures*

---

6.16	(a) Linear sweep voltammetry of blank CC, Ni <sub>0.85</sub> Se, Ce <sub>0.1</sub> Ni <sub>0.85</sub> Se, and RuO <sub>2</sub> for OER, (b) histogram plot at 1.65 V vs. RHE, (c) comparative OER of other doped samples.	224
6.17	(a) Tafel slope, and (b) impedance of Ni <sub>0.85</sub> Se, Ce <sub>0.1</sub> Ni <sub>0.85</sub> Se, and RuO <sub>2</sub> . The inset of Figure 6.14b represents an equivalent circuit for impedance (c) CV analysis for bare and doped samples.	226
6.18	(a) LSV analysis of the two-electrode setup of Ce <sub>0.1</sub> Ni <sub>0.85</sub> Se    Ce <sub>0.1</sub> Ni <sub>0.85</sub> Se and blank CC, (b) chronoamperometric data of Ce <sub>0.1</sub> Ni <sub>0.85</sub> Se    Ce <sub>0.1</sub> Ni <sub>0.85</sub> Se cell in 1.0 M KOH solution	227
6.19	Post electrocatalysis (a) FESEM (b) EDS analysis of Ce <sub>0.1</sub> Ni <sub>0.85</sub> Se sample	228
6.20	Post electrocatalysis XPS analysis of Ce <sub>0.1</sub> Ni <sub>0.85</sub> Se sample.	229
7.1	(a) PXRD pattern (b) FESEM (c) EDS analysis for Fe doped Ni-Co urea precursor complex.	241
7.2	(a) PXRD analysis of NiCo <sub>2</sub> Se <sub>4</sub> and Fe <sub>0.2</sub> NiCo <sub>1.8</sub> Se <sub>4</sub> with standard JCPDS card (b) Peak shift in XRD (c) Williamson-Hall plot of NiCo <sub>2</sub> Se <sub>4</sub> and Fe <sub>0.2</sub> NiCo <sub>1.8</sub> Se <sub>4</sub> .	244
7.3	XPS analysis of NiCo <sub>2</sub> Se <sub>4</sub> (a) deconvoluted spectra of Ni 2p, (b) deconvoluted spectra of Co 2p, and (c) deconvoluted spectra of Se 3d and (d) survey spectrum.	246
7.4	XPS analysis of Fe <sub>0.2</sub> NiCo <sub>1.8</sub> Se <sub>4</sub> (a) Ni 2p, (b) Co 2p, (c) Fe 2p, (d) Se 3d deconvoluted spectra, and (e) survey spectrum.	248
7.5	FESEM images of (a) NiCo <sub>2</sub> Se <sub>4</sub> (b) Fe <sub>0.2</sub> NiCo <sub>1.8</sub> Se <sub>4</sub> (c) Fe <sub>0.1</sub> NiCo <sub>1.9</sub> Se <sub>4</sub> and (b) Fe <sub>0.4</sub> NiCo <sub>1.6</sub> Se <sub>4</sub> . Inset of Figure 7.5a and 7.5b show uniform distribution of sample.	250
7.6	High magnification FESEM images (a) NiCo <sub>2</sub> Se <sub>4</sub> and (b) Fe <sub>0.2</sub> NiCo <sub>1.8</sub> Se <sub>4</sub> .	250
7.7	(a) EDS mapping and (b) elemental distribution of NiCo <sub>2</sub> Se <sub>4</sub> sample.	251
7.8	(a) EDS mapping and (b) elemental distribution of Fe <sub>0.2</sub> NiCo <sub>1.8</sub> Se <sub>4</sub> sample.	251
7.9	Line mapping analysis of Fe <sub>0.2</sub> NiCo <sub>1.8</sub> Se <sub>4</sub> sample showing the uniform distribution of elements.	252
7.10	(a) TEM, (b) HRTEM image, and (c) SAED of bare NiCo <sub>2</sub> Se <sub>4</sub> .	253
7.11	(a) TEM, (b) HRTEM (yellow circle shows lattice distortion), and (c) SAED analysis of Fe <sub>0.2</sub> NiCo <sub>1.8</sub> Se <sub>4</sub> .	253

## List of Figures

7.12	(a) Linear sweep voltammetry of blank CC, NiCo <sub>2</sub> Se <sub>4</sub> , Fe <sub>0.1</sub> NiCo <sub>1.9</sub> Se <sub>4</sub> , Fe <sub>0.2</sub> NiCo <sub>1.8</sub> Se <sub>4</sub> , Fe <sub>0.4</sub> NiCo <sub>1.6</sub> Se <sub>4</sub> , and Pt/C for HER, (b) histogram plot at -0.3 V vs. RHE, (c) Tafel slope, and (d) impedance of NiCo <sub>2</sub> Se <sub>4</sub> and Fe <sub>0.2</sub> NiCo <sub>1.8</sub> Se <sub>4</sub> . The inset of Figure 7.12d represents an equivalent circuit for impedance.	256
7.13	Effect of KSCN on the HER current of Fe <sub>0.2</sub> NiCo <sub>1.8</sub> Se <sub>4</sub> sample (a) LSV (b) chronoamperometric data.	258
7.14	Cyclic voltammetry curves of NiCo <sub>2</sub> Se <sub>4</sub> and Fe <sub>0.2</sub> NiCo <sub>1.8</sub> Se <sub>4</sub> at different scan rates (a) and (b) capacitive current at 0.525 (V vs. RHE) as a function of scan rate for ECSA calculation (c).	259
7.15	(a) Polarization curve of Fe <sub>0.2</sub> NiCo <sub>1.8</sub> Se <sub>4</sub> initial and after 1000 cycles (b) 48 hours chronoamperometric data of Fe <sub>0.2</sub> NiCo <sub>1.8</sub> Se <sub>4</sub> for HER.	260
7.16	(a) PXRD pattern (b) FESEM of Fe <sub>0.2</sub> NiCo <sub>1.8</sub> Se <sub>4</sub> sample after HER analysis.	260
7.17	Post HER XPS analysis of Fe <sub>0.2</sub> NiCo <sub>1.8</sub> Se <sub>4</sub> (a) deconvoluted spectra of Ni 2p, (b) deconvoluted spectra of Co 2p, and (c) deconvoluted spectra of Fe 2p (d) deconvoluted spectra of Se 3d, and (e) survey spectrum	261
7.18	(a) Linear sweep voltammetry of blank CC, NiCo <sub>2</sub> Se <sub>4</sub> , Fe <sub>0.1</sub> NiCo <sub>1.9</sub> Se <sub>4</sub> , Fe <sub>0.2</sub> NiCo <sub>1.8</sub> Se <sub>4</sub> , Fe <sub>0.4</sub> NiCo <sub>1.6</sub> Se <sub>4</sub> , and RuO <sub>2</sub> for OER, (b) histogram plot at 1.65 V vs. RHE, (c) Tafel slope, and (d) impedance of NiCo <sub>2</sub> Se <sub>4</sub> and Fe <sub>0.2</sub> NiCo <sub>1.8</sub> Se <sub>4</sub> . The inset of Figure 7.18d shows an equivalent circuit for impedance.	262
7.19	(a) Polarization curve of Fe <sub>0.2</sub> NiCo <sub>1.8</sub> Se <sub>4</sub> initial and after 1000 cycles (b) 48 hours chronoamperometric data of Fe <sub>0.2</sub> NiCo <sub>1.8</sub> Se <sub>4</sub> for OER.	264
7.20	(a) FESEM image and (b) EDS mapping of Fe <sub>0.2</sub> NiCo <sub>1.8</sub> Se <sub>4</sub> after electrocatalysis.	264
7.21	XPS of Fe <sub>0.2</sub> NiCo <sub>1.8</sub> Se <sub>4</sub> after OER electrocatalysis (a) deconvoluted spectra of Ni 2p (b) deconvoluted spectra of Co 2p (c) deconvoluted spectra of Fe 2p (d) deconvoluted spectra of Se 3d deconvoluted spectra, and (e) survey spectrum.	265
7.22	CV analysis of NiCo <sub>2</sub> Se <sub>4</sub> and Fe <sub>0.2</sub> NiCo <sub>1.8</sub> Se <sub>4</sub> in a particular potential window.	266
7.23	Effect of KSCN on the OER current of Fe <sub>0.2</sub> NiCo <sub>1.8</sub> Se <sub>4</sub> sample (a) LSV and (b) chronoamperometric data.	267
7.24	(a) Linear sweep voltammetry of the two electrode setup of Fe <sub>0.2</sub> NiCo <sub>1.8</sub> Se <sub>4</sub>    Fe <sub>0.2</sub> NiCo <sub>1.8</sub> Se <sub>4</sub> and blank CC, (b) 24 hours chronoamperometric data of Fe <sub>0.2</sub> NiCo <sub>1.8</sub> Se <sub>4</sub>    Fe <sub>0.2</sub> NiCo <sub>1.8</sub> Se <sub>4</sub> cell in 1.0 M KOH solution, and (c) theoretically calculated and experimentally measured H <sub>2</sub> and O <sub>2</sub> gas vs. time for overall water-splitting of Fe <sub>0.2</sub> NiCo <sub>1.8</sub> Se <sub>4</sub>    Fe <sub>0.2</sub> NiCo <sub>1.8</sub> Se <sub>4</sub> cell.	269

## *List of Figures*

---

7.25	Effect of KSCN on the overall current (for two-electrode system) of $\text{Fe}_{0.2}\text{NiCo}_{1.8}\text{Se}_4$ sample (a) LSV and (b) chronoamperometric data.	270
7.26	(a) FESEM image and (b) EDS mapping of $\text{Fe}_{0.2}\text{NiCo}_{1.8}\text{Se}_4$ after two electrode electrocatalysis.	270
7.27	XPS of $\text{Fe}_{0.2}\text{NiCo}_{1.8}\text{Se}_4$ (a) deconvoluted spectra of Ni 2p, (b) deconvoluted spectra of Co 2p, (c) deconvoluted spectra of Fe 2p, (d) deconvoluted spectra of Se 3d, (e) deconvoluted spectra of O 2p, and (f) survey spectrum after two electrode electrocatalysis.	271
7.28	Upper and lower panels represent the optimized crystal structures of the bare and Fe-doped $\text{NiCo}_2\text{Se}_4$ compounds ( $\text{Fe}_{0.12}\text{NiCo}_{1.88}\text{Se}_4$ , $\text{Fe}_{0.2}\text{NiCo}_{1.8}\text{Se}_4$ , and $\text{Fe}_{0.5}\text{NiCo}_{1.5}\text{Se}_4$ ) respectively as estimated from the first-principle calculations.	273
7.29	Defect formation energies per dopant ( $\Delta E_{\text{df}}$ ) for different Fe-doped $\text{NiCo}_2\text{Se}_4$ systems as obtained from DFT+Udd level of theory.	273
7.30	The electronic band structures along the $\Gamma \rightarrow \text{R} \rightarrow \text{M} \rightarrow \Gamma \rightarrow \text{X} \rightarrow \text{R}$ high-symmetry points of (a) $\text{NiCo}_2\text{Se}_4$ and (b) $\text{Fe}_{0.2}\text{NiCo}_{1.8}\text{Se}_4$ systems as obtained from the DFT+Udd level of calculations. [The band gaps in Figure (a) and the Fermi energies ( $E_{\text{F}}$ ) are marked with green arrows and horizontal dashed lines, respectively].	275
7.31	(a to d) Left and right panels depict the total, orbital resolved partial atomic density of states of $\text{NiCo}_2\text{Se}_4$ and $\text{Fe}_{0.2}\text{NiCo}_{1.8}\text{Se}_4$ compounds, respectively, as obtained from the DFT+Udd level of theory. [The Fermi energies ( $E_{\text{F}}$ ) are marked with vertical dashed lines].	276
7.32	Total density of states of $\text{Fe}_{0.12}\text{NiCo}_{1.88}\text{Se}_4$ and $\text{Fe}_{0.5}\text{NiCo}_{1.5}\text{Se}_4$ compounds as estimated from DFT+Udd level of theory.	277
7.33	The Gibbs free energy ( $\Delta G$ ) vs. (A) hydrogen and (B) oxygen coverage and the exchange current density ( $J$ ) as a function of $\Delta G$ for (a) HER and (b) OER activities of Fe-doped $\text{NiCo}_2\text{Se}_4$ compounds.	279



# Chapter 1

## Introduction

- \* *The chapter contains an insight of thesis and brief idea about the nanomaterials and their wide application.*
- \* *The chapter emphasizes the different ways of water-splitting, the parameters of electrocatalyst, and their use in electrochemical water- splitting.*
- \* *It contains the factors which are affecting the EC water-splitting performance and strategies to enhance the performance of electrode in EC water- splitting.*

### 1.1 Nanoscience and Nanotechnology: Historical Background

Nanomaterials are defined as materials that have at least one dimension in the range of 1-100 nm. The concept of nanomaterials can be traced back to Richard Feynman's talk in 1959 titled "There's Plenty of Room at the Bottom," in which he envisioned the possibility of directing and controlling the materials at the atomic and molecular level.<sup>1</sup> The manipulation and engineering of the materials on the nanomaterial scale are related to nanoscience, whereas the application of nanomaterials and nanoscience is relevant to nanotechnology. In 1974, Norio Taniguchi was the first person to use the term nanotechnology. Norio Taniguchi stated: "Nanotechnology mainly consists of the processing of, separation, consolidation, and deformation of materials by one atom or one molecule."<sup>2</sup> Almost all fields of science and technology now include nanotechnology as a crucial component due to its widespread influence in research and applications. Nonetheless, we will discuss nanoscience in the field of electrochemistry in the following part.

In the late 20th and early 21st centuries, significant improvements in the field of electrochemistry have evolved into an interdisciplinary research domain, blending insights from chemistry, material science, physics, nanotechnology, and engineering. Cost-competitive renewable energy sources are one of the driving forces behind the surge of interest in electrochemistry.<sup>3</sup> As green electricity produced from wind, solar, wave, biomass, and geothermal farms have become more accessible, it is now an important urgency to explore how this sustainable energy can be effectively harnessed to reduce greenhouse gas emissions. Subsequently, the scope and application of electrochemical principles have significantly expanded, encompassing a wide range of activities. These include hydrogen ( $H_2$ ) production and utilization, carbon dioxide ( $CO_2$ ) conversion into fuels and value-added chemicals, nitrogen ( $N_2$ ) electroreduction, and electrochemical synthesis of crucial organic compounds.<sup>4-5</sup> The schematic representation of nanomaterials in the field of electrochemistry is given in Figure 1.1. This extension shows the pivotal role of electrochemistry, which plays in addressing environmental challenges and advancing sustainable technologies.

Nanomaterials have emerged as a potent tool in modern electrochemistry, capitalizing on a range of nanoscale effects that improve their catalytic capabilities.<sup>6</sup> These effects, including their high surface area, favorable electronic structure, boosted conductivity, plenty of surface atomic sites, and improved charge transfer kinetics, jointly contribute to their exceptional electrocatalytic performance. In order to understand the precise mechanism of these nano electrocatalysts, the

development of advanced characterization techniques is imperative.<sup>7</sup> These techniques are widely used in the construction of microelectronic circuits and a range of technologies, such as water-splitting, lithium-air batteries, supercapacitors, and hydrogen storage.<sup>8-10</sup> Lithium-ion batteries are widely utilized in devices like laptops, electric vehicles, mobile phones, and cameras as energy storage solutions.<sup>11</sup> Presently, there's a significant focus on developing high-energy-density electrical power capacitors to meet the increasing demands of industries and consumers. Supercapacitors incorporating nanostructured electrode materials offer higher power density storage compared to conventional batteries.<sup>12</sup> This makes nanomaterials highly appealing for various applications. Nanomaterials have gained substantial attention in the storage of molecular hydrogen due to their unique properties. Molecular hydrogen serves as an energy source that can be produced from both renewable and non-renewable resources. However, renewable resources are preferred for clean hydrogen production.<sup>13</sup> One of the intriguing options is water-splitting, which uses renewable resources to make clean hydrogen efficiently and cost-effectively. Furthermore, scientists are working on the development of a low-cost solar cell device with efficient solar energy conversion capabilities to replace fossil fuels.<sup>14</sup> The electrochemical water-splitting technique is a more efficient and environmentally friendly way of producing H<sub>2</sub> with electrical energy. The hydrogen produced can be immediately stored and used in hydrogen fuel cells, replacing carbon fiber tanks in fuel cell-powered cars.<sup>15</sup>

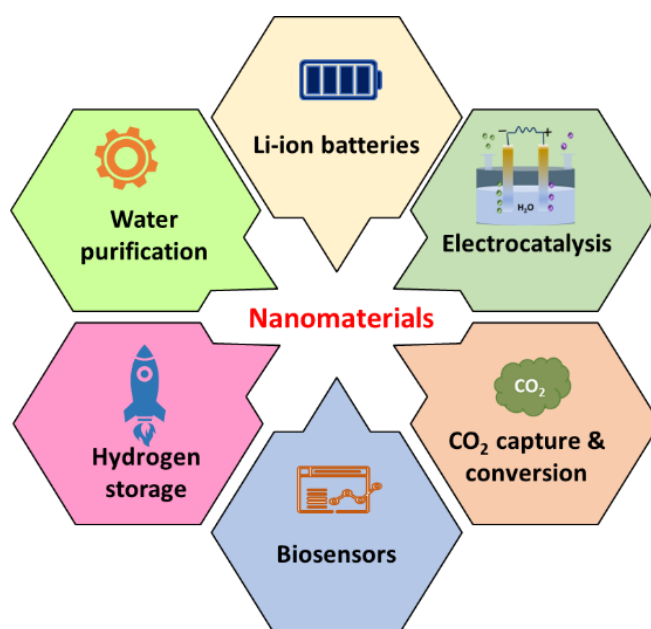


**Figure 1.1:** Representation of application of nanomaterials in the field of electrochemistry.

### 1.2 Nanomaterials: Brief Overview

#### 1.2.1 Uniqueness of Nanomaterials

Nanomaterials demonstrate different properties than their bulk counterparts because of two main factors: the confinement effect and the high surface-to-volume ratio.<sup>16</sup> Strong electron confinement in nanoscale material causes discrete energy levels to lead to a rise in the bandgap, which in turn leads to the confinement effect.<sup>17</sup> Conversely, when particle size reduces, the number of surface atoms increases relatively to its volume, which is the reason for the high surface-to-volume ratio. This improved surface area provides more active sites for chemical reactions and generates nanomaterials that are highly reactive and useful for catalytic applications.<sup>18</sup> Furthermore, high surface energies of nanomaterials are a factor in their higher reactivity, which has important ramifications for the study of electronics, medicine, energy, and the environment. Therefore, nanomaterials are valuable for a variety of applications due to their unique electrical and chemical properties.<sup>19</sup>

Quantum dots, mere nanometers in size, possess optical and electronic characteristics distinct from their larger counterparts. These characteristics result from significant quantization effects caused by the high quantum confinement of electrons and holes in the nanocrystals. Excitons are created when electrons and holes are bound together by Coulomb interactions or by differing polarities. This phenomenon is known as quantum confinement.<sup>20</sup> The most asserted quantum confinement occurs when the radius of nanoparticles is smaller than the exciton Bohr radius. This confinement creates discrete energy levels of electronic states in nanomaterials, unlike the continuous energy bands found in bulk materials. When two atoms come together during the synthesis of molecules perturbs the energy level, creating the lowest unoccupied molecular orbital (LUMO) and the highest occupied molecular orbital (HOMO). The number of energy levels rises with the number of atoms, and the energy difference between HOMO and LUMO decreases. In bulk materials, the empty and filled states form a separate continuum, namely the conduction band (CB) and valence band (VB), respectively (Figure 1.2). In contrast, the energy levels within the empty and filled states of quantum-size particles remain discrete. This is known as the quantum size effect, which is vital in understanding the unique properties of nanomaterials.<sup>21</sup>

Another important factor that influences the distinct properties of nanomaterials is their high surface-to-volume ratio compared to bulk materials.<sup>22</sup> The surface area to volume ratio increases as the material's size decreases, resulting in a greater number of active atoms on the

surface. When compared to their bulk equivalents, nanoparticles have improved adsorption, adhesion, storage capacity, and catalytic activity. Because of the increased number of surface-active atoms, chemical reactions occur at a faster rate, making nanomaterials highly reactive.<sup>23</sup> So, nanomaterials are ideal for a variety of applications such as chemical reactions, catalytic processes, sensing, detection, and adsorption.

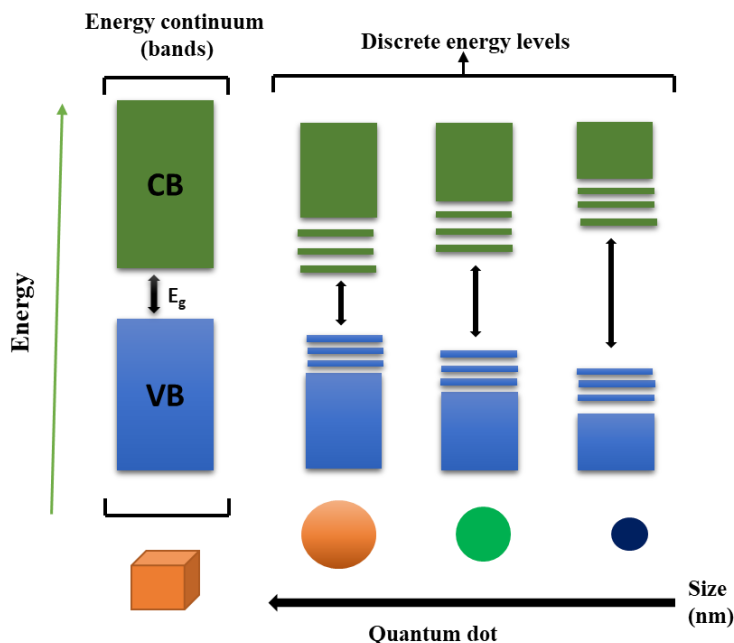


**Figure 1.2:** Representation of discretization of electronic energy levels with size variation.

### 1.2.2 Dimensionality of Nanomaterials

Nanomaterials are divided into four categories based on their dimensions: 0D, 1D, 2D, and 3D. These materials' characteristics and behavior are significantly reliant on their dimensionality. Quantum dots, for example, which fall within the 0D category, exhibit unique electrical and optical features due to quantum confinement effects. 1D nanomaterials, on the other hand, have large aspect ratios and can display better mechanical, electrical, and thermal properties.<sup>24</sup> Graphene, a 2D nanomaterial, because of its two-dimensional structure, has exceptional electrical and thermal conductivity.<sup>25</sup> Finally, 3D nanomaterials with unique hierarchical structures and optical characteristics, such as nano-cubes and nanoflowers, do not restrict electrons.<sup>26</sup> (Figure 1.3)

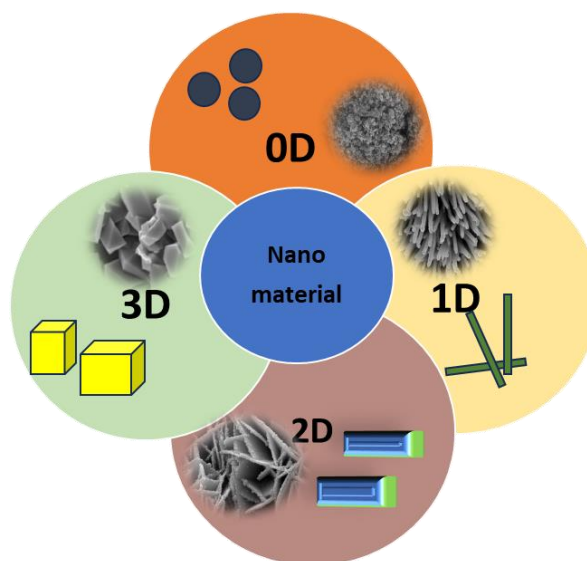


**Figure 1.3:** Schematic illustration of 0D, 1D, 2D, and 3D nanostructures.

### 1.2.3 Synthetic Approaches of Nanomaterials

The synthetic approach to nanomaterials entails producing materials with controlled nanoscale architectures and features. It involves creating nanoscale structures with exact control over size, shape, composition, and surface qualities. Top-down and bottom-up approaches are the most often used strategies for synthesizing nanomaterials.<sup>27</sup>

#### 1.2.3.1 Top-down approaches

Top-down approaches to creating nanomaterials involve breaking down larger particles into smaller to produce the particles in nanometer length scale. This can be achieved through various methods, such as mechanical or ball milling, laser ablation, arc discharge, electrospinning, sonication, sputtering, and lithography, among others. There are some problems with following the top-down approach because of imperfection and crystallographic to surface structure, the physical properties and surface chemistry of nanomaterials will be changed, which would have a significant impact on the other properties (Figure 1.4).<sup>28</sup>

#### 1.2.3.2 Bottom-up approaches

The bottom-up technique is a way of generating nanomaterials by assembling individual atoms or molecules into bigger structures. The atoms or ions are synthesized, reduced and stabilized, and then assembled into nanostructures using this process. Chemical vapor deposition

(CVD), solvothermal and hydrothermal methods, sol-gel method, reverse micelle method, electrodeposition method, soft and hard template method, combustion method, chemical reduction, and co-precipitation are some of the techniques available for bottom-up nanomaterial synthesis. The method chosen is determined by the qualities and applications of the nanomaterial to be synthesized. The bottom-up approach keeps a high degree of control over the size, shape, and composition of the nanomaterials, making it a promising approach for a wide range of applications, including energy, electronics, and medicine (Figure 1.4).<sup>28</sup>

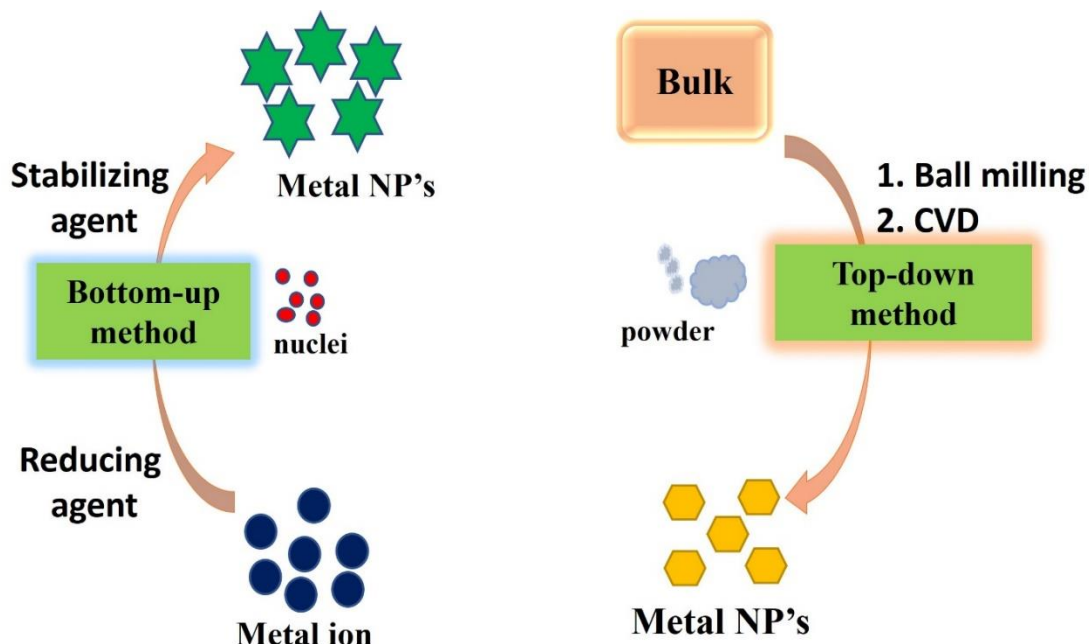


**Figure 1.4:** Top-down and bottom-up approaches for the synthesis of nanomaterials.

### 1.3 Application of Nanomaterials in Energy Conversion

Nanomaterials provide unique qualities like high surface area-to-volume ratio, superior conductivity, and tunable optical and electrical properties, which make them intriguing for use in energy conversion and storage. This chapter provides a detailed discussion of energy conversion via a water-splitting reaction.<sup>29</sup>

### 1.3.1 Methods of water splitting

Water splitting is the process of breaking water ( $\text{H}_2\text{O}$ ) into its constituent elements, hydrogen ( $\text{H}_2$ ) and oxygen ( $\text{O}_2$ ).<sup>30</sup> This can be achieved through various methods, primarily categorized into different types based on the energy source used:

#### 1.3.1.1 Thermal Water Splitting:

This process splits water into hydrogen and oxygen by using high temperatures produced by nuclear reactors, concentrated solar electricity, or other heat sources. Water splitting is facilitated by a sequence of chemical events known as thermochemical cycles. It is true that water can be broken down into its component elements of  $\text{H}_2$  and  $\text{O}_2$  in a single step; however, this is not feasible due to thermodynamics, kinetics and the high temperatures needed. As a result, thermochemical cycles are suggested as a substitute strategy. These cycles usually entail two or more steps and a sequence of chemical reactions to divide water using thermal energy at temperatures below 2000 °C. To accomplish the desired water splitting, a series of regulated reactions take place in these thermochemical cycles. Using such cycles has the advantage of being more practical and energy-efficient than the single-step breakdown of water since they can be engineered to function at lower temperatures and with better thermodynamic efficiency.<sup>31-32</sup> This strategy makes it feasible to use waste heat or renewable energy sources to power the water-splitting reactions, which advances the development of sustainable hydrogen generation techniques. For water splitting, thermochemical cycles are still not as cost competitive as traditional techniques. A synergistic integration with nuclear or concentrated solar reactors is necessary for continued advancement in order to improve their economic viability.<sup>32</sup>

#### 1.3.1.2 Photoelectrochemical Water Splitting (PEC):

PEC water splitting combines the principles of solar cells and electrolysis, where a semiconductor material absorbs sunlight to generate electron-hole pairs. These electron hole pair drive the water-splitting reaction when an external bias is applied.<sup>33</sup> In a photoelectrochemical (PEC) water-splitting reaction, a semiconductor material is used as a light absorber and energy converter because the energy provided by light alone is insufficient to drive the electrolysis of water. In a PEC cell, the two half-cell reactions occur simultaneously at two different electrodes, resulting in the separate evolution of  $\text{H}_2$  and  $\text{O}_2$ . At the photoanode's surface, water is oxidized to  $\text{O}_2$ , while at the photocathode's surface, water is reduced to  $\text{H}_2$ . PEC cells differ structurally from



conventional electrolytic cells, as the photoelectrode is illuminated through an optically transparent window. The critical component in a PEC system is the photoactive semiconductor, which serves as a working electrode, either as a photocathode or a photoanode.<sup>34</sup>

In an ideal scenario, water splitting can be carried out under unbiased conditions using the components mentioned in a PEC device (Figure 1.5), which are essential for transforming water and solar energy into H<sub>2</sub> and O<sub>2</sub>. However, an additional bias is required to drive the water-splitting reaction. Furthermore, several precautions should be taken when constructing the PEC system. The working and counter electrodes should be placed apart from each other to prevent contamination with the reactants or intermediates from the other electrode and to avoid reverse reactions. To prevent the crossover of gaseous products, a membrane can be used, allowing the separate evolution of H<sub>2</sub> and O<sub>2</sub>. A PEC cell must meet several criteria for practical application, including the arrangement of photoelectrodes, effective penetration of light into the photoelectrodes through the cell, resistance to corrosive electrolytes, continuous electrolyte supply, and the use of a membrane to keep the evolved gases separate.

The primary concern with PEC systems is improving the efficiency of the photoactive material to achieve the 10% solar to hydrogen energy conversion threshold is benchmark for commercialization. In 1972, pioneering work by Honda and Fujishima used TiO<sub>2</sub> for PEC water-splitting, but the efficiency of this system was very low (<1%). To meet the threshold efficiency, an efficient PEC cell is crucial.<sup>35</sup> An efficient cell relies on an affordable photoactive material that meets several key requirements for the ideal photoelectrode: strong light absorption across the entire solar spectrum, high chemical stability in aqueous electrolytes under both dark and illuminated conditions, proper band edge positions for the evolution of H<sub>2</sub> and O<sub>2</sub>, low kinetic over-potentials, and proper charge transfer at the semiconductor/electrolyte interface for water-splitting. Efficiency remains a significant challenge, as converting a substantial portion of solar energy into hydrogen can be difficult. The choice of photoactive materials is critical, with many efficient options being expensive or rare. Maintaining the stability of PEC cells in corrosive electrolytes is another hurdle, and reducing costs while preserving efficiency is essential. Scaling up PEC systems for commercial use is complex, and improving reaction kinetics is necessary to enhance efficiency. The inherent complexity of PEC systems, including various components and electrodes, makes their design and operation more challenging. Researchers are actively working to overcome these limitations through advances in materials, technology, and sustainable practices,

aiming to make PEC water splitting a more practical and environmentally friendly method for hydrogen production.<sup>36-37</sup>

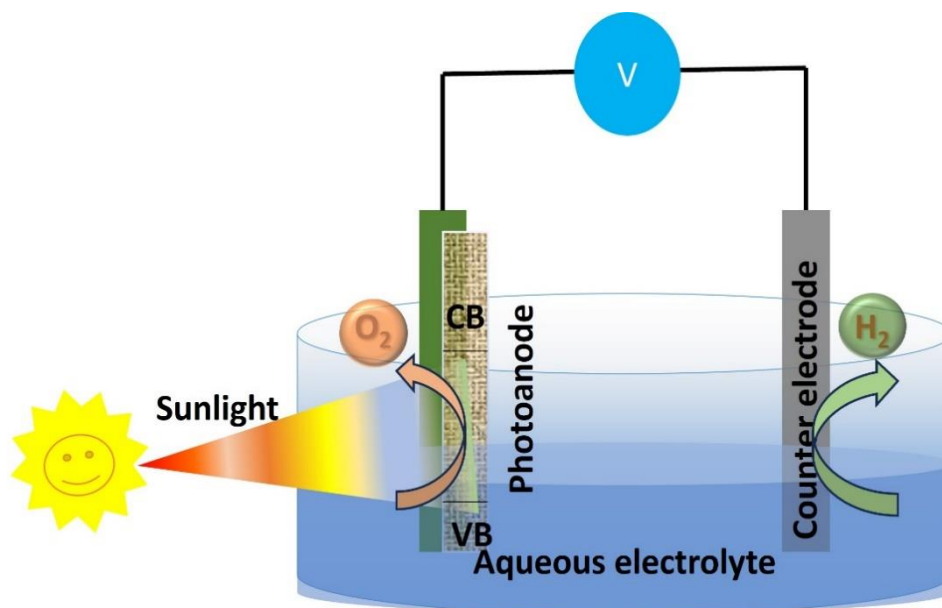


**Figure 1.5:** A schematic diagram of the PEC cell for water splitting.

### 1.3.1.3 Biological Water Splitting:

Certain microorganisms, such as some types of algae and bacteria, are capable of photosynthesis, a process similar to water splitting. These organisms use light energy to split water and produce oxygen and organic compounds. The complexity of the biological system is really high; its basic principles are still debatable and researched for a decade. Biological water splitting is an incredibly efficient and sustainable method for harnessing solar energy and producing oxygen, which is vital for all aerobic life forms. Researchers are studying this natural process to gain insights into developing artificial photosynthetic systems that could potentially be used for renewable energy production and sustainable fuel generation, such as hydrogen production through artificial photosynthesis. Efficiency, speed, susceptibility to environmental factors, substrate dependence, rivalry with other metabolic pathways, scaling issues, and the requirement for purification are some of the drawbacks of biological hydrogen generation.

Through comprehending the complexities of biological water splitting, researchers want to imitate and enhance natural processes for more sustainable energy sources.<sup>38-39</sup>

### 1.3.1.4 Photocatalytic Water Splitting:

Photocatalysts are used in catalytic water splitting to speed up the chemical process by using light. Metals, metal oxides, or other materials can serve as the basis for these catalysts. Catalytic water splitting can be accomplished by thermal or electrochemical. There are several crucial processes that can be used to distil the basic mechanism of photocatalytic water splitting. Initially, if the energy of the photons surpasses the photocatalyst's band gap, charge carriers are produced when the photons hit the surface of the catalyst. These generated charge carriers drive the entire water-splitting reaction. The bandgap of the photocatalyst and the alignment of its valence band maxima and conduction band minima with the water redox potential have a significant impact on the process's effectiveness. Aside from this, choosing an effective photocatalyst is crucial to successfully achieving water splitting because of the quick creation and efficient separation of charge carriers.<sup>40</sup> A schematic representation of this process can be found in Figure 1.6.

The main disadvantage of using a single photocatalyst is that the oxygen and hydrogen created recombine quickly, making it impossible for them to be released separately. On the other hand, a more viable option is provided by the two-step photoexcitation mechanism, which uses the Z-scheme and two different photocatalysts. Z-scheme photocatalysis is a more useful technique for splitting water since it takes inspiration from natural processes. Z-scheme photocatalysts guarantee the distinct evolution of H<sub>2</sub> and O<sub>2</sub> by utilizing the full visible light spectrum. In addition, the cost-effectiveness and adaptability of powdered photocatalyst systems make them beneficial for solar water-splitting applications. Their primary obstacle, though, is going to be getting more efficiency because the production of H<sub>2</sub> and O<sub>2</sub> happens on a single electrode surface, meaning that their separation and avoidance of recombination will require an external procedure that might be expensive.<sup>41</sup>

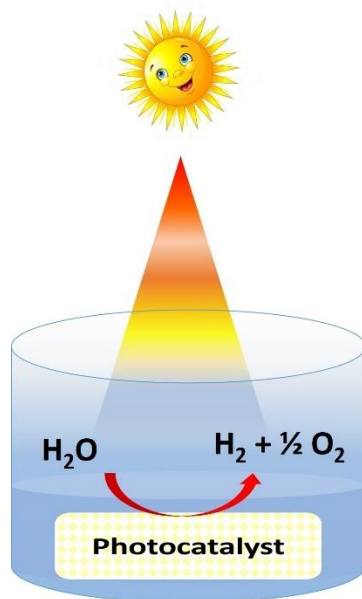
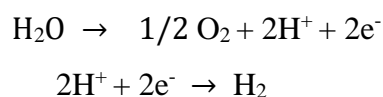


**Figure 1.6:** A schematic representation of the photocatalytic cell.

### 1.3.1.5 Electrochemical water splitting

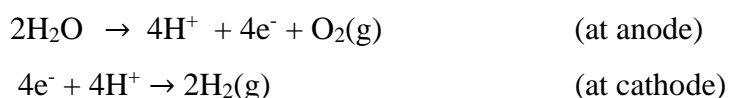
Electrochemical water splitting is becoming more and more well-liked as a sustainable way to create hydrogen for use as fuel in the future. Compared to conventional fuels like gasoline, hydrogen has a number of benefits, including a high energy density and no carbon dioxide emissions.<sup>42</sup> However, it uses finite fossil fuels and releases carbon dioxide into the atmosphere, the existing process of producing hydrogen by steam-reforming hydrocarbons is not sustainable. Furthermore, the hydrogen that is produced is frequently tainted with C, N, and S oxides, which shortens the catalyst's life. Some techniques, such as photoelectrochemical water splitting and metal hydride hydrolysis, are limited by factors like hazardous precursors and low solar-to-hydrogen conversion efficiency. Electrolysis of water is currently the most environmentally friendly method to produce large-scale hydrogen, and researchers are focused on developing cost-effective electrocatalysts with excellent efficiency to improve the performance of water electrolyzers.<sup>43</sup> Nowadays, electrochemical water splitting is one of the important fields of research, it is the only method to produce clean and carbonaceous-free hydrogen. As per a recent survey of the future availability of coal and hydrocarbons, it is clear that there will not be sufficient carbon in the coming years to meet the energy requirements. Apart from energy requirements, the use of fossil fuels leads to critical environmental issues throughout the world. Hydrogen is an important fuel that is the solution to energy-related issues because of its abundance and high energy

density. An engine that burns hydrogen produces no pollution, so it is a form of clean energy. Hydrogen does not occur naturally on the earth it combines with the other atoms such as combine with oxygen and makes water. It is found in other organic compounds known as a hydrocarbon: gasoline, methanol, and other natural gases. Water splitting reaction involves two half-reactions, hydrogen and oxygen evolution. First, at the cathode, the reduction of protons takes place which generates hydrogen as given in the schematic Figure 1.7. Another at the anode oxidation of water takes place which evolves oxygen. Among HER and OER, OER is a sluggish reaction because four-electron transfer processes involve oxygen-oxygen bond formation. Water splitting requires thermodynamically 1.23 V which is potentially related to OER reaction. Hence, practically, water splitting requires more potential of 1.23-2.5 V, which is due to extra overpotential.<sup>44</sup> The OER and HER reactions are as follows-

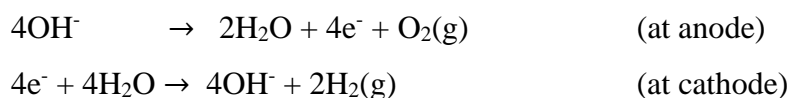


At present Ru and Ir-based catalysts are considered the most efficient catalyst for OER, and carbon-based Pt catalysts are best for HER in an acidic medium. In alkaline medium metal oxides, sulfides and selenides show good activity in the alkaline medium. Though Pt, Ru, and Ir-based catalysts are having low activation energy for the water splitting reaction energy barrier but have scarcity in different pH mediums.<sup>42, 45</sup> One of the basic approaches for the replacement of noble catalysts is to apply metal chalcogenides for water splitting due to their cost effectiveness and large abundance. Nevertheless, the industrial application still deals with some gaps due to electrocatalytic activity and stability of the catalyst. Therefore, it is important to notice some non-noble electrocatalysts with improved stability and activity. It is important to know the mechanistic pathways for water-splitting reactions in different pH mediums.<sup>46</sup> There are different types of mechanisms is proposed in the reported literature-

In acidic medium



In alkaline medium



In a water-splitting reaction, the Faradaic efficiency is never 100 % for an electrolytic cell due to various kinetic and thermodynamic hindrances. As previously mentioned, platinum (Pt) is recognized as an efficient catalyst for the HER, while Ir and Ru and their compounds are favored catalysts for the OER. However, the use of these relatively scarce and precious metals in water electrolysis presents challenges, increasing the cost of hydrogen ( $H_2$ ) production and hindering scalability. Recently, researchers have discovered that oxides and hydroxides of 3d transition metals from Group VIII, such as Fe, Co, and Ni, either individually or in combination with other metals, can efficiently catalyze the OER under alkaline conditions, rivaling the performance of Ir and Ru.<sup>47</sup> However, the issue lies in the kinetics of the counter-reaction, the HER, in alkali, which remains sluggish even with Pt due to the following mentioned reasons. 1. The larger concentration of  $OH^-$  ions in alkaline solution competes with the proton adsorption on the Pt surface. 2. The abundance of hydroxide ions can lead to adsorption of  $OH^-$  species blocking active sites of Pt. 3. Pt catalyst surfaces may undergo restructuring, diminishing the number of active sites available for the reaction. To address these challenges and enhance HER performance in alkaline media, researchers explore alternative catalysts and design strategies to improve the stability, activity, and selectivity of catalysts under alkaline conditions.

There are two alternative techniques for addressing this difficulty. The first entails developing efficient and long-lasting non-noble OER catalysts for usage in acidic conditions, as well as replacing Pt with non-noble metal-based catalysts such as sulfides, selenides, and phosphides for the HER. However, this strategy may result in asymmetric electrolytic cells, adding technical challenges. The second strategy is to create a bifunctional catalyst out of non-noble metals that can accelerate both the OER and HER without the use of a separator. Bifunctional catalysts made of Fe, Co, and Ni, particularly in nanostructures, have been demonstrated to exhibit equivalent or higher HER and OER activity than Pt, Ir, and Ru. These bifunctional catalysts are frequently made up of nanostructured phosphides, sulfides, and selenides of Fe, Co, and Ni.<sup>48</sup> While the energy sector is actively investigating these materials, detailed evaluations of sulfide, selenide, and phosphide catalysts generated from Fe, Co, and Ni, as well as their applications in water splitting are lacking. The other common problems associated with electrochemical water splitting reactions include corrosion and durability issues that must be addressed to ensure long-lasting electrochemical cells. Effective mass transport of reactants and products, stable electrolytes, and safety measures for handling flammable hydrogen are all critical considerations.

Additionally, the scalability, economic viability, high energy input, and environmental impact of water-splitting technologies need to be addressed to realize their potential in a sustainable hydrogen economy. Researchers and engineers are actively working on solutions to overcome these challenges and make electrochemical water splitting a practical and environment friendly hydrogen production method.<sup>44</sup>

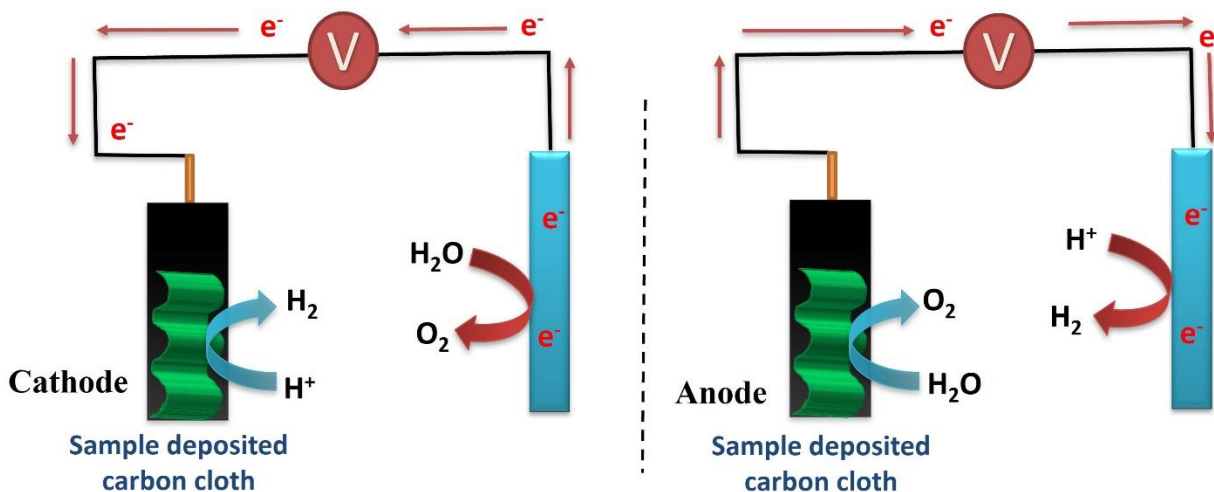


**Figure 1.7:** Schematic representation of electrochemical cell reactions (HER & OER).

Photovoltaic-electrochemical (PV-EC) water-splitting stands out as a pivotal, advanced, and potent method for hydrogen generation.<sup>49</sup> This technique combines a photovoltaic cell with an electrocatalyst, where the PV cell serves as the energy source, and the electrocatalyst facilitates water splitting as given in Figure 1.8. In a PV-EC system, two electrolyzers are connected in series with the PV cell, and these electrolyzers are linked to compartments for collecting H<sub>2</sub> and O<sub>2</sub> gases. Due to its reliance on solar radiation for power generation, the photovoltaic cell, also known as a solar cell, directly converts solar energy into electrical energy. These cells are made of semiconductor materials, which collect light from the sun and use a specific method to produce electricity. Electrons in the semiconductor shift from the valence band to the conduction band in the crystal structure when exposed to sunlight. The migration of electrons caused by this excess energy leaves holes in their wake, and it is the combination of these free electrons and holes that causes the PV cell to produce electricity. The greater the intensity of solar light and the surface area of the semiconductor, the greater the flow of photocurrent. Usually, an anti-reflective layer is applied to the PV cell's surface to reduce the amount of incident light lost. PV-EC water-splitting

provides low fuel expenses, durability, high efficiency, and freedom from fuel supply concerns, in addition to being environmentally friendly. PV-EC systems provide a clean and sustainable way to produce hydrogen gas, a flexible and eco-friendly fuel, they are of great interest in the field of renewable energy. Hydrogen produced through PV-EC water splitting can be used in fuel cells to generate electricity, stored for later use, or utilized in various industrial processes. The development and optimization of PV-EC systems are ongoing research areas, with a focus on improving efficiency, cost-effectiveness, and the selection of suitable materials and catalysts to enhance the performance of both the photovoltaic cells and the electrochemical components. These systems hold promise for addressing the challenges of clean energy production and storage while reducing the environmental impact of traditional energy sources.<sup>50</sup>

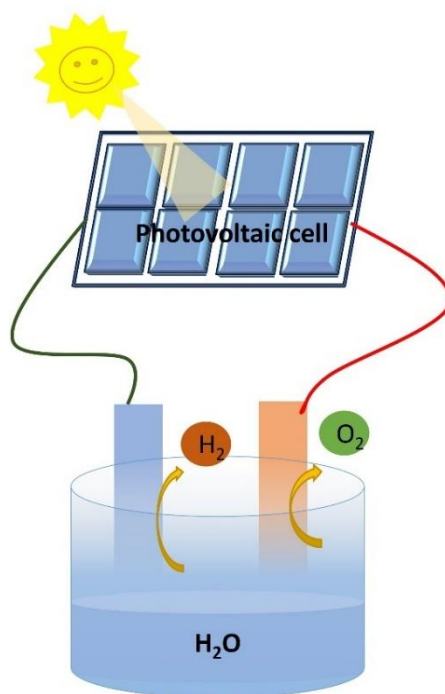


**Figure 1.8:** Schematic representation of PV-EC cell.

### 1.3.2 The Mechanisms of Hydrogen Evolution Reaction and Oxygen Evolution Reaction in an alkaline medium

#### 1.3.2.1 Hydrogen evolution reaction (HER)

Hydrogen is considered a highly attractive replacement to depleting traditional fossil fuels because of its environmentally friendly nature and recyclability. Among numerous hydrogen



production techniques, electrochemical water splitting emerges as an efficient and durable technology, particularly in contrast to other approaches. One of its significant advantages lies in its seamless integration with renewable energy sources like solar and wind power.<sup>51</sup> Notably, alkaline water electrolysis plays a crucial role in industrial applications. It offers a prime solution for treating alkaline water discharge from processes such as water-alkali and chloralkali electrolyzers.<sup>52</sup> However, it is essential to recognize that these technologies are energy-intensive, with water-alkali and chloralkali electrolyzer alone consuming a greater part of electrical energy consumption. Therefore, optimizing and improving the efficiency of alkaline water electrolysis becomes essential to mitigate energy demands and maximize the benefits of hydrogen production through water splitting. The inefficiency of high-performing acidic catalysts in alkaline electrolytes can be attributed to the higher overpotentials required and the inherent challenges associated with the reaction chemistry. Hence, there is a critical need to investigate the underlying mechanism and electrode kinetics, which can be a solid foundation for researchers to develop novel and highly efficient electrocatalysts.<sup>53</sup>

There are numerous active electrocatalysts that have been reported for HER in an acidic medium. However, the formation of acid fog and high rate of corrosion in the electrocatalytic cell make it contaminated. On the contrary, in an alkaline medium, there is a need for extra energy to produce hydrogen by breaking the H<sub>2</sub>O molecule. The electrolysis of water in different electrolytes follows distinct pathways. In acidic electrolytes, the abundance of available protons promotes HER catalysis, making it comparatively easier to accomplish at low overpotentials. In an alkaline medium, the produced hydrogen is clear, and this provides improved stability to non-noble metals, preventing their erosion and dissolution, which leads to long effect and makes alkaline catalysis a substitute to acidic environment.<sup>54</sup>

According to theoretical and experimental evidence, the HER mechanism in an alkaline medium mainly involves water dissociation, hydroxyl desorption, H<sub>2</sub> desorption, and H\* adsorption. Therefore, HER mechanism follows two pathways, first, Volmer-Tafel (V-T) and second, Volmer-Herovosky (V-H) pathway. The Volmer step is the common step in both pathways; in this case, water dissociation takes place and the formation of intermediate species on the active surface. Subsequent to the Volmer step, either another H<sub>2</sub>O molecule attacks the adsorbed H\* to form H<sub>2</sub> (equation 2), or two adsorbed H\* species unite to produce H<sub>2</sub> (equation

3).<sup>55</sup> As a result, the alkaline HER can proceed through whichever the V-H or the V-T pathway, as illustrated in Figure 1.9.

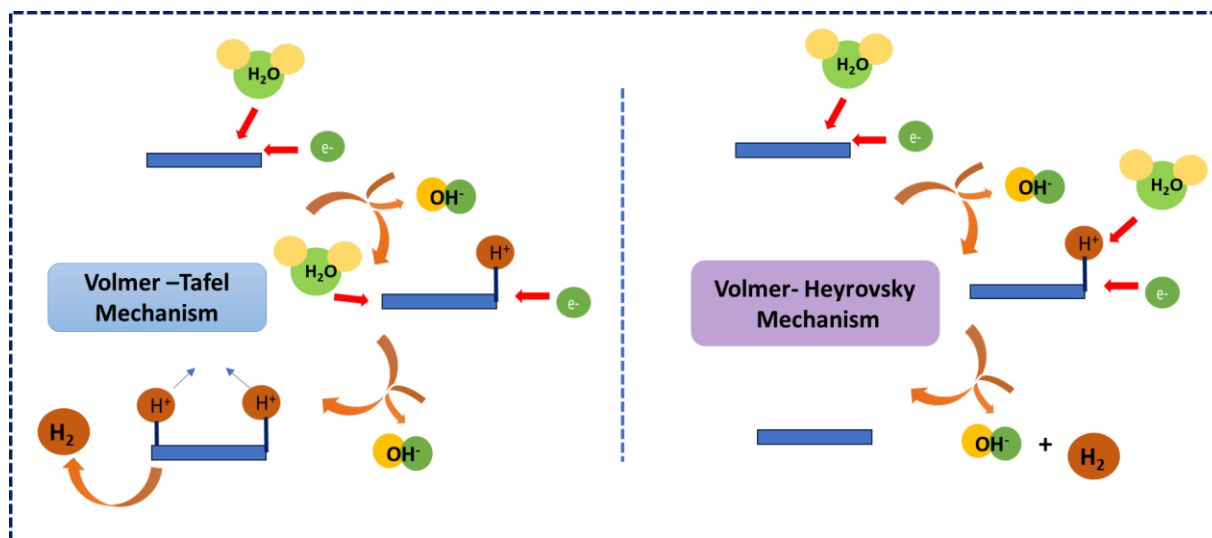
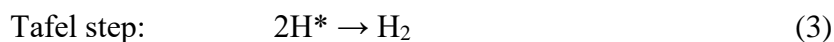
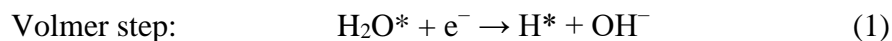


**Figure 1.9:** Schematic representation of HER mechanism in an alkaline medium.

Thus, in alkaline electrolytes, the HER is governed by specific reaction mechanisms. Two essential factors significantly influence the intrinsic activity of the HER in this environment: 1. Catalyst's H–OH bond cleavage ability during the Volmer step: This step involves breaking the H–OH bond in water molecules to generate crucial hydrogen intermediates ( $\text{H}^*$ ). The catalyst's effectiveness in facilitating this bond cleavage is vital for the overall reaction efficiency. 2. The binding energy of hydrogen intermediates on the catalyst's surface: Once the  $\text{H}^*$  species are formed, their subsequent interactions with the catalyst's surface are essential. The strength of their binding (binding energy) influences the stability and reactivity of the intermediates, further impacting the overall performance of the HER.<sup>56</sup> These two factors play pivotal roles in determining how efficiently the HER proceeds in alkaline mediums, making them crucial considerations in the construct and optimization of electrocatalysts for this important reaction. The adsorption-free energy of  $\text{H}_2\text{O}$  or  $\text{OH}^*$ , calculated using density functional theory (DFT), for

evaluating the energy barrier of H<sub>2</sub>O dissociation ( $E_{\text{H}_2\text{O}}$ ) for active sites is a descriptor. It is crucial to regulate the adsorption free energy of H<sub>2</sub>O/OH\* to promote the HER process while avoiding solid adsorption that could hinder the reaction.<sup>55</sup> Furthermore, the binding energy of H\* on the active surface is closely related to the acceleration of hydrogen molecule formation and the overall HER activity of catalysts. The Sabatier Principle in catalysis suggests that an optimal hydrogen binding energy (HBE), neither too strong nor too weak, leads to high HER activity. The Gibbs free energy of hydrogen intermediates ( $\Delta G_{\text{H}^*}$ ) calculated using DFT is used to evaluate the HBE on active surfaces. For efficient HER, the ideal HBE is close to zero ( $\Delta G_{\text{H}^*} = 0$ ), indicating that further optimization of hydrogen adsorption energy on the catalyst's surface that further speed up the alkaline HER kinetics. In recent years, with advances in synthetic strategies and nanotechnology, numerous advanced Ni-based electrocatalysts have been designed for the HER in alkaline medium, exhibiting excellent performance with low overpotentials, high current density, and long-term durability. Nørskov's and others have well correlated the determined exchange current density of the HER (how quickly hydrogen is produced in the reaction) with the calculated energy of hydrogen adsorption ( $\Delta G_{\text{H}}$ ). They have plotted these values, leading to a classic "volcano-shaped plot." The volcano-shaped plot is a graphical representation that shows the correlation between the exchange current density and the energy of hydrogen adsorption ( $\Delta G_{\text{H}}$ ).<sup>57</sup> In this plot, you typically observe a peak or maximum activity at a certain value of  $\Delta G_{\text{H}}$  (Figure 1.10). Catalysts with this specific energy of hydrogen adsorption exhibit optimal performance in the HER. Precious metals, like platinum, often have near-zero  $\Delta G_{\text{H}}$ , making them excellent catalysts for the HER. Non-precious metals, on the other hand, tend to have either too strong or too weak  $\Delta G_{\text{H}}$  values, making them fewer effective catalysts for this reaction.

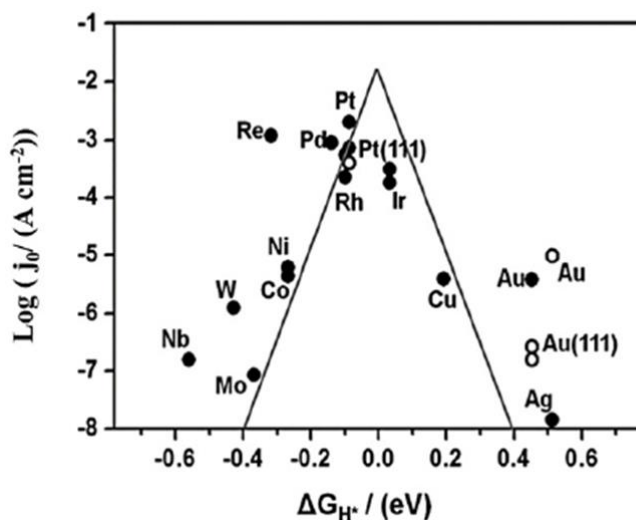


**Figure 1.10:** Volcano plot of exchange current density ( $j_0$ ) as a function of DFT-calculated Gibbs free energy ( $\Delta G_{H^*}$ ) of adsorbed atomic hydrogen on pure metals.

### 1.3.2.2 Oxygen evolution reaction (OER)

The kinetics of OER show distinct characteristics depending on the pH of the medium and catalyst. In acidic medium,  $\text{RuO}_2$  and  $\text{IrO}_2$  demonstrate heightened OER efficiency whereas in alkaline medium oxides and hydroxides of Mn, Ni, Fe, and Co are more active. The OER mechanisms in both media involve multiple steps, with the rate-determining step (RDS) being crucial in determining overall efficiency. Catalysts with stable oxidation states, such as  $\text{IrO}_2$  and  $\text{RuO}_2$  in acidic media and Ni, Co, Fe, and Mn oxides and hydroxides in alkaline media, undergo oxidation-reduction cycles, producing  $\text{O}_2$  while restoring active sites for subsequent reactions. The electrocatalytic activity is intricately linked to the catalyst's capability to absorb intermediates, and the rate of reaction is influenced by factors including electronic configuration and the strength of attachment of intermediates to active sites.

The electrocatalytic Oxygen Evolution Reaction (OER) is a complicated process that consists of four different phases, forming a multistep, four-electron transfer mechanism. This process necessitates an additional potential as compared to thermodynamic equilibrium potentials, stressing the need of understanding the reaction mechanism, particularly the rate-determining step, while building new OER electrocatalysts. The initial phase of alkaline OER comprises the

coordination of OH ions with metal ions [M-OH], followed by the production of [M-O] and [M-OOH]. Notably, the creation of [M-OOH] is the most thermodynamically unfavorable process, as evidenced by the associated positive free energy, which could be due to a weak contact between -OOH ions and the metal surface. The metal oxide derivative is then oxidized, resulting in the creation of oxyhydroxide to act as a catalyst. The following Figure 1.11 represent the OER reaction alkaline medium-

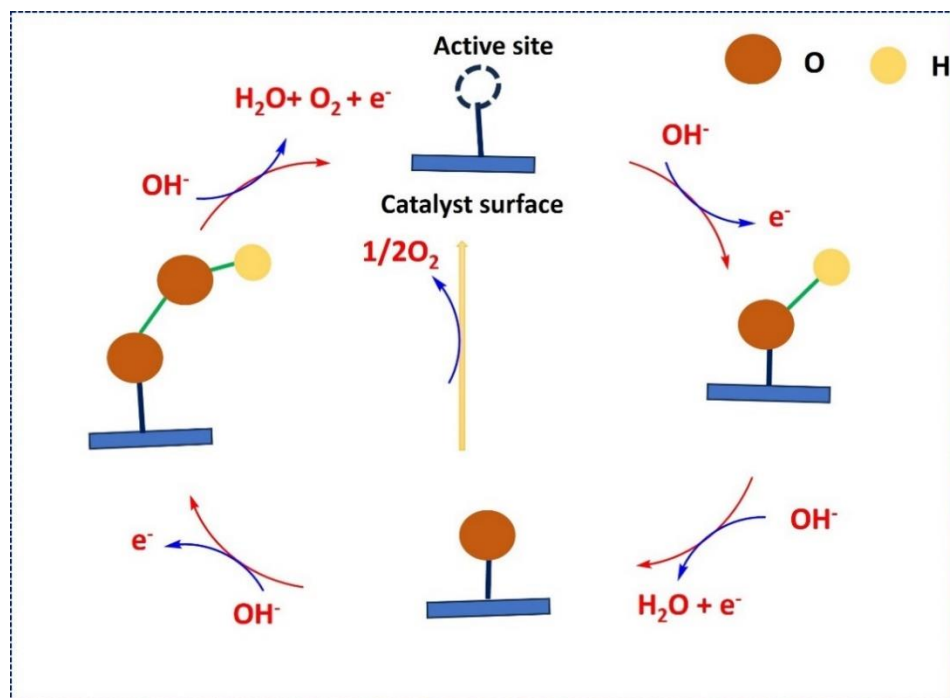


**Figure 1.11:** Schematic mechanism of OER in alkaline medium.

In alkaline conditions, the formation of intermediates in the OER is relatively facile. This ease of formation is attributed to the abundance of hydroxide ions, which serve as active reactants. However, as the pH of the solution decreases, moving towards acidic conditions, the formation of these intermediates becomes more challenging. This difficulty arises because, in alkaline environments, hydroxide ions are readily available as reactants. In contrast, at lower pH values, especially in acidic conditions, the source of hydroxide ions is water molecules. Consequently, breaking O-H bonds in water demands additional energy, leading to an increase in overpotential for the OER at lower pH conditions. The scarcity of hydroxide ions in acidic environments complicates the formation of intermediates, adding an energy barrier to the reaction process. This

pH-dependent behavior underscores the importance of considering the specific conditions in which OER occurs when designing electrocatalysts for optimal performance.

The OER process can typically involve two different electron-transfer routes: the adsorbate evolution mechanism (AEM) and the lattice oxygen oxidation mechanism (LOM) (Figure 1.12). In AEM, metal bands serve as the redox center, and the reaction proceeds through various oxygen intermediates, such as  $\text{OH}^*$ ,  $\text{OOH}^*$ ,  $\text{O}^*$ , and  $\text{O}_2$ . During this mechanism, concerted electron-proton transfer steps take place between the metal and the intermediates. This type of process is contemplated as a metal redox catalytic reaction. On the other hand, LOM is recently recognized as an alternative electron-transfer route observed in electrochemistry, including applications in Li-ion batteries and OER. In LOM, oxygen states act as the redox center, and the pathway involves  $\text{OH}^-$ ,  $\text{O}_2^{2-}$ , and  $\text{O}_2$  species, with a direct O-O bond coupling (O-O) step. Unlike AEM, LOM avoids the rate-determining step, which is the O-O bond formation ( $\text{OOH}^*$ ) in AEM. As a result, LOM is considered more efficient in achieving the OER process. In recent years, continuous attempts have been made to understand the mechanism behind complex OER reactions (due to the multistep reaction involved).<sup>58</sup>

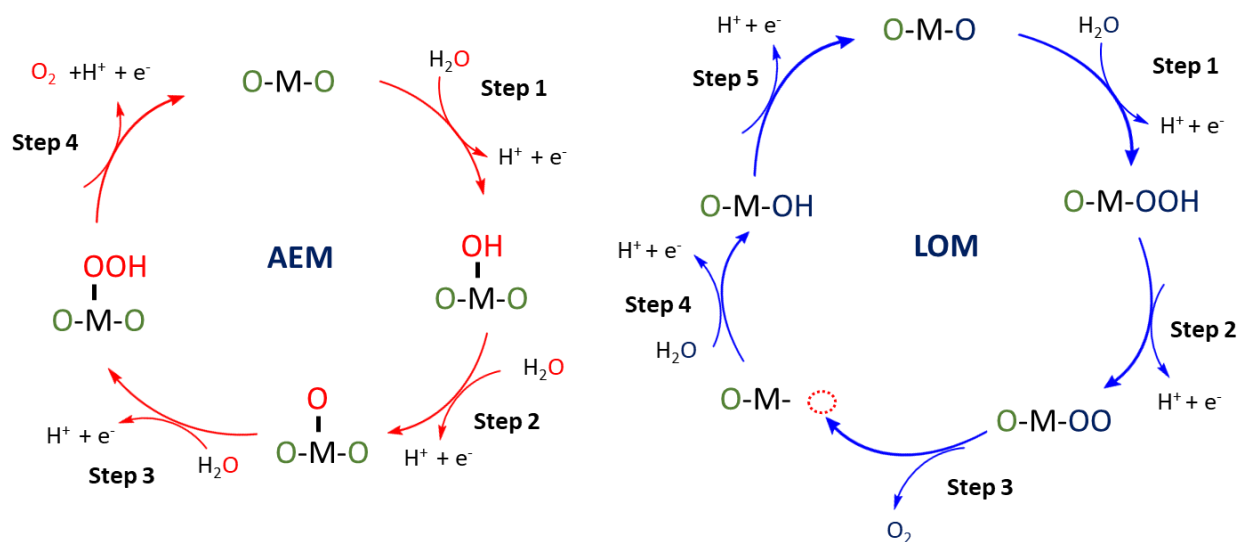


**Figure 1.12:** Schematic representation of OER in an alkaline medium through AEM and LOM pathways.

### 1.4 Evaluation parameter for water splitting reaction

Electrochemical splitting evaluation parameters (Figure 1.13) comprise overpotential at a specific current density, Tafel slope, electrochemical surface area (ECSA), Faradaic efficiency (FE), Impedance, mass and specific activities. These parameters collectively provide insights into the efficiency, kinetics, and selectivity of the electrochemical reaction.<sup>44</sup> Lower overpotential and higher ECSA favor reduced energy consumption and improved performance. Exchange current density, and Tafel slope, the reaction's kinetic activity. Faradaic efficiency measures the selectivity of the desired product. Researchers must consider the interdependence of these parameters and their experimental complexities while optimizing electrochemical processes. We will discuss all the parameters as given below-

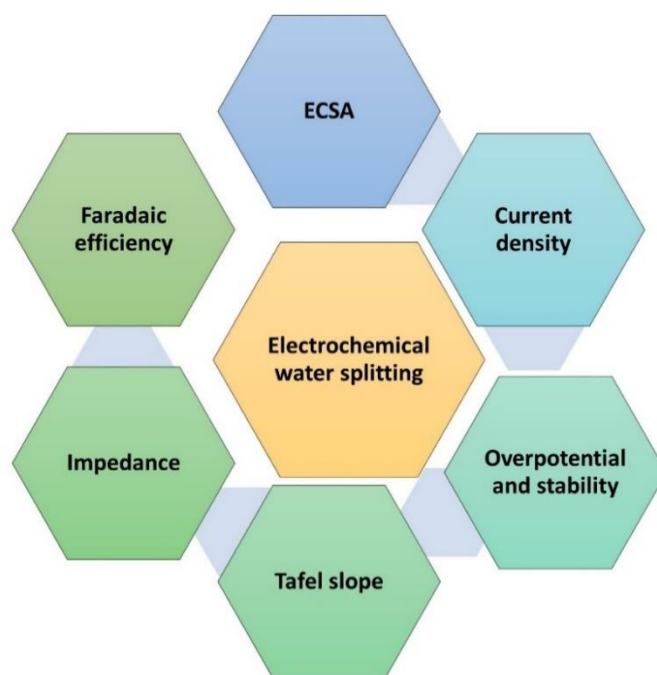


**Figure 1.13:** Diagrammatic scheme of parameters for evaluation of electrochemical reaction.

#### 1.4.1 Overpotential

In electrochemical water splitting, overpotential (symbolized as the  $\eta$ ) represents the additional potential needed to reduce the intrinsic kinetic hindrance during both the HER and OER. The thermodynamic potentials for HER and OER are 0 V and 1.23 V *vs.* NHE, respectively, the overpotential at the desired current density without  $iR$  compensation. In commercial water electrolysis, the electrochemical setup operates at a constant cell voltage, typically ranging from

1.6 V to 2.0 V, depending on the electrocatalyst for HER and OER and the electrolyte pH. The standard for comparing HER and OER electrocatalysts is a current density of 10 mA/cm<sup>2</sup> under different pH conditions. The origin of the overpotential ( $\eta$ ) at 10 mA/cm<sup>2</sup> in the context of solar-to-fuel (STF) energy conversion devices is related to measuring the cell potential at this specific current density to evaluate the efficiency of the STF device. However, using the same overpotential benchmark for assessing an electrocatalyst that catalyzes a half-cell reaction (either HER or OER) independently may not be entirely appropriate. The STF device converts solar energy into fuel, where multiple electrochemical reactions occur at different interfaces. In contrast, the half-cell reaction focuses solely on one of the reactions (HER or OER). Therefore, the overpotential requirements and performance criteria may differ between the two scenarios, and a direct comparison of overpotentials in these contexts might not provide a comprehensive understanding of the catalyst's efficiency for a specific application.<sup>46</sup>

In electrochemical water splitting, various overpotentials affect the reaction kinetics and efficiency. Concentration overpotential arises from differences in ion concentrations between the electrode surface and bulk solution and leads to decrement in concentration at the interfaces. Ohmic overpotential results from resistance within the electrochemical system, causing an additional voltage drop. Activation overpotential accounts for the activation energy needed for charge transfer at the reaction site. The total overpotential is the sum of these components, and understanding and minimizing these overpotentials are essential for optimizing the efficiency of water-splitting processes and improving overall system performance. Bubble overpotential arises when hydrogen or oxygen bubbles generated on the electrode's surface hinder the reaction. These bubbles can't be quickly removed from the electrolytic system, leading to a loss of effective active area for electrolysis and resulting in a high overpotential and ohmic voltage drop. The kinetic overpotentials of the HER and OER are related to the interfacial charge-transfer kinetics, and the exchange current density ( $j_0$ ) and the parameter 'a' determine the relationship between overpotential and current density. Kinetic overpotentials vary depending on the materials and the reaction conditions. Hence, for evaluating electrocatalysts in HER and OER, the overpotential at a fixed current density (e.g., 10 mA/cm<sup>2</sup>) or higher current densities (e.g., 50 mA/cm<sup>2</sup> and 100 mA/cm<sup>2</sup>) are considered as quantitative parameters. Additionally, the overpotential of a catalyst varies with different mass loading as it is mass dependent.<sup>59</sup>



### 1.4.2 Electrochemically accessible/active surface area (ECSA)

ECSA stands for electrochemically active surface area and is credited to represent the actual surface area of the catalyst exposed to the electrolyte rather than the geometrical surface area. This distinction is crucial because electrochemical reactions take place on the surface to contact with the electrolyte. The BET surface area normalized activity has lost ground to the ECSA normalized activity, mostly because the former may offer a more precise evaluation of the catalytic characteristics of electrochemical materials. The ECSA normalized activity, also known as  $j_{ECSA}$ , is a more useful metric for comparing different kinds of catalysts since it accounts for variations in electrocatalyst size, shape, morphology, topography, and porosity. It is a crucial metric that seeks to demonstrate the electrocatalysts' inherent catalytic qualities. However, quantifying ECSA is not without its difficulties. There are various ways to calculate ECSA, but the catalyst's physicochemical characteristics influence which approach is used. When employing multiple methods to get the same material, this can result in differences in the ECSA values. This can lead to inconsistencies in ECSA values obtained for the same material when using different methods, affecting the reproducibility of results.<sup>46, 60</sup>

Due to the difficulties in accurately determining ECSA and the need for consistent measurements, the utilization of ECSA-normalized activity is still a subject of argument within the scientific community. Consequently, only a limited number of researchers currently employ this parameter for evaluating catalysts performance in water splitting reaction. Furthermore, the significant variations in ECSA values obtained using different measurement techniques make it challenging to recommend ECSA-normalized activity as an essential activity parameter for electrocatalytic water-splitting. Despite these drawbacks, some researchers may choose to measure ECSA with other activity parameters if they believe it could provide valuable insights and complement their evaluations.<sup>60</sup>

### 1.4.3 Tafel slope

Tafel slope is a vital parameter to forecast the nature of the kinetics of an electrolytic reaction at the catalytic interface.<sup>46</sup> The Butler-Volmer equation describe the relationship between current ( $I$ ) and overpotential ( $\eta$ ) at the electrolyte interface is given as-

$$I = I_0 \times [\exp(aAnF/RT \times \eta) - \exp(-aCnF/RT \times \eta)] \quad (4)$$

$I$  is the current at particular overpotential,  $I_0$  is the exchange current at equilibrium potential,  $n$  is the number of electrons transferred,  $R$  is the ideal gas constant,  $F$  is the Faraday constant, and  $a_A$  and  $a_C$  are charge transfer coefficients at the anodic and cathodic reaction,  $T$  is the absolute temperature in K, and  $\eta$  is the overpotential. At equilibrium conditions, where there is no net current flow, then the anodic and cathodic terms in the Butler-Volmer equation cancel each other, and the observed current ( $I$ ) is equal to the exchange current ( $I_0$ ).

In the Tafel analysis, we assume that the electrochemical reaction is dominated by either the cathodic or the anodic process at a time (high overpotential approximation). Based on this, we can derive the Tafel equations for the cathodic and anodic polarizations separately. For the cathodic Tafel equation, when the cathodic reaction dominates (high overpotential on the cathodic side), the anodic term can be neglected, and the Butler-Volmer equation reduces to:

$$I = I_0 \times \exp(-aCnF/RT \times \eta) \quad (5)$$

Similarly, for the anodic Tafel equation, when the anodic reaction dominates (high overpotential on the anodic side), the cathodic term can be neglected, and the Butler-Volmer equation reduces to:

$$I = I_0 \times \exp(aAnF/RT \times \eta) \quad (6)$$

By measuring the current ( $I$ ) at different overpotentials ( $\eta$ ) during electrocatalysis, researchers can plot Tafel curves for both cathodic and anodic processes. The Tafel slopes obtained from these curves provide valuable information about the inherent kinetics of the electrocatalytic reaction. The expression gives the Tafel slope:

$$\text{Tafel slope } (b) = (RT) / (nF) \times (1 / a) \quad (7)$$

Where “ $a$ ” is the charge transfer coefficient of the dominant reaction.

The Tafel slope can give insights into the reaction mechanism and the RDS in the electrocatalytic process. Steeper Tafel slopes indicate a faster RDS and a more efficient electrocatalyst. By studying the Tafel slopes obtained from Tafel curves, researchers can semi-quantitatively predict the relative rate of electrochemical processes. Specifically, for the HER, a low Tafel slope (around 30 to 40 mV /dec) indicates a faster and more efficient Tafel pathway, which involves adsorption and electrochemical discharge of protons on adjacent active sites, leading to the evolution of  $H_2$ . This describes the reaction V-T mechanism. This process is favored in electrocatalytic interfaces rich in electroactive sites exposed to the electrolyte, when many adjacent active sites are available. Material like Pt follows this pathway in an acidic medium. In

contrast, non-noble metal HER electrocatalysts, such as iron (Fe), cobalt (Co), nickel (Ni), tungsten (W), and molybdenum (Mo), chalcogenides commonly follow the V-H mechanism, which involves additional adsorption and electrochemical discharge. In alkaline conditions, the mechanism of HER is more complicated compared to acidic conditions. This is because there is no free H in a solution in alkaline medium for instant adsorption and discharge. Instead, protons must be generated through the oxidation of H<sub>2</sub>O or OH<sup>-</sup> at the anode, which requires extra work to be accomplished on the cathode, leading to a more sluggish HER process.<sup>47</sup>

OER involves the generation of oxygen from water or hydroxide ions at the anode. The complexity of the reaction makes it more challenging to directly relate the Tafel slope to the reaction mechanism. OER can proceed through different pathways with several intermediate steps, and the rate-determining step can vary based on the catalyst and the conditions. However, it is still possible to gain some understanding of the OER mechanism using the Tafel slope. By deducting the number of e<sup>-</sup> transferred during OER from the Tafel slope values, researchers can partially predict the mechanism. For instance, a Tafel slope around 30 mV/dec suggests a four-electron transfer pathway, as observed with iridium dioxide (IrO<sub>2</sub>) and ruthenium dioxide (RuO<sub>2</sub>). On the other hand, Tafel slopes between 60 and 120 mV/dec indicate a two-electron transfer pathway, characteristic of iron group metal oxides/hydroxides like Fe, Co, and Ni in alkaline conditions.<sup>47</sup>

### 1.4.4 Faradaic efficiency

The Faradaic efficiency (FE) is used to show the selectivity of catalysts for HER and OER. Selectivity is an important aspect of electrocatalysis. Through an experiment, the evaluated amount of evolved gas is compared to the amount of gas calculated using Faraday's equations of electrolysis to determine FE.<sup>46</sup> Gas chromatography (GC) and the conventional water-gas displacement method are the two widely used techniques for determining FE. The traditional method involves dispensing the water-gas method, which collects the gas produced inside a graduated cylindrical measuring jar. Avogadro's principle is then used to convert the volume of the collected gas into moles, and Faraday's second rule of electrolysis is used to calculate the number of moles of gas molecules based on the charge transmitted when the volumes that are computed and collected line up, the catalyst is said to have 100% Faradaic efficiency (FE), which indicates that it is very selective for the specific gas evolution reaction. Nevertheless, there may be practical problems when gathering evolved gases with the water-gas displacement approach.

As a result, the most extensively used technique for determining the amount of evolved gas is GC. With the use of GC, researchers may monitor the reaction course over time and gain knowledge about how the applied voltage affects the response rate. When the catalyst experiences large surface alterations under applied voltage, which impacts FE, this approach becomes especially helpful. Recently, fluorescence spectroscopy has been used as an alternative to GC for measuring evolved gases electrolysis for both OER and HER during electrolysis. This technique allows accurate measurement of FE for electrocatalysts. For OER, another consistent electrochemical technique involves using the rotating ring-disk electrode (RRDE) setup. FE is independent of the size, shape, and morphology of the catalyst, making it a valuable metric for comparing catalysts. Providing FE along with other activity parameters is essential when screening or evaluating electrocatalysts for water splitting or other electrochemical processes.<sup>61</sup>

### 1.4.5 Electrochemical stability

One important factor that establishes its potential for large-scale commercial operations is its electrochemical stability, which is assessed by analyzing its activity over an extended period of time. Two methods that are frequently used to investigate the stability of HER and OER catalysts are prolonged potentiostat electrolysis measurements (or chronoamperometry), CV and LSV at faster scan rates, also referred to as accelerated deterioration testing. In HER, the polarization curve begins at 0 V vs. NHE, allowing the catalyst to go through millions of cycles. An electrocatalyst's stability is indicated by the shift in both the onset potential and overpotential at a specific current density of 10 mA/cm<sup>2</sup>. A constant current density such as 10, 50, or 100 mA/cm<sup>2</sup> sustained for more than 12 hours in chronoamperometric measurements, or a small increase in overpotential at a current density of 10 mA/cm<sup>2</sup> for more than 12 hours, is another commonly accepted criterion for assessing stability. Stabilizing the electrocatalyst under investigation is influenced by several variables, including the substrate, the electrode being utilized, and the catalyst fixation technique. In general, evaluating an electrocatalyst's stability is essential to figuring out whether it can be used in large-scale water splitting or other electrochemical processes.

### 1.4.6 Impedance

Electrochemical impedance spectroscopy (EIS) is a useful technique for determining the electrochemical properties of catalysts, surfaces, interfaces, coatings, and other materials. Its use

in a wide range of energy research disciplines has become indispensable, particularly in areas where performance is dependent on parameters such as current, potential, and charge. One such field is electrocatalytic water splitting, which aims to produce high-purity hydrogen. EIS plays a critical role here by allowing the correlation of activity trends via the measurement of charge transfer resistance ( $R_{CT}$ ). The charge transfer process, in particular, governs the kinetics of these processes (HER and OER). As a result, Warburg's impedance makes no substantial impact in these circumstances. Under these conditions, the investigated interface is analogous to a simplified Randle's cell (Inset figure 1.14), especially if the substrate electrode plays no significant role in the ongoing electrocatalytic activity. Impedance spectroscopy is a widely used technique for measuring the impedance of an electrochemical system. The technique involves applying a small AC voltage or current to the system and measuring the resulting AC response. The measured impedance is then used to extract information about the electrochemical properties of the system, such as the charge transfer resistance, the double-layer capacitance, and the solution resistance.<sup>46</sup>

The resulting Nyquist plot has a distinct shape, like a depressed semi-circle, as shown in Figure 1.14. A solution resistance ( $R_S$ ) and a charge-transfer resistance ( $R_{CT}$ ) are connected in series in this scenario, with a Constant Phase Element (CPE) connected in parallel to  $R_{CT}$ . As previously stated, at high frequencies, the CPE's contribution is insignificant, operating as a short circuit, and its impedance is substantially lower than  $R_S$ . This means that under these conditions,  $R_S$  controls the charge transfer process primarily, and the measured impedance effectively represents  $R_S$ . At low frequencies, however, the CPE acts as an open circuit, which is effectively erased by  $R_{CT}$ . In this case, the charge transfer inside the circuit is solely determined by the series-connected impedances  $R_S$  and  $R_{CT}$ . As a result, by adding the real components of impedances at both high and low frequencies, the total impedance of the interface may be calculated. Similarly,  $R_{CT}$  can be calculated by subtracting  $R_S$  from total impedance. These  $R_{CT}$  values form the basis for making valid comparisons between different electrocatalysts, allowing for an assessment of their activity trends.<sup>60</sup>

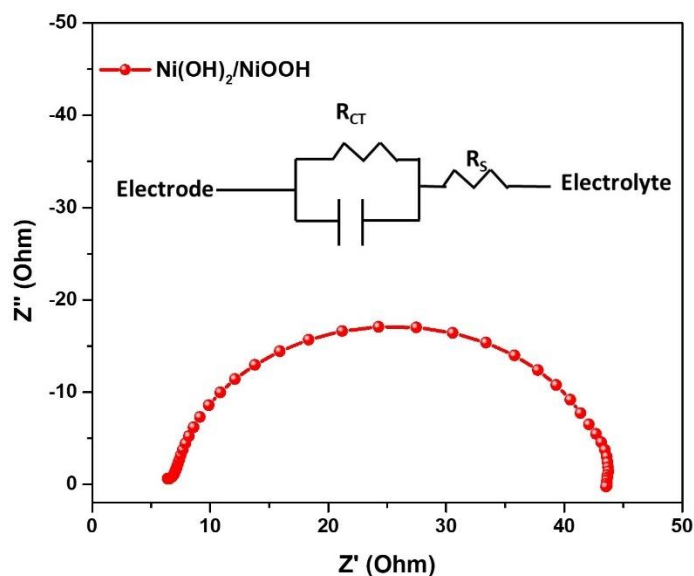


**Figure 1.14:** Impedance plot of one of the developed samples showing semicircle. Inset of Figure 1.14 is the Randles circuit.

## 1.5 Transition metal chalcogenides as an important candidate for water splitting

There is one chalcogen element and one transition metal atom at least in transition metal chalcogenide nanomaterials. Group 16 elements are referred to as chalcogen elements in the periodic table. Transition metal chalcogenides come in a variety of forms and compositions, including  $\text{Co}_3\text{O}_4$ ,  $\text{Fe}_2\text{O}_3$ ,  $\text{NiO}$ ,  $\text{TiO}_2$ ,  $\text{ZnO}$ ,  $\text{NiCo}_2\text{O}_4$ ,  $\text{MoS}_2$ ,  $\text{WSe}_2$ , and others.<sup>62</sup> Transition metal chalcogenides, with their superior properties (chemical, electrical, physical, and magnetic) over bulk materials, have a significant role to play in fundamental science and practical applications (Figure 1.15). Electrochemical water splitting for  $\text{H}_2$  production offers a cleaner and more sustainable alternative, as it utilizes water as both the starting material and the byproduct in the hydrogen economy cycle, where the combustion of  $\text{H}_2$  regenerates water. Noble-metal-based catalysts, such as Pt,  $\text{IrO}_2$ , and  $\text{RuO}_2$ , have historically been regarded as the most efficient water-splitting catalysts. However, their exorbitant cost and scarcity prevent widespread usage. As a result, there is an urgent demand for low-cost, earth-abundant, and highly active non-noble-metal-based catalysts to enable sustainable energy conversion. A great deal of work has gone into

creating non-noble-metal-based electrocatalysts, mostly concentrating on transition metal-based chalcogenides (TMCs) that are common in the earth, such as phosphides, carbides, nitrides, oxides, hydroxides, and more. TMCs are one of these materials that have attracted a lot of interest because of their exceptional catalytic activity, distinct electrical characteristics, and structural arrangements. TMCs are adaptable for a variety of applications due to their broad spectrum of electrical properties, which include those of metals, semiconductors, and insulators. Furthermore, TMCs can exist in a variety of phases, including rhombohedral, hexagonal, or trigonal, and under some circumstances, they can undergo phase transitions that present new possibilities for electrocatalysis. The edges of 2D TMC nanosheets have been found to exhibit remarkable electrocatalytic activity, acting as HER active sites. However, despite their promise, TMC-based electrocatalysts face challenges related to low electrical conductivity, poor stability, aggregation, and unfavorable water adsorption and dissociation abilities.<sup>63-64</sup>

Energy demand is expected to increase from 16 terawatts (TW) in 2010 to 30 TW by 2050. Currently, traditional fossil resources such as oil, coal, and gas account for 77% of global energy consumption, while renewable energy sources such as solar, wind, and hydroelectric power account for only 23% of energy consumption in 2024. This high reliance on fossil fuels depletes scarce resources while also contributing to environmental issues such as global warming. To solve these issues, the development of sustainable and renewable energy sources has become critical in order to combat environmental deterioration and ensure long-term development. Hydrogen has emerged as a possible replacement to fossil fuels as a clean, zero-carbon energy transporter with high energy density. Unfortunately, the majority of H<sub>2</sub> is now produced by steam reforming of fossil fuels, which is inefficient and emits CO<sub>2</sub>, aggravating global warming. Elemental hydrogen is typically found in the gaseous form as molecular hydrogen. It is a colorless, odorless, non-toxic, and lightweight gas. When uncompressed, hydrogen occupies a large volume of 11250 L/Kg at room temperature. However, when subjected to high pressure, around 35.5 MPa or 350 atm, its volume is greatly reduced to 56 L/Kg. H<sub>2</sub> undergoes liquefaction at an extremely low temperature of 20 K (-253 °C), and in its liquid state, it occupies a much smaller volume of only 14.1 L/kg. This property of hydrogen makes it a highly efficient carrier of energy, with a high energy density of 120 MJ/Kg, significantly surpassing gasoline, which has an energy density of 44.4 MJ/Kg. Furthermore, the anticipated cost of green hydrogen is projected to be in the range of INR 75-150 per kilogram, which is competitive with the prices of existing fossil fuels. This indicates that

hydrogen has the potential to serve as a cost-effective and environmentally friendly alternative to traditional fuels.<sup>65</sup>

Numerous strategies have been developed to enhance the electrocatalytic activity of TMCs, broadly categorized as increasing the number of active sites through structural engineering or increasing the intrinsic activity of each active site through electronic structure regulation. The latter approach involves modifying the electronic properties of TMCs to optimize their catalytic performance, particularly by tuning the energy band structure and electron distribution. Increasing the intrinsic activity leads to significant improvements in electrode activity while mitigating mass/charge transport issues. The adsorption strength of intermediates plays a pivotal role in reaction kinetics, with the Gibbs free energy for intermediate adsorption serving as a crucial parameter to explain catalytic behavior. The relationship between electronic structure regulation and electrochemical performance provides valuable insights for designing highly efficient electrocatalysts for water splitting. Recently, Ni-based materials have been especially attractive among transition metals due to their versatile chemical activity, corrosive resistance, crystal and electronic structure types, redox behavior, and thermodynamic stability. However, single type Ni-based electrocatalysts experience insufficient active sites, low intrinsic activity, and stability as bifunctional catalysts in an alkaline medium. Researchers continuously try to improve Ni-based material's electrochemical performance by following different strategies such as morphology tuning, doping, structural engineering, creating defects, and regulating electronic properties. Therefore, designing a bifunctional nickel-based electrocatalyst is more appealing for practical and business aspects.<sup>66</sup>

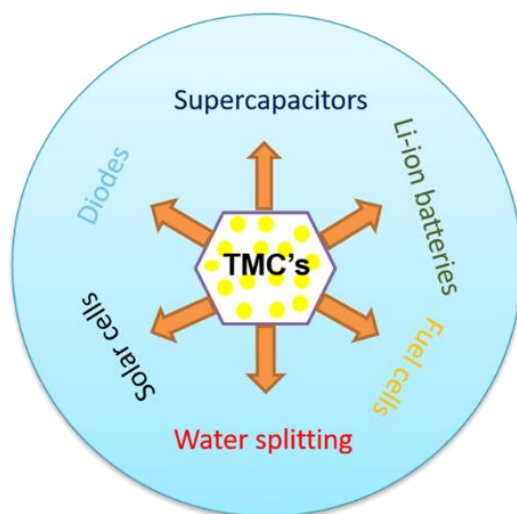


**Figure 1.15:** Schematic presentation of transition metal chalcogenides in various field



### 1.6 Important strategies to enhance electrocatalytic activity

Electrocatalytic water splitting is a promising process for generating hydrogen fuel and oxygen using electricity. Enhancing the electrocatalytic water-splitting activity can improve the efficiency of this process. Here are some different strategies to enhance electrocatalytic water-splitting activity:

#### 1.6.1 Morphology

##### 1.6.1.1 1D nanomaterial

1D structures, like nanowires (NWs) and nanotubes (NTs), offer distinct advantages due to their anisotropic nature, unique structure, and surface properties compared to their nanoparticle counterparts. These attributes hold significant promise for enhancing both the activity and stability of water-splitting processes. Specifically, 1D nanomaterials have fewer lattice boundaries, facilitating electron and mass transport. They also feature longer stretches of smooth crystal planes along specific crystal surfaces and offer control over surface defect sites.<sup>67</sup>

Several investigations have shown that Pt-based nanowires have superior electrocatalytic activity. However, their prohibitively high cost has hindered their widespread use. As a result, there is an increasing need to create novel, plentiful, non-precious nanomaterials with higher electrocatalytic activity to replace Pt-based materials. Cost-effective, inherently anisotropic metal-based 1D nanostructures with increased activity have recently been manufactured in nanotechnology. Arrays of 1D nanowires on carbon fiber paper, nickel foam (NF), copper foam, and other conductive materials, for example, not only retain the distinctive features of nanowires but also display improved conductivity. As a result, they can be used as self-supporting electrodes without the usage of additional conducting polymers such as Nafion or carbon black. Furthermore, these materials aid in the prevention of corrosion and are extremely durable for water splitting. Herein, for all the materials, we have used carbon cloth as a substrate for the synthesis of a binder-free catalyst.<sup>68</sup>

Sancho and co-workers<sup>69</sup> reported NiCo<sub>2</sub>Se<sub>4</sub> nanowires (Figure 1.16a) as a promising electrocatalyst for OER. The nanowire morphology increases the material's electrochemically active surface area and porosity, which leads to better activity. Recently, Wang and co-workers<sup>70</sup> reported a phosphorous-doped NiCo<sub>2</sub>Se<sub>4</sub> nanoneedle (Figure 1.16b) array for efficient HER

activity in different pH mediums. P doped  $\text{NiCo}_2\text{Se}_4$  electrocatalyst fabricated on carbon fiber paper shows outstanding HER performance with low overpotentials of 33, 57, and 69 mV in acidic, alkaline, and neutral medium, respectively, to achieve  $10 \text{ mA/cm}^2$  current density. They have done DFT studies also to know the atomic level modulation and prove that P doping can optimize the charge densities in metallic and non-metallic centers of  $\text{NiCo}_2\text{Se}_4$ , improving the electrocatalytic HER activity. Xia and their research team<sup>71</sup> synthesized metallic  $(\text{Ni, Co})_{0.85}\text{Se}$  nanotube arrays (Figure 1.16c), boasting a distinctive structure and an exceptionally high number of defect sites. These nanotube arrays demonstrated superior activity and stability in the OER when compared to pure  $\text{Co}_{0.85}\text{Se}$ . Our group also developed  $\text{NiCo}_2\text{Se}_4$  and Fe-doped  $\text{NiCo}_2\text{Se}_4$  nanorod array for electrochemical water splitting.

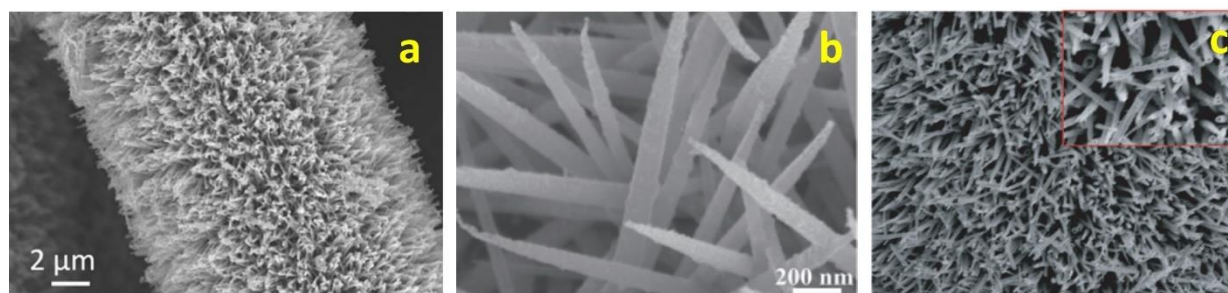


**Figure 1.16:** FESEM image representing 1D nanostructure of (a)  $\text{NiCo}_2\text{Se}_4$  (b) P doped  $\text{NiCo}_2\text{Se}_4$  (c)  $(\text{NiCo})_{0.85}\text{Se}$  [Ref. 69, 70, and 71].

### 1.6.1.2 2D nanomaterial

In recent years, 2D nanosheets, especially ultrathin 2D nanostructures, have gained significant attention across various fields, including catalysis, optics, and electronics. There are several key advantages associated with the use of 2D nanomaterials in water-splitting applications. First, 2D nanocrystals, particularly ultrathin ones, expose a greater number of active sites, leading to improved catalytic activity. Second, the strong coupling between atoms in both the in-plane and out-of-plane directions within 2D nanostructures results in unique electrical performance, which plays a crucial role in electrocatalysis. Third, 2D nanomaterials, with their ultrahigh specific surface area, provide abundant sites for the adsorption of active species involved in electrocatalytic reactions.<sup>72</sup>

The 2D nanocrystals obtained through methods like liquid exfoliation often possess a high density of defects, including vacancies, lattice disorder, and distortion. These defects, especially

when prepared by liquid exfoliation, can serve as additional active sites for various catalytic processes. Furthermore, surface functionalization offers a straightforward approach to fabricating catalysts based on 2D nanostructure. The unique properties of doped 2D nanostructure underscore the importance of careful characterization techniques to understand better and utilize their potential in diverse applications. For example, Cui *et al.*<sup>73</sup> have developed nickel doped CoS<sub>2</sub> thin nanosheets as a productive electrocatalyst through simple hydrothermal technique (Figure 1.17a). After the incorporation of 10% wt. Ni in CoS<sub>2</sub> material, the bimetal catalyst displays the best activity with a smaller overpotential of 156 mV and a lower Tafel slope of 52 mVdec<sup>-1</sup> as well as stability of 3000 cycles in acidic conditions. The favorable kinetics and energetics for hydrogen adsorption and desorption contribute to the excellent HER activity. Co-doped NiSe<sub>2</sub> supported on Ni foam was developed by Liu and co-workers.<sup>74</sup> Novel 3D mesoporous nanosheets of Co-doped NiSe<sub>2</sub> (Figure 1.17b) show the best activity in all pH medium, after optimum doping of Co. The same group has shown both theoretically and experimentally that the doped catalyst is durable for HER with peculiar morphology and electronic structure. Recently, M. Basu *et al.*<sup>75</sup> have reported iron-doped Ni(OH)<sub>2</sub>/NiOOH (Figure 1.17c) electrocatalyst on carbon cloth through a simple hydrothermal technique; the optimum ratio was obtained through ratio variation. They have shown that after doping with Fe, tuning in morphology, high electronic conductivity, and strain in the system originated. Iron behaves as a strong Lewis acid in the system, which can accommodate electron density from Nickel and enhances the O<sub>2</sub> evolution in alkaline medium. Our group also developed Ni/Ni(OH)<sub>2</sub>/NiOOH nano worm, W doped Ni(OH)<sub>2</sub>/NiOOH nanosheets, CuCoS nanosheets, Ce doped Ni<sub>0.85</sub>Se nanosheets, and Cu and V doped MoS<sub>2</sub> nanosheets for electrocatalytic water splitting.<sup>76-77</sup>

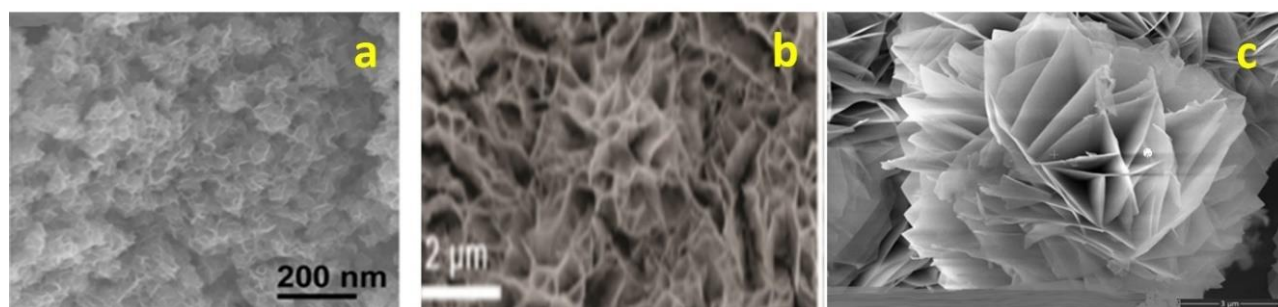


**Figure 1.17:** FESEM image of (a) Ni doped ultrathin CoS<sub>2</sub>, (b) Mesoporous Co doped NiSe<sub>2</sub> nanosheets, (c) Fe-doped Ni(OH)<sub>2</sub>/NiOOH nanoflower[Ref. 72, 73, and 74].

### 1.6.1.2 3D nanomaterial

3D Materials with mesoporous and hollow structures have shown great potential in various fields, as they facilitate several essential processes such as providing active sites, adsorbing intermediates, and storing and releasing gases. When these 3D nanostructures are employed in electrocatalysis, they significantly enhance the efficiency of the reaction. This enhancement is achieved through several mechanisms, including increasing the contact surface area, reducing electron transfer resistance, creating more active sites, and facilitating the connection between the electrolyte and catalysts. Moreover, the presence of mesoporous and hollow structures further benefits electrocatalysis by promoting the efficient release of evolved gases, leading to improved catalytic performance. For instance, Gong and group<sup>78</sup> reported 3D electrode pair of NiCoS/NiCoP (Figure 1.18a) as good electrocatalyst for water splitting, the nano brush structure of the developed is beneficial for exposed area and active sites. This cell requires 1.57 V to obtain 20 mA/cm<sup>2</sup> current density as electrolyze in alkaline medium. The crystal-plane-dependent electrocatalytic activity of NiCo<sub>2</sub>O<sub>4</sub> crystals was examined by Fang and colleagues.<sup>79</sup> In a 1.0 M KOH solution, the overpotential of the NiCo<sub>2</sub>O<sub>4</sub> octahedron (Figure 1.18b) with exposed (110) and (111) crystal surfaces is 330 mV at 5 mA/cm<sup>2</sup> for the OER and 157 mV at 5 mA/cm<sup>2</sup> for the HER.

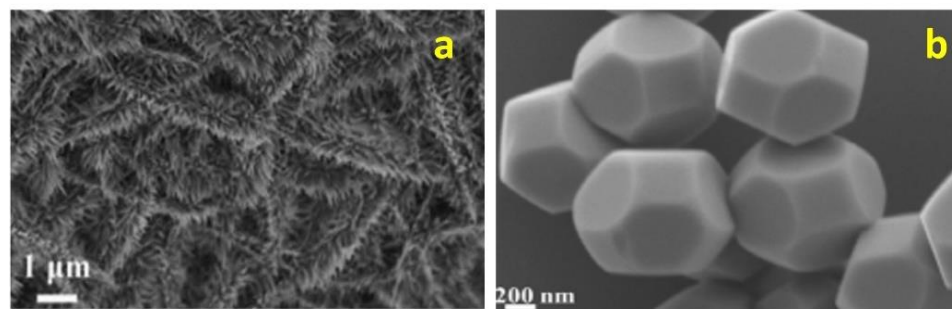


**Figure 1.18:** 3D nanostructure of (a) NiCoS/NiCoP electrode (b) NiCo<sub>2</sub>O<sub>4</sub> octahedron [Ref. 77, and 78].

### 1.6.2 Structure

#### 1.6.2.1 Phase change

Nanomaterial features such as conductivity, surface adsorption energy, energy band structure, and others can vary rapidly as crystal phases change. This process may result in unanticipated increases in electrocatalytic activity. Metal chalcogenides, with their various atomic and electronic structures, enable the fabrication of materials with a variety of crystal phases. Materials based on MoS<sub>2</sub> or WS<sub>2</sub>, for example, often exhibit two phases: the semiconducting trigonal prismatic phase (2H) and the metallic octahedral phase (1T).<sup>80-81</sup> It is quite simple to transition from the 2H phase to the 1T phase using phase-transformation procedures. This phase change increases electron density in the d orbitals, which enhances electrocatalytic activity. Liang and their team<sup>82</sup> reported on the orthorhombic-CoSe<sub>2</sub> and cubic-CoSe<sub>2</sub> structures. The lengths of the Co-Se bonds in these materials vary, resulting in varying free adsorption energies for both hydrogen atoms (H<sub>ads</sub>) and water molecules. Notably, the cubic-CoSe<sub>2</sub> structure has much higher activity than the orthorhombic-CoSe<sub>2</sub>. According to experimental data and density functional theory (DFT) calculations, cubic-CoSe<sub>2</sub> has greater electrical conductivity, optimized adsorption energy, and increased hydrogen generation efficiency. This illustrates that creating active electrocatalysts via phase-transformation engineering is a highly efficient approach.

#### 1.6.2.2 High index crystal face

A high density of atomic steps, ledges, and kinks is generally present in high-index planar nanocrystals, and these can behave as very active sites for a variety of catalytic, energy conversion, and other chemical events. Thus, the synthesis of high-index nanocrystals offers a viable route towards the production of extremely efficient next-generation nanocatalysts. Shape-controlled syntheses can produce these unique high-index aspects. It is critical to remember that high-index facets are not fundamentally stable and can change and vanish quickly during synthesis or in reaction conditions due to their high surface energy. To make extremely effective electrocatalysts, high-index faceted nanosheets with abundant of active sites and great structural stability are required.<sup>83</sup>

#### 1.6.2.3 Amorphous structure

Unlike crystalline nanoparticles, amorphous materials have attracted a lot of attention from a variety of industries. Amorphous materials only exhibit short-range order across a small number of atoms, in contrast to crystalline solids, which display long-range atomic order. Amorphous materials also possess special qualities like a large number of flaws, metastability, and isotropic qualities (such as soft magnetic, mechanical, corrosion-resistant, electrical, and catalytic qualities). Despite their intriguing features, amorphous nanomaterials require further exploration. This is due to amorphous materials' extraordinarily intricate internal structure, which makes it difficult to develop a complete model or systematic theory that can appropriately represent or describe them. Nonetheless, the less studied amorphous materials are, the more intriguing they become to researchers. Significant efforts have also been made to investigate the local atomic environment and ion transport in amorphous materials.<sup>84</sup>

### 1.6.3 Electronic structure

#### 1.6.3.1 Chemical Doping

Chemical doping has been demonstrated as an effective method to improve electrocatalytic performance via multiple mechanisms in the electrochemical reaction. The interest in doped nanoscale materials as catalysts originates from the fact that these particles display better electrocatalytic activity due to more active sites, chemical stability compared to bare nanomaterial. Chemical doping has proven a significant role in optimizing the morphology, crystal structure, and hydrogen adsorption Gibbs free energy, which plays a dynamic role in enhancing the activity. Transition metal-based electrocatalysts behave like a noble metal substitute and show excellent activity both for cathodic and anodic electrocatalytic reaction. Among them, various elements based doping materials, for example, transition metals of 3d, 4d and 5d in the periodic table and their chalcogenides, phosphides, nitrides, carbides, and other molecular subordinates have been investigated even though their erosion susceptibility to acidic or basic electrolytes, show better electrocatalytic performance. After doping, these materials exhibit activity comparable to the state-of-the-art metals, such as Pt, Pd and RuO<sub>2</sub> materials. Chemical doping in materials with foreign atoms is also an impressive method to manipulate surface chemistry, morphology, modify the elemental composition, and to tailor the electronic properties of host materials. Common dopants used in water splitting catalysts include transition metals (e.g., Fe, Co, Ni), non-metal elements

(e.g., N, P, S), and even heteroatoms like carbon. The choice of dopant and the doping method are critical in tailoring the properties of the catalyst to improve its performance in water splitting. Researchers continue to explore and develop new doping strategies to create more efficient and cost-effective catalysts for this sustainable energy conversion process.<sup>85-86</sup>

### 1.6.3.1.1 Anion doping

Researchers have focused on heteroatom-based (N, P, S, and Se) doping in transition metal electrocatalysts to catalyze the water-splitting reaction. This approach has demonstrated significant improvements in electrocatalytic performance by increasing the number of active sites and modifying the electronic and catalytic properties of the materials. Heteroatom doping involves the introduction of electronegative atoms, which leads to charge reorganization and changes in the material's electronic and catalytic properties. Importantly, the intrinsic properties of the host material can be retained even after heteroatom doping. For example, Ouyang and co-workers<sup>87</sup> have reported P doped CoS<sub>2</sub> nanosheets for the hydrogen evolution reaction as an advanced electrocatalyst. They have emphasized that after phosphorous doping surface morphology of CoS<sub>2</sub> was tuned uniformly on the surface of carbon fiber, erected structure of P doped CoS<sub>2</sub> could be more attainable by the electrolyte at the same time as water electrolysis. After P-doping, the enhanced charge transfer and promoted proton adsorption efficiently increase the kinetics of HER. The Ni-Co based catalyst (NiCo<sub>2</sub>S<sub>4</sub>) shows higher activity due to active redox couple of Co<sup>+3/+2</sup> and Ni<sup>+2/+3</sup>, which are effective centres for overall water splitting reaction but the high value of overpotential, onset potential, and inferior stability suppress the role in the water-splitting reaction. So, to overcome this problem, F. Li *et al.*<sup>88</sup> have reported nitrogen-doped Ni-Co based sulphide hollow nanotubes with carbon layer coating by following a simple solvothermal method, after doping hollow nanotube's structure not only maximize the number of active sites but also sheltered from electrolyte deterioration to upgrade the durability for electrolysis. The integrated catalyst exhibited low overpotential of 295 and 330 mV to generate 100 mA/cm<sup>2</sup> for HER and OER, respectively. Recently, in 2019 Z. Shao *et al.*<sup>89</sup> have synthesized heteroatom doped with oxygen vacancies in nitride and phosphide hybrid of Ni-Co for boosting OER. The remarkable performance of catalyst devoted to the particular heterojunction, available active sites and sufficient oxygen vacancies due to which charge transport increases and release O<sub>2</sub> bubble, that makes catalyst to achieve low value of 41 mV dec<sup>-1</sup> Tafel slope and an overpotential of 290 mV

in 1.0 M KOH, superior to the commercial IrO<sub>2</sub> catalyst. Nitrogen dopant in tungsten carbide nanoarray was developed by Han and co-workers,<sup>90</sup> it behaves as good bifunctional electrocatalyst for water splitting in acidic medium. They have claimed that HER kinetics increased through N-doping, which modulated the surface energy level to revise hydrogen binding sites. After doping, not only active sites were increasing, but there is a formation of a superaerophobic interface under water that leads to weaker bubble adhesion that favors more gas evolution. Because of N-doping surface morphology was maintained except the nanoarray become thinner as N can easily replace oxygen without any disturbance in the system.

### 1.6.3.1.2 Cation doping

Water splitting reaction can also be promoted through metallic (Fe<sup>+2/+3</sup>, W<sup>+6</sup>, Co<sup>+2/+3</sup>, Ni<sup>+2/+3</sup>, Ce<sup>+4</sup>, and Mo<sup>+6</sup>, etc.) doping in transition metal electrocatalysts. Due to vacant/filled d-orbitals, metal can accept or donate the electrons to the system that make feasible adsorption or desorption of gaseous products, which can faster the reaction kinetics. Doped transition metal chalcogenides can be developed from various synthetic routes with different morphology, which give insight into the advancement of these material. Tungsten-doped CoP nanoneedles array was developed on carbon cloth as a bifunctional electrocatalyst by Ren and co-workers.<sup>91</sup> The catalyst performed high activity and stability in acidic as well as in the alkaline medium. Theoretical (DFT calculations) results also prove W doped CoP as a promising catalyst because doping increases and optimizes the water and hydrogen adsorption energy, respectively. The synthesized W/CoP electrode exhibits low overpotential (32 and 77 mV) with small Tafel slopes of 57 and 65 mVdec<sup>-1</sup> in acidic and alkaline medium, respectively. Two electrode systems were also established with the same material accomplishing a stable current density of 10 mA/cm<sup>2</sup> at a fixed potential of 1.59 V. Reducing the thickness of transition metal-based material nanosheets cation doping is a prominent way as reported in the literature. For example, Fei and co-workers<sup>92</sup> developed Fe-doped ultrathin Ni<sub>3</sub>S<sub>2</sub> nanosheets on Ni foam as a well active electrocatalyst towards alkaline HER. The experimental and theoretical evidence proves that Fe doping modulates the size of Ni<sub>3</sub>S<sub>2</sub> nanosheets and surface electron density, which really helps in boosting electrochemical active surface area for HER. The atomic force microscopy (AFM) confirms the size of the Fe<sub>0.9</sub>Ni<sub>2.1</sub>S<sub>2</sub> sample is around 5 nm; this ultrathin Ni<sub>3</sub>S<sub>2</sub> nanosheet could increase the system's conductivity. 2D nanosheets characterized by their substantial specific surface area, abundant active sites, and



excellent conductivity have been extensively documented as catalysts for the HER. Our group also reported cation ( $W^{6+}$ ,  $Fe^{3+}$ , and  $Co^{2+}$ ) doping on Ni-based nanomaterials for electrocatalytic water splitting.<sup>93-95</sup>

By introducing foreign cationic species into the crystal lattice, it becomes possible to fine-tune the electronic structure, enhance catalytic activity, and improve charge transport, making them well-suited for various aspects of the water-splitting process. Furthermore, cation doping can influence the material's structural stability, mechanical properties, and optical characteristics, offering opportunities for innovation in water-splitting applications, such as catalysis for the HER and OER, as well as photocatalytic water splitting. This strategy remains a focal point of research to create advanced materials with customized properties for more efficient and sustainable water splitting technologies.

### 1.6.3.2 Heterostructure formation

A successful strategy for synthesizing extremely active electrocatalysts is the formation of heterogeneous nanocrystals with highly active nanointerfaces. Metals and metal oxides, metal compounds, carbon materials, inorganic substances, and metal-organic frameworks (MOFs) can all be combined to create these nanointerfaces. A distinct and extremely active nanointerface is formed because of the electrical structure of these many components changing close to the nanointerface. The fabrication of these nanointerfaces leads to the optimization of crucial factors like charge transfer, adsorption energy, and active sites. As a result, the electrocatalytic performance is significantly enhanced. Recent research has demonstrated the pivotal role that nanointerfaces play in improving electrocatalysis, showcasing their importance in the development of highly efficient electrocatalytic materials.<sup>96</sup>

Enhancing the electronic structure and optimizing charge transport and mass transfer properties of heterostructures in catalytic processes can be achieved through chemical and physical modifications. This approach can lead to improved overall performance. For example, one effective method involves growing heterostructures on conductive substrates like nickel foam and carbon cloth, which serves to enhance their electrical conductivity. The modulation of surface electrons is closely associated with the transfer of charges across heterointerfaces within heterostructures, and this is influenced by the alignment of their band structures. Electron transfer occurs across the interface until the work function reaches equilibrium. For example, Huang *et*

*al.*<sup>97</sup> conducted a synthesis of Mo<sub>2</sub>C/VC nanoparticle-embedded 3D graphite carbon through a phase separation process. This material demonstrated the capability to achieve a current density of 10 mA/cm<sup>2</sup> for the HER at a low overpotential of 122 mV. Notably, it exhibited exceptional long-term durability, withstanding over 10,000 cycles. Sharma and group<sup>98</sup> synthesized MoS<sub>2</sub>/MoSe<sub>2</sub> as an HER electrocatalyst in wide pH range. The heterostructure composed of MoSe<sub>2</sub>-ts@MoS<sub>2</sub>-ts exhibits superior electrocatalytic efficiency and stability when compared to bare MoS<sub>2</sub> and MoSe<sub>2</sub> thin sheets. The formation of a heterojunction in MoSe<sub>2</sub>-ts/MoS<sub>2</sub>-ts leads to accelerated charge-carrier transport and provides a significantly larger and more active surface area for the adsorption and desorption of H<sup>+</sup> ions. MoSe<sub>2</sub>-ts/MoS<sub>2</sub>-ts has an overpotential of -0.186 V vs. RHE with a low Tafel value of 71 mV/decade. Our group also developed Ni/Ni(OH)<sub>2</sub>/NiOOH electrodeposited sample on carbon cloth for better HER performance.<sup>68</sup>

### 1.7 Doping of transition metal ions in Nickel-based electrocatalyst

To date, the utilization of Ni-based materials has garnered significant attention due to their widespread availability and promising electrochemical efficiency. Notably, researchers have extensively explored Ni-based catalysts featuring heterogeneous nanostructures. Various Ni-based catalyst types have been investigated, including Ni-based oxides/hydroxides, chalcogenides, sulfides, selenides, phosphides, and nitrides. These catalysts demonstrate impressive electrochemical performance for processes like the HER or OER, along with bifunctional capabilities for overall water splitting.<sup>99</sup> In order to enhance catalytic activity and decrease required overpotentials, diverse strategies have been developed. Examples include modifying the microstructure of nanomaterials, configuring developed electrocatalysts with multiple active phases, doping, alloying, and hybridizing with conductive materials. Significant advancements have focused on designing materials with nanostructures to finely control morphology, optimize surface-related properties, and facilitate charge transfer among different components. Beyond singular Ni-based catalysts, introducing additional elements to create multiple active sites can substantially enhance electrochemical properties because of synergistic effects and cooperative interactions. Moreover, incorporating metal or non-metal atoms via doping can fine-tune electronic structures, surface properties, and conductivity, rendering the catalysts more suitable for electrochemical reactions. Capitalizing on the cost-efficiency, excellent conductivity, and

exceptional stability of Ni-based materials to improve electrochemical performance for water splitting.<sup>66, 100</sup>

### **1.8 Synthetic approaches for the development of doped nanomaterials**

#### **1.8.1 Hydrothermal route:**

Hydrothermal synthesis is a powerful technique to control the morphology of nanomaterials, according to the temperature and pressure variation, different types of transition metal nanostructure (0D, 1D, 2D, and 3D) can be prepared.<sup>101</sup> It is a solution reaction approach, and the composition can also be controlled through the liquid phase reaction. Nanomaterials with higher vapor pressure can be synthesized with minimum loss by this approach. Doping of heteroatom and metal can be carried out in transition metal nanostructure by using the following hydrothermal process. An advantage of using inorganic salts lies in the ease with which the source of metal ions can be dissolved in water. This method offers several benefits, including rapid reaction kinetics, high crystallinity, short processing times, phase purity, and cost-effectiveness. It is particularly useful for fine-tuning the architecture, morphology, crystalline phase, and unique shape and size of materials. This control is achieved through the regulation of factors such as the addition of small quantities of organic ligands, the composition of the solution, as well as the temperature and pressure during the reaction process.<sup>94, 102</sup>

#### **1.8.2 Electrodeposition method:**

This method presents an attractive approach for creating nanostructures on conducting surfaces via a cathodic reduction reaction. The process involves a two or three-electrode system where a specific voltage is applied in an appropriate electrolyte, often with the support of a growth-directing agent that influences both nucleation rate and morphology. Electrodeposition can be conducted using techniques like cyclic voltammetry, linear sweep voltammetry, and chronoamperometry. Conductive surfaces such as carbon cloth (CC) or Ni foam are commonly used as working electrodes for the growth of desired nanomaterials.<sup>68</sup>

Electrodeposition offers the advantage of enabling the conformal fabrication of structures while allowing for the control of material thickness by adjusting factors such as temperature, precursor solution concentration, and applied potential. This method is characterized by its rapid synthesis, minimal material wastage, low energy consumption, absence of chemical oxidants and reductants, and the elimination of unwanted byproducts. Importantly, electrodeposition allows for

the synthesis of nanomaterials directly on binder-free conducting substrates, fulfilling the requirements of electrocatalysts for efficient charge carrier transportation and improved catalytic activity within the substrate material. Therefore, it is well-suited for the development of metal chalcogenides, oxides, and various other nanomaterials, which hold promise for applications in energy conversion technologies.<sup>103</sup>

### **1.8.3 Microwave-assisted method:**

In this method, electromagnetic energy is converted into thermal energy, signifying an energy transformation process rather than a simple heat transfer. The fundamental mechanism involves the penetration of microwaves into materials, resulting in direct interactions that generate heat. Microwaves, which are primarily electromagnetic rays within a frequency range of 0.3 to 2.45 GHz, exhibit a superheating effect by interacting with solvent molecules, causing a rapid temperature increase. The use of a sealed container amplifies this effect by raising the pressure, consequently reducing reaction times. Because of the fast changes in their electric and magnetic fields, microwaves cause molecules to reorient, which results in the absorption of energy. Owing to a number of benefits, such as its affordability, excellent reaction yields, suitability for one-pot reactions, and capacity to reduce side reactions through reduced reaction periods, the microwave approach has become widely used in the synthesis of diverse nanomaterials.<sup>104</sup>

### **1.8.4 Wet-Chemical Method:**

The wet-chemical synthesis method is a versatile method for producing nanomaterials at low temperatures and pressures. This method employs a variety of processes, such as the sequential ionic layer and adsorption reaction process (SILAR), dip coating, sol-gel, co-precipitation, microemulsion, and simple reduction.<sup>105-106</sup> At or near ambient temperature, the simple reduction process is routinely used to manufacture metal nanoparticles. Through hydrolysis and condensation stages, a colloidal suspension of solid particles (sol) and polymers (gel) is formed. This approach yields nanoparticles with regulated size and shape, as well as homogeneity and monodispersity. The co-precipitation method is a simple way to create metal or metal chalcogenide nanoparticles. It entails the use of metal salts in aqueous solutions along with a precipitating agent. By altering parameters such as precursor ratios, temperature, surface ligands, stabilizing agents, and pH, the morphology, shape, and size of the nanomaterials can be adjusted. Microemulsion is

another important wet-chemical process that involves dispersing small water droplets (polar phase) inside an oil medium (non-polar phase) and stabilizing them with surfactant molecules. The SILAR deposition method allows for the creation of various thin films and layers of metal chalcogenides, offering simplicity, easy control over deposition and growth rates, and a shorter processing time compared to other methods. In this approach, the substrate is successively immersed in cationic and anionic precursors, facilitating the controlled growth of thin films.<sup>107</sup>

### 1.9 Gaps in existing research

The interest in nanoscale materials as electrocatalyst arises from the fact that these particles display characteristic physical, chemical, and optoelectronic properties, which are noticeably different from those of the corresponding bulk materials. Moreover, a catalyst having thin sheets, porous, and layered structure with increased reactive sites through doping decreases the required catalyst amount and also contributes to alleviating the overpotential. Mainly Pt, RuO<sub>2</sub>, and IrO<sub>2</sub> are used as efficient hydrogen and oxygen evolution catalysts, but the potential of large-scale deployment is hindered by higher cost and stability of these noble metal resources. Therefore, it becomes more and more essential to unveil an alternative bifunctional electrocatalyst within a single catalyst composed of non-precious metals or earth-abundant elements with high efficiency and stability. Incorporation of second metal as dopant generally improves the electrocatalytic activity by increasing charge transportation. Moreover, doping with heteroatom makes the catalyst more metallic and influences the chemical environment of the catalytic surface.

In order to carry out water splitting reaction at practical scale, an extra overall operational voltage is required to apply on cell for the reaction, which can be equated as-

$$V_{op} = 1.23 \text{ V} + |\eta_a| + \eta_c + \eta_\Omega$$

In the above equation,  $\eta_a$  and  $\eta_c$  are anodic and cathodic overpotential, respectively and  $\eta_\Omega$  is excess potential required to compensate the internal resistance. To improve the efficiency of water splitting reaction these overpotential should be minimized. Highly active OER and HER catalyst can minimize the intrinsic activation barrier of the anode and cathode, which can give the solution to the existing literature problem. Higher activity can be generated through a bifunctional active catalyst via doping.

Most reported results are paying attention on the development of separately active HER or OER electrocatalyst. Therefore, the challenge is to generate bifunctionality (HER and OER) in a

single catalyst. So far, the origin of bifunctional activity is not clearly known and is sometimes controversial. Therefore, to develop bifunctional active site in a single catalyst for electrocatalytic water splitting by incorporating many active components via doping, alloying, composing, etc. approaches is very much essential. Furthermore, the developed electrocatalyst exhibits better OER but poor HER in alkaline electrolyte, whereas poor OER but higher HER in acidic electrolyte solution. Therefore, to overcome the gaps in existing research, we must develop an efficient strategy for a superior electrocatalyst with bifunctional active sites in a single catalyst for overall water splitting in a particular electrolyte solution. After doping in transition metal chalcogenides, higher activity, chemical stability, and catalytic durability can be seen, but the interaction between dopant and transition metal chalcogenides is still missing, which plays a vital role for better electrocatalytic activity. Another critical challenge is to fabricate two-electrode configuration using doped thin sheets as both an anode and cathode. For two-electrode system, overall water splitting apparatus are assembled as sample deposited carbon cloth as a working, counter and reference electrode and in a single electrolyte, which is very much challenging.

### 1.10 Thesis Objectives and Outline

The following objectives were proposed initially in the research proposal-

1. Syntheses of various transition metal chalcogenides (hydroxides, oxyhydroxides, sulphides and selenides etc.) of Ni, Co, Fe, and Cu using different chemical techniques.
2. Effect of doping on transition metal chalcogenides. The dopants are W, Fe, Co, Ce, S, P, and N.
3. Characterization of doped and undoped transition metal chalcogenides using various techniques.
4. Application in overall water splitting using doped and undoped transition metal chalcogenides in a wide pH range including sea water condition.
5. Development of two electrode system by using bifunctional active site in a single catalyst both as a cathode and anode.

In our current study, Nickel based different nanomaterials are explored as cathode, anode and bifunctional electrocatalyst for electrochemical water splitting reaction. Nickel-based transition metal chalcogenides ( $M_aX_b$ , where X = S, Se, Te) have appeared as highly promising substitutes to Pt, and  $RuO_2$  for water splitting. The remarkable synergistic effect between nickel

(Ni) and neighboring atoms leads to significantly enhanced surface adsorption properties, thereby attributing to the improved electrocatalytic characteristics of the resulting materials. The advantages of Ni-based materials are manifold, including their cost-effectiveness, abundant elemental availability, robust strength, excellent ductility, high corrosion resistance, efficient heat conduction, and remarkable electrical conductivity. While many well-known Ni compounds are divalent, Ni has the unique capability to exhibit various valences ranging from -1 to +4. This versatility in electronic transitions, combined with its exceptional electronic properties, high conductivity, and thermal stability, has made Ni a popular choice for designing electrocatalytic material. Due to its highly oxidizing nature single Ni based materials show lower conductivity and stability for HER, OER and bifunctional properties. Herein, we have followed the different strategies such as heterostructuring, morphology control and chemical doping to improve the electrochemical activity and stability of various material as Ni/Ni(OH)<sub>2</sub>/NiOOH, Ni(OH)<sub>2</sub>/NiOOH, Ni<sub>9</sub>S<sub>8</sub>, Ni<sub>0.85</sub>Se and NiCo<sub>2</sub>Se<sub>4</sub> etc. The theoretical studies result are also included to support the tuning in the electronic structure, synergistic effect, Lewis acidity, metallic nature and reaction mechanism of HER and OER of Ni(OH)<sub>2</sub>/NiOOH, Ni<sub>9</sub>S<sub>8</sub>, Ni<sub>0.85</sub>Se and NiCo<sub>2</sub>Se<sub>4</sub> material after doping with W<sup>6+</sup>, Co<sup>2+</sup>, Ce<sup>4+</sup>, and Fe<sup>3+</sup> cations, respectively. The specifics of each of these processes are elucidated within their respective chapters.

### 1.11 References

1. Lewis, N. S.; Nocera, D. G., Powering the planet: Chemical challenges in solar energy utilization. *PNAS* **2006**, *103* (43), 15729-15735.
2. Bayda, S.; Adeel, M.; Tuccinardi, T.; Cordani, M.; Rizzolio, F., The history of nanoscience and nanotechnology: from chemical–physical applications to nanomedicine. *Molecules* **2019**, *25* (1), 112-127.
3. Li, Q., *Nanomaterials for sustainable energy*. Springer: 2016.
4. Xie, Z.; Duo, Y.; Lin, Z.; Fan, T.; Xing, C.; Yu, L.; Wang, R.; Qiu, M.; Zhang, Y.; Zhao, Y., The rise of 2D photothermal materials beyond graphene for clean water production. *Adv. Sci.* **2020**, *7* (5), 1902236-1902259.

5. Ashley, M.; Magiera, C.; Ramidi, P.; Blackburn, G.; Scott, T. G.; Gupta, R.; Wilson, K.; Ghosh, A.; Biswas, A., Nanomaterials and processes for carbon capture and conversion into useful by-products for a sustainable energy future. *Greenh. gases* **2012**, *2* (6), 419-444.
6. Chen, X.; Li, C.; Grätzel, M.; Kostecky, R.; Mao, S. S., Nanomaterials for renewable energy production and storage. *Chem. Soc. Rev.* **2012**, *41* (23), 7909-7937.
7. Bowman, D. M., More than a decade on: Mapping today's regulatory and policy landscapes following the publication of nanoscience and nanotechnologies: Opportunities and uncertainties. *NanoEthics* **2017**, *11*, 169-186.
8. Fatikow, S.; Eichhorn, V.; Bartenwerfer, M., Nanomaterials Enter the Silicon-Based CMOS Era: Nanorobotic Technologies for Nanoelectronic Devices. *IEEE Nanotechnol. Mag.* **2012**, *6* (1), 14-18.
9. Li, Y.; Sun, Y.; Qin, Y.; Zhang, W.; Wang, L.; Luo, M.; Yang, H.; Guo, S., Recent advances on water-splitting electrocatalysis mediated by noble-metal-based nanostructured materials. *Adv. Energy Mater.* **2020**, *10* (11), 1903120-1903140.
10. Plonska-Brzezinska, M. E.; Echegoyen, L., Carbon nano-onions for supercapacitor electrodes: recent developments and applications. *J. Mater. Chem. A* **2013**, *1* (44), 13703-13714.
11. Wang, Y.; Li, H.; He, P.; Hosono, E.; Zhou, H., Nano active materials for lithium-ion batteries. *Nanoscale* **2010**, *2* (8), 1294-1305.
12. Chen, G. Z., Understanding supercapacitors based on nano-hybrid materials with interfacial conjugation. *PNAS: Mater. Int.* **2013**, *23* (3), 245-255.
13. Zohuri, B., Hydrogen energy. *Cryogenics and Liquid Hydrogen Storage: Challenges and Solutions for a Cleaner Future; Springer: New York, NY, USA* **2019**, 121-139.
14. Tee, S. Y.; Win, K. Y.; Teo, W. S.; Koh, L. D.; Liu, S.; Teng, C. P.; Han, M. Y., Recent progress in energy-driven water splitting. *Adv. Sci.* **2017**, *4* (5), 1600337-1600361.
15. Ayers, K., Gigawatt-scale renewable hydrogen via water splitting as a case study for collaboration: The need to connect fundamental and applied research to accelerate solutions. *MRS Energy Sustain.* **2017**, *4*, 1-10.
16. Saleh, T. A., Nanomaterials: Classification, properties, and environmental toxicities. *Environmental Technology & Innovation* **2020**, *20*, 101067-101098.



17. Ramalingam, G.; Kathirgamanathan, P.; Ravi, G.; Elangovan, T.; Manivannan, N.; Kasinathan, K., Quantum confinement effect of 2D nanomaterials. In *Quantum Dots-Fundamental and Applications*, IntechOpen: **2020**, 1-11.
18. Baig, N.; Kammakakam, I.; Falath, W., Nanomaterials: a review of synthesis methods, properties, recent progress, and challenges. *Mater. Adv.* **2021**, 2 (6), 1821-1871.
19. Roduner, E., Size matters: why nanomaterials are different. *Chem. Soc. Rev.* **2006**, 35 (7), 583-592.
20. Mohammad, N. S., Understanding quantum confinement in nanowires: basics, applications and possible laws. *J. Physics: Condensed Matter* **2014**, 26 (42), 423202.
21. Chen, G.; Seo, J.; Yang, C.; Prasad, P. N., Nanochemistry and nanomaterials for photovoltaics. *Chem. Soc. Rev.* **2013**, 42 (21), 8304-8338.
22. Padmanabhan, J.; Kyriakides, T. R., Nanomaterials, inflammation, and tissue engineering. *Wiley Int. Rev. Nanomedicine Nanobiotechnol* **2015**, 7 (3), 355-370.
23. Vollath, D., Nanomaterials an introduction to synthesis, properties and application. *Environ Eng Manag J* **2008**, 7 (6), 865-870.
24. Bukowski, T. J.; Simmons, J. H., Quantum dot research: current state and future prospects. *Crit. Rev. Solid State Mater. Sci.* **2002**, 27 (3-4), 119-142.
25. Geim, A. K., Graphene: status and prospects. *Science* **2009**, 324 (5934), 1530-1534.
26. Luo, W.; Li, F.; Li, H.; Zhang, Z.; Zhang, X.; Liang, Y.; Huang, G., From 0D to 3D nanomaterial-based composite membranes for CO<sub>2</sub> capture: recent advances and perspectives. *J. Environ. Chem. Engg.* **2023**, 110657-110678.
27. Arole, V.; Munde, S., Fabrication of nanomaterials by top-down and bottom-up approaches-an overview. *J. Mater. Sci* **2014**, 1, 89-93.
28. Thiruvengadathan, R.; Korampally, V.; Ghosh, A.; Chanda, N.; Gangopadhyay, K.; Gangopadhyay, S., Nanomaterial processing using self-assembly-bottom-up chemical and biological approaches. *Rep. Progress Phy.* **2013**, 76 (6), 066501-066555.
29. Zhang, Q.; Uchaker, E.; Candelaria, S. L.; Cao, G., Nanomaterials for energy conversion and storage. *Chem. Soc. Rev.* **2013**, 42 (7), 3127-3171.
30. Ong, W.-J.; Zheng, N.; Antonietti, M., Advanced nanomaterials for energy conversion and storage: current status and future opportunities. *Nanoscale* **2021**, 13 (22), 9904-9907.

31. O'Brien, J. In *Thermodynamic considerations for thermal water splitting processes and high temperature electrolysis*, ASME International Mechanical Engineering Congress and Exposition, **2008**; 639-651.
32. Mehrpooya, M.; Habibi, R., A review on hydrogen production thermochemical water-splitting cycles. *J. Cleaner Product.* **2020**, *275*, 123836.
33. Minggu, L. J.; Daud, W. R. W.; Kassim, M. B., An overview of photocells and photoreactors for photoelectrochemical water splitting. *Int. J. hydrog. Energy* **2010**, *35* (11), 5233-5244.
34. Joy, J.; Mathew, J.; George, S. C., Nanomaterials for photoelectrochemical water splitting—review. *Int. J. hydrog. Energy* **2018**, *43* (10), 4804-4817.
35. Döscher, H.; Young, J. L.; Geisz, J. F.; Turner, J. A.; Deutsch, T. G., Solar-to-hydrogen efficiency: shining light on photoelectrochemical device performance. *Energy Environ. Sci.* **2016**, *9* (1), 74-80.
36. Abe, R., Recent progress on photocatalytic and photoelectrochemical water splitting under visible light irradiation. *J. Photochem. Photobiology C Photochem Rev.* **2010**, *11* (4), 179-209.
37. Mahala, C.; Sharma, M. D.; Basu, M., ZnO nanosheets decorated with graphite-like carbon nitride quantum dots as photoanodes in photoelectrochemical water splitting. *ACS Appl. Nano Mater.* **2020**, *3* (2), 1999-2007.
38. Rossmeisl, J.; Dimitrievski, K.; Siegbahn, P.; Nørskov, J. K., Comparing electrochemical and biological water splitting. *J. Phy. Chem. C* **2007**, *111* (51), 18821-18823.
39. Renger, G., Biological exploitation of solar energy by photosynthetic water splitting. *Angewandte Chemie International Edition in English* **1987**, *26* (7), 643-660.
40. Maeda, K., Photocatalytic water splitting using semiconductor particles: history and recent developments. *Journal of Photochemistry and Photobiology C: Photochemistry Reviews* **2011**, *12* (4), 237-268.
41. Maeda, K.; Domen, K., Photocatalytic water splitting: recent progress and future challenges. *J. Phys. Chem. Lett.* **2010**, *1* (18), 2655-2661.
42. Li, X.; Hao, X.; Abudula, A.; Guan, G., Nanostructured catalysts for electrochemical water splitting: current state and prospects. *J. Mater. Chem. A* **2016**, *4* (31), 11973-12000.

43. Ifkovits, Z. P.; Evans, J. M.; Meier, M. C.; Papadantonakis, K. M.; Lewis, N. S., Decoupled electrochemical water-splitting systems: a review and perspective. *Energy Environ. Sci.* **2021**, *14* (9), 4740-4759.
44. Wei, C.; Xu, Z. J., The comprehensive understanding of as an evaluation parameter for electrochemical water splitting. Wiley Online Library: 2018; Vol. 2, p 1800168.
45. Li, L.; Wang, B.; Zhang, G.; Yang, G.; Yang, T.; Yang, S.; Yang, S., Electrochemically modifying the electronic structure of IrO<sub>2</sub> nanoparticles for overall electrochemical water splitting with extensive adaptability. *Adv. Energy Mater.* **2020**, *10* (30), 2001600-2001609.
46. Anantharaj, S.; Ede, S.; Karthick, K.; Sankar, S. S.; Sangeetha, K.; Karthik, P.; Kundu, S., Precision and correctness in the evaluation of electrocatalytic water splitting: revisiting activity parameters with a critical assessment. *Energy Environ. Sci.* **2018**, *11* (4), 744-771.
47. Anantharaj, S.; Ede, S. R.; Sakthikumar, K.; Karthick, K.; Mishra, S.; Kundu, S., Recent trends and perspectives in electrochemical water splitting with an emphasis on sulfide, selenide, and phosphide catalysts of Fe, Co, and Ni: a review. *ACS Catal.* **2016**, *6* (12), 8069-8097.
48. Darband, G. B.; Aliofkhaezai, M.; Hyun, S.; Rouhaghdam, A. S.; Shanmugam, S., Electrodeposition of Ni–Co–Fe mixed sulfide ultrathin nanosheets on Ni nanocones: a low-cost, durable and high performance catalyst for electrochemical water splitting. *Nanoscale* **2019**, *11* (35), 16621-16634.
49. Zhao, H.; Yuan, Z. Y., Progress and Perspectives for Solar-Driven Water Electrolysis to Produce Green Hydrogen. *Adv. Energy Mater.* **2023**, *13* (16), 2300254-2300274.
50. Xiao, Y.-X.; Yu, F.; Yang, X.; Yang, X.-Y., Photovoltaic Electrocatalytic Seawater Splitting. In *Photo-Driven Seawater Splitting for Hydrogen Production*, Springer: 2023; pp 225-294.
51. Rand, D. A. J.; Dell, R. M., Hydrogen energy: challenges and prospects. **2007**.
52. Rosen, M. A.; Koochi-Fayegh, S., The prospects for hydrogen as an energy carrier: an overview of hydrogen energy and hydrogen energy systems. *Energy Ecology Environ.* **2016**, *1*, 10-29.
53. Tilak, B.; Chen, C.-P., Generalized analytical expressions for Tafel slope, reaction order and ac impedance for the hydrogen evolution reaction (HER): mechanism of HER on platinum in alkaline media. *J. Appl. Electrochem.* **1993**, *23* (6), 631-640.

54. Hu, C.; Zhang, L.; Gong, J., Recent progress made in the mechanism comprehension and design of electrocatalysts for alkaline water splitting. *Energy Environ. Sci.* **2019**, *12* (9), 2620-2645.
55. Mahmood, N.; Yao, Y.; Zhang, J. W.; Pan, L.; Zhang, X.; Zou, J. J., Electrocatalysts for hydrogen evolution in alkaline electrolytes: mechanisms, challenges, and prospective solutions. *Adv. Sci.* **2018**, *5* (2), 1700464-1700487.
56. Mengting, L.; Xingqun, Z.; Li, L.; Zidong, W., Research progress of hydrogen oxidation and hydrogen evolution reaction mechanism in alkaline media. *Acta Physico-Chimica Sinica* **2021**, *37* (9), 21-37.
57. Zeng, M.; Li, Y., Recent advances in heterogeneous electrocatalysts for the hydrogen evolution reaction. *J Mater. Chem. A* **2015**, *3* (29), 14942-14962.
58. Liu, X.; He, Z.; Ajmal, M.; Shi, C.; Gao, R.; Pan, L.; Huang, Z.-F.; Zhang, X.; Zou, J.-J., Recent Advances in the Comprehension and Regulation of Lattice Oxygen Oxidation Mechanism in Oxygen Evolution Reaction. *Trans. Tianjin Univ.* **2023**, *29* (4), 247-253.
59. Bulakhe, S.; Shinde, N.; Kim, J. S.; Mane, R. S.; Deokate, R., Recent advances in non-precious Ni-based promising catalysts for water splitting application. *Int. J. Energy Res.* **2022**, *46* (13), 17829-17847.
60. Anantharaj, S.; Kundu, S., Do the evaluation parameters reflect intrinsic activity of electrocatalysts in electrochemical water splitting? *ACS Energy Lett.* **2019**, *4* (6), 1260-1264.
61. Svengren, H.; Chamoun, M.; Grins, J.; Johnsson, M., Water Splitting Catalysis Studied by using Real-Time Faradaic Efficiency Obtained through Coupled Electrolysis and Mass Spectrometry. *ChemElectroChem* **2018**, *5* (1), 44-50.
62. Huang, J.; Jiang, Y.; An, T.; Cao, M., Increasing the active sites and intrinsic activity of transition metal chalcogenide electrocatalysts for enhanced water splitting. *J. Mater. Chem. A* **2020**, *8* (48), 25465-25498.
63. Zhao, Y.; Wei, S.; Pan, K.; Dong, Z.; Zhang, B.; Wu, H.-H.; Zhang, Q.; Lin, J.; Pang, H., Self-supporting transition metal chalcogenides on metal substrates for catalytic water splitting. *Chem. Eng. J.* **2021**, *421*, 129645-129688.
64. Sumesh, C.; Peter, S. C., Two-dimensional semiconductor transition metal based chalcogenide based heterostructures for water splitting applications. *Dalton Trans.* **2019**, *48* (34), 12772-12802.

65. Marbán, G.; Valdés-Solís, T., Towards the hydrogen economy? *Int. J. Hydrog. Energy* **2007**, *32* (12), 1625-1637.
66. Li, Y.; Bao, X.; Chen, D.; Wang, Z.; Dewangan, N.; Li, M.; Xu, Z.; Wang, J.; Kawi, S.; Zhong, Q., A Minireview on Nickel-Based Heterogeneous Electrocatalysts for Water Splitting. *ChemCatChem* **2019**, *11* (24), 5913-5928.
67. Li, J.; Zheng, G., One-dimensional earth-abundant nanomaterials for water-splitting electrocatalysts. *Adv. Sci.* **2017**, *4* (3), 1600380-1600395.
68. Rathore, D.; Sharma, M. D.; Sharma, A.; Basu, M.; Pande, S., Aggregates of Ni/Ni(OH)<sub>2</sub>/NiOOH Nanoworms on Carbon Cloth for Electrocatalytic Hydrogen Evolution. *Langmuir* **2020**, *36* (46), 14019-14030.
69. Sancho, H.; Zhang, Y.; Liu, L.; Barevadia, V. G.; Wu, S.; Zhang, Y.; Huang, P.-W.; Zhang, Y.; Wu, T.-H.; You, W.; Liu, N., NiCo<sub>2</sub>Se<sub>4</sub> Nanowires as a High-Performance Bifunctional Oxygen Electrocatalyst. *J Electrochem. Soc.* **2020**, *167* (5), 056503-056512.
70. Wang, G.; Sun, Y.; Zhao, Y.; Zhang, Y.; Li, X.; Fan, L.; Li, Y., Phosphorus-induced electronic structure reformation of hollow NiCo<sub>2</sub>Se<sub>4</sub> nanoneedle arrays enabling highly efficient and durable hydrogen evolution in all-pH media. *Nano Research* **2022**, 8771-8782.
71. Xia, C.; Jiang, Q.; Zhao, C.; Hedhili, M. N.; Alshareef, H. N., Selenide-Based Electrocatalysts and Scaffolds for Water Oxidation Applications. *Adv. Mater.* **2016**, *28* (1), 77-85.
72. Subhramannia, M.; Pillai, V. K., Shape-dependent electrocatalytic activity of platinum nanostructures. *J. Mater. Chem.* **2008**, *18* (48), 5858-5870.
73. Cui, Y.; Zhou, C.; Li, X.; Gao, Y.; Zhang, J., High performance electrocatalysis for hydrogen evolution reaction using nickel-doped CoS<sub>2</sub> nanostructures: experimental and DFT insights. *Electrochim. Acta* **2017**, *228*, 428-435.
74. Liu, B.; Zhao, Y.-F.; Peng, H.-Q.; Zhang, Z.-Y.; Sit, C.-K.; Yuen, M.-F.; Zhang, T.-R.; Lee, C.-S.; Zhang, W.-J., Nickel–Cobalt Diselenide 3D Mesoporous Nanosheet Networks Supported on Ni Foam: An All-pH Highly Efficient Integrated Electrocatalyst for Hydrogen Evolution. *Adv. Mater.* **2017**, *29* (19), 1606521-1606554.
75. Mahala, C.; Devi Sharma, M.; Basu, M., Fe-Doped Nickel Hydroxide/Nickel Oxyhydroxide Function as an Efficient Catalyst for the Oxygen Evolution Reaction. *ChemElectroChem* **2019**, *6* (13), 3488-3498.

76. Mahala, C.; Sharma, R.; Sharma, M. D.; Pande, S., Development of copper cobalt sulfide with Cu: Co ratio variation on carbon cloth as an efficient electrode material for the oxygen evolution reaction. *ChemElectroChem* **2019**, *6* (20), 5301-5312.
77. Sharma, M. D.; Mahala, C.; Modak, B.; Pande, S.; Basu, M., Doping of MoS<sub>2</sub> by “Cu” and “V”: an efficient strategy for the enhancement of hydrogen evolution activity. *Langmuir* **2021**, *37*, 4847-4858.
78. Gong, Y.; Xu, Z.; Pan, H.; Lin, Y.; Yang, Z.; Wang, J., A 3D well-matched electrode pair of Ni–Co–S//Ni–Co–P nanoarrays grown on nickel foam as a high-performance electrocatalyst for water splitting. *J Mater Chem A* **2018**, *6* (26), 12506-12514.
79. Fang, L.; Jiang, Z.; Xu, H.; Liu, L.; guan, Y.; Gu, X.; Wang, Y., Crystal-plane engineering of NiCo<sub>2</sub>O<sub>4</sub> electrocatalysts towards efficient overall water splitting. *J. Catal.* **2018**, *357*, 238-246.
80. Gan, X.; Lee, L. Y. S.; Wong, K.-y.; Lo, T. W.; Ho, K. H.; Lei, D. Y.; Zhao, H., 2H/1T Phase Transition of Multilayer MoS<sub>2</sub> by Electrochemical Incorporation of S Vacancies. *ACS Appl. Energy Materi.* **2018**, *1*, 4754-4765.
81. Leong, S. X.; Mayorga-Martinez, C. C.; Chia, X.; Luxa, J.; Sofer, Z.; Pumera, M., 2H → 1T Phase Change in Direct Synthesis of WS<sub>2</sub> Nanosheets via Solution-Based Electrochemical Exfoliation and Their Catalytic Properties. *ACS Appl. Mater. Interfaces* **2017**, *9*, 26350-26356.
82. Liang, L.; Cheng, H.; Lei, F.; Han, J.; Gao, S.; Wang, C.; Sun, Y.; Qamar, S.; Wei, S.; Xie, Y., Metallic Single-Unit-Cell Orthorhombic Cobalt Diselenide Atomic Layers: Robust Water-Electrolysis Catalysts. *Angew. Chem. Int. Ed.* **2015**, *54* (41), 12004-12008.
83. Wang, F.; Li, C.; Sun, L.-D.; Wu, H.; Ming, T.; Wang, J.; Yu, J. C.; Yan, C.-H., Heteroepitaxial Growth of High-Index-Faceted Palladium Nanoshells and Their Catalytic Performance. *JACS* **2011**, *133* (4), 1106-1111.
84. Wang, X.; Tian, H.; Yu, X.; Chen, L.; Cui, X.; Shi, J., Advances and insights in amorphous electrocatalyst towards water splitting. *Chinese J. Catal.* **2023**, *51*, 5-48.
85. Deng, Y.; Lai, W.; Xu, B., A mini review on doped nickel-based electrocatalysts for hydrogen evolution reaction. *Energies* **2020**, *13* (18), 4651-4672.
86. Ji, Y.; Du, J.; Chen, A., Review on heteroatom doping carbonaceous materials toward electrocatalytic carbon dioxide reduction. *Trans. Tianjin Univ.* **2022**, 1-16.

87. Ouyang, C.; Wang, X.; Wang, S., Phosphorus-doped CoS<sub>2</sub> nanosheet arrays as ultra-efficient electrocatalysts for the hydrogen evolution reaction. *Chem. Commun.* **2015**, *51* (75), 14160-14163.
88. Li, F.; Xu, R.; Li, Y.; Liang, F.; Zhang, D.; Fu, W.-F.; Lv, X.-J., N-doped carbon coated NiCo<sub>2</sub>S<sub>4</sub> hollow nanotube as bifunctional electrocatalyst for overall water splitting. *Carbon* **2019**, *145*, 521-528.
89. Shao, Z.; Sun, J.; Guo, N.; He, F.; Huang, K.; Tian, F.; Wang, Q., Boosting electrocatalysis by heteroatom doping and oxygen vacancies in hierarchical Ni-Co based nitride phosphide hybrid. *J. Power Source* **2019**, *422*, 33-41.
90. Han, N.; Yang, K. R.; Lu, Z.; Li, Y.; Xu, W.; Gao, T.; Cai, Z.; Zhang, Y.; Batista, V. S.; Liu, W., Nitrogen-doped tungsten carbide nanoarray as an efficient bifunctional electrocatalyst for water splitting in acid. *Nat. Commun.* **2018**, *9*, 924-935.
91. Ren, Z.; Ren, X.; Zhang, L.; Fu, C.; Li, X.; Zhang, Y.; Gao, B.; Yang, L.; Chu, P. K.; Huo, K., Tungsten-Doped CoP Nanoneedle Arrays Grown on Carbon Cloth as Efficient Bifunctional Electrocatalysts for Overall Water Splitting. *ChemElectroChem* **2019**, *6* (20), 5229-5236.
92. Fei, B.; Chen, Z.; Liu, J.; Xu, H.; Yan, X.; Qing, H.; Chen, M.; Wu, R., Ultrathinning Nickel Sulfide with Modulated Electron Density for Efficient Water Splitting. *Adv. Energy Mater.* **2020**, *10*, 2001963-2001982.
93. Rathore, D.; Ghosh, S.; Chowdhury, J.; Pande, S., Fe-Doped NiCo<sub>2</sub>Se<sub>4</sub> Nanorod Arrays as Electrocatalysts for Overall Electrochemical Water Splitting. *ACS Appl. Nano Mater.* **2023**, *6* (4), 3095-3110.
94. Rathore, D.; Ghosh, S.; Chowdhury, J.; Pande, S., Co-Doped Ni<sub>9</sub>S<sub>8</sub> Nanostructures for Electrocatalytic Water Splitting over a Wide pH Range. *ACS Appl. Nano Mater.* **2022**, *5*, 11823-11838.
95. Rathore, D.; Banerjee, A.; Pande, S., Bifunctional Tungsten-Doped Ni(OH)<sub>2</sub>/NiOOH Nanosheets for Overall Water Splitting in an Alkaline Medium. *ACS Appl. Nano Mater.* **2022**, *5* (2), 2664-2677.
96. Yang, J. W.; Ahn, S. H.; Jang, H. W., Crucial role of heterostructures in highly advanced water splitting photoelectrodes. *Curr. Opin. Green Sustain. Chem* **2021**, *29*, 100454-100463.

97. Huang, C.; Miao, X.; Pi, C.; Gao, B.; Zhang, X.; Qin, P.; Huo, K.; Peng, X.; Chu, P. K., Mo<sub>2</sub>C/VC heterojunction embedded in graphitic carbon network: An advanced electrocatalyst for hydrogen evolution. *Nano Energy* **2019**, *60*, 520-526.
98. Sharma, M. D.; Mahala, C.; Basu, M., 2D thin sheet heterostructures of MoS<sub>2</sub> on MoSe<sub>2</sub> as efficient electrocatalyst for hydrogen evolution reaction in wide pH range. *Inorg. Chem.* **2020**, *59* (7), 4377-4388.
99. Al-Naggar, A. H.; Shinde, N. M.; Kim, J.-S.; Mane, R. S., Water splitting performance of metal and non-metal-doped transition metal oxide electrocatalysts. *Coord. Chem. Rev.* **2023**, *474*, 214864-214881.
100. Yan, Y.; Wang, P.; Lin, J.; Cao, J.; Qi, J., Modification strategies on transition metal-based electrocatalysts for efficient water splitting. *J. Energy Chem.* **2021**, *58*, 446-462.
101. Liu, N.; Chen, X.; Zhang, J.; Schwank, J. W., A review on TiO<sub>2</sub>-based nanotubes synthesized via hydrothermal method: Formation mechanism, structure modification, and photocatalytic applications. *Catal. Today* **2014**, *225*, 34-51.
102. Jitputti, J.; Pavasupree, S.; Suzuki, Y.; Yoshikawa, S., Synthesis and photocatalytic activity for water-splitting reaction of nanocrystalline mesoporous titania prepared by hydrothermal method. *J. Solid State Chem.* **2007**, *180* (5), 1743-1749.
103. Jayakrishnan, D. S., Electrodeposition: the versatile technique for nanomaterials. In *Corrosion protection and control using nanomaterials*, Elsevier: 2012; pp 86-125.
104. Dąbrowska, S.; Chudoba, T.; Wojnarowicz, J.; Łojkowski, W., Current trends in the development of microwave reactors for the synthesis of nanomaterials in laboratories and industries: a review. *Crystals* **2018**, *8* (10), 379-405.
105. Tan, C.; Zhang, H., Wet-chemical synthesis and applications of non-layer structured two-dimensional nanomaterials. *Nat. Commun.* **2015**, *6* (1), 7873-7884.
106. Zhao, H.; Li, F.; Wang, S.; Guo, L., Wet chemical synthesis of amorphous nanomaterials with well-defined morphologies. *Accounts Mater. Res.* **2021**, *2* (9), 804-815.
107. Kulkarni, S. K.; Kulkarni, S. K., Synthesis of nanomaterials—II (Chemical methods). *Nanotechnology: principles and practices* **2015**, 77-109.



## Chapter 2

### Materials, Methods, and Instrumentation

- \* *The chapter includes details of chemical and experimental methods used for the synthesis of different types of pristine and doped nickel-based nanomaterials.*
- \* *It contains the characterization methods, calculation methods, and instruments used for all the experiments included in the thesis.*

This chapter provides a comprehensive overview of the chemicals, reagents, and conducting materials employed in the fabrication of all pristine and doped Ni-based electrocatalysts. The characterization of Ni-based nanomaterials is conducted through diverse techniques, including powder X-ray diffraction (PXRD), field emission scanning electron microscopy (FESEM), transmission electron microscopy (TEM), X-ray photoelectron spectroscopy (XPS), Fourier-transform infrared (FTIR) spectroscopy, Raman spectroscopy, BET (Brunauer–Emmett–Teller) analysis and inductively coupled plasma atomic emission spectroscopy (ICP-AES). The electrocatalytic activity studies are carried out using the CH instrument.

### 2.1 Used Chemicals

The below-mentioned chemicals are used for the synthesis of various doped and undoped electrodes.

**Table 2.1:** List of the chemicals used in this thesis work with their purchasing company.

S. No.	Chemicals	Name of Supplier
1	Nickel chloride (II) hexahydrate ( $\text{NiCl}_2 \cdot 6\text{H}_2\text{O}$ )	SRL, India
2	Cobalt chloride (II) hexahydrate ( $\text{CoCl}_2 \cdot 6\text{H}_2\text{O}$ )	Merck, India
3	Urea, Extra pure	SD fine, India
4	Ethanol	Merck, India
5	Sodium selenite ( $\text{Na}_2\text{SeO}_3$ )	Loba Chemie, India
6	Ferric chloride ( $\text{FeCl}_3$ )	SRL, India
7	Hydrazine hydrate ( $\text{H}_2\text{N-NH}_2$ )	Spectrochem, India
8	Potassium hydroxide (KOH)	SRL, India
9	Sodium hydroxide (NaOH)	SRL, India
10	Nafion	Sigma Aldrich, India
11	Isopropanol	Merck, India
12	Sulfuric acid	Spectrochem, India
13	Nitric acid	Spectrochem, India
14	Acetone [ $\text{C}_3\text{H}_6\text{O}$ ]	MolyChem, India
15	Pt-C 5%	Spectrochem, India
16	Ammonium fluoride ( $\text{NH}_4\text{F}$ )	SRL, India

17	Thioacetamide	SRL, India
18	Nickel nitrate hexahydrate ( $\text{Ni}(\text{NO}_3)_2 \cdot 6\text{H}_2\text{O}$ )	SRL, India
19	Sodium tungstate dihydrate $\text{Na}_2\text{WO}_4 \cdot 2\text{H}_2\text{O}$	SRL, India
20	Ammonium ceric (IV) nitrate	Merck, India
21	Commercial $\text{RuO}_2$	Sigma Aldrich, India

## 2.2 Materials Used:

### 2.2.1 Carbon Cloth:

A conducting surface, specifically carbon cloth (CC), obtained from Shiree Balaji Scientific Company, served as the substrate for electrocatalyst development. The cleaning process involved immersing a small CC piece in concentrated  $\text{HNO}_3$  solution for 24 hours. Subsequently, the CC underwent ultrasonication in distilled water, followed by a 12-hour wash with acetone and a 12-hour wash with ethanol. After thorough drying, the cleaned CC was employed in the stepwise process for electrocatalyst development.

## 2.3 Methods

### 2.3.1 Synthesis Method

#### 2.3.1.1 Ultra-sonication Method:

The ultra-sonication method is a highly effective technique for achieving the proper dissolution of metal precursors. This process involves the transmission of high-intensity ultrasound waves (greater than 20 kHz) through a liquid medium. These waves induce acoustic cavitation, leading to the rapid formation of microbubbles. The resulting local heating facilitates the breakdown of the metal precursor into its ions, allowing for efficient dissolution in the solvent medium.<sup>1-2</sup>

#### 2.3.1.2 Hydrothermal Method

Hydrothermal synthesis stands out as an advantageous and emerging technique for crafting diverse nanostructures. Notably, it offers a greener, simpler, and more cost-effective alternative to the solvothermal method by utilizing water as a solvent in lieu of organic solvents. The reaction temperature surpasses the boiling point of water, creating self-generated pressure within the closed system due to vapor saturation. A key merit of the hydrothermal method lies in its ability to yield

nanomaterials with remarkable uniformity. This technique boasts a shorter reaction time compared to conventional methods and produces nanomaterials with a high degree of phase homogeneity. Several pivotal reaction parameters exert influence over the physicochemical properties of the resulting nanostructures in hydrothermal syntheses. These include reaction temperature, pressure, reaction time, pH of the reaction precursor, concentration of the initial metal precursor, and the presence of growth-directing agents. In the hydrothermal method, the reaction precursor solution is contained within a Teflon-lined container and maintained at a constant temperature for the specified reaction duration. Other parameters, such as the concentration of initial components, solubility, and pH of the solution, must be carefully set prior to initiating the reaction.<sup>3-4</sup>

### **2.3.1.3 Electrodeposition Method**

Electrodeposition, often known as electroplating, is a very useful process noted for its precision, adaptability, and low cost. One of its primary advantages is the exact control it provides over the thickness and composition of deposited materials, which is critical for applications needing specialized coating characteristics. Even on intricate and irregular surfaces, the method ensures a homogeneous coating, making it important in industries such as electronics. The capacity of electrodeposition to produce high-purity deposits is very useful in industries such as microelectronics and semiconductor production. Furthermore, because it is versatile across a wide spectrum of materials, from metals to alloys and specific compounds, it is applicable in a variety of industrial applications. Because of its simplicity and minimal equipment expenses, the approach is frequently cost-effective, making it an economically viable option. Furthermore, electrodeposition saves energy. Furthermore, electrodeposition is energy-efficient, particularly when employing aqueous solutions, benefiting both economic and environmental concerns. Electrodeposition has emerged as a preferred approach in a variety of industrial applications due to its capabilities for selective deposition, strong substrate adherence, scalability for mass production, and lower waste generation as compared to competing methods.<sup>5-6</sup>

### **2.3.2 Sample Preparation method for Analysis**

#### **2.3.2.1 Sample Preparation for TEM**

The samples were deposited onto 400-mesh carbon-coated copper grids by placing 3-4 droplets of a recently prepared dilute ethanolic solution of the specimen, followed by overnight

drying of the grids. For solid powder samples, dispersion was achieved in ethanol, whereas liquid samples were promptly utilized for drop casting onto the grids.

### 2.3.2.2 Sample Preparation for XPS

To perform XPS analysis, palates of the developed material were prepared, keeping the thickness at 8 mm. To compensate for any charging effect, the binding energy of the C1s peak has been used as a reference.

## 2.4 Instrumentation

For the detailed characterization and to study the EC activity of the developed electrodes following instruments and techniques are used.

### 2.4.1 List of Instruments

1. Magnetic stirrer, IKA RCT basic.
2. Centrifuge Machine, Tarsons (SPINWIN-MC03).
3. Sonicator, Leelasonic.
4. Balance, Denver Instrument, Japan.
5. Teflon lined container (autoclave) and Oven, Genetix (GX-A5030A).
6. Hot Air Ovan, MAC (MSW-211).
7. PXRD analysis: For PXRD, a Rigaku Mini Flex II diffractometer with Cu-K $\alpha$  radiation was used. The PXRD analysis was carried out with  $2\theta$  values ranging from  $10^\circ$ -  $80^\circ$  and a scanning rate of  $2^\circ$  per minute and  $1^\circ$  per minute at  $25^\circ\text{C}$ .
8. XPS Analysis: For XPS measurements, a commercial Omicron EA 125 spectrometer equipped with a seven-channel detection system was used. Monochromatic light of Al-K $\alpha$  radiation with 1486.7 eV energy was used as an X-ray source. The emission current was set to 15 mA, and chamber base pressure was maintained below  $<10^{-9}$  mbar during the measurement.
9. FESEM analysis: To determine the morphology of the synthesized samples FESEM FEI microscope (Model- "APREO S") was used. To carry out EDS analysis, X-MaxN, Aztec (software), NS: 77887 (Detector) was used, which was attached to the FESEM. Before FESEM and EDS analysis, the synthesized materials were coated with gold or chromium by sputtering.

10. TEM analysis: TEM and HRTEM analysis were carried out using a Bruker microscope and FEI Technai G2 instrument operated with an electron beam with an energy of 200 kV.
11. Fourier Transform Infrared Spectroscopy (FTIR): To acquire FTIR spectra, a Shimadzu IR Affinity-1S spectrometer was used.
12. Raman Analysis: HORIBASCI Raman instrument (Model: LabRAM HR EVO) was used to carry out Raman analysis. The detector was a thermoelectrically cooled charged coupled device (CCD) detector of 576×384 pixels.
13. BET analysis: The BET surface area was done with Autosorb iQ-C-XR-XR-XR and BELSORP mini-X. The preheating treatment for samples was done at 300°C for 3 and 6 hours.
14. ICP-AES analysis: ICP analysis was done with model ARCOS, a Simultaneous ICP spectrometer, and a Perkin Elmer AVIO spectrometer. Before ICP analysis, the sample was digested and mixed with a digestion reagent, often an acid or a combination of acids. Commonly used acids include nitric acid (HNO<sub>3</sub>), hydrochloric acid (HCl), sulfuric acid (H<sub>2</sub>SO<sub>4</sub>),
15. All the electrochemical data was recorded in CH Instrument (CHI604E) at 25 °C.

The details of the characterization techniques are as follows:

### 2.4.2 Powder X-ray Diffraction

In 1912, the German physicist Max von Laue made a groundbreaking contribution by demonstrating X-ray diffraction (XRD), a non-destructive, versatile, and widely employed analytical technique. X-ray diffraction is extensively utilized for analyzing crystallinity, phase identification, purity assessment, determination of particle size, investigation of crystal structure, and determination of lattice parameters. X-rays, characterized by their short wavelengths in the range of  $10^{-7}$  to about  $10^{-15}$  meters, are generated through the interaction of high-energy accelerated electrons (typically at 30 kilovolts) with the core electrons of a metal. When these accelerated electrons displace core electrons from their orbits, electrons from outer orbitals drop down to fill the vacancies. The energy produced during this process manifests as an electromagnetic wave known as an X-ray. A cathode ray tube acts as the X-ray source in the X-ray diffraction apparatus.

The generated X-rays are filtered before being directed onto the sample to produce monochromatic radiation with a single wavelength. The sample is then exposed to this monochromatic radiation. The X-rays interact with the sample's crystal lattice, and reflection

occurs only when the Bragg diffraction condition is met. When the angle of incidence equals the angle of reflection, the X-ray is reflected by the sample's lattice planes, meeting the relationship indicated by Bragg's law. To sum up, X-ray diffraction is an effective analytical method that uses the concepts of X-ray generation, monochromatic radiation, and the Bragg diffraction condition to yield important details about the phase composition, crystalline structure, and other critical properties of the materials being studied.<sup>7</sup>

$$2d_{hkl} \sin \theta = n\lambda$$

Here,  $\lambda$  is the wavelength of the X-ray,  $\theta$  is the scattering angle,  $d_{hkl}$  represents the spacing between crystal planes with Miller indices  $hkl$ , and  $n$  is an integer. The characteristic diffraction pattern is produced by the relationship between the angle of incidence, the wavelength of incident X-rays, and the spacing between crystal planes, which is described by this equation. When used in X-ray diffraction, the powerful X-rays can reveal important details about the molecular and atomic structures of a material. These X-rays interact with the crystal structure as they go deeper into the substance. Each crystalline material has a different diffraction pattern because of its own atomic structure.<sup>8-9</sup>

### 2.4.2.1 Determination of Particle Size

The diffraction method uses the measurement of diffraction peak broadening to determine particle size. Particle size has a direct bearing on this occurrence. In order to obtain diffraction maxima in a crystal, the incident X-ray beam needs to line up at precise angles with a reflection plane for an accurate analysis. Using X-ray diffraction (XRD) examination, the width of the peak can be used to determine the size of the crystallite. For this, Scherer's equation is frequently used. The equation is expressed as:

$$B(2\theta) = \frac{K\lambda}{\cos\theta}$$

In this case,  $d$  stands for particle size,  $\lambda$  for incident X-ray wavelength, and  $B$  for full width at half maximum (FWHM) intensity expressed in terms of  $2\theta$ . Peak broadening results from a decrease in crystallite size, according to the equation provided.<sup>10-12</sup>

### 2.4.2.2 Determination of strain (W-H method)

The broadening of diffraction peaks in X-ray diffraction (XRD) can be analyzed and interpreted using the Williamson-Hall method, particularly when considering crystallite size and lattice strain. The contributions of crystallite size ( $D$ ) and lattice strain ( $\epsilon$ ) to the widening of XRD peaks are separated using the Williamson-Hall equation. The equation is given by:

$$\beta \cos \theta = \frac{k\lambda}{D} + 4\epsilon \sin \theta$$

The variables, in this case, are  $\beta$  (full width half maxima),  $\lambda$  (wavelength),  $k$  (constant),  $D$  (size),  $\theta$  (diffraction angle), and  $\epsilon$  (system strain value). The intercept and slope values are shown in Figure by the plot of  $\beta \cos \theta$  and  $4 \sin \theta$ ; the slope value indicates the increased strain in the system. Based on XRD peak broadening, the Williamson-Hall equation offers researchers a useful tool for understanding the structural characteristics of materials.<sup>12-13</sup>

### 2.4.3 X-ray Photoelectron Spectroscopy (XPS)

In X-ray photoelectron spectroscopy (XPS), atoms, molecules, or solid surfaces expel their core electrons when exposed to X-rays. For the XPS procedure, photons of Al  $K\alpha$  (1486.6 eV) or Mg  $K\alpha$  (1253.6 eV) are usually used. Every element has a unique core electron binding energy, which indicates the oxidation state. One can ascertain the elemental makeup of the substance by examining the peaks linked to these binding energies. The oxidation state of every element can be determined by using the core electron binding energies. These binding energies are represented by the peaks in the XPS spectrum, which can be examined to ascertain the material's composition. In addition, XPS can shed light on chemical bonding. The binding energy and peak shape provide important insights into the chemical environment of the material since they are sensitive to the oxidation and chemical state of the emitting atom. To sum up, XPS is an effective analytical method that uses X-ray irradiation to examine the material's surface composition. XPS is a useful tool in surface science and materials analysis because it allows researchers to obtain quantitative information about elemental composition, oxidation states, and chemical bonding by studying the resultant spectra and examining the core electron binding energies.<sup>14-15</sup>

### 2.4.4 Electron Microscopy

Energetic electron beams are used in electron microscopy, an imaging method, to study objects at extremely tiny scales. Although there are many different types of electron microscopes,



field emission scanning and transmission electron microscopes are the most commonly utilized.

### 2.4.4.1 Field Emission Scanning Electron Microscope (FESEM)

A popular electron microscopy method is field emission scanning electron microscopy (FESEM), which is renowned for its adaptability, range of imaging modes, simple sample preparation, and simple picture interpretation. The source of the electron beam in a FESEM is a cathode, usually made of  $\text{LaB}_6$  or tungsten filament. The specimen loses energy through a variety of processes as it interacts with the electron beam. Then, this lost energy is transformed into a variety of other forms, including heat, high-energy backscattered electrons, Auger electrons, low-energy secondary electrons, cathodoluminescence (light emission), or X-ray emission. Each of these processes sends out signals that carry important details about the specimen's composition and topography. In a typical FESEM image, only secondary electrons are detected. After being identified, these electrons are sent as signals to the processor, where they undergo additional processing to create an image of the specimen. The surface topography and composition of the sample can be seen in this image, which makes the FESEM a useful instrument for characterizing and analyzing materials. The technique is widely used in many scientific disciplines since it is simple to prepare samples and interpret images.<sup>16</sup>

### 2.4.4.2 Transmission Electron Microscope (TEM)

In terms of its fundamental elements, Transmission Electron Microscopy (TEM) and Scanning Electron Microscopy (SEM) are identical. TEM, on the other hand, varies in that it uses transmitted electrons to produce images of the sample. This method involves directing an electron beam through a thin specimen, focusing the transmitted electrons onto an image medium—fluorescent screens or photographic films, for example. SEM uses beam scattering to only provide information on the surface morphology of the sample; TEM uses transmitted electrons to create images that provide a more complete picture. provide information regarding magnetic domains, tensions, size, lattice planes, and crystal structures. TEM is notable for achieving a better resolution than SEM. Transmission electron microscopy (TEM) comes in two primary varieties: high-resolution transmission electron microscopy (HRTEM) and low-resolution TEM. Especially HRTEM provides incredibly detailed images. Lattice spacing ( $d$ ) can be computed from HRTEM pictures, which yields details about individual crystal planes ( $dhkl$ ). TEM has drawbacks despite

its great resolution and adaptability, including the requirement for experienced operators and complex sample preparation.<sup>17-18</sup>

### 2.4.4.3 Energy-Dispersive X-ray (EDX) Spectroscopy

Analytical methods like as Transmission Electron Microscopy (TEM) and Scanning Electron Microscopy (SEM) are frequently used with Energy Dispersive X-ray Spectroscopy (EDS), or EDX. This method is used to examine a sample's elemental composition. EDS analysis produces distinctive X-rays from the material being analyzed by subjecting a conducting sample to an electron beam, usually with energy between 10 and 20 kilo electron volts (keV). These X-rays originate in an area that is about two micrometers deep. An image of the distribution of each element is produced as the electron beam is traversed across the material, giving important details about the sample's chemical makeup. All photons released in EDS are concurrently gathered and quantified by a solid-state X-ray detector. Since every element has a distinct collection of peaks in its electromagnetic emission spectrum, it is possible to identify individual components and fully characterize the composition of the material.<sup>19</sup>

### 2.4.5 Fourier Transform Infrared (FTIR) Spectroscopy

The study of matter's interaction with the infrared portion of the electromagnetic spectrum is known as infrared (IR) spectroscopy. The related photon energies (from 1 to 15 kcal/mole) are too low in this spectral range to excite electrons, but they can cause vibrational excitation in atoms that are covalently bound. The infrared spectrum is commonly observed in the range of 4000 to 400  $\text{cm}^{-1}$ , whereby both inorganic and organic functional groups absorb radiation. According to the IR spectroscopy gross selection criteria, a 'IR active' vibrational mode needs to be connected to variations in the electric dipole moment. The molecule needs a change in dipole moment throughout the vibration, but it does not necessarily need a permanent dipole. IR spectroscopy plays a crucial role in identifying functional groups present on the surface of materials, as it provides insights into the vibrational characteristics associated with different chemical bonds and helps in material characterization.<sup>20</sup>

### 2.4.6 Raman Spectroscopy

Raman spectroscopy is an analytical method that uses scattered light to measure a sample's vibrational energy modes. Using this technique, a microscope focuses lasers at particular wavelengths (such 354 nm, 532 nm, and 785 nm) onto a tiny area on the sample. Next, the Raman

effect, also called the Raman shift, or frequency difference between the incident monochromatic light and the scattered light is measured. The ensuing plot of the Raman shift against the measured photons produces the Raman spectrum. This spectrum provides specific details on the sample's rotational, vibrational, and other low-frequency modes. Raman spectroscopy is a flexible technique that offers insights into both structure and chemistry. It also enables the identification of substances using their unique Raman "fingerprint." Determining details regarding the sample's symmetry, crystalline structure, disorders, and flaws is another useful application of this approach. Raman spectroscopy provides an unparalleled insight into the molecular and structural makeup of materials, making it a vital tool in many scientific domains such as biology, chemistry, and material science.<sup>21</sup>

### 2.4.7 BET Analysis

This is a popular analytical method in surface science for figuring out a porous material's specific surface area is Brunauer-Emmett-Teller. The BET method, which bears the names of its creators, Edward Teller, Paul Hugh Emmett, and Stephen Brunauer, is especially useful for determining the surface area of substances like powders, adsorbents, and catalysts that have complex pore architectures. The method relies on the adsorption of gas molecules at various relative pressures onto the surface of the material. The BET equation is used to compute the specific surface area and ascertain the monolayer capacity by examining the adsorption isotherm data. The BET technique has been widely used in many different industries, offering vital information about the textural characteristics of materials and supporting the optimization of procedures, including catalysis, gas adsorption, and material synthesis.<sup>22</sup>

### 2.4.8 ICP-AES Analysis

ICP-AES, or inductively coupled plasma atomic emission spectroscopy, is a potent analytical method that is applied to elemental analysis of various kinds of samples. This technique ionizes an inert gas, usually argon, to create a high-temperature inductively coupled plasma. When the sample—which is frequently liquid—is added to the plasma, the atoms are excited and release a distinctive light. The light that has been released is then scattered by a spectrometer, and the elemental makeup of the sample can be determined and measured using the spectrum that is produced. Because of its great sensitivity and precision, ICP-AES can be used in metallurgy,

environmental analysis, pharmaceuticals, and geochemistry. ICP-AES has become a popular and adaptable method in analytical chemistry due to its capacity to evaluate many elements at once over a wide concentration range.<sup>23</sup>

### 2.5 Techniques for Electrochemical Application and Calculations

#### 2.5.1 Voltammetry

Voltammetry is a type of electroanalysis where the current through a cell is measured when a voltage (V) is applied. Voltammetry depends on the oxidation or reduction reactions that take place at the working electrode in response to the applied voltage. It is generally carried out in a three-electrode setup that consists of a working electrode, a counter electrode, and a reference electrode. Completing the circuit, the counter electrode assumes the role of either an anode or a cathode, contingent upon the conduct of the working electrode. In the meanwhile, it is essential to measure the potential of the working electrode using the reference electrode, which has a known electrode potential. There are several voltammetry methods utilized, the most widely used ones being CV, and LSV.<sup>24</sup>

##### 2.5.1.1 Cyclic voltammetry

In the cyclic phase of an electrochemical technique called CV, the electrode's potential increases linearly with time. In CV analysis, the working electrode's potential is linearly ramped in the opposite direction to revert to the initial potential after the set potential is attained. The relationship between the applied voltage (V) and the current (i) at the working electrode is depicted in the ensuing diagram, which is called a voltammogram. Characterizing the electrochemical characteristics of analytes in solution and adsorbed species on the electrode surface is a common use for this approach. The analyte and adsorbed species must show redox activity within the potential window being scanned in order to yield significant results. A useful method for examining the redox behavior and their electrochemical characteristics is cyclic voltammetry.<sup>25</sup>

##### 2.5.1.2.1 Linear Sweep Voltammetry

An electrochemical approach called linear sweep voltage monitoring, or LSV, measures the current at the working electrode while the potential between it and the reference electrode sweeps linearly over time. The rate of electron exchange at the electrode-electrolyte interface can

be directly determined by the measured current. At a point where there is little current and no electrochemical reaction, the curve scanning starts. The current becomes noticeable as the potential rises, indicating the start of charge transport. After that, as the potential increases, the current increases until it reaches its maximum value, creating a peak current plateau. The depletion of reactive species at the interface then causes the current to begin to drop. Key outcomes of interest in LSV include the onset potential and the corresponding current resulting from the reacting species, providing valuable insights into the electrochemical behavior of the system under investigation.<sup>26</sup>

### 2.5.2 Amperometry

#### 2.5.2.1 Chronoamperometry

A technique used in electrochemistry called chronoamperometry involves stepping the voltage of the working electrode and measuring the current ( $i$ ) that results from the faradaic process at the electrode surface over a period of time ( $t$ ). The relationship between current and time is closely investigated by providing the working electrode in the electrochemical system with a single or double-stepped potential. Chronoamperometry has a higher signal-to-noise ratio than other amperometry methods. Because it allows for the measurement and integration of current over long time intervals, this technique is very useful for investigating the stability of created electrodes. It provides detailed insights into the electrochemical behavior of the system being studied.<sup>27</sup>

#### 2.5.2.2 Chronocoulometry

Chronocoulometry, like chronoamperometry, is an electrochemical technique that shares a similar principle. However, instead of focusing on the correlation between current and time, chronocoulometry examines the relationship between charge ( $Q$ ) and time ( $t$ ). In this method, the potential of the working electrode is stepped, and the resulting charge generated from the electrochemical reactions occurring at the electrode surface is monitored over a specific time duration. This approach provides valuable information about the quantity of charge transferred during the electrochemical process, offering insights into the kinetics and behavior of the system under study.

### 2.5.3 Impedance Spectroscopy

Electrochemical Impedance Spectroscopy (EIS) stands as a potent technique employed to understand the electron transfer kinetics occurring at the electrode/electrolyte interface during water-splitting reactions. The Nyquist plot, derived from EIS analysis, portrays the imaginary part of impedance against the real part. This plot provides dual insights into the electrode/electrolyte interface. Firstly, the solution resistance is determined when the semicircle shifts from the starting point to high frequency, and the disparity between the endpoint (low frequency) and the starting point of the semicircle (high frequency) calculates the charge transfer resistance of the electrode. The solution resistance remains independent of light intensity and applied bias. For the calculation of the resistance of a single electrode/electrolyte interface, the Randles model is applied, wherein the polarization resistor ( $R_{CT}$  or  $R_1$ ) is connected in parallel with the constant phase element (CPE) and in series with the bulk resistor ( $R_S$  or  $R_2$ ). The use of CPE accommodates the non-ideal behavior of the electric double layer attributed to porosity, roughness, poly-crystallinity, and dynamic disorders associated with diffusion.<sup>28</sup>

### 2.5.4 Faradaic efficiency

We have used the chronopotentiometry reaction to compare the amount of gas calculated theoretically with that which was quantified experimentally in order to calculate the Faradaic efficiency (FE). The Faradaic efficiency calculation was done using the equation below.

Faradaic efficiency = Experimental gas evolution / Theoretical gas evolution  $\times$  100 %

$$\text{Theoretical gas evolution} = Q = i \times t / n \times F$$

Here;  $i$  = current in amper,  $t$  = Time,  $n$  = Number of electrons, and  $F$  = Faraday constant

### 2.5.5 Rate constant calculation

The rate constant  $k$  can be related to the exchange current density by the following relationship:

$$k = \frac{i_0}{nFA} = J_0/nF$$

where:  $J_0$  is exchange current density,  $n$  is the number of electrons transferred, and  $F$  is the Faraday constant (96485 C/mol).

### 2.5 Electrochemical Cell to Perform the Water-Splitting reaction

#### 2.5.1 Three-electrode system

The electrolysis cell depicted in Figure 2.1 is employed for evaluating the electrocatalytic performance of an electrocatalyst. In this configuration, the glassy carbon electrode (GCE) bearing the deposited sample serves as the working electrode, with the potential for functioning either as a cathode or an anode determined by the catalyst's nature. If the working electrode operates as a cathode, the counter electrode functions as an anode, and vice versa. The counter electrode in this setup is made of platinum/graphite, while the reference electrode is Ag/AgCl. This experimental arrangement allows for a comprehensive assessment of the electrocatalytic properties of the tested materials in various electrode configurations. The electrocatalytic water-splitting process was conducted in either an acidic or alkaline medium. This process involves the application of an external potential to facilitate the splitting of water into hydrogen ( $H_2$ ) and oxygen ( $O_2$ ).<sup>29</sup>

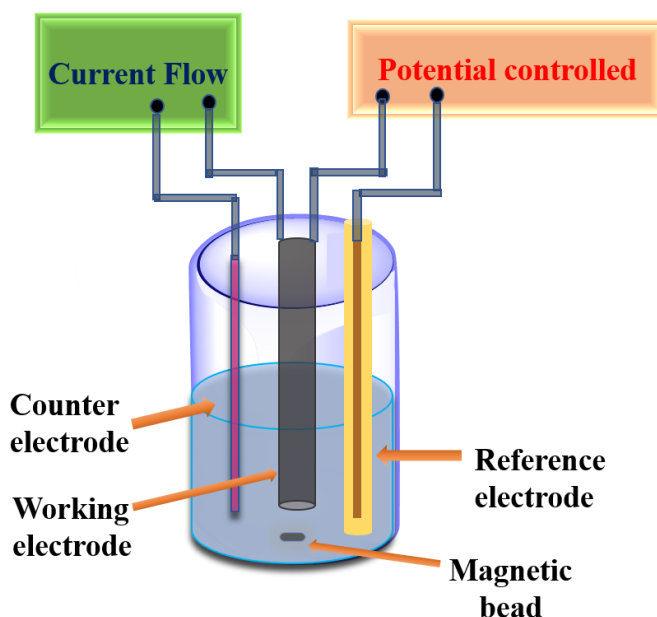


**Figure 2.1:** Schematic representation of three electrode system for electrochemical water splitting.

#### 2.5.2 Two-electrode system

A two-electrode system (Figure 2.2) is a basic configuration for water splitting in electrocatalytic applications. It consists of two electrodes submerged in an electrolyte solution. An

anode is one electrode that undergoes oxidation to produce oxygen gas ( $O_2$ ), and a cathode is another electrode that undergoes reduction to produce hydrogen gas ( $H_2$ ). Through the use of an external power source, the anode and cathode are linked externally to complete the electrical circuit. When an external voltage is supplied during the electrolysis of water, the water molecules at the anode oxidize, releasing positively charged protons ( $H^+$ ) and oxygen gas. Concurrently, reduction occurs at the cathode, where protons from the water mix with electrons from the outside circuit to generate hydrogen gas. The overall reaction is represented as  $2H_2O \rightarrow 2H_2 + O_2$ . For the purpose of researching the effectiveness and electrocatalytic performance of materials in water splitting, the two-electrode system is essential. To optimize the kinetics of the individual reactions and raise the overall efficiency of the water-splitting process, different catalysts can be used at the anode and cathode. The advancement of sustainable hydrogen production methods requires an understanding of and attention to the behavior of these catalysts in a two-electrode system.<sup>29</sup>

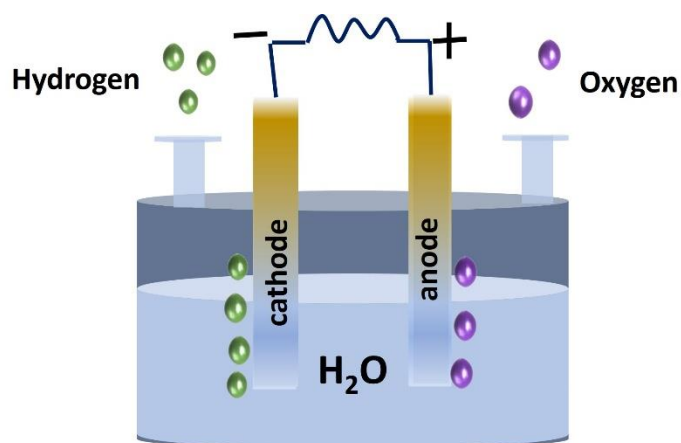


**Figure 2.2:** Schematic representation of two electrode systems for electrochemical water splitting.

## 2.7 References

1. Kirgiz, M. S., Advancements in Properties of Cements Containing Pulverised Fly Ash and Nanomaterials by Blending and Ultrasonication Method (Review-Part II). *Nano hybrids and composites* **2019**, *24* (12), 37-44.
2. Gedanken, A., Using sonochemistry for the fabrication of nanomaterials. *Ultrason Sonochem* **2004**, *11* (2), 47-55.



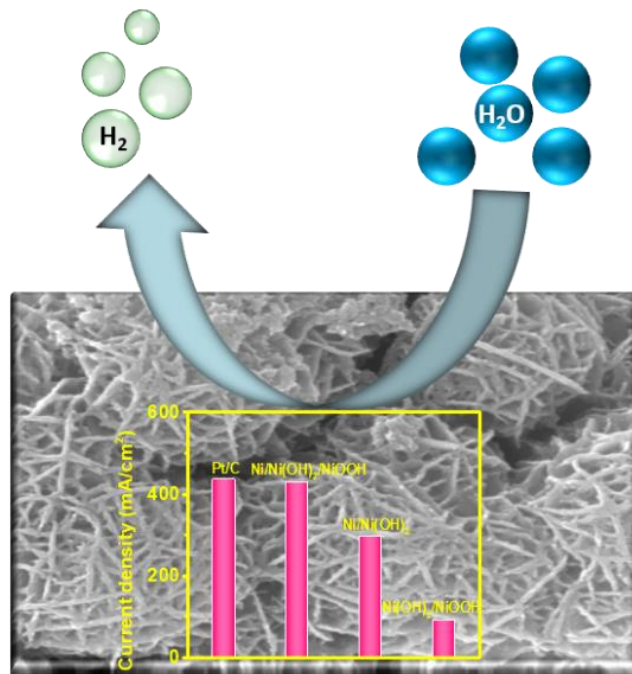
3. Gan, Y. X.; Jayatissa, A. H.; Yu, Z.; Chen, X.; Li, M., Hydrothermal synthesis of nanomaterials. *J. Nanomater.* **2020**, *2020*, 1-3.
4. Li, J.; Wu, Q.; Wu, J., Synthesis of Nanoparticles via Solvothermal and Hydrothermal Methods 12. **2016**.
5. Sun, I.-W.; Chang, J.-K., Electrodeposition of nanomaterials. *Springer Handbook of Electrochemical Energy* **2017**, 835-895.
6. Purohit, B.; Kumar, A.; Mahato, K.; Chandra, P., Electrodeposition of metallic nanostructures for biosensing applications in health care. *J. Sci. Res* **2020**, *64* (01), 68-73.
7. Jiang, Y.; Cao, L.; Hu, X.; Ren, Z.; Zhang, C.; Wang, C., Simulating powder X-ray diffraction patterns of two-dimensional materials. *Inorg. Chem.* **2018**, *57* (24), 15123-15132.
8. Beltrán-Suito, R.; Menezes, P. W.; Driess, M., Amorphous outperforms crystalline nanomaterials: surface modifications of molecularly derived CoP electro (pre) catalysts for efficient water-splitting. *J. Mater. Chem. A* **2019**, *7* (26), 15749-15756.
9. Sharma, R.; Bisen, D.; Shukla, U.; Sharma, B., X-ray diffraction: a powerful method of characterizing nanomaterials. *Recent Res Sci Technol* **2012**, *4* (8), 77-79.
10. Boddolla, S.; Thodeti, S., A review on characterization techniques of nanomaterials. *Int. j. eng. sci. math.* **2018**, *7* (1), 169-175.
11. Giannini, C.; Ladisa, M.; Altamura, D.; Siliqi, D.; Sibillano, T.; De Caro, L., X-ray diffraction: a powerful technique for the multiple-length-scale structural analysis of nanomaterials. *Crystals* **2016**, *6* (8), 87.
12. Zak, A. K.; Majid, W. A.; Abrishami, M. E.; Yousefi, R.; Parvizi, R., Synthesis, magnetic properties and X-ray analysis of  $Zn_{0.97}X_{0.03}O$  nanoparticles (X= Mn, Ni, and Co) using Scherrer and size-strain plot methods. *Solid State Sci.* **2012**, *14* (4), 488-494.
13. Prabhu, Y. T.; Rao, K. V.; Kumar, V. S. S.; Kumari, B. S., X-ray analysis by Williamson-Hall and size-strain plot methods of ZnO nanoparticles with fuel variation. *World j. nano sci. eng.* **2014**, *2014*.
14. Baer, D. R.; Engelhard, M. H., XPS analysis of nanostructured materials and biological surfaces. *J Electron Spectros Relat Phenomena* **2010**, *178*, 415-432.
15. Baer, D. R.; Engelhard, M. H.; Johnson, G. E.; Laskin, J.; Lai, J.; Mueller, K.; Munusamy, P.; Thevuthasan, S.; Wang, H.; Washton, N., Surface characterization of nanomaterials and nanoparticles: Important needs and challenging opportunities. *J. Vac. Sci. Technol. A* **2013**, *31* (5).

16. Akhtar, K.; Khan, S. A.; Khan, S. B.; Asiri, A. M., Scanning electron microscopy: Principle and applications in nanomaterials characterization. *Handbook of materials characterization* **2018**, 113-145.
17. Oku, T., Direct structure analysis of advanced nanomaterials by high-resolution electron microscopy. *Nanotech. Rev.* **2012**, *1* (5), 389-425.
18. Anjum, D. H. In *Characterization of nanomaterials with transmission electron microscopy*, IOP Conference Series: Materials Science and Engineering, IOP Publishing: 2016; p 012001.
19. Song, Y.; Li, X.; Wang, L.; Rojanasakul, Y.; Castranova, V.; Li, H.; Ma, J., Nanomaterials in humans: identification, characteristics, and potential damage. *Toxicol. Pathol.* **2011**, *39* (5), 841-849.
20. Khan, S. A.; Khan, S. B.; Khan, L. U.; Farooq, A.; Akhtar, K.; Asiri, A. M., Fourier transform infrared spectroscopy: fundamentals and application in functional groups and nanomaterials characterization. *Handbook of materials characterization* **2018**, 317-344.
21. Havel, M.; Colomban, P., Smart Raman and Rayleigh spectroscopy for the analysis of nanomaterials. *Microscopy and Analysis* **2006**, *113*, 13-16.
22. Brame, J. A.; Griggs, C. S., Surface area analysis using the Brunauer-Emmett-Teller (BET) method: scientific operation procedure series: SOP-C. **2016**.
23. Jiang, X.; Huang, K.; Deng, D.; Xia, H.; Hou, X.; Zheng, C., Nanomaterials in analytical atomic spectrometry. *TrAC Trends in Analytical Chemistry* **2012**, *39*, 38-59.
24. Majhi, K. C.; Yadav, M., Bimetallic chalcogenide nanocrystallites as efficient electrocatalyst for overall water splitting. *J. Alloys Compd.* **2021**, *852*, 156736-156752.
25. Doyle, R. L.; Godwin, I. J.; Brandon, M. P.; Lyons, M. E., Redox and electrochemical water splitting catalytic properties of hydrated metal oxide modified electrodes. *Phys. Chem. Chem. Phys.* **2013**, *15* (33), 13737-13783.
26. Anantharaj, S.; Noda, S.; Driess, M.; Menezes, P. W., The pitfalls of using potentiodynamic polarization curves for tafel analysis in electrocatalytic water splitting. *ACS Energy Lett.* **2021**, *6* (4), 1607-1611.
27. Ren, J.; Antonietti, M.; Feller, T. P., Efficient water splitting using a simple Ni/N/C paper electrocatalyst. *Adv. Energy Mater.* **2015**, *5* (6), 1401660-140672.

28. Anantharaj, S.; Noda, S., Appropriate use of electrochemical impedance spectroscopy in water splitting electrocatalysis. *ChemElectroChem* **2020**, *7* (10), 2297-2308.
29. Li, X.; Zhao, L.; Yu, J.; Liu, X.; Zhang, X.; Liu, H.; Zhou, W., Water splitting: from electrode to green energy system. *Nano-Micro Lett.* **2020**, *12*, 1-29.

## Chapter 3

### *Ni/Ni(OH)<sub>2</sub>/NiOOH Nanoworms on Carbon Cloth for Electrocatalytic Hydrogen Evolution*



- \* In this chapter, electrodeposited Ni/Ni(OH)<sub>2</sub>/NiOOH nanoworm heterostructure was developed on carbon cloth.
- \* The electrodeposited Ni/Ni(OH)<sub>2</sub>/NiOOH nanoworm applied for electrochemical HER activity, which shows good activity compared to Ni/Ni(OH)<sub>2</sub> and Ni(OH)<sub>2</sub>/NiOOH.

## *Abstract*

The development of an efficient electrocatalyst for hydrogen evolution reaction (HER) is essential to facilitate the practical application of water splitting. Here, an electrocatalyst; Ni/Ni(OH)<sub>2</sub>/NiOOH is aimed to develop via electrodeposition technique on carbon cloth, which shows efficient activity and durability for HER in alkaline medium. Phase purity and morphology of the electrodeposited catalyst are determined through powder x-ray diffraction and electron microscopic techniques. The compositional and thermal stability of the catalyst is checked by x-ray photoelectron spectroscopy and thermogravimetry analysis. Electrodeposited Ni/Ni(OH)<sub>2</sub>/NiOOH material is an efficient, stable, and low-cost electrocatalyst for hydrogen evolution reaction in 1.0 M KOH medium. The catalyst exhibits remarkable performance, achieving a current density of 10 mA/cm<sup>2</sup> at a potential of -0.045 V *vs.* RHE and the Tafel slope value is 99.6 mV/dec. The overall electrocatalytic water splitting mechanism using Ni/Ni(OH)<sub>2</sub>/NiOOH catalyst is well explained, where formation and desorption of OH<sup>-</sup> ion on the catalyst surface is significant in alkaline pH. The developed electrocatalyst shows significant durability up to 200 h at a negative potential window in a highly corrosive alkaline environment along with an efficient activity. The electrocatalyst can generate 165.6 μmol of H<sub>2</sub> in ~145 min of reaction time with 81.5% Faradaic efficiency.

### 3.1 Introduction

To meet the daily energy requirement, strong consumption of fossil fuels is going on, which increases global warming and environmental pollution significantly. Thus, searching for clean and renewable energy sources as the replacement of fossil fuels is of utmost urgency. Water electrolysis steered by renewable sources is recognized as a clean and sustainable way to produce eco-friendly and high-purity hydrogen.<sup>1-2</sup> Hydrogen evolution reaction (HER) is a process that is effectively assisted by platinum and its alloys and requires a small overpotential to generate high cathodic current.<sup>3-5</sup> However, the large-scale application for HER is hindered by the scarcity and cost of noble metals; therefore, the replacement of Pt metal is very much essential. In this aspect, earth-abundant 3d metals, including metal chalcogenides, hydroxides, phosphides, and nitrides, are studied to enhance the activity and durability in such potential clean hydrogen energy.<sup>6-12</sup>

In the past few years, various studies have observed that Ni and its derivatives are efficient, cost-effective, and abundant electrocatalytic candidates for HER.<sup>13-15</sup> The higher electrocatalytic activity of Ni based derivatives is due to superior hydrogen adsorption energy on Ni surfaces. In alkaline solution, metallic Ni and stainless steel are used in industry for water splitting reaction. However, due to the very high overpotential and large Tafel slope, metallic Ni is not an ideal electrocatalyst.<sup>16-17</sup> Furthermore, Ni metal abundance also attracts its uses as an alternative electrode for HER. However, in the form of pure Ni metal, it is not stable and easily oxidized by environmental oxygen.<sup>18-19</sup> So, the improvement of an efficient and stable non-precious Ni-based electrocatalyst for HER in an alkaline medium is an imminent need to be addressed. In this context, Ofoli and co-workers developed a catalytic film of walnut-shaped Ni/Ni(OH)<sub>2</sub> core-shell structure for HER using 0.1 M phosphate buffer and 1.0 M KOH solution.<sup>20</sup> In a phosphate buffer solution, cv-Ni (developed catalyst) and cc-Ni (traditional catalyst) have a Tafel slope of 0.25 V/dec and 0.34 V/dec, respectively reported by the same group. Wu *et al.* reported the synthesis of Ni(OH)<sub>2</sub> nanosheets on Ni foam through a single-step hydrothermal technique with the homogeneous distribution.<sup>21</sup> The developed unique binder-free electrocatalyst show remarkable activity for HER with 172 mV overpotential for the generation of 10 mA/cm<sup>2</sup> current density in 1.0 M KOH solution.

Similarly, Wang *et al.* reported heterostructured Ni@NiO wrapped carbon fiber effectively participated as a bifunctional catalyst for HER and OER in alkaline pH.<sup>22</sup> The heterojunction like nano-interface and the formation of Ni(III) species are beneficial for HER and OER. The integrated Ni@NiO on carbon fiber shows excellent electrocatalytic performance with a lower Tafel slope value and

overpotential as a durable electrocatalyst with the stability of 60 hours without any sign of decay in current density. Markovic et al. developed  $\text{Ni}(\text{OH})_2/\text{M}$  catalyst for water splitting reaction with different metals like Ni, V, and Ti and demonstrated the best result with  $\text{Ni}(\text{OH})_2/\text{Ni}$  in alkaline electrolysis.<sup>23</sup> The same group showed that in an alkaline medium, the metallic Ni surface is responsible for H atom adsorption and  $\text{H}_2$  gas collection, whereas  $\text{Ni}(\text{OH})_2$  is responsible for water splitting reaction.  $\text{Ni}(\text{OH})_2@/\text{Ni}$  was electrodeposited on carbon cloth by Yang and co-workers, which behave as an electrocatalyst for water splitting reaction.<sup>24</sup> The developed nanoporous  $\text{Ni}(\text{OH})_2@/\text{Ni}$  exhibits superior performance in alkaline medium, achieving a potential of 1.58 V for 10  $\text{mA}/\text{cm}^2$  current density. Theoretical studies also proved that the synergistic effect between Ni and  $\text{Ni}^{2+}$  favors the chemisorption of hydrogen intermediates, which leads to higher activity. Recently, Liu and co-workers reported electrodeposition of  $\text{Ni}/\text{Ni}(\text{OH})_2$  on a Ni foam substrate for HER in alkaline media with a lower Tafel slope of 54.5  $\text{mV}/\text{dec}$ .<sup>25</sup> Huang *et al.* developed  $\text{NiWO}_4$  decorated  $\text{Ni}_3\text{S}_2$  heterostructure with a two-step hydrothermal method as an efficient HER active electrocatalyst in 1.0 M KOH medium.<sup>26</sup> Improved HER activity using the heterostructure electrocatalyst is due to highly active interfaces between  $\text{NiWO}_4$  amorphous nanoparticles and  $\text{Ni}_3\text{S}_2$  surface. Yang and co-workers develop  $\text{Ni}_3\text{S}_2/\text{VS}_4$  electrocatalyst on the surface of Ni foam by self-driven synthetic method for water splitting reaction in an alkaline medium.<sup>27</sup> After the formation of the heterostructure, a highly active  $\text{S}_2^{2-}$  bridging site on the interface between  $\text{Ni}_3\text{S}_2$  and  $\text{VS}_4$  enhanced HER kinetics.

Based on the above literature, it is clear that  $\text{Ni}(\text{OH})_2$  or NiO present on Ni can serve as an efficient electrocatalyst in the alkaline medium. It is also reported that  $\text{Ni}(\text{OH})_2$  surface offers the preferential adsorption of  $\text{OH}^-$  ion to promote water splitting reaction. Furthermore, the synergistic effect of metal and metal hydroxide plays a significant role in transferring the adsorbed H atom onto Ni(0) surface for the  $\text{H}_2$  molecule generation. Further, the adsorption of  $\text{OH}^-$  can be accelerated by generating a more d-electron deficient system (e.g., NiOOH) into the heterostructure matrix. Therefore, the development of an electrocatalyst with a combination of metallic Ni,  $\text{Ni}(\text{OH})_2$ , and NiOOH species in a simple and clean way with high efficiency and durability is very much essential. A heterostructure could significantly enhance the active sites to increase HER performance. To develop heterostructure, electrodeposition is a simple, environmental friendly, and hassle free technique to grow an electrocatalyst on a conducting substrate, which can generate a nanoscale 2D structure with higher activity and durability.<sup>28</sup> 2D structured materials can also provide large surface area, which is beneficial to achieve high activity during the hydrogen

evolution reaction. The crystal orientation of the electrodeposited sample depends on applied potential, the composition of the electrolyte, pH, and temperature, etc. factors.<sup>29-31</sup> Furthermore, the electrodeposition process also produced a binder-free electrode, which could diminish the catalytic activity by reducing the active sites.<sup>32</sup>

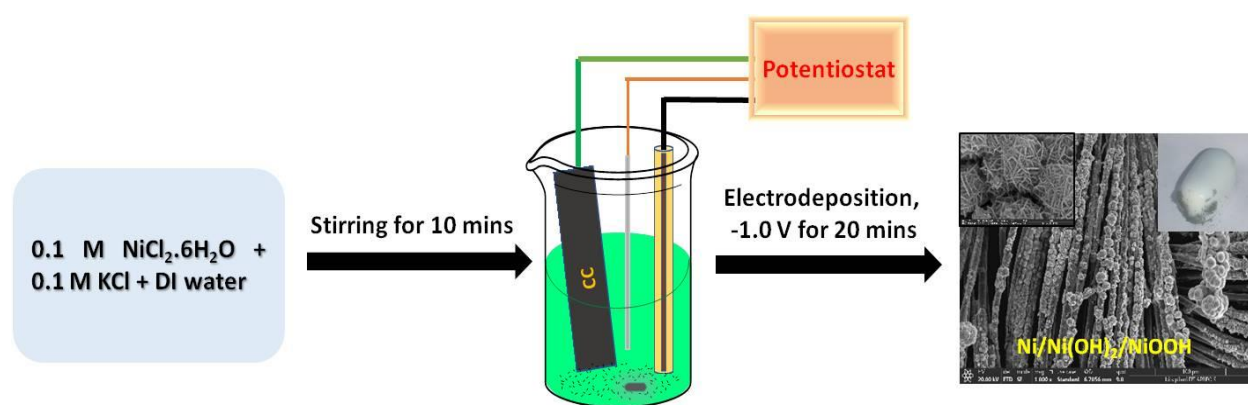
Being motivated from the above studies herein, we develop a facile electrodeposited approach for the synthesis of Ni/Ni(OH)<sub>2</sub>/NiOOH heterostructure on carbon cloth (CC). The fabrication of composite materials is simple, economical, and easy to scale up. The samples are characterized by XRD, XPS, FESEM, TEM, TGA, FTIR, and Raman techniques. The electrodeposited material represents the best electrocatalytic performance for HER in alkaline media, achieving a current density of 10 mA/cm<sup>2</sup> at the potential of -0.045 V vs. RHE. The overall electrocatalytic mechanism is well explained. FESEM analysis of reused catalyst confirms the retention of morphology. The advantages of this research are manifold. First, the electrodeposition process is straightforward and facile, producing a pure phase of Ni/Ni(OH)<sub>2</sub>/NiOOH heterostructure. The formation of other products during the synthesis is negligible. Second, the experimental time scale during electrodeposition is very less than any other developed method. Third, Ni metal is cost-effective, and earth-abundant rather than noble metals and fibrous like morphology of the catalyst provides more active sites. Fourth, the synergistic effect between Ni, Ni(OH)<sub>2</sub>, and NiOOH ions favor more active surface area and sites, thus leading to higher activity for HER in alkaline medium. These results prominently offer an active, durable, and economic heterostructure for HER.

## 3.2 Experimental Section

**3.2.1 Synthesis of electrodeposited Ni/Ni(OH)<sub>2</sub>/NiOOH heterostructure on CC:** For electrodeposition, cleaned carbon cloth, platinum wire, and Ag/AgCl were used as the working electrode, counter electrode, and reference electrode, respectively. Electrodeposition was performed under the potential of -1.0 V vs. Ag/AgCl (-0.3894 V vs. RHE) for 20 minutes at room temperature. The mixture of 0.1 M nickel (II) chloride hexa-hydrate and 0.1 M KCl (pH = ~ 7) was used as an electrolyte for electrodeposition. After electrodeposition, the sample was dried in air for 40 minutes at 35 °C. This process helps to acquire the optimized sample of Ni/Ni(OH)<sub>2</sub>/NiOOH heterostructure. Then the as-prepared electrode was washed with DI water and alcohol before electrochemical application. A similar



experiment was carried out for 10 and 30 minutes of deposition, keeping the other reaction parameters unchanged to optimize the electrodeposition time. The optimized time for electrodeposition was 20 minutes to avoid over deposition or less deposition. An external magnet attracts the electrodeposited sample due to the presence of 'Ni(0)', and the overall electrodeposition process is shown in Scheme 3.1. To check the physical stability of the developed species: Ni(0), Ni(OH)<sub>2</sub>, and NiOOH in the matrix of a heterostructure for a longer period, the samples were preserved separately for 2 and 7 days in a laboratory environment. Until otherwise indicated, the preserved samples are named as Ni-2d and Ni-7d for 2 days and 7 days, respectively.



**Scheme 3.1:** Schematic illustration for the synthesis of Ni/Ni(OH)<sub>2</sub>/NiOOH on carbon cloth via electrodeposition.

**3.2.2 Synthesis of Ni(OH)<sub>2</sub>/NiOOH on CC:** Hydrothermal method was used to decorate Ni(OH)<sub>2</sub>/NiOOH on CC following reported literature.<sup>33</sup> Briefly, 40 mL water was used to dispersed 0.6 gm of Ni(NO<sub>3</sub>)<sub>2</sub> and 0.6 gm of urea. 0.15 gm of NH<sub>4</sub>F was separately dispersed in 30 mL distilled water. After mixing and sonicating both solutions for 10 minutes, it was transferred into a 100 mL Teflon-lined autoclave. Fixed-size carbon cloth was used to develop Ni(OH)<sub>2</sub>/NiOOH and dipped in the hydrothermal container. The hydrothermal reaction condition was maintained at 105 °C for 6 h. The catalyst deposited CC was rinsed with DI water and alcohol before using for electrocatalysis.

**3.2.3 Synthesis of Ni/Ni(OH)<sub>2</sub>:** The hydrothermal method was used to synthesize Ni/Ni(OH)<sub>2</sub> by following existing literature.<sup>34</sup> In brief, 0.9 gm NiCl<sub>2</sub>.6H<sub>2</sub>O was added in 15 mL of 1 M NaOH solution and stirred for 15 minutes. After that, 1.5 mL of hydrazine hydrate was added to the solution, and the

whole solution was stirred for 30 minutes. The overall solution was transferred into the Teflon-lined autoclave, and the hydrothermal reaction was carried out for 15 h at 180 °C. The obtained black powder was rinsed with the DI water and alcohol several times and dried well. PXRD analysis (Figure 3.1a) was carried out to confirm the synthesis of the pure phase of Ni/Ni(OH)<sub>2</sub>. To verify the hexagonal morphology of Ni/Ni(OH)<sub>2</sub> material, FESEM analysis was performed and is shown in Figure 3.1b. All the peak positions in XRD and morphology of Ni/Ni(OH)<sub>2</sub> are well-matched with the existing literature.<sup>34</sup>

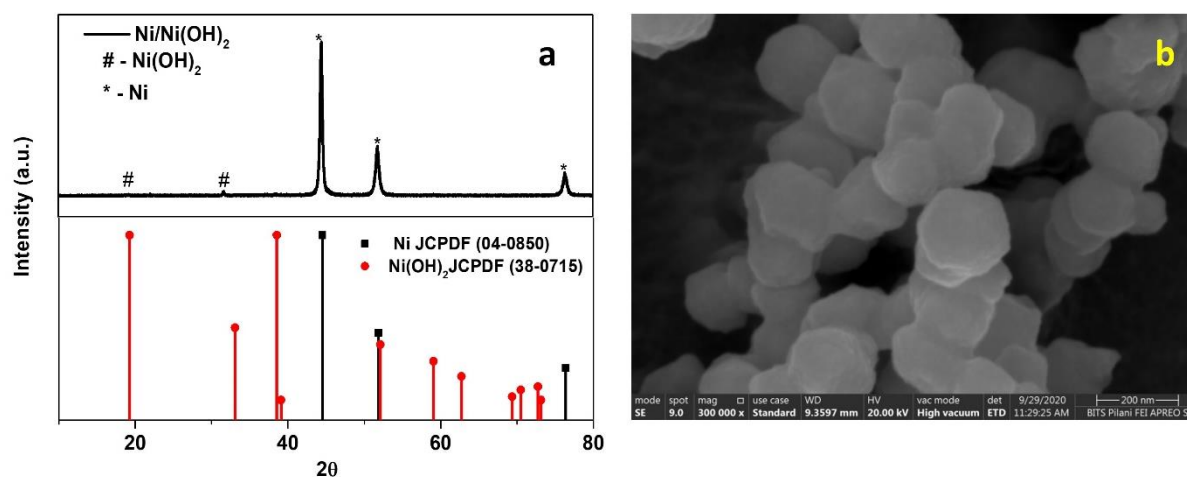


**Figure 3.1:** (a) PXRD analysis and (b) FESEM image of Ni/Ni(OH)<sub>2</sub>

**3.2.4 Electrochemical Measurement:** For electrochemical application, Ag/AgCl, graphite rod, and the sample deposited CC was used as the reference electrode, counter electrode, and working electrode, respectively, with a scan rate of 2 mV/sec. 1.0 M KOH solution (pH ~14) was used as an electrolyte throughout the study. 1 cm × 1 cm size of carbon cloth was used during the synthesis of Ni/Ni(OH)<sub>2</sub>/NiOOH samples. Therefore, the amount of heterostructure was deposited on carbon cloth is 3.8 mg/cm<sup>2</sup>. However, during electrocatalysis, 0.4 cm × 0.4 cm area of the working electrode (sample deposited carbon cloth) was maintained, and the amount of catalyst was 0.60 mg. For all the controlled experiments (Ni(OH)<sub>2</sub>/NiOOH, Ni/Ni(OH)<sub>2</sub>, and Pt/C), the ink was prepared with 0.60 mg of the electrocatalyst, 200 μL of isopropyl alcohol, and 20 μL of Nafion and then quantitatively transferred into 0.4 cm × 0.4 cm area of carbon cloth. The electrochemically insulating epoxy paste was used to fix the specific area of the working electrode. All the electrochemical data was collected with respect to Ag/AgCl with a potential window of -0.8 to -1.8 V for HER. Finally, all the potential data were reported with respect to a reversible hydrogen

electrode (RHE). For impedance analysis, a frequency range of 50 kHz to 1 Hz and onset potential was used at room temperature in 1.0 M KOH solution.

### 3.3 Results and Discussions

#### 3.3.1 Synthesis and structural analysis of electrodeposited sample:

##### 3.3.1.1 PXRD analysis

Crystallinity and phase purity of electrodeposited materials are determined by powder X-ray diffraction analysis. Figure 3.2a shows three significant peaks at  $44.5^\circ$ ,  $51.8^\circ$ , and  $76.3^\circ$  for (111), (200), and (220) planes of cubic Ni (JCPDS 04-0850). The other diffraction peaks at  $11.2^\circ$  and  $22.4^\circ$  for (003) and (006) planes, respectively, of NiOOH (JCPDS 6-0075). Furthermore,  $33.6^\circ$ ,  $39^\circ$ , and  $59.8^\circ$  are well-matched with (100), (101), and (110) planes, respectively of Ni(OH)<sub>2</sub> (JCPDS 38-0715). Therefore, the electrodeposited sample consists of a heterostructure of Ni/Ni(OH)<sub>2</sub>/NiOOH. All the species, Ni(0), Ni(OH)<sub>2</sub>, and NiOOH, are present within the crystal lattice of the heterostructure. All the diffraction peaks for Ni(0) and Ni(OH)<sub>2</sub>/NiOOH are well-matched with the literature.<sup>35-37</sup> PXRD analysis is performed for Ni-2d and Ni-7d samples and represented in Figure 3.2b and 3.2c. Figure 3 shows the presence of all the peaks at  $44.5^\circ$ ,  $51.8^\circ$ , and  $76.3^\circ$  for Ni(0) and  $33.6^\circ$ ,  $39^\circ$ , and  $59.8^\circ$  for Ni(OH)<sub>2</sub> in the heterostructure. The remaining peaks confirm the formation of NiOOH within the structure. The absence of any extra peak substantiates the sample is in pure phase. Therefore, the electrodeposited sample on CC is crystalline and physically very stable. Furthermore, Ni(0) within the heterostructure is stabilized by Ni(OH)<sub>2</sub> and NiOOH species for a more extended period.

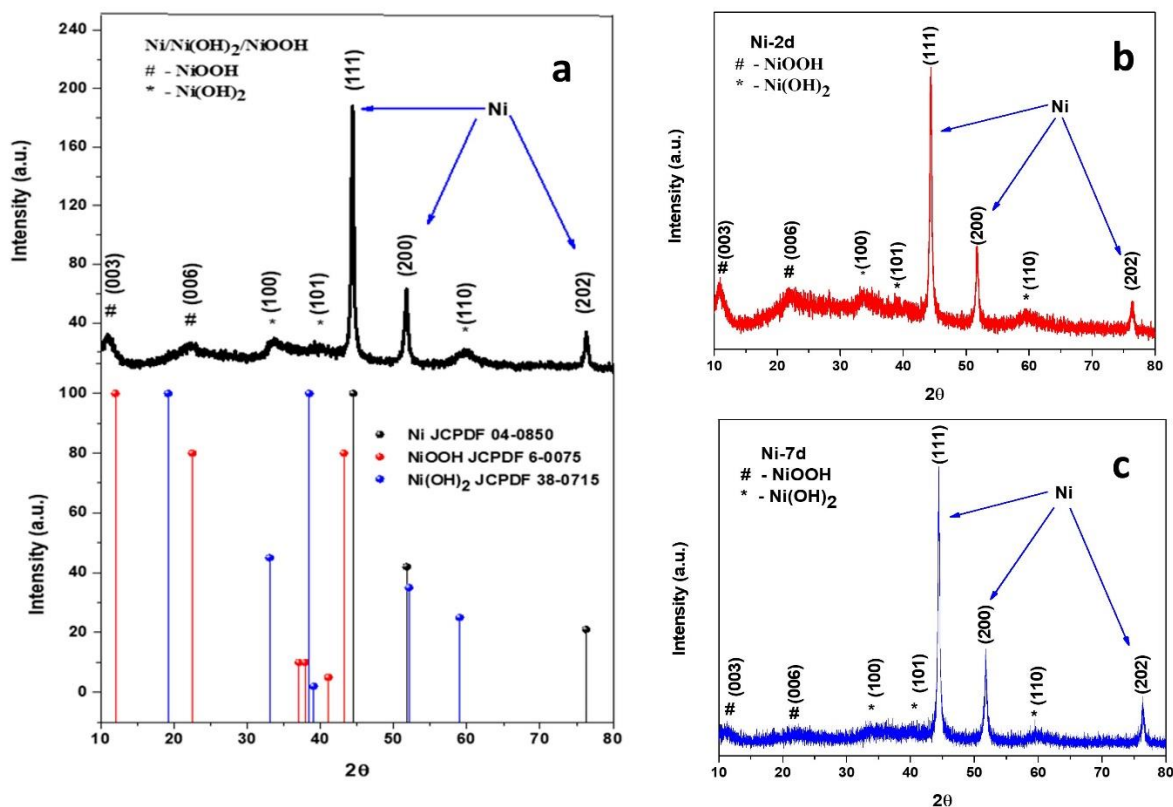


**Figure 3.2:** PXRD pattern of (a) fresh (b) 2-day (c) 7-day Ni/Ni(OH)<sub>2</sub>/NiOOH heterostructure.

### 3.3.1.2 TGA, FTIR and Raman analysis

Thermogravimetric analysis is performed for the developed heterostructure to check the thermal and physical stability. The typical thermogravimetric plot, weight (%) vs. temperature (°C) shows two temperature intervals as well as weight (%) loss of the sample (Figure 3.3a). The corresponding weight (%) losses are 12.1% and 9.6% at a temperature of 40-140 °C and 210-360 °C. The first weight (%) loss signifies eliminating adsorbed and intercalated water molecules within the heterostructure. The second loss is due to the thermal decomposition of Ni(OH)<sub>2</sub> to NiO and water molecules.<sup>38-40</sup>

FTIR and Raman analysis is performed for the electrodeposited sample. FTIR analysis exhibit (Figure 3.3b) 1334 and 1645 cm<sup>-1</sup> peaks represent the stretching and bending vibration of NO<sub>3</sub><sup>-</sup> or CO<sub>3</sub><sup>2-</sup> and H<sub>2</sub>O, respectively.<sup>41-43</sup> The other peak at 601 cm<sup>-1</sup> for Ni-OH vibration and 456 cm<sup>-1</sup> for Ni-O stretching mode, indicates the formation of Ni(OH)<sub>2</sub>.<sup>43</sup> An intense and broad peak

centered at  $3448\text{ cm}^{-1}$  symbolizes O-H stretching vibration.<sup>44-45</sup> Raman analysis represent three peaks at  $542\text{ cm}^{-1}$ ,  $689\text{ cm}^{-1}$ , and  $1062\text{ cm}^{-1}$ , shown in Figure 3.3.c. The first two peaks at  $542$  and  $689\text{ cm}^{-1}$  corresponds to the presence of Ni(III)-O and Ni(OH)<sub>2</sub> within the heterostructure. The third peak at  $1062\text{ cm}^{-1}$  represents the Ni-O-O stretching mode in the NiOOH structure. All the FTIR and Raman peaks for Ni/Ni(OH)<sub>2</sub>/NiOOH heterostructure are well-matched with existing literature.<sup>33, 46-48</sup>

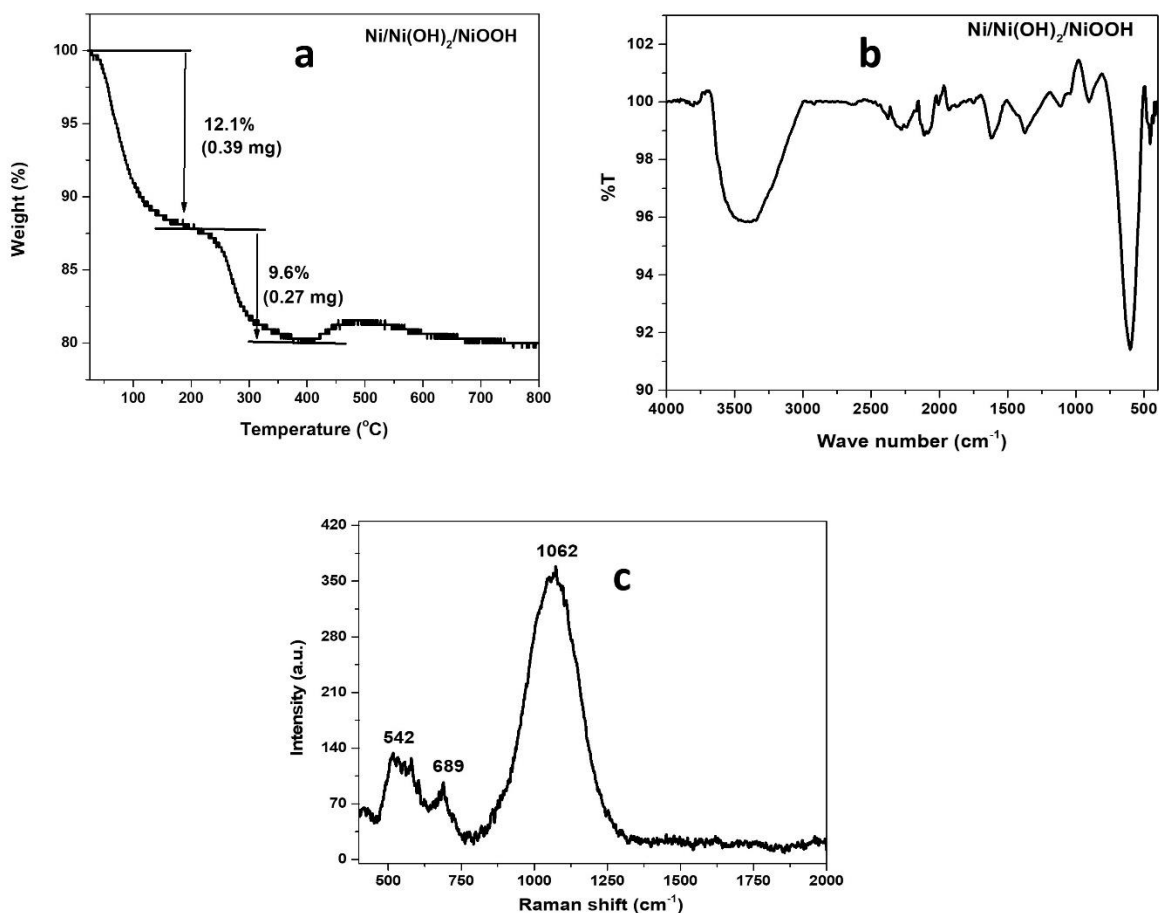


**Figure 3.3:** (a) TGA analysis, (b) FTIR spectra, (c) Raman analysis of Ni/Ni(OH)<sub>2</sub>/NiOOH heterostructure.

### 3.3.1.3 XPS analysis

X-ray photoelectron spectroscopy (XPS) confirms the presence of Ni(0), Ni(OH)<sub>2</sub>, and NiOOH species and chemical composition in the electrodeposited heterostructure. All the

deconvoluted and survey XPS spectra are given in Figure 3.4. Survey spectra (Figure 3.4a) show peaks for Ni(0), Ni<sup>2+</sup>, oxygen, and carbon. The peak is located at 284.6 eV attributed to C 1s. The deconvoluted spectrum of Ni 2p binding energy is fitted with two Ni doublets and a pair of satellites. The binding energies at 855.07 eV and 872.60 eV for 2P<sub>3/2</sub> and 2P<sub>1/2</sub> symbolize the formation of Ni<sup>2+</sup> ion as Ni(OH)<sub>2</sub> (Figure 3.4b and c). The spin-energy separation between the two doublets is 17.6 eV, which represents a characteristic of the Ni(OH)<sub>2</sub> phase. The two shake-up satellite peaks (represented as "sat") due to Ni<sup>2+</sup> are observed at 860.85 eV and 879.9 eV. The presence of Ni(OH)<sub>2</sub> is confirmed from the binding energy values and well-matched with the literature.<sup>49-51</sup> Other than Ni(OH)<sub>2</sub>, another two peaks are observed at 856.89 eV and 874.66 eV binding energies, which signifies the formation of NiOOH (Figures 3.4b and c).<sup>33</sup> Along with Ni<sup>2+</sup> and Ni<sup>3+</sup>, peaks due to Ni(0) is also observed. The deconvoluted spectra of metallic Ni 2p exhibit two spin-orbit doublets, shown in Figure 3.4b and c. The observed binding energies at 852.68 eV and 869.95 eV for 2P<sub>3/2</sub> and 2P<sub>1/2</sub>, respectively, are due to the presence of Ni(0) in the system.<sup>52</sup> The peak intensity of Ni(0) is significantly less; it may be due to the surface oxidation to Ni(OH)<sub>2</sub> and NiOOH species, which limits the detection of Ni(0) in the inner core of the developed heterostructure. From the deconvoluted spectrum of O1s indicates the presence of two peaks at 530.6, and 532.4 eV corresponds to the presence of O<sup>2-</sup> and OH<sup>-</sup>, respectively (Figure 3.4d).<sup>53</sup> The deconvoluted spectra indicate the presence of Ni(0), Ni(OH)<sub>2</sub>, and NiOOH in the electrodeposited sample. Therefore, XPS analysis confirmed the oxidation state and composition (Ni/Ni(OH)<sub>2</sub>/NiOOH) of the heterostructure, which is well-matched with our XRD result.

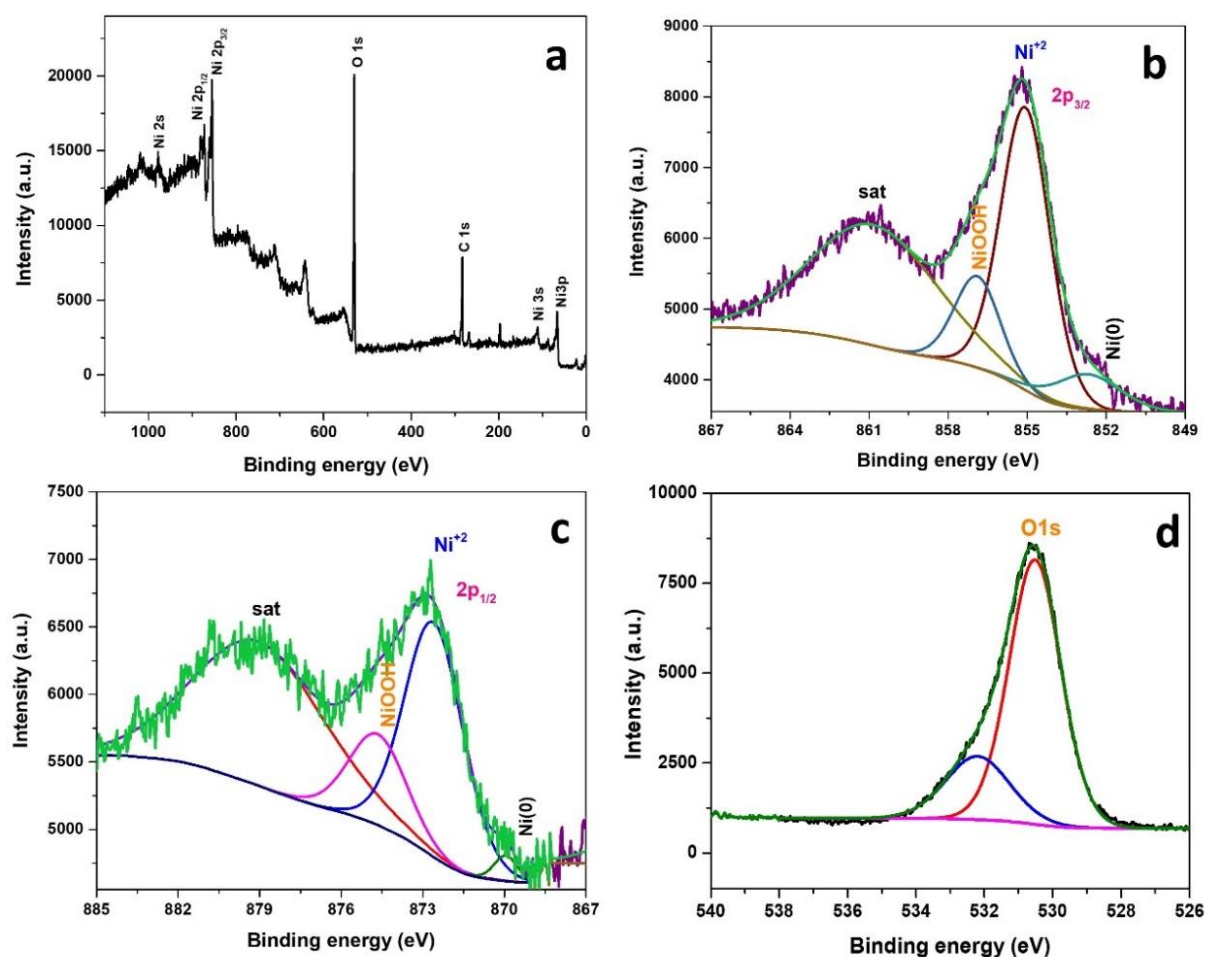


**Figure 3.4:** XPS analysis of Ni/Ni(OH)<sub>2</sub>/NiOOH heterostructure (a) survey spectrum, (b) and (c) deconvoluted spectra of Ni(0), Ni(OH)<sub>2</sub>, and NiOOH, and (d) deconvoluted spectra of O 1s.

### 3.3.2 FESEM, TEM, and EDS analysis of electrodeposited sample:

The composition, size, and shape of the samples are determined from electron microscopy analysis. Low- and high-resolution FESEM images (Figure 3.5a to d) indicate that the composite sample is assembled of vertically grown nano-worm like structure. It is clear from Figure 3.5c that the 2D nanoworms are interconnected and having sharp edges of 36 nm. It is observed that the entire CC is covered with vertically grown nanoworms (Figures 3.5a and b). Therefore, the electrodeposition technique helps in uniform coverage of CC. It is also observed that Ni/Ni(OH)<sub>2</sub>/NiOOH heterostructures have a larger number of pores on the surface, which may



facile electrolyte penetration and provide active sites during electrocatalysis. Therefore, the open porous structure of interconnected 2D Ni/Ni(OH)<sub>2</sub>/NiOOH nanoworms would be convenient for electrolyte penetration, diffusion, and faster electron transfer. 2D nanostructure of an electrocatalyst shows higher electrocatalytic performance, and it is well-matched with the literature.<sup>20, 54,55</sup>

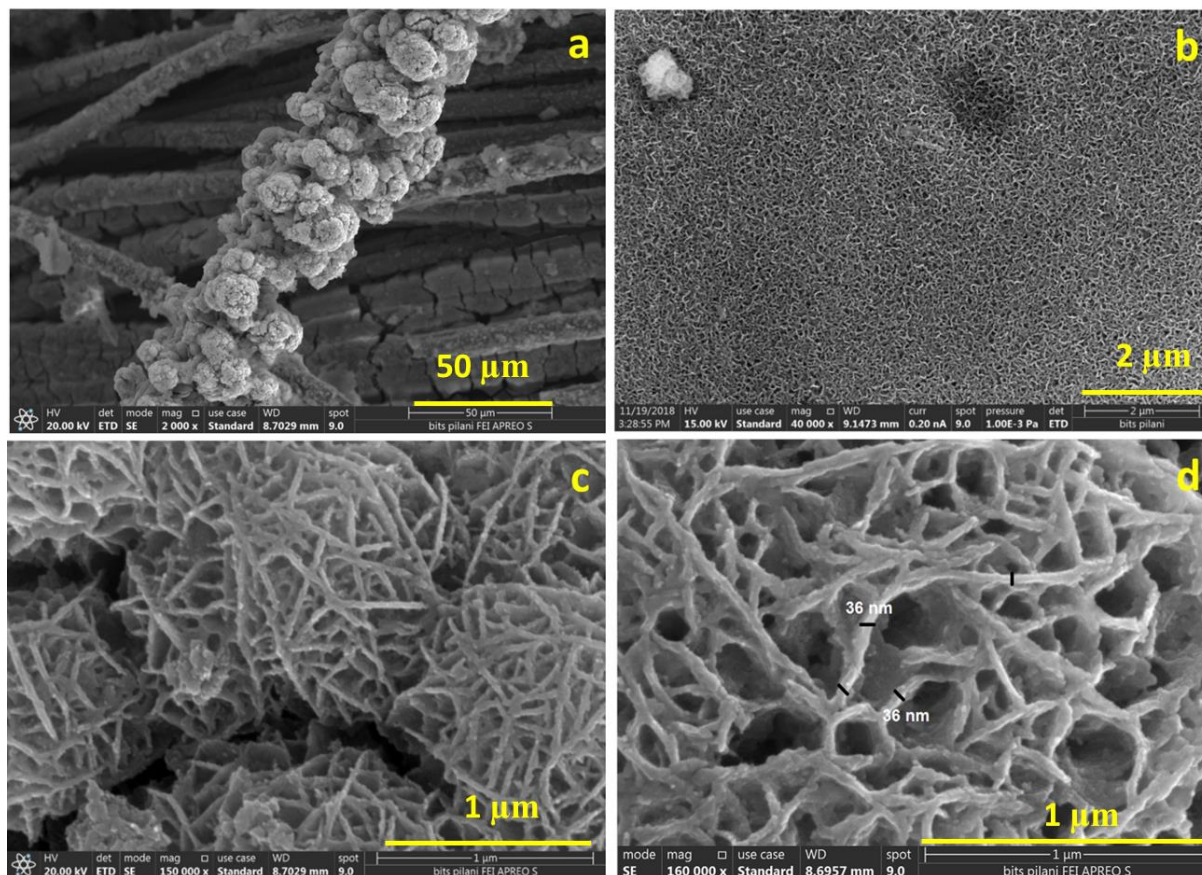


**Figure 3.5:** FESEM images of Ni/Ni(OH)<sub>2</sub>/NiOOH heterostructure at different magnifications, (a) low, (b) medium, (c and d) high.

To check the composition of the sample, EDS mapping analysis is carried out, which confirms the presence of Ni, O, and C with uniform elemental distribution on CC (Figure 3.6a). Line mapping analysis also confirms the presence of C, O, and Ni uniformly throughout the heterostructure (Figure 3.6b).



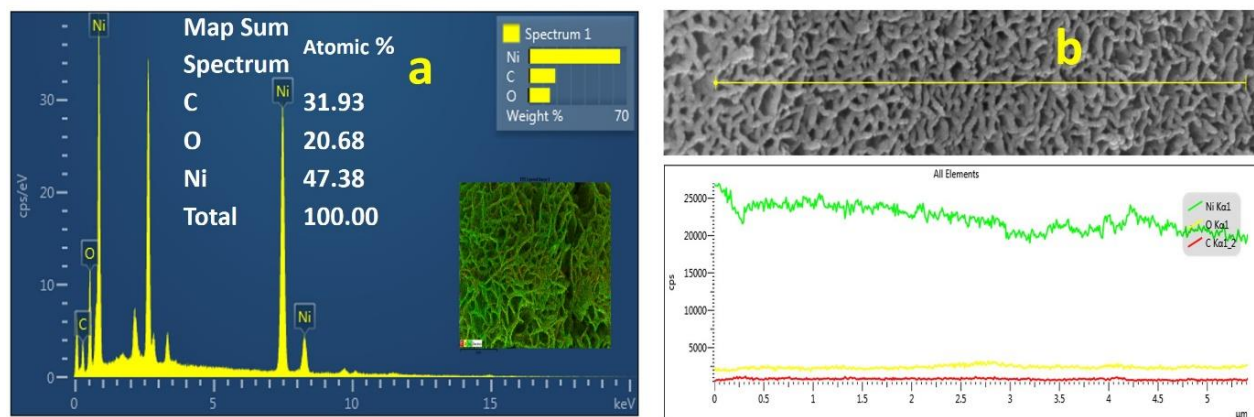


**Figure 3.6:** (a) EDS spectra (b) Line mapping analysis of Ni/Ni(OH)<sub>2</sub>/NiOOH heterostructure.

Further confirmation of morphology, transmission electron microscopy analysis is performed. For TEM analysis, electrodeposited samples are collected from CC via ultrasonication. Figure 3.7a represents nanoworm like morphology of Ni/Ni(OH)<sub>2</sub>/NiOOH heterostructure with a sharp edge. The inset of Figure 3.7a also confirms the cross-linked structure of the electrodeposited sample. It can be seen from Figure 3.7b that the as-prepared composite is composed of nanoworm architecture of 37 nm edge length, which is well-matched with FESEM analysis. From the high-resolution TEM image, the interconnected worm-like morphology with uniform size of Ni/Ni(OH)<sub>2</sub>/NiOOH is confirmed. The high-resolution TEM image in Figure 3.7c confirms the existence of different lattice fringes. The interplanar distances in different lattice fringes are calculated to be 0.20 nm and 0.23 nm for (111) and (101) planes of Ni(0) and Ni(OH)<sub>2</sub> ion, respectively. The interplanar distance values for Ni(0) and Ni(OH)<sub>2</sub> are well-matched, as in the literature.<sup>25, 56</sup> The crystalline nature of the Ni/Ni(OH)<sub>2</sub>/NiOOH sample is further confirmed from SAED analysis (Figure 3.7d). The selected area diffraction pattern exhibit various diffraction ring, which could be indexed to (006), (100), and (110) planes for NiOOH and Ni(OH)<sub>2</sub>, respectively. The presence of (111), (200), and (202) planes are due to metallic Ni. Therefore, TEM analysis also confirms the interconnected worm-like structure with different crystal planes orientation, which increases the active site and electronic conductivity in the catalyst. These effects of the electrodeposited catalyst will be beneficial during electrocatalysis. Furthermore, the distribution of both Ni(0) and Ni(OH)<sub>2</sub> on the catalyst surface represents the synergistic effect, which is advantageous for an efficient electrocatalyst.

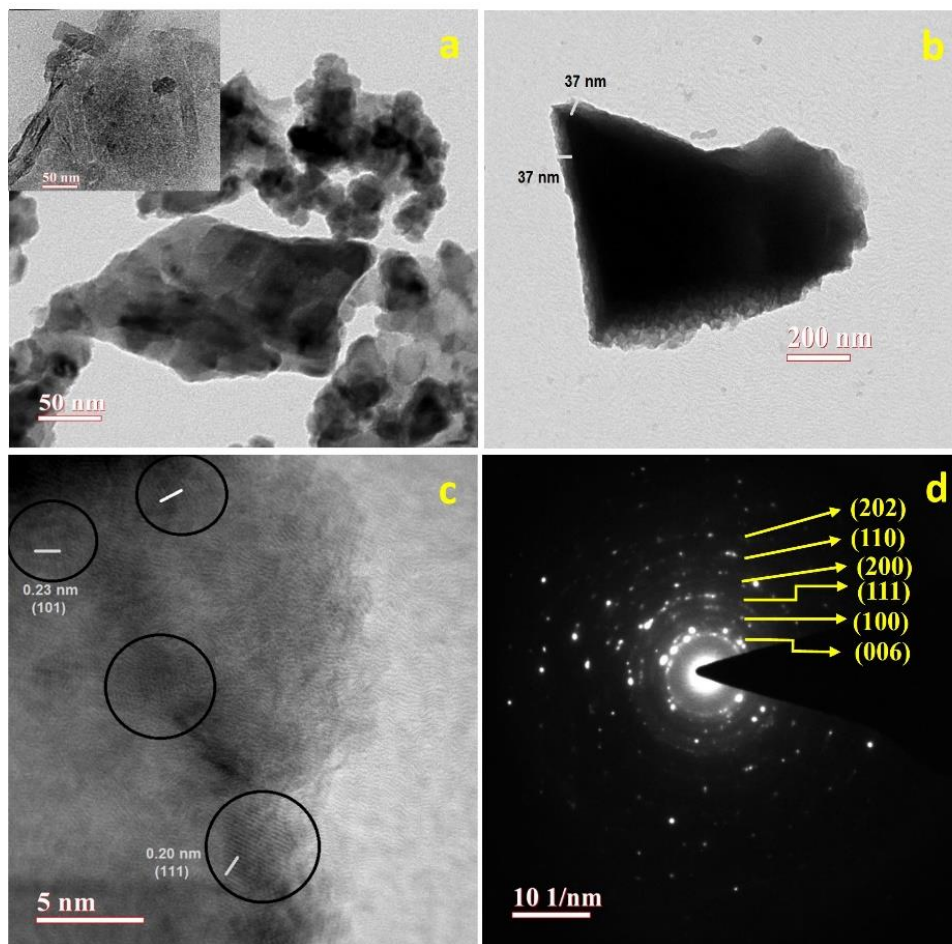
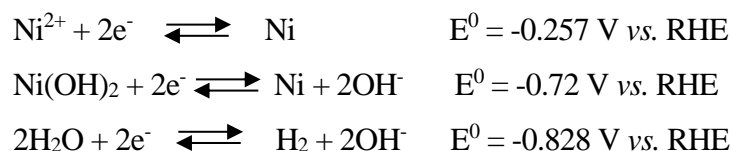


**Figure 3.7:** (a) TEM and (b) HRTEM image of Ni/Ni(OH)<sub>2</sub>/NiOOH heterostructure. The inset of figure (a) exhibits the distribution of nano worms. HRTEM for d-spacing calculation (c) and SAED (d) for Ni/Ni(OH)<sub>2</sub>/NiOOH heterostructure.

**3.3.3 Mechanism of formation of Ni/Ni(OH)<sub>2</sub>/NiOOH heterostructure:** During electrodeposition, an aqueous solution of 0.1 M nickel (II) chloride hexahydrate as a metal precursor and 0.1 M KCl as an electrolyte are used. The process is performed at room temperature under the cathodic potential of -1.0 V vs. Ag/AgCl (-0.389 V vs. RHE) for 20 minutes. Few reported standard electrode potentials in aqueous solutions at 25 °C in V vs. NHE are given below.<sup>57</sup>



From the above electrode potentials, it is clear that  $\text{NiCl}_2 \cdot 6\text{H}_2\text{O}$  is reduced to  $\text{Ni}(0)$  on CC at an applied potential of  $-0.389 \text{ V vs. RHE}$ .  $\text{Ni}(0)$  being a magnetically attractive material, the CC is attracted by an external magnet, and few stepwise digital images for the electrodeposited sample are shown in Figure 3.8. PXRD, XPS, and HRTEM analyses are used to confirm the formation of metallic Ni. The preformed  $\text{Ni}(0)$  behave as a redox-active reagent to reduce water to generate  $\text{H}_2$  and  $\text{OH}^-$  ion in the solution and undergo oxidation. Further, the developed  $\text{OH}^-$  and surface oxidized  $\text{Ni}^{2+}$  combine to develop  $\text{Ni}(\text{OH})_2$  on unreacted  $\text{Ni}(0)$ . In support of this phenomenon, it is also observed from the literature that Chen and co-workers reported the synthesis of Ni/NiO nanosheet as an active and stable HER electrocatalyst in alkaline media, where the effect of  $\text{Ni}(0)$  is prominent on amorphous NiO surface for HER.<sup>58</sup> The occurrence of  $\text{Ni}(\text{OH})_2$  on the same surface is confirmed from lattice spacing calculation using HRTEM images. PXRD and XPS analyses also exhibit the formation of  $\text{Ni}(\text{OH})_2$  on the  $\text{Ni}(0)$  surface. However, the chance of further reducing  $\text{Ni}(\text{OH})_2$  to  $\text{Ni}(0)$  can be eliminated because it requires more cathodic potential for the reduction process, which is  $-0.72 \text{ V vs. NHE}$ , and the working potential for electrodeposition is only  $-0.389 \text{ V vs. RHE}$ . Further, in-situ surface oxidation of  $\text{Ni}(\text{OH})_2$  represents the formation of Ni(III) oxy-hydroxide. The existence of NiOOH on Ni/Ni(OH)<sub>2</sub> surface is confirmed by PXRD and XPS analyses. The unreacted  $\text{Ni}(0)$  in the heterostructure getting stabilized by the presence of  $\text{Ni}(\text{OH})_2$  and NiOOH species on its surface are confirmed by PXRD analyses of Ni-2d and Ni-7d samples. There is no further change in crystallinity, physical stability, and phase purity within the heterostructure for a more extended period in PXRD analysis.

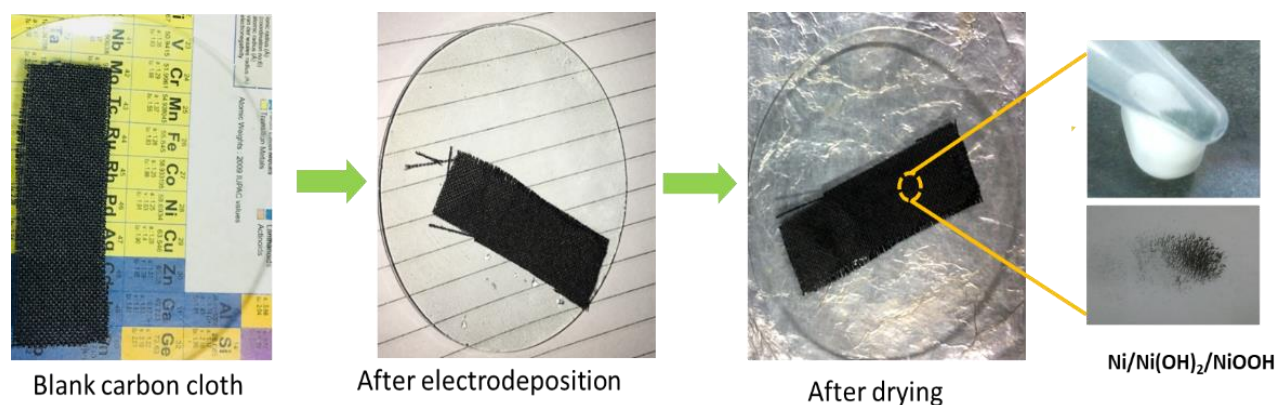


**Figure 3.8:** Digital pictures of electrodeposited Ni/Ni(OH)<sub>2</sub>/NiOOH before and after drying on CC.

### 3.3.4 Application in hydrogen evolution reaction (HER):

The overall HER is carried out with the help of linear sweep voltammetry (LSV) technique in 1.0 M KOH solution applying a 2 mV/sec scan rate. Ag/AgCl, graphite rod, and the sample deposited CC is used as a reference electrode, counter electrode, and the working electrode, respectively, and data is reported against RHE. To compare the electrochemical activity of the electrodeposited sample, Ni(OH)<sub>2</sub>/NiOOH and Ni/Ni(OH)<sub>2</sub> was also hydrothermally developed on CC. All the HER activity of electrodeposited Ni/Ni(OH)<sub>2</sub>/NiOOH is compared with bare carbon cloth, Ni(OH)<sub>2</sub>/NiOOH, Ni/Ni(OH)<sub>2</sub>, and Pt/C (5%) on CC. The polarization curve in Figure 3.9a and b depicts that Ni/Ni(OH)<sub>2</sub>/NiOOH heterostructure exhibits good electrocatalytic activity and requires a low onset potential of -0.045 V vs. RHE for the generation of 10 mA/cm<sup>2</sup> current density. In the case of bare CC, negligible activity is observed in the potential experimental window. In alkaline pH, the electrocatalytic activity of Ni/Ni(OH)<sub>2</sub>/NiOOH is comparable with Pt/C (5%). Figure 3.9c shows the plot between the potential required to generate 50 mA/cm<sup>2</sup> current density and onset potential (V) vs. RHE. Electrodeposited Ni/Ni(OH)<sub>2</sub>/NiOOH heterostructure shows better activity in comparison with other electrocatalysts. It can be seen from Figure 3.9d that Ni/Ni(OH)<sub>2</sub>/NiOOH is an efficient HER electrocatalyst with the highest current density at -0.60 V vs. RHE. The effect of Ni (0) in the heterostructure is further judged by using hydrothermally developed Ni(OH)<sub>2</sub>/NiOOH and Ni/Ni(OH)<sub>2</sub> electrocatalysts. The onset potential of the electrodeposited composite is -0.045 V vs. RHE, whereas Ni(OH)<sub>2</sub>/NiOOH, Ni/Ni(OH)<sub>2</sub>, and Pt/C (5%) catalysts show -0.421 V, -0.099, and -0.038 V vs. RHE, respectively.

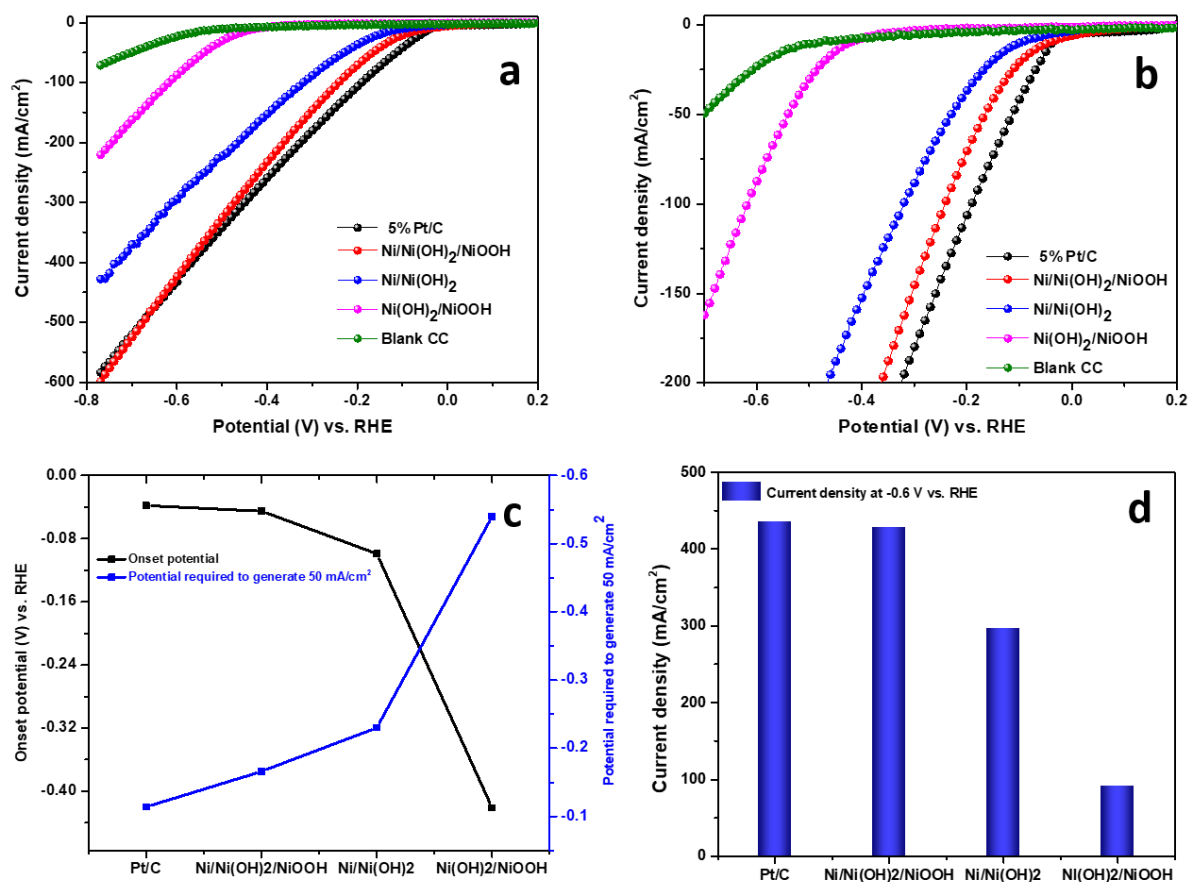


**Figure 3.9:** Polarization curve at (a) low scale and (b) large scale using Ni/Ni(OH)<sub>2</sub>/NiOOH, Ni(OH)<sub>2</sub>/NiOOH, Ni/Ni(OH)<sub>2</sub>, and Pt/C samples. A plot between potential required to produce 50 mA/cm<sup>2</sup> current density and onset potential (V) vs. RHE (c) and histogram plot of current density obtained at -0.6 V vs. RHE (d) for all the developed Ni(OH)<sub>2</sub>/NiOOH, Ni/Ni(OH)<sub>2</sub>/NiOOH, Ni/Ni(OH)<sub>2</sub> and Pt/C (5%) on carbon cloth.

LSV of Ni/Ni(OH)<sub>2</sub>/NiOOH heterostructure, Ni-2d, and Ni-7d are also checked in 1.0 M KOH solution, but there is no significant difference in the efficiency (Figure 3.10a). So, electrodeposited samples remain very active for longer period time or it can be claimed that under such surface protected condition Ni(0) remain very stable in air. Therefore, the electrocatalytic result proves that electrodeposited nanoworms of Ni/Ni(OH)<sub>2</sub>/NiOOH heterostructure are highly active towards HER in alkaline pH. LSV of Ni/Ni(OH)<sub>2</sub>/NiOOH heterostructure with 10, 20, and 30 min electrodeposition in HER are compared (Figure 3.10b). It can be seen that 20 min



electrodeposition is optimum to get the best HER activity in 1.0 M KOH medium. Otherwise, HER efficiency is reduced by less or over deposition, which is also confirmed from FESEM analysis (Figures 3.10 c and d). This hierarchical 2D interconnected nanoworm structure has high amounts of active sites and the open space between the interconnected nanoworms, enhancing the evolution of gaseous products. Therefore, interconnected nanoworms help for electrolyte penetration, diffusion, and faster electron transportation. However, Ni(OH)<sub>2</sub>/NiOOH sample exhibits 2D sheet-like morphology, but the synergy between Ni(0) and Ni(OH)<sub>2</sub> is completely missing resulting in poor performance in HER activity.

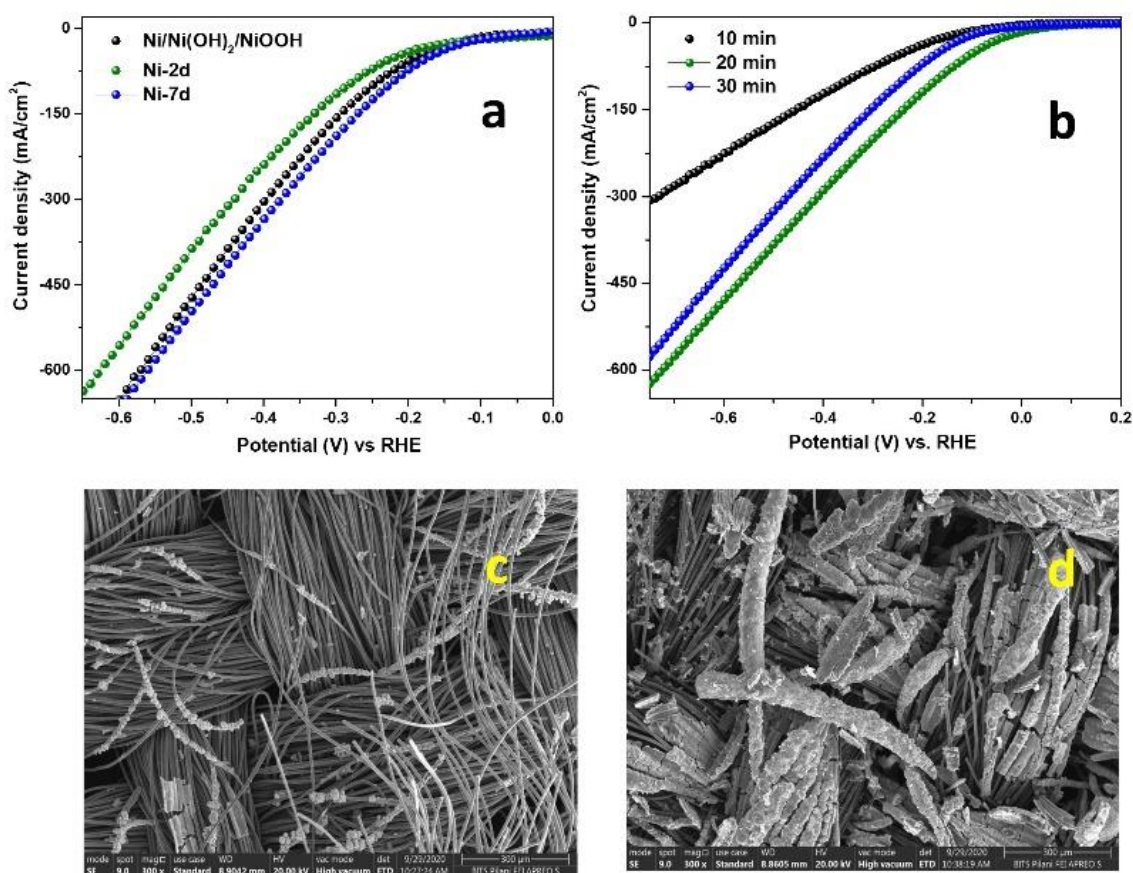


**Figure 3.10:** (a) Comparative polarization curve of Ni/Ni(OH)<sub>2</sub>/NiOOH, Ni-2d, and Ni-7d samples. (b) LSV of Ni/Ni(OH)<sub>2</sub>/NiOOH electrocatalyst via 10 min, 20 min, and 30 min electrodeposition. (c and d) FESEM of 10 and 30 min deposited sample.

The electrochemical performance of an electrocatalyst is correlated with its electrochemically active surface area (ECSA) and electron transportation. CV analysis is

performed (Figure 3.11a and b) using a potential range of 0.825-1.025 V vs. RHE at a different scan rate of 40-200 mV/s using 1.0 M KOH solution to determine the value of electrochemical double-layer capacitance ( $C_{dl}$ ). To determine the value of the slope, which corresponds to  $C_{dl}$ , the observed current at a fixed potential of 0.925 V vs. RHE is plotted against the scan rate (Figure 3.11 c). The  $C_{dl}$  value for Ni/Ni(OH)<sub>2</sub>/NiOOH and Ni(OH)<sub>2</sub>/NiOOH samples are 0.942 mF and 0.06 mF, respectively. The calculated ECSA and  $R_f$  values are 15.7 cm<sup>2</sup>, 1.02 cm<sup>2</sup>, 98.12, 6.25 for Ni/Ni(OH)<sub>2</sub>/NiOOH, and Ni(OH)<sub>2</sub>/NiOOH samples, respectively. Higher ECSA signifies the presence of more active sites, generated from porous 2D interconnected nanoworms in electrodeposited Ni/Ni(OH)<sub>2</sub>/NiOOH heterostructure. A higher roughness factor also indicates better activity in HER.

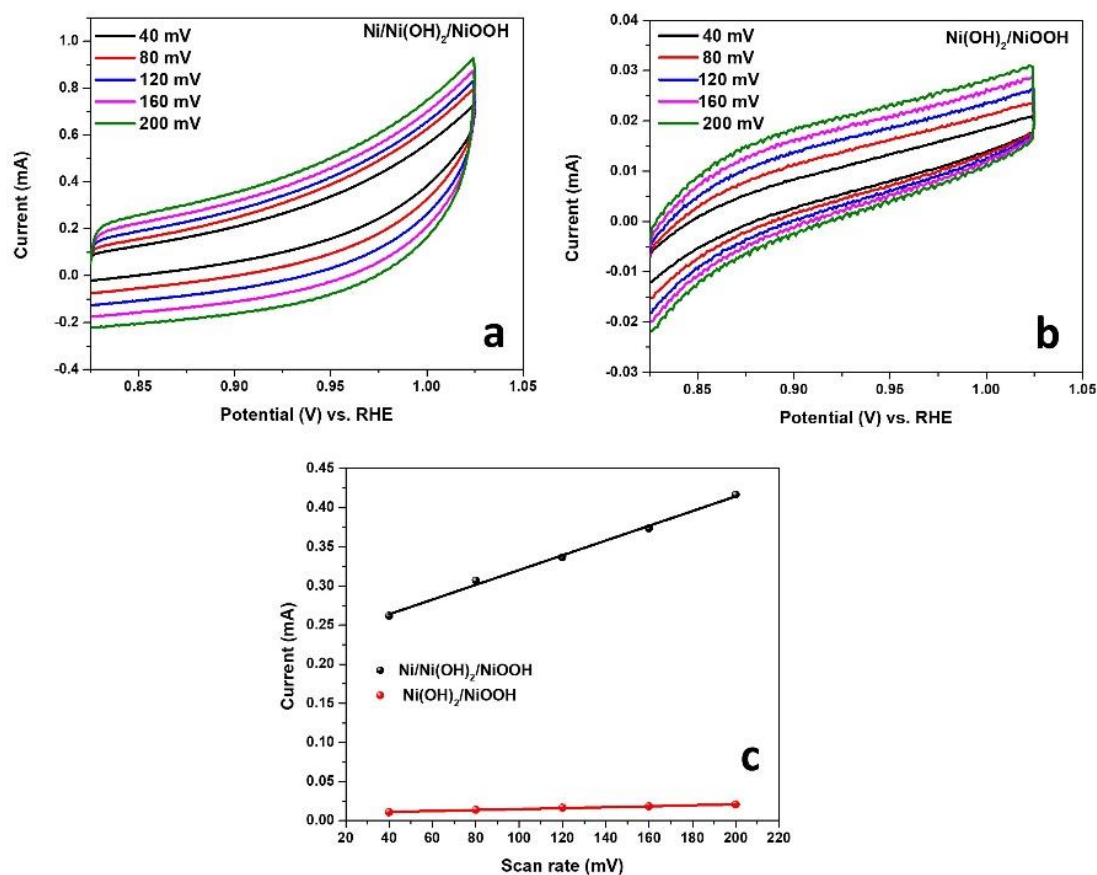


**Figure 3.11:** Cyclic voltammetry curves of (a) electrodeposited Ni/Ni(OH)<sub>2</sub>/NiOOH, (b) Ni(OH)<sub>2</sub>/NiOOH recorded in 1 M KOH recorded with different scan rates, (c) capacitive current at 0.925 (V vs. RHE) as a function of scan rate for Ni/Ni(OH)<sub>2</sub>/NiOOH and Ni(OH)<sub>2</sub>/NiOOH.

The higher electrocatalytic activity can also be supported by the calculation of mass activity. During electrocatalysis, the amount of catalyst loading is 0.60 mg with an area of 0.16 cm<sup>2</sup> for Ni/Ni(OH)<sub>2</sub>/NiOOH, Ni(OH)<sub>2</sub>/NiOOH, Ni/Ni(OH)<sub>2</sub>, and Pt/C (5%). However, the value of mass activity for Ni/Ni(OH)<sub>2</sub>/NiOOH, Ni(OH)<sub>2</sub>/NiOOH, Ni/Ni(OH)<sub>2</sub>, and Pt/C is 38.5 A/g, 8.1 A/g, 23.3 A/g, and 47.5 A/g, respectively. In the heterostructure, Ni(0), Ni(OH)<sub>2</sub>, and NiOOH species are distributed on the catalyst surface and exhibit a synergistic effect, which is incredibly advantageous for an efficient HER activity. Therefore, all the above results confirm the electrodeposited Ni/Ni(OH)<sub>2</sub>/NiOOH heterostructure is highly efficient in HER in alkaline medium. In Ni/Ni(OH)<sub>2</sub>/NiOOH hybrid structure, the presence of all the species, Ni(0), Ni(OH)<sub>2</sub>, and NiOOH, as close as possible, are essential for an efficient HER activity. The close proximity between Ni(0), Ni(OH)<sub>2</sub>, and NiOOH can create more active sites within the heterostructure. Moreover, stable Ni(0) covered by surface oxidized Ni(OH)<sub>2</sub> and NiOOH are significant for H atom and molecular hydrogen production adsorption. Furthermore, the synergistic effect between Ni(0) and Ni(OH)<sub>2</sub> endorsed higher HER activity. For a quick comparison, all the electrochemical (C<sub>dl</sub>, R<sub>f</sub>, and mass activity, etc.) values are tabulated in Table 3.1.

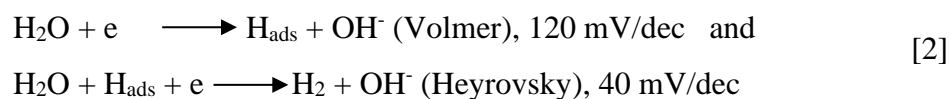
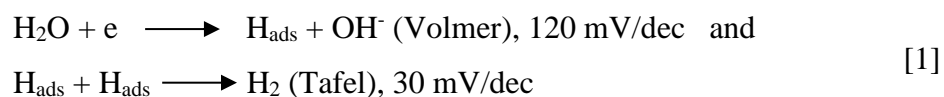
**Table 3.1:** All the electrochemical parameters for Ni/Ni(OH)<sub>2</sub>/NiOOH, Ni(OH)<sub>2</sub>/NiOOH, and Pt/C electrocatalyst.

Electrodes	Potential (V) vs. RHE required to generate 10 mA/cm <sup>2</sup>	ECSA (cm <sup>2</sup> )	R <sub>f</sub>	Mass Activity (A/g) at -0.3 V vs. RHE	Tafel Slope (mV/decade)	R <sub>s</sub> (Ω)	R <sub>CT</sub> (Ω)
Ni/Ni(OH) <sub>2</sub> /NiOOH	-0.045	15.7	98.12	38.5	99.6	6.84	4.70
Ni(OH) <sub>2</sub> /NiOOH	-0.421	1.02	6.25	8.1	167.1	6.88	36.01
Ni/Ni(OH) <sub>2</sub>	-0.099	-	-	23.3	129.4	-	-
Pt/C	-0.038	-	-	47.5	81.4	-	-

The effectiveness of Ni/Ni(OH)<sub>2</sub>/NiOOH electrocatalyst and HER mechanism can also be explained from the Tafel slope calculation. The linear fitted curve in Figure 3.12a leads to the Tafel equation [ $\eta = a + b \log(j)$ ] where,  $\eta$  = overpotential,  $j$  = current density, and  $b$  = Tafel slope.<sup>59-60</sup>



Ni/Ni(OH)<sub>2</sub>/NiOOH heterostructure exhibit the Tafel slope value of 99.6 mV/dec. The Tafel slope value for 5% Pt/C is 81.4 mV/dec in alkaline medium. The Tafel slope value for Ni(OH)<sub>2</sub>/NiOOH and Ni/Ni(OH)<sub>2</sub> catalysts is 167.1 mV/dec and 129.4 mV/dec, respectively. Therefore, Ni/Ni(OH)<sub>2</sub>/NiOOH heterostructure shows efficient activity in HER. In alkaline media, HER mechanism depends on two steps.<sup>61</sup> Based on the literature, the steps are either Volmer-Heyrovsky or Volmer-Tafel steps. Both the HER pathways and their corresponding Tafel slope values are given below.



However, the calculated Tafel slope for electrodeposited heterostructure is 99.6 mV/dec, which follows the Volmer-Heyrovsky mechanism. In the case of the hybrid heterostructure, the higher activity is due to the synergistic effect between Ni(0) and Ni(OH)<sub>2</sub>, as well as the presence of NiOOH. Metallic Ni can bind H atom more efficiently ( $\Delta G_{\text{H}} \sim 0$ ) but is not a suitable catalyst for HER, whereas Ni(OH)<sub>2</sub> aided water splitting reaction.<sup>61</sup> The presence of Ni(OH)<sub>2</sub> rich-region is beneficial for water splitting to produce Ni/Ni(OH)<sub>2</sub>/NiOOH[H<sub>ads</sub>+OH<sup>-</sup>], Volmer step. The formation and desorption of OH<sup>-</sup> ion on Ni(OH)<sub>2</sub> surface is essential during HER so that the Ni(OH)<sub>2</sub> surface can split more H<sub>2</sub>O molecule (Heyrovsky step). In Ni/Ni(OH)<sub>2</sub>/NiOOH heterostructure, due to the presence of Ni(OH)<sub>2</sub> and NiOOH species (more unfilled d-orbital), the preferential adsorption and desorption of OH<sup>-</sup> ion is more. At the same time, Ni(0) surface would facilitate more H atom adsorption, leading to molecular hydrogen formation. Therefore, The overall process follows the Volmer-Heyrovsky mechanism.<sup>62-63</sup>

Electrochemical impedance spectroscopy (EIS) analysis further regulates the higher activity of Ni/Ni(OH)<sub>2</sub>/NiOOH electrocatalyst over Ni(OH)<sub>2</sub>/NiOOH. For both the materials, impedance analysis is performed at their respective onset potentials, and corresponding Nyquist plots are shown (Figure 3.12b). All the experimental data are fitted using the equivalent circuit (inset of Figure 3.12b), which is composed of charge transfer resistance (R<sub>CT</sub>), solution resistance

( $R_s$ ), and constant phase element (CPE). During electrocatalysis, ease of charge transportation on the electrode surface is essential, and the idea can be obtained from charge transfer resistance. The lower value of  $R_{CT}$  signifies higher conductivity of the developed material. In Ni/Ni(OH)<sub>2</sub>/NiOOH heterostructure,  $R_{CT}$  and  $R_s$  values are 4.70  $\Omega$  and 6.84  $\Omega$ , respectively. However,  $R_{CT}$  and  $R_s$  values for Ni(OH)<sub>2</sub>-hyd electrocatalyst are 36.01  $\Omega$  and 6.88  $\Omega$ , respectively. Therefore, based on  $R_{CT}$  value, electrodeposited heterostructure shows higher conductivity, which enhances HER activity. All the charge transfer resistance and solution resistance values for electrodeposited and Ni(OH)<sub>2</sub>/NiOOH samples are shown in Table-3.1. The following reasons can attribute the higher electronic conductivity of Ni/Ni(OH)<sub>2</sub>/NiOOH heterostructure; (i) the presence of stable Ni(0) makes this material more metallic, (ii) the presence of Ni(0), Ni(OH)<sub>2</sub>, and NiOOH species in close proximity (larger surface area) show more contact between electrolyte and catalyst, which increases ease of charge transportation during the reaction, and (iii) the cross-linked nanoworm morphology increases the interfacial structure with heteroatom Ni(0) and Ni(OH)<sub>2</sub>.

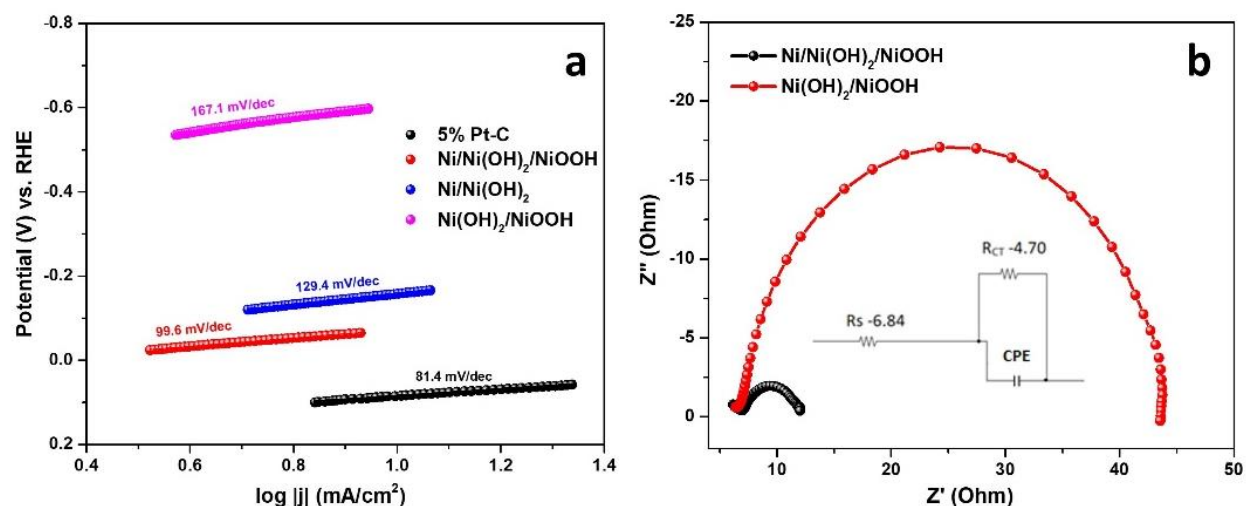


**Figure 3.12 :** (a) Tafel plot and (b) Nyquist plots of Ni/Ni(OH)<sub>2</sub>/NiOOH, Ni(OH)<sub>2</sub>/NiOOH, and Ni/Ni(OH)<sub>2</sub> electrocatalysts. Inset of figure b represents equivalent circuit of Ni/Ni(OH)<sub>2</sub>/NiOOH heterostructure.

Apart from excellent electrocatalytic activity, the durability of an electrocatalyst is an essential parameter. The stability of Ni/Ni(OH)<sub>2</sub>/NiOOH heterostructure is checked over

consecutive 1000 LSV cycles in 1.0 M KOH medium. Figure 3.13a shows that there is no significant change before and after the 1000 cycle LSV run. To further cross-check, we have also performed a chronoamperometric analysis for a prolonged time. The electrodeposited heterostructure is stable up to 200 hours at a fixed potential of  $-0.375$  V vs. RHE. Figure 3.13b represents the generated current density ( $260$  mA/cm<sup>2</sup>) remain constant up to 200 hours. Therefore, the electrocatalyst is highly durable and robust in the alkaline medium. After electrocatalysis, FESEM and PXRD analyses are carried out to confirm the retention of morphology and physical stability of the heterostructure. PXRD pattern in Figure 3.13c shows the presence of peaks for Ni(0), Ni(OH)<sub>2</sub>, and NiOOH for a reused catalyst as well as there is no change in morphology after electrocatalysis (Figure 3.13d), which proves that the fabricated heterostructure is showing excellent electrocatalytic stability and robustness in alkaline electrolyte.

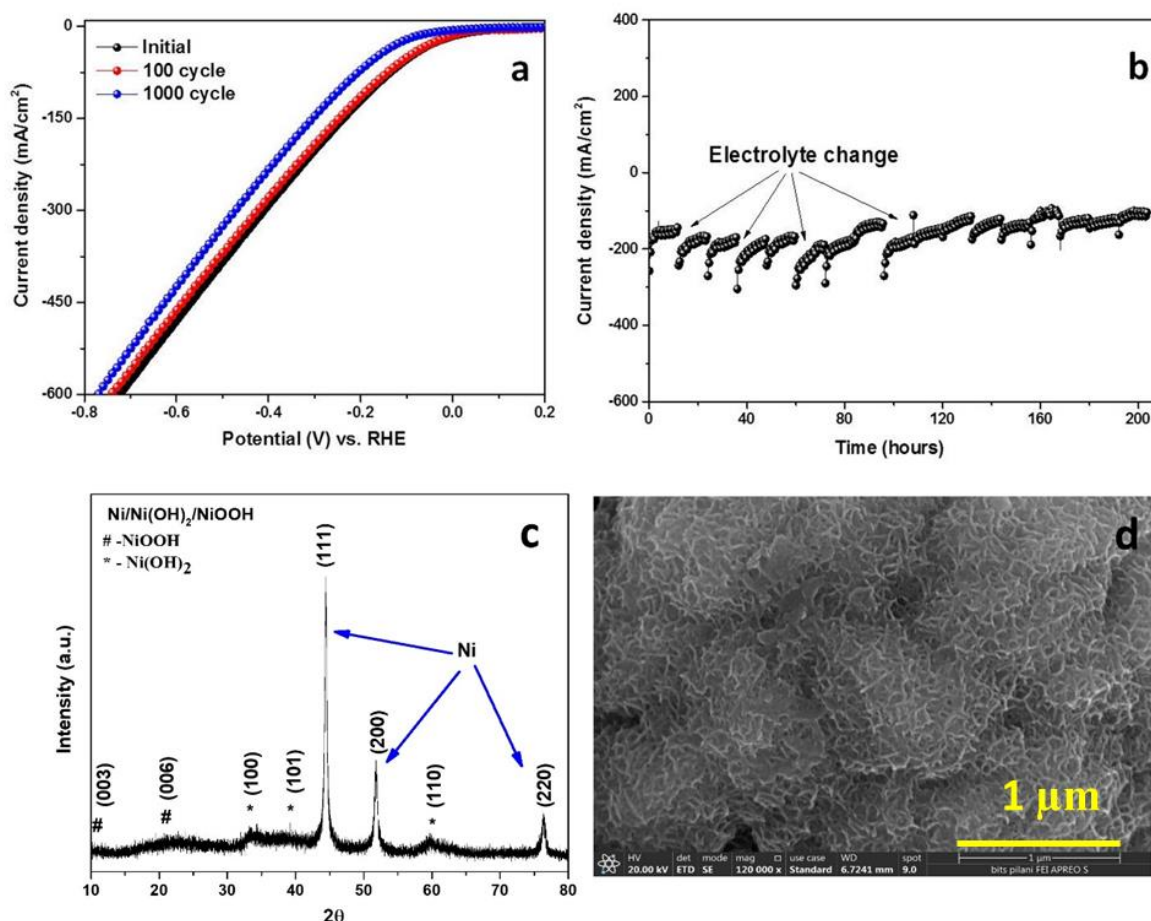


**Figure 3.13:** (a) Polarization curves of Ni/Ni(OH)<sub>2</sub>/NiOOH electrocatalyst for initial, 100 cycles, and after 1000 cycles. (b) Amperometric data recorded at a fixed potential. (c) PXRD and (d) FESEM analyses of Ni/Ni(OH)<sub>2</sub>/NiOOH heterostructure after electrocatalysis.

EDS mapping analysis was also performed for the reused electrocatalyst, and Figure 3.14a represents the presence of Ni, O, and C elements properly. Faradaic efficiency for hydrogen evolution is calculated at an applied potential of  $-0.12$  V vs. RHE for  $\sim 145$  min using the Ni/Ni(OH)<sub>2</sub>/NiOOH electrocatalyst. The electrocatalyst shows  $165.6$   $\mu\text{mol}$  of H<sub>2</sub> generation in 145 min, whereas the theoretical amount of H<sub>2</sub> generation within the time is  $203.1$   $\mu\text{mol}$ . The determined Faradaic efficiency is 81.5% with Ni/Ni(OH)<sub>2</sub>/NiOOH heterostructure electrocatalyst. The theoretically and experimentally calculated H<sub>2</sub> generation (in  $\mu\text{mol}$ ) in various time scale is shown in Figure 3.14b.

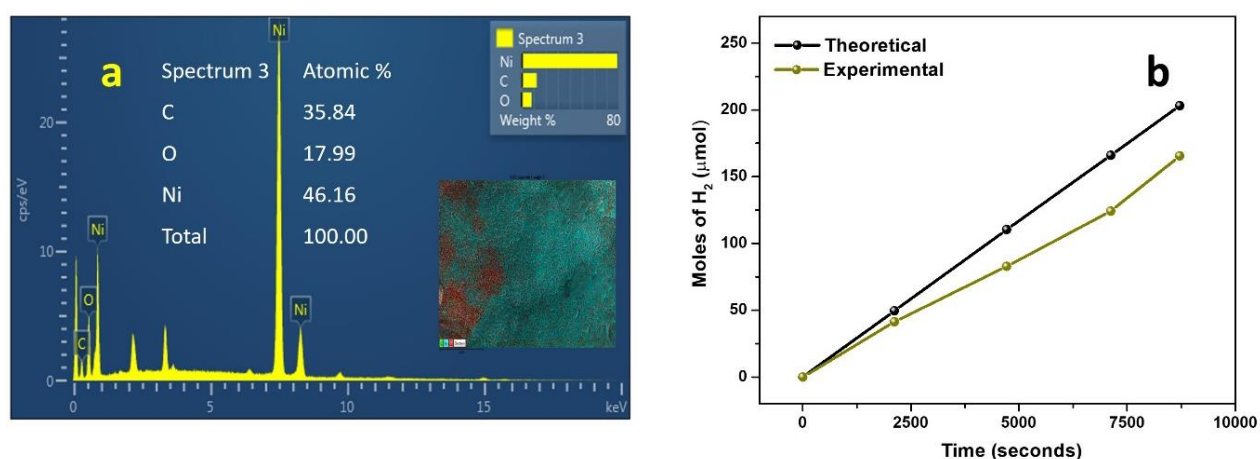


**Figure 3.14:** (a) EDS mapping analysis of post electrolysis. (b) Hydrogen gas evolution of Ni/Ni(OH)<sub>2</sub>/NiOOH electrode under applied potential of  $-0.225$  V vs. RHE.

### 3.3.5 Application in oxygen evolution reaction (OER):

The electrodeposited carbon cloth, graphitic rod, and Ag/AgCl electrode was used as a working, counter, and reference electrode during OER, respectively. In Figure 3.15a comparative polarization curve of commercial RuO<sub>2</sub>, electrodeposited Ni/Ni(OH)<sub>2</sub>/NiOOH, bare CC, Ni/Ni(OH)<sub>2</sub>, and hydrothermally grown Ni(OH)<sub>2</sub>/NiOOH are given for OER. Bare CC exhibit lesser electrochemical activity than others. To compare OER activity, the potential to generate  $50$  mA/cm<sup>2</sup> current density and overpotential are compared. The onset potential for electrodeposited Ni/Ni(OH)<sub>2</sub>/NiOOH is  $1.588$  V vs. RHE, and overpotential is  $358$  mV, which is much better than commercial RuO<sub>2</sub> and Ni(OH)<sub>2</sub>/NiOOH. For commercial RuO<sub>2</sub> onset potential is  $1.608$  V vs. RHE and overpotential is  $378$  mV, and Ni(OH)<sub>2</sub>/NiOOH sample show onset potential at  $1.638$  V vs.

RHE and overpotential is 408 mV. The efficient electrocatalytic activity was observed with Ni/Ni(OH)<sub>2</sub> deposited on carbon cloth; it is having overpotential of 312 mV, and 1.542 V vs. RHE is required to obtain 50 mA/cm<sup>2</sup> current density (Figure 3.15a). The anodic peak at 1.417 V vs. RHE is attributed to the redox reaction of Ni<sup>2+</sup> to Ni<sup>3+</sup> formation, promoting in situ formation of NiOOH species during oxygen evolution. Besides, in Ni/Ni(OH)<sub>2</sub>, the formation of this redox peak appeared at 1.39 V vs. RHE. The Figure 3.15b shows the Tafel slope value of electrodeposited Ni/Ni(OH)<sub>2</sub>/NiOOH is 72.5 mV/dec, which is lower compare to other catalysts. The commercial RuO<sub>2</sub> exhibits a Tafel slope of 84.1 mV/dec. However, the stability of electrodeposited Ni/Ni(OH)<sub>2</sub>/NiOOH for OER is poor in an alkaline medium. The sample is not electrocatalytically stable.

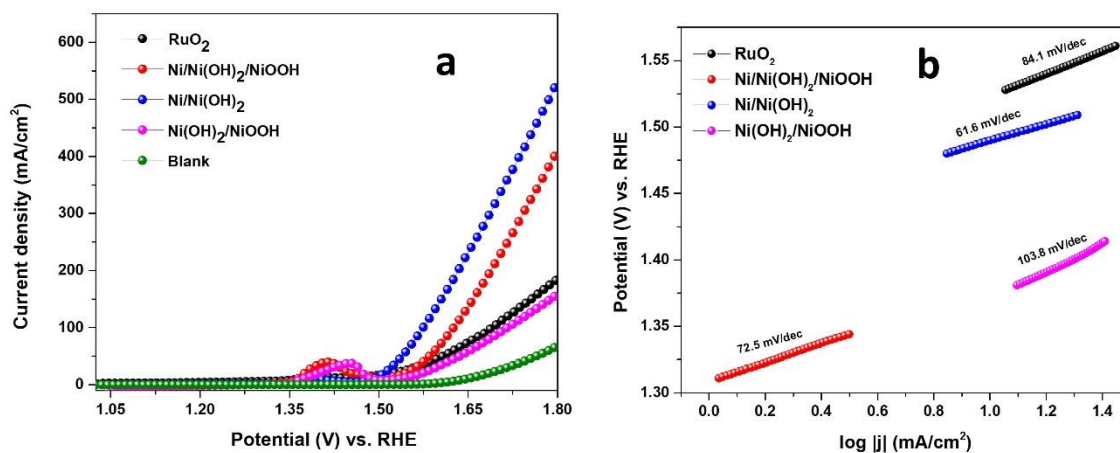


**Figure 3.15:** (a) Polarization OER curve (b) Tafel slope of Ni/Ni(OH)<sub>2</sub>/NiOOH, Ni(OH)<sub>2</sub>/NiOOH, Ni/Ni(OH)<sub>2</sub>, and RuO<sub>2</sub> samples.

### 3.3.6 Comparative Study

A comparative study of all the electrochemical parameters with the as-developed electrocatalysts is tabulated in Table 3.2.

**Table 3.2:** A comparative study of all the electrochemical parameters with the as-developed electrocatalysts.

S.N.	Electrocatalyst	Electrode reaction	Electrolyte	Potential (mV vs. RHE) at 10 mA/cm <sup>2</sup> Current density	Tafel slope	Substrate	Ref.
1.	Ni/Ni(OH) <sub>2</sub>	HER	1 M KOH	-	250	FTO	20
2.	Ni(OH) <sub>2</sub>	HER & OER	1 M KOH	1.68 V	140 & 150	Ni foam	21
3.	Ni/NiO	OER & HER	1 M KOH	300 & 153	60 & 84	Carbon fiber	22
4.	Ni(OH) <sub>2</sub> /Ni	HER & OER	0.1 M KOH	-	128	RRDE	23
5.	Ni/Ni(OH) <sub>2</sub>	HER & OER	1 M KOH	168 & 310	95.7 & 74.8	GCE	34
6.	Ni(OH) <sub>2</sub> @ Ni	HER	1 M KOH	68	97	Ni film	24
7.	Ni/Ni(OH) <sub>2</sub>	HER	1 M KOH	53	54.5	Ni foam	25
8.	Ni/Ni(OH) <sub>2</sub> /NiOOH	HER	1 M KOH	45	99.6	Carbon cloth	This work

### 3.4 Conclusion

We have developed an environment friendly and easily scaled up electrodeposition method for 2D nanoworms of Ni/Ni(OH)<sub>2</sub>/NiOOH on conductive CC surface as an efficient electrocatalyst for hydrogen evolution. The reduction of NiCl<sub>2</sub> leads to the formation of Ni(0) on the CC surface upon application of a cathodic potential of -1.0 V vs. Ag/AgCl. The sample is attracted by an external magnet, which confirms the presence of metallic Ni in the system. The presence of Ni(0) is important in the HER, and Ni(OH)<sub>2</sub> and NiOOH surface can participate in adsorption and desorption of OH<sup>-</sup> ion on its surface. Therefore, the combined effect of Ni(0), Ni(OH)<sub>2</sub>, and NiOOH in the heterostructure leads to better HER activity. The optimized catalyst has a lower onset potential and a smaller Tafel slope value of 99.6 mVdec<sup>-1</sup> in HER. The ultrafine 2D nanoworms of electrodeposited heterostructure have more active sites, and the synergistic effect leads to stability up to 200 in HER. The electrocatalytic activity of Ni/Ni(OH)<sub>2</sub>/NiOOH heterostructure is compared with Ni-7d and shows similar HER activity. The developed heterostructure electrocatalyst can generate 165.6 μmol of H<sub>2</sub> in ~145 min of reaction time with 81.5% Faradaic efficiency. This work provides us an efficient and robust electrocatalyst for HER, comparable to the performance of noble Pt metal electrocatalyst in an alkaline medium. We need to modify the

developed catalyst with some strategy to make it bifunctional and further improve the electrocatalytic stability.

### 3.5 References

1. Turner, J. A., A realizable renewable energy future. *Science* **1999**, *285*, 687-689.
2. Lewis, N. S.; Nocera, D. G., Powering the planet: Chemical challenges in solar energy utilization. *Proc. Natl. Acad. Sci.* **2006**, *103*, 15729-15735.
3. Sharma, M. D.; Mahala, C.; Basu, M.; 2D Thin Sheet Heterostructures of MoS<sub>2</sub> on MoSe<sub>2</sub> as Efficient Electrocatalyst for Hydrogen Evolution Reaction in Wide pH Range. *Inorg. Chem.* **2020**, *59*, 4377-4388.
4. Grigoriev, S.; Millet, P.; Fateev, V., Evaluation of carbon-supported Pt and Pd nanoparticles for the hydrogen evolution reaction in PEM water electrolyzers. *J. Power Sources* **2008**, *177*, 281-285.
5. Strmcnik, D.; Lopes, P. P.; Genorio, B.; Stamenkovic, V. R.; Markovic, N. M., Design principles for hydrogen evolution reaction catalyst materials. *Nano Energy* **2016**, *29*, 29-36.
6. Ming, F.; Liang, H.; Shi, H.; Mei, G.; Xu, X.; Wang, Z., Hierarchical (Ni, Co) Se<sub>2</sub>/carbon hollow rhombic dodecahedra derived from metal-organic frameworks for efficient water-splitting electrocatalysis. *Electrochim. Acta* **2017**, *250*, 167-173.
7. Jin, Y.; Wang, H.; Li, J.; Yue, X.; Han, Y.; Shen, P. K.; Cui, Y., Porous MoO<sub>2</sub> nanosheets as non-noble bifunctional electrocatalysts for overall water splitting. *Adv. Mater.* **2016**, *28*, 3785-3790.
8. Friebel, D.; Louie, M. W.; Bajdich, M.; Sanwald, K. E.; Cai, Y.; Wise, A. M.; Cheng, M.-J.; Sokaras, D.; Weng, T.-C.; Alonso-Mori, R., Identification of highly active Fe sites in (Ni, Fe) OOH for electrocatalytic water splitting. *J. Am. Chem. Soc.* **2015**, *137*, 1305-1313.
9. Yang, Y.; Zhang, K.; Lin, H.; Li, X.; Chan, H. C.; Yang, L.; Gao, Q., MoS<sub>2</sub>-Ni<sub>3</sub>S<sub>2</sub> heteronanorods as efficient and stable bifunctional electrocatalysts for overall water splitting. *ACS Catal.* **2017**, *7*, 2357-2366.
10. Hussain, N.; Yang, W.; Dou, J.; Chen, Y.; Qian, Y.; Xu, L., Ultrathin mesoporous F-doped  $\alpha$ -Ni(OH)<sub>2</sub> nanosheets as an efficient electrode material for water splitting and supercapacitors. *J. mater. chem. A* **2019**, *7*, 9656-9664.

11. Liu, J.; Ji, Y.; Nai, J.; Niu, X.; Luo, Y.; Guo, L.; Yang, S., Ultrathin amorphous cobalt–vanadium hydr (oxy) oxide catalysts for the oxygen evolution reaction. *Energy Environ. Sci.* **2018**, *11*, 1736-1741.
12. Zhou, J.; Dou, Y.; Zhou, A.; Guo, R.-M.; Zhao, M.-J.; Li, J.-R., MOF Template-Directed Fabrication of Hierarchically Structured Electrocatalysts for Efficient Oxygen Evolution Reaction. *Adv. Energy Mater.* **2017**, *7*, 1602643.
13. Ahn, S. H.; Choi, I.; Park, H.-Y.; Hwang, S. J.; Yoo, S. J.; Cho, E.; Kim, H.-J.; Henkensmeier, D.; Nam, S. W.; Kim, S.-K., Effect of morphology of electrodeposited Ni catalysts on the behavior of bubbles generated during the oxygen evolution reaction in alkaline water electrolysis. *Chem. Commun.* **2013**, *49*, 9323-9325.
14. Meguro, S.; Sasaki, T.; Katagiri, H.; Habazaki, H.; Kawashima, A.; Sakaki, T.; Asami, K.; Hashimoto, K., Electrodeposited Ni-Fe-C Cathodes for Hydrogen Evolution. *J. Electrochem. Soc.* **2000**, *147*, 3003-3009.
15. Huang, H.; Yan, M.; Yang, C.; He, H.; Jiang, Q.; Yang, L.; Lu, Z.; Sun, Z.; Xu, X.; Bando, Y., Graphene Nanoarchitectonics: Recent Advances in Graphene Based Electrocatalysts for Hydrogen Evolution Reaction. *Adv. Mater.* **2019**, *31*, 1903415.
16. Janjua, M.; Le Roy, R., Electrocatalyst performance in industrial water electrolyzers. *Int. J. Hydrogen Energy* **1985**, *10*, 11-19.
17. Hall, D., Electrodes for alkaline water electrolysis. *J. Electrochem. Soc.* **1981**, *128*, 740.
18. Stern, L.-A.; Hu, X., Enhanced oxygen evolution activity by NiO<sub>x</sub> and Ni(OH)<sub>2</sub> nanoparticles. *Faraday Discuss.* **2014**, *176*, 363-379.
19. Shalom, M.; Ressnig, D.; Yang, X.; Clavel, G.; Fellingner, T. P.; Antonietti, M., Nickel nitride as an efficient electrocatalyst for water splitting. *J. Mater. Chem. A* **2015**, *3*, 8171-8177.
20. Yuan, H.; Lunt, R. R.; Thompson, J. I.; Ofoli, R. Y., Electrodeposition of Ni/Ni(OH)<sub>2</sub> Catalytic Films for the Hydrogen Evolution Reaction Produced by using Cyclic Voltammetry. *Chemelectrochem* **2017**, *4*, 241-245.
21. Rao, Y.; Wang, Y.; Ning, H.; Li, P.; Wu, M., Hydrotalcite-like Ni(OH)<sub>2</sub> Nanosheets in Situ Grown on Nickel Foam for Overall Water Splitting. *ACS Appl. Mater. Interfaces* **2016**, *8*, 33601-33607.



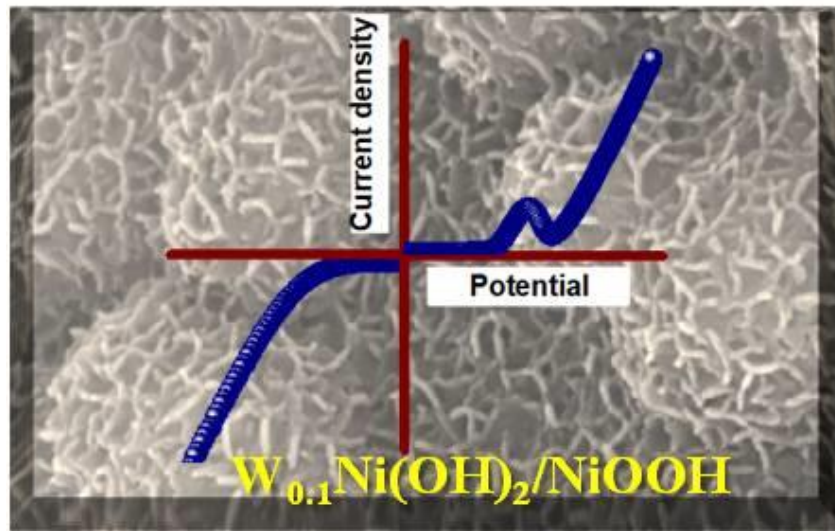
22. Zhang, Z.; Liu, S.; Xiao, F.; Wang, S., Facile synthesis of heterostructured nickel/nickel oxide wrapped carbon fiber: flexible bifunctional gas-evolving electrode for highly efficient overall water splitting. *ACS Sustain. Chem. Eng.* **2017**, *5*, 529-536.
23. Danilovic, N.; Subbaraman, R.; Strmcnik, D.; Chang, K. C.; Paulikas, A.; Stamenkovic, V.; Markovic, N. M., Enhancing the alkaline hydrogen evolution reaction activity through the bifunctionality of Ni (OH)<sub>2</sub>/metal catalysts. *Angew. Chem. Int. Ed.* **2012**, *51*, 12495-12498.
24. Xing, Z.; Gan, L.; Wang, J.; Yang, X., Experimental and theoretical insights into sustained water splitting with an electrodeposited nanoporous nickel hydroxide@ nickel film as an electrocatalyst. *J. Mater. Chem. A* **2017**, *5*, 7744-7748.
25. Liu, Y.; Wang, J.; Tian, Q.; Liu, M.; Wang, X.; Li, P.; Li, W.; Cai, N.; Chen, W.; Yu, F., Papillae-like morphology of Ni/Ni(OH)<sub>2</sub> hybrid crystals by stepwise electrodeposition for synergistically improved HER. *CrystEngComm* **2019**, *21*, 3431-3438.
26. Huang, S.; Meng, Y.; Cao, Y.; Yao, F.; He, Z.; Wang, X.; Pan, H.; Wu, M., Amorphous NiWO<sub>4</sub> nanoparticles boosting the alkaline hydrogen evolution performance of Ni<sub>3</sub>S<sub>2</sub> electrocatalysts. *Appl. Catal. B: Environ.* **2020**, *274*, 119120.
27. Yang, D.; Cao, L.; Feng, L.; Huang, J.; Kajiyoshi, K.; Feng, Y.; Liu, Q.; Li, W.; Feng, L.; Hai, G., Formation of hierarchical Ni<sub>3</sub>S<sub>2</sub> nanohorn arrays driven by in-situ generation of VS<sub>4</sub> nanocrystals for boosting alkaline water splitting. *Appl. Catal. B: Environ.* **2019**, *257*, 117911.
28. Ahn, S. H.; Hwang, S. J.; Yoo, S. J.; Choi, I.; Kim, H.-J.; Jang, J. H.; Nam, S. W.; Lim, T.-H.; Lim, T.; Kim, S.-K., Electrodeposited Ni dendrites with high activity and durability for hydrogen evolution reaction in alkaline water electrolysis. *J. Mater. Chem.* **2012**, *22*, 15153-15159.
29. Chang, Y.-H.; Feng, S.-P., Stepwise anodic electrodeposition of nanoporous NiOOH/Ni(OH)<sub>2</sub> with controllable wettability and its applications. *HKIE Transactions* **2015**, *22*, 202-211.
30. Hwang, S. J.; Yoo, S. J.; Jang, S.; Lim, T.-H.; Hong, S. A.; Kim, S.-K., Ternary Pt– Fe– Co alloy electrocatalysts prepared by electrodeposition: elucidating the roles of Fe and Co in the oxygen reduction reaction. *J. Phys. Chem. C* **2011**, *115*, 2483-2488.
31. Scavetta, E.; Mignani, A.; Prandstraller, D.; Tonelli, D., Electrosynthesis of thin films of Ni, Al hydrotalcite like compounds. *Chem. Mater.* **2007**, *19*, 4523-4529.

32. Fan, M.; Chen, H.; Wu, Y.; Feng, L.-L.; Liu, Y.; Li, G.-D.; Zou, X., Growth of molybdenum carbide micro-islands on carbon cloth toward binder-free cathodes for efficient hydrogen evolution reaction. *J. Mater. Chem. A* **2015**, *3*, 16320-16326.
33. Mahala, C.; Devi Sharma, M.; Basu, M., Fe-Doped Nickel Hydroxide/Nickel Oxyhydroxide Function as an Efficient Catalyst for the Oxygen Evolution Reaction. *ChemElectroChem* **2019**, *6*, 3488-3498.
34. Lim, D.; Kim, S.; Kim, N.; Oh, E.; Shim, S. E.; Baeck, S.-H., Strongly Coupled Ni/Ni(OH)<sub>2</sub> Hybrid Nanocomposites as Highly Active Bifunctional Electrocatalysts for Overall Water Splitting. *ACS Sustain. Chem. Eng.* **2020**, *8*, 4431-4439.
35. Ullah, N.; Zhao, W.; Lu, X.; Oluigbo, C. J.; Shah, S. A.; Zhang, M.; Xie, J.; Xu, Y., In situ growth of M-MO (M= Ni, Co) in 3D graphene as a competent bifunctional electrocatalyst for OER and HER. *Electrochim. Acta* **2019**, *298*, 163-171.
36. Tong, X.; Chen, S.; Guo, C.; Xia, X.; Guo, X. Y., Mesoporous NiCo<sub>2</sub>O<sub>4</sub> Nanoplates on Three-Dimensional Graphene Foam as an Efficient Electrocatalyst for the Oxygen Reduction Reaction. *ACS Appl. Mater. Interfaces* **2016**, *8*, 28274-28282.
37. Zhang, Y.; Liu, Y.; Guo, Y.; Yeow, Y. X.; Duan, H.; Li, H.; Liu, H., In situ preparation of flower-like  $\alpha$ -Ni(OH)<sub>2</sub> and NiO from nickel formate with excellent capacitive properties as electrode materials for supercapacitors. *Mater. Chem. Phys.* **2015**, *151*, 160-166.
38. Wang, Y.; Cao, D.; Wang, G.; Wang, S.; Wen, J.; Yin, J., Spherical clusters of  $\beta$ -Ni(OH)<sub>2</sub> nanosheets supported on nickel foam for nickel metal hydride battery. *Electrochim. Acta* **2011**, *56*, 8285-8290.
39. Freitas, M., Nickel hydroxide powder for NiOOH/Ni(OH)<sub>2</sub> electrodes of the alkaline batteries. *J. Power Sources* **2001**, *93*, 163-173.
40. Mani, B.; de Neufville, J., Dehydration of chemically and electrochemically impregnated (CI and EI) nickel hydroxide electrodes. *J. Electrochem. Soc.* **1988**, *135*, 800.
41. Li, Y.; Yao, J.; Zhu, Y.; Zou, Z.; Wang, H., Synthesis and electrochemical performance of mixed phase  $\alpha/\beta$  nickel hydroxide. *J. Power Sources* **2012**, *203*, 177-183.
42. Shruthi, B.; Raju, V. B.; Madhu, B., Synthesis, spectroscopic and electrochemical performance of pasted  $\beta$ -nickel hydroxide electrode in alkaline electrolyte. *Spectrochim. Acta A Biomol. Spectrosc.* **2015**, *135*, 683-689.

43. Su, Y.-Z.; Xiao, K.; Li, N.; Liu, Z.-Q.; Qiao, S.-Z., Amorphous Ni(OH)<sub>2</sub>@ three-dimensional Ni core-shell nanostructures for high capacitance pseudocapacitors and asymmetric supercapacitors. *J. Mater. Chem. A* **2014**, *2*, 13845-13853.
44. Fu, G.; Hu, Z.; Xie, L.; Jin, X.-q.; Xie, Y.-l.; Wang, Y.-x.; Zhang, Z.-y.; Yang, Y.; Wu, H., Electrodeposition of nickel hydroxide films on nickel foil and its electrochemical performances for supercapacitor. *Int. J. Electrochem. Sci.* **2009**, *4*, 1052.
45. Kamath, P. V.; Subbanna, G., Electroless nickel hydroxide: synthesis and characterization. *J. Appl. Electrochem.* **1992**, *22*, 478-482.
46. Diaz-Morales, O.; Ferrus-Suspedra, D.; Koper, M. T., The importance of nickel oxyhydroxide deprotonation on its activity towards electrochemical water oxidation. *Chem. Sci.* **2016**, *7*, 2639-2645.
47. Mironova-Ulmane, N.; Kuzmin, A.; Steins, I.; Grabis, J.; Sildos, I.; Pärss, M., Raman scattering in nanosized nickel oxide NiO. *J. Phys.: Conf. Ser.* **2007**, *93*, 012039.
48. Hall, D. S.; Lockwood, D. J.; Bock, C.; MacDougall, B. R., Nickel hydroxides and related materials: a review of their structures, synthesis, and properties. *Proc. R. Soc. A* **2015**, *471*, 20140792.
49. Yan, J.; Fan, Z.; Sun, W.; Ning, G.; Wei, T.; Zhang, Q.; Zhang, R.; Zhi, L.; Wei, F., Advanced asymmetric supercapacitors based on Ni(OH)<sub>2</sub>/graphene and porous graphene electrodes with high energy density. *Adv. Funct. Mater.* **2012**, *22*, 2632-2641.
50. Min, S.; Zhao, C.; Chen, G.; Qian, X., One-pot hydrothermal synthesis of reduced graphene oxide/Ni(OH)<sub>2</sub> films on nickel foam for high-performance supercapacitors. *Electrochim. Acta* **2014**, *115*, 155-164.
51. Jiang, H.; Guo, Y.; Wang, T.; Zhu, P.-L.; Yu, S.; Yu, Y.; Fu, X.-Z.; Sun, R.; Wong, C.-P., Electrochemical fabrication of Ni(OH)<sub>2</sub>/Ni 3D porous composite films as integrated capacitive electrodes. *RSC Adv.* **2015**, *5*, 12931-12936.
52. Grosvenor, A. P.; Biesinger, M. C.; Smart, R. S. C.; McIntyre, N. S., New interpretations of XPS spectra of nickel metal and oxides. *Surf. Sci.* **2006**, *600*, 1771-1779.
53. Lee, J. W.; Ahn, T.; Soundararajan, D.; Ko, J. M.; Kim, J.-D., Non-aqueous approach to the preparation of reduced graphene oxide/ $\alpha$ -Ni(OH)<sub>2</sub> hybrid composites and their high capacitance behavior. *Chem. Commun.* **2011**, *47*, 6305-6307.

54. Mahala, C.; Basu, M., Nanosheets of NiCo<sub>2</sub>O<sub>4</sub>/NiO as efficient and stable electrocatalyst for oxygen evolution reaction. *ACS Omega* **2017**, *2*, 7559-7567.
55. Mahala, C.; Sharma, R.; Sharma, M. D.; Pande, S., Development of Copper Cobalt Sulfide with Cu: Co Ratio Variation on Carbon Cloth as an Efficient Electrode Material for the Oxygen Evolution Reaction. *ChemElectroChem* **2019**, *6*, 5301-5312.
56. Zhou, Y.; Sun, C.; Yang, X.; Zou, G.; Wu, H.; Xi, S., Flame-like Ni(OH)<sub>2</sub> strongly promotes the dissociation of water and can be used to produce an excellent hybrid electrocatalyst for the hydrogen evolution reaction in alkaline media. *Electrochem. Commun.* **2018**, *91*, 66-70.
57. Bard, A. J.; Faulkner, L. R.; Leddy, J.; Zoski, C. G., *Electrochemical methods: fundamentals and applications*. Wiley New York: 1980; Vol. 2.
58. Yan, X.; Tian, L.; Chen, X., Crystalline/amorphous Ni/NiO core/shell nanosheets as highly active electrocatalysts for hydrogen evolution reaction. *J. Power Sources* **2015**, *300*, 336-343.
59. Fageria, P.; Sudharshan, K.; Nazir, R.; Basu, M.; Pande, S., Decoration of MoS<sub>2</sub> on g-C<sub>3</sub>N<sub>4</sub> surface for efficient hydrogen evolution reaction. *Electrochim. Acta* **2017**, *258*, 1273-1283.
60. Basu, M.; Nazir, R.; Mahala, C.; Fageria, P.; Chaudhary, S.; Gangopadhyay, S.; Pande, S., Ag<sub>2</sub>S/Ag Heterostructure: A Promising Electrocatalyst for the Hydrogen Evolution Reaction. *Langmuir* **2017**, *33*, 3178-3186.
61. Gong, M.; Zhou, W.; Tsai, M.-C.; Zhou, J.; Guan, M.; Lin, M.-C.; Zhang, B.; Hu, Y.; Wang, D.-Y.; Yang, J., Nanoscale nickel oxide/nickel heterostructures for active hydrogen evolution electrocatalysis. *Nat. Commun.* **2014**, *5*, 4695.
62. Xing, Z.; Wang, D.; Li, Q.; Asiri, A. M.; Sun, X., Self-standing Ni-WN heterostructure nanowires array: A highly efficient catalytic cathode for hydrogen evolution reaction in alkaline solution. *Electrochim. Acta* **2016**, *210*, 729-733.
63. Wu, Y.; He, H., Direct-current electrodeposition of Ni-S-Fe alloy for hydrogen evolution reaction in alkaline solution. *Int. J. Hydrogen Energy* **2018**, *43*, 1989-1997.

### Bifunctional Tungsten-doped Ni(OH)<sub>2</sub>/NiOOH Nanosheets for Overall Water Splitting in Alkaline Medium



- \* In this chapter, W doped Ni(OH)<sub>2</sub>/NiOOH heterostructure was developed on carbon cloth.
- \* The  $W_{0.1}Ni(OH)_2/NiOOH$  nanosheet applied for electrochemical HER and OER activity, which shows good bifunctional activity.

## *Abstract*

The development of a cost-effective and proficient bifunctional electrocatalyst is highly fascinating. Herein, we have synthesized tungsten ( $W^{6+}$ ) doped vertically grown nanosheet-like structure of  $Ni(OH)_2/NiOOH$  on carbon cloth for HER and OER activity in KOH solution. Doping with  $W^{6+}$  ion in  $Ni(OH)_2/NiOOH$  is performed by electrodeposition followed by hydrothermal method. Various amount of dopant ( $W^{6+}$ ) is used to confirm the role of W but  $W_{0.1}Ni(OH)_2/NiOOH$  nanosheet shows the highest efficiency in electrocatalysis. The surface composition and oxidation state of the developed electrocatalyst are confirmed by ICP-AES and XPS analysis. After doping the lattice suffers a tensile strain, which is confirmed by Raman and PXRD analysis. FESEM and TEM analyses confirm the nanosheet morphology of  $W_{0.1}Ni(OH)_2/NiOOH$ . The electrocatalyst,  $W_{0.1}Ni(OH)_2/NiOOH$  is having a lower value of overpotential of 56 and 293 mV to obtain 10 and 50 mA/cm<sup>2</sup> current density for HER and OER, respectively, in a basic medium. The corresponding Tafel slope values are 63.5 and 48.2 mVdec<sup>-1</sup> for HER and OER, respectively. In  $W_{0.1}Ni(OH)_2/NiOOH$ ,  $W^{6+}$  ion is a  $d^0$  system that behaves as a strong Lewis acid and helps in electron pulling from  $Ni^{2+}$  ion, which facilitates the formation of  $Ni^{3+}$  ion as an active site for HER and OER. The electron pulling nature of the  $W^{6+}$  ion is further confirmed from Bader's charge analysis. Moreover, the synergistic effect between  $Ni^{2+}$  and  $W^{6+}$  ions play an important role in higher electrocatalytic efficiency. Density Functional Theory calculations revealed the change in the Gibbs free energy of H adsorption in the presence of W, suggesting an enhanced HER activity for  $W_{0.1}Ni(OH)_2/NiOOH$ .

### 4.1 Introduction

Electrochemical water splitting reaction is a prominent way to generate hydrogen and oxygen with high purity and zero pollution, a clean and sustainable source of energy.<sup>1-2</sup> Hydrogen and oxygen evolution reactions (HER and OER) are the two important half-reactions for electrochemical water splitting for sustainable clean energy production.<sup>3-4</sup> HER is a two-electron process, whereas, OER is a four-electron process. OER shows more sluggish kinetics than HER and requires very high overpotential. The theoretical potential value of 1.23 V ( $\Delta G = 237.2$  kJ/mol) is required for water splitting.<sup>5</sup> Therefore, it is essential to minimize the value of large overpotential and sluggish reaction kinetics by developing a desirable electrocatalyst in nanometre length scale with better efficiency. Noble metal-based materials like Pt and RuO<sub>2</sub>, IrO<sub>2</sub> is an excellent electrocatalyst for HER and OER, respectively, but due to high cost and low availability large-scale application is restricted.<sup>6-8</sup>

Oxides, hydroxides, sulphides, and selenides of transition metals (e.g., Ni, Co, and Fe) are investigated as a better electrocatalyst with low-cost element composition and well functionality in the acidic and basic medium for electrocatalytic HER and OER, respectively.<sup>9-10</sup> Although these electrocatalysts show efficient activity in HER and OER reaction using an acidic and basic electrolyte, however, their activity diminished for either HER or OER using the same electrolyte (alkaline or acidic) because of the incongruity among activity and stability. It becomes more and more essential to unveil alternative bifunctional (HER and OER) electrocatalysts within a single catalyst composed of nonprecious metals or earth-abundant elements with high efficiency and stability in a single electrolyte solution.<sup>11-13</sup> So, there are many strategies like heterostructuring, morphology control, and incorporation of dopant to create a bifunctional active site for electrocatalytic water splitting using the same electrolyte.<sup>14-16</sup> The incorporation of the second metal as a dopant generally improves the electrocatalytic activity by increasing charge transportation. Moreover, doping with heteroatom makes the catalyst more metallic and influences the chemical environment of the catalytic surface.<sup>17</sup>

An effort is being dedicated to developing a new cost-effective, durable, and bifunctional electrocatalyst for HER and OER but the exact role of dopant is not yet clear. The literature report confirms that the integration of dopant in Ni(OH)<sub>2</sub> enhances the electrocatalytic activity and electrical conductivity. Basu and co-workers<sup>18</sup> developed Fe<sup>3+</sup> doped Ni(OH)<sub>2</sub>/NiOOH as an effective electrocatalyst for OER and confirmed the strong Lewis acid behaviour of Fe<sup>3+</sup> ion, which

pulls the electron from the neighbouring nickel results in peak shifting during CV analysis. Similarly, few other scientists also reported Fe doping in Ni(OH)<sub>2</sub> structures. Wang and co-workers<sup>19</sup> developed Ni(OH)<sub>2</sub> from Ni foam and Fe doping via electrochemically assisted technique for OER. They have reported high efficiency, durability, and lower Tafel slope value (48.3 mVdec<sup>-1</sup>) with Fe doped electrocatalyst, where Fe doping modifies the electronic structure of Ni(OH)<sub>2</sub>. Furthermore, Yuan and co-workers<sup>20</sup> reported integrated architectures with multiple pores of Fe doped Ni(OH)<sub>2</sub> for electrocatalytic reactions (HER and OER). These architectures and high porosity help in exposing sufficient electrocatalytically active sites, electrical and structural properties during electrochemical reactions. Later on, single-atom tungsten doping in ultrathin Ni(OH)<sub>2</sub>, where, W<sup>6+</sup> sites present in the system behave as the exothermic site for H<sub>2</sub>O adsorption, and oxygen radical formation favors the oxygen evolution in 1.0 M KOH solution is reported by Yan and co-workers.<sup>21</sup> Using DFT calculation the same group has confirmed that the site of W<sup>6+</sup> is responsible for the generation of O radical and O-O coupling, which promptly enhances the oxygen evolution. Wang and co-workers<sup>22</sup> developed Ru doping in Ni(OH)<sub>2</sub> following hydrothermal method and represented best HER activity in alkaline medium. They have mentioned that Ru doped Ni(OH)<sub>2</sub> propagates increment of charge transfer rate, higher electrochemically active surface area, acceleration in Volmer step, and an active site for hydrogen adsorption. Ce doped Ni(OH)<sub>2</sub> nanosheet via one-step electrodeposition on a conducting carbon fiber paper is reported by Huang and co-workers.<sup>23</sup> They have mentioned that the electrodeposition technique increases the active sites during oxygen generation. Recently, Ning and co-workers<sup>24</sup> introduced a small amount of W<sup>6+</sup> into Fe<sub>x</sub>Ni<sub>1-x</sub>(O)OH to develop the target product as Fe<sub>0.03</sub>W<sub>0.03</sub>-Ni layered double hydroxide for OER. Based on various characterization techniques and electrochemical studies the same group has claimed a synergistic interaction between nickel, iron, and tungsten metal ions which produced a favourable environment and electronic structure for enhanced OER activity. Therefore, the above-mentioned literature directed us for doping in Ni(OH)<sub>2</sub> substrate, which can effectively increase the conductivity and stability of the system. In this study, we have chosen Ni(OH)<sub>2</sub>/NiOOH system as a heterostructure and doped it with tungsten to develop a bifunctional electrocatalyst for both HER and OER in a single electrolyte medium.

Being motivated by the above studies, herein, we have synthesized tungsten doping with Ni(OH)<sub>2</sub>/NiOOH on a conductive surface through electrodeposition followed by the hydrothermal method. The catalyst exhibits superior performance for HER and OER in 1.0 M KOH. Afterward,



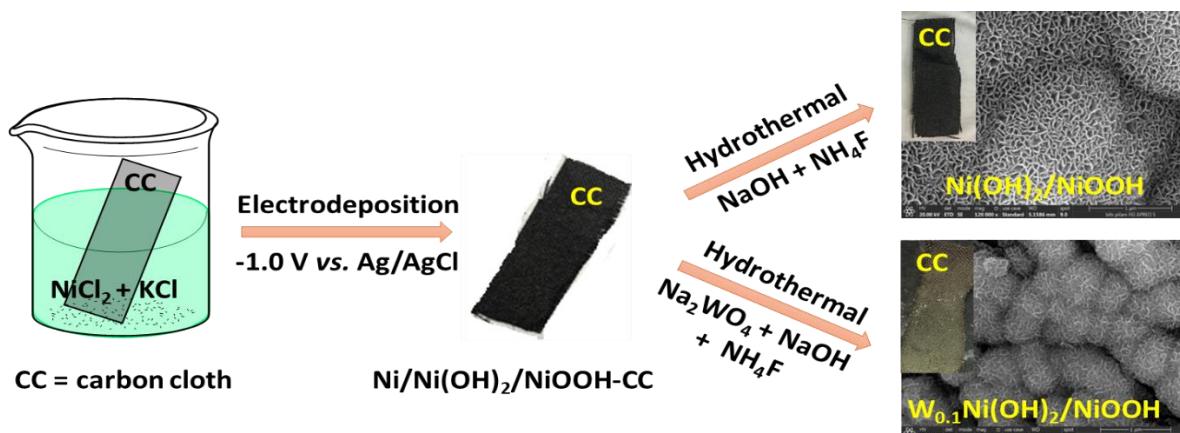
through doping of W in Ni(OH)<sub>2</sub>/NiOOH with ratio variation (W:Ni) the electrocatalyst shows more electrocatalytic activity. W<sup>6+</sup> has a d<sup>0</sup> system, which can improve the adsorption energies for intermediates, resulting in increasing the electrocatalytic efficiency. All the nanomaterials are well characterized by various techniques like PXRD, FESEM, TEM, XPS, etc. The advantage of this work can be folded as, first, the development of electrocatalyst is an easy and cost-effective method. Carbon cloth is working as better conductive support, which could be used without any polymer binder. Second, the doped electrocatalyst exhibits higher activity and stability. There is a synergistic consequence among W<sup>6+</sup> and Ni<sup>2+</sup> ions to increase the electronic conductivity of the system. The best electrocatalytic activity was obtained with W<sub>0.1</sub>Ni(OH)<sub>2</sub>/NiOOH nanosheet, which exhibits a very low overpotential value of 56 and 293 mV to obtain 10 and 50 mA/cm<sup>2</sup> current density for HER and OER, respectively. The calculated Tafel slope is 63.5 and 48.2 mVdec<sup>-1</sup> for HER and OER, respectively, which is outstanding among the non-noble metal-based electrocatalysts. Third, the developed doped nanomaterials can behave as a bifunctional electrocatalyst in an alkaline electrolyte. Fourth, Density Functional Theory calculations confirm the higher Gibbs free energy of H adsorption in W<sub>0.1</sub>Ni(OH)<sub>2</sub>/NiOOH for enhanced HER activity.

## 4.2 Experimental Section

**4.2.1 Synthesis of Ni(OH)<sub>2</sub>/NiOOH:** For the synthesis of Ni(OH)<sub>2</sub>/NiOOH, firstly, Ni/Ni(OH)<sub>2</sub>/NiOOH composite was developed by a facile electrodeposition process on carbon cloth following our recently reported method.<sup>25</sup> A brief procedure is also given here. Three-electrode systems (carbon cloth = WE, Pt wire = CE, and Ag/AgCl = RE) were used during electrodeposition. At the time of electrodeposition, 10 mM NiCl<sub>2</sub>·6H<sub>2</sub>O and 0.1 M KCl were used as precursor salt and an electrolyte. Chronoamperometry technique with cathodic potential of -1.0 V vs. Ag/AgCl was applied for 20 minutes to deposit Ni/Ni(OH)<sub>2</sub>/NiOOH composite. Subsequently, after electrodeposition, the sample deposited carbon cloth was kept for hydrothermal reaction (105 °C for 6 hours) in a sealed autoclave using a Teflon container along with 0.63 gm NaOH, 0.15 gm NH<sub>4</sub>F, and 50 mL DI water, and the solution was sonicated for 10 minutes for proper mixing. Finally, ethanol was used to clean the sample deposited carbon cloth and dried in a conventional oven.

**4.2.2 Synthesis of W doped Ni(OH)<sub>2</sub>/NiOOH:** For W doping, 0.329 gm of Na<sub>2</sub>WO<sub>4</sub> (1.0 mM), 0.63 gm NaOH, and 0.15 gm NH<sub>4</sub>F were mixed properly in 50 mL DI water via sonication. After that, the 50 mL solution consisting of Na<sub>2</sub>WO<sub>4</sub>, NaOH, and NH<sub>4</sub>F was transferred into a Teflon-lined autoclave. In the same autoclave previously developed Ni/Ni(OH)<sub>2</sub>/NiOOH on a CC was dipped for the hydrothermal reaction at 105 °C for 6 hours. After the reaction, the CC was removed and washed with ethanol followed by drying. Following this technique, W<sub>0.1</sub>Ni(OH)<sub>2</sub>/NiOOH was developed on CC.

To vary the amount of "W" during doping various amount of Na<sub>2</sub>WO<sub>4</sub> was taken keeping unchanged the other conditions. 0.658 and 0.197 gm of Na<sub>2</sub>WO<sub>4</sub> (2.0 mM and 0.6 mM) were used to develop W<sub>0.2</sub>Ni(OH)<sub>2</sub>/NiOOH, and W<sub>0.06</sub>Ni(OH)<sub>2</sub>/NiOOH electrocatalyst, respectively. Unless otherwise indicated the three developed electrocatalysts on CC are represented as W<sub>0.1</sub>Ni(OH)<sub>2</sub>/NiOOH, W<sub>0.2</sub>Ni(OH)<sub>2</sub>/NiOOH, and W<sub>0.06</sub>Ni(OH)<sub>2</sub>/NiOOH. Schematic representation for the synthesis of doped and undoped Ni(OH)<sub>2</sub>/NiOOH nanomaterials is shown in Scheme 4.1.



**Scheme 4.1** : Schematic illustration for the synthesis of Ni(OH)<sub>2</sub>/NiOOH and W<sub>0.1</sub>Ni(OH)<sub>2</sub>/NiOOH on carbon cloth.

**4.2.3 Electrochemical measurement:** For electrochemical analysis, three-electrode systems were used. The electrodes were sample (doped and undoped) deposited carbon cloth as WE, Ag/AgCl as RE, and graphite rod as CE using 1.0 M KOH as an electrolyte. No further polymer binder was used during electrocatalysis. The area of the working electrode was fixed (0.4×0.4 cm<sup>2</sup>) and

insulated epoxy paste was applied to the sample deposited carbon cloth. In the fixed area of  $0.4 \times 0.4 \text{ cm}^2$ , the amount of catalyst was loaded for  $\text{Ni}(\text{OH})_2/\text{NiOOH}$  and W doped  $\text{Ni}(\text{OH})_2/\text{NiOOH}$  as 0.624 mg. All the electrochemical analysis was performed using the CHI604E instrument. During linear sweep voltammetry (LSV) analysis,  $-0.9$  to  $-1.8 \text{ V vs. Ag/AgCl}$  and  $0$  to  $0.8 \text{ V vs. Ag/AgCl}$  for HER and OER, respectively were used at a scan rate of  $2.0 \text{ mV/s}$ . The obtained data was converted to RHE using the equation,  $E_{\text{RHE}} = E_{\text{Ag/AgCl}} + 0.0591 \text{ pH} + E^0_{\text{Ag/AgCl}}$ . For electrochemical impedance spectroscopy (EIS) analysis bare and W doped  $\text{Ni}(\text{OH})_2/\text{NiOOH}$  material was used and the onset potential was selected as the execution bias for data recording. A frequency ranges of  $50 \text{ kHz}$  to  $1 \text{ Hz}$  with applying a voltage of onset potential in  $1.0 \text{ M KOH}$  solution was used for EIS analysis.

**4.2.4 Preparation of standard electrocatalyst for HER and OER:**  $5\% \text{ Pt/C}$  and  $\text{RuO}_2$  were used as standard electrocatalyst for HER and OER, respectively. To compare the electrocatalytic activity same amount ( $0.624 \text{ mg}$ ) of catalyst was used. For HER, in a small glass vial  $0.624 \text{ mg}$  of  $5\% \text{ Pt/C}$  was added with  $200 \mu\text{L}$  isopropyl alcohol and  $20 \mu\text{L}$  Nafion (as adhesive), and the mixture was shaken well. After that, the whole mixture was transferred quantitatively into  $0.4 \times 0.4 \text{ cm}^2$  carbon cloth and was used for HER. The same process was followed for OER except  $\text{RuO}_2$  was used instead of  $5\% \text{ Pt/C}$ .

**4.2.5 Computational Methods:** Periodic spin-polarized density functional theory calculations were performed using the Vienna ab initio Simulation package as developed at the Fakultät für Physik of Universität Wien.<sup>26-27</sup> A plane-wave basis set with an energy cutoff of  $450 \text{ eV}$  and the Projector augmented wave potentials (PAW)<sup>28-29</sup> was employed in the calculations. The PBE functional<sup>30</sup> in the generalized gradient approximation (GGA) was utilized for describing the exchange-correlation energy. The DFT+U formalism proposed by Dudarev was chosen to account for the better description of the d electrons of transition metal oxides.<sup>31</sup> An effective U-J value of  $5.5 \text{ eV}$  for Ni was found to accurately predict the lattice constant for  $\text{NiOOH}$ .<sup>32-33</sup> The bulk unit cell of  $\beta\text{-NiOOH}$  created by Selloni and co-workers was adapted for this work.<sup>32-33</sup> A higher indexed  $\beta\text{-NiOOH}$  (015) surface was considered for this study as they are highly reactive. The  $\beta\text{-NiOOH}$  (015) surface was modeled as a 6 layer slab with a  $15 \text{ \AA}$  vacuum spacing to avoid inter slab interactions. The W doped surface was modeled by replacing one of the surface Ni atoms. The Brillouin zone was sampled with a  $3 \times 3 \times 1$  Monkhorst-Pack grid, and a tetrahedron method of

smearing having a width of 0.2 eV was employed. Geometry optimization was done using a conjugate gradient algorithm with a force convergence criterion of 0.05 eV/Å.

The Gibbs free energy for hydrogen adsorption on the  $\beta$ -NiOOH surface was calculated as follows:

$$\Delta G_{\text{H}}(298\text{K}, 1\text{bar}) = \Delta H(298\text{K}) + \text{ZPE} - T\Delta S(298\text{K})$$

Where  $\Delta H$  and  $\Delta S$  are the enthalpy and entropy change at 298K and ZPE is the zero-point energy correction. ZPE was calculated from a vibrational analysis and enthalpy and entropy corrections for  $\text{H}_2$  (gas). The d band center of the surface Ni atom is computed as follows

$$\varepsilon_d = \frac{\int_{-\infty}^{E_F} E D(E) dE}{\int_{-\infty}^{E_F} D(E) dE}$$

Where  $D(E)$  is the density of states at energy  $E$ . A Bader charge analysis<sup>34</sup> was also performed to quantify the charge transfer between the metals.

## 4.3 Results and discussion

### 4.3.1 Material synthesis and characterization

Electrodeposition followed by the hydrothermal method was used for the synthesis of bare and W doped  $\text{Ni}(\text{OH})_2/\text{NiOOH}$  nanomaterials on carbon cloth. The Chronoamperometry technique was used for electrodeposition using KCl as an electrolyte. After electrodeposition,  $\text{Ni}(\text{OH})_2/\text{NiOOH}$  sample was doped with W using  $\text{Na}_2\text{WO}_4$  following hydrothermal technique. The amount of W was varied to optimize the role of dopant in the electrocatalytic activity.

To find out the phase, crystallinity, and purity, XRD analysis is carried out, which is given in Figure 4.1a. All the peaks are well indexed to the  $\text{Ni}(\text{OH})_2/\text{NiOOH}$ , in which  $\text{Ni}(\text{OH})_2$  is present in the form of both alpha and beta phase (JCPDS 38-0715) and (JCPDS 14-0117) representing  $2\theta$  values at  $19.2^\circ$ ,  $33.2^\circ$ ,  $38.9^\circ$ , and  $59.4^\circ$ . All the assigned peaks are well-matched with the diffraction plane with (hkl) values of (001), (100), (101), and (110). The other peaks at  $29.3^\circ$ ,  $44.3^\circ$ , and  $47.1^\circ$  are observed for NiOOH (JCPDS 78-4225). The remaining broad peaks at  $2\theta = 25.6^\circ$ ,  $42.8^\circ$ , and  $52.1^\circ$  are due to the presence of carbon cloth.<sup>18, 25</sup> After doping with W in  $\text{Ni}(\text{OH})_2/\text{NiOOH}$  all the peak positions are the same except the peaks at  $29.3^\circ$ ,  $33.2^\circ$ , and  $38.9^\circ$  are shifted. The shifting of peaks to the lower diffraction angle suggested that the dopant arises

tensile strain in the system of Ni(OH)<sub>2</sub>/NiOOH.<sup>24</sup> All the observed peaks in the PXRD pattern of W<sub>0.2</sub>Ni(OH)<sub>2</sub>/NiOOH and W<sub>0.06</sub>Ni(OH)<sub>2</sub>/NiOOH samples are well-matched with the W<sub>0.1</sub>Ni(OH)<sub>2</sub>/NiOOH (Figure 4.1b). The calculation of the lattice strain is performed following Williamson-Hall (W-H) method and the diffraction angles (2θ) = 29.3, 38.9, and 47.1 for (003), (101), and (203) planes of Ni(OH)<sub>2</sub>/NiOOH are used. The value of stain (ε) is co-related to the slope value, which shows 0.854, 1.12, 0.867, and 0.728 for Ni(OH)<sub>2</sub>/NiOOH, W<sub>0.1</sub>Ni(OH)<sub>2</sub>/NiOOH, W<sub>0.2</sub>Ni(OH)<sub>2</sub>/NiOOH and W<sub>0.06</sub>Ni(OH)<sub>2</sub>/NiOOH, respectively (Figure 4.1c). The positive value of strain confirms the presence of tensile strain in the doped sample, which is well matched with the literature.<sup>24,35</sup> The absence of any extra peak in W<sub>0.1</sub>Ni(OH)<sub>2</sub>/NiOOH for WO<sub>x</sub> and hydroxides species, which confirms the successful doping of W in the heterostructure system, and the synthesized sample is highly pure.

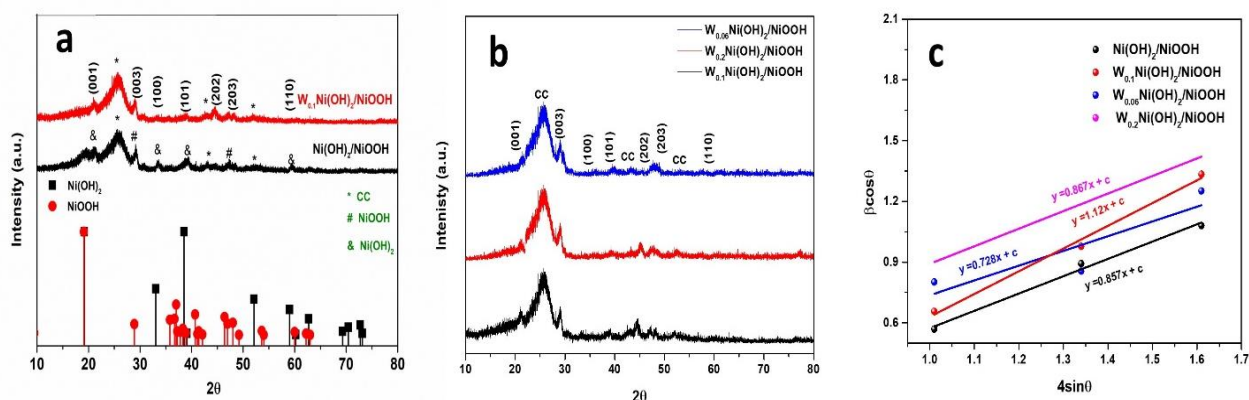


**Figure 4.1:** (a) PXRD pattern of Ni(OH)<sub>2</sub>/NiOOH and W<sub>0.1</sub>Ni(OH)<sub>2</sub>/NiOOH materials. JCPDS values for Ni(OH)<sub>2</sub> and NiOOH are shown at the bottom of the graph (b) PXRD analysis of W<sub>0.1</sub>Ni(OH)<sub>2</sub>/NiOOH, W<sub>0.2</sub>Ni(OH)<sub>2</sub>/NiOOH, and W<sub>0.06</sub>Ni(OH)<sub>2</sub>/NiOOH. (c) W-H plot.

Raman spectra of Ni(OH)<sub>2</sub>/NiOOH and W<sub>0.1</sub>Ni(OH)<sub>2</sub>/NiOOH samples are shown in Figure 4.2. In Ni(OH)<sub>2</sub>/NiOOH sample, the peaks are observed at 309 cm<sup>-1</sup> and 444 cm<sup>-1</sup> for E<sub>g(T)</sub> and A<sub>1g</sub> mode of Ni-OH lattice vibration and stretching vibration, respectively.<sup>36</sup> Another peak that appeared at 1058 cm<sup>-1</sup> confirms the presence of active oxygen in NiOOH.<sup>37</sup> Raman spectra of W<sub>0.1</sub>Ni(OH)<sub>2</sub>/NiOOH consist of similar peaks but shifted to higher wavenumber, which is due to the doping. The peak shifting in Raman analysis also symbolizes the presence of strain in the system after doping. The Raman spectra of W<sub>0.2</sub>Ni(OH)<sub>2</sub>/NiOOH and W<sub>0.06</sub>Ni(OH)<sub>2</sub>/NiOOH also exhibit broad peaks shifted at 545 cm<sup>-1</sup>. No new peak appeared in W<sub>0.1</sub>Ni(OH)<sub>2</sub>/NiOOH indicates the formation of oxides and hydroxides is insignificant.<sup>38</sup>

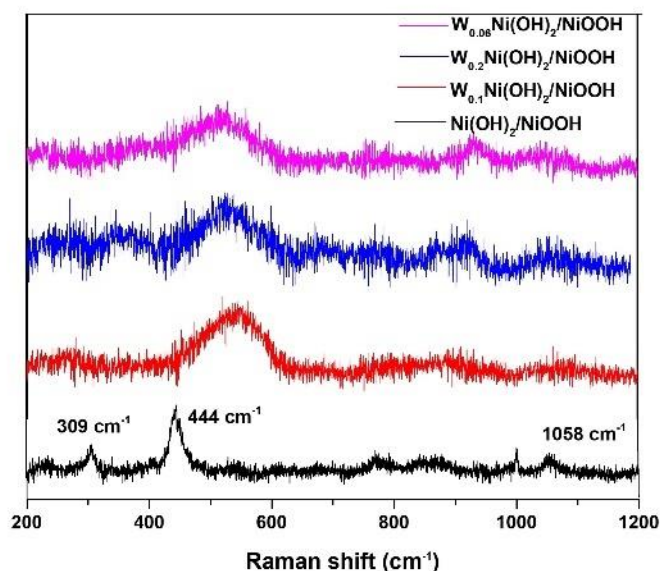


**Figure 4.2:** Raman spectrum of  $\text{Ni(OH)}_2/\text{NiOOH}$ ,  $\text{W}_{0.1}\text{Ni(OH)}_2/\text{NiOOH}$ ,  $\text{W}_{0.2}\text{Ni(OH)}_2/\text{NiOOH}$ , and  $\text{W}_{0.06}\text{Ni(OH)}_2/\text{NiOOH}$  materials.

### 4.3.2 XPS analysis

Furthermore, XPS analysis was performed to confirm the oxidation states of all the ions and doping of W in the developed materials. The presence of W, Ni, and O in the system is confirmed from the XPS survey scan. The absence of any extra peak in survey scans confirms that the synthesized sample is pure and contaminant-free. XPS survey scan for  $\text{Ni(OH)}_2/\text{NiOOH}$  is represented in Figure 4.3a, which exhibits the peaks for Ni and O. In  $\text{Ni(OH)}_2/\text{NiOOH}$  sample, the deconvoluted Ni 2p spectra (Figure 4.3b) are fitted with two doublet peaks along with satellite peaks. Figure 4.3b symbolizes two binding energies at 855.7 eV and 873.17 eV for Ni 2p<sub>3/2</sub> and Ni 2p<sub>1/2</sub>, respectively ascribed to the presence of Ni<sup>2+</sup>. Moreover, two-fold satellite peaks with the binding energies of 862.03 eV and 879.9 eV are also characteristic of Ni<sup>2+</sup>. The other binding energies of 856.9 eV (2p<sub>3/2</sub>) and 874.6 eV (2p<sub>1/2</sub>) for the existence of NiOOH in the sample. The above binding energies for Ni<sup>2+</sup> and Ni<sup>3+</sup> ions are well corroborated with the literature.<sup>18, 22</sup> The deconvoluted spectra (Figure 4.4b) of Ni 2p consists of two spin-orbit doublets in addition to satellite peaks in  $\text{W}_{0.1}\text{Ni(OH)}_2/\text{NiOOH}$  sample. The binding energy values for Ni 2p peaks are at 856.2 eV (2p<sub>3/2</sub>), and 873.9 eV (2p<sub>1/2</sub>) for the presence of Ni<sup>2+</sup> ion and 857.5 eV (2p<sub>3/2</sub>) and 875.4 eV (2p<sub>1/2</sub>) for NiOOH species, respectively. Figures 4.4b and 4.3b show that there is a clear shift of ~ 0.6 eV and ~ 0.7 eV towards higher binding energy for Ni<sup>2+</sup> and Ni<sup>3+</sup> species, respectively.

Therefore, the shift in binding energy in  $W_{0.1}Ni(OH)_2/NiOOH$  represents a strong interaction between nickel and tungsten.<sup>18</sup> High-resolution deconvoluted XPS analysis of W 4f in W doped  $Ni(OH)_2/NiOOH$  sample is shown in Figure 4.4c. XPS spectra of W 4f exhibit dual peaks with the binding energies of 36.1 eV ( $4f_{7/2}$ ) and 38.1 eV ( $4f_{5/2}$ ), which represents W is present in the +6 oxidation state in the doped sample.<sup>24, 39</sup> Apart from the two binding energies of the  $W^{6+}$  species, there is no other peak present in Figure 4.4c, which confirms the absence of  $WO_3$  or another impurity in the  $W_{0.1}Ni(OH)_2/NiOOH$  sample.

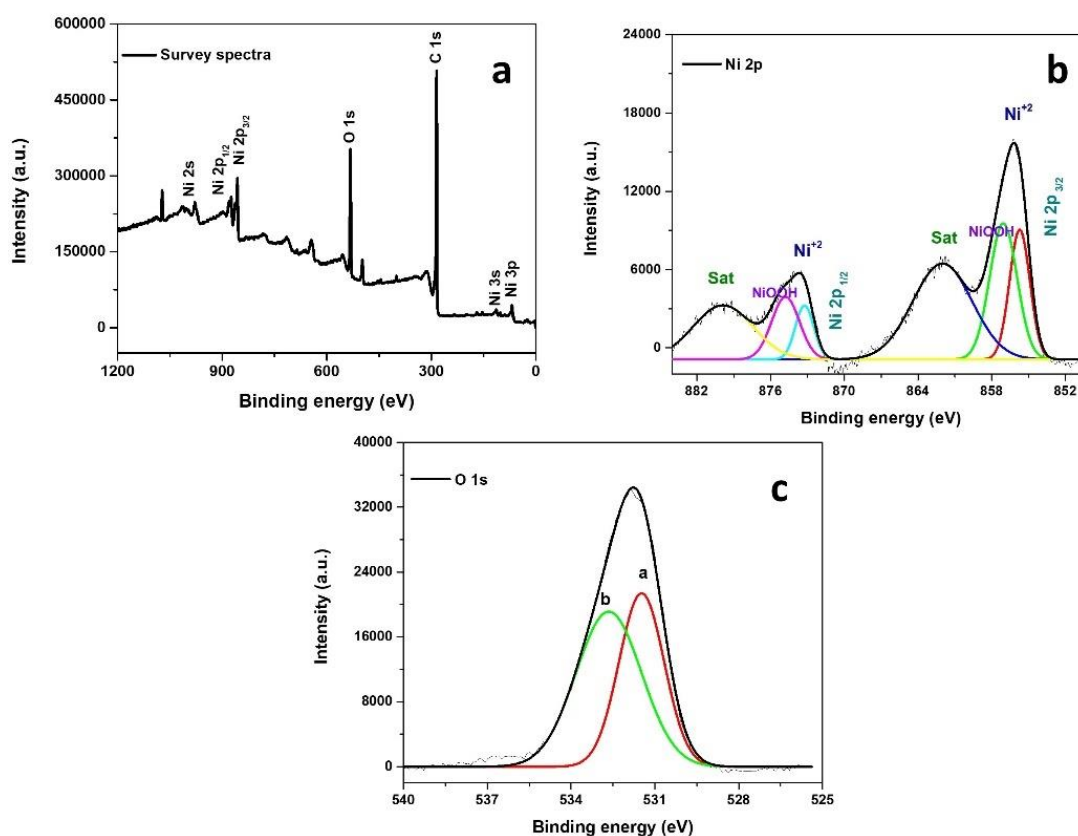


**Figure 4.3:** XPS analysis of  $Ni(OH)_2/NiOOH$  (a) survey spectrum, (b) deconvoluted spectra of Ni 2p and (c) deconvoluted spectra of O 1s.



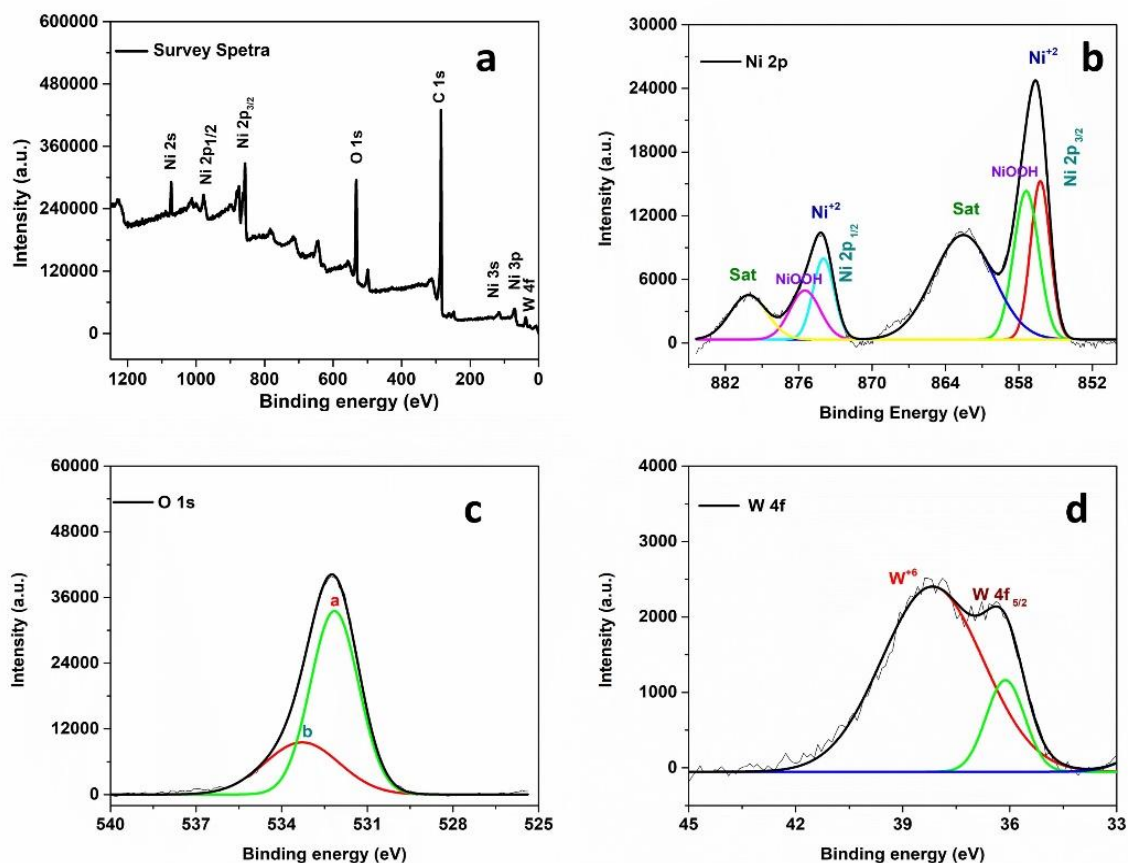


**Figure 4.4:** XPS analysis of  $W_{0.1}Ni(OH)_2/NiOOH$  (a) survey spectrum, (b) deconvoluted spectra of Ni 2p, (c) high-resolution spectra of W 4f, and (d) deconvoluted spectra of O 1s.

The sample,  $W_{0.1}Ni(OH)_2/NiOOH$  consists of  $W^{6+}$ , a  $d^0$  system, which can behave as a strong Lewis acid and withdraw adjacent electrons from the Ni site for the generation of more catalytically active  $Ni^{3+}$  species in the system. To confirm the electron pulling nature of  $W^{6+}$  species the atomic percentage of  $Ni^{2+}/Ni^{3+}$  are calculated as 7.82 and 5.89 in both  $Ni(OH)_2/NiOOH$  and  $W^{6+}$  doped  $Ni(OH)_2/NiOOH$  samples, respectively. So, a lower ratio of  $Ni^{2+}/Ni^{3+}$  in the doped sample confirms the electron pulling behaviour of  $W^{6+}$  and the generation of more  $Ni^{3+}$  species. Furthermore, O 1s binding energy also plays an important role to prove the electron-withdrawing effect of the ‘W’ dopant, shown in Figures 4.4c. XPS spectra of O 1s peak for  $Ni(OH)_2/NiOOH$  sample (Figure 4.3c) shows two peaks around 531.4 eV and 532.6 eV, which is due to lattice  $O^{2-}$  and adsorbed  $OH^-$ , respectively. On the other hand, XPS spectra of  $W^{6+}$  doped  $Ni(OH)_2/NiOOH$  show two peaks at 532.2 eV and 533.3 eV for  $O^{2-}$  and adsorbed  $OH^-$  ion, respectively (Figure 4.4d). In the doped sample, the higher binding energy of adsorbed  $OH^-$  further confirms the



electron-withdrawing effect and also indicates a higher affinity of Ni site for both  $O^{2-}$  and adsorbed  $OH^-$ .<sup>18</sup>

The survey spectrum and the deconvoluted spectra of  $W_{0.2}Ni(OH)_2/NiOOH$  and  $W_{0.06}Ni(OH)_2/NiOOH$  show similar binding energy values for  $Ni^{2+}$ ,  $Ni^{3+}$ ,  $O^{2-}$ , and  $W^{6+}$  ions. All the binding energy values for bare and doped samples are tabulated in Table 4.1, which confirms the highest shift is observed in  $W_{0.1}Ni(OH)_2/NiOOH$  sample. XPS analysis result is well-corroborated with the PXRD analysis and further confirms the absence of impurities in the doped samples.

**Table 4.1:** XPS binding energy values of  $Ni(OH)_2/NiOOH$ ,  $W_{0.1}Ni(OH)_2/NiOOH$ ,  $W_{0.2}Ni(OH)_2/NiOOH$ , and  $W_{0.06}Ni(OH)_2/NiOOH$ .

Metal ions	$Ni(OH)_2/NiOOH$	$W_{0.2}Ni(OH)_2/NiOOH$	$W_{0.1}Ni(OH)_2/NiOOH$	$W_{0.06}Ni(OH)_2/NiOOH$
$Ni^{2+}(2p_{3/2})$	855.7 eV	855.9 eV	856.2 eV	855.8 eV
$Ni^{3+}(2p_{3/2})$	856.9 eV	857.3 eV	857.5 eV	857.1 eV
$O^{2-}$	531.4 eV	531.6 eV	532.2 eV	531.3 eV
$W^{6+}(4f_{7/2})$	-	35.7 eV	36.1 eV	35.6 eV

### 4.3.3 FESEM, EDS, ICP-AES and TEM analysis

Electron microscopy technique is used to determine the size, shape, and morphology of the as-developed samples. Figures 4.5a show the FESEM images of  $Ni(OH)_2/NiOOH$ . The inset image of Figure 4.5a shows the uniform distribution of  $Ni(OH)_2/NiOOH$  on the surface of carbon cloth. Low and high-resolution images confirm the formation of the vertically grown nanosheet structure of  $Ni(OH)_2/NiOOH$  on the surface of carbon cloth. These vertically grown sheet-like structures of  $Ni(OH)_2/NiOOH$  function as a basic unit and accumulate into an aggregated structure. A higher magnification image also confirms the 2D nanosheet structures are well interconnected with each other having a sharp edge. FESEM images at low and high-resolution of  $W_{0.1}Ni(OH)_2/NiOOH$  are shown in Figures 4.5b, which confirms the uniform distribution throughout the carbon cloth. After doping the morphology is retained and shows a stacked nanosheet structure. A higher

magnification image clearly shows the interconnecting 2D sheets of W doped  $\text{Ni}(\text{OH})_2/\text{NiOOH}$  materials (Figure 4.5b). In a closer view, the outer edge of W doped materials is thick and rough than the undoped materials. The uniformly distributed nanosheet morphology with many interspaces and rough surfaces can significantly increase the surface area of the electrocatalyst, which can increase the electrocatalytic activity.<sup>40</sup> However, FESEM analysis of  $\text{W}_{0.2}\text{Ni}(\text{OH})_2/\text{NiOOH}$  and  $\text{W}_{0.06}\text{Ni}(\text{OH})_2/\text{NiOOH}$  represents non-uniform and aggregated structures (Figures 4.5c and d).

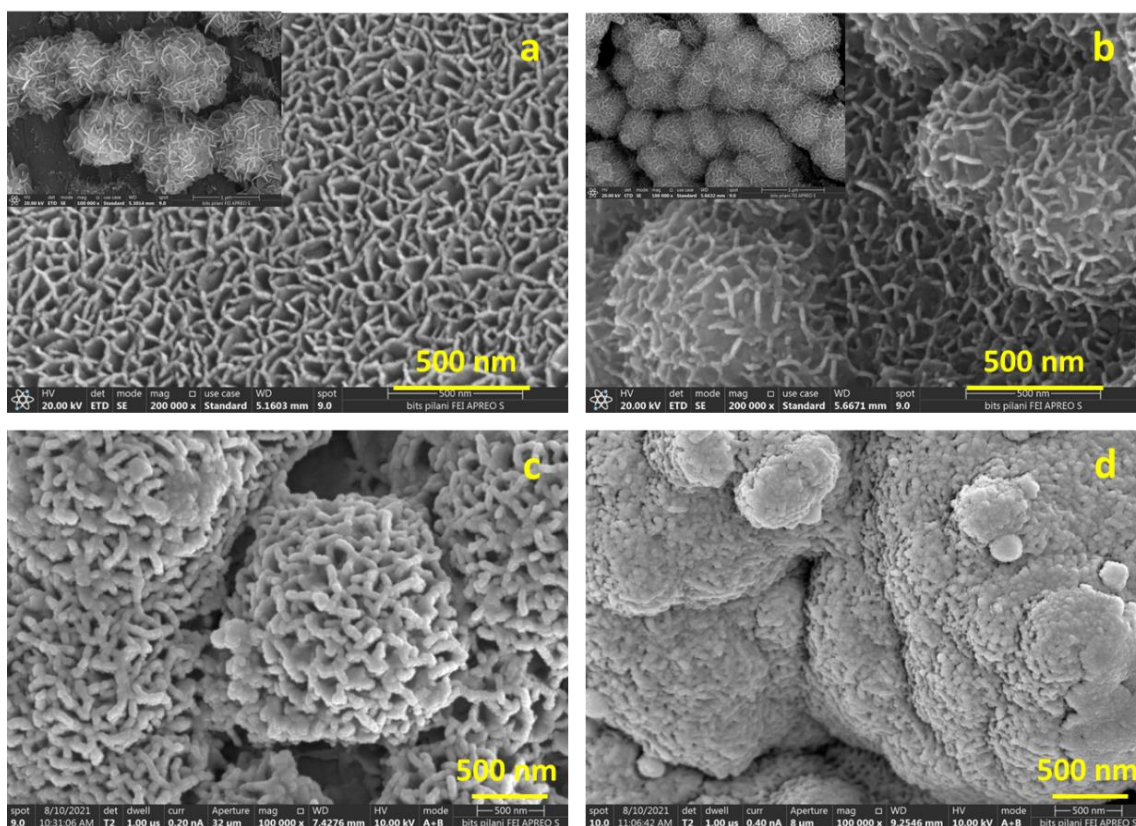


**Figure 4.5:** FESEM images of (a)  $\text{Ni}(\text{OH})_2/\text{NiOOH}$ . The inset of figure 4.5 a shows the uniform coverage of carbon cloth surface with  $\text{Ni}(\text{OH})_2/\text{NiOOH}$ . (b)  $\text{W}_{0.1}\text{Ni}(\text{OH})_2/\text{NiOOH}$  (with inset of CC surface) (c)  $\text{W}_{0.2}\text{Ni}(\text{OH})_2/\text{NiOOH}$  (d)  $\text{W}_{0.06}\text{Ni}(\text{OH})_2/\text{NiOOH}$ .

The difference in morphology could be due to the presence of the different amounts of W dopant. By changing the dopant concentration, the surplus atoms are aggregated and influence the surface kinetics, which leads to the change in morphology. The nucleation and growth of the  $\text{Ni}(\text{OH})_2/\text{NiOOH}$  lattice may also be affected by the lower and higher amount of W in  $\text{W}_{0.06}\text{Ni}(\text{OH})_2/\text{NiOOH}$  and  $\text{W}_{0.2}\text{Ni}(\text{OH})_2/\text{NiOOH}$  samples. EDS mapping analysis of the bare

sample shows the signals of Ni, O, and C elements with uniform distribution of Ni, O, and C in the material (Figure 4.6). The presence of W is further confirmed from EDS mapping analysis of doped materials along with the distribution of Ni, O, and C (Figures 4.7).

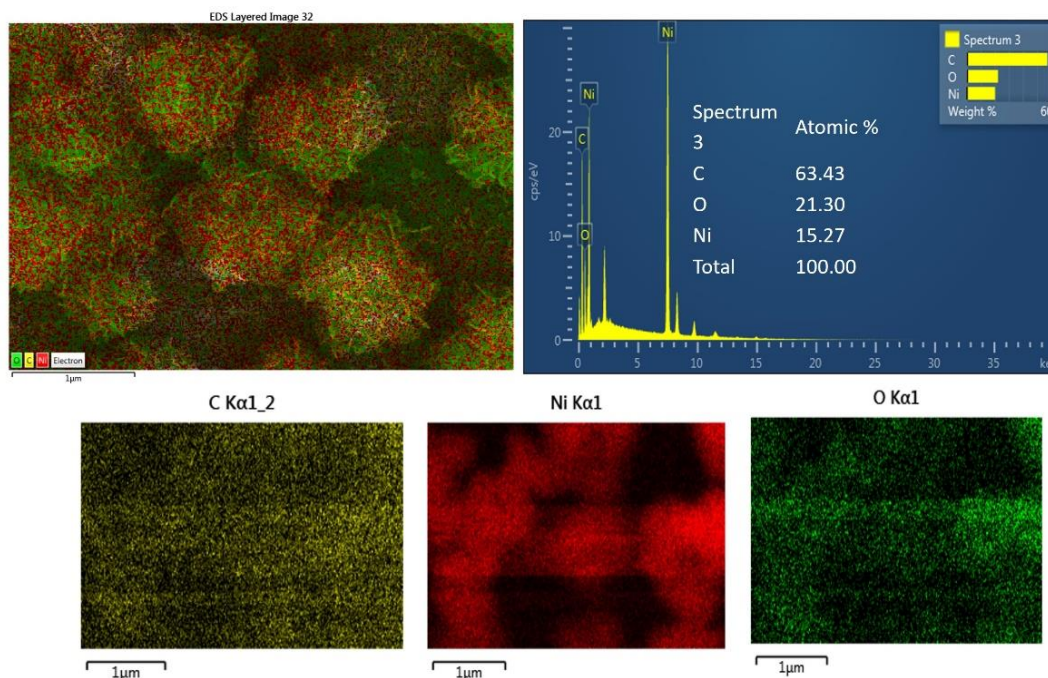


**Figure 4.6:** Elemental composition and EDS mapping showing the distribution of Ni and O on the carbon cloth in Ni(OH)<sub>2</sub>/NiOOH.

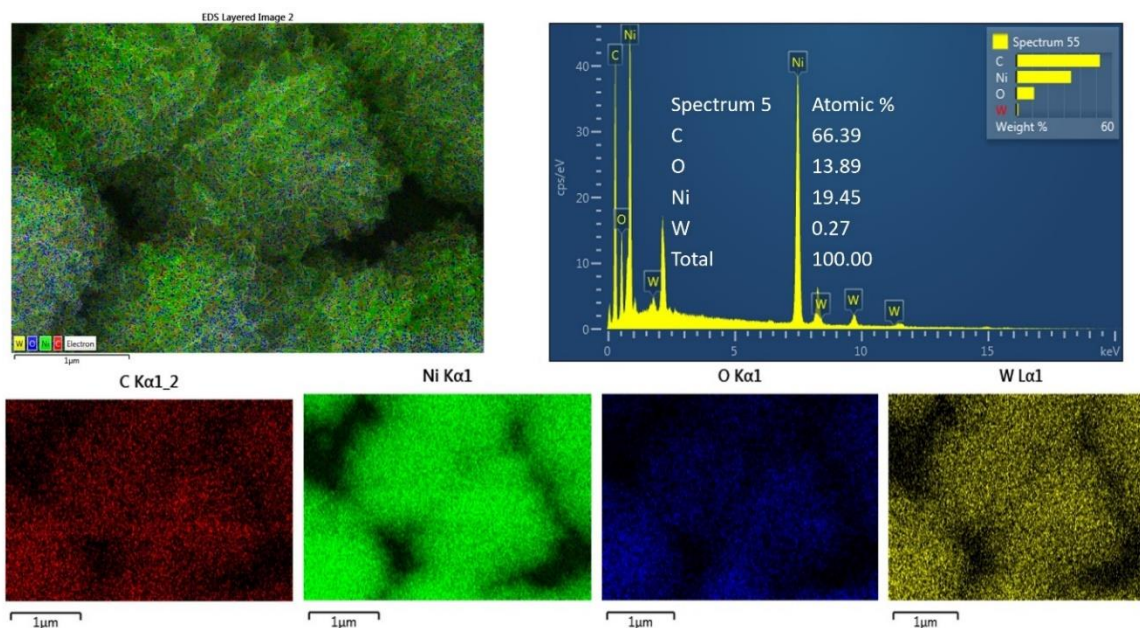


**Figure 4.7:** Elemental composition and EDS mapping showing the distribution of W, Ni and O on the carbon cloth in W<sub>0.1</sub>Ni(OH)<sub>2</sub>/NiOOH.



The amount of W in  $W_{0.1}Ni(OH)_2/NiOOH$  is verified by using ICP-AES analysis and shown in Table 4.2. ICP-AES result confirms the presence of 0.106, 0.143, and 0.052 wt% of W in  $W_{0.1}Ni(OH)_2/NiOOH$ ,  $W_{0.2}Ni(OH)_2/NiOOH$ , and  $W_{0.06}Ni(OH)_2/NiOOH$ , respectively, which is well-matched with the experimental amount of W.

**Table 4.2:** ICP-AES analysis of  $W_{0.1}Ni(OH)_2/NiOOH$ ,  $W_{0.2}Ni(OH)_2/NiOOH$ , and  $W_{0.06}Ni(OH)_2/NiOOH$ .

ICP-AES	W 239.708 (wt%)	Ni 231.604 (wt%)
$W_{0.1}Ni(OH)_2/NiOOH$	0.106	0.911
$W_{0.2}Ni(OH)_2/NiOOH$	0.143	0.857
$W_{0.06}Ni(OH)_2/NiOOH$	0.052	0.952

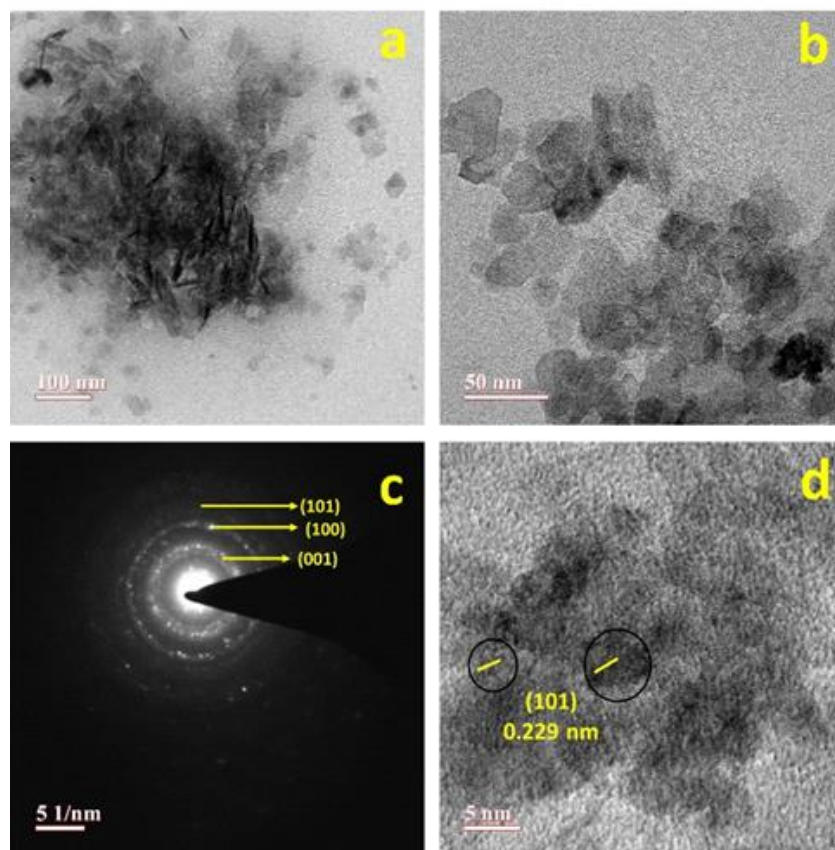


**Figure 4.8:** (a and b) TEM and (c) HRTEM image (d) SAED pattern of  $Ni(OH)_2/NiOOH$ .

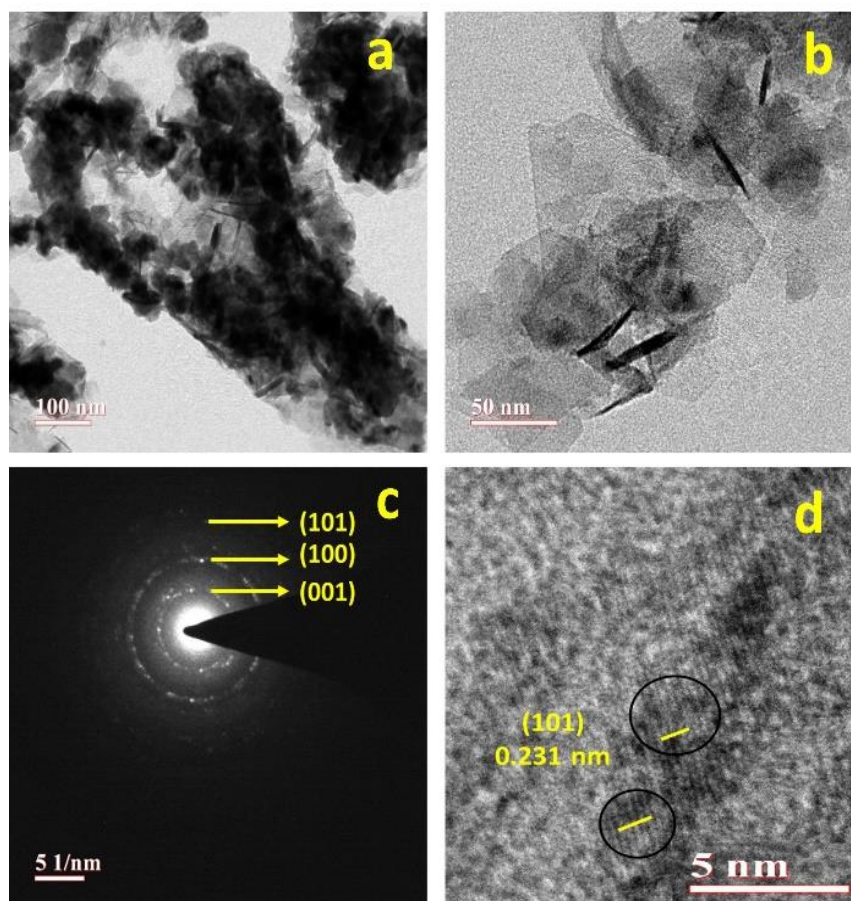


**Figure 4.9:** (a and b) TEM and (c) HRTEM image (d) SAED pattern of  $W_{0.1}Ni(OH)_2/NiOOH$ .

To reconfirm the morphology and crystallinity, TEM analysis is performed with doped and bare samples. Nanosheet morphology with a sharp edge of  $Ni(OH)_2/NiOOH$  is confirmed from the lower and higher magnification TEM images (Figures 4.8a and b). Afterward, doping with W in  $Ni(OH)_2/NiOOH$  ( $W_{0.1}Ni(OH)_2/NiOOH$ ) there is no change in morphology only the edges become thick and rough (Figures 4.9a and b). HRTEM analysis in Figure 4.8c is carried out to calculate the d-spacing in  $Ni(OH)_2/NiOOH$  lattice and reported as 0.229 nm, which is well-matched with the (101) plane. In  $W_{0.1}Ni(OH)_2/NiOOH$  sample, the d spacing value increases to 0.231 nm corresponding with the same plane in XRD (Figure 4.9c). The increment in d spacing value for the doped sample is well-matched with the XRD analysis. The blue-shifted peak in XRD analysis, as well as the change in d-spacing value altogether, represents a tensile strain in the  $Ni(OH)_2/NiOOH$  lattice after W doping ( $W_{0.1}Ni(OH)_2/NiOOH$ ). The crystallinity of the W doped  $Ni(OH)_2/NiOOH$

sample is also confirmed with SAED analysis. In Figures 4.8d and 4.9d, the SAED pattern shows the presence of many diffraction rings, which are well-matched with (001), (100), and (101) diffraction planes of Ni(OH)<sub>2</sub>.

Therefore, a few important points have emerged from the above analyses. First, the PXRD pattern and Raman spectra confirm that W<sub>0.1</sub>Ni(OH)<sub>2</sub>/NiOOH lattice suffers a tensile strain, which is due to the incorporation of W<sup>6+</sup> ion as a dopant. The increment in the d-spacing value from the HRTEM image also infer the change in tensile strain after doping. Second, a vertically grown nanosheet structure along with the optimum edge of W<sub>0.1</sub>Ni(OH)<sub>2</sub>/NiOOH is confirmed from FESEM and TEM. Third, a strong interaction is observed between nickel and tungsten due to the higher binding energy of W<sub>0.1</sub>Ni(OH)<sub>2</sub>/NiOOH. Fourth, XPS analysis confirms the electron pulling effect of the W<sup>6+</sup> ion, which also behaves as a strong Lewis acid. All these points are very important to improve the electrocatalytic HER and OER performances of W<sub>0.1</sub>Ni(OH)<sub>2</sub>/NiOOH than the other doped and bare materials.

### 4.3.4 Electrocatalytic performance

#### 4.3.4.1 Hydrogen evolution reaction (HER) study

The HER activity is studied using a three-electrode system and 1.0 M KOH solution. Ag/AgCl, graphitic rod, and sample (doped and bare) deposited CC is used as RE, CE, and WE, respectively. Bare Ni(OH)<sub>2</sub>/NiOOH on CC is also used to compare the HER activity. LSV analysis was examined at a 2 mVs<sup>-1</sup> scan rate for all the materials. Onset potential and overpotential are primarily two important parameters to determine electrocatalytic activity. Figures 4.10a and b represent the onset potential of bare Ni(OH)<sub>2</sub>/NiOOH is -0.312 V vs. RHE to obtain 10 mA/cm<sup>2</sup> current density, whereas W<sub>0.1</sub>Ni(OH)<sub>2</sub>/NiOOH shows at -0.056 V vs. RHE. Therefore, after doping the shift in the cathodic potential of -0.256 V vs. RHE confirms higher conductivity. 5% Pt/C is used to compare the current density at 10 mA/cm<sup>2</sup> and the required onset potential is -0.038 V vs. RHE. The effect of blank CC is insignificant within the potential region. Various amount of W dopant is used to optimize the role of W in the electrocatalytic activity. The electrocatalysts, W<sub>0.1</sub>Ni(OH)<sub>2</sub>/NiOOH, W<sub>0.2</sub>Ni(OH)<sub>2</sub>/NiOOH, and W<sub>0.06</sub>Ni(OH)<sub>2</sub>/NiOOH exhibits onset potentials at -0.056 V, -0.110 V, and -0.119 V vs. RHE to generate 10 mA/cm<sup>2</sup> current density in alkaline medium (Figures 4.10a and b). The difference in onset potentials during the generation of 10 mA/cm<sup>2</sup> current density represents the variation in conductivity in various doped samples. Figure

4.10c shows the plot between onset potential (V) vs. RHE and potential required to generate 100 mA/cm<sup>2</sup> current density, W<sub>0.1</sub>Ni(OH)<sub>2</sub>/NiOOH shows the best electrocatalytic performance in comparison with another developed electrocatalyst. The histogram plot (Figure 4.10d) of current density generated at -0.3 V vs. RHE of all the developed electrocatalyst represents the best active electrocatalyst is W<sub>0.1</sub>Ni(OH)<sub>2</sub>/NiOOH. In the W doped sample, the hierarchically interconnected nanosheet morphology produces a large number of active sites, which enhanced the evolution of hydrogen gases during the electrochemical reactions. The electrocatalyst, W<sub>0.1</sub>Ni(OH)<sub>2</sub>/NiOOH lattice suffers tensile strain which also produced active sites to enhance HER reaction.

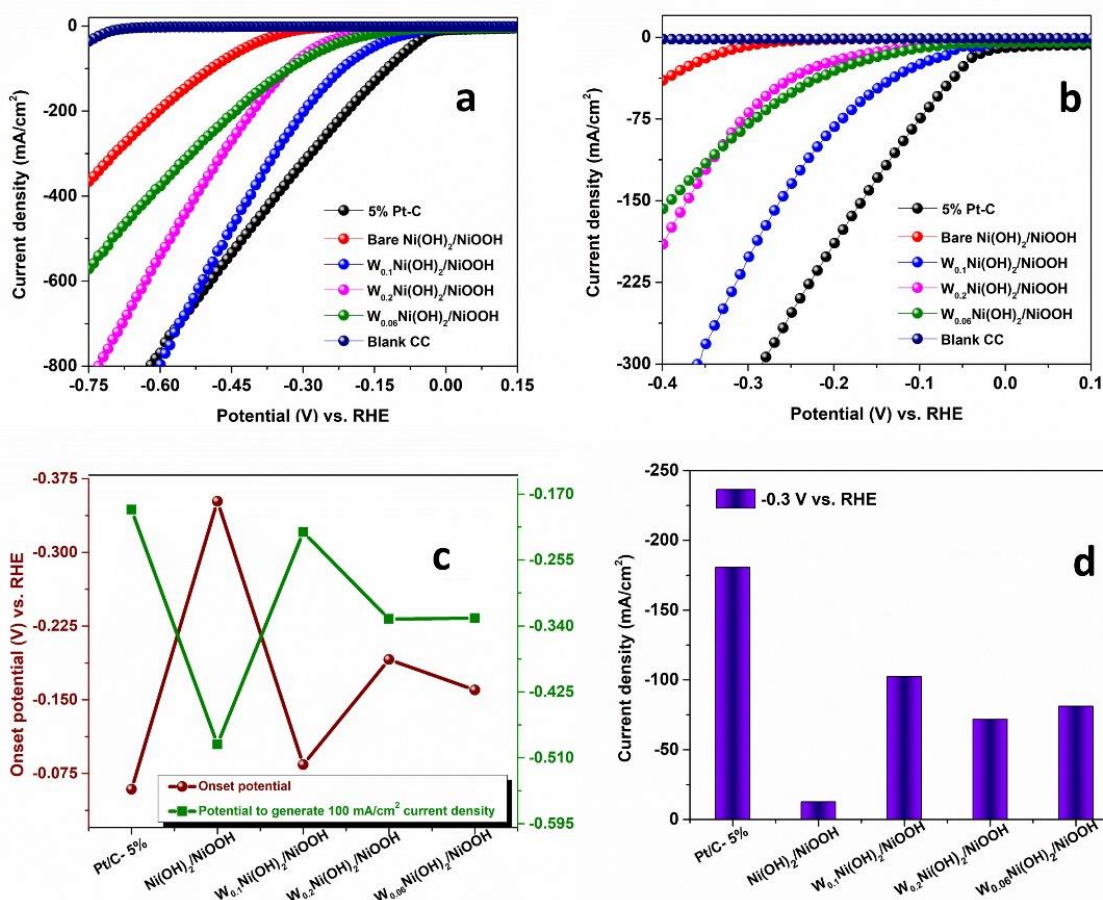


**Figure 4.10:** Polarization HER curve at (a) low scale and (b) high scale. (c) Plot between potential required to produce 100 mA/cm<sup>2</sup> current density and onset potential (V) vs. RHE (d) Histogram plot of current density obtained at -0.3 V vs. RHE of Ni(OH)<sub>2</sub>/NiOOH, W<sub>0.1</sub>Ni(OH)<sub>2</sub>/NiOOH, W<sub>0.2</sub>Ni(OH)<sub>2</sub>/NiOOH, W<sub>0.06</sub>Ni(OH)<sub>2</sub>/NiOOH, and Pt/C samples.

To determine the electrochemical performance of the developed electrocatalysts the electrochemically active surface area (ECSA) is calculated.<sup>25,41</sup> Cyclic voltammetry (CV) analysis is performed at altered scan rates (40 mV/s to 200 mV/s) within the potential range of 0.825 to 1.025 V vs. RHE using 1.0 M KOH solution (Figures 4.11a to d) for the calculation of double-layer capacitance ( $C_{dl}$ ). Observed current at a fixed potential of 0.925 V vs. RHE is plotted against the scan rate and the calculated  $C_{dl}$  values are 0.30 mF, 1.88 mF, 1.56 mF, and 0.696 mF for Ni(OH)<sub>2</sub>/NiOOH, W<sub>0.1</sub>Ni(OH)<sub>2</sub>/NiOOH, W<sub>0.2</sub>Ni(OH)<sub>2</sub>/NiOOH, and W<sub>0.06</sub>Ni(OH)<sub>2</sub>/NiOOH, respectively (Figure 4.11e). The obtained ECSA and roughness factor ( $R_f$ ) values are 31.33 cm<sup>2</sup>, 26 cm<sup>2</sup>, 11.6 cm<sup>2</sup>, 5.01 cm<sup>2</sup> and 195.81, 162.5, 72.5, 31.35 for W<sub>0.1</sub>Ni(OH)<sub>2</sub>/NiOOH, W<sub>0.2</sub>Ni(OH)<sub>2</sub>/NiOOH, W<sub>0.06</sub>Ni(OH)<sub>2</sub>/NiOOH and Ni(OH)<sub>2</sub>/NiOOH samples, respectively. So, W<sub>0.1</sub>Ni(OH)<sub>2</sub>/NiOOH sample shows ~ 6.3 times higher surface area than the bare sample. The higher value of ECSA for the W<sub>0.1</sub>Ni(OH)<sub>2</sub>/NiOOH sample represents more active sites, which is generated from the interconnected rough sheet-like structure and strong interaction between W and Ni site in the lattice. The larger value of  $R_f$  also indicates higher efficiency in HER. In this context, Li and co-workers<sup>40</sup> observed that after doping with phosphorus atom on Ni(OH)<sub>2</sub>/NiMoO<sub>4</sub> structure, nanosheets become rougher and the decrease in interspaces value. This decrement facilitates the rapid release of gas bubbles and the roughened nanosheets exhibit enhanced electrocatalytic efficiency.

Mass activity calculation is also very helpful to show the higher efficiency of an electrocatalyst. For all the electrocatalyst, Ni(OH)<sub>2</sub>/NiOOH, W<sub>0.1</sub>Ni(OH)<sub>2</sub>/NiOOH, and 5% Pt/C the amount of catalyst loading is 0.624 mg on 0.4×0.4 cm<sup>2</sup> carbon cloth. The calculated value of mass activity at a fixed potential of -0.4 V vs. RHE is 10.28 A/g, 96.34 A/g, and 66.58 A/g for Ni(OH)<sub>2</sub>/NiOOH, W<sub>0.1</sub>Ni(OH)<sub>2</sub>/NiOOH, and 5% Pt/C, respectively. The other W<sup>6+</sup> doped catalysts, W<sub>0.2</sub>Ni(OH)<sub>2</sub>/NiOOH and W<sub>0.06</sub>Ni(OH)<sub>2</sub>/NiOOH show the mass activity values are 49.01 A/g and 40.73 A/g, respectively. Therefore, the mass activity value of W<sub>0.1</sub>Ni(OH)<sub>2</sub>/NiOOH is highest than the other electrocatalyst. This higher electrocatalytic activity of W<sub>0.1</sub>Ni(OH)<sub>2</sub>/NiOOH can be explained by a strong synergistic effect between W<sup>6+</sup> and Ni<sup>2+</sup> ions. The proof of synergistic effect between the ions is well corroborated with the peak position shifting in PXRD, Raman, and XPS analyses. Moreover, stable W<sup>6+</sup> ions (d<sup>0</sup> system) as a dopant are significant for the adsorption of H atom and molecular hydrogen. Recently, our group has reported an efficient and durable electrocatalyst for HER based on Ni/Ni(OH)<sub>2</sub>/NiOOH, where, we have



mentioned that all the associated metal and ions (metallic Ni, Ni<sup>2+</sup>, and Ni<sup>3+</sup>) are randomly distributed on the surface of the catalyst and shows synergistic effect between the ions.<sup>25</sup> Table 4.3 represents the values of C<sub>dl</sub>, ECSA, R<sub>f</sub>, mass activity, etc. for a quick understanding of all the developed electrocatalysts.

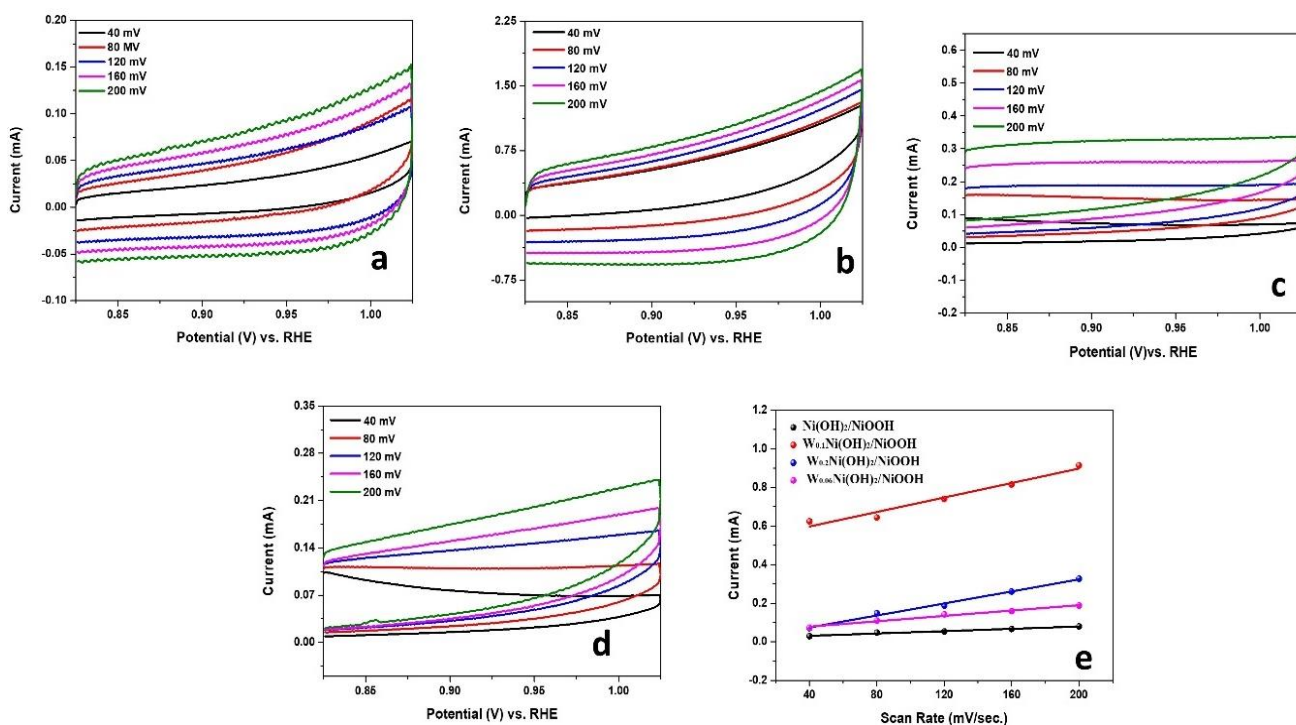
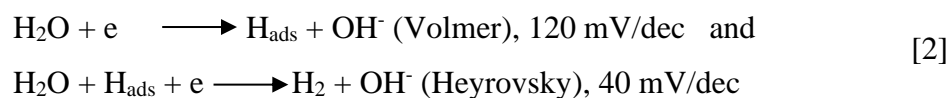
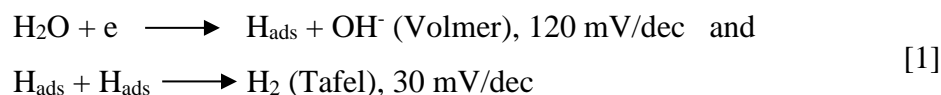


**Figure 4.11:** . Cyclic voltammograms of (a) Ni(OH)<sub>2</sub>/NiOOH (b) W<sub>0.1</sub>Ni(OH)<sub>2</sub>/NiOOH (c) W<sub>0.2</sub>Ni(OH)<sub>2</sub>/NiOOH (d) W<sub>0.06</sub>Ni(OH)<sub>2</sub>/NiOOH recorded in 1 M KOH recorded with different scan rates, (e) capacitive current at 0.925 (V vs. RHE) as a function of scan rate for all the samples.

**Table 4.3:** All the electrochemical HER parameters for Ni(OH)<sub>2</sub>/NiOOH, W<sub>0.1</sub>Ni(OH)<sub>2</sub>/NiOOH, W<sub>0.2</sub>Ni(OH)<sub>2</sub>/NiOOH, W<sub>0.06</sub>Ni(OH)<sub>2</sub>/NiOOH, and Pt/C electrocatalysts.

Electrodes	Potential (V) vs. RHE ) required to generate 20 mA/cm <sup>2</sup>	ECSA (cm <sup>2</sup> )	R <sub>f</sub>	Mass Activity (A/g) at -0.4 V vs. RHE	Tafel Slope (mV/decade)	R <sub>s</sub> (Ω)	R <sub>CT</sub> (Ω)
Ni(OH) <sub>2</sub> /NiOOH	-0.352	5.01	31.35	10.28	126.7	10.25	26.26
W <sub>0.1</sub> Ni(OH) <sub>2</sub> /NiOOH	-0.084	31.33	195.81	96.34	63.5	9.46	16.26
W <sub>0.2</sub> Ni(OH) <sub>2</sub> /NiOOH	-0.191	26	162.5	49.01	95.8	10.73	18.59
W <sub>0.06</sub> Ni(OH) <sub>2</sub> /NiOOH	-0.160	11.6	72.5	40.73	101.6	10.74	20.08
Pt/C (5%)	-0.059	-	-	66.58	59.8	-	-

To explain the mechanism of HER and higher activity of W<sub>0.1</sub>Ni(OH)<sub>2</sub>/NiOOH the calculation of Tafel slope is very important. The linear fitted graph (Figure 4.12a) is performed using the Tafel slope equation,  $\eta = b \log(J) + a$ , where,  $\eta$  = overpotential,  $b$  = Tafel slope, and  $J$  = current density.<sup>6, 42</sup> The electrocatalyst, Ni(OH)<sub>2</sub>/NiOOH, W<sub>0.1</sub>Ni(OH)<sub>2</sub>/NiOOH, W<sub>0.2</sub>Ni(OH)<sub>2</sub>/NiOOH, W<sub>0.06</sub>Ni(OH)<sub>2</sub>/NiOOH, and 5% Pt/C are having Tafel slope values of 126.7, 63.5, 95.8, 101.6, and 59.8 mVdec<sup>-1</sup>, respectively (Table 4.3). Therefore, W<sub>0.1</sub>Ni(OH)<sub>2</sub>/NiOOH shows the best Tafel slope value amongst all other electrocatalysts. Furthermore, with the increase or decrease of W<sup>6+</sup> amount the Tafel slope values are larger than W<sub>0.1</sub>Ni(OH)<sub>2</sub>/NiOOH. The Tafel slope value of W<sub>0.1</sub>Ni(OH)<sub>2</sub>/NiOOH and 5% Pt/C are comparable, which confirms the existence of an alternative electrocatalyst for HER in KOH solution. The HER reaction proceeds through the Volmer step at the beginning and then is followed by either Heyrovsky or Tafel step according to their Tafel slope value (alkaline medium), which is represented below.<sup>43</sup>



However, based on the Tafel slope value of  $W_{0.1}Ni(OH)_2/NiOOH$  heterostructure the HER reaction followed the Volmer-Heyrovsky pathway.<sup>25,33</sup> The obvious higher HER activity is due to the synergistic effect between  $W^{6+}$  and  $Ni^{2+}$  ions and the presence of  $NiOOH$  within the heterostructure. The presence of  $Ni(OH)_2$  facilitates water splitting to produce the Volmer step,  $W_{0.1}Ni(OH)_2/NiOOH[H_{ads} + OH^-]$ . In the heterostructure, the existence of  $Ni(OH)_2$  ( $d^8$  system) and  $NiOOH$  ( $d^7$  system, more unfilled d-orbital's) species increases the superior adsorption followed by desorption of  $OH^-$  ions and also favors water splitting, generation of Heyrovsky step. Further,  $W^{6+}$  doping ( $d^0$  system) distinctly promotes water dissociation reaction and expedites the adsorption of atomic hydrogen, leading to the formation of  $H_2$  molecules. Therefore,  $W_{0.1}Ni(OH)_2/NiOOH$  follows the fastest HER kinetics, and the process is conquered by the Volmer-Heyrovsky path. Similar phenomena of higher electrocatalytic activity after doping (single W atom doping in  $\alpha-Ni(OH)_2$ ) are reported by Yan and co-workers.<sup>21</sup> Based on DFT calculation, they have explained W itself can behave as an active site for water splitting reaction and having exothermic steps of water splitting. Wang and co-workers<sup>39</sup> developed W doped  $NiO/NiS_2$  heterostructure for overall water splitting reaction. They have shown that the W site is superior for hydrogen adsorption, whereas, the Ni site favors the water dissociation process. This mutual interaction between W and Ni sites further enhanced the HER reaction kinetics. Jin and co-workers<sup>44</sup> reported W-doped cobalt carbonate hydroxide (CCH) for electrocatalytic water splitting. Using the DFT study they have observed that the low-level W doping in CCH induced electron density near the Fermi level, which enhanced the charge transfer and active sites for intermediate adsorption.

The higher HER activity of  $W_{0.1}Ni(OH)_2/NiOOH$  is further verified by Electrochemical impedance spectroscopy (EIS) analysis. For all the developed electrocatalysts respective onset potentials are used to calculate the EIS and the corresponding Nyquist plot is shown (Figure 4.12b). An equivalent circuit was drawn with  $W_{0.1}Ni(OH)_2/NiOOH$  using all the experimental values. All the recorded values are listed in Table 4.3. It is reported in Table 4.3 that bare  $Ni(OH)_2/NiOOH$  shows the value of  $R_S$  and  $R_{CT}$  are  $10.25 \Omega$  and  $26.26 \Omega$ , respectively. Whereas, the value of  $R_S$  and  $R_{CT}$  are  $9.46 \Omega$  and  $16.26 \Omega$  for  $W_{0.1}Ni(OH)_2/NiOOH$ , which is the lowest than  $W_{0.2}Ni(OH)_2/NiOOH$  and  $W_{0.06}Ni(OH)_2/NiOOH$ . Therefore, the lowest value of  $R_{CT}$  for  $W_{0.1}Ni(OH)_2/NiOOH$  indicates higher electronic conductivity. After doping with W the charge transport efficiency increases, enduring more electron transfer and interactions, which further

increases HER performance. The plausible reasons for higher conductivity of  $W_{0.1}Ni(OH)_2/NiOOH$  heterostructure can be demonstrated by the presence of  $W^{6+}$  ions in the lattice, which creates tensile strain in the lattice structure (PXRD and Raman analyses) and close contact between the electrolyte and catalyst. Furthermore, the vertically grown nanosheet structure of the doped sample increases the interfacial structure and thus allows faster diffusion of reactant. The long-term stability of the developed catalyst is very important for an efficient and durable electrocatalyst. To check the stability of  $W_{0.1}Ni(OH)_2/NiOOH$ , the consecutive 1000 cycles are carried out in KOH solution (Figure 4.12c). It is observed that after 1000 cycles there is no change in the value of onset potential and current density, so the developed catalyst is highly stable for HER in an alkaline medium. Apart from 1000 cycle stability, chronoamperometry is also checked for long-term stability with a current density of  $160 \text{ mA/cm}^2$ . Figure 4.12d represents the unaltered current density for  $W_{0.1}Ni(OH)_2/NiOOH$ , which is stable for up to 5 days.

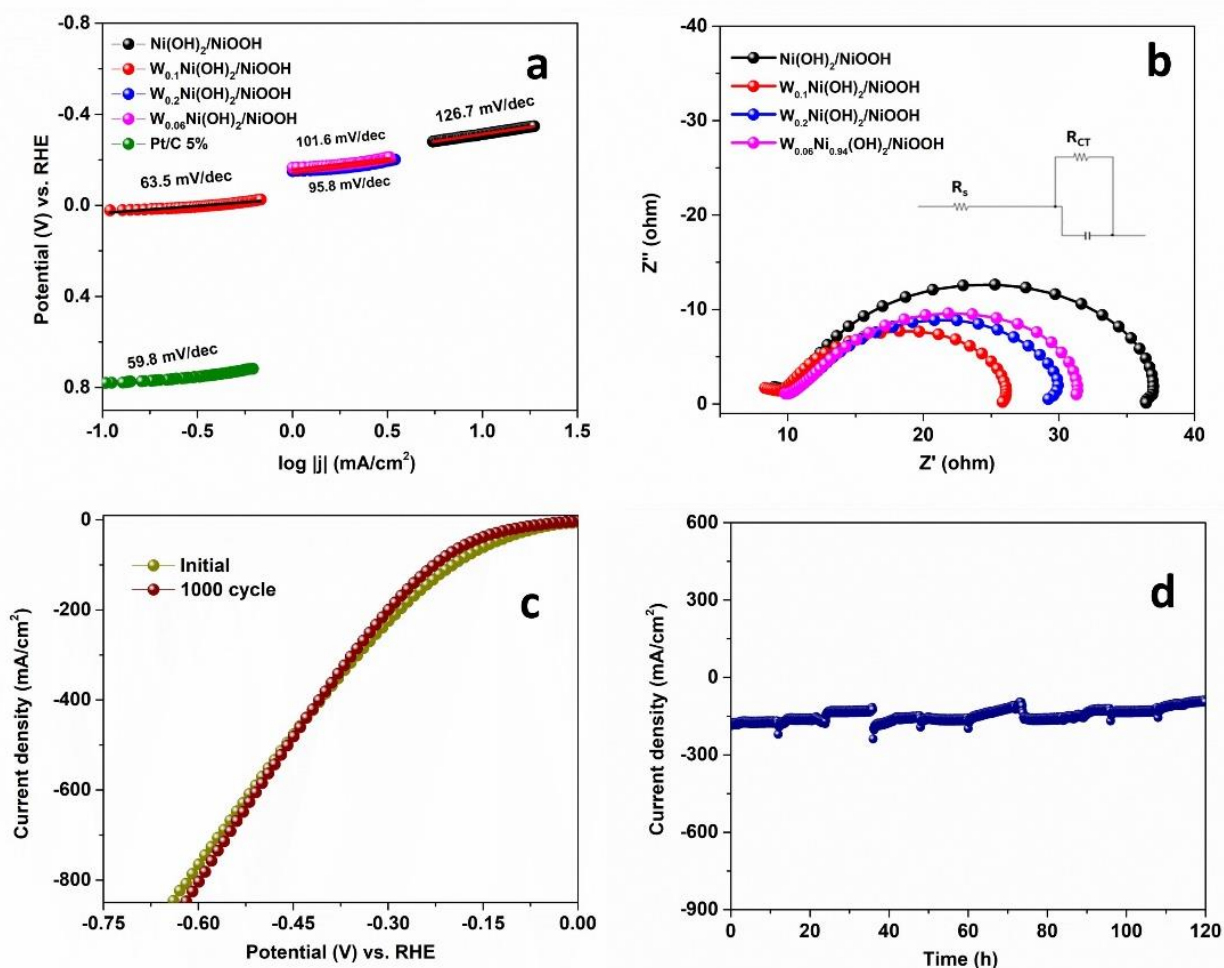


**Figure 4.12:** (a) Tafel plot and (b) Nyquist plots of  $\text{Ni}(\text{OH})_2/\text{NiOOH}$ ,  $\text{W}_{0.1}\text{Ni}(\text{OH})_2/\text{NiOOH}$ ,  $\text{W}_{0.2}\text{Ni}(\text{OH})_2/\text{NiOOH}$ , and  $\text{W}_{0.06}\text{Ni}(\text{OH})_2/\text{NiOOH}$  materials. The inset of Figure (b) shows the corresponding equivalent circuit. (c) Polarization HER curve of  $\text{W}_{0.1}\text{Ni}(\text{OH})_2/\text{NiOOH}$  electrocatalyst for initial, and after 1000 cycles. (d) chronoamperometric data recorded for 120 hours at a fixed potential for HER. All the data are recorded using a 1.0 M KOH solution.

#### 4.3.4.2 Oxygen evolution reaction (OER) study

Similar to HER, W doped  $\text{Ni}(\text{OH})_2/\text{NiOOH}$  is also used for OER in an alkaline medium. The OER activity is performed with bare, doped, and standard  $\text{RuO}_2$  electrocatalyst. The LSV measurement is accomplished at a scan rate of  $2 \text{ mVs}^{-1}$  in 1.0 M KOH solution for all the samples. Figures 4.13a and b represent LSV plots of all the doped and bare samples along with bare CC. The onset potential of  $\text{Ni}(\text{OH})_2/\text{NiOOH}$  is 1.57 V vs. RHE to generate  $50 \text{ mA/cm}^2$  current density,

while,  $W_{0.1}Ni(OH)_2/NiOOH$  shows an onset potential of 1.52 V *vs.* RHE. To compare with other W doped samples,  $W_{0.2}Ni(OH)_2/NiOOH$ , and  $W_{0.06}Ni(OH)_2/NiOOH$  electrocatalyst exhibits an onset potential of 1.53 V and 1.54 V *vs.* RHE, respectively for 50 mA/cm<sup>2</sup> current density generation. Commercial  $RuO_2$  catalyst is having an onset potential of 1.61 V *vs.* RHE. Bare CC has no contribution within this potential window. The overpotential value for  $Ni(OH)_2/NiOOH$  and  $W_{0.1}Ni(OH)_2/NiOOH$  represents 340 mV and 293 mV, respectively to obtain the current density of 50 mA/cm<sup>2</sup>. On the other hand,  $W_{0.2}Ni(OH)_2/NiOOH$ , and  $W_{0.06}Ni(OH)_2/NiOOH$  show an overpotential of 300 and 314 mV to generate 50 mA/cm<sup>2</sup> current density. After incorporation of W in  $Ni(OH)_2/NiOOH$  structure a reduction of overpotential occurs for the same current density generation but the maximum reduction of ~ 47 mV in case of optimized  $W_{0.1}Ni(OH)_2/NiOOH$  sample. Therefore,  $W_{0.1}Ni(OH)_2/NiOOH$  exhibits superior OER performance and a cathodic shift in onset and overpotential than the other electrocatalyst. During LSV analysis (Figures 4.13 a and b), all the  $Ni(OH)_2/NiOOH$  samples exhibited an obvious peak at a potential window of 1.35 - 1.46 V *vs.* RHE for the conversion of  $Ni^{2+}$  to  $Ni^{3+}/Ni^{4+}$  species. Additionally, the peak intensity is maximum in W doped samples, which represents the electron pulling effect of  $W^{6+}$  ion (XPS analysis) for the conversion of  $Ni^{2+}$  to  $Ni^{3+}/Ni^{4+}$  during OER. Figures 4.13c and d show the plot between onset potential (V) *vs.* RHE and current density generated at 1.8 V *vs.* RHE potential and histogram plot of all the developed electrocatalyst, which signifies  $W_{0.1}Ni(OH)_2/NiOOH$  is the best OER active catalyst than others.

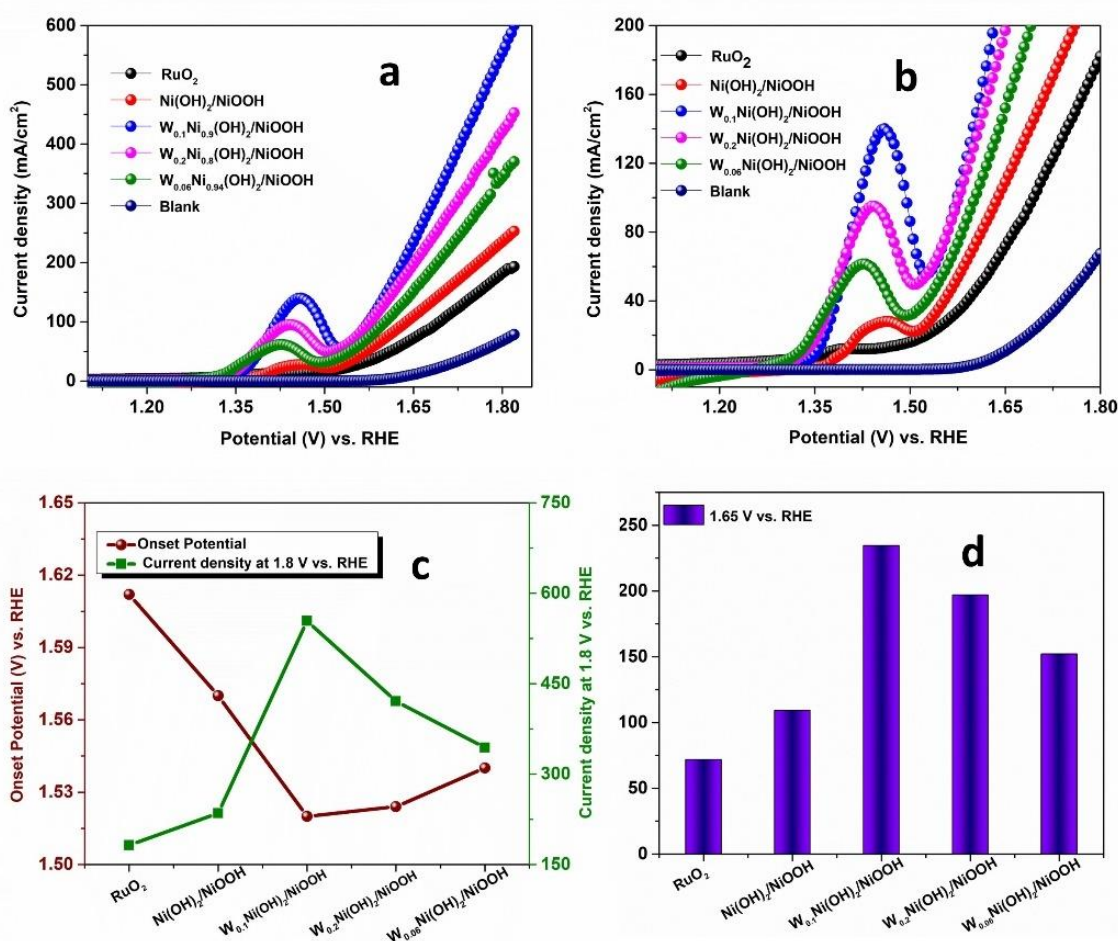


**Figure 4.13:** Polarization OER curve at (a) low scale and (b) high scale. (c) The plot of current density obtained at 1.8 V vs. RHE and onset potential (V) vs. RHE (d) histogram plot of current density obtained at 1.65 V vs. RHE of Ni(OH)<sub>2</sub>/NiOOH, W<sub>0.1</sub>Ni(OH)<sub>2</sub>/NiOOH, W<sub>0.2</sub>Ni(OH)<sub>2</sub>/NiOOH, W<sub>0.06</sub>Ni(OH)<sub>2</sub>/NiOOH, and RuO<sub>2</sub> samples.

To further recognize the betterment in the electrocatalytic activity of doped and bare samples few parameters like mass activity is analyzed in alkaline solution.<sup>18, 45</sup> The mass activity of all the materials is calculated at a particular potential of 1.65 V vs. RHE (mass loading is 0.624 mg and area is 0.16 cm<sup>2</sup>). The obtained mass activity for Ni(OH)<sub>2</sub>/NiOOH and W<sub>0.1</sub>Ni(OH)<sub>2</sub>/NiOOH samples are 18.9 A/g and 60.12 A/g, respectively. Whereas, the mass activity value for W<sub>0.2</sub>Ni(OH)<sub>2</sub>/NiOOH, W<sub>0.06</sub>Ni(OH)<sub>2</sub>/NiOOH, and RuO<sub>2</sub> are calculated as 50.53 A/g, 38.98 A/g, and 18.9 A/g, respectively. After doping with W the mass activity value increases

and the maximum value is represented by  $W_{0.1}Ni(OH)_2/NiOOH$ . With the enhancement in mass activity, the oxygen evolution reaction also reflects higher efficiency. So, W doping increases the active sites within the catalyst and helps in electron transfer as well as electronic interaction in the electrode-electrolyte interfaces. The higher OER activity of  $W_{0.1}Ni(OH)_2/NiOOH$  structure is mainly due to a strong synergistic effect between  $W^{6+}$  and  $Ni^{2+}$  ions in the lattice structure, well corroborated with PXRD and XPS results. Moreover, vertically grown nanosheet structures provide a more electrochemically active surface area (FESEM and TEM analyses). All the determined electrochemical values (ECSA,  $R_f$ , and mass activity) are tabulated in Table 4.4.

**Table 4.4:** All the electrochemical OER parameters for  $Ni(OH)_2/NiOOH$ ,  $W_{0.1}Ni(OH)_2/NiOOH$ ,  $W_{0.2}Ni(OH)_2/NiOOH$ ,  $W_{0.06}Ni(OH)_2/NiOOH$ , and  $RuO_2$  electrocatalysts.

Electrodes	Potential (V) vs. RHE ) required to generate 50 mA/cm <sup>2</sup>	Mass Activity (A/g) at 1.65 V vs. RHE	Tafel Slope (mV/decade)	$R_s$ ( $\Omega$ )	$R_{CT}$ ( $\Omega$ )
$Ni(OH)_2/NiOOH$	1.57	27.97	75.4	12.04	37.65
$W_{0.1}Ni(OH)_2/NiOOH$	1.523	60.12	48.2	10.51	11.3
$W_{0.2}Ni(OH)_2/NiOOH$	1.53	50.53	68.1	11.64	21.99
$W_{0.06}Ni(OH)_2/NiOOH$	1.544	38.98	68.9	11.59	30.61
$RuO_2$	1.612	18.9	84.1	-	-

The exact role of W dopant in  $Ni(OH)_2/NiOOH$  system during OER is verified with the help of CV analysis, which is recorded in alkaline medium (1.0 M KOH) and 10 mV/s scan rate. Figure 4.14 exhibits the CV analysis of  $Ni(OH)_2/NiOOH$ ,  $W_{0.1}Ni(OH)_2/NiOOH$ ,  $W_{0.2}Ni(OH)_2/NiOOH$ , and  $W_{0.06}Ni(OH)_2/NiOOH$  electrodes. Both bare and doped samples show redox (oxidation & reduction) peaks due to simultaneous conversion between  $Ni^{2+} \rightleftharpoons Ni^{3+}$  system of  $Ni(OH)_2$  and  $NiOOH$ , respectively.<sup>18, 21</sup> In the case of the  $Ni(OH)_2/NiOOH$  sample, the oxidation peak appears at 1.42 V and reduction at 1.25 V vs. RHE. Whereas,  $W_{0.1}Ni(OH)_2/NiOOH$  shows the oxidation and reduction peak at 1.49 and 1.13 V vs. RHE for  $Ni^{2+}/Ni^{3+}$  couple. The other W doped samples,  $W_{0.2}Ni(OH)_2/NiOOH$ , and  $W_{0.06}Ni(OH)_2/NiOOH$  also exhibit the oxidation and



reduction peaks at 1.44, 1.50 V and 1.16, 1.17 V vs. RHE, respectively. Therefore, in the doped sample, the oxidation peak suffers an anodic shift, which is due to the doping of the  $W^{6+}$  ion. The electron pulling nature of the  $W^{6+}$  ion (strong Lewis acid) withdraws electrons from the neighbouring ion  $Ni^{2+}$ , which results in positive peak shifting and increases the amount of  $Ni^{3+}$  ion in the system. It can be seen from Figure 4.14 that for  $W_{0.1}Ni(OH)_2/NiOOH$  sample the area under the curve is steeper than  $Ni(OH)_2/NiOOH$ , which represents the formation of more  $Ni^{3+}$  species, an active species in OER. So, W doped sample consists of more  $Ni^{3+}$  ion i.e.,  $NiOOH$ , and generate more electroactive sites for oxygen evolution reaction. The number of generated electroactive species is more in the case of the  $W_{0.1}Ni(OH)_2/NiOOH$  structure as the area under the curve (anodic and cathodic) is high than other W doped electrocatalyst,  $W_{0.2}Ni(OH)_2/NiOOH$ , and  $W_{0.06}Ni(OH)_2/NiOOH$ . This CV analysis result is well-matched with XPS analysis and further confirms the presence of  $W^{6+}$  ion which facilitates the formation of more active  $Ni^{3+}$  ions in the system. Basu and co-workers also reported a similar anodic peak shift of  $Ni^{2+}/Ni^{3+}$  couple while doped with  $Fe^{3+}$  ion in  $Ni(OH)_2/NiOOH$  structure.<sup>18</sup>

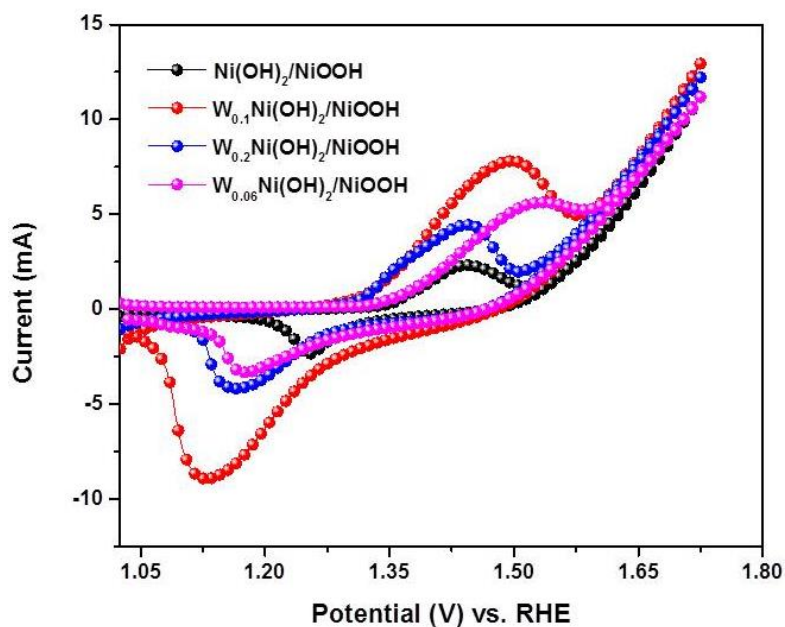
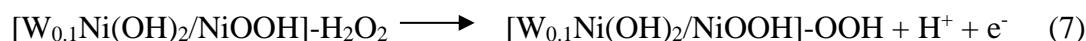
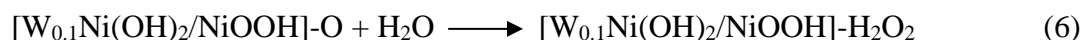
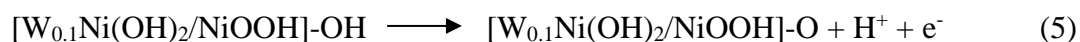
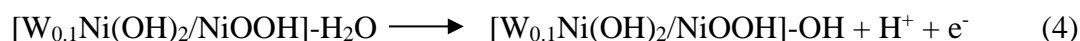


**Figure 4.14.** CV analysis of  $Ni(OH)_2/NiOOH$ ,  $W_{0.1}Ni(OH)_2/NiOOH$ ,  $W_{0.2}Ni(OH)_2/NiOOH$ , and  $W_{0.06}Ni(OH)_2/NiOOH$  electrocatalysts.

To further verify the superior activity of  $W^{6+}$  doped  $Ni(OH)_2/NiOOH$ , the OER mechanism, and reaction kinetics the calculation of Tafel slope is important. The Tafel slope values of

Ni(OH)<sub>2</sub>/NiOOH, W<sub>0.1</sub>Ni(OH)<sub>2</sub>/NiOOH, W<sub>0.2</sub>Ni(OH)<sub>2</sub>/NiOOH, W<sub>0.06</sub>Ni(OH)<sub>2</sub>/NiOOH, and RuO<sub>2</sub> are 75.4, 48.2, 68.1, 68.9, and 84.1 mVdec<sup>-1</sup>, respectively (Figure 4.15a). Commercial RuO<sub>2</sub> is having the highest value of Tafel slope and represents slower OER kinetics compared to other developed W doped catalysts. W<sub>0.1</sub>Ni(OH)<sub>2</sub>/NiOOH is having the lowest value of the Tafel slope that indicates higher electrocatalytic activity due to faster electrode kinetics. Based on the reported literature the OER reaction mechanism consists of the following steps in an alkaline medium.<sup>46</sup>



In the above reactions, step 3 represents the surface adsorption of the water molecule. Steps 4 and 5 proceeds via the deprotonation step. Step 6 exhibits further adsorption of a water molecule on the pre-adsorbed O radical results O-O coupling and adsorbed OOH on the surface-active site (step 7). The O-O coupling formation prefers the low-spin sites as Ni<sup>3+</sup> (d<sup>7</sup> system), W<sup>6+</sup> (d<sup>0</sup> system) ions rather than Ni<sup>2+</sup> (d<sup>8</sup> configuration). Therefore, W<sub>0.1</sub>Ni(OH)<sub>2</sub>/NiOOH electrocatalyst produced more surface electroactive sites for OER. In the final step (step 8), deprotonation of [W<sub>0.1</sub>Ni(OH)<sub>2</sub>/NiOOH]-OOH results in the removal of the O<sub>2</sub> molecule, and the catalyst (surface active site) remain free for further reaction. Yan and co-workers<sup>21</sup> also reported the similar phenomena, the stabilization of O-O coupling occurs more on the low spin state of the W atom than the high spin state of atomic Ni.

Further to judge the higher electrochemical activity of the doped sample, EIS analysis is performed in alkaline electrolytes. The charge transfer nature and electronic property are examined by impedance spectra and the corresponding Nyquist plot is shown in Figure 4.15b. Using all the experimental values for W<sub>0.1</sub>Ni(OH)<sub>2</sub>/NiOOH electrocatalyst an equivalent circuit is drawn. The value of R<sub>S</sub> and R<sub>CT</sub> for Ni(OH)<sub>2</sub>/NiOOH are 12.04 Ω and 37.65 Ω, respectively. After doping, in the case of W<sub>0.1</sub>Ni(OH)<sub>2</sub>/NiOOH, the values of R<sub>S</sub> and R<sub>CT</sub> are 10.51 Ω and 11.3 Ω, respectively, which is the lowest compared to other catalysts. Therefore, W<sub>0.1</sub>Ni(OH)<sub>2</sub>/NiOOH shows the

firmest electron transfer kinetics and higher conductivity due to the lower value of charge transfer resistance.<sup>22</sup> It is noteworthy that incorporation of  $W^{6+}$  dopant creates tensile strain in the lattice, which affects the local electronic structure and increases the adsorption of oxygenated species, thereby improving intrinsic activity of  $W_{0.1}Ni(OH)_2/NiOOH$  materials.

Apart from efficient electrocatalytic activity, stability is also very important to achieve an effective water-splitting reaction. The stability of  $W_{0.1}Ni(OH)_2/NiOOH$  is observed by applying consecutive 1000 LSV cycles (Figure 4.15c). After 1000 cycle, there is no variation in onset potential as well as current density, which prove the robust nature of  $W_{0.1}Ni(OH)_2/NiOOH$ . Long-term stability is also checked for continuously 5 days with the chronoamperometry technique at the potential of 1.56 V vs. RHE. and 140 mA/cm<sup>2</sup> current density. During the chronoamperometry analysis at a fixed potential, the current density remains unchanged and further confirmed that the electrocatalyst,  $W_{0.1}Ni(OH)_2/NiOOH$  is highly stable and robust for OER (Figure 4.15d).

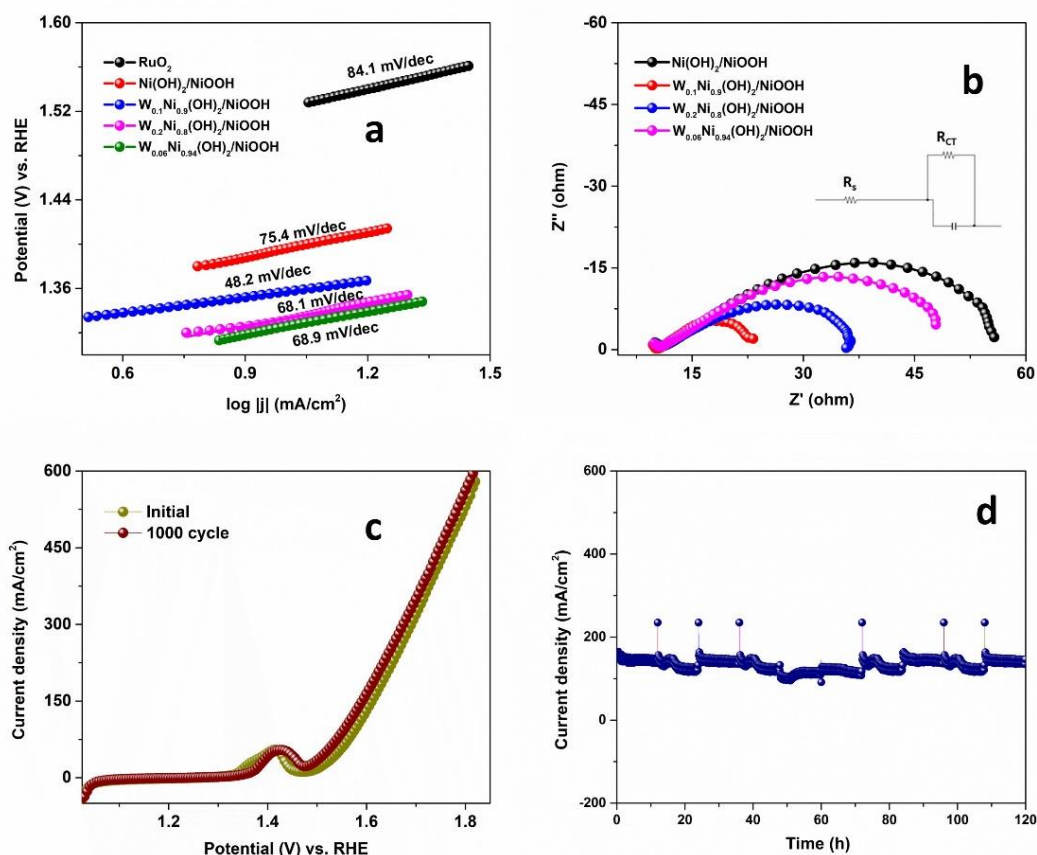


**Figure 4.15:** (a) Tafel plot, and (b) Nyquist plots of  $Ni(OH)_2/NiOOH$ ,  $W_{0.1}Ni(OH)_2/NiOOH$ ,  $W_{0.2}Ni(OH)_2/NiOOH$ , and  $W_{0.06}Ni(OH)_2/NiOOH$  electrocatalysts. The corresponding equivalent

circuit is shown in the inset of Figure (b). (c) Polarization OER curve of  $W_{0.1}Ni(OH)_2/NiOOH$  electrocatalyst for initial, and after 1000 cycles. (d) Chronoamperometric data were recorded for 120 hours at a fixed potential for OER. All the data are recorded using a 1.0 M KOH solution.

#### 4.3.4.3 Two electrode system

Inspired from efficient HER and OER activity, similar electrode system is used in two electrode system with best optimized ratio of  $W_{0.1}Ni(OH)_2/NiOOH$  in an alkaline medium. Figure 4.16a demonstrates the LSV curves of assembled  $W_{0.1}Ni(OH)_2/NiOOH$  (+) ||  $W_{0.1}Ni(OH)_2/NiOOH$  (-) cells, which show onset cell voltage of 1.62 V in 1 M KOH. The chronoamperometric stability of cell,  $W_{0.1}Ni(OH)_2/NiOOH$  (+) ||  $W_{0.1}Ni(OH)_2/NiOOH$  (-) is also checked for 12-hour at a fixed potential of 1.65 V *vs.* RHE in alkaline medium, shown in Figure 4.16b. The developed cell,  $W_{0.1}Ni(OH)_2/NiOOH$  (+) ||  $W_{0.1}Ni(OH)_2/NiOOH$  (-) exhibits good stability for overall water splitting reaction.

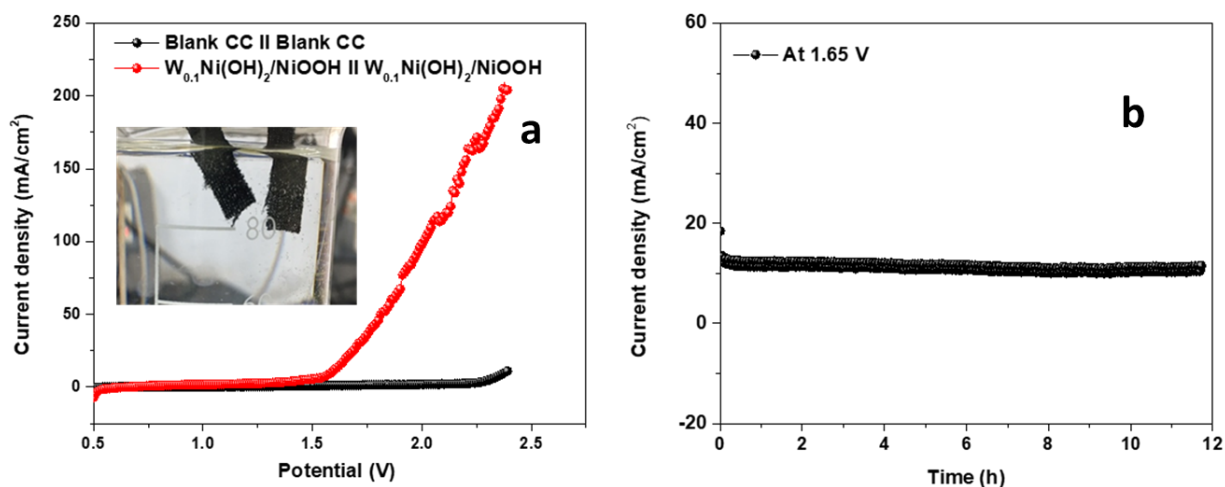


**Figure 4.16:** (a) Two electrode system activity with  $W_{0.1}Ni(OH)_2/NiOOH$  (+) ||  $W_{0.1}Ni(OH)_2/NiOOH$  (-) cell (b) chronoamperometric stability of 12 hours in 1 M KOH. Inset in Figure a is digital image of  $W_{0.1}Ni(OH)_2/NiOOH$  (+) ||  $W_{0.1}Ni(OH)_2/NiOOH$  (-) cell.

#### 4.3.4.4 Post electrocatalytic study

To verify the morphology after prolonged electrochemical study in alkaline medium FESEM analysis is performed and shown in Figure 4.17a. It is clear from Figure 4.17a that there is no noticeable change in the morphology of vertically grown nanosheet structure with a thick edge of  $W_{0.1}Ni(OH)_2/NiOOH$ . Therefore, the durability and robustness of W doped  $Ni(OH)_2/NiOOH$  structure is maintained throughout the electrochemical study. After electrocatalysis, the uniform distribution of all the elements (W, Ni, and O) is further confirmed by EDS mapping analysis (Figure 4.17b). The XPS of the  $W_{0.1}Ni(OH)_2/NiOOH$  sample is performed after electrocatalysis to check the composition and oxidation state of the elements (Figure 4.18). The deconvoluted spectra of Ni 2p shows doublet peak at binding energy values of 856.1 eV ( $2p_{3/2}$ ), and 873.8 eV ( $2p_{1/2}$ ) for the presence of  $Ni^{2+}$  ion and 857.5 eV ( $2p_{3/2}$ ) and 875.4 eV ( $2p_{1/2}$ ) for  $Ni^{3+}$  species. The binding energy values of O 1s show the peak at 532.2 eV and 534.1 eV for  $O^{2-}$  and adsorbed hydroxide. The W 4f deconvoluted spectra show peaks at 35.8 eV ( $4f_{7/2}$ ) and 38.2 eV ( $4f_{5/2}$ ), confirming the presence of  $W^{6+}$  ion. Thus, the composition and oxidation state of all the elements in the electrocatalyst remain unchanged after the water-splitting reaction in an alkaline medium.

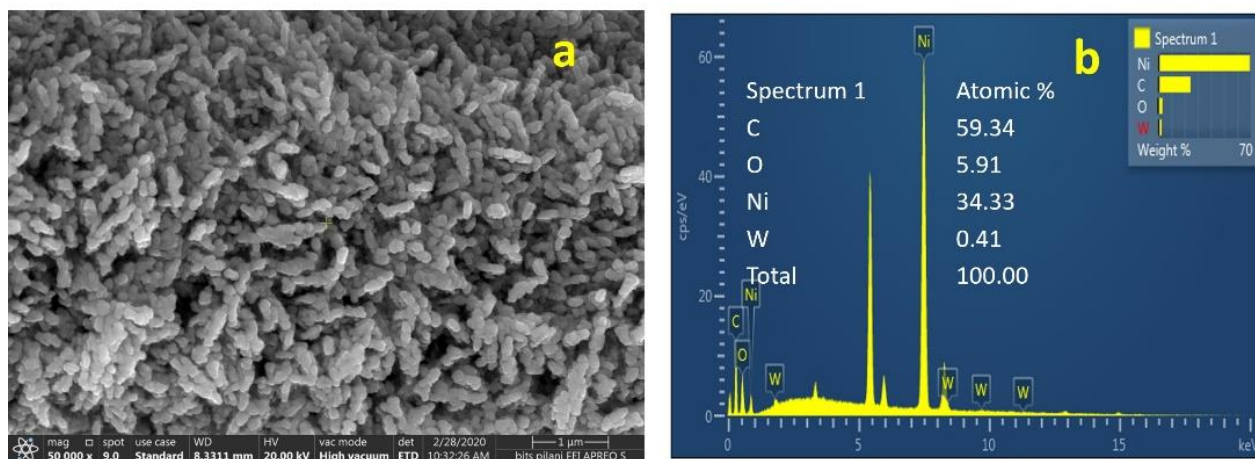


**Figure 4.17:** (a) FESEM analysis (b) EDS spectra of  $W_{0.1}Ni(OH)_2/NiOOH$  post electrolysis.

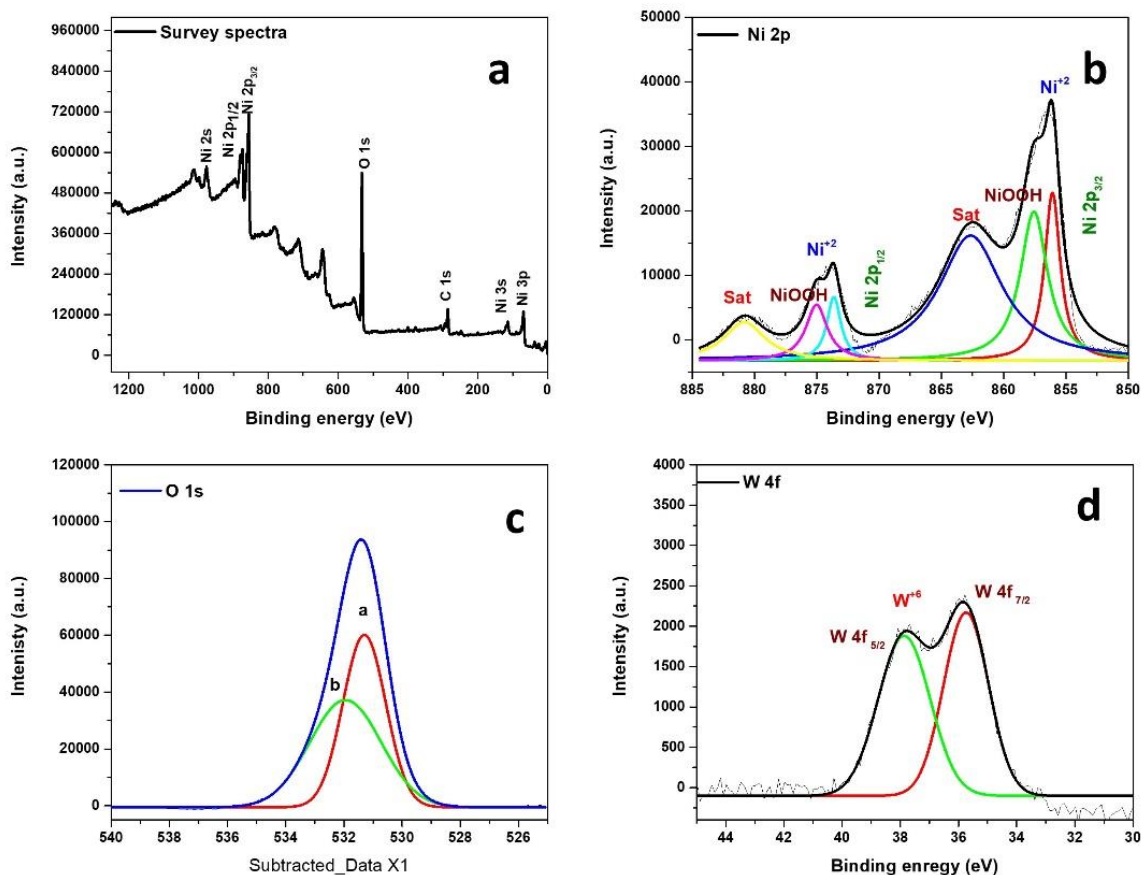


**Figure 4.18:** XPS of  $W_{0.1}Ni(OH)_2/NiOOH$  after OER electrolysis (a) survey spectrum, (b) deconvoluted spectra of Ni 2p and (c) deconvoluted spectra of O 1s (d) deconvoluted spectra of W.

#### 4.3.4.5 Comparative study

All the above results prove that after doping with W, the electrocatalyst shows better HER and OER performance. Out of all the variations, 0.329 gm of  $Na_2WO_4$  (1.0 mM) in  $W_{0.1}Ni(OH)_2/NiOOH$  material exhibit the best activity in both HER and OER, a proven electrocatalyst for electrochemical water splitting reaction. Doping is an important strategy to enhance the overall electrocatalytic activity for water-splitting reactions. Therefore, a few important points have emerged regarding the highest efficiency of  $W_{0.1}Ni(OH)_2/NiOOH$  electrocatalyst for HER and OER. First, PXRD and Raman analysis confirm that dopant



incorporation causes tensile strain in the lattice, which affects the electronic environment within the lattice. Second, W doping can generate more catalytically active sites, which is due to the formation of nanosheet structures. Third, direct growth of W doped interconnected nanosheet morphology on a conducting carbon cloth substrate allows interfacial electron transfer between the electrode surface and the catalyst and increases the dispersion of the sheet-like structure, which facilitates the electrocatalytic activity. Fourth, after W doping the electrocatalyst is much more durable with high conductivity resulting in a faster reaction rate. Fifth, W dopant has a unique role in modulating the electronic structure and surface chemical property of the catalyst. Sixth, the synergistic effect between the dopant (W) and the metal center ( $\text{Ni}^{2+}$ ) plays an important role during the electrocatalytic reaction. Seventh, low spin  $\text{W}^{6+}$  ( $d^0$  system) stabilized oxygen unpaired electron and facilitated O-O coupling during OER. An overall comparative table using another doped sample for HER and OER is shown in Table 4.5.

**Table 4.5:** A comparative study of all the electrochemical parameters with the  $\text{W}_{0.1}\text{Ni}(\text{OH})_2/\text{NiOOH}$  electrocatalyst.

S.N.	Electrocatalyst	Electrode reaction	Electrolyte	Potential (mV vs. RHE) at 10 mA/cm <sup>2</sup> Current density	Tafel slope	Substrate	Ref.
1.	$\text{Fe}_{0.06}\text{Ni}_{0.94}(\text{OH})_2/\text{NiOOH}$	OER	1 M KOH	220 mV	48	CC	18
2.	P doped $\text{Ni}(\text{OH})_2/\text{NiMoO}_4$	OER & HER	1 M KOH	1.55 V & 60 mV	130	Ni foam	40
3.	W-doped $\alpha\text{-Ni}(\text{OH})_2$	OER	1 M KOH	237 mV	33	GCE	21
4.	Fe doped $\text{Ni}(\text{OH})_2$	OER	1 M KOH	220 mV	48.3	Ni foam	19
5.	NiFe LDH@NiCoP	OER & HER	1 M KOH	220 & 120 mV	48.6 & 88.2	Ni foam	12
6.	5 wt% W-CCH/PCCH	OER & HER	1 M KOH	318 & 106 mV	65.7 & 59	CC	44
7.	W,Fe- $\text{Ni}(\text{OH})_2$	OER	1 M KOH	205 mV	60	CC	24
8.	$\text{W}_{0.1}\text{Ni}(\text{OH})_2/\text{NiOOH}$	OER & HER	1 M KOH	293 mV (@ 50mA/cm <sup>2</sup> current density) & 56 mV	48.2 & 63.5	Carbon cloth	This work

## 4.3.5 Theoretical studies

To verify the higher electrocatalytic performance of  $W_{0.1}Ni(OH)_2/NiOOH$  electrocatalyst Density Functional Theory calculations are performed to determine the hydrogen adsorption energy. In addition, the d band center for the bare and doped sample is also analyzed by a density of states (DOS) calculation. For this calculation,  $\beta$ -NiOOH is used as a bare substrate and W doped surface is modeled by replacing one Ni surface atom with W. The  $\beta$ -NiOOH and W doped  $\beta$ -NiOOH surface is shown in Figure 4.19.  $\Delta G_H$  (Gibbs free energy of adsorption of H) is considered to be an excellent indicator of HER activity.<sup>38, 47-48</sup> A value of  $\Delta G_H$  closer to zero suggests ease of H adsorption and release.  $\Delta G_H$  was calculated to be 1.4 eV on the surface Ni atom of a bare  $\beta$ -NiOOH surface (Figure 4.19c). In the presence of a nearby W, the  $\Delta G_H$  on a surface Ni increased to 1.27 eV, suggesting an enhanced HER activity (Figure 4.19d). The difference in adsorption behavior of H on the doped  $\beta$ -NiOOH surface can be further explained by a density of states analysis projected on the surface Ni atom (Figure 4.20). The d band center of the surface Ni atom relative to the Fermi level shifts from -4.35 eV for a  $\beta$ -NiOOH surface to -3.65 eV for the W doped  $\beta$ -NiOOH surface (where Ni is adjacent to the W). According to d band theory<sup>49-50</sup>, a higher d band center (closer to Fermi level) indicates stronger binding energy of adsorbates to the surface due to a lower occupancy of the anti-bonding orbital's. Li and co-workers<sup>51</sup> also reported a similar trend in bare  $Ni(OH)_2$  and Cu doped  $Ni(OH)_2$  during DOS calculations, where, d-band center values are -1.70 eV and -1.38 eV for bare and doped samples, respectively. A Bader charge analysis revealed a decrease in charge of  $0.06 e^-$  on the surface Ni atom adjacent to W, in agreement with the electron-withdrawing nature of W, which is in agreement with XPS analysis.

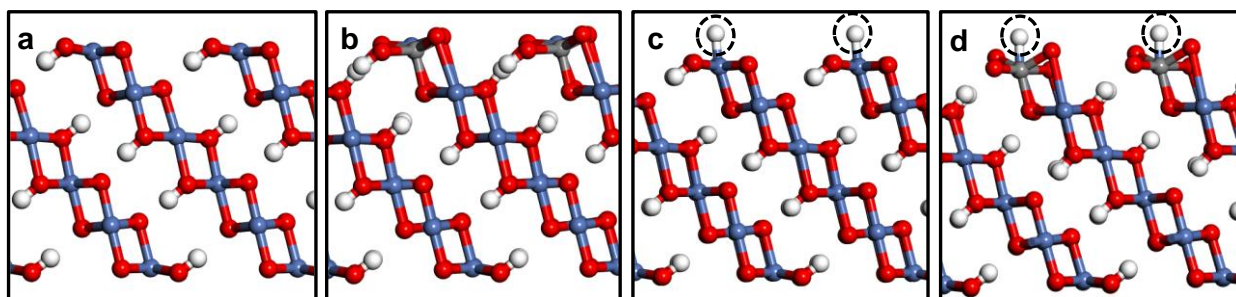


**Figure 4.19:** H adsorption on the NiOOH surface. (a)  $\beta$ -NiOOH (015) surface; (b) W doped  $\beta$ -NiOOH (015) surface; (c-d) H adsorbed (indicated by dotted line) at a surface Ni of  $\beta$ -NiOOH (015) and W doped  $\beta$ -NiOOH (015) surface. The Ni atoms are in blue, W in gray, O in red, and H in white.



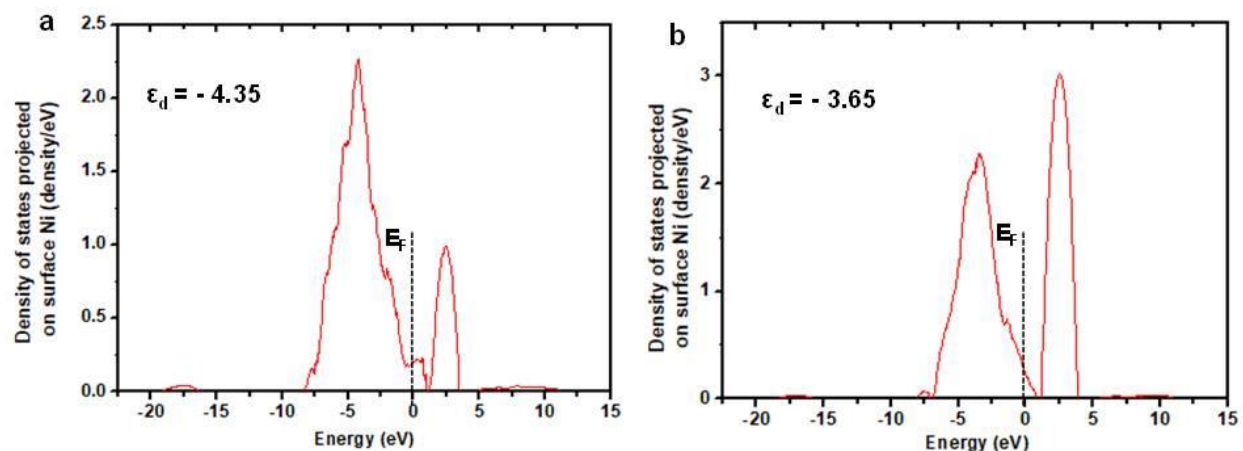


**Figure 4.20:** Density of states projected on the d-band for the surface Ni site. a)  $\beta$ -NiOOH (015) surface; b) W doped  $\beta$ -NiOOH (015) surface. The d band centres (in eV) are indicated with respect to the Fermi level ( $E_F$ ).

## 4.4 Conclusion

In summary, we have developed a simple and facile method to synthesize W doped Ni(OH)<sub>2</sub>/NiOOH nanosheet with ratio variation of W:Ni as an efficient bifunctional electrocatalyst. Electrodeposition followed by the hydrothermal method is tracked for the development of W doped sample. PXRD, XPS, FESEM, and TEM along with other techniques are used to confirm the purity, composition, morphology, etc. for the doped and undoped samples. Vertically grown nanosheet morphology of W<sub>0.1</sub>Ni(OH)<sub>2</sub>/NiOOH is highly active towards HER and OER in an alkaline medium. The developed electrocatalyst (W<sub>0.1</sub>Ni(OH)<sub>2</sub>/NiOOH) is durable for 120 hours in an alkaline medium. Doping with W<sup>6+</sup> ion in Ni(OH)<sub>2</sub>/NiOOH structure can change the electronic environment and conductivity within the electrocatalyst. The synergistic effect between W<sup>6+</sup> and Ni<sup>2+</sup> ions play a vital role to enhance the active surface area and electrocatalytic activities. A Bader charge analysis is followed to confirm the electron pulling effect of W<sup>6+</sup> ion in W<sub>0.1</sub>Ni(OH)<sub>2</sub>/NiOOH. Moreover, low spin W<sup>6+</sup> (d<sup>0</sup> system) ion in W<sub>0.1</sub>Ni(OH)<sub>2</sub>/NiOOH facilitates O-O coupling and H<sub>2</sub> molecule formation during OER and HER, respectively. The presence of W promotes H adsorption and release, by shifting the free energy of adsorption towards the optimum value of  $G_H = 0$ . All these results prove the simple strategy to develop W doped Ni(OH)<sub>2</sub>/NiOOH, a non-expensive, efficient, and ultra-stable electrocatalyst for

water splitting reaction. It is still very important and challenging to produce a non-precious metal electrocatalyst with similar activity to noble metal catalysts.

### 4.5 References

1. Turner, J. A. A realizable renewable energy future. *Science* **1999**, 285 (5428), 687-689,.
2. Hall, D. Electrodes for alkaline water electrolysis. *J. Electrochem. Soc.* **1981**, 128 (4), 740-747.
3. Fominykh, K.; Chernev, P.; Zaharieva, I.; Sicklinger, J.; Stefanic, G.; Döblinger, M.; Müller, A.; Pokharel, A.; Böcklein, S.; Scheu, C.; Bein, T.; Fattakhova-Rohlfing, D. Iron-Doped Nickel Oxide Nanocrystals as Highly Efficient Electrocatalysts for Alkaline Water Splitting. *ACS Nano* **2015**, 9 (5), 5180-5188.
4. Ullah, N.; Zhao, W.; Lu, X.; Oluigbo, C. J.; Shah, S. A.; Zhang, M.; Xie, J.; Xu, Y. In situ growth of M-MO (M= Ni, Co) in 3D graphene as a competent bifunctional electrocatalyst for OER and HER. *Electrochim. Acta* **2019**, 298, 163-171.
5. Montoya, J. H.; Garcia-Mota, M.; Nørskov, J. K.; Vojvodic, A. Theoretical evaluation of the surface electrochemistry of perovskites with promising photon absorption properties for solar water splitting. *Phys. Chem. Chem. Phys.* **2015**, 17 (4), 2634-2640.
6. Sharma, M. D.; Mahala, C.; Basu, M. 2D Thin Sheet Heterostructures of MoS<sub>2</sub> on MoSe<sub>2</sub> as Efficient Electrocatalyst for Hydrogen Evolution Reaction in Wide pH Range. *Inorg. Chem.* **2020**, 59 (7), 4377-4388.
7. Mahala, C.; Sharma, M. D.; Basu, M. 2D nanostructures of CoFe<sub>2</sub>O<sub>4</sub> and NiFe<sub>2</sub>O<sub>4</sub>: efficient oxygen evolution catalyst. *Electrochim. Acta* **2018**, 273, 462-473.
8. Yang, D.; Cao, L.; Feng, L.; Huang, J.; Kajiyoshi, K.; Feng, Y.; Liu, Q.; Li, W.; Feng, L.; Hai, G. Formation of hierarchical Ni<sub>3</sub>S<sub>2</sub> nanohorn arrays driven by in-situ generation of VS<sub>4</sub> nanocrystals for boosting alkaline water splitting. *Appl. Catal. B: Environ.* **2019**, 257, 117911-117950.
9. Kim, J. E.; Bae, K.-k.; Park, C.-s.; Jeong, S.-u.; Kim, J.-w.; Yoon, J.; Cho, H.; Lee, K. B.; Kang, K. S. Nickel-iron hydroxide oxygen evolution electrocatalysts prepared by a simple chemical bath deposition method. *Int. J. Hydrogen Energy* **2021**, 46 (39), 20313-20324.

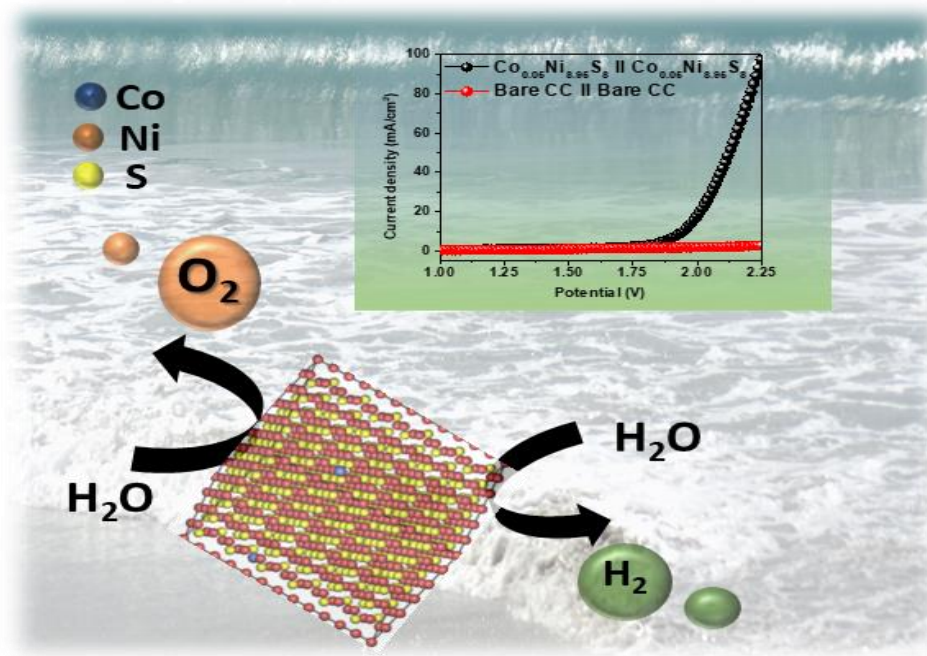
10. McKone, J. R.; Sadtler, B. F.; Werlang, C. A.; Lewis, N. S.; Gray, H. B. Ni–Mo Nanopowders for Efficient Electrochemical Hydrogen Evolution. *ACS Catal.* **2013**, *3* (2), 166-169.
11. Li, J.; Jiang, L.; He, S.; Wei, L.; Zhou, R.; Zhang, J.; Yuan, D.; Jiang, S. P. Heterostructured Ni(OH)<sub>2</sub>/Ni<sub>3</sub>S<sub>2</sub> Supported on Ni Foam as Highly Efficient and Durable Bifunctional Electrodes for Overall Water Electrolysis. *Energy & Fuels* **2019**, *33* (11), 12052-12062.
12. Zhang, H.; Li, X.; Hähnel, A.; Naumann, V.; Lin, C.; Azimi, S.; Schweizer, S. L.; Maijenburg, A. W.; Wehrspohn, R. B. Bifunctional Heterostructure Assembly of NiFe LDH Nanosheets on NiCoP Nanowires for Highly Efficient and Stable Overall Water Splitting. *Adv. Funct. Mater.* **2018**, *28* (14), 1706847-1706857.
13. Sun, H.; Zhang, W.; Li, J.-G.; Li, Z.; Ao, X.; Xue, K.-H.; Ostrikov, K. K.; Tang, J.; Wang, C. Rh-engineered ultrathin NiFe-LDH nanosheets enable highly-efficient overall water splitting and urea electrolysis. *Appl. Catal. B: Environ.* **2021**, *284*, 119740-119787.
14. Lim, D.; Kim, S.; Kim, N.; Oh, E.; Shim, S. E.; Baeck, S.-H. Strongly Coupled Ni/Ni(OH)<sub>2</sub> Hybrid Nanocomposites as Highly Active Bifunctional Electrocatalysts for Overall Water Splitting. *ACS Sustain. Chem. & Engg.* **2020**, *8* (11), 4431-4439.
15. Han, N.; Yang, K. R.; Lu, Z.; Li, Y.; Xu, W.; Gao, T.; Cai, Z.; Zhang, Y.; Batista, V. S.; Liu, W. Nitrogen-doped tungsten carbide nanoarray as an efficient bifunctional electrocatalyst for water splitting in acid. *Nat. Commun.* **2018**, *9* (1), 1-10.
16. Nazir, R.; Fageria, P.; Basu, M.; Pande, S. Decoration of Carbon Nitride Surface with Bimetallic Nanoparticles (Ag/Pt, Ag/Pd, and Ag/Au) via Galvanic Exchange for Hydrogen Evolution Reaction. *J. Phys. Chem. C* **2017**, *121* (36), 19548-19558.
17. Zhang, H.; Tian, Y.; Zhao, J.; Cai, Q.; Chen, Z. Small Dopants Make Big Differences: Enhanced Electrocatalytic Performance of MoS<sub>2</sub> Monolayer for Oxygen Reduction Reaction (ORR) by N- and P-Doping. *Electrochim. Acta* **2017**, *225*, 543-550.
18. Mahala, C.; Devi Sharma, M.; Basu, M. Fe-Doped Nickel Hydroxide/Nickel Oxyhydroxide Function as an Efficient Catalyst for the Oxygen Evolution Reaction. *ChemElectroChem* **2019**, *6* (13), 3488-3498.
19. Wang, P.; Lin, Y.; Wan, L.; Wang, B. Autologous growth of Fe-doped Ni(OH)<sub>2</sub> nanosheets with low overpotential for oxygen evolution reaction. *Int. J. Hydrogen Energy* **2020**, *45* (11), 6416-6424.

20. Ren, J.-T.; Yuan, G.-G.; Weng, C.-C.; Chen, L.; Yuan, Z.-Y. Uniquely integrated Fe-doped Ni(OH)<sub>2</sub> nanosheets for highly efficient oxygen and hydrogen evolution reactions. *Nanoscale* **2018**, *10* (22), 10620-10628.
21. Yan, J.; Kong, L.; Ji, Y.; White, J.; Li, Y.; Zhang, J.; An, P.; Liu, S.; Lee, S.-T.; Ma, T. Single atom tungsten doped ultrathin  $\alpha$ -Ni(OH)<sub>2</sub> for enhanced electrocatalytic water oxidation. *Nat. Commun.* **2019**, *10* (1), 2149-2159.
22. Wang, Y.; Wang, J.; Xie, T.; Zhu, Q.; Zeng, D.; Li, R.; Zhang, X.; Liu, S. Ru doping in Ni(OH)<sub>2</sub> to accelerate water reduction kinetics for efficient hydrogen evolution reaction. *Appl. Surf. Sci.* **2019**, *485*, 506-512.
23. Fang, G.; Cai, J.; Huang, Z.; Zhang, C. One-step electrodeposition of cerium-doped nickel hydroxide nanosheets for effective oxygen generation. *RSC Adv.* **2019**, *9* (31), 17891-17896.
24. Li, C.; Tian, P.; Pang, H.; Gong, W.; Ye, J.; Ning, G. Trace tungsten and iron-doped nickel hydroxide nanosheets for an efficient oxygen evolution reaction. *Sustain. Energy & Fuels* **2020**, *4* (6), 2792-2799.
25. Rathore, D.; Sharma, M. D.; Sharma, A.; Basu, M.; Pande, S. Aggregates of Ni/Ni(OH)<sub>2</sub>/NiOOH Nanoworms on Carbon Cloth for Electrocatalytic Hydrogen Evolution. *Langmuir* **2020**, *36* (46), 14019-14030.
26. Kresse, G.; Furthmüller, J. Efficient iterative schemes for ab initio total-energy calculations using a plane-wave basis set. *Phys. Rev. B* **1996**, *54* (16), 11169-11187.
27. Kresse, G.; Furthmüller, J. Efficiency of ab-initio total energy calculations for metals and semiconductors using a plane-wave basis set. *Compt. Mater. Sci.* **1996**, *6* (1), 15-50.
28. Blöchl, P. E. Projector augmented-wave method. *Phys. Rev. B* **1994**, *50* (24), 17953-17980.
29. Kresse, G.; Joubert, D. From ultrasoft pseudopotentials to the projector augmented-wave method. *Phys. Rev. b* **1999**, *59* (3), 1758-1778.
30. Perdew, J. P.; Burke, K.; Ernzerhof, M. Generalized gradient approximation made simple. *Phys. Rev. Lett.* **1996**, *77* (18), 3865-3869.
31. Dudarev, S.; Botton, G.; Savrasov, S.; Humphreys, C.; Sutton, A. Electron-energy-loss spectra and the structural stability of nickel oxide: An LSDA+ U study. *Phys. Rev. B* **1998**, *57* (3), 1505-1510.

32. Li, Y.-F.; Selloni, A. Mosaic texture and double c-axis periodicity of  $\beta$ -NiOOH: insights from first-principles and genetic algorithm calculations. *J. Phys. Chem. Lett.* **2014**, *5* (22), 3981-3985.
33. Li, Y.-F.; Selloni, A. Mechanism and activity of water oxidation on selected surfaces of pure and Fe-doped NiOx. *ACS Catal.* **2014**, *4* (4), 1148-1153.
34. Kutzelnigg, W., Atoms in molecules. a quantum theory.(reihe: International series of monographs on chemistry, vol. 22.) von RFW bader. clarendon press, oxford: 1990.
35. Khorsand Zak, A.; Abd. Majid, W. H.; Abrishami, M. E.; Yousefi, R. X-ray analysis of ZnO nanoparticles by Williamson–Hall and size–strain plot methods. *Solid State Sci.* **2011**, *13* (1), 251-256.
36. Kirubasankar, B.; Palanisamy, P.; Arunachalam, S.; Murugadoss, V.; Angaiah, S. 2D MoSe<sub>2</sub>-Ni(OH)<sub>2</sub> nanohybrid as an efficient electrode material with high rate capability for asymmetric supercapacitor applications. *Chem. Eng. J.* **2019**, *355*, 881-890.
37. Diaz-Morales, O.; Ferrus-Suspedra, D.; Koper, M. T. The importance of nickel oxyhydroxide deprotonation on its activity towards electrochemical water oxidation. *Chem. Sci.* **2016**, *7* (4), 2639-2645.
38. Ren, Z.; Ren, X.; Zhang, L.; Fu, C.; Li, X.; Zhang, Y.; Gao, B.; Yang, L.; Chu, P. K.; Huo, K. Tungsten-Doped CoP Nanoneedle Arrays Grown on Carbon Cloth as Efficient Bifunctional Electrocatalysts for Overall Water Splitting. *ChemElectroChem* **2019**, *6* (20), 5229-5236.
39. Wang, H.; Liu, T.; Bao, K.; Cao, J.; Feng, J.; Qi, J. W doping dominated NiO/NiS<sub>2</sub> interfaced nanosheets for highly efficient overall water splitting. *J. Colloid Interface Sci.* **2020**, *562*, 363-369.
40. Xi, W.; Yan, G.; Tan, H.; Xiao, L.; Cheng, S.; Khan, S. U.; Wang, Y.; Li, Y. Superaerophobic P-doped Ni(OH)<sub>2</sub>/NiMoO<sub>4</sub> hierarchical nanosheet arrays grown on Ni foam for electrocatalytic overall water splitting. *Dalton Trans.* **2018**, *47* (26), 8787-8793.
41. Fageria, P.; Sudharshan, K.; Nazir, R.; Basu, M.; Pande, S. Decoration of MoS<sub>2</sub> on g-C<sub>3</sub>N<sub>4</sub> surface for efficient hydrogen evolution reaction. *Electrochim. Acta* **2017**, *258*, 1273-1283.
42. Sharma, M. D.; Mahala, C.; Basu, M. Nanosheets of MoSe<sub>2</sub>@ M (M= Pd and Rh) function as widespread pH tolerable hydrogen evolution catalyst. *J. Colloid Interface Sci.* **2019**, *534*, 131-141.

43. Gong, M.; Zhou, W.; Tsai, M.-C.; Zhou, J.; Guan, M.; Lin, M.-C.; Zhang, B.; Hu, Y.; Wang, D.-Y.; Yang, J. Nanoscale nickel oxide/nickel heterostructures for active hydrogen evolution electrocatalysis. *Nat. Commun.* **2014**, *5* (1), 1-6.
44. Jin, M.; Li, J.; Gao, J.; Liu, W.; Han, J.; Liu, H.; Zhan, D.; Lai, L. Atomic-level tungsten doping triggered low overpotential for electrocatalytic water splitting. *J. Colloid Interface Sci.* **2021**, *587*, 581-589.
45. Mahala, C.; Sharma, R.; Sharma, M. D.; Pande, S. Development of Copper Cobalt Sulfide with Cu: Co Ratio Variation on Carbon Cloth as an Efficient Electrode Material for the Oxygen Evolution Reaction. *ChemElectroChem* **2019**, *6* (20), 5301-5312.
46. Feng, C.; Faheem, M.; Fu, J.; Yequan, X.; Li, C.; Li, Y. Fe-Based Electrocatalysts for Oxygen Evolution Reaction: Progress and Perspectives. *ACS Catal.* **2020**.
47. Zhang, L.; Amiin, I. S.; Ren, X.; Liu, Z.; Du, G.; Asiri, A. M.; Zheng, B.; Sun, X. Surface Modification of a NiS<sub>2</sub> Nanoarray with Ni(OH)<sub>2</sub> toward Superior Water Reduction Electrocatalysis in Alkaline Media. *Inorg. Chem.* **2017**, *56* (22), 13651-13654.
48. Wang, P.; Zhang, X.; Zhang, J.; Wan, S.; Guo, S.; Lu, G.; Yao, J.; Huang, X. Precise tuning in platinum-nickel/nickel sulfide interface nanowires for synergistic hydrogen evolution catalysis. *Nat. Commun.* **2017**, *8* (1), 14580-14589.
49. Hammer, B.; Nørskov, J. K. Theoretical surface science and catalysis-calculations and concepts. *Adv. Catal.* **2000**, *45*, 71-129.
50. Nørskov, J. K.; Bligaard, T.; Rossmeisl, J.; Christensen, C. H. Towards the computational design of solid catalysts. *Nat. Chem.* **2009**, *1* (1), 37-46.
51. Zhong, W.; Yang, C.; Wu, J.; Xu, W.; Zhao, R.; Xiang, H.; Shen, K.; Li, X. Adsorption site engineering: Cu-Ni(OH)<sub>2</sub> sheets for efficient hydrogen evolution. *J. Mater. Chem. A* **2021**, *9* (32), 17521-17527.

### Co-Doped Ni<sub>9</sub>S<sub>8</sub> Nanostructures for Electrocatalytic Water-Splitting in a Wide pH Region



- \* In this chapter, Co doped Ni<sub>9</sub>S<sub>8</sub> nanoparticles was developed on carbon cloth through hydrothermal route.
- \* The Co<sub>0.05</sub>Ni<sub>8.95</sub>S<sub>8</sub> structure show good HER and OER activity in all pH medium.

## *Abstract*

As a replacement for renewable energy sources an earth-abundant electrocatalyst for water splitting is effectively explored. In this work, Ni<sub>9</sub>S<sub>8</sub> and cobalt-doped Ni<sub>9</sub>S<sub>8</sub> nanostructure is fabricated on carbon cloth through hydrothermal technique. The developed electrocatalysts are characterized through various techniques, e.g., PXRD, Raman, XPS, FESEM, HRTEM, BET, and ICP-AES. Tuning of cobalt doping is performed to optimize the best ratio of Co:Ni for electrocatalytic activity. All the developed materials are applied in a water-splitting reaction in an alkaline electrolyzer and Co<sub>0.05</sub>Ni<sub>8.95</sub>S<sub>8</sub> is an optimized material for both hydrogen and oxygen evolution. The electrocatalysts, Co<sub>0.05</sub>Ni<sub>8.95</sub>S<sub>8</sub> only require -0.151 V vs. RHE to obtain 10 mA/cm<sup>2</sup> current density in HER, and in OER it requires 1.557 V vs. RHE to generate 30 mA/cm<sup>2</sup> current density. The corresponding Tafel slope values for HER and OER are 125 mV/dec and 49.8 mV/dec, respectively by using Co<sub>0.05</sub>Ni<sub>8.95</sub>S<sub>8</sub> electrocatalysts in 1.0 M KOH solution. The stability of Co<sub>0.05</sub>Ni<sub>8.95</sub>S<sub>8</sub> is also checked and it is stable up to 60 and 80 hours for both HER and OER, respectively. The cell voltage of 1.89 V is required to generate 10 mA/cm<sup>2</sup> current density for overall water splitting. The electrocatalyst is also used for HER and OER in wide pH regions for practical applicability. The overall experimental findings were verified by theoretical calculations, which state higher metallic nature of Co doped Ni<sub>9</sub>S<sub>8</sub>, facilitates efficient electrocatalytic activity. The optimum Gibbs free energy, hydrogen, and oxygen coverage calculation also proves the optimized Co<sub>0.05</sub>Ni<sub>8.95</sub>S<sub>8</sub> electrocatalyst exhibits the best HER and OER activity. Therefore, this work provides a robust electrocatalyst for electrocatalytic water-splitting reaction.



### 5.1 Introduction

Electrocatalytic water splitting reaction, which generates hydrogen and oxygen is extensively considered a prominent approach for the production of clean, secure, and sustainable forms of energy.<sup>1, 2</sup> Water-splitting involves hydrogen and oxygen evolution (HER and OER) at the cathode and anode, respectively, with a requirement of 1.23 V potential difference to split water.<sup>3</sup> Due to the very high overpotential of OER and HER, in practical, a voltage of 1.8-2.0 V pertains commercially during the water-splitting reaction.<sup>4</sup> The wide application of water splitting is still limited due to the use of noble catalysts such as Pt, and RuO<sub>2</sub>, IrO<sub>2</sub> for HER and OER, respectively.<sup>5, 6</sup> These noble catalysts' are higher cost, lower abundance, and scarcity in different pH. The major limitations of these electrocatalysts are efficiency and durability in alkaline and acidic medium for HER and OER, respectively. Moreover, most noble metal catalysts in the alkaline electrolyte are either high onset overpotential or unstable, especially at high current density.<sup>7</sup> So, to overcome these issues we need an alternative electrocatalyst with high efficiency and stability in a wide pH. Consequently, investigation for the substitution of these noble catalysts with transition metal-based electrocatalysts having low overpotential and higher stability is being considered.<sup>8, 9</sup> Over the past years, transition metal hydroxides, oxides, and sulfides are extensively surveyed for electrocatalytic water-splitting.<sup>10</sup> Out of all these catalysts, nickel-based materials (hydroxides, oxides, chalcogenides, nitrides, phosphides, etc.) and their derivatives have drawn immense importance in OER.<sup>11, 12</sup>

Transition metal sulfides and selenides like WS<sub>2</sub>, NiS<sub>2</sub>, MoS<sub>2</sub>, MoSe<sub>2</sub>, etc. are potential candidates for HER due to their low price and high durability.<sup>13, 14</sup> Whereas, due to less activity and stability of Ni-based sulphides like NiS<sub>2</sub>, Ni<sub>3</sub>S<sub>2</sub>, and Ni<sub>9</sub>S<sub>8</sub>, etc. are less explored as HER and OER catalysts.<sup>11, 15</sup> Synthesis of the pure phase of godlevskite (Ni<sub>9</sub>S<sub>8</sub>) is also less reported. Godlevskite has a specific crystal structure and mixed valence state of Ni atom due to which it shows slightly better efficiency in OER than HER.<sup>16</sup> Mixed valence state configuration and the eight-valence electron in the 3d orbital of Ni(II) facilitated the regulation of electronic structure during HER and OER through heterostructuring, surface modification, shape tuning, defects, etc. methodologies.<sup>17-19</sup> Doping is an effective strategy to enhance electrocatalytic performance by increasing active sites. The doped atom itself can generate a new active site in the system and can regulate the change in the electronic environment of the existing active site.<sup>16</sup> In the current scenario, it becomes more important to reveal alternative HER and OER catalysts with low price,

high efficiency and stability. Therefore, attention has been diverted towards low-cost nickel sulphides doped with non-noble metals to create active sites for overall electrocatalytic water-splitting.

Till now, doping with NiS, Ni<sub>3</sub>S<sub>2</sub>, etc. is widely investigated but the effect of doping on Ni<sub>9</sub>S<sub>8</sub> is rarely reported.<sup>20, 21</sup> In this context, Wang and co-workers<sup>16</sup> reported OER activity of porous nickel sulphides, Ni<sub>x</sub>S<sub>y</sub> (Ni<sub>9</sub>S<sub>8</sub>, Ni<sub>9</sub>S<sub>8</sub>-NiS<sub>1.03</sub> alloy, and NiS<sub>1.03</sub>) mixed with N and S co-doped carbon matrix. They have shown that the co-doped carbon nanoparticles improved the conductivity of nickel sulphides and the porous structure increased the active sites, which facilitates the OER activity. They have reported low overpotential of 270 mV vs. RHE by using co-doped NiS<sub>1.03</sub>, whereas, Tafel slope value of 63.8 mV/dec is shown by Ni<sub>9</sub>S<sub>8</sub>-NiS<sub>1.03</sub> alloy. Qiao and co-workers<sup>22</sup> developed catalyst electrodes based on 3D Ni/Ni<sub>8</sub>P<sub>3</sub> and Ni/Ni<sub>9</sub>S<sub>8</sub> by activating Ni-foam for water splitting in an alkaline medium. They have shown that the activation of Ni-foam assists charge transfer and produces an efficient and durable electrocatalyst. Yang and co-workers<sup>23</sup> produced ultrathin nanosheets of metallic Fe-Ni sulfide by topotactic conversion using hydroxide precursor for HER activity in 0.5 M H<sub>2</sub>SO<sub>4</sub> solution. The developed catalyst shows overpotential of 105 mV to obtain 10 mA/cm<sup>2</sup> and a Tafel slope value of 40 mV/dec. They have shown that Fe doping increases active surface area, facile ion transfer, and suitable hydrogen adsorption energy in Fe-Ni sulfide for an cost effective and durable HER electrocatalyst. Copper-nickel sulfide (Cu<sub>2</sub>S, NiS, and Ni<sub>3</sub>S<sub>2</sub>) nanowires by one-pot multi-step strategy for overall water splitting in an alkali medium have been reported by Cheng and co-workers.<sup>24</sup> They have shown that the active center for water-splitting reactions is generated by Cu<sub>2</sub>S, NiS, and Ni<sub>3</sub>S<sub>2</sub> phases because of metallic Cu, which helps in the transfer of electron. Different phases of nickel sulfides, hexagonal-NiS, and orthorhombic-Ni<sub>9</sub>S<sub>8</sub> are developed by Leite and co-workers<sup>25</sup> following microwave energy and solvothermal technique by changing the sulfur precursor. They have used the as-developed sulfides for HER in 1.0 M KOH solution with the value of overpotential is 266 mV after electrolysis to generate a 10 mA/cm<sup>2</sup> current density. Lee and co-workers<sup>26</sup> reported Co<sub>x</sub>Ni<sub>y</sub>S<sub>z</sub> nanostructure for oxygen evolution reaction following hydrothermal route. The developed Co<sub>9-x</sub>Ni<sub>x</sub>S<sub>8</sub> nanostructure exhibit 362 mV vs. RHE overpotential to obtain 10 mA/cm<sup>2</sup> current density, which is better than Co<sub>9</sub>S<sub>8</sub> and Ni<sub>9</sub>S<sub>8</sub>. Wang and co-workers<sup>27</sup> developed Ni<sub>9</sub>S<sub>8</sub>/CuS/Cu<sub>2</sub>O composite on Ni foam via hydrothermal and used for hydrogen evolution reaction. The developed catalyst shows good electrocatalytic activity with low onset potential of -

0.147 V *vs.* RHE to achieve 10 mA/cm<sup>2</sup> current density. Ni<sub>9</sub>S<sub>8</sub> nanorod/O-MoS<sub>2</sub> nanosheet developed through hydrothermal technique was reported by Li and co-workers.<sup>28</sup> The catalyst shows good stability along with 150 mV *vs.* RHE to obtain 10 mA/cm<sup>2</sup> current density. Ni<sub>3</sub>S<sub>2</sub>/Fe-NiP<sub>x</sub> magic cube via hydrothermal and phosphorization techniques with higher water oxidation efficiency was developed by Mu and co-workers.<sup>29</sup> The catalyst exhibit remarkable activity with the overpotential value of 336 and 351 mV *vs.* RHE to generate 500 and 1000 mA/cm<sup>2</sup> current density. The presence of rich oxygen vacancies and grain boundaries between Ni(OH)<sub>2</sub>, NiOOH, and FeOOH create abundant active sites for oxygen evolution. The same group<sup>30</sup> also reported nickel sulfide nanoflower with dual phase of NiS-NiS<sub>2</sub>, the developed catalyst exhibits superior HER performance in alkaline medium. However, nickel sulfide materials are either HER or OER active as low price and high abundance but the efficiency and durability during the water-splitting reaction are questionable. Therefore, to develop bifunctional activity (both HER and OER) within a single electrocatalyst with high activity and stability we have synthesized transition metal-doped Ni<sub>9</sub>S<sub>8</sub>.

Inspired by the above studies, herein, we have synthesized the pure phase of Ni<sub>9</sub>S<sub>8</sub> with cobalt doping on conductive carbon cloth (CC), through a simple hydrothermal technique. The presence of Co in the Ni<sub>9</sub>S<sub>8</sub> is optimized through ratio variation of Co:Ni (0.1:8.9, 0.05:8.95, and 0.03:8.97). The characterization of the developed Co doped Ni<sub>9</sub>S<sub>8</sub> is done by various techniques, e.g., PXRD, XPS, Raman, FESEM, and HRTEM. After successful Co doping in Ni<sub>9</sub>S<sub>8</sub>, all the materials are applied in an electrocatalytic water-splitting reaction using an alkaline medium (pH-14). The best electrocatalytic activity is observed with the Co<sub>0.05</sub>Ni<sub>8.95</sub>S<sub>8</sub> in both HER as well as OER. The optimized ratio of Co<sub>0.05</sub>Ni<sub>8.95</sub>S<sub>8</sub> shows a lower value of Tafel slope of 125 mV/dec and requires -0.151 V *vs.* RHE to achieve 10 mA/cm<sup>2</sup> current density for HER. In the case of OER, it requires 1.557 V *vs.* RHE to generate a 30 mA/cm<sup>2</sup> current density with the 49.8 mV/dec of Tafel slope value. The morphology of Co<sub>0.05</sub>Ni<sub>8.95</sub>S<sub>8</sub> is checked after electrocatalysis and confirms the retention in morphology. The Co<sub>0.05</sub>Ni<sub>8.95</sub>S<sub>8</sub> is also used as a cathode and anode in an alkaline medium, which needs cell voltage of 1.89 V to generate 10 mA/cm<sup>2</sup> current density. There are many advantages of this work. First, the synthesis process is very simple and straightforward for the development of Co doped Ni<sub>9</sub>S<sub>8</sub> in the pure phase. Second, Co and Ni metals are cost-effective and earth-abundant compared to noble metals. Third, Co doped Ni<sub>9</sub>S<sub>8</sub> is very effective for both hydrogen and oxygen evolution in 1 M KOH. Fourth, the synergistic effect between the metals

(Co and Ni) increases the electrocatalytic performance. Fifth, bifunctional activity of Co doped  $\text{Ni}_9\text{S}_8$  for overall water-splitting by generating new active sites. Sixth, the metallic nature of Co doped  $\text{Ni}_9\text{S}_8$  is also supported by DFT calculation, and the defect formation energy values suggest the favorable formation of  $\text{Co}_{0.05}\text{Ni}_{8.95}\text{S}_8$ . The minimum Gibbs free hydrogen adsorption energy, hydrogen, and oxygen coverages of  $\text{Co}_{0.05}\text{Ni}_{8.95}\text{S}_8$  show better HER and OER performance. The energy barriers for HER and OER are calculated using various dopant concentrations to comprehend precisely the electrocatalytic performances of Co doped  $\text{Ni}_9\text{S}_8$ . Therefore, these advantages transform Co doped  $\text{Ni}_9\text{S}_8$  electrocatalysts as an active, robust, and economically favorable candidate for overall water-splitting reactions.

## 5.2 Experimental Section

**5.2.1 Synthesis of  $\text{Ni}_9\text{S}_8$ :** The hydrothermal process was used for the synthesis of  $\text{Ni}_9\text{S}_8$  on the surface of CC. The synthesis was carried out in two-step processes. First, 1 mmol of  $\text{NiCl}_2 \cdot 6\text{H}_2\text{O}$  and 1 mmol of urea were collected along with 30 mL DI water and sonicated for 10 minutes. After that, the carbon cloth ( $1.5 \text{ cm} \times 3 \text{ cm}$ ) was placed in the  $\text{NiCl}_2 \cdot 6\text{H}_2\text{O}$  and urea solution and transferred into Teflon-lined autoclave for hydrothermal reaction ( $110 \text{ }^\circ\text{C}$  for 10 hours). The deposited material was characterized by PXRD (Figure 5.1a), FESEM (Figure 5.1b), and EDS mapping analysis (Figure 5.1c), which confirms the formation of  $\text{Ni}(\text{OH})_2$ . Therefore, in this process  $\text{Ni}(\text{OH})_2$  was developed on CC. Second, the deposited  $\text{Ni}(\text{OH})_2$  on the surface of CC was transferred for the sulphidation process, 0.346 gm of thioacetamide was taken in 30 mL DI water followed by sonication. The entire solution was transferred for hydrothermal reaction at  $180 \text{ }^\circ\text{C}$  for 10 hours. Finally, a black deposition was observed on CC and rinsed with DI water and ethanol followed by drying.

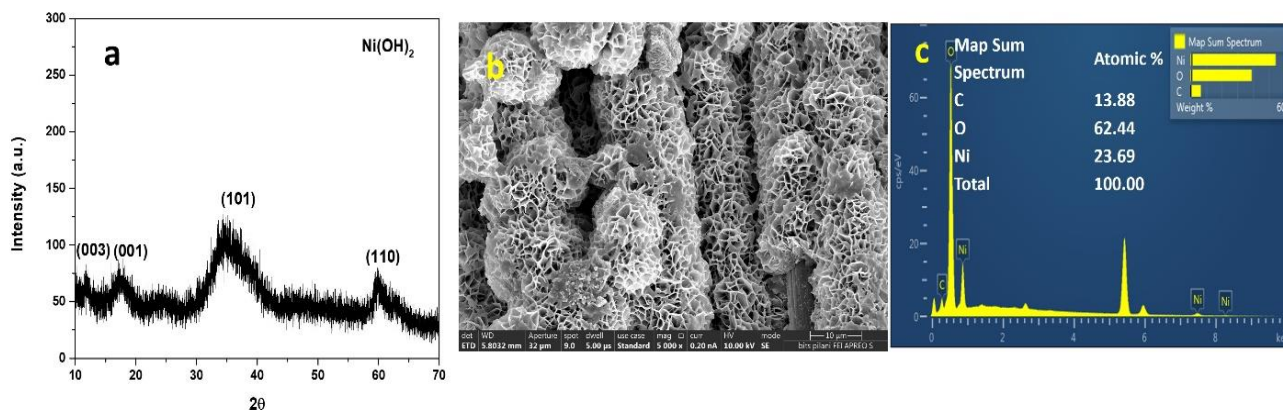
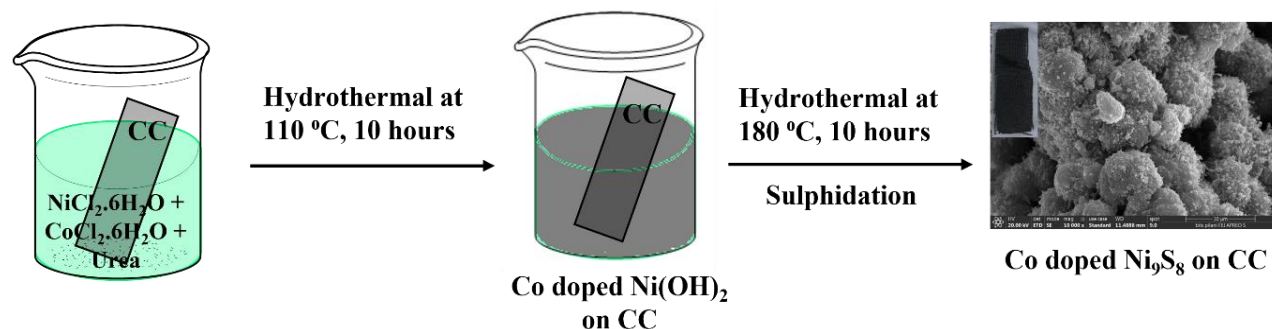


**Figure 5.1:** (a) PXRD (b) FESEM, (c) EDS analysis of  $\text{Ni}(\text{OH})_2$ .

**5.2.2 Synthesis of Co doped Ni<sub>9</sub>S<sub>8</sub>:** The synthesis of Co doped Ni<sub>9</sub>S<sub>8</sub> was also performed in two-step hydrothermal processes. First, for the synthesis of Ni(OH)<sub>2</sub> in presence of Co<sup>2+</sup> ion, 0.9 mmol of NiCl<sub>2</sub>.6H<sub>2</sub>O and 1 mmol of urea into 30 mL DI water followed by the addition of 0.1 mmol CoCl<sub>2</sub>.6H<sub>2</sub>O in the same mixture. The overall solution was transferred into a Teflon-lined autoclave for hydrothermal reaction at 110 °C for 10 hours. During the hydrothermal reaction CC (1.5 cm × 3 cm) was poured into the Teflon container. At the end of the first step, Co doped Ni(OH)<sub>2</sub> was deposited on the surface of CC. Second, sulphidation of Co doped Ni(OH)<sub>2</sub> complex was performed followed by hydrothermal using 0.346 gm thioacetamide at 180 °C for 10 hours. The doped Ni<sub>9</sub>S<sub>8</sub> was washed with DI water and ethanol followed by drying. This step developed the formation of Co<sub>0.1</sub>Ni<sub>8.9</sub>S<sub>8</sub> on CC (Scheme 5.1).

To tune the amount of dopant, the same procedure was followed except for the change in NiCl<sub>2</sub>.6H<sub>2</sub>O and CoCl<sub>2</sub>.6H<sub>2</sub>O quantity. 0.95 and 0.97 mmol of NiCl<sub>2</sub>.6H<sub>2</sub>O were used while the amount of CoCl<sub>2</sub>.6H<sub>2</sub>O was 0.05, and 0.03 mmol. Rest all the steps remain unchanged. Finally, three different ratios of Co:Ni (0.1:8.9, 0.05:8.95, and 0.03:8.97) were developed as Co doped Ni<sub>9</sub>S<sub>8</sub>. Unless otherwise indicated all the ratios are represented as Co<sub>0.1</sub>Ni<sub>8.9</sub>S<sub>8</sub>, Co<sub>0.05</sub>Ni<sub>8.95</sub>S<sub>8</sub>, and Co<sub>0.03</sub>Ni<sub>8.97</sub>S<sub>8</sub>.



**Scheme 5.1:** Schematic representation for the synthesis of Co doped Ni<sub>9</sub>S<sub>8</sub> on CC surface.

**5.2.3 Electrochemical Measurement:** For the electrochemical HER and OER study, graphite rod, Ag/AgCl, and the sample (doped and undoped Ni<sub>9</sub>S<sub>8</sub>) deposited CC were used as the counter, reference, and working electrode, respectively. 1.0 M KOH solution (pH ~14) was used as an electrolyte throughout the study with a scan rate of 2 mV/sec. The catalyst loading for both the

doped and undoped samples was calculated as  $1.63 \text{ mg/cm}^2$ . However, during electrocatalysis (HER and OER),  $0.4 \text{ cm} \times 0.4 \text{ cm}$  working area of CC was retained, and the catalyst was  $0.26 \text{ mg}$ . The epoxy paste was used to fix the area of the CC for electrochemical application. All the electrochemical measurement were performed concerning Ag/AgCl (reference electrode) with a potential window of  $-0.9$  to  $-1.8 \text{ V}$  for HER and  $0$  to  $0.8 \text{ V}$  for OER, respectively. Finally, all the potential data were reported as reversible hydrogen electrodes (RHE) using the following equation,  $E_{\text{RHE}} = E_{\text{Ag/AgCl}} + 0.0591 \text{ pH} + E_{\text{Ag/AgCl}}^0$ . For EIS (electrochemical impedance spectroscopy) analysis, a frequency ranges of higher  $50 \text{ kHz}$  and lower  $0.1 \text{ Hz}$  was used at room temperature in a  $1.0 \text{ M KOH}$  solution.

### 5.2.4 Computational Details

The first-principle density functional theory (DFT) calculations have been accomplished from the generalized gradient approximation (GGA) in conjunction with the Perdew-Burke-Ernzerhof (PBE) exchange-correlation functional<sup>31</sup> as implemented in the Quantum ESPRESSO (QE) software<sup>32-34</sup>. The geometry optimization of the orthorhombic ( $C222$ )  $\text{Ni}_9\text{S}_8$  system at ambient pressure ( $P = 0 \text{ GPa}$ ) has been performed using variable cell relaxation scheme following Broyden-Fletcher-Goldfarb-Shanno (BFGS) method<sup>35-38</sup>. The electron-ion interactions have been considered from the pseudopotential approach using projector augmented wave (PAW) method<sup>39</sup>. The valance electrons  $3d^84s^2$  for Ni and  $3s^23p^4$  for S atoms of the  $\text{Ni}_9\text{S}_8$  system are represented as plane wave with kinetic energy cut-off of  $60 \text{ Ry}$ . The orthorhombic  $\text{Ni}_9\text{S}_8$  system is allowed to relax until the Hellman–Feynman force acting on it attains a value less than  $0.003 \text{ Ry/Bohr}$  for the maximum cell pressure of  $0.01 \text{ GPa}$  and the total electronic energy difference  $< 10^{-11} \text{ Ry}$ . A gamma-centered k-point mesh of  $10 \times 10 \times 10$  Monkhorst–Pack grid has been employed for the geometry optimization and self-consistent-field (SCF) calculations. However, for estimating the total and projected atomic density of states (TDOS and PDOS), denser grid of  $20 \times 20 \times 20$  k-point mesh has been chosen in the DFT calculations. The on-site Coulomb interaction ( $+U_{\text{dd}} = 8 \text{ eV}$ ) has been included in the GGA-PBE calculations to estimate the band gap energies of pristine and doped  $\text{Ni}_9\text{S}_8$  systems<sup>40, 41</sup>.

For the estimations of the electronic band structures, TDOS, PDOS of the pristine and Co-doped  $\text{Ni}_9\text{S}_8$  ( $\text{Co}_x\text{Ni}_{9-x}\text{S}_8$ ) systems and the defect formation energies ( $\Delta E_{\text{df}}$ ) for  $\text{Co}_x\text{Ni}_{9-x}\text{S}_8$  systems,  $6 \times 6 \times 6$  supercells have been used at ambient pressure. The replacement of Ni by Co in

the doped systems has been accomplished on the optimized  $6 \times 6 \times 6$  supercell. The number of Co dopants has been varied from 2 to 24 in place of Ni atoms to obtain the final dopant concentration of Co to vary between  $\sim 0.5\%$  and  $6\%$  in  $\text{Ni}_9\text{S}_8$  system. The Gibbs free energies ( $\Delta G_{\text{H}}$ ) for the hydrogen and subsequent oxygen adsorbed  $\text{Co}_x\text{Ni}_{9-x}\text{S}_8$  compounds have been elucidated in terms of hydrogen and oxygen coverage as reported elsewhere<sup>42-46</sup>. The hydrogen and oxygen coverages are estimated by adsorbing 'n' hydrogens followed by 'n' oxygens on the dopant Co atoms of the  $\text{Co}_x\text{Ni}_{9-x}\text{S}_8$  systems. The energy barriers and the electrochemical reaction pathways for the HER and OER activities have been estimated from the nudged elastic band (NEB) method<sup>47</sup> using QE software.

### 5.3 Results & Discussions

The detailed synthesis of Co doped  $\text{Ni}_9\text{S}_8$  is reported in the experimental section. Two-step hydrothermal processes are followed for the synthesis of doped  $\text{Ni}_9\text{S}_8$ . Tuning of Co doping in  $\text{Ni}_9\text{S}_8$  is also performed. Finally, the material is cleaned properly for further use.

**5.3.1 Structural analysis of doped and undoped  $\text{Ni}_9\text{S}_8$ :** The phase purity and crystallinity are checked with powder X-ray diffraction analysis (PXRD). Figure 5.2a shows the prominent peaks at  $2\theta = 15.4^\circ, 27.1^\circ, 31.3^\circ, 35.2^\circ, 38.8^\circ, 53.2^\circ,$  and  $56.1^\circ$  are indexed to (111), (202), (222), (312), (241), (261) and, (531) planes, respectively. All the peaks correspond to the orthorhombic  $\text{Ni}_9\text{S}_8$  phase as in Figure 5.2a, which is well-matched with JCPDF 22-1193.<sup>18</sup> After Co doping in orthorhombic  $\text{Ni}_9\text{S}_8$  ( $\text{Co}_{0.05}\text{Ni}_{8.95}\text{S}_8$ ) the peaks at  $2\theta = 31.3^\circ$  and  $38.8^\circ$  are shifted at a higher diffraction angle, as shown in Figure 5.3a. Therefore, the peak shifting in the PXRD analysis of Co doped  $\text{Ni}_9\text{S}_8$  confirms the change in the lattice. The calculation of strain in the Co doped  $\text{Ni}_9\text{S}_8$  is further confirmed with the value of " $\epsilon$ " from the Williamson-Hall equation.<sup>48</sup> The diffraction angle ( $2\theta$ ) values of  $31.3^\circ, 35.2^\circ,$  and  $38.8^\circ$  are selected for the calculation of the strain in the doped and undoped samples. The plot of  $\beta\cos\theta$  and  $4\sin\theta$  in Figure 5.3b gives the value of intercept as the size of the lattice (D) and slope represent the raised strain ( $\epsilon$ ) in the system. In the Co doped  $\text{Ni}_9\text{S}_8$  sample the slope value appears to be negative, which symbolizes the nature of the strain is compressive.<sup>49</sup> The strain that arises in the doped sample is probably due to the higher ionic radius of  $\text{Co}^{2+}$  ion (88.5 pm) than  $\text{Ni}^{2+}$  ion (83 pm). In the PXRD pattern of the doped sample, the intensity of the major peaks ( $2\theta = 27.1^\circ, 31.3^\circ, 35.2^\circ, 38.8^\circ, 53.2^\circ,$  and  $56.1^\circ$ ) are decreased than the bare

sample. This decrement in the peak intensity signifies that after doping the grain size of  $\text{Ni}_9\text{S}_8$  is reduced. To confirm the deduction in grain size, the Debye-Scherrer formula is used and the calculated sizes are 41.7 nm and 30.6 nm for bare  $\text{Ni}_9\text{S}_8$  and Co doped  $\text{Ni}_9\text{S}_8$ , respectively. In this context, Ismail and co-workers<sup>49</sup> also reported the decrease in ZnO crystallite size after doping with Fe metal. In the doped sample ( $\text{Co}_{0.05}\text{Ni}_{8.95}\text{S}_8$ ), the absence of any additional peak proves that the formation of cobalt sulphide is negligible, which signifies the successful Co doping. The PXRD analysis of  $\text{Co}_{0.1}\text{Ni}_{8.9}\text{S}_8$  and  $\text{Co}_{0.03}\text{Ni}_{8.97}\text{S}_8$  samples are also performed (Figure 5.2b) and the peaks are well-matched with  $\text{Co}_{0.05}\text{Ni}_{8.95}\text{S}_8$ . The crystallinity of the sample is decreased upon increasing the amount of dopant, which can be seen from the peaks at  $2\theta = 31.3^\circ$ ,  $35.2^\circ$ , and  $38.8^\circ$ . Similar phenomena were observed after Fe doping in  $\text{TiO}_2$  nanoparticles by Bharti and co-workers.<sup>48</sup>

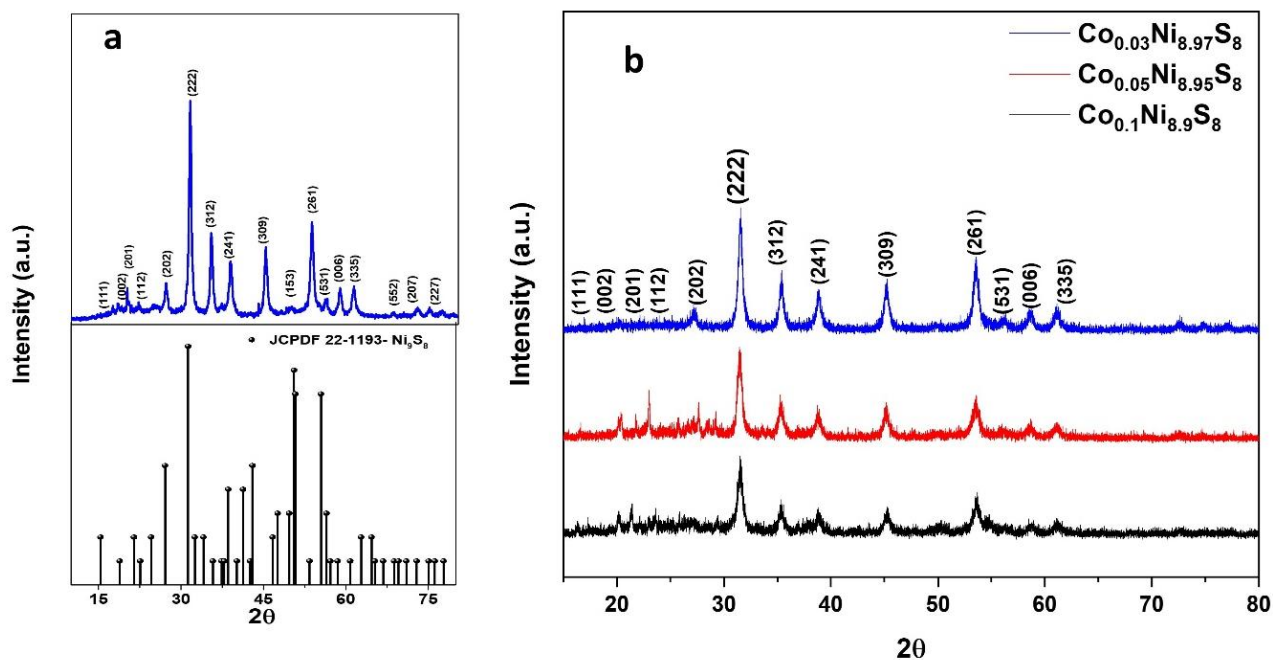


**Figure 5.2:** (a) XRD of  $\text{Ni}_9\text{S}_8$ , stacked with JCPDF 22-1193 and (b) XRD analysis of  $\text{Co}_{0.1}\text{Ni}_{8.9}\text{S}_8$ ,  $\text{Co}_{0.05}\text{Ni}_{8.95}\text{S}_8$  and  $\text{Co}_{0.03}\text{Ni}_{8.97}\text{S}_8$ .



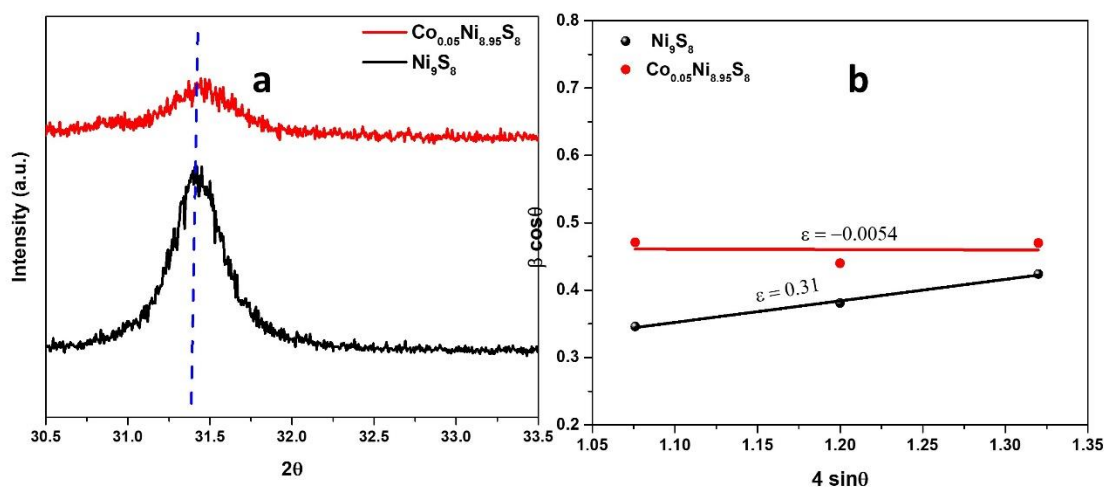


**Figure 5.3:** (a) low scan rate XRD profile of  $\text{Ni}_9\text{S}_8$  and  $\text{Co}_{0.05}\text{Ni}_{8.95}\text{S}_8$  with peak shifting. (b) Williamson-Hall plot of  $\text{Ni}_9\text{S}_8$  and  $\text{Co}_{0.05}\text{Ni}_{8.95}\text{S}_8$ .

Raman spectra of bare  $\text{Ni}_9\text{S}_8$  and Co doped  $\text{Ni}_9\text{S}_8$  ( $\text{Co}_{0.05}\text{Ni}_{8.95}\text{S}_8$ ) are shown in Figure 5.4a, which represents a broad peak located at  $508 \text{ cm}^{-1}$  for bare  $\text{Ni}_9\text{S}_8$ . The peak at  $508 \text{ cm}^{-1}$  is responsible for Ni-S vibration, which is well-matched with the literature.<sup>50</sup> In the doped sample the Raman peak is shifted at a higher value,  $527 \text{ cm}^{-1}$ . The dopant plays an important role in peak shifting. It is confirmed from the reported literature that the position and intensity of the Raman peak can effectively be changed by doping. Therefore, the shift in Ni-S vibrations and decrease in intensity confirms the incorporation of cobalt in the  $\text{Ni}_9\text{S}_8$  lattice, which is well-coordinated with the XRD analysis. The absence of any new Raman peak after doping signifies the formation of cobalt sulphide is negligible. Based on the classification of IUPAC, the curve nature suggests that it is a type-III (Figure 5.4 b) isotherm with a hysteresis loop for both bare and doped  $\text{Ni}_9\text{S}_8$ .<sup>51</sup> This type-III isotherm also confirms the initial formation of multilayer adsorption well before the fulfilment of monolayer adsorption. The specific surface area of the doped and bare catalyst is performed through the BET (Brunauer–Emmett–Teller) method. The increment in surface area is observed from  $11.3 \text{ m}^2/\text{gm}$  to  $13.7 \text{ m}^2/\text{gm}$  after Co doping in  $\text{Ni}_9\text{S}_8$ , which indicate that after doping contact area of electrode-electrolyte increases (Figure 5.4c). The BJH pore diameter is calculated from BET data, which represents  $38.6$  and  $49.3 \text{ nm}$  for bare  $\text{Ni}_9\text{S}_8$  and Co doped  $\text{Ni}_9\text{S}_8$  nanostructure, respectively. According to the pore diameter the materials can be classified as

mesoporous or nanoporous, which is in the range of 2-50 nm. An increase in pore diameter reflects the diffusion kinetics within the electrode material. The same phenomena were observed by Mishra and co-workers in the electrochemical performance of iron-doped cobalt oxide.<sup>52</sup>

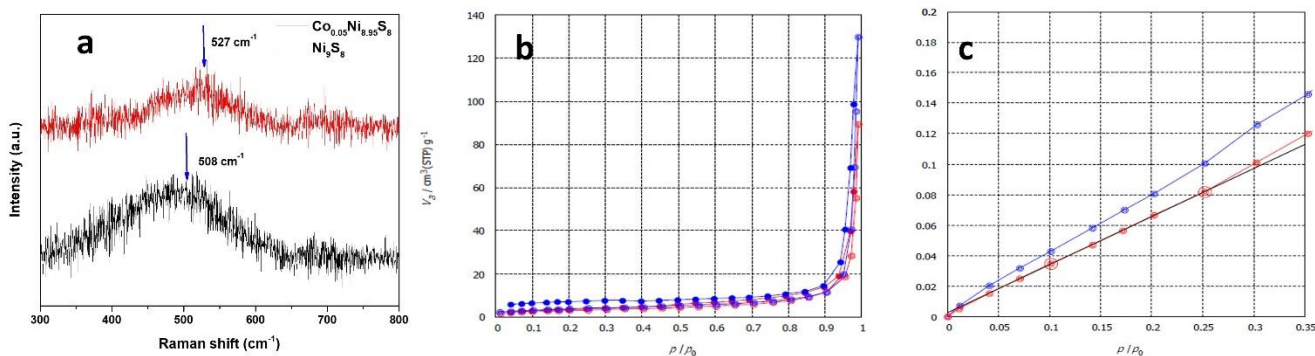


**Figure 5.4:** (a) Raman analysis of Ni<sub>9</sub>S<sub>8</sub> and Co<sub>0.05</sub>Ni<sub>8.95</sub>S<sub>8</sub> (b and c) BET adsorption isotherm and surface area of Co<sub>0.05</sub>Ni<sub>8.95</sub>S<sub>8</sub>.

The X-ray photoelectron spectroscopy (XPS) analysis confirms the oxidation state and composition of the synthesized material. Figure 5.5a shows the survey spectra of bare Ni<sub>9</sub>S<sub>8</sub> in which the peaks for Ni, S, C, and O are present. The signal of O 1s arises due to surface oxidation of the deposited material on carbon cloth. Figures 5.5b represents the deconvoluted XPS spectrum of the Ni<sub>9</sub>S<sub>8</sub> sample, which is well-fitted with spin-orbit doublets and a shakeup satellite. The binding energy values at 853.9 eV and 871.3 eV represent 2P<sub>3/2</sub> and 2P<sub>1/2</sub>, respectively of the Ni<sup>+2</sup> oxidation state in bare Ni<sub>9</sub>S<sub>8</sub>. The other binding energies at 856.4 eV and 874.7 eV show the existence of Ni<sup>+3</sup> species for 2P<sub>3/2</sub> and 2P<sub>1/2</sub> state, respectively. Furthermore, the satellite peaks at 860.7 eV and 879.9 eV also confirm the presence of Ni<sup>+2</sup> and Ni<sup>+3</sup> species. The binding energies at 163 eV and 164.05 eV for sulphide ion can be assigned to S2p<sub>3/2</sub> and S2p<sub>1/2</sub>, respectively due to the co-ordination of metal and sulphide ion (Figure 5.5c). The satellite peak for sulphide ion appears at 169.4 eV. All the binding energy values for Ni<sub>9</sub>S<sub>8</sub> are well consistent with the previous reports.<sup>16, 18, 27</sup>

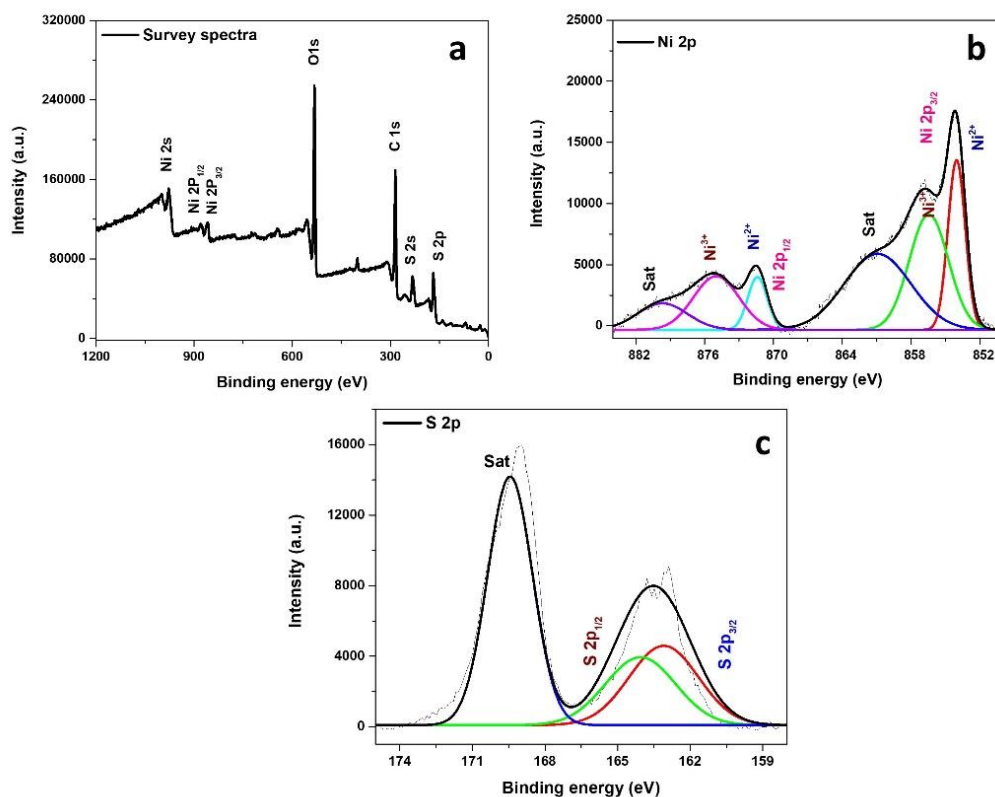


**Figure 5.5:** XPS analysis of Ni<sub>9</sub>S<sub>8</sub> (a) survey spectrum, (b) deconvoluted spectra of Ni 2p and (c) deconvoluted spectra of S 2p.

After Co doping in Ni<sub>9</sub>S<sub>8</sub> (Co<sub>0.05</sub>Ni<sub>8.95</sub>S<sub>8</sub>), the survey spectra in Figure 5.6a show a peak corresponding to Ni, S, C, O, and C. The Ni 2p spectra show two spin-orbit doublets with binding energy at 854.2 eV and 871.6 eV for 2P<sub>3/2</sub> and 2P<sub>1/2</sub>, respectively due to Ni<sup>2+</sup> ion. The binding energy of 857.06 eV and 874.8 eV are due to the presence of Ni<sup>3+</sup> ion for 2P<sub>3/2</sub> and 2P<sub>1/2</sub>, respectively (Figure 5.5b). The shakeup satellite peaks are also present in the doped sample at 862.3 eV and 880 eV. The positive shifting in the binding energy values of Ni 2p confirms the charge transfer of Co in the Ni<sub>9</sub>S<sub>8</sub> system.<sup>53</sup> In the doped sample, the S 2p spectrum shows the binding energy at 162.7 eV and 163.5 eV for 2p<sub>3/2</sub> and 2p<sub>1/2</sub>, respectively, and 169.4 eV is due to the satellite peak (Figure 5.5c). The deconvoluted XPS spectrum of Co doping in Ni<sub>9</sub>S<sub>8</sub> is shown in Figure 5.5d. The Co 2p region exhibits a spin-orbit doublet including Co 2p<sub>3/2</sub> and Co 2p<sub>1/2</sub> at 778.6 eV and 795.5 eV, respectively suggesting the existence of Co<sup>2+</sup> ion in the system. In addition, two satellite peaks are observed at 783.9 and 802.58 eV binding energy. In the XPS study, there is no other peak for Co-S bond formation, which confirms the Co<sup>2+</sup> ion is used as a dopant and the

absence of impurity in the system. Therefore, XPS analysis confirms the charge transfer between  $\text{Co}^{2+}$  and  $\text{Ni}^{2+}/\text{Ni}^{3+}$  systems in the doped sample. The XPS deconvoluted spectra of  $\text{Co}_{0.1}\text{Ni}_{8.9}\text{S}_8$  show analogous binding energy values for  $\text{Ni}^{2+}$ ,  $\text{Ni}^{3+}$ ,  $\text{S}^{2-}$ , and  $\text{Co}^{2+}$  ions. All the binding energy values are tabulated in Table 5.1, which confirms the maximum shift in the binding energy values of the  $\text{Co}_{0.05}\text{Ni}_{8.95}\text{S}_8$  sample.

**Table 5.1:** Comparative table for XPS binding energy values.

Metal ions	$\text{Ni}_9\text{S}_8$	$\text{Co}_{0.1}\text{Ni}_{8.9}\text{S}_8$	$\text{Co}_{0.05}\text{Ni}_{8.95}\text{S}_8$
$\text{Ni}^{2+}(2p_{3/2})$	853.9 eV	854.0 eV	854.2 eV
$\text{Ni}^{3+}(2p_{3/2})$	856.4 eV	856.9 eV	857.06 eV
$\text{S}^{2-}(2p_{3/2})$	163 eV	162.8 eV	162.7 eV
$\text{Co}^{2+}(2p_{3/2})$	-	778.9 eV	779.8 eV
$\text{Co}^{2+}(2p_{1/2})$	-	795.5 eV	797.5 eV

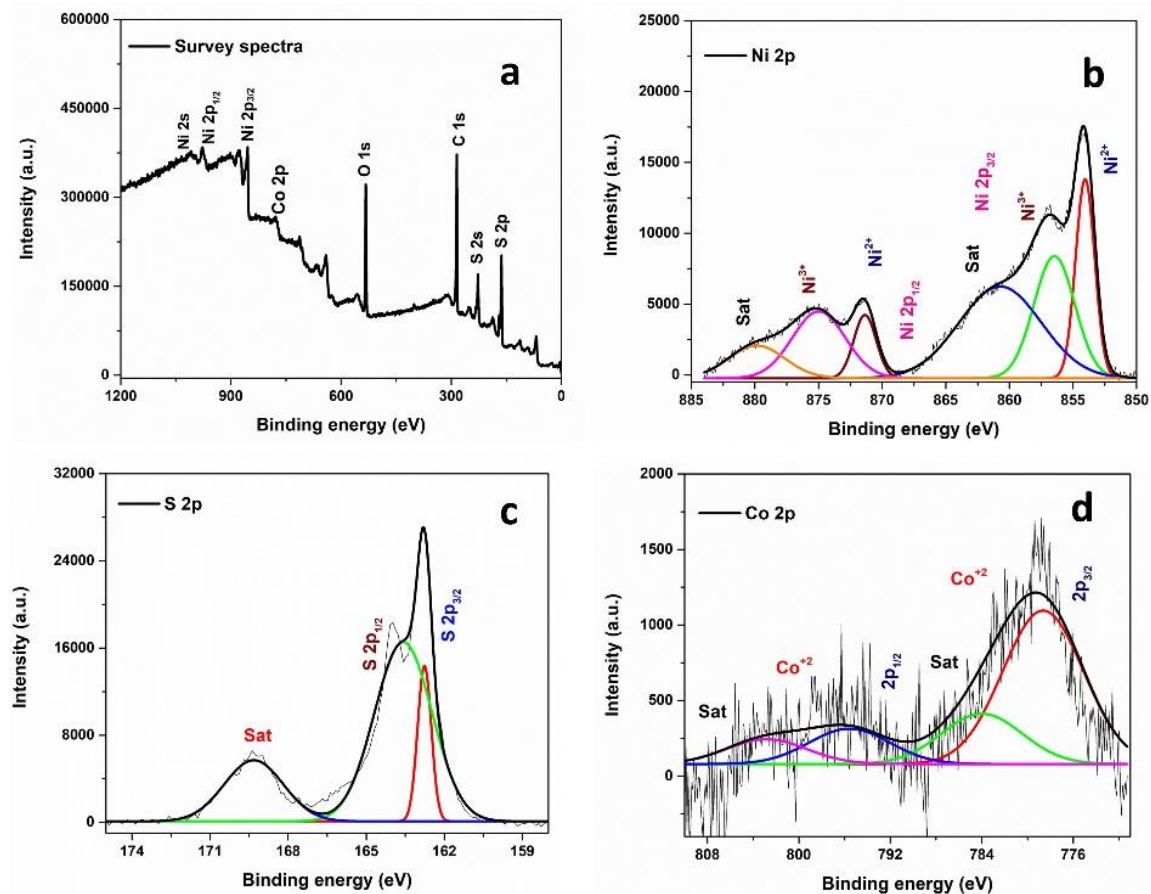


**Figure 5.6:** XPS analysis of  $\text{Co}_{0.05}\text{Ni}_{8.95}\text{S}_8$  (a) survey spectrum, (b) deconvoluted spectra of Ni 2p, (c) deconvoluted spectra of S 2p, and (d) high-resolution spectra of Co 2p.

The shift in the binding energy of Ni 2p at a higher value confirm the Lewis acid behaviour of the  $\text{Co}^{2+}$  ion. Therefore, the electron transfer from  $\text{Ni}^{2+}$  to  $\text{Co}^{2+}$  system is possible due to its Lewis acid nature, which originates the formation of  $\text{Ni}^{3+}$  ion. After Co doping the formation of  $\text{Ni}^{3+}$  ion is favored, which generates active sites for water splitting reaction. Furthermore, to confirm the electron-withdrawing nature of  $\text{Co}^{2+}$  the atomic percentage of  $\text{Ni}^{2+}/\text{Ni}^{3+}$  is calculated before and after doping. The area under the curve for  $\text{Ni}^{2+}$  2p<sub>1/2</sub> peak is 9844.9 before and after doping, whereas, the area for  $\text{Ni}^{3+}$  2p<sub>1/2</sub> peak is 21843 and 26455 in bare and doped  $\text{Ni}_9\text{S}_8$ , respectively. The calculated  $\text{Ni}^{2+}/\text{Ni}^{3+}$  ratio is 0.45 for  $\text{Ni}_9\text{S}_8$  and 0.37 for  $\text{Co}_{0.05}\text{Ni}_{8.95}\text{S}_8$  samples. The decrease in the atomic percentage ratio (0.37) of  $\text{Ni}^{2+}/\text{Ni}^{3+}$  in the  $\text{Co}_{0.05}\text{Ni}_{8.95}\text{S}_8$  sample again confirmed the formation of more  $\text{Ni}^{3+}$  in the system.



**5.3.2 Morphological analysis of doped and undoped Ni<sub>9</sub>S<sub>8</sub>:** FESEM analysis is executed to confirm the morphology and shape of the as-developed materials on the surface of CC. FESEM images of undoped Ni<sub>9</sub>S<sub>8</sub> are shown in Figures 5.7a in different magnifications. At high magnifications, the spherical Ni<sub>9</sub>S<sub>8</sub> nanoparticles are agglomerated and porous in nature, which is uniformly distributed on the surface of CC. FESEM images of Co doped Ni<sub>9</sub>S<sub>8</sub> (Co<sub>0.05</sub>Ni<sub>8.95</sub>S<sub>8</sub>) at low and high magnification are shown in Figures 5.7b, which exhibit agglomerated spherical nanoparticles. After doping with Co there is no change in the shape of the nanoparticles. The FESEM analysis of other doped samples, Co<sub>0.1</sub>Ni<sub>8.9</sub>S<sub>8</sub>, and Co<sub>0.03</sub>Ni<sub>8.97</sub>S<sub>8</sub> are also performed and given in Figure 5.7 c and d. It can be seen from Figures 5.7 that with the increase or decrease in Co doping the particles are aggregated and non-uniform.

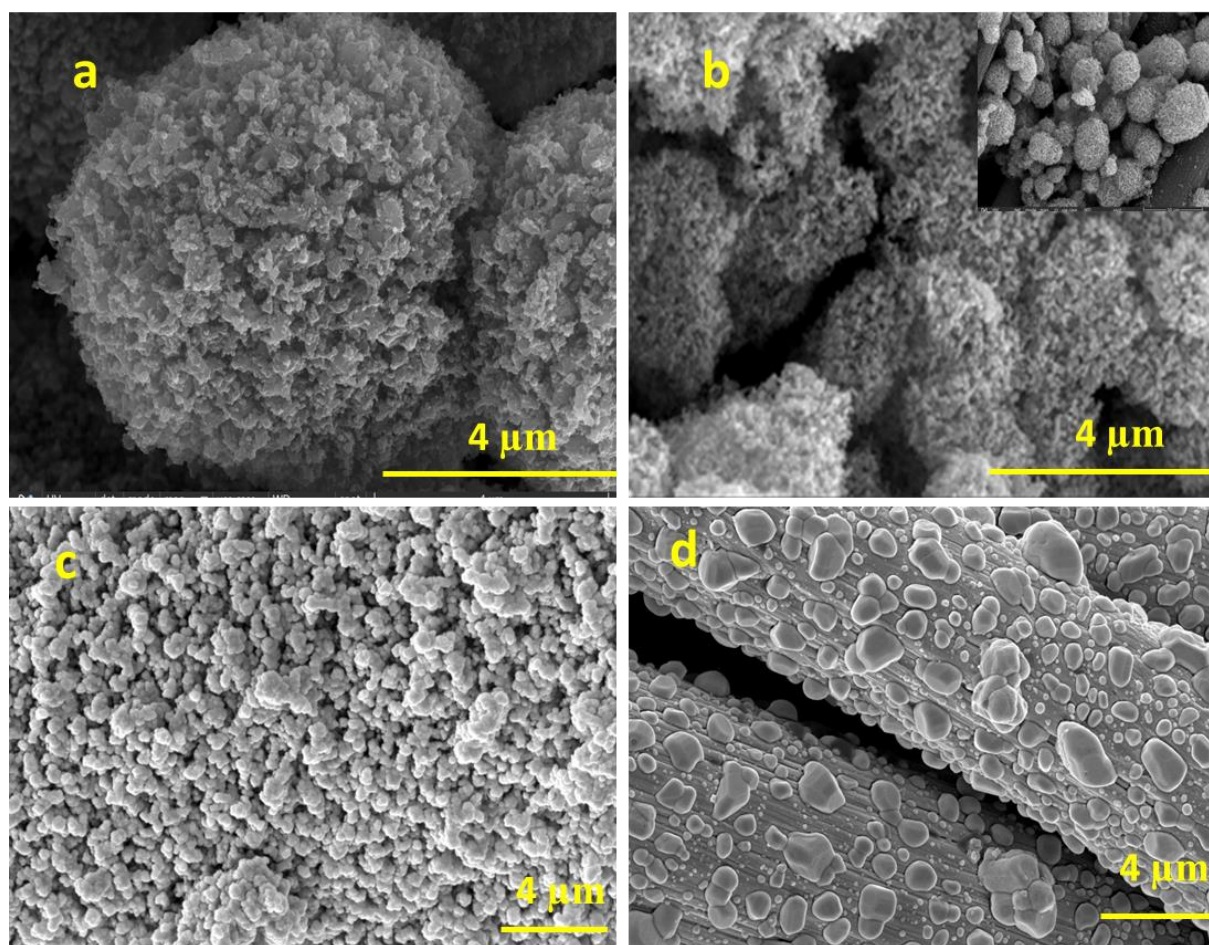


**Figure 5.7:** FESEM images of (a) Ni<sub>9</sub>S<sub>8</sub> (b) Co<sub>0.05</sub>Ni<sub>8.95</sub>S<sub>8</sub> (c) Co<sub>0.1</sub>Ni<sub>8.9</sub>S<sub>8</sub> and (d) Co<sub>0.03</sub>Ni<sub>8.97</sub>S<sub>8</sub> samples. Inset of b represent low magnification image of Co<sub>0.05</sub>Ni<sub>8.95</sub>S<sub>8</sub> catalyst.

The uniform distribution of Ni and S elements in bare Ni<sub>9</sub>S<sub>8</sub> is performed using EDS mapping analysis (Figure 5.8). EDS analysis (Figure 5.9) also confirms the existence and uniform distribution of Co, Ni, and S in the Co doped Ni<sub>9</sub>S<sub>8</sub>. The weight percentage ratio of Co:Ni is 1:20, which is well acquainted with the experimental observation. Furthermore, the ratio of Co:Ni is confirmed from ICP-OES analysis, which represents Co:Ni = 0.87:23.5 in the Co<sub>0.05</sub>Ni<sub>8.95</sub>S<sub>8</sub> sample (Table 5.2).

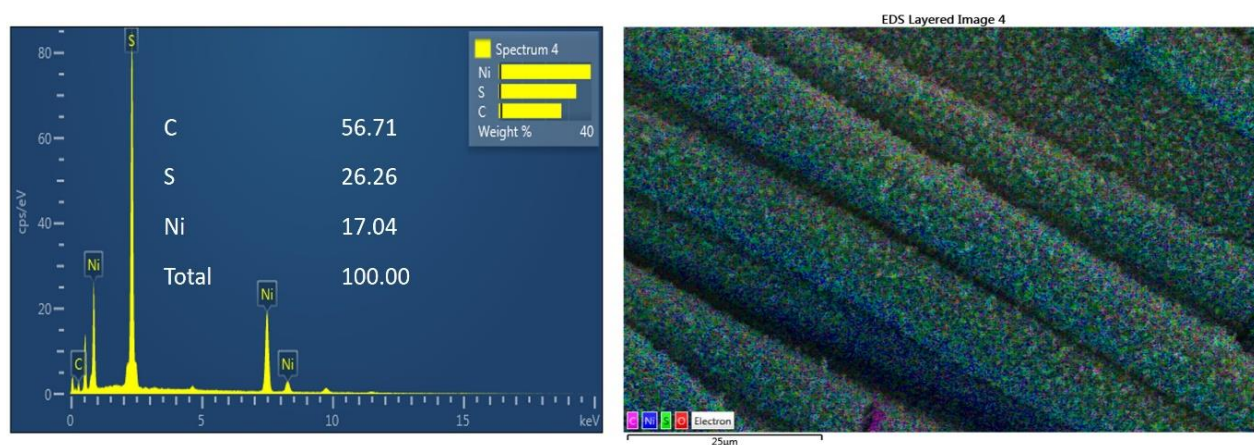


**Figure 5.8:** Elemental composition and EDS mapping showing the distribution of Ni and S on the carbon cloth for Ni<sub>9</sub>S<sub>8</sub> sample.

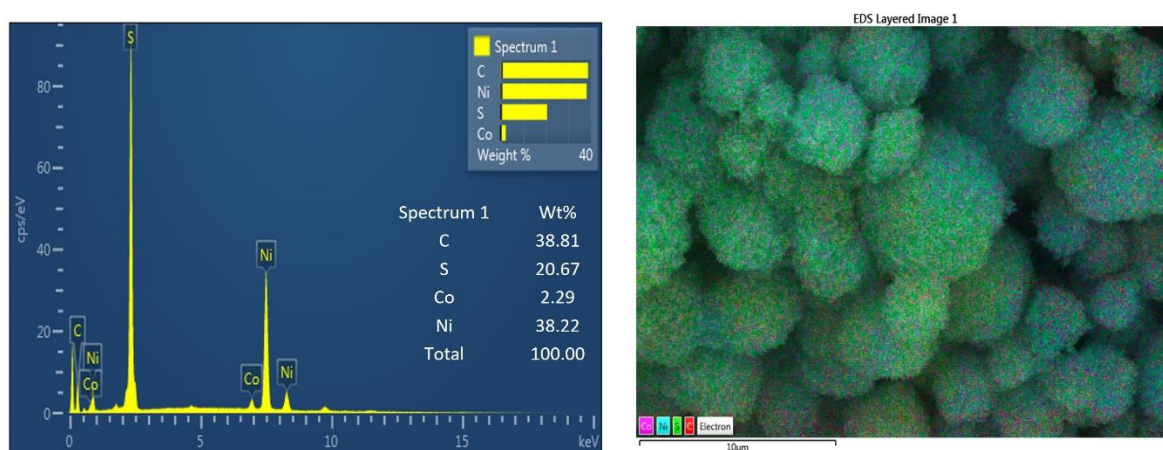


**Figure 5.9:** Elemental composition and EDS mapping showing the distribution of Co, Ni and S on the carbon cloth for Co<sub>0.05</sub>Ni<sub>8.95</sub>S<sub>8</sub> sample.

**Table 5.2:** ICP-AES data for Co<sub>0.05</sub>Ni<sub>8.95</sub>S<sub>8</sub>

Sample	Co	Ni
Co <sub>0.05</sub> Ni <sub>8.95</sub> S <sub>8</sub>	0.87 %	23.5 %



Morphology and crystallinity of the sample are confirmed through TEM, and HRTEM analysis. The high-resolution TEM image of bare  $\text{Ni}_9\text{S}_8$  in Figure 5.10a shows the size of nanoparticle ranges between 60-70 nm with clear lattice fringes. The calculated d-spacing values in Figure 5.10b is 0.27 nm for (222) plane of  $\text{Ni}_9\text{S}_8$  samples. After doping with Co ( $\text{Co}_{0.05}\text{Ni}_{8.95}\text{S}_8$ ) the shape of the nanoparticles remains unchanged and the estimated size is 50-60 nm (5.10c). HRTEM image (Figure 5.10d) of the doped sample shows the d-spacing value of 0.26 nm indexed to (222) planes. The decrement in the d-spacing value confirms the presence of lattice contraction. HRTEM results are well consistent with the XRD analysis.

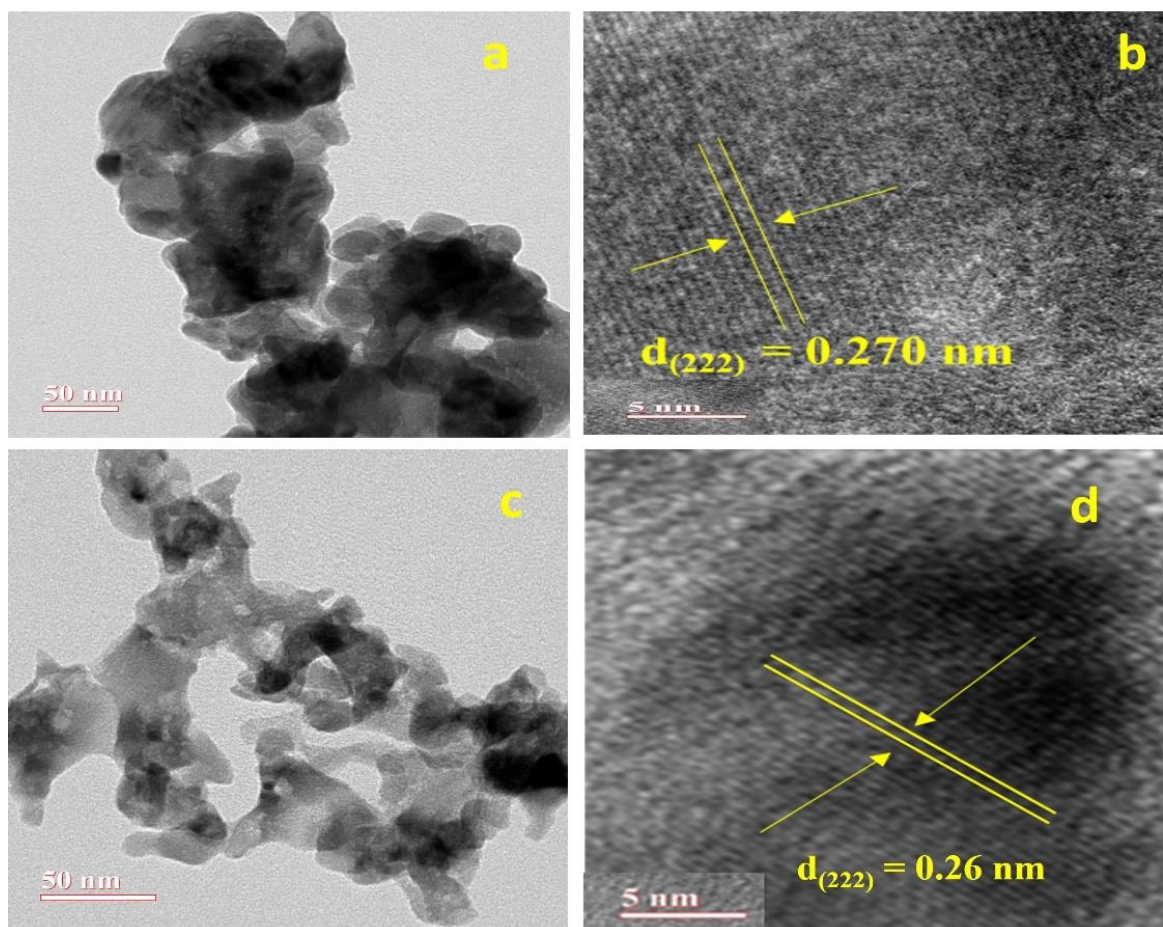


**Figure 5.10:** (a) TEM and (b) HRTEM image of bare  $\text{Ni}_9\text{S}_8$  (c) TEM and (d) HRTEM image of  $\text{Co}_{0.05}\text{Ni}_{8.95}\text{S}_8$ .



### 5.3.3 Electrocatalytic study for HER:

The electrocatalytic HER activity of all the prepared samples, Ni<sub>9</sub>S<sub>8</sub>, Co<sub>0.05</sub>Ni<sub>8.95</sub>S<sub>8</sub>, blank CC, and Pt/C (5%) on the surface of carbon cloth is performed in 1 M KOH solution. Linear sweep voltammogram (LSV) analysis is executed by using sample deposited CC with an area of 0.4×0.4 cm<sup>2</sup> as a working electrode. Figure 5.11a represents the comparative polarization curve of blank CC, bare Ni<sub>9</sub>S<sub>8</sub>, Co<sub>0.05</sub>Ni<sub>8.95</sub>S<sub>8</sub>, and Pt/C catalysts. It is clear from Figure 5.11a that blank CC has negligible conductivity in the potential window. Co<sub>0.05</sub>Ni<sub>8.95</sub>S<sub>8</sub> has the best electrocatalytic activity in comparison with Ni<sub>9</sub>S<sub>8</sub>, which exhibits higher current density and lowest onset potential. It requires only -0.151 V *vs.* RHE potential to generate 10 mA/cm<sup>2</sup> current density, whereas, -0.214 V *vs.* RHE potential is required for Ni<sub>9</sub>S<sub>8</sub>. However, 5% Pt/C catalyst is having the lowest onset potential of -0.04 V *vs.* RHE for 10 mA/cm<sup>2</sup> current density during HER and a comparable current density with Co<sub>0.05</sub>Ni<sub>8.95</sub>S<sub>8</sub>. To optimize the electrocatalytic activity of Co<sub>0.05</sub>Ni<sub>8.95</sub>S<sub>8</sub> two other ratios of Co doping in Ni<sub>9</sub>S<sub>8</sub> are developed, the compared LSV of all the ratios is given in Figure 5.11b. The electrocatalysts, Co<sub>0.1</sub>Ni<sub>8.9</sub>S<sub>8</sub> and Co<sub>0.03</sub>Ni<sub>8.97</sub>S<sub>8</sub> have onset potential of -0.20 V and -0.281 V *vs.* RHE, respectively to produce 10 mA/cm<sup>2</sup> current density. Furthermore, the electrocatalytic activity of bare Co<sub>9</sub>S<sub>8</sub> is checked and shows -0.393 V *vs.* RHE to obtain 10 mA/cm<sup>2</sup> current density (Figure 5.11c). Therefore, the efficient HER activity in 1.0 M KOH solution is observed with Co<sub>0.05</sub>Ni<sub>8.95</sub>S<sub>8</sub>. The graph between onset potential (V) *vs.* RHE and the potential required to generate 50 mA/cm<sup>2</sup> current density is shown in Figure 5.11d, where, Co<sub>0.05</sub>Ni<sub>8.95</sub>S<sub>8</sub> shows the best electrocatalytic activity among other developed electrocatalysts. The histogram plot at potential -0.4 V *vs.* RHE (Figure 5.11e) also confirms the best electrocatalytic activity of Co<sub>0.05</sub>Ni<sub>8.95</sub>S<sub>8</sub>. Thus, the optimum amount of dopant (Co:Ni = 0.05:8.95) in the system enhanced the electrocatalytic activity in an alkaline medium.

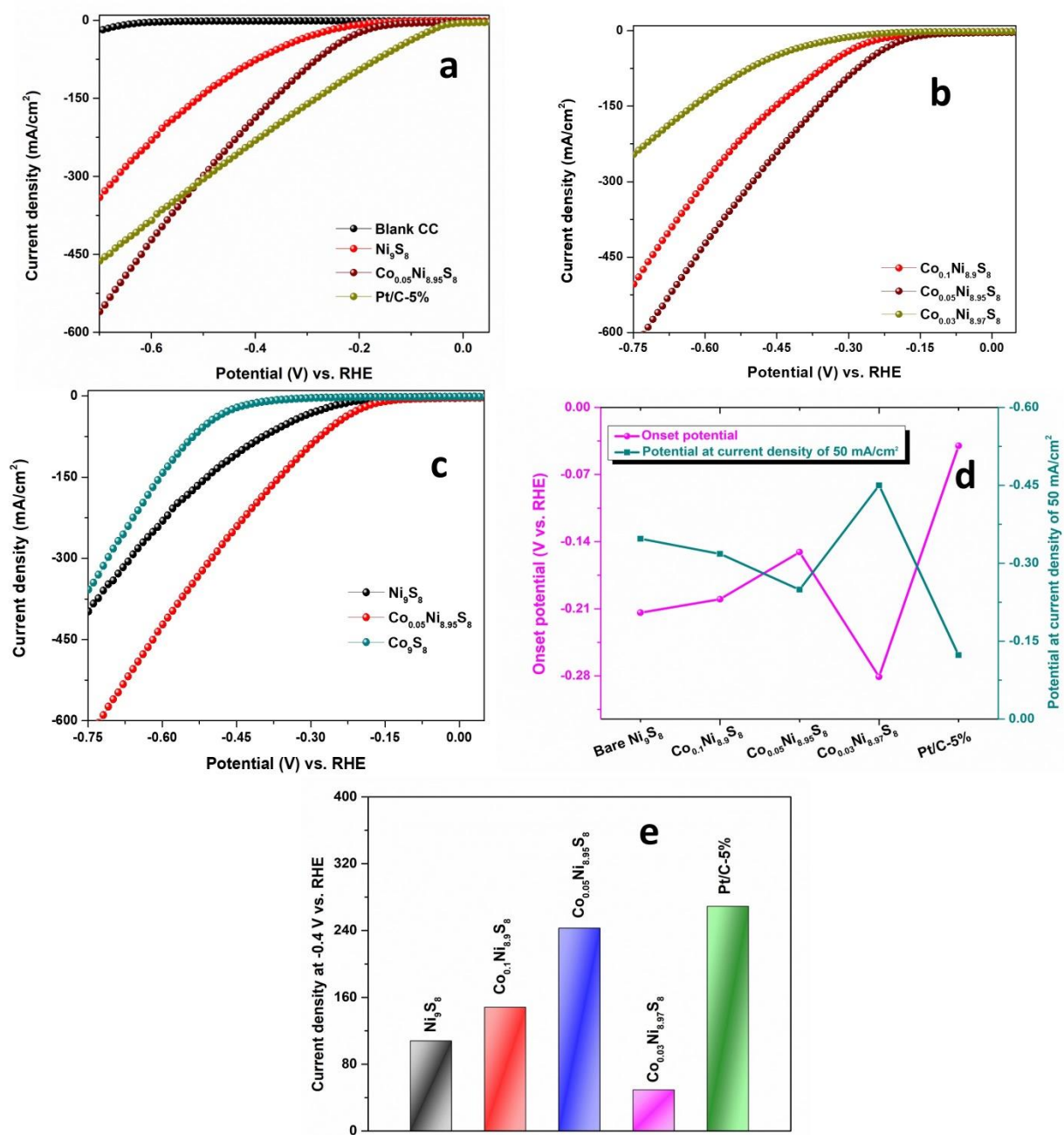


**Figure 5.11:** Polarization HER curve at (a) low scale and (b) Co<sub>0.05</sub>Ni<sub>8.95</sub>S<sub>8</sub>, Co<sub>0.1</sub>Ni<sub>8.9</sub>S<sub>8</sub> and Co<sub>0.03</sub>Ni<sub>8.97</sub>S<sub>8</sub> (c) comparative HER of Co<sub>9</sub>S<sub>8</sub> and Co<sub>0.05</sub>Ni<sub>8.95</sub>S<sub>8</sub> (d) Plot between potential required to produce 50 mA/cm<sup>2</sup> current density and onset potential (V) vs. RHE (e) Histogram plot of current density obtained at -0.4 V vs. RHE of Ni<sub>9</sub>S<sub>8</sub>, Co<sub>0.1</sub>Ni<sub>8.9</sub>S<sub>8</sub>, Co<sub>0.05</sub>Ni<sub>8.95</sub>S<sub>8</sub>, Co<sub>0.03</sub>Ni<sub>8.97</sub>S<sub>8</sub>, and Pt/C samples.

To further explore the effectiveness of  $\text{Co}_{0.05}\text{Ni}_{8.95}\text{S}_8$ , HER activity is checked in wide pH range by using 0.5 M  $\text{H}_2\text{SO}_4$  (pH = 0.0), 0.5 M KOH (pH = 13.69), 1 M KOH (pH = 14), saline water (3.5% NaCl, pH = 6.5), and buffer solution (pH 7) as electrolytes. All the pH-dependent results are shown in Figures 5.12a and b. Figure 5.12b shows the comparative histogram of different pH mediums in which best activity is observed in 1.0 M KOH solution with an onset potential of -151 mV vs. RHE to generate  $10 \text{ mA/cm}^2$  current density. Mass activity is analyzed at potential of -0.3 V vs. RHE and the values are 19.21 A/g, 24.9 A/g, 55.26 A/g, and 7.75 A/g for  $\text{Ni}_9\text{S}_8$ ,  $\text{Co}_{0.1}\text{Ni}_{8.9}\text{S}_8$ ,  $\text{Co}_{0.05}\text{Ni}_{8.95}\text{S}_8$ , and  $\text{Co}_{0.03}\text{Ni}_{8.97}\text{S}_8$ , respectively as mentioned in Table 5.3. Therefore, the above results indicate the higher activity of  $\text{Co}_{0.05}\text{Ni}_{8.95}\text{S}_8$  towards HER in an alkaline medium. After doping with Co the change in the electronic environment of the  $\text{Ni}_9\text{S}_8$  enhances active sites in the system which makes it more efficient towards HER. The orthorhombic structure of  $\text{Ni}_9\text{S}_8$  consists of the average oxidation state of the Ni, which is favorable for electrocatalytic activity. Lee and co-workers<sup>26</sup> also reported the average oxidation state of Ni metal in  $\text{Ni}_9\text{S}_8$  during the growth of mixed metal sulphide hollow cage structure.

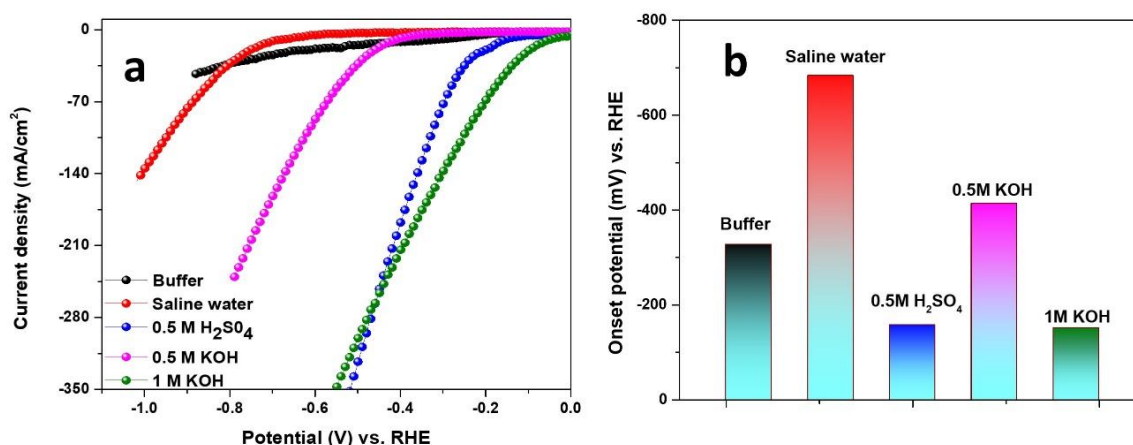


**Figure 5.12:** (a) Comparative LSV of  $\text{Co}_{0.05}\text{Ni}_{8.95}\text{S}_8$  working under different pH medium. (b) Histogram of onset potential to generate  $10 \text{ mA/cm}^2$  current density in different pH medium.

**Table 5.3:** All the electrochemical HER parameters for Ni<sub>9</sub>S<sub>8</sub>, Co<sub>0.1</sub>Ni<sub>8.9</sub>S<sub>8</sub>, Co<sub>0.05</sub>Ni<sub>8.95</sub>S<sub>8</sub>, Co<sub>0.03</sub>Ni<sub>8.97</sub>S<sub>8</sub>, and 5% Pt-C deposited on carbon cloth.

Electrodes	Potential (V) vs. RHE ) required to generate 10 mA/cm <sup>2</sup>	Mass Activity (A/g) at -0.3 V vs. RHE	Tafel Slope (mV/d decade)	R <sub>s</sub> (Ω)	R <sub>CT</sub> (Ω)
Bare Ni <sub>9</sub> S <sub>8</sub>	-0.214	19.21	216	11.52	67.28
Co <sub>0.1</sub> Ni <sub>8.9</sub> S <sub>8</sub>	-0.20	24.9	168	8.93	51.84
Co <sub>0.05</sub> Ni <sub>8.95</sub> S <sub>8</sub>	-0.151	55.26	125	8.58	22.85
Co <sub>0.03</sub> Ni <sub>8.97</sub> S <sub>8</sub>	-0.281	7.75	430	10.48	88.1
Pt/C (5%)	-0.04	-	81.15	-	-

The Tafel slope values are determined to know the kinetics of the HER reaction. The noble catalyst, 5% Pt/C has the Tafel slope value of 81.15 mV/dec (Figure 5.13a). The other Tafel slope value of bare Ni<sub>9</sub>S<sub>8</sub>, Co<sub>0.1</sub>Ni<sub>8.9</sub>S<sub>8</sub>, Co<sub>0.05</sub>Ni<sub>8.95</sub>S<sub>8</sub>, and Co<sub>0.03</sub>Ni<sub>8.97</sub>S<sub>8</sub> are 216, 168, 125, and 430 mV/dec, respectively (Figure 5.13a). The smallest value of the Tafel slope implies the highest electrocatalytic performance. Therefore, Co<sub>0.05</sub>Ni<sub>8.95</sub>S<sub>8</sub> is having higher activity and faster kinetics apart from other doped materials. The calculated exchange current density values for bare Ni<sub>9</sub>S<sub>8</sub> and Co<sub>0.05</sub>Ni<sub>8.95</sub>S<sub>8</sub> are 0.52 and 0.61 mA/cm<sup>2</sup>, respectively, which also favors the higher electrocatalytic activity of the doped sample. To determine the possible mechanism of HER, the detailed processes are given in the SI.<sup>54</sup> The first path is known as Volmer-Tafel and the second is Volmer-Heyrovsky. In the beginning, chemical adsorption of water molecules takes place on the surface of the catalyst through the Volmer step, which is a common step in both mechanisms. Thereafter, in the first path spontaneous desorption of the H<sub>2</sub> molecule, which is known as the Tafel step. In the Heyrovsky step, adsorption of another water molecule and desorption of H<sub>2</sub> molecules happen. Therefore, based on the Tafel slope value Co<sub>0.05</sub>Ni<sub>8.95</sub>S<sub>8</sub> electrocatalyst follows the Volmer-Heyrovsky mechanism for the HER in an alkaline medium. The advantage with the Co doped Ni<sub>9</sub>S<sub>8</sub> materials is Co can promote active site creation for H-H bond formation. Co doping enhances the formation of a higher oxidation state of Ni as explained in XPS results, thus Co doping promotes the formation of Ni<sup>3+</sup> species which is useful for OH<sup>-</sup> adsorption. Furthermore, the synergistic effect of Co and Ni makes the developed catalyst more beneficial for the adsorption

of H ( $H_{\text{ads}}$ ).  $\text{Co}_{0.05}\text{Ni}_{8.95}\text{S}_8$  is highly active and has a faster rate towards HER. Gong and coworkers<sup>55</sup> reported Co doping in  $\text{Ni}_3\text{S}_2$  materials, which is helpful for H-H bond formation by lowering the kinetic energy barrier. Using DFT calculation, they have explained that Co doping enhanced the hydrogen adsorption leading to superior HER activity.

The higher electrocatalytic activity of  $\text{Co}_{0.05}\text{Ni}_{8.95}\text{S}_8$  is examined by electrochemical impedance spectroscopy (EIS) analysis. The onset potential is chosen as executed bias and Figure 5.13b shows the semicircle curve of the materials. EIS analysis of other materials, bare  $\text{Ni}_9\text{S}_8$ ,  $\text{Co}_{0.05}\text{Ni}_{8.95}\text{S}_8$ ,  $\text{Co}_{0.1}\text{Ni}_{8.9}\text{S}_8$ , and  $\text{Co}_{0.03}\text{Ni}_{8.97}\text{S}_8$  are also performed. The obtained data are fitted into the equivalent circuit as given in the inset of Figure 5.13b, which provides the value of the solution resistance ( $R_s$ ) and charge transfer resistance ( $R_{\text{CT}}$ ). The lower value of  $R_{\text{CT}}$  signifies the higher charge transportation, which shows the higher conductivity of the synthesized material.  $\text{Co}_{0.05}\text{Ni}_{8.95}\text{S}_8$  has the lowest value of 8.58  $\Omega$  and 22.85  $\Omega$  for  $R_s$  and  $R_{\text{CT}}$ , respectively than other developed materials, as shown in Table 5.3. Therefore, the amount of Co is optimized in  $\text{Co}_{0.05}\text{Ni}_{8.95}\text{S}_8$  (Co:Ni = 0.05:8.95), where, Co enhances the conductivity of  $\text{Ni}_9\text{S}_8$ . The observed results confirm that doping increases the conductivity, which may be due to the following reasons. First, doping arises compressive strain in the  $\text{Ni}_9\text{S}_8$  matrix, which further increases the number of active sites. Second, doping can modulate the electronic environment of  $\text{Ni}^{+2/+3}$  in the  $\text{Ni}_9\text{S}_8$ . Third, higher charge transportation and faster kinetics improve the electrocatalytic activity.

An important parameter for the practical application of water splitting reactions is long-term stability. Figure 5.13c represents the consecutive 1000 cycle LSV of  $\text{Co}_{0.05}\text{Ni}_{8.95}\text{S}_8$  which signifies the insignificant change in the value of current density as well as onset potential. For long-term stability, chronoamperometry is checked at a fixed potential to generate a 100  $\text{mA}/\text{cm}^2$  current density for continuous 60 hours (Figure 5.13d). There is no alteration in current density after 60 hours, so, the developed  $\text{Co}_{0.05}\text{Ni}_{8.95}\text{S}_8$  is having robust nature and is highly durable for HER in 1.0 M KOH solution. The comparative table with reported literature for HER is given in Table 5.4.

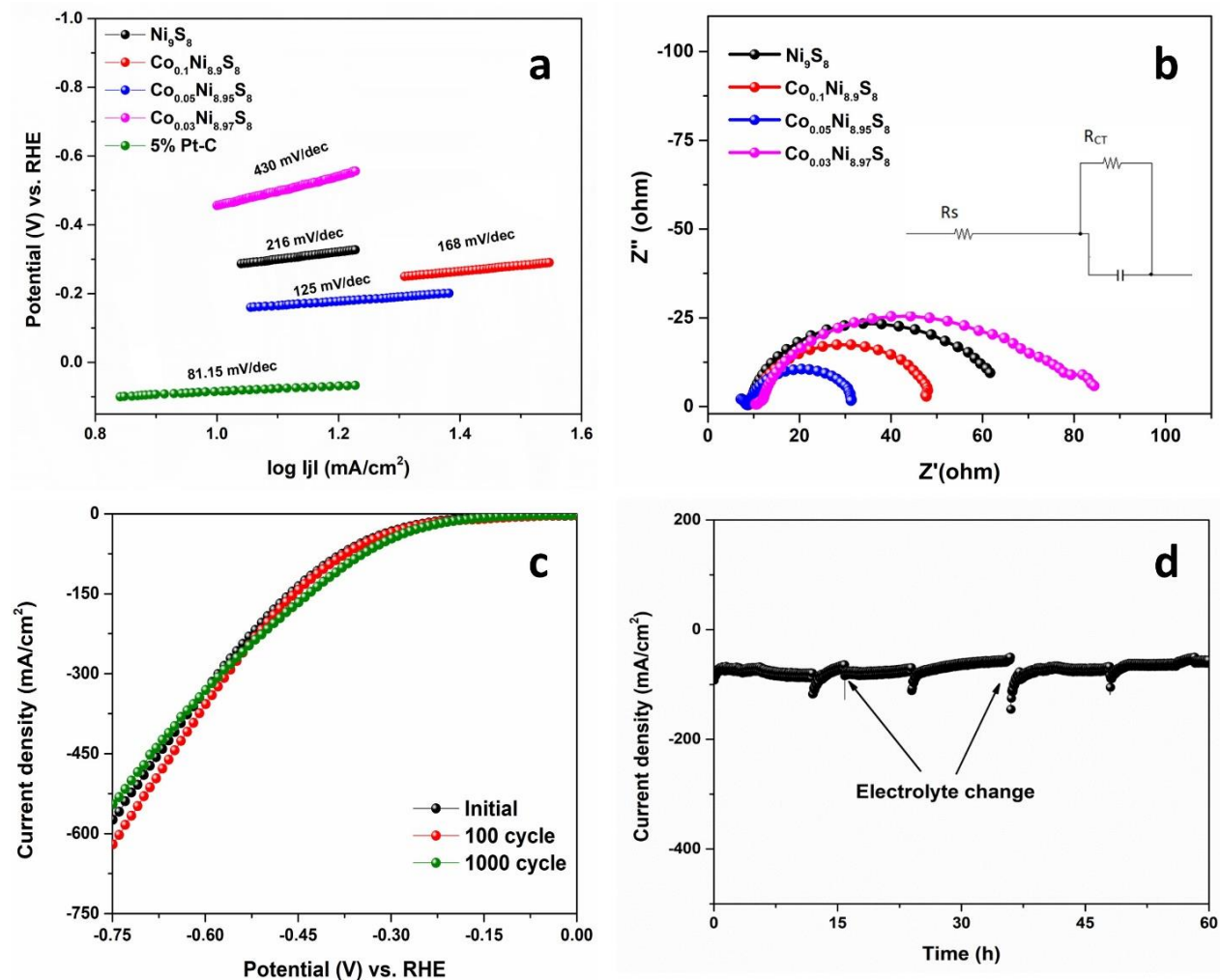


**Figure 5.13:** (a) Tafel plot and (b) Nyquist plots of materials. Tafel slope of Ni<sub>9</sub>S<sub>8</sub>, Co<sub>0.1</sub>Ni<sub>8.9</sub>S<sub>8</sub>, Co<sub>0.05</sub>Ni<sub>8.95</sub>S<sub>8</sub>, Co<sub>0.03</sub>Ni<sub>8.97</sub>S<sub>8</sub>, and Pt/C is included in Fig. (a). The inset of Fig. (b) shows the corresponding equivalent circuit. (c) Polarization HER curve of Co<sub>0.05</sub>Ni<sub>8.95</sub>S<sub>8</sub> electrocatalyst for initial, and after 1000 cycles. (d) Chronoamperometric data was recorded for 60 hours at a fixed potential for HER.

**Table 5.4:** A comparative HER study of all the electrochemical parameters with the electrocatalyst.

S.N.	Electrocatalyst	Electrolyte	Current density (mA/cm <sup>2</sup> )	Potential (mV vs. RHE)	Tafel slope	Ref.
1.	Co-Ni <sub>3</sub> S <sub>2</sub> /Ni foam	1 M KOH	10	80	75	55
2.	CuNiS nanowires/ Carbon paper	1 M KOH	10	71	44	24
3.	Fe doped NiS <sub>2</sub>	1 M KOH	10	121	37	21
4.	Ni/Ni <sub>9</sub> S <sub>8</sub>	1 M KOH	10	230	123.3	22
5.	Co <sub>0.05</sub> Ni <sub>8.95</sub> S <sub>8</sub>	1 M KOH	10	151	125	This work

### 5.3.3 Electrocatalytic study for OER

The outstanding electrocatalytic activity of Co doped Ni<sub>9</sub>S<sub>8</sub> is confirmed through OER in an alkaline medium. Three-electrode setup and 1.0 M KOH solution is used as an electrolyte to evaluate the OER performance of Ni<sub>9</sub>S<sub>8</sub>, Co<sub>0.1</sub>Ni<sub>8.9</sub>S<sub>8</sub>, Co<sub>0.05</sub>Ni<sub>8.95</sub>S<sub>8</sub>, and Co<sub>0.03</sub>Ni<sub>8.97</sub>S<sub>8</sub> with a scan rate of 2 mV/sec. Figures 5.14a represent the polarization LSV of bare CC, Ni<sub>9</sub>S<sub>8</sub>, Co<sub>0.05</sub>Ni<sub>8.95</sub>S<sub>8</sub>, and commercial RuO<sub>2</sub>, which exhibits the negligible effect of bare CC in the applied potential window. Figure 5.14b shows the comparative LSV curve of Co<sub>0.05</sub>Ni<sub>8.95</sub>S<sub>8</sub> and the other two ratios. The onset potential for Ni<sub>9</sub>S<sub>8</sub>, Co<sub>0.1</sub>Ni<sub>8.9</sub>S<sub>8</sub>, Co<sub>0.05</sub>Ni<sub>8.95</sub>S<sub>8</sub>, and Co<sub>0.03</sub>Ni<sub>8.97</sub>S<sub>8</sub> are 1.588 V, 1.574 V, 1.557 V, and 1.607 V *vs.* RHE, respectively, to generate 30 mA/cm<sup>2</sup> current density, where, Co<sub>0.05</sub>Ni<sub>8.95</sub>S<sub>8</sub> shows the best OER performance with the lowest value of onset potential and larger current density compared to other electrocatalysts (Table 5.5). The superior electrocatalytic performance of Co<sub>0.05</sub>Ni<sub>8.95</sub>S<sub>8</sub> is further compared with commercial RuO<sub>2</sub>, which is having a high value of onset potential (1.562 V *vs.* RHE). By changing the Co amount in the Ni<sub>9</sub>S<sub>8</sub> system, onset potential also shifted cathodically with a value of 0.04 V *vs.* RHE. The plot of onset potential *vs.* potential required to generate 100 mA/cm<sup>2</sup> current density is represented in Figure 5.14c which again confirms the superior activity of Co<sub>0.05</sub>Ni<sub>8.95</sub>S<sub>8</sub>. Figure 5.14d represents the comparative



current density at 1.65 V vs. RHE, in which  $\text{Co}_{0.05}\text{Ni}_{8.95}\text{S}_8$  exhibits the best electrocatalytic activity than commercial  $\text{RuO}_2$  and other developed electrocatalysts.

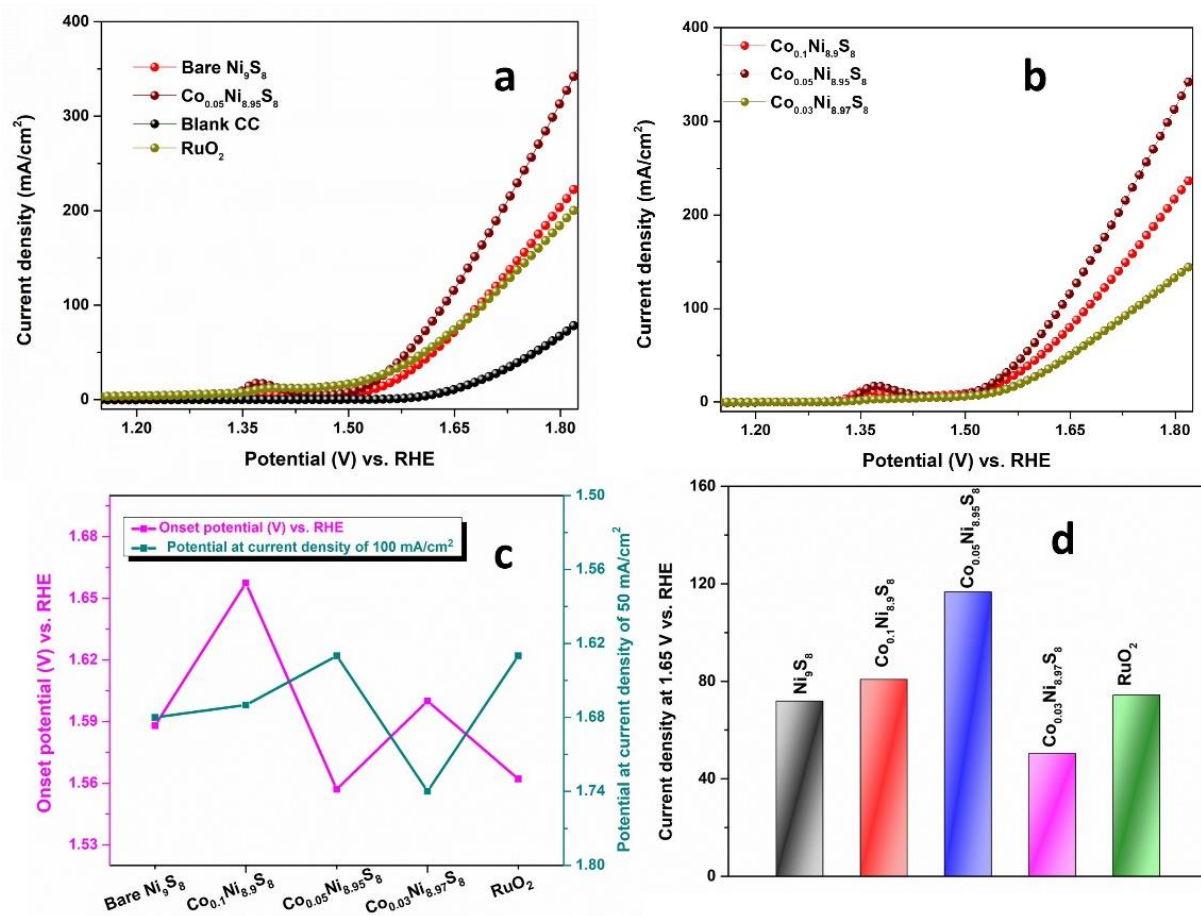


**Figure 5.14:** Polarization OER curve at (a) low scale and (b) comparative (c) Plot between potential required to produce 100 mA/cm<sup>2</sup> current density and onset potential (V) vs. RHE (d) Histogram plot of current density obtained at 1.65 V vs. RHE of Ni<sub>9</sub>S<sub>8</sub>, Co<sub>0.1</sub>Ni<sub>8.9</sub>S<sub>8</sub>, Co<sub>0.05</sub>Ni<sub>8.95</sub>S<sub>8</sub>, Co<sub>0.03</sub>Ni<sub>8.97</sub>S<sub>8</sub>, and RuO<sub>2</sub> samples.

To further explore the effectiveness of  $\text{Co}_{0.05}\text{Ni}_{8.95}\text{S}_8$ , OER activity is checked in wide pH range by using 0.5 M  $\text{H}_2\text{SO}_4$  (pH = 0.0), 0.5 M KOH (pH = 13.69), 1 M KOH (pH = 14), saline water (3.5% NaCl, pH = 6.5), and buffer solution (pH=7) as electrolytes. All the pH-dependent electrocatalytic results are shown in Figure 5.15. The optimized  $\text{Co}_{0.05}\text{Ni}_{8.95}\text{S}_8$  shows the best electrocatalytic activity in 1 M KOH solution.



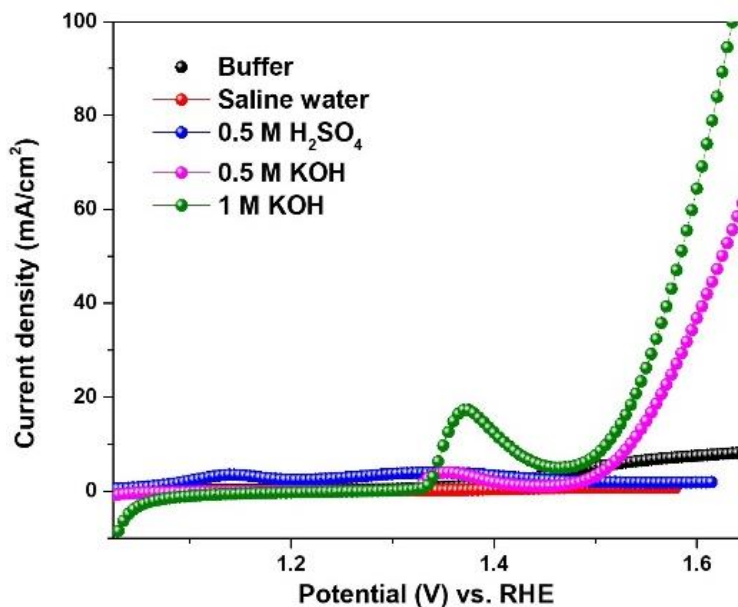


**Figure 5.15:** Comparative pH study for OER of  $\text{Co}_{0.05}\text{Ni}_{8.95}\text{S}_8$ .

To further confirm the higher electrocatalytic activity of the efficient electrocatalyst, other parameters like ECSA and mass activity are calculated. A higher value of ECSA signifies a larger number of active sites and better electrocatalytic activity. Figure 5.16 shows the CV analysis at various scan rates in the non-faradaic area and after that, at the fixed potential of 1.125 V vs. RHE, the current is plotted versus the scan rate and the fitted slope value represents double-layer capacitance ( $C_{dl}$ ). Bare  $\text{Ni}_9\text{S}_8$  is having an ECSA value of  $1.06 \text{ cm}^2$ , whereas,  $\text{Co}_{0.05}\text{Ni}_{8.95}\text{S}_8$  shows an ECSA value of  $23 \text{ cm}^2$ . The ECSA values for  $\text{Co}_{0.1}\text{Ni}_{8.9}\text{S}_8$  and  $\text{Co}_{0.03}\text{Ni}_{8.97}\text{S}_8$  electrocatalysts are  $7.68 \text{ cm}^2$  and  $0.389 \text{ cm}^2$ , respectively. The roughness factor is also calculated from the ECSA value,  $\text{Co}_{0.05}\text{Ni}_{8.95}\text{S}_8$  is 21.7 times higher than  $\text{Ni}_9\text{S}_8$ , thus doping of Co enhances the roughness and electrocatalytic activity. The mass activity is determined at a fixed potential of 1.65 V vs. RHE for  $\text{Ni}_9\text{S}_8$ ,  $\text{Co}_{0.1}\text{Ni}_{8.9}\text{S}_8$ ,  $\text{Co}_{0.05}\text{Ni}_{8.95}\text{S}_8$ , and  $\text{Co}_{0.03}\text{Ni}_{8.97}\text{S}_8$ , as mentioned in Table 5.5. The  $\text{Co}_{0.05}\text{Ni}_{8.95}\text{S}_8$  is having a higher mass activity value of  $71.57 \text{ A/g}$  which further confirms higher OER activity.

**Table 5.5:** All the electrochemical OER parameters for  $\text{Ni}_9\text{S}_8$ ,  $\text{Co}_{0.1}\text{Ni}_{8.9}\text{S}_8$ ,  $\text{Co}_{0.05}\text{Ni}_{8.95}\text{S}_8$ ,  $\text{Co}_{0.03}\text{Ni}_{8.97}\text{S}_8$ , and commercial  $\text{RuO}_2$ .

Electrodes	Potential (V) vs. RHE ) required to generate 30 $\text{mA}/\text{cm}^2$	ECSA ( $\text{cm}^2$ )	$R_f$	Mass Activity ( $\text{A}/\text{g}$ ) at 1.65 V vs. RHE	Tafel Slope ( $\text{mV}/\text{d}$ ecade)	$R_s$ ( $\Omega$ )	$R_{CT}$ ( $\Omega$ )
Bare $\text{Ni}_9\text{S}_8$	1.588	1.06	6.625	44.04	128.8	9.85	40.52
$\text{Co}_{0.1}\text{Ni}_{8.9}\text{S}_8$	1.574	7.68	48	49.52	83.7	9.02	36.84
$\text{Co}_{0.05}\text{Ni}_{8.95}\text{S}_8$	1.557	23	143.75	71.57	49.8	8.97	8.14
$\text{Co}_{0.03}\text{Ni}_{8.97}\text{S}_8$	1.607	0.389	2.43	30.85	135.9	13.7	66.35
$\text{RuO}_2$	1.562	-	-	-	82.3	-	-

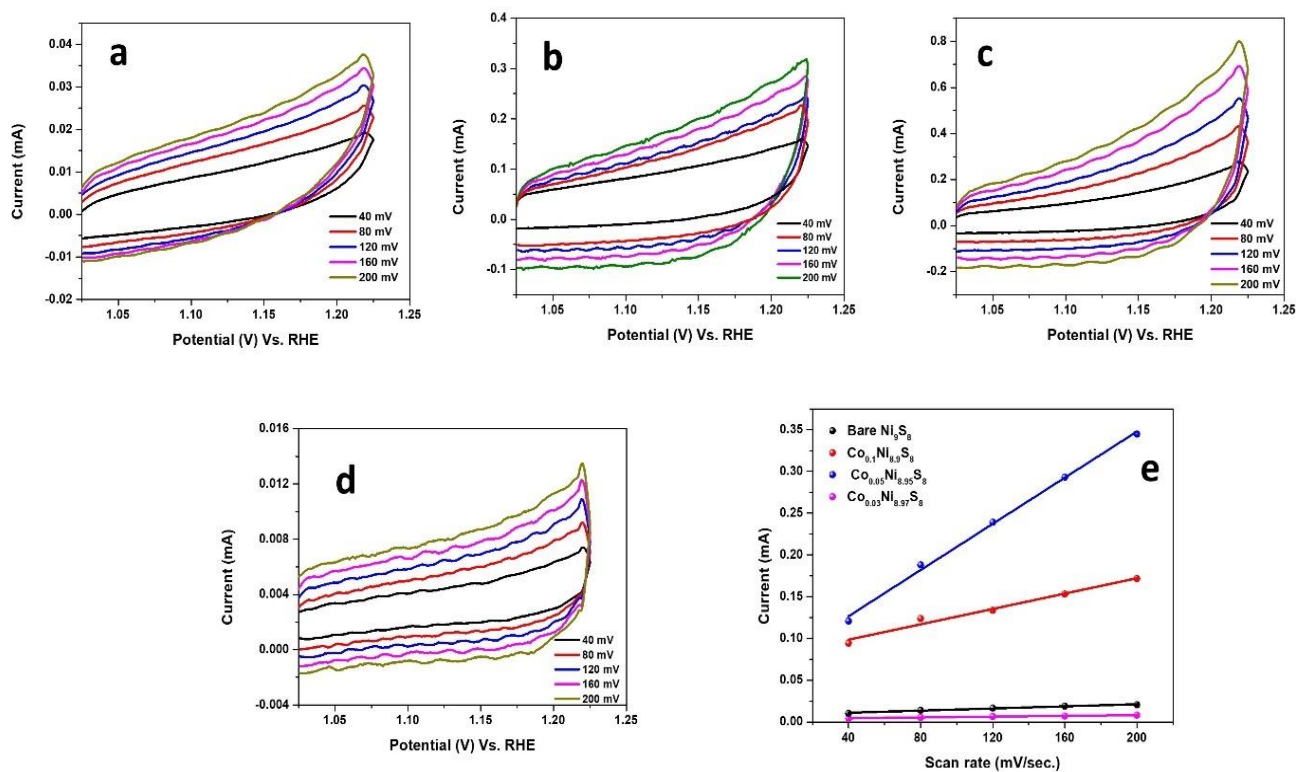


**Figure 5.16:** Cyclic voltammetry curves of  $\text{Co}_{0.05}\text{Ni}_{8.95}\text{S}_8$  at different scan rate (a) (b) (c) (d) capacitive current at 1.125 (V vs. RHE) as a function of scan rate for ECSA calculation (e).

To judge the role of dopants in the  $\text{Ni}_9\text{S}_8$  system cyclic voltammogram (CV) analysis is done and shown in Figure 5.17. CV curves of bare  $\text{Ni}_9\text{S}_8$ ,  $\text{Co}_{0.1}\text{Ni}_{8.9}\text{S}_8$ ,  $\text{Co}_{0.05}\text{Ni}_{8.95}\text{S}_8$ , and

$\text{Co}_{0.03}\text{Ni}_{8.97}\text{S}_8$  catalysts show one anodic and the cathodic peak in 1.025 to 1.65 V vs. RHE potential window. In  $\text{Ni}_9\text{S}_8$  the peak present at 1.40 V and 1.28 V vs. RHE represents the redox couple,  $\text{Ni}^{2+}/\text{Ni}^{3+}$ . After Co doping the redox peak of  $\text{Ni}^{2+}/\text{Ni}^{3+}$  shifted towards 1.48 V and 1.27 V vs. RHE, the anodic shift in the oxidation peak is well corroborated with the effect of doping. By increasing the dopant amount the peak shifted again into the cathodic side which shows the conductivity of  $\text{Ni}_9\text{S}_8$  remains unchanged. Therefore, the optimized ratio of Co:Ni = 0.05:8.95 is developed for an efficient and robust electrocatalyst. In the CV analysis, the area under the curve is directly proportional to the conductivity of the electrocatalyst, where,  $\text{Co}_{0.05}\text{Ni}_{8.95}\text{S}_8$  is having the highest value of the area, which further confirms higher conductivity and better efficiency for OER. In this context, Akbari and co-workers<sup>56</sup> also reported peak shifting of the  $\text{Ni}^{2+}/\text{Ni}^{3+}$  system in the Ni/NiO interface with an impurity of Fe.

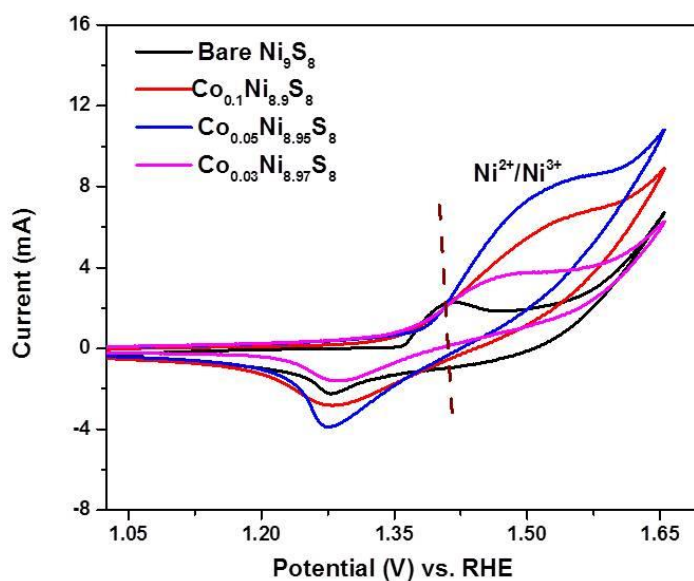


**Figure 5.17:** CV analysis of all the developed electrocatalyst in a particular potential window.

The Tafel slope is an important parameter to decide the kinetics of OER. The slope value is determined using the standard Tafel equation (given in SI). The electrocatalyst,  $\text{Co}_{0.05}\text{Ni}_{8.95}\text{S}_8$  is having the lowest value (49.8 mV/dec) of the Tafel slope, whereas, bare  $\text{Ni}_9\text{S}_8$  shows 128.8 mV/dec (Figure 5.18a). The faster kinetics of the OER process occurs at the  $\text{Co}_{0.05}\text{Ni}_{8.95}\text{S}_8$  surface. Commercial  $\text{RuO}_2$  is having 82.3 mV/dec Tafel slope, which is well-matched with the literature.<sup>57</sup> Furthermore, the better conductivity and ease of electron transportation of Co doped  $\text{Ni}_9\text{S}_8$  EIS

analysis is performed by applying onset potential with a frequency range of 50 kHz to 0.5 Hz (Figure 5.18b). The fitted Nyquist plot gives the value of the solution resistance ( $R_S$ ) and charge transfer resistance ( $R_{CT}$ ) of 8.97  $\Omega$  and 8.14  $\Omega$ , respectively for  $\text{Co}_{0.05}\text{Ni}_{8.95}\text{S}_8$ . The smaller value of  $R_{CT}$  provides more charge transportation and higher conductivity. Finally, the OER stability of the optimized electrocatalyst is checked up to 1000 consecutive LSV cycles (Figure 5.18c), which shows unchanged current density. For long-term stability, chronoamperometry analysis is performed for 80 hours at an applied potential of 1.60 V vs. RHE. Figure 5.18d exhibits unaltered current density by using  $\text{Co}_{0.05}\text{Ni}_{8.95}\text{S}_8$ . Therefore,  $\text{Co}_{0.05}\text{Ni}_{8.95}\text{S}_8$  is a highly stable and robust electrocatalyst for oxygen evolution.

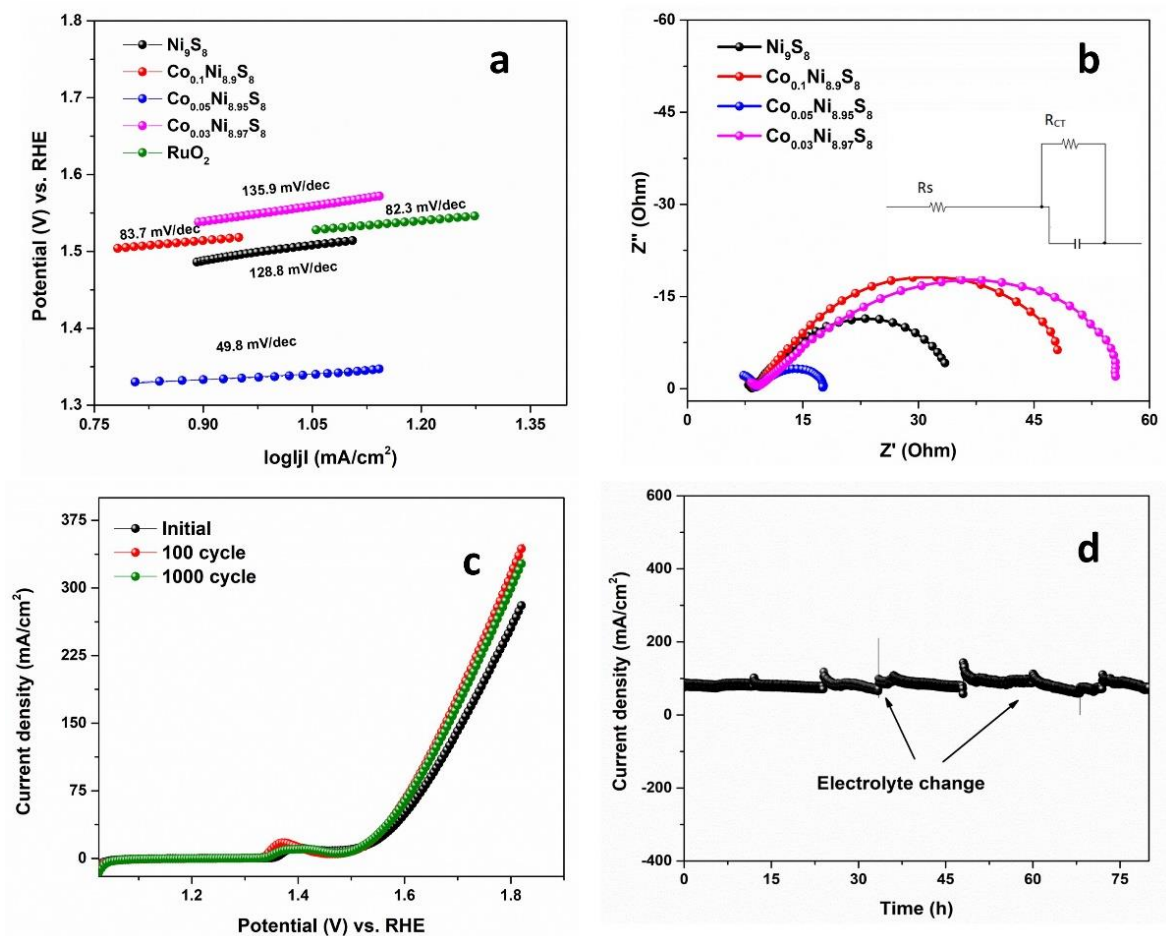


**Figure 5.18:** (a) Tafel plot for OER and (b) Nyquist plots of materials. Tafel slope of  $\text{Ni}_9\text{S}_8$ ,  $\text{Co}_{0.1}\text{Ni}_{8.9}\text{S}_8$ ,  $\text{Co}_{0.05}\text{Ni}_{8.95}\text{S}_8$ , and  $\text{Co}_{0.03}\text{Ni}_{8.97}\text{S}_8$ , is included in Fig. (a). The inset of Fig. (b) shows the corresponding equivalent circuit. (c) Polarization OER curve of  $\text{Co}_{0.05}\text{Ni}_{8.95}\text{S}_8$  electrocatalyst

for initial, and after 1000 cycles. (d) Chronoamperometric data for 80 hours at a fixed negative potential.

Moreover, FESEM analysis (Figure 5.19a) is performed after long-term electrocatalysis. There is no significant change in the morphology of  $\text{Co}_{0.05}\text{Ni}_{8.95}\text{S}_8$  materials after OER in an alkaline medium. EDS analysis (Figure 5.19b) is also done which gives the uniform distribution of Co, Ni, S, and C elements. The PXRD result (Figure 5.20) shows that the peaks of  $\text{Co}_{0.05}\text{Ni}_{8.95}\text{S}_8$  samples are retained after the OER study. However, two new small intense peaks ( $2\theta = 37.8^\circ$  and  $54.8^\circ$ ) appear for NiOOH species, which may be due to surface oxidation of  $\text{Co}_{0.05}\text{Ni}_{8.95}\text{S}_8$  during OER.

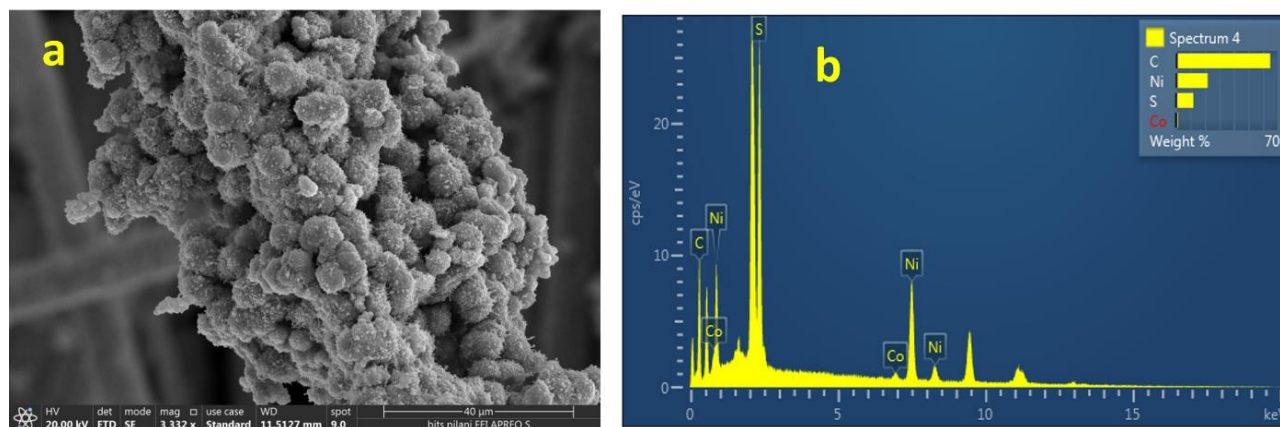


**Figure 5.19:** (a) FESEM image (b) EDS of  $\text{Co}_{0.05}\text{Ni}_{8.95}\text{S}_8$  after electrocatalysis.

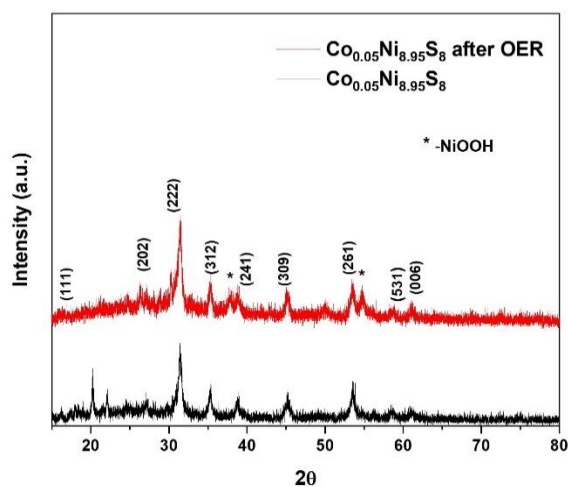


**Figure 5.20:** XRD of  $\text{Co}_{0.05}\text{Ni}_{8.95}\text{S}_8$  after electrocatalysis.

XPS analysis (Figure 5.21) of the electrocatalyst is also performed after OER activity that exhibits similar binding energy values of  $\text{Ni}^{2+}$ ,  $\text{Ni}^{3+}$ ,  $\text{Co}^{2+}$ , and  $\text{S}^{2-}$  ions. Compared with the fresh electrocatalyst, the sulfide ion intensities are decreased. In literature also there are reports which suggest that in metal sulfides post-OER hydroxide/oxyhydroxide species is formed which is also an active site.<sup>58, 59</sup> Zhu and group<sup>60</sup> also hypothesized  $\text{NiOOH}@ \text{NiS}$  to behave as an active site post-long-term OER analysis.

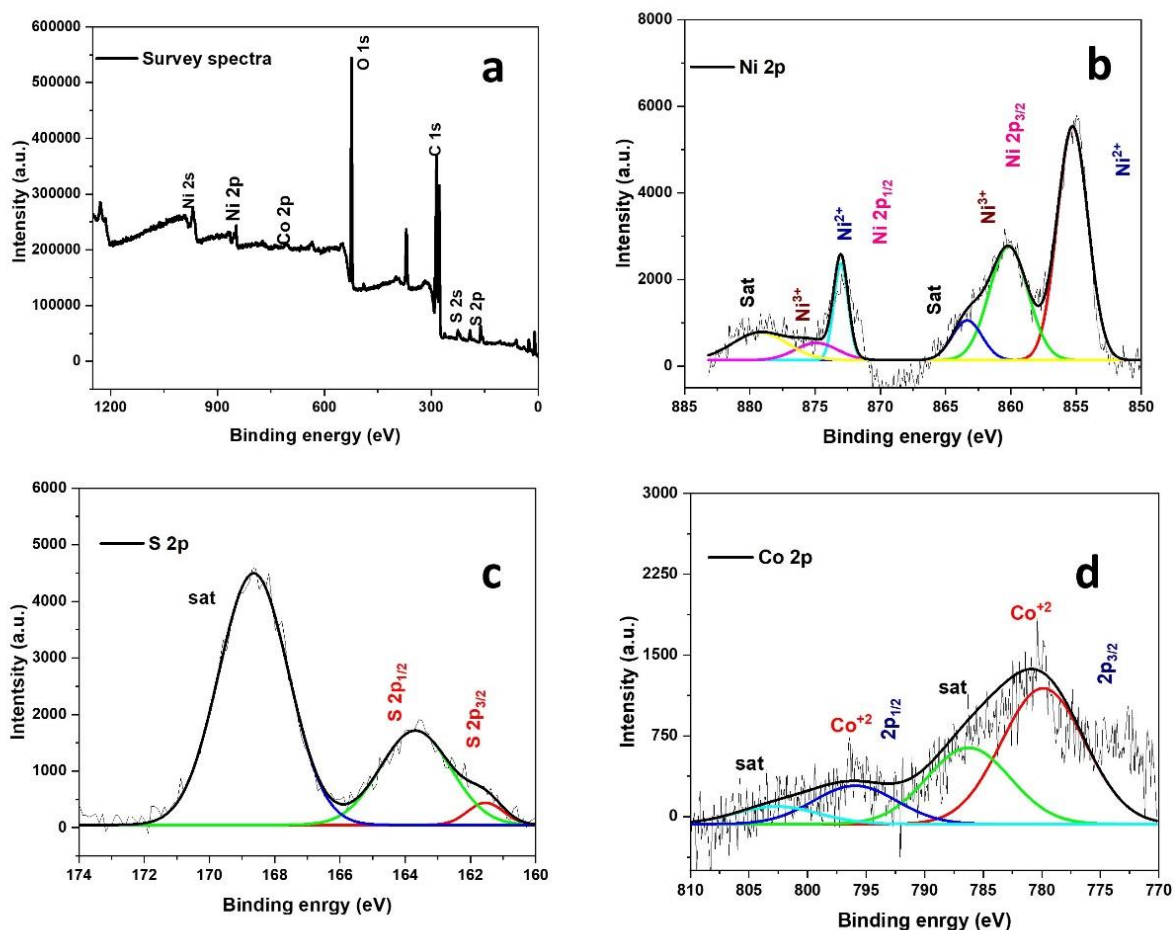


**Figure 5.21:** XPS analysis of  $\text{Co}_{0.05}\text{Ni}_{8.95}\text{S}_8$  after OER electrocatalysis.

Thus, all the above results validate that due to doping with Co, the electrocatalyst shows improved electrocatalytic performance. The best-optimized ratio,  $\text{Co}_{0.05}\text{Ni}_{8.95}\text{S}_8$  nanomaterial exhibits maximum efficiency in water-splitting reaction. Doping of cation is an important approach to improve the electrocatalytic activity due to the availability of unfilled d-orbital. Therefore, a few important factors are evolved for better electrocatalytic efficiency of  $\text{Co}_{0.05}\text{Ni}_{8.95}\text{S}_8$ . First,



PXRD analysis confirmed that the material shows compressive strain, which changes the electronic environment. Second, XPS analysis authorizes the shifting in the binding energy of Ni to a higher value and the electropositive behaviour of Ni enhanced, which promotes the reaction kinetics and formation of a more active site. Third, the lattice contraction after doping is confirmed by the HRTEM analysis. Fourth, the composition of Co:Ni in the  $\text{Co}_{0.05}\text{Ni}_{8.95}\text{S}_8$  sample is confirmed through ICP-AES and EDS mapping analyses, which gives 1:20 ratio of Co:Ni and is well-matched with the experimental condition. Therefore, the optimized doped electrocatalyst authorizes efficient activity and durability during electrocatalytic applications. The comparative study of OER with reported literature is given Table 5.6.

**Table 5.6:** A comparative OER study of all the electrochemical parameters with the electrocatalyst.

S.N.	Electrocatalyst	Electrolyte	Current density (mA/cm <sup>2</sup> )	Overpotential (mV vs. RHE)	Tafel slope	Ref.
1.	Co-Ni <sub>3</sub> S <sub>2</sub> /Ni foam	1 M KOH	10	228	84	55
2.	CuNiS nanowires/ Carbon paper	1 M KOH	30	307	81	24
3.	Co <sub>9-x</sub> Ni <sub>x</sub> S <sub>8</sub>	1 M KOH	10	362	74.7	21
4.	Ni/Ni <sub>9</sub> S <sub>8</sub>	1 M KOH	30	340	109.8	22
5.	$\text{Co}_{0.05}\text{Ni}_{8.95}\text{S}_8$	1 M KOH	30	327	49.8	This work

### 5.3.4 Overall water splitting: Two electrode system

Being inspired by the above results of the Co doped sample for both HER and OER in an alkaline medium, we have checked the overall water splitting reaction using the  $\text{Co}_{0.05}\text{Ni}_{8.95}\text{S}_8$  electrode as an anode and a cathode. Figure 5.22a demonstrates the LSV curves of assembled  $\text{Co}_{0.05}\text{Ni}_{8.95}\text{S}_8$  (+) ||  $\text{Co}_{0.05}\text{Ni}_{8.95}\text{S}_8$  (-) cells. To compare the cell voltage to generate a 10 mA/cm<sup>2</sup> current density the  $\text{Co}_{0.05}\text{Ni}_{8.95}\text{S}_8$  (+) ||  $\text{Co}_{0.05}\text{Ni}_{8.95}\text{S}_8$  (-) cells require only 1.89 V. The cell  $\text{Co}_{0.05}\text{Ni}_{8.95}\text{S}_8$  (+) ||  $\text{Co}_{0.05}\text{Ni}_{8.95}\text{S}_8$  (-), is also showing 24-hour stability at a fixed potential of 1.89 V in alkaline medium, shown in Figure 5.22b. Thus, the developed cell,  $\text{Co}_{0.05}\text{Ni}_{8.95}\text{S}_8$  (+) ||  $\text{Co}_{0.05}\text{Ni}_{8.95}\text{S}_8$  (-) exhibits good activity for overall water splitting reaction.

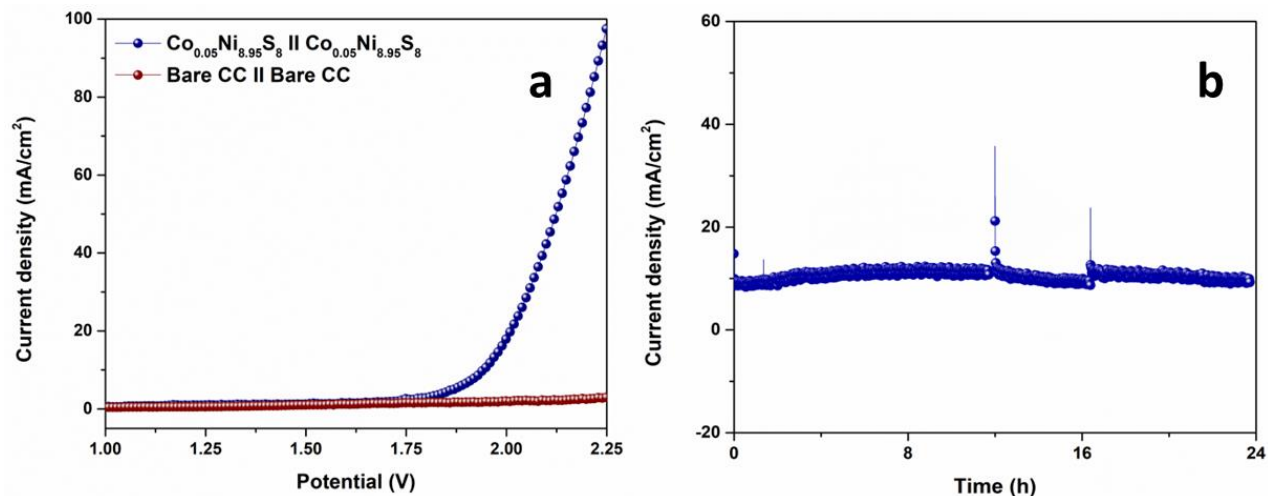


**Figure 5.22:** (a) LSV and (b) 24 hours stability test of constructed two electrode system of  $\text{Co}_{0.05}\text{Ni}_{8.95}\text{S}_8$  (+) ||  $\text{Co}_{0.05}\text{Ni}_{8.95}\text{S}_8$  (-).

### 5.3.5 Theoretical calculations

#### 5.3.5.1 Structures of pristine, Co doped Ni<sub>9</sub>S<sub>8</sub> systems and their relative stabilities

At room temperature and under ambient pressure Ni<sub>9</sub>S<sub>8</sub> crystallizes in the orthorhombic phase and belongs to *C222* space group symmetry (space group no. 21). The crystal structure, the associated lattice and structural parameters of Ni<sub>9</sub>S<sub>8</sub> compound were experimentally determined from the X-ray single-crystal and powder diffraction data<sup>61, 62</sup>. The unit cell of Ni<sub>9</sub>S<sub>8</sub> consists of 36 Ni and 32 S atoms with the formula unit  $Z = 4$ . Starting from the experimentally determined lattice parameters ( $a = 9.33590 \text{ \AA}$ ,  $b = 11.21850 \text{ \AA}$  and  $c = 9.430 \text{ \AA}$ ) the crystal structure of Ni<sub>9</sub>S<sub>8</sub> has been further optimized using GGA-PBE level of theory. The optimized geometry of Ni<sub>9</sub>S<sub>8</sub> compound is shown in Figure 5.23.



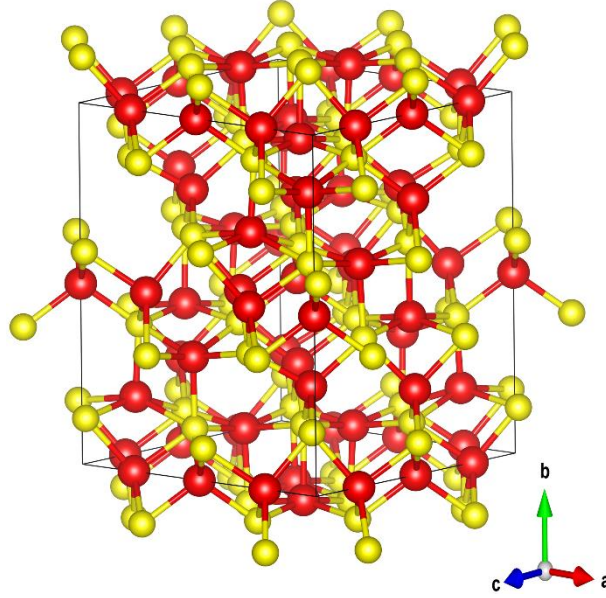


**Figure 5.23:** Optimized geometry of pristine Ni<sub>9</sub>S<sub>8</sub> as obtained from GGA-PBE level of theory. Red and yellow colours represent Ni and S atoms respectively.

The optimized geometry for 0.5%, 0.75%, 3%, and 6% Co doped Ni<sub>9</sub>S<sub>8</sub> systems are shown in Figure 5.24. To understand the structural stabilities of Co doped Ni<sub>9</sub>S<sub>8</sub> crystal systems, the defect formation energy per dopant ( $\Delta E_{df}$ ) for each doping percentage has been estimated from the following relation:

$$\Delta E_{df} = \frac{1}{m_{Co}} [E_{doped} - E_{pristine} - m_{Co}(\mu_{Co} - \mu_{Ni})] \quad (1)$$

where  $E_{doped}$  and  $E_{pristine}$  are the total energies of Ni<sub>9</sub>S<sub>8</sub> supercell with and without Co dopants respectively,  $m_{Co}$  is the number of doped Co atoms,  $\mu_{Co}$  and  $\mu_{Ni}$  are the chemical potentials of single isolated Co and Ni atoms respectively. The defect formation energies per dopant for 0.5% (Co<sub>0.05</sub>Ni<sub>8.95</sub>S<sub>8</sub>), 0.75% (Co<sub>0.075</sub>Ni<sub>8.925</sub>S<sub>8</sub>), 3% (Co<sub>0.3</sub>Ni<sub>8.7</sub>S<sub>8</sub>) and 6% (Co<sub>0.6</sub>Ni<sub>8.4</sub>S<sub>8</sub>) Co - doped Ni<sub>9</sub>S<sub>8</sub> systems are estimated to be -22.80 Ry, -15.04 Ry, -3.82 Ry and -1.87 Ry respectively. From the defect formation energy values, it is clearly seen that the 0.5% Co doped Ni<sub>9</sub>S<sub>8</sub> system (Co<sub>0.05</sub>Ni<sub>8.95</sub>S<sub>8</sub>) is energetically most favorable in comparison with other Co doped systems with 0.75%, 3%, and 6% of doping.

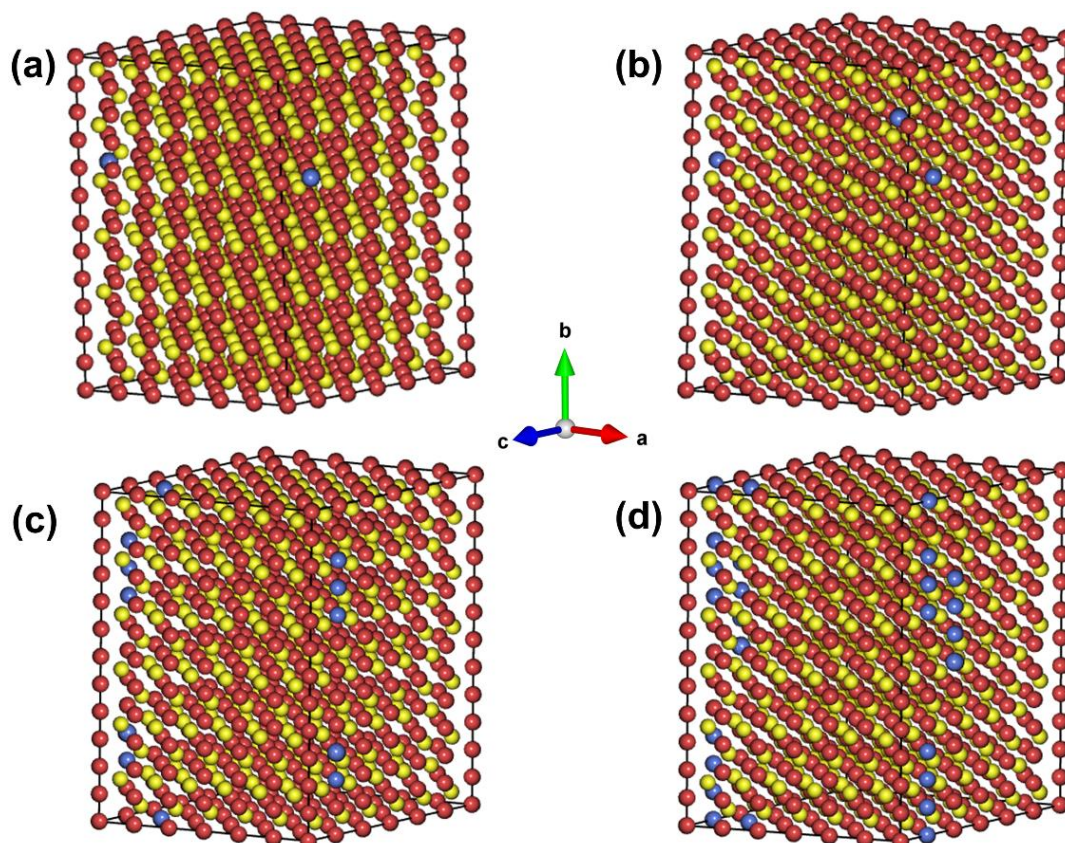


**Figure 5.24:** Optimized geometries of Co - doped  $\text{Ni}_9\text{S}_8$  system for (a) 0.5%, (b) 0.75%, (c) 3% and (d) 6% doping of Co as obtained from GGA-PBE level of theory. Red, yellow, and blue colors represent Ni, S, and Co atoms respectively.

### 5.3.5.2 The electronic band structures and density of states (DOS) of the pristine ( $\text{Ni}_9\text{S}_8$ ) and 0.5% Co doped $\text{Ni}_9\text{S}_8$ ( $\text{Co}_{0.05}\text{Ni}_{8.95}\text{S}_8$ ) systems

To understand the improved electrocatalytic performance of the 0.5% Co doped  $\text{Ni}_9\text{S}_8$  ( $\text{Co}_{0.05}\text{Ni}_{8.95}\text{S}_8$ ) system in comparison with the pristine  $\text{Ni}_9\text{S}_8$  counterpart, the electronic band structures for the pristine and 0.5% Co doped  $\text{Ni}_9\text{S}_8$  systems have been estimated. The respective E- $\mathbf{k}$  diagrams along  $Y \rightarrow \Gamma \rightarrow T \rightarrow \Gamma \rightarrow Z \rightarrow S$  high-symmetry points are shown in Figures 5.25 a and b. From Figure 5.25a, various dispersive energy bands emanating from the valence and conduction band edges of the pristine  $\text{Ni}_9\text{S}_8$  compound are noticed around the Fermi energy level ( $E_F$ ). While the valence band maximum for the  $\text{Ni}_9\text{S}_8$  system is estimated at the high symmetric  $\Gamma$  point, the conduction band minimum is localized along the Y-  $\Gamma$  direction with bandgap energy ( $E_g$ )  $\sim$  0.8 eV. This result signifies that the pristine  $\text{Ni}_9\text{S}_8$  system is an indirect bandgap semiconductor.

Interestingly, upon 0.5% Co doping in  $\text{Ni}_9\text{S}_8$ , remarkable changes in the E-k diagram have been estimated. The E-k diagram for the doped  $\text{Co}_{0.05}\text{Ni}_{8.95}\text{S}_8$  system is represented in Figure 5.25b. The E-k diagram for  $\text{Co}_{0.05}\text{Ni}_{8.95}\text{S}_8$  is marked by the dense nesting of energy bands contributing from the valence and conduction band edges of the compound around the  $E_F$ . This observation suggests a zero bandgap or the metallic nature of the  $\text{Co}_{0.05}\text{Ni}_{8.95}\text{S}_8$  compound. The metallic nature of the 0.5% Co doped  $\text{Ni}_9\text{S}_8$  system may promote HER activity of the compound due to the presence of excess free electrons around  $E_F$ . This observation is in agreement with the experimental results which indeed show enhanced electrocatalytic activity for the doped  $\text{Co}_{0.05}\text{Ni}_{8.95}\text{S}_8$  system in comparison to its pristine  $\text{Ni}_9\text{S}_8$  counterpart. The reduction in bandgap enhanced the electron transport probability and conductivity, which improves the electrocatalytic performance of  $\text{Co}_{0.05}\text{Ni}_{8.95}\text{S}_8$ .

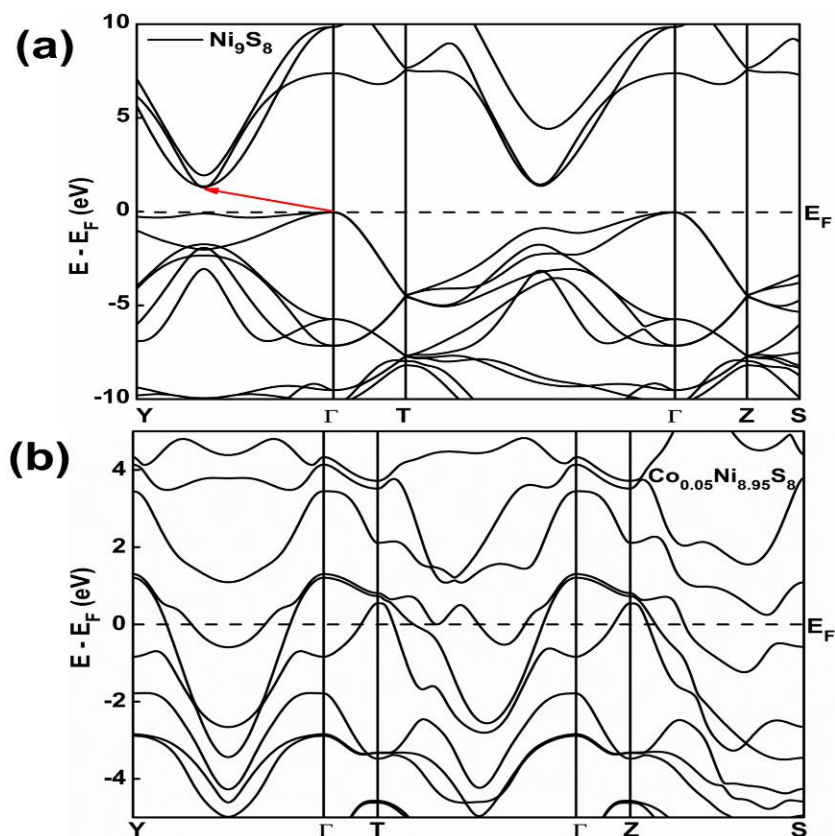


**Figure 5.25:** Electronic band structures of (a) pristine  $\text{Ni}_9\text{S}_8$  and (b) doped  $\text{Co}_{0.05}\text{Ni}_{8.95}\text{S}_8$  systems along with the high-symmetry points  $Y \rightarrow \Gamma \rightarrow T \rightarrow \Gamma \rightarrow Z \rightarrow S$  as obtained from the GGA+ $U_{dd}$  level of theory. The indirect bandgap of pristine  $\text{Ni}_9\text{S}_8$  and the Fermi energy level ( $E_F$ ) are marked with the red arrow and black dashed line respectively.

To get deeper insights into the density of energy states, the total (TDOS) and the orbital resolved projected atomic density of states (TDOS and PDOS) of the pristine  $\text{Ni}_9\text{S}_8$  and doped  $\text{Co}_{0.05}\text{Ni}_{8.95}\text{S}_8$  systems have been estimated and are depicted in Figure 5.26. The TDOS plot of the pristine  $\text{Ni}_9\text{S}_8$  system, as shown in Figure 5.26A, exhibits small but finite depletion in energy states near  $E_F$ . The corresponding PDOS plot is shown in Figure 5.26a. From Figure 5.26a it is clearly seen that the top of the valence bands of the pristine compound around  $E_F$  ranging in the range -1 to 0 eV are dominated by S-3p and Ni-3d orbitals. The relative weight of the S-3p exceeds from that of the Ni-3d orbitals. Akin to the top of the valence bands, the bottom of the conduction bands of the pristine compound near  $E_F$ , ranging from 0 to 1 eV, is largely dominated by Ni-3d and S-3p orbitals, albeit weak contributions from the Ni-4s and S-3s are also noticed. Interestingly for the 0.5% Co doped  $\text{Ni}_9\text{S}_8$  ( $\text{Co}_{0.05}\text{Ni}_{8.95}\text{S}_8$ ) system, the corresponding TDOS plot, as depicted in Figure 5.26B, shows dramatic changes in features in comparison to its pristine counterpart (Figure 5.26A). The TDOS plot shows sharp energy states not only confined around the  $E_F$  but also exhibit the van-Hove singularity at  $E_F$ . These observations suggest the metallic behavior of the  $\text{Co}_{0.05}\text{Ni}_{8.95}\text{S}_8$  compound and are in accordance with the inference so predicted from the corresponding E- $\mathbf{k}$  diagram (Figure 5.25b, *vide supra*). The reason behind the metallic behavior of the doped  $\text{Co}_{0.05}\text{Ni}_{8.95}\text{S}_8$  compound is easily unveiled from the associated PDOS plot as shown in Figure 5.26b. The PDOS plot clearly shows the predominant contribution from the doped Co-4s orbital at  $E_F$ . Thus the contribution from the doped Co-4s orbital may account for the metallic behavior of the doped  $\text{Co}_{0.05}\text{Ni}_{8.95}\text{S}_8$  system which in turn may stand responsible for the enhanced electrocatalytic activity of the compound as observed from the experimental results. Therefore, the generation of more active sites and the adsorption of intermediates during the electrocatalytic activity are more pronounced in the  $\text{Co}_{0.05}\text{Ni}_{8.95}\text{S}_8$  catalyst. Furthermore, the synergistic effect between Co and Ni also plays a significant role in the change in the electronic structure and conductivity enhancement. All the above results confirm the potential use of Co as a dopant in the  $\text{Ni}_9\text{S}_8$  system for boosting electrocatalytic performance.



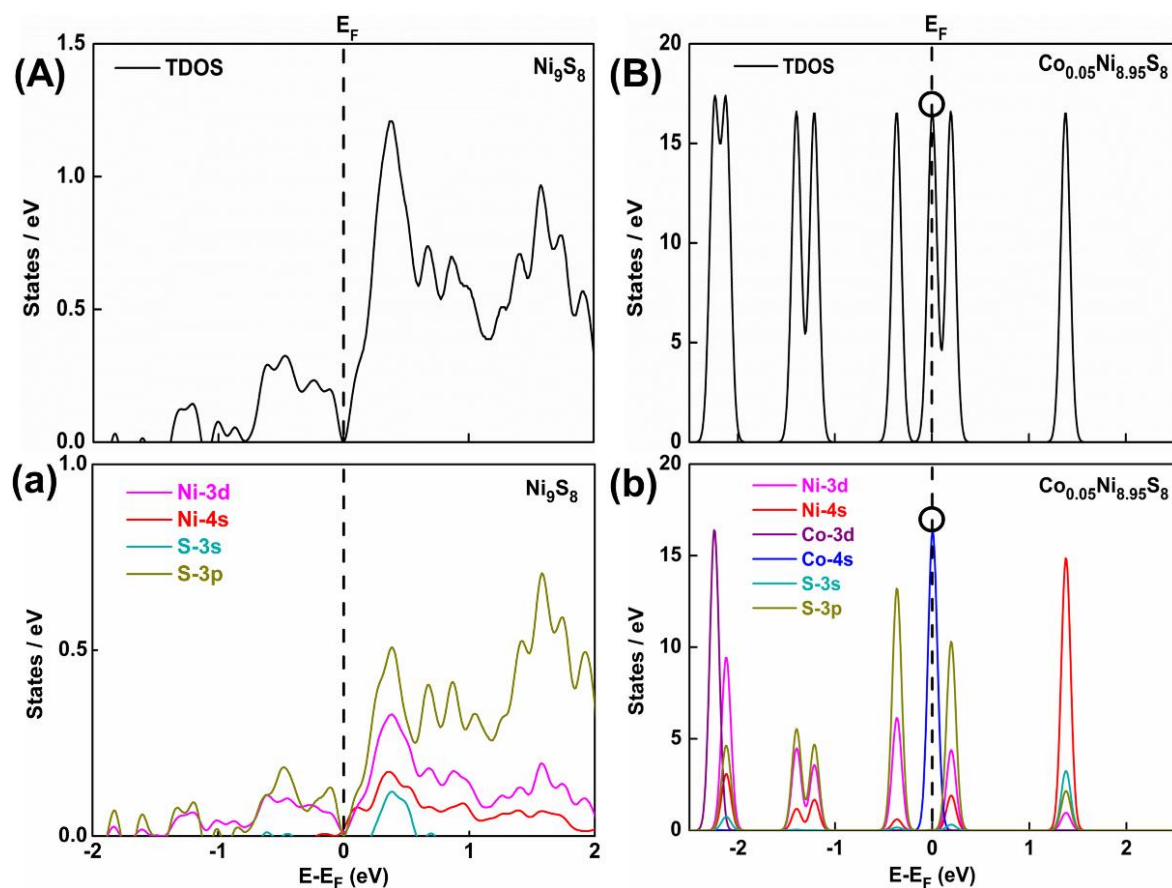


**Figure 5.26:** Left panel shows (A) TDOS and (a) PDOS spectra for pristine  $\text{Ni}_9\text{S}_8$  compounds. Right panel shows (B) TDOS and (b) PDOS spectra for the doped  $\text{Co}_{0.05}\text{Ni}_{8.95}\text{S}_8$  system as obtained from the GGA+ $U_{\text{dd}}$  level of theory. The van-Hove singularity and the Fermi energy level ( $E_{\text{F}}$ ) are marked with a black circle and black dashed line respectively.

### 5.3.5.3 Hydrogen/ oxygen coverage and current density

To introspect the HER and OER activities of Co doped  $\text{Ni}_9\text{S}_8$  systems for various dopant concentrations, the variations in Gibbs free energy ( $\Delta G_{\text{H}}$ ) values as a function of hydrogen and oxygen coverages for  $\text{Co}_{0.05}\text{Ni}_{8.95}\text{S}_8$ ,  $\text{Co}_{0.075}\text{Ni}_{8.925}\text{S}_8$ ,  $\text{Co}_{0.3}\text{Ni}_{8.7}\text{S}_8$ ,  $\text{Co}_{0.6}\text{Ni}_{8.4}\text{S}_8$  systems have been elucidated at zero overpotential value ( $U = 0$ ). The results are shown in Figures 5.27A and 5.27B. From Figure 5.27, it is observed that  $\Delta G_{\text{H}}$  attains minimum value  $-7.22$  ( $-3.03$ ) eV for 8% of hydrogen (oxygen) coverage for the doped  $\text{Co}_{0.05}\text{Ni}_{8.95}\text{S}_8$  system. However, for  $\text{Co}_{0.075}\text{Ni}_{8.925}\text{S}_8$ ,  $\text{Co}_{0.3}\text{Ni}_{8.7}\text{S}_8$  and  $\text{Co}_{0.6}\text{Ni}_{8.4}\text{S}_8$  systems the lowest  $\Delta G_{\text{H}}$  values are estimated to be  $-6.59$  ( $-1.6$ ) eV, -

3.09 (-0.49) eV and -6.92 (-1.25) eV for 16%, 48% and 100% hydrogen (oxygen) coverage respectively. All these observations collectively suggest the minimum  $\Delta G_H$  value [-7.22 (-3.03) eV for 8% hydrogen (oxygen) coverage] for  $\text{Co}_{0.05}\text{Ni}_{8.95}\text{S}_8$  system which may be responsible for the enhanced HER and OER activities of the Co doped  $\text{Ni}_9\text{S}_8$  compounds. In this connection it is relevant to mention that the variations of  $\Delta G_H$  as a function of hydrogen and oxygen coverages for  $\text{Co}_{0.3}\text{Ni}_{8.7}\text{S}_8$  system are found to be quite different from the other Co doped systems [Figures 5.27A and 9B]. This may be rationalized from the position and the rate of hydrogen/ oxygen adsorption at the active sites with HER/ OER activities. The large positive values of  $\Delta G_H$  between 8 - 40% and 72 - 100% represents weak hydrogen adsorption and poor HER activity of  $\text{Co}_{0.3}\text{Ni}_{8.7}\text{S}_8$  compound in comparison to its other Co doped systems [ca. Figure 5.27A].

The volcano plots associated with the exchange current densities ( $J_0$ ) have been estimated to analyse further the HER and OER activities of the active sites of the compounds<sup>43, 63-65</sup>. The logarithm of  $J_0$  as a function of  $\Delta G_H$  for HER and OER processes are shown in Figures 5.27 a and b respectively. From Figures 5.27a and 5.27b, it is observed that in the region  $\Delta G_H < 0$ , where the relative adsorption of hydrogen and oxygen is strong, the highest  $J_0$  values are found to be -7.31 and -0.693  $\text{Am}^{-2}$  for  $\text{Co}_{0.05}\text{Ni}_{8.95}\text{S}_8$  compound for the HER and OER activities, respectively. Moreover, the  $J_0$  values of  $\text{Co}_{0.05}\text{Ni}_{8.95}\text{S}_8$  system are found near  $\Delta G_H = 0$  which represents the ideal scenario of generation of hydrogen and oxygen. These observations are also in agreement with our experimental results where  $\text{Co}_{0.05}\text{Ni}_{8.95}\text{S}_8$  shows the best HER/ OER performance with the lowest value of onset potential and higher current density in comparison to its other Co doped counterparts (*vide supra*). Moreover, Co doping also catalyzes the formation of  $\text{Ni}^{3+}$  ion, which is an active center for  $\text{OH}^-$  adsorption followed by the generation of molecular hydrogen.

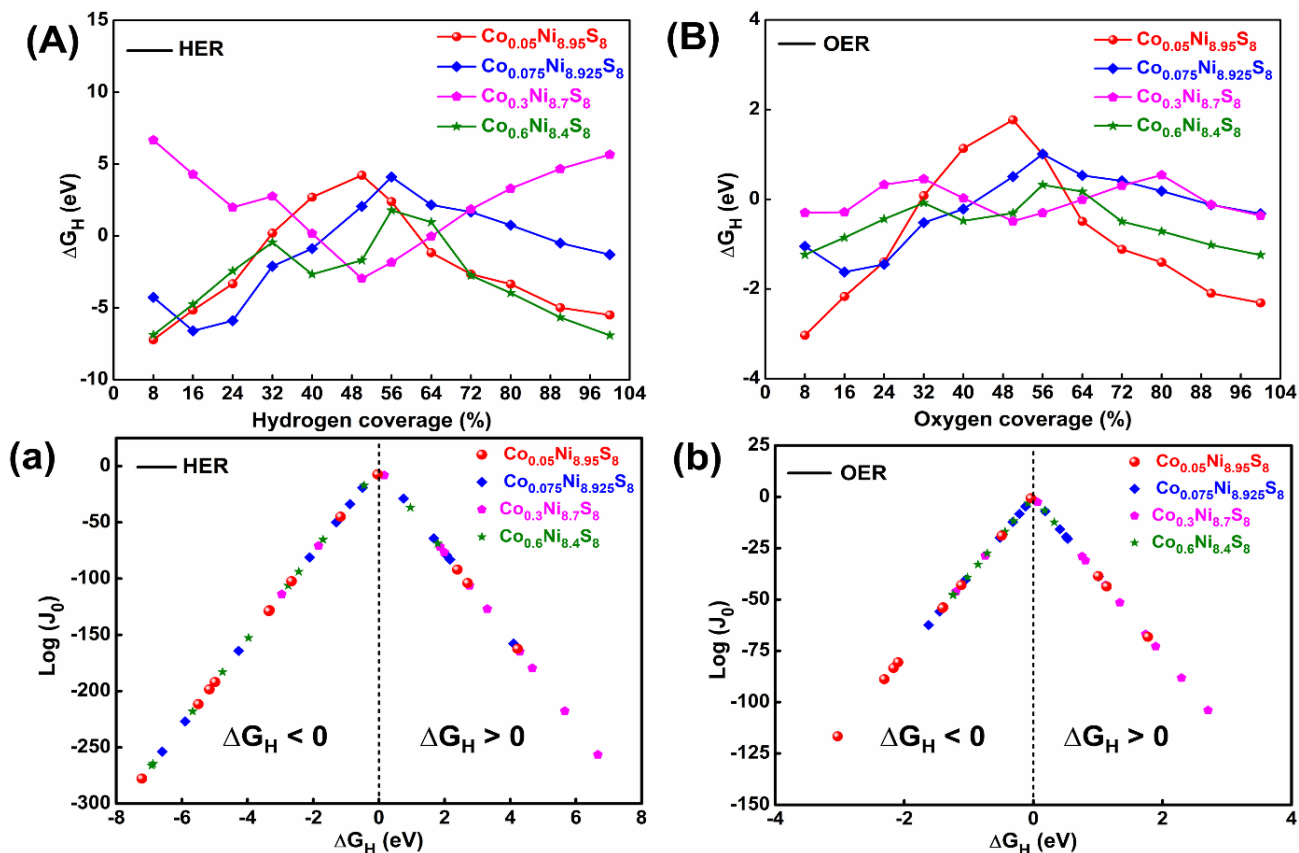


**Figure 5.27:** The Gibbs free energy versus (A) hydrogen, (B) oxygen coverage, and the exchange current density as a function of Gibbs free energy for (a) HER, (b) OER activities of Co - doped  $\text{Ni}_9\text{S}_8$  systems as obtained from GGA+ $U_{\text{dd}}$  level of theory.

### Electrochemical reaction pathways for HER and OER activities

To understand precisely the HER and OER performances of Co doped  $\text{Ni}_9\text{S}_8$  systems for various dopant concentrations, the energy barriers for HER and OER have been calculated. The associated free energy diagrams for the Volmer-Heyrovsky (V-H), Volmer-Tafel (V-T) reaction pathways<sup>66, 67</sup> at zero work function difference ( $\Delta U = 0$ ) for HER and OER are shown in Figure 5.28a and b respectively. From the left panel of Figure 5.28, the free energy values at the final transition point for  $\text{Co}_{0.05}\text{Ni}_{8.95}\text{S}_8$ ,  $\text{Co}_{0.075}\text{Ni}_{8.925}\text{S}_8$ ,  $\text{Co}_{0.3}\text{Ni}_{8.7}\text{S}_8$  and  $\text{Co}_{0.6}\text{Ni}_{8.4}\text{S}_8$  systems are found to be -7.22, -6.60, -2.96 and -6.92 eV respectively in V-H reaction pathways. However, for V-T reaction path the free energy values for the above referred systems are estimated to be -5.90, -5.67, -1.86, and -5.55 eV, respectively at the final transition point. The right panel of Figure 5.28, which illustrates the energy barriers for OER activities, shows the free energy values of -3.03 (-2.48), -1.62 (-1.39),

-1.19 (-0.75) and -1.24 (-0.99) eV in V-H (V-T) reaction paths at the final transition point for  $\text{Co}_{0.05}\text{Ni}_{8.95}\text{S}_8$ ,  $\text{Co}_{0.075}\text{Ni}_{8.925}\text{S}_8$ ,  $\text{Co}_{0.3}\text{Ni}_{8.7}\text{S}_8$  and  $\text{Co}_{0.6}\text{Ni}_{8.4}\text{S}_8$  compounds respectively. Interestingly, from the estimations of the energy barriers for the V-H and V-T reaction paths, it is observed that  $\text{Co}_{0.05}\text{Ni}_{8.95}\text{S}_8$  system, which shows minimum free energy values (ca. -7.22 eV for HER and -3.03 eV for OER of V-H reaction pathway), is responsible for the enhanced HER and OER performances. The V-H reaction pathway is found to be more favourable compared to the V-T reaction path for both the HER and OER performances. These results are in well accordance with our experimental observations where the  $\text{Co}_{0.05}\text{Ni}_{8.95}\text{S}_8$  electrocatalyst is found to follow the V-H mechanism for the HER and OER in an alkaline medium (*vide supra*).

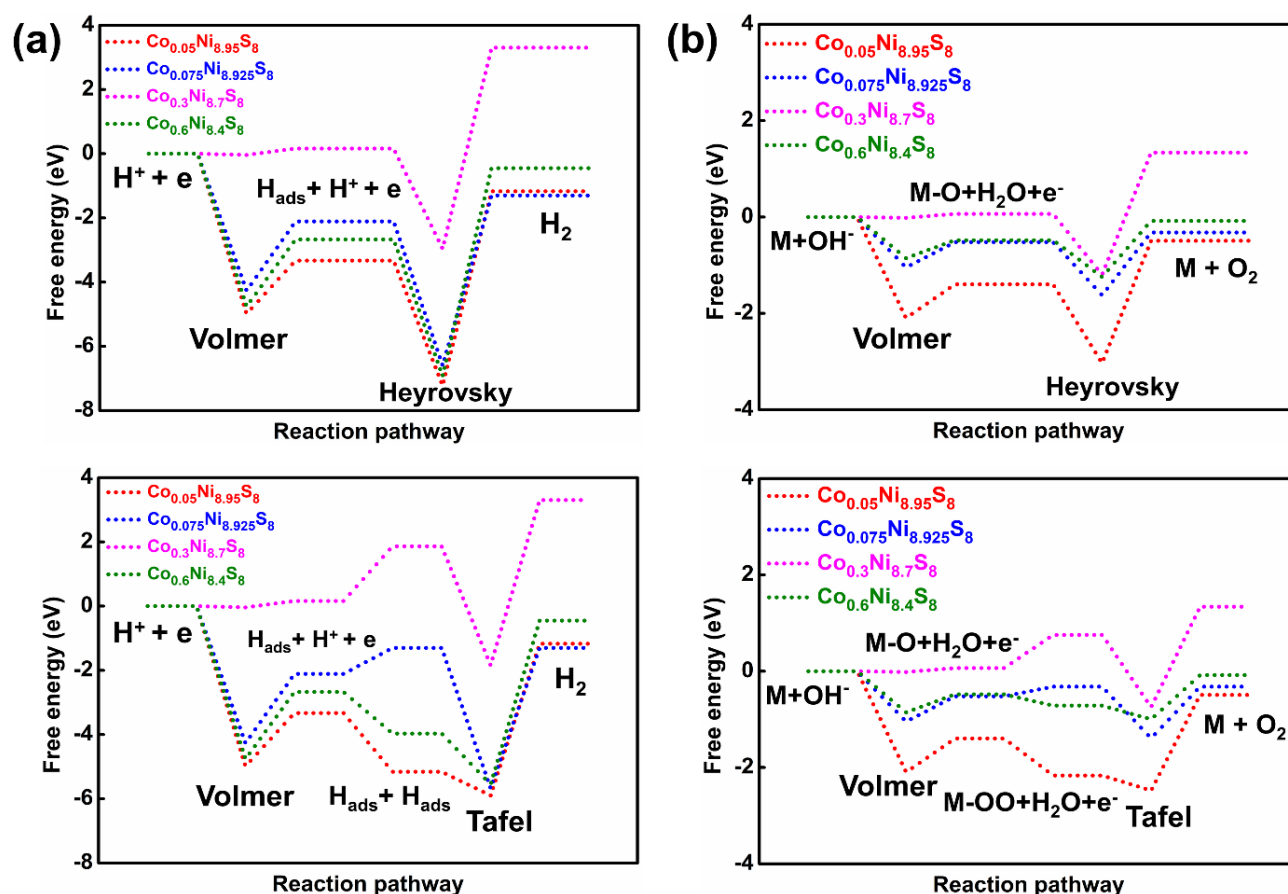


**Figure 5.28 :** The energy barriers for the Volmer-Heyrovsky, Volmer-Tafel reaction pathways for (a) HER and (b) OER activities of Co - doped  $\text{Ni}_9\text{S}_8$  systems as obtained from the NEB method. [“M” is the metal center or catalyst surface].



### 5.4 Conclusion

Two-step synthesis for the development of Co doped Ni<sub>9</sub>S<sub>8</sub> nanomaterials supported on carbon cloth is performed for both HER and OER in an alkaline medium. Different ratios of Co:Ni, Co<sub>0.1</sub>Ni<sub>8.9</sub>S<sub>8</sub>, Co<sub>0.05</sub>Ni<sub>8.95</sub>S<sub>8</sub>, and Co<sub>0.03</sub>Ni<sub>8.97</sub>S<sub>8</sub> are developed but, Co<sub>0.05</sub>Ni<sub>8.95</sub>S<sub>8</sub> exhibits superior electrocatalytic activity. The cobalt doping arises compressive strain in the Ni<sub>9</sub>S<sub>8</sub> system, which impacts in the electronic environment and conductivity in the developed sample. Williamson-Hall equation is used to confirm the presence of strain in the doped sample. The d-spacing calculation from HRTEM analysis also corroborates the lattice contraction in the doped sample. XPS analysis confirms the synergistic effect between Co and Ni, which makes the electrocatalysts more effective for HER and OER. The Lewis acid behaviour of the Co<sup>2+</sup> ion is confirmed by shifting the binding energy of Ni 2p at a higher region, which shows the electron transfer from Ni<sup>2+</sup> to the Co<sup>2+</sup> system. Finally, the introduction of dopant Co enhances the number of active sites and roughness factor in Ni<sub>9</sub>S<sub>8</sub> nanomaterials. The constructed Co<sub>0.05</sub>Ni<sub>8.95</sub>S<sub>8</sub> (+) || Co<sub>0.05</sub>Ni<sub>8.95</sub>S<sub>8</sub> (-) cell, exhibits 24-hour stability at a fixed potential of 1.89 V in an alkaline medium. The metallic nature of Co<sub>0.05</sub>Ni<sub>8.95</sub>S<sub>8</sub> is confirmed from theoretical calculation, which further supports an efficient electrocatalytic activity. Better HER performance is also confirmed from the minimum Gibbs free hydrogen adsorption energy and hydrogen coverage calculation of Co<sub>0.05</sub>Ni<sub>8.95</sub>S<sub>8</sub> electrocatalyst. Variations in Gibbs free energy ( $\Delta G_H$ ) values as a function of oxygen coverages are also calculated for all the ratios where, Co<sub>0.05</sub>Ni<sub>8.95</sub>S<sub>8</sub> shows maximum OER efficiency. Therefore, Co doped Ni<sub>9</sub>S<sub>8</sub> supported on carbon cloth exhibits high efficiency and stability in an alkaline medium for overall water-splitting reaction.

### 5.5 References

1. Jiao, Y.; Zheng, Y.; Jaroniec, M.; Qiao, S. Z., Design of electrocatalysts for oxygen-and hydrogen-involving energy conversion reactions. *Chem. Soc. Rev.* **2015**, *44* (8), 2060-2086.
2. Suen, N.-T.; Hung, S.-F.; Quan, Q.; Zhang, N.; Xu, Y.-J.; Chen, H. M., Electrocatalysis for the oxygen evolution reaction: recent development and future perspectives. *Chem. Soc. Rev.* **2017**, *46* (2), 337-365.
3. Xiang, C.; Papadantonakis, K. M.; Lewis, N. S., Principles and implementations of electrolysis systems for water splitting. *Mater. Horizons* **2016**, *3* (3), 169-173.

- Sabba, D.; Kumar, M. H.; Wong, L. H.; Barber, J.; Grätzel, M.; Mathews, N., Perovskite–hematite tandem cells for efficient overall solar driven water splitting. *Nano Lett.* **2015**, *15* (6), 3833-3839.
- Cheng, N.; Stambula, S.; Wang, D.; Banis, M. N.; Liu, J.; Riese, A.; Xiao, B.; Li, R.; Sham, T.-K.; Liu, L.-M., Platinum single-atom and cluster catalysis of the hydrogen evolution reaction. *Nat. Commun.* **2016**, *7* (1), 1-9.
- Exner, K. S., Boosting the Stability of RuO<sub>2</sub> in the Acidic Oxygen Evolution Reaction by Tuning Oxygen-Vacancy Formation Energies: A Viable Approach Beyond Noble-Metal Catalysts? *ChemElectroChem* **2021**, *8* (1), 46-48.
- Zadick, A.; Dubau, L.; Sergent, N.; Berthomé, G.; Chatenet, M., Huge Instability of Pt/C Catalysts in Alkaline Medium. *ACS Catal.* **2015**, *5* (8), 4819-4824.
- Yan, Y.; Xia, B. Y.; Zhao, B.; Wang, X., A review on noble-metal-free bifunctional heterogeneous catalysts for overall electrochemical water splitting. *J. Mater. Chem. A* **2016**, *4* (45), 17587-17603.
- Nazir, R.; Fageria, P.; Basu, M.; Pande, S., Decoration of carbon nitride surface with bimetallic nanoparticles (Ag/Pt, Ag/Pd, and Ag/Au) via galvanic exchange for hydrogen evolution reaction. *J. Phys. Chem. C* **2017**, *121* (36), 19548-19558.
- Zou, X.; Zhang, Y., Noble metal-free hydrogen evolution catalysts for water splitting. *Chem. Soc. Rev.* **2015**, *44* (15), 5148-5180.
- Li, X.; Walsh, F. C.; Pletcher, D., Nickel based electrocatalysts for oxygen evolution in high current density, alkaline water electrolyzers. *Phys. Chem. Chem. Phys.* **2011**, *13* (3), 1162-1167.
- Fageria, P.; Sudharshan, K.; Nazir, R.; Basu, M.; Pande, S., Decoration of MoS<sub>2</sub> on g-C<sub>3</sub>N<sub>4</sub> surface for efficient hydrogen evolution reaction. *Electrochim. Acta* **2017**, *258*, 1273-1283.
- Guo, Y.; Park, T.; Yi, J. W.; Henzie, J.; Kim, J.; Wang, Z.; Jiang, B.; Bando, Y.; Sugahara, Y.; Tang, J., Nanoarchitectonics for transition metal sulfide based electrocatalysts for water splitting. *Adv. Mater.* **2019**, *31* (17), 1807134.
- Yu, X. Y.; Lou, X. W., Mixed Metal Sulfides for Electrochemical Energy Storage and Conversion. *Adv. Energy Mater.* **2018**, *8* (3), 1701592.

15. Gong, M.; Wang, D.-Y.; Chen, C.-C.; Hwang, B.-J.; Dai, H., A mini review on nickel-based electrocatalysts for alkaline hydrogen evolution reaction. *Nano Res.* **2016**, *9* (1), 28-46.
16. Yang, H.; Wang, C.; Zhang, Y.; Wang, Q., Chemical Valence Dependent Electrocatalytic Activity for Oxygen Evolution Reaction: A Case of Nickel Sulfides Hybridized with N and S Co-Doped Carbon Nanoparticles. *Small* **2018**, *14* (8), 1703273.
17. Chen, X.; Wang, X.; Zhang, X.; Srinivas, K.; Liu, D.; Zhao, X.; Yu, H.; Wang, B.; Zhang, W.; Chen, Y., Vertical Fe (OH)<sub>3</sub>/Ni<sub>9</sub>S<sub>8</sub> nanoarrays electrodeposited on stainless steel as binder-free electrocatalyst for highly efficient and stable oxygen evolution reaction. *J. Mater. Sci.* **2021**, 1-11.
18. Hussain, S.; Ullah, N.; Zhang, Y.; Shaheen, A.; Javed, M. S.; Lin, L.; Shah, S. B.; Liu, G.; Qiao, G., One-step synthesis of unique catalyst Ni<sub>9</sub>S<sub>8</sub>@ C for excellent MOR performances. *Int. J. Hydrog. Energy* **2019**, *44* (45), 24525-24533.
19. Basu, M.; Nazir, R.; Mahala, C.; Fageria, P.; Chaudhary, S.; Gangopadhyay, S.; Pande, S., Ag<sub>2</sub>S/Ag heterostructure: a promising electrocatalyst for the hydrogen evolution reaction. *Langmuir* **2017**, *33* (13), 3178-3186.
20. Mahmood, N.; Zhang, C.; Hou, Y., Nickel Sulfide/nitrogen doped graphene composites: phase-controlled synthesis and high performance anode materials for lithium ion batteries. *Small* **2013**, *9* (8), 1321-1328.
21. Yan, J.; Wu, H.; Chen, H.; Jiang, R.; Liu, S. F., Fe (III) doped NiS<sub>2</sub> nanosheet: a highly efficient and low-cost hydrogen evolution catalyst. *J. Mater. Chem. A* **2017**, *5* (21), 10173-10181.
22. Chen, G. F.; Ma, T. Y.; Liu, Z. Q.; Li, N.; Su, Y. Z.; Davey, K.; Qiao, S. Z., Efficient and stable bifunctional electrocatalysts Ni/Ni<sub>x</sub>M<sub>y</sub> (M= P, S) for overall water splitting. *Adv. Funct. Mater.* **2016**, *26* (19), 3314-3323.
23. Long, X.; Li, G.; Wang, Z.; Zhu, H.; Zhang, T.; Xiao, S.; Guo, W.; Yang, S., Metallic iron–nickel sulfide ultrathin nanosheets as a highly active electrocatalyst for hydrogen evolution reaction in acidic media. *J. Am. Chem. Soc.* **2015**, *137* (37), 11900-11903.
24. Cao, D.; Cheng, D., One-pot synthesis of copper–nickel sulfide nanowires for overall water splitting in alkaline media. *ChemComm* **2019**, *55* (56), 8154-8157.

25. da Silva, M. G.; Leite, C. M.; Cordeiro, M. A.; Mastelaro, V. R.; Leite, E. R., One-Step Synthesis of Nickel Sulfides and Their Electrocatalytic Activities for Hydrogen Evolution Reaction: A Case Study of Crystalline h-NiS and o-Ni<sub>9</sub>S<sub>8</sub> Nanoparticles. *ACS Appl. Energy Mater.* **2020**, *3* (10), 9498-9503.
26. Kim, J.; Jin, H.; Oh, A.; Baik, H.; Joo, S. H.; Lee, K., Synthesis of compositionally tunable, hollow mixed metal sulphide Co<sub>x</sub>Ni<sub>y</sub>S<sub>z</sub> octahedral nanocages and their composition-dependent electrocatalytic activities for oxygen evolution reaction. *Nanoscale* **2017**, *9* (40), 15397-15406.
27. Wei, D.; Tang, W.; Wang, Y., Hairy sphere-like Ni<sub>9</sub>S<sub>8</sub>/CuS/Cu<sub>2</sub>O composites grown on nickel foam as bifunctional electrocatalysts for hydrogen evolution and urea electrooxidation. *Int. J Hydrog. Energy* **2021**, *46* (40), 20950-20960.
28. Li, S.; Chen, T.; Wen, J.; Gui, P.; Fang, G., Insitu grown Ni<sub>9</sub>S<sub>8</sub> nanorod/O-MoS<sub>2</sub> nanosheet nanocomposite on carbon cloth as a free binder supercapacitor electrode and hydrogen evolution catalyst. *Nanotechnology* **2017**, *28* (44), 445407.
29. Luo, X.; Ji, P.; Wang, P.; Tan, X.; Chen, L.; Mu, S., Spherical Ni<sub>3</sub>S<sub>2</sub>/FeNiP<sub>x</sub> Magic Cube with Ultrahigh Water/Seawater Oxidation Efficiency. *Adv. Sci.* **2022**, *9*.
30. Wang, P.; Wang, T.; Qin, R.; Pu, Z.; Zhang, C.; Zhu, J.; Chen, D.; Feng, D.; Kou, Z.; Mu, S.; Wang, J., Swapping Catalytic Active Sites from Cationic Ni to Anionic S in Nickel Sulfide Enables More Efficient Alkaline Hydrogen Generation. *Adv. Energy Mater.* **2022**, *12* (8), 2103359.
31. Perdew, J. P.; Burke, K.; Ernzerhof, M., Generalized Gradient Approximation Made Simple. *Phys. Rev. Lett.* **1996**, *77* (18), 3865-3868.
32. Giannozzi, P.; Barone, P.; Bonfà, P.; Brunato, D.; Car, R.; Carnimeo, I.; Cavazzoni, C.; de Gironcoli, S.; Delugas, P.; Ferrari Ruffino, F.; Ferretti, A.; Marzari, N.; Timrov, I.; Urru, A.; Baroni, S., Quantum ESPRESSO toward the exascale. *J. Chem. Phys.* **2020**, *152* (15), 154105.
33. Giannozzi, P.; Andreussi, O.; Brumme, T.; Bunau, O.; Buongiorno Nardelli, M.; Calandra, M.; Car, R.; Cavazzoni, C.; Ceresoli, D.; Cococcioni, M.; Colonna, N.; Carnimeo, I.; Dal Corso, A.; de Gironcoli, S.; Delugas, P.; DiStasio, R. A.; Ferretti, A.; Floris, A.; Fratesi, G.; Fugallo, G.; Gebauer, R.; Gerstmann, U.; Giustino, F.; Gorni, T.; Jia, J.; Kawamura, M.; Ko, H. Y.; Kokalj, A.; Küçükbenli, E.; Lazzeri, M.; Marsili,

- M.; Marzari, N.; Mauri, F.; Nguyen, N. L.; Nguyen, H. V.; Otero-de-la-Roza, A.; Paulatto, L.; Poncé, S.; Rocca, D.; Sabatini, R.; Santra, B.; Schlipf, M.; Seitsonen, A. P.; Smogunov, A.; Timrov, I.; Thonhauser, T.; Umari, P.; Vast, N.; Wu, X.; Baroni, S., Advanced capabilities for materials modelling with Quantum ESPRESSO. *J. Phys.: Condens. Matter* **2017**, *29* (46), 465901.
34. Giannozzi, P.; Baroni, S.; Bonini, N.; Calandra, M.; Car, R.; Cavazzoni, C.; Ceresoli, D.; Chiarotti, G. L.; Cococcioni, M.; Dabo, I.; Dal Corso, A.; de Gironcoli, S.; Fabris, S.; Fratesi, G.; Gebauer, R.; Gerstmann, U.; Gougoussis, C.; Kokalj, A.; Lazzeri, M.; Martin-Samos, L.; Marzari, N.; Mauri, F.; Mazzarello, R.; Paolini, S.; Pasquarello, A.; Paulatto, L.; Sbraccia, C.; Scandolo, S.; Sclauzero, G.; Seitsonen, A. P.; Smogunov, A.; Umari, P.; Wentzcovitch, R. M., QUANTUM ESPRESSO: a modular and open-source software project for quantum simulations of materials. *J. Phys.: Condens. Matter* **2009**, *21* (39), 395502.
35. Shanno, D. F., Conditioning of quasi-Newton methods for function minimization. *Math. Comp.* **1970**, *24*, 647-656.
36. Goldfarb, D., A family of variable-metric methods derived by variational means. *Math. Comp.* **1970**, *24*, 23-26.
37. Fletcher, R., A new approach to variable metric algorithms. *Comput. J.* **1970**, *13* (3), 317-322.
38. Broyden, C. G., The Convergence of a Class of Double-rank Minimization Algorithms 1. General Considerations. *IMA J. Appl. Math.* **1970**, *6* (1), 76-90.
39. Dal Corso, A., Pseudopotentials periodic table: From H to Pu. *Comput. Mater. Sci.* **2014**, *95*, 337-350.
40. Anisimov, V. I.; Zaanen, J.; Andersen, O. K., Band theory and Mott insulators: Hubbard U instead of Stoner I. *Phys. Rev. B* **1991**, *44* (3), 943-954.
41. Cococcioni, M.; de Gironcoli, S., Linear response approach to the calculation of the effective interaction parameters in the  $\text{LDA}+\text{U}$  method. *Phys. Rev. B* **2005**, *71* (3), 035105.
42. Behera, S. K.; Deb, P.; Ghosh, A., Mechanistic Study on Electrocatalytic Hydrogen Evolution by High Efficiency Graphene/MoS<sub>2</sub> Heterostructure. *ChemistrySelect* **2017**, *2* (13), 3657-3667.

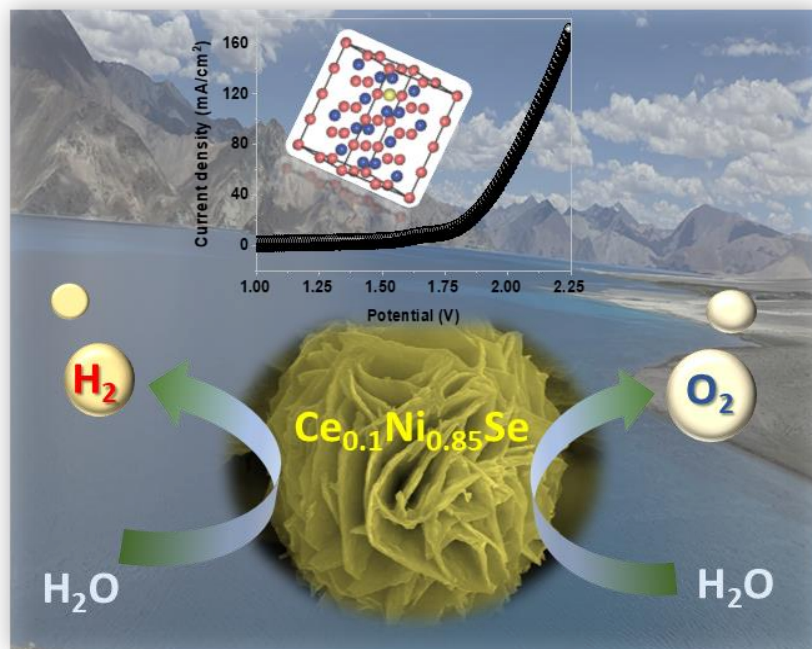
43. Behera, S. K.; Deb, P.; Ghosh, A., Driving electrocatalytic activity by interface electronic structure control in a metalloprotein hybrid catalyst for efficient hydrogen evolution. *Phys. Chem. Chem. Phys.* **2016**, *18* (33), 23220-23230.
44. Zacharia, R.; Ulbricht, H.; Hertel, T., Interlayer cohesive energy of graphite from thermal desorption of polyaromatic hydrocarbons. *Phys. Rev. B* **2004**, *69* (15), 155406.
45. Pan, H., Metal Dichalcogenides Monolayers: Novel Catalysts for Electrochemical Hydrogen Production. *Sci Rep* **2014**, *4* (1), 5348.
46. Li, Y.; Wang, H.; Xie, L.; Liang, Y.; Hong, G.; Dai, H., MoS<sub>2</sub> Nanoparticles Grown on Graphene: An Advanced Catalyst for the Hydrogen Evolution Reaction. *J. Am. Chem. Soc.* **2011**, *133* (19), 7296-7299.
47. Mills, G.; Jónsson, H., Quantum and thermal effects in H<sub>2</sub> dissociative adsorption: Evaluation of free energy barriers in multidimensional quantum systems. *Phys. Rev. Lett.* **1994**, *72* (7), 1124-1127.
48. Bharti, B.; Barman, P. B.; Kumar, R., XRD analysis of undoped and Fe doped TiO<sub>2</sub> nanoparticles by Williamson Hall method. *AIP Conf. Proc.* **2015**, *1675* (1), 030025.
49. Ismail, A. S.; Mamat, M. H.; Shameem Banu, I. B.; Amiruddin, R.; Malek, M. F.; Parimon, N.; Zoolfakar, A. S.; Md. Sin, N. D.; Suriani, A. B.; Ahmad, M. K.; Rusop, M., Structural modification of ZnO nanorod array through Fe-doping: Ramification on UV and humidity sensing properties. *Nano-Struct. Nano-Objects* **2019**, *18*, 100262.
50. Liu, S.; Li, B.; Mohite, S. V.; Devaraji, P.; Mao, L.; Xing, R., Ultrathin MoS<sub>2</sub> nanosheets in situ grown on rich defective Ni<sub>0.96</sub>S as heterojunction bifunctional electrocatalysts for alkaline water electrolysis. *Int. J Hydrog. Energy* **2020**, *45* (55), 29929-29937.
51. Huo, J.; Wu, J.; Zheng, M.; Tu, Y.; Lan, Z., Flower-like nickel cobalt sulfide microspheres modified with nickel sulfide as Pt-free counter electrode for dye-sensitized solar cells. *J Power Sources* **2016**, *304*, 266-272.
52. Guragain, D.; Karna, S.; Choi, J.; Bhattarai, R.; Poudel, T. P.; Gupta, R. K.; Shen, X.; Mishra, S. R., Electrochemical Performance of Iron-Doped Cobalt Oxide Hierarchical Nanostructure. *Processes* **2021**, *9* (12), 2176.
53. Wang, T.; Guo, X.; Zhang, J.; Xiao, W.; Xi, P.; Peng, S.; Gao, D., Electronic structure modulation of NiS<sub>2</sub> by transition metal doping for accelerating the hydrogen evolution reaction. *J. Mater. Chem. A* **2019**, *7* (9), 4971-4976.

54. Rathore, D.; Sharma, M. D.; Sharma, A.; Basu, M.; Pande, S., Aggregates of Ni/Ni(OH)<sub>2</sub>/NiOOH Nanoworms on Carbon Cloth for Electrocatalytic Hydrogen Evolution. *Langmuir* **2020**, *36* (46), 14019-14030.
55. Jin, C.; Zhai, P.; Wei, Y.; Chen, Q.; Wang, X.; Yang, W.; Xiao, J.; He, Q.; Liu, Q.; Gong, Y., Ni (OH)<sub>2</sub> Templated Synthesis of Ultrathin Ni<sub>3</sub>S<sub>2</sub> Nanosheets as Bifunctional Electrocatalyst for Overall Water Splitting. *Small* **2021**, *17* (33), 2102097.
56. Ali Akbari, M. S.; Bagheri, R.; Song, Z.; Najafpour, M. M., Oxygen-evolution reaction by nickel/nickel oxide interface in the presence of ferrate(VI). *Sci. Rep.* **2020**, *10* (1), 8757.
57. Mahala, C.; Sharma, R.; Sharma, M. D.; Pande, S., Development of copper cobalt sulfide with Cu: Co ratio variation on carbon cloth as an efficient electrode material for the oxygen evolution reaction. *ChemElectroChem* **2019**, *6* (20), 5301-5312.
58. Lin, J.; Wang, P.; Wang, H.; Li, C.; Si, X.; Qi, J.; Cao, J.; Zhong, Z.; Fei, W.; Feng, J., Defect-Rich Heterogeneous MoS<sub>2</sub>/NiS<sub>2</sub> Nanosheets Electrocatalysts for Efficient Overall Water Splitting. *Adv. Sci.* **2019**, *6* (14), 1900246.
59. Chen, Y.; Xu, Y.; Niu, S.; Yan, J.; Wu, Y.; Du, F.; Zhao, Y.; Zhu, Z.; Jiang, Z.; Tan, X., A highly efficient Fe–Ni–S/NF hybrid electrode for promoting oxygen evolution performance. *Chem. Commun.* **2021**, *57* (37), 4572-4575.
60. Zhu, W.; Yue, X.; Zhang, W.; Yu, S.; Zhang, Y.; Wang, J.; Wang, J., Nickel sulfide microsphere film on Ni foam as an efficient bifunctional electrocatalyst for overall water splitting. *Chem. Commun.* **2016**, *52* (7), 1486-1489.
61. Kulagov, E. A., The new nickel sulfide godlevskite. *Geol. Rudn. Mestorozhd.* **1969**, *11*, 115-121.
62. Fleet, M., Structure of godlevskite, Ni<sub>9</sub>S<sub>8</sub>. *Acta Cryst.* **1987**, *43* (12), 2255-2257.
63. Nørskov, J. K.; Rossmeisl, J.; Logadottir, A.; Lindqvist, L.; Kitchin, J. R.; Bligaard, T.; Jónsson, H., Origin of the Overpotential for Oxygen Reduction at a Fuel-Cell Cathode. *J. Phys. Chem. B* **2004**, *108* (46), 17886-17892.
64. Parsons, R., The rate of electrolytic hydrogen evolution and the heat of adsorption of hydrogen. *Trans. Faraday Soc.* **1958**, *54* (0), 1053-1063.
65. Würger, T.; Feiler, C.; Vonbun-Feldbauer, G. B.; Zheludkevich, M. L.; Meißner, R. H., A first-principles analysis of the charge transfer in magnesium corrosion. *Sci Rep* **2020**, *10* (1), 15006.

66. Doyle, R. L.; Lyons, M. E. G., An electrochemical impedance study of the oxygen evolution reaction at hydrous iron oxide in base. *Phys. Chem. Chem. Phys.* **2013**, *15* (14), 5224-5237.
67. de Chialvo, M. R. G.; Chialvo, A. C., Hydrogen evolution reaction: Analysis of the Volmer-Heyrovsky-Tafel mechanism with a generalized adsorption model. *J. Electroanal. Chem.* **1994**, *372* (1), 209-223.



# Ce-Doped $Ni_{0.85}Se$ 2D Nanosheets Developed on Carbon Cloth for Electrochemical Water-Splitting



- \* In this chapter, Ce doped  $Ni_{0.85}Se$  in pure phase was developed on carbon cloth by following hydrothermal route.
- \* The Ce doped  $Ni_{0.85}Se$  2D nanosheet applied for electrochemical HER and OER activity, which shows good bifunctional activity.

## *Abstract*

Developing a new, affordable, and efficient electrocatalyst for bifunctional activity is crucial for the advancement of water electrolysis technology. The doping with foreign atoms in electrocatalysts can tune the electronic properties, which further improves the water-splitting process. Herein, we have developed Ce doped Ni<sub>0.85</sub>Se as a bifunctional electrocatalyst in an alkaline medium. Hydrothermal method was used to develop a 2D nanosheet of Ce doped Ni<sub>0.85</sub>Se electrocatalyst. The as-developed pristine and doped electrocatalysts were characterized through various techniques. The optimized Ce<sub>0.1</sub>Ni<sub>0.85</sub>Se electrocatalyst represents -0.238 and 1.56 V vs. RHE as an onset potential for HER and OER, respectively, to generate 20 and 50 mA/cm<sup>2</sup> current density. The Ce<sub>0.1</sub>Ni<sub>0.85</sub>Se electrocatalyst works as a suitable cell in an alkaline medium with 1.73 V to generate 10 mA/cm<sup>2</sup> and 24 h stability. The introduction of Ce doping plays a pivotal role in tuning the electronic environment and facilitating a synergistic effect, ultimately improving the overall efficiency. Moreover, the active sites for water-splitting were generated by expansion and distortion in the Ni<sub>0.85</sub>Se lattice. The enhanced specific surface area and porous 2D nanosheets of the doped sample are beneficial for water splitting. Therefore, this idea can generate a route for developing a doped electrocatalyst with an efficient and stable activity.

### 6.1 Introduction

Amid the ongoing depletion of non-renewable resources and the deterioration of the environment, current research is focused on finding reproducible and clean energy.<sup>1-2</sup> Electrochemical water splitting reaction has emerged as an obvious way to generate green hydrogen, which can deal with the energy crisis.<sup>3</sup> Hydrogen fuel has attracted much attention due to its abundance, clean, and good recyclability nature. Electrochemical water splitting is an effective approach that involves two redox reactions for hydrogen and oxygen generation.<sup>4-5</sup> The theoretical electric voltage is 1.23 V; however, because of slow kinetics and the multistep electron transfer process, the electric voltage for water splitting is higher than the theoretical value.<sup>6</sup> In the current scenario, noble catalysts such as Pt, RuO<sub>2</sub>, and IrO<sub>2</sub> are effective in hydrogen and oxygen evolution reactions (HER and OER). However, the higher cost, low availability, and scarcity of different pH mediums impede their commercialization. Therefore, electrochemical water splitting faces significant challenges in achieving widespread adoption.<sup>7-9</sup>

In recent times, transition metal-based chalcogenides (oxides, sulfides, and selenides) have been extensively investigated due to their cost effectiveness and promising electrocatalytic activity.<sup>10</sup> Nevertheless, there are still some drawbacks of transition metal-based chalcogenides due to less active sites and poor conductivity.<sup>11</sup> Selenide-based materials are better due to the larger atomic radius, high metallic properties, and conductivity of the Se atom. Some transition metal selenides, such as MoSe<sub>2</sub>, WSe<sub>2</sub>, and CoSe<sub>2</sub>, are well explored for HER.<sup>12-13</sup> Among them, nickel-based selenides are interesting due to their excellent electrolytic performance. Due to their multiple oxidation states and tuneable electronic configuration, various nickel-based selenides (NiSe<sub>2</sub>, NiSe, and Ni<sub>1-x</sub>Se) are reported in the literature for energy-related applications.<sup>14</sup> The existence of a metal vacancy and the large number of unsaturated atoms in Ni<sub>0.85</sub>Se play a leading role in HER and OER performances. However, poor electron transfer and aggregation tendency reduce the electrical conductivity of Ni<sub>0.85</sub>Se, which requires further improvement.<sup>15-16</sup>

To improve the electrocatalytic performance of Ni<sub>0.85</sub>Se, numerous strategies are reported, such as morphology tuning, doping, and composite formation. Among them, doping is considered an effective method for fine-tuning electrocatalytic activity. The intrinsic activity of transition metal-based selenides can be improved by incorporating metal ions via doping.<sup>17-18</sup> The doping process can also change the electronic environment, leading to the creation of more active sites

and improving intrinsic activity. For instance, Liu and co-workers<sup>16</sup> engineered Fe-doped Ni<sub>0.85</sub>Se on Ni foam for water splitting. They found that introducing Fe as a dopant influenced the 2D nanosheet structure, enhancing the exposed surface area and active sites. This catalyst displayed outstanding performance in overall water splitting, attaining 100 mA/cm<sup>2</sup> current density at 1.52 V potential and providing stability over 40 hours. Zhao and co-workers<sup>19</sup> developed an electrocatalyst for HER in an acidic environment by supporting Co-doped Ni<sub>0.85</sub>Se with graphene oxide (GO). The Co<sub>0.1</sub>Ni<sub>0.75</sub>Se/GO catalyst exhibited superior performance, with a low onset potential of 103 mV *vs.* RHE to generate 10 mA/cm<sup>2</sup> current density and a reduced Tafel slope of 43 mV/dec. The introduction of Co as a dopant reduced the kinetic barrier by facilitating H-H bond formation, thereby enhancing the active sites and improving electronic conductivity. Yang and co-workers<sup>20</sup> developed Mo-doped Ni<sub>0.85</sub>Se on nickel foam for hydrogen generation along with electrooxidation of hydroxymethylfurfural. Mo doping can tune the *d* band center in Ni, which can decrease the hydrogen adsorption energy and further improve the hydrogen desorption process that helps in the electrooxidation process. Our group also reported cation (W<sup>6+</sup>, Fe<sup>3+</sup>, and Co<sup>2+</sup>) doping<sup>4, 21-22</sup> on Ni-based nanomaterials for electrocatalytic water splitting. W<sup>6+</sup> doped Ni(OH)<sub>2</sub>/NiOOH catalyst require an onset potential of 56 mV and 293 mV *vs.* RHE to obtain 10 and 50 mA/cm<sup>2</sup> current density for HER and OER, respectively. Fe-doped NiCo<sub>2</sub>Se<sub>4</sub> nanorods require a potential of 1.51 V to obtain 10 mA/cm<sup>2</sup> current density and 24 hours of stability. The better electrocatalytic performance is due to the presence of W<sup>6+</sup> and Fe<sup>3+</sup>, which behave as Lewis acid and tune the electronic properties of electrocatalyst.

Apart from the 3d transition metals, rare earth metals (Ce, La, etc.) show interesting characteristics due to available 4f orbitals. Specifically, the Ce element shows good redox behavior due to different redox centers, which offer good catalytic activity in CO oxidation and hydrogen production. Concerning this, Rong and co-workers<sup>23</sup> reported lanthanum-doped CoFe-layered double hydroxide (LDH) for better OER. The improved performance of CoFe-LDH is due to more defects and electrochemical active sites generated after the introduction of La<sup>3+</sup> and Ce<sup>3+</sup> in the system. Li and others<sup>24</sup> developed Ce-doped CoP for water splitting reaction, where they have also shown DFT calculations to prove the electronic environment change of CoP after Ce doping. The optimized Ce<sub>0.1</sub>CoP electrocatalyst offers good electrocatalytic performance with the voltage of 1.65 V to acquire a current density of 10 mA/cm<sup>2</sup>. Therefore, Ce introduction in the host matrix can improve the electrocatalytic performance.

Getting inspiration from the previously discussed research, we embarked on the development of Ce-doped Ni<sub>0.85</sub>Se nanosheets anchored on a carbon cloth substrate. This synthesis was achieved through a straightforward hydrothermal method, and the resulting materials were applied in a comprehensive water-splitting process. Our investigation encompassed a thorough characterization of both the pristine and doped materials, using analytical techniques such as XRD, XPS, FESEM, TEM, ICP-AES, and BET analysis. To fine-tune the Ce dopant content within Ni<sub>0.85</sub>Se, we systematically varied the concentration of the Ce<sup>4+</sup> precursor salt. Among the tested compositions, the Ce<sub>0.1</sub>Ni<sub>0.85</sub>Se sample exhibited the most promising performance in both the HER and OER. It displayed a low onset potential of -0.238 V *vs.* RHE and 1.56 V *vs.* RHE for HER and OER, enabling current densities of 20 and 50 mA/cm<sup>2</sup>, respectively. The Tafel slope is 118 and 58.8 mV/dec for HER and OER, respectively. The optimized Ce<sub>0.1</sub>Ni<sub>0.85</sub>Se sample is applied as a bifunctional electrocatalyst with an onset potential of 1.73 V for 10 mA/cm<sup>2</sup>. The advantages of this work can be folded as. First, the Ce dopant increases the electrochemical activity and stability of the Ni<sub>0.85</sub>Se sample. Second, simple hydrothermal method enables the synthesis of various Ce-doped Ni<sub>0.85</sub>Se ratios, adding versatility to the process. Third, the synergistic effect of different metal ions and morphological tuning regulates electrochemical activity. Fourth, after Ce doping, the change in the electronic environment in Ni<sub>0.85</sub>Se improves the active sites and enhances the overall electrocatalytic activity. Fifth, Ce-doped Ni<sub>0.85</sub>Se catalyst effectively functions as a bifunctional electrocatalyst with exceptional stability over a continuous 24-hour operation in an alkaline environment.

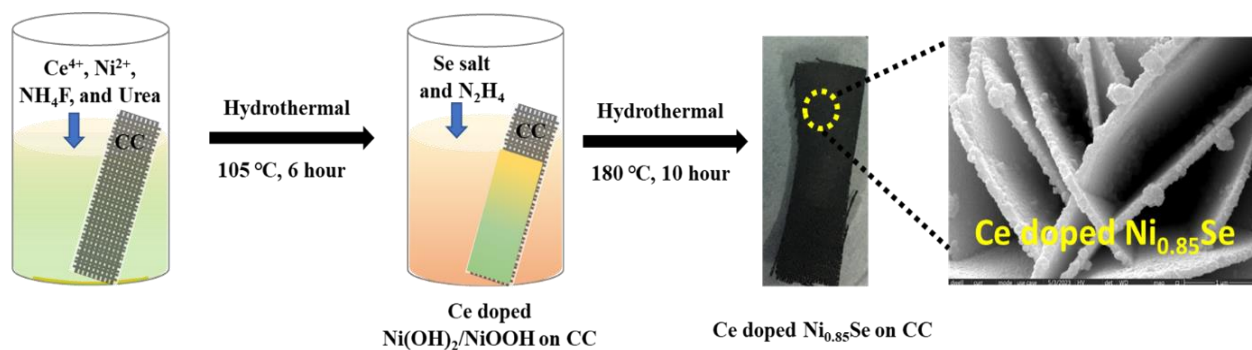
## 6.2 Experimental Section

**6.2.1 Synthesis of bare Ni<sub>0.85</sub>Se:** To synthesize pristine Ni<sub>0.85</sub>Se, a simple hydrothermal process was carried out. In the first step, 2.09 mmol Ni(NO<sub>3</sub>)<sub>2</sub>·6H<sub>2</sub>O, 9.0 mmol urea, and 4.04 mmol NH<sub>4</sub>F were dispersed in 60 mL DI water. The solution was sonicated for 10 minutes and transferred into a 100 mL capacity Teflon-lined autoclave. The 2×3 cm<sup>2</sup> carbon cloth was transferred along with the solution for hydrothermal reaction at 105 °C for 6 hours. In the next step, the Ni(OH)<sub>2</sub>/NiOOH deposited carbon cloth was transferred for the second hydrothermal reaction, i.e., for selenization. During the process of selenization, 0.3 gm of sodium selenite was dissolved in 4 mL N<sub>2</sub>H<sub>4</sub> and 26 mL Milli Q. The selenization process was executed at 180 °C for 10 hours, resulting in a black product on the CC. This product was then thoroughly washed with Milli-Q water and ethanol.

**6.2.2 Synthesis of Ce-doped Ni<sub>0.85</sub>Se:** Scheme 6.1 1 represents the synthesis of Ce-doped Ni<sub>0.85</sub>Se; a two-step hydrothermal procedure was carried out. In the first step, 2.09 mmol Ni(NO<sub>3</sub>)<sub>2</sub>·6H<sub>2</sub>O, 9.0 mmol urea, and 4.04 mmol NH<sub>4</sub>F were dispersed in 60 mL DI water. Additionally, we introduced 0.209 mmol of ammonium ceric nitrate into the solution for doping purposes. The entire solution was subjected to a 10-minute sonication process. The complete solution was taken into a Teflon-lined autoclave, with the carbon cloth positioned along the autoclave's wall. The hydrothermal reaction was conducted at 105 °C for a duration of six hours. For the subsequent step, 0.3 gm of Na<sub>2</sub>SeO<sub>3</sub> was dissolved in 4 mL of hydrazine hydrate and 26 mL DI water for selenization and transferred into a Teflon container. The sample developed earlier, which had been deposited on the carbon cloth, was immersed in the 30 mL selenization solution. Another hydrothermal reaction was executed at 180 °C, and the process was allowed to continue for 10 hours. The resultant Ce-doped Ni<sub>0.85</sub>Se sample on the carbon cloth was black color, washed with ethanol and DI water before being dried in a conventional oven.

For the ratio variation of Ce dopant two, another concentration of ammonium ceric nitrate was used, keeping unchanged the remaining procedure of Ce-doped Ni<sub>0.85</sub>Se synthesis. 0.105 mmol and 0.05 mmol of ammonium ceric nitrate were taken, and the same procedure was repeated. As per the concentration (mmol) of ceric ammonium nitrate, the developed electrocatalysts were named Ce<sub>0.2</sub>Ni<sub>0.85</sub>Se, Ce<sub>0.1</sub>Ni<sub>0.85</sub>Se, and Ce<sub>0.05</sub>Ni<sub>0.85</sub>Se throughout the MS.

**Scheme 6.1:** Diagram representation for the synthesis of Ce doped Ni<sub>0.85</sub>Se on CC surface.



### 6.2.3 Electrochemical Study

The electrochemical investigation was conducted within a three-electrode system. The working electrode was developed by depositing the sample on carbon cloth (CC) and securing it in place with an insulating epoxy paste. This electrode was allowed to dry under normal air

conditions, resulting in a working electrode area of 0.16 cm<sup>2</sup>. Graphite served as the counter electrode, while Ag/AgCl electrode was implied as the reference electrode. Electrochemical measurements were conducted using a CHI604E workstation. For both the doped and pristine Ni<sub>0.85</sub>Se samples, the catalyst loading was calculated as 2.89 mg/cm<sup>2</sup> on the 3.5 × 2 cm<sup>2</sup> area of the CC. The electrolyte employed for the electrochemical reactions in HER and OER was a 1.0 M KOH solution. The primary technique utilized for the electrochemical analysis was linear sweep voltammetry (LSV). In the case of the HER, LSV measurements were conducted within a potential window of -0.9 to -1.8 V *vs.* Ag/AgCl, utilizing a scan rate of 2 mV/sec. Conversely, for the OER, the LSV was carried out within the potential range of 0 to 0.8 V *vs.* Ag/AgCl, also employing of 2 mV/sec scan rate. Impedance measurements were recorded using the three-electrode system, with the onset potential serving as the operational bias for these measurements. The frequency range for the impedance analysis was configured from 50 kHz to 0.1 Hz, and an AC perturbation of 5 mV was applied.

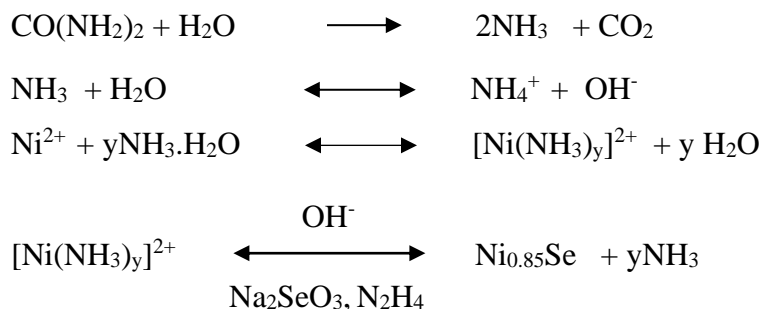
### 6.3 Result and discussion

The detailed synthesis of Ce-doped Ni<sub>0.85</sub>Se is reported in the experimental section. Tuning of Ce dopant in Ni<sub>0.85</sub>Se is also performed.

#### 6.3.1 Mechanism of formation

The detailed synthesis of Ce-doped Ni<sub>0.85</sub>Se is reported in the experimental section. Bare Ni<sub>0.85</sub>Se and Ce-doped Ni<sub>0.85</sub>Se sample is deposited on the surface of CC by following a two-step hydrothermal method. In the first step, Ni(OH)<sub>2</sub>/NiOOH was formed as an intermediate species on the surface of CC. Urea was used as a hydrolyzing agent, and NH<sub>4</sub>F works as a growth-regulating agent.<sup>25-26</sup> Initially, *y*NH<sub>3</sub>·H<sub>2</sub>O reacted with Ni<sup>2+</sup> salt and [Ni(NH<sub>3</sub>)<sub>*y*</sub>]<sup>2+</sup> complex was formed. In the next step, [Ni(NH<sub>3</sub>)<sub>*y*</sub>]<sup>2+</sup> complex reacted with OH<sup>-</sup> ion for the generation of Ni(OH)<sub>2</sub>/NiOOH. However, Ni(OH)<sub>2</sub>/NiOOH was transformed to Ni<sub>0.85</sub>Se in the second hydrothermal step by selenization. An aqueous solution of sodium selenite and N<sub>2</sub>H<sub>4</sub>·2H<sub>2</sub>O was used during hydrothermal step, where, Na<sub>2</sub>SeO<sub>3</sub> was reduced to Se<sup>2-</sup> ions and reacted with Ni(OH)<sub>2</sub>/NiOOH to form black-colored bare Ni<sub>0.85</sub>Se sample.<sup>27</sup> During Ce doping Ce<sub>0.1</sub>Ni<sub>0.85</sub>Se was developed without

any change in the chemical reaction. No cerium hydroxide was formed before selenization. The following possible reaction occurs in the reaction medium during the formation of Ni<sub>0.85</sub>Se.



### 6.3.2 XRD, Raman, BET and XPS analysis

The structural composition, phase, and purity of doped and undoped samples were confirmed with powder XRD analysis, which is shown in Figure 6.1a. It becomes evident from Figure 6.1a that the peak position at 33.6°, 45.2°, 50.8°, 60.4°, 62.1°, and 70.1° corresponds to the (101), (102), (110), (103), (201), and (202) lattice planes, respectively, which is well acquainted with the hexagonal lattice of Ni<sub>0.85</sub>Se (JCPDS no. 18-0888). The peak positions for Ni<sub>0.85</sub>Se are well corroborated with the reported literature.<sup>28-29</sup> After the introduction of Ce dopant in the system, the XRD peaks are shifted towards lower diffraction angles at 33.0°, 44.4°, 50.2°, 59.6°, 61.4°, and 69.4° associated with (101), (102), (110), (103), (201), and (202) lattice planes. It can be observed from Figure 6.1b that the peak at 2θ = 33.6 (bare Ni<sub>0.85</sub>Se) is shifted at 33.0 for Ce doped Ni<sub>0.85</sub>Se. The calculated distance value for the (101) plane is ~0.26 nm and ~0.29 nm for bare Ni<sub>0.85</sub>Se and Ce doped Ni<sub>0.85</sub>Se, respectively. The increase in the distance value for the Ce doped Ni<sub>0.85</sub>Se sample is due to the larger ionic radii of the Ce<sup>4+</sup> (97 pm) than Ni<sup>2+</sup> (78 pm), which induces lattice distortion. The absence of any new peak in the Ce doped Ni<sub>0.85</sub>Se lattice confirms partial substitution of Ni by Ce. The Debye Scherer equation is used to calculate the crystallite size of bare Ni<sub>0.85</sub>Se and Ce-doped Ni<sub>0.85</sub>Se and reported as 32.1 nm and 25.7 nm, respectively. The decrease in crystallite size may be due to the doping with Ce. Therefore, the lattice distortion and crystallite size reduction correlate with the presence of Ce dopant in the Ni<sub>0.85</sub>Se lattice. Our group reported similar phenomena of crystallite size reduction and lattice distortion after Co doping in Ni<sub>9</sub>S<sub>8</sub> lattice.<sup>22</sup>



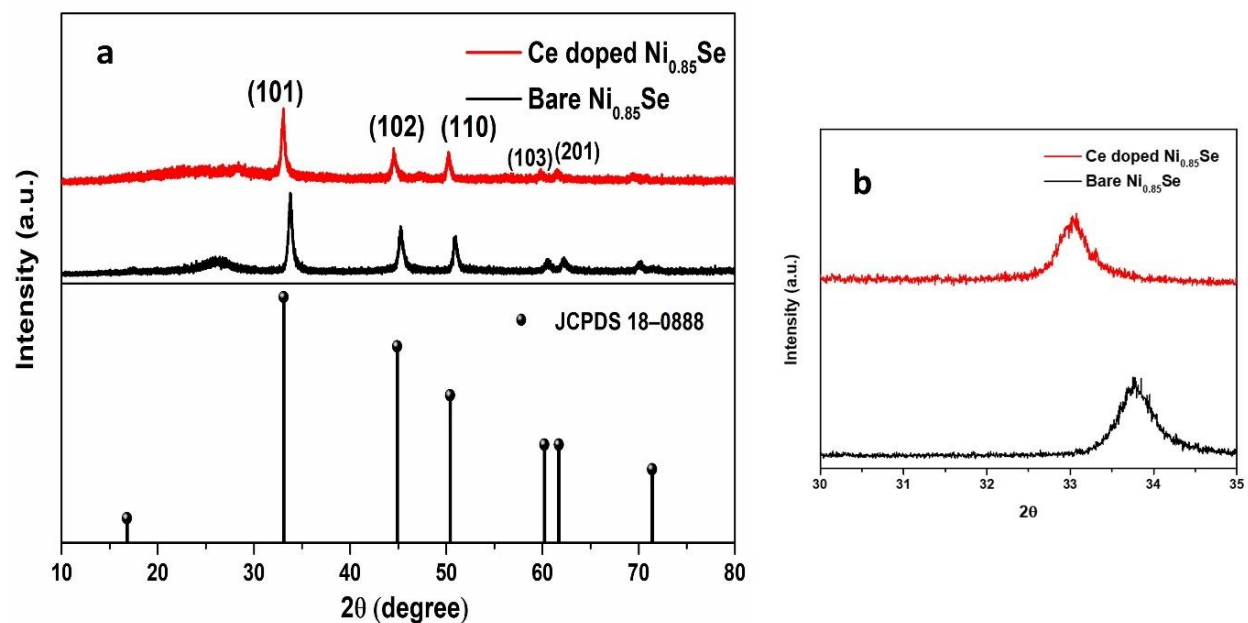


**Figure 6.1:** (a) XRD analysis of pristine and Ce doped  $\text{Ni}_{0.85}\text{Se}$  catalysts (b) low scan XRD of pristine and Ce doped  $\text{Ni}_{0.85}\text{Se}$  catalysts.

Raman analysis was further performed to confirm the bonding in pristine and doped  $\text{Ni}_{0.85}\text{Se}$  samples. Figure 6.2 represent the Raman peaks of  $\text{Ni}_{0.85}\text{Se}$  and  $\text{Ce}_{0.1}\text{Ni}_{0.85}\text{Se}$  sample. The Raman peak at  $188\text{ cm}^{-1}$  represents Se-Se stretching mode of the  $\text{Ni}_{0.85}\text{Se}$  sample, which is indicative of a selenium-enriched environment. The other peak at  $512\text{ cm}^{-1}$  is the indicative peak of the Ni-Se bond in the  $\text{Ni}_{0.85}\text{Se}$  sample. These peaks are well matched with the existing literature.<sup>30-31</sup> After doping with Ce, there is no new or extra Raman peak in the  $\text{Ce}_{0.1}\text{Ni}_{0.85}\text{Se}$  sample. The peaks are shifted towards higher wave numbers at  $191\text{ cm}^{-1}$  and  $533\text{ cm}^{-1}$  representing Se-Se and Ni-Se bonding, respectively. There is no peak corresponding to Ce-Se bond in the sample, which further confirms that Ce dopant partially substitute the Ni in  $\text{Ni}_{0.85}\text{Se}$  sample. Liu and coworkers<sup>32</sup> reported Fe-doped  $\text{Ni}_{0.85}\text{Se}$ , which shows peak shift in  $\text{Fe}_{0.08}\text{Ni}_{0.77}\text{Se}$  sample to a larger wave number than the pristine sample.

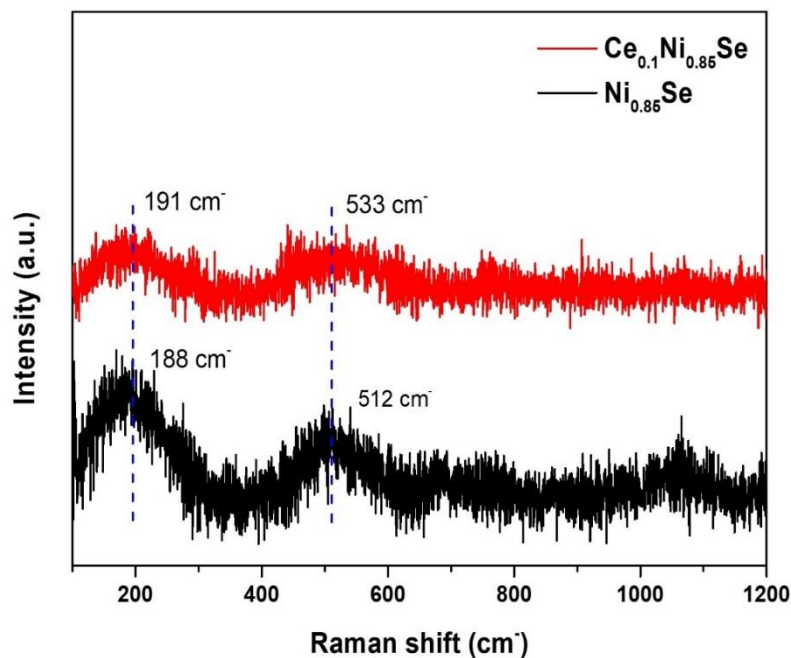


**Figure 6.2:** Raman analysis of Ni<sub>0.85</sub>Se, and Ce<sub>0.1</sub>Ni<sub>0.85</sub>Se.

The analysis of the specific surface area of pristine and Ce doped Ni<sub>0.85</sub>Se catalysts is accomplished using the BET (Brunauer–Emmett–Teller) analysis. The N<sub>2</sub> adsorption-desorption isotherm of Ce doped Ni<sub>0.85</sub>Se sample is given in Figure 6.3a, which shows that the isotherm with an increment in the relative low-pressure region specifies the presence of micropores. The appearance of mesopores is confirmed by a significant hysteresis loop, which appears at relatively high pressure.<sup>33-34</sup> The BET-specific surface area is 9.34 m<sup>2</sup>/g to 12.8 m<sup>2</sup>/g for pristine Ni<sub>0.85</sub>Se and Ce doped Ni<sub>0.85</sub>Se, respectively. The BJH pore diameter distribution of Ce doped Ni<sub>0.85</sub>Se is calculated (Figure 6.3b), which represents the doped sample consisting of mesopores around 3 nm and a few larger mesopores around 19 nm. This structural characteristic is favorable for increasing the exposure of active sites and better contact with electrolytes, thereby improving the catalytic performance of the material. The substantial specific surface area and tiny mesopores facilitated the effective mass transfer and offered good active sites for electrochemical reactions.

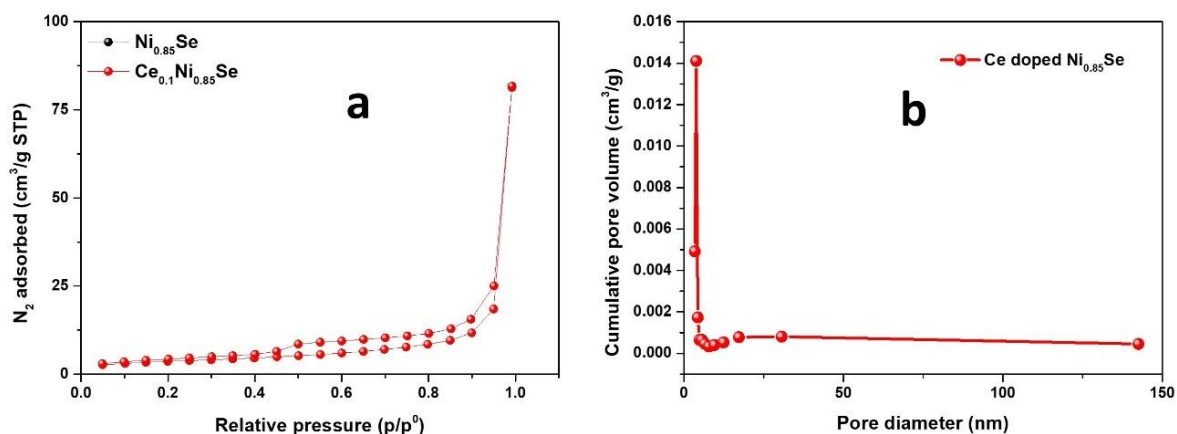


**Figure 6.3:** (a) BET adsorption-desorption isotherm (b) BJH plot of Ce doped Ni<sub>0.85</sub>Se.

The chemical valence state and the electronic environment of Ni<sub>0.85</sub>Se and Ce doped Ni<sub>0.85</sub>Se was investigated by using XPS analysis. Figure 6.4a illustrates the deconvoluted XPS spectra of Ni 2p of pristine Ni<sub>0.85</sub>Se. Ni 2p spectra are present with two doubles and a shake-up satellite. The binding energy (BE) values for the first two peaks of the Ni 2p<sub>3/2</sub> spin-orbit state are represented at 855.4 eV and 856.4 eV, indicative of the existence of Ni<sup>2+</sup> and Ni<sup>3+</sup>, respectively. The first satellite peak of Ni 2p<sub>3/2</sub> is at 861.2 eV. Another doublet peak of Ni 2p<sub>1/2</sub> state appeared at 872.8 eV and 874.2 eV, representing the appearance of Ni<sup>2+</sup> and Ni<sup>3+</sup> states, respectively. The remaining peak at 879.4 eV is due to other shake-up satellites of Ni 2p<sub>1/2</sub> state. The BE values of Ni 2P align well with the values reported in the literature.<sup>35</sup> Deconvoluted XPS spectra (Figure 6.4b) of Se 3d show the BE value at 54.2 eV (3d<sub>5/2</sub>) and 55.2 eV (3d<sub>3/2</sub>), which confirms the presence of selenide ion (Se<sup>2-</sup>). The peaks at BE values of 58.1 eV and 59.07 eV represent the presence of SeOx, which is due to the surface oxidation. The survey spectrum depicted in Figure 6.4c exhibits peaks corresponding to Ni, Se, C, and O in the pristine Ni<sub>0.85</sub>Se sample. Therefore, pristine Ni<sub>0.85</sub>Se consist of Ni<sup>2+</sup>, Ni<sup>3+</sup> and Se<sup>2-</sup> ions.<sup>36</sup>



representing the  $\text{Ce}^{4+}$  and  $\text{Ce}^{3+}$  in the doped sample. Further the peaks found at 881.3 eV and 884.9 eV are due to  $\text{Ce } 3d_{5/2}$  and represent the mixed valence state of  $\text{Ce}^{4+}$  and  $\text{Ce}^{3+}$ . The peaks at 898.6 eV and 902.8 eV are due to  $\text{Ce } 3d_{3/2}$ , which also exhibits the diverse valence state of Ce. Moreover, the BE values at 891.2, 906.9, and 913.1 eV also show the presence of a  $\text{Ce}^{4+}$  state. The survey spectrum represents the Ce, Ni, O, Se, and C elements in the  $\text{Ce}_{0.1}\text{Ni}_{0.85}\text{Se}$  sample (Figure 6.5d). The existing literature well supports the BE values of Ce, Ni, and Se.<sup>19, 37-38</sup>

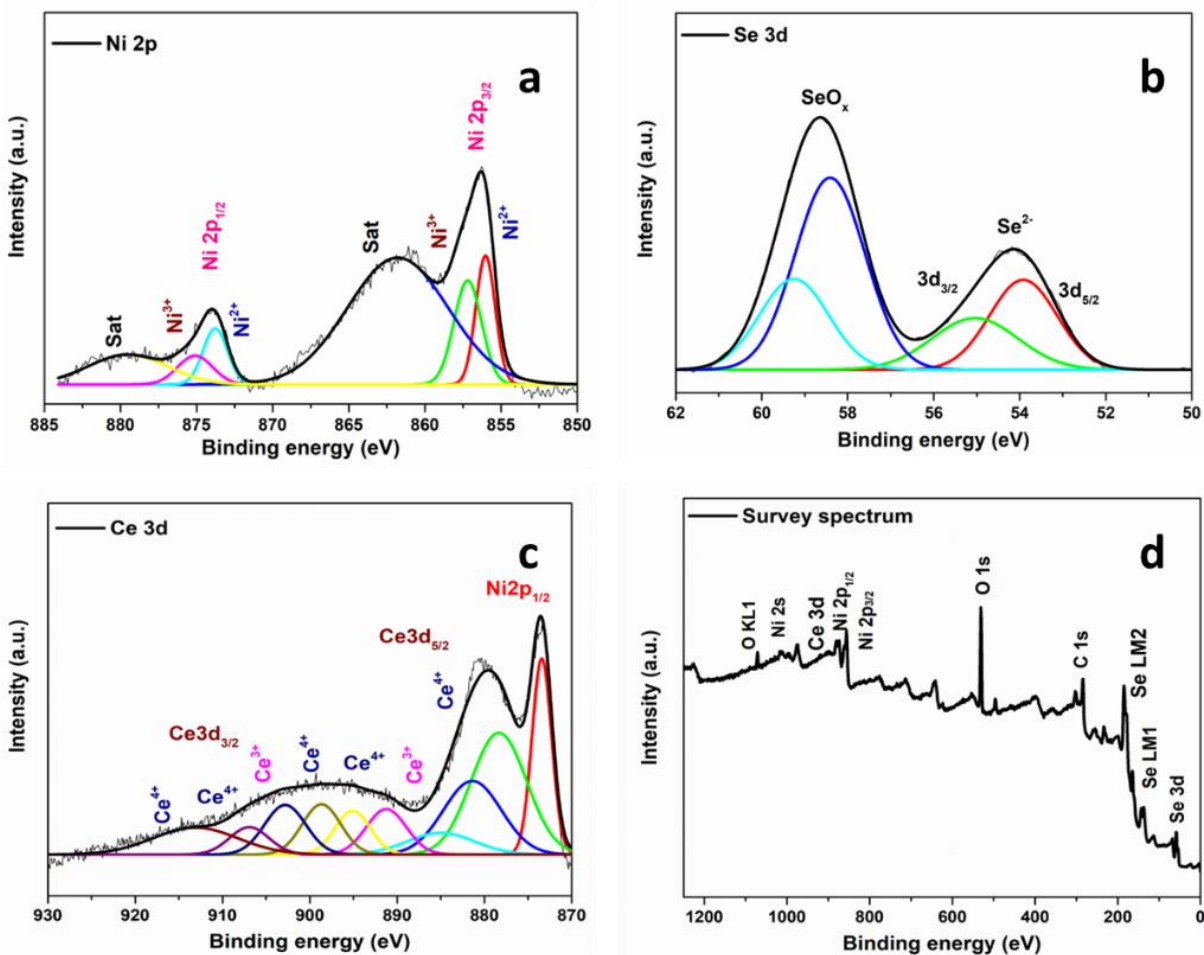


**Figure 6.5:** XPS analysis of  $\text{Ce}_{0.1}\text{Ni}_{0.85}\text{Se}$  (a) deconvoluted spectra of Ni 2p, (b) deconvoluted spectra of Se 3d, (c) high-resolution spectra of Ce 3d, and (d) high-resolution spectra of Co 2p survey spectrum.

The XPS depth profile analysis of pristine  $\text{Ni}_{0.85}\text{Se}$  and  $\text{Ce}_{0.1}\text{Ni}_{0.85}\text{Se}$  samples was investigated, which shows the presence of Ni 2p and Se 3d in both the sample (Figure 6.6 and 6.7). Depth profiling of Ni 2p exhibits similar peak up to 135 nm etching of the sample. The Se 3d spectra also display the continuous presence of Se in  $\text{Ni}_{0.85}\text{Se}$  up to 135 nm. This study confirms the presence of Ni-Se bond throughout the composite.

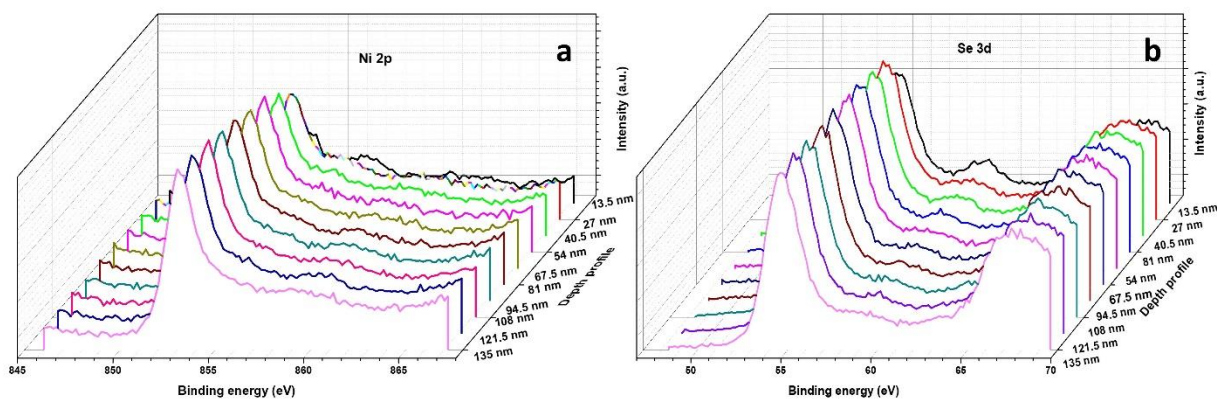


**Figure 6.6:** Depth XPS analysis of pristine  $\text{Ni}_{0.85}\text{Se}$  (a) Ni 2p and (b) Se 3d.

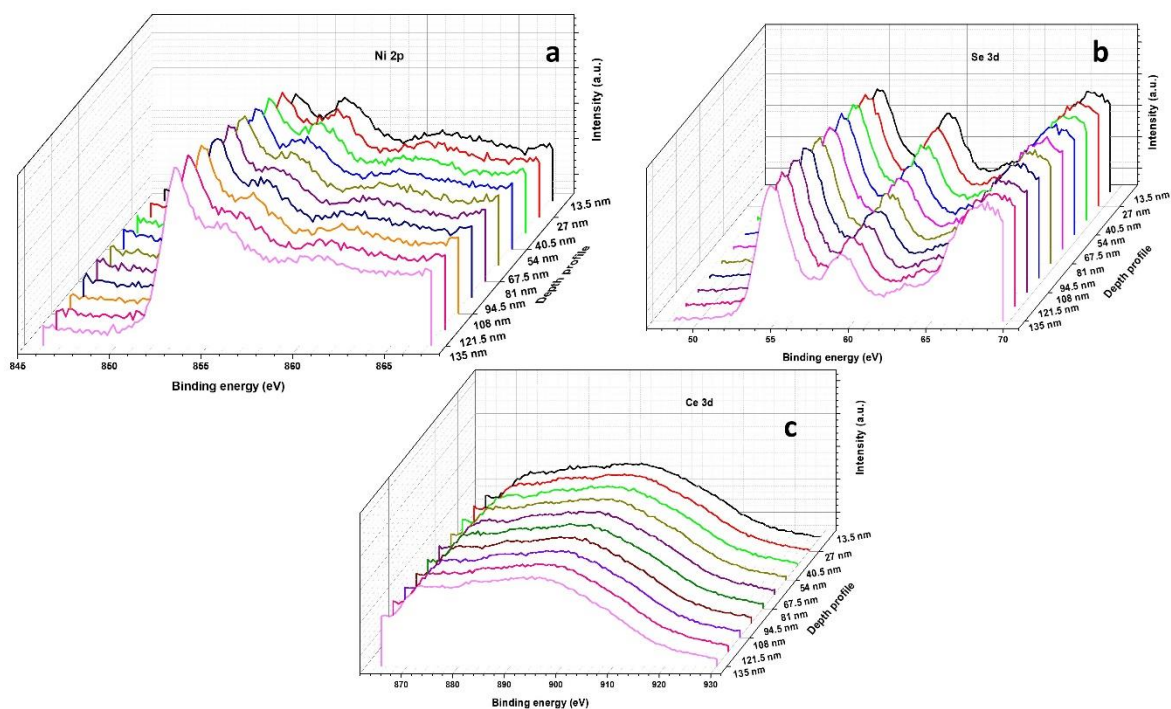


**Figure 6.7:** Depth XPS analysis of pristine  $\text{Ce}_{0.1}\text{Ni}_{0.85}\text{Se}$  (a) Ni 2p (b) Se 3d and (c) Ce 3d.



The dopant Ce can act as a Lewis acid in the  $\text{Ce}_{0.1}\text{Ni}_{0.85}\text{Se}$  sample, which can attract electrons from the Ni site. The available 4f orbital of the Ce dopant can attract electrons, which changes the electronic environment of Ni and Se sites, which can induce the synergistic effect. After doping with  $\text{Ce}^{4+}$ , the BE values for Ni 2p are shifted towards higher BE values (0.6 eV~0.8 eV). The Se 3d BE values are shifted to a lower BE of approximately 0.3 eV. The shifting in BE may be due to the high electronegativity of the Se atom. The charge transfer from Ni and Ce takes place towards Se atom, due to which, after doping, the BE values of Ni shifted to the higher side and Se towards the lower. The Lewis acid nature of Ce can be proven with the percentage ratio of  $\text{Ni}^{2+}/\text{Ni}^{3+}$  after doping. The calculated ratio of  $\text{Ni}^{2+}/\text{Ni}^{3+}$  in the pristine sample is 1.84, which reduces to 0.87 after doping. This ratio decrement shows the increased number of  $\text{Ni}^{3+}$  sites after doping with  $\text{Ce}^{4+}$ , leading to better electrocatalytic activity. Basu and co-workers reported a decrease in the ratio of  $\text{Ni}^{2+}/\text{Ni}^{3+}$  after doping with  $\text{Fe}^{3+}$ , which represents a higher quantity of  $\text{Ni}^{3+}$  in  $\text{Ni}(\text{OH})_2/\text{NiOOH}$ . Our group also stated the Lewis acidity of Fe in the  $\text{NiCo}_2\text{Se}_4$  system.<sup>4</sup> This change in BE values and synergistic effect between metal ions ( $\text{Ce}^{3+}$ ,  $\text{Ce}^{4+}$ ,  $\text{Ni}^{2+}$ ,  $\text{Ni}^{3+}$ ) and  $\text{Se}^{2-}$  are attributed to better electrocatalytic performance.

### 6.3.3 FESEM, ICP-AES and TEM analysis

FESEM analysis was conducted to analyze the surface morphology, structure, and shape of the pristine and doped  $\text{Ni}_{0.85}\text{Se}$ . Figure 6.8 a and b represents the vertically grown 2D nanosheet morphology of  $\text{Ni}_{0.85}\text{Se}$  on the surface of carbon cloth. These 2D nanosheets are interconnected to each other and made up of hexagonal shapes with an average thickness of 200-350 nm, as given in Figure 6.8b. The outer surface of the  $\text{Ni}_{0.85}\text{Se}$  sample has a porous and rough structure. The FESEM images of Ce doped  $\text{Ni}_{0.85}\text{Se}$  are represented in Figures 6.8c and 6.8d, which exhibit that Ce dopant does not affect the regular morphology and shape of  $\text{Ni}_{0.85}\text{Se}$ . It can be observed from Figure 6.8c that Ce-doped  $\text{Ni}_{0.85}\text{Se}$  nanosheets are distributed on the surface of CC. However, Ce dopant reduces the thickness of  $\text{Ni}_{0.85}\text{Se}$  nanosheets, which shows 70-130 nm (Figure 6.8d). Furthermore, vertically grown nanosheets of Ce doped  $\text{Ni}_{0.85}\text{Se}$  sample are also rough and porous in nature. The porous and uniform distribution of the  $\text{Ce}_{0.1}\text{Ni}_{0.85}\text{Se}$  sample is more favorable for the complete exposure of catalytic active sites. The decrease in thickness is presumably due to the doping of the Ce atom. The reduction in thickness of the Ce doped  $\text{Ni}_{0.85}\text{Se}$  sample is well corroborated with the literature. Basu and co-workers<sup>39</sup> reported thinner 2D nanosheets of Fe-

doped  $\text{Ni}(\text{OH})_2/\text{NiOOH}$  sample. Our group<sup>4</sup> also reported Fe-doped  $\text{NiCo}_2\text{Se}_4$  thinner nanorod after the addition of dopant Fe in the system.

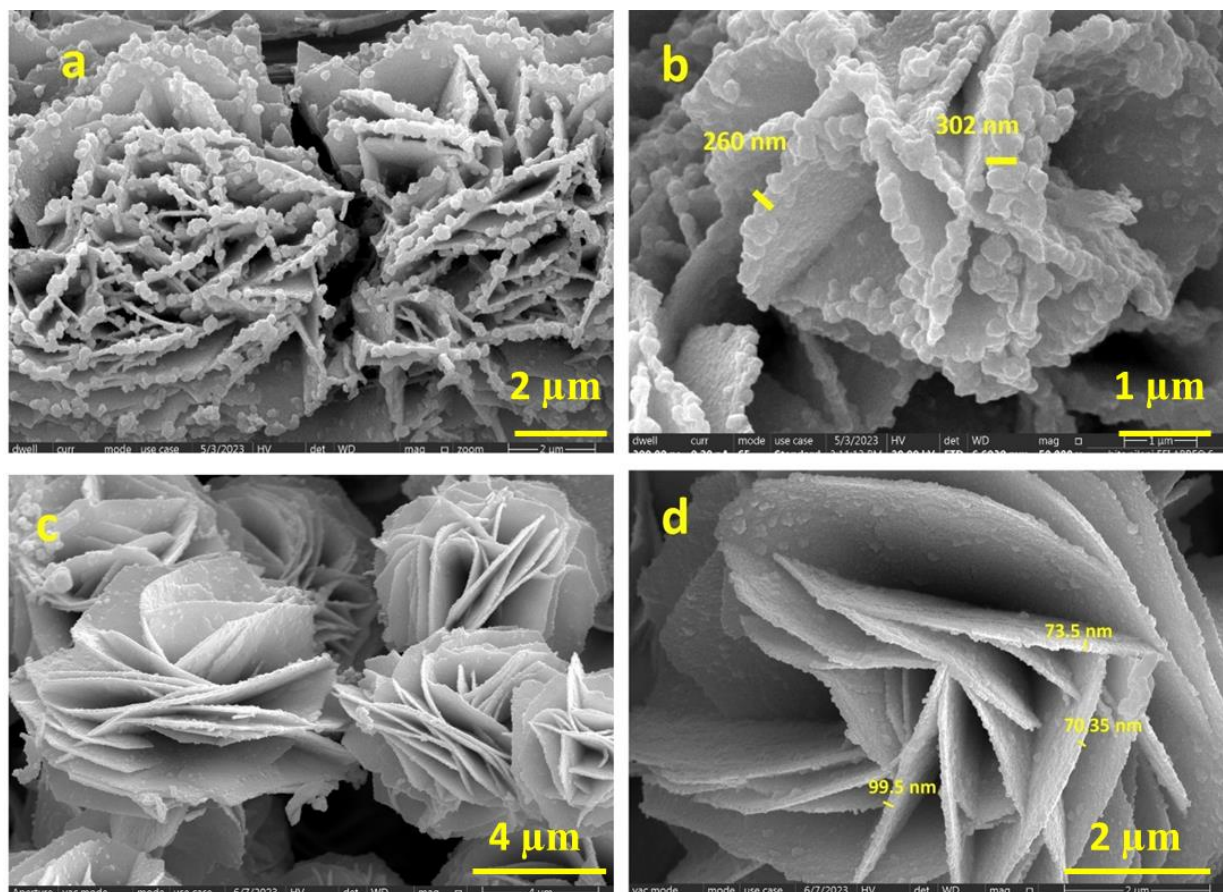


**Figure 6.8:** FESEM images of  $\text{Ni}_{0.85}\text{Se}$  catalyst at various magnifications (a and b)  $\text{Ce}_{0.1}\text{Ni}_{0.85}\text{Se}$  catalyst at various magnifications, (c and d).

EDS analysis confirms the existence of Ni, Se, and C in the pristine  $\text{Ni}_{0.85}\text{Se}$  (Figure 6.9), whereas the analysis of Ce doped  $\text{Ni}_{0.85}\text{Se}$  nanosheets confirms the presence of Ni, Se, C, and Ce in the sample (Figure 6.10). The mapping analysis of the Ce doped  $\text{Ni}_{0.85}\text{Se}$  sample also shows the uniform distribution of Ce, Ni, Se, and C elements after doping. To ensure the elemental distribution and exact amount of dopant in the  $\text{Ce}_{0.1}\text{Ni}_{0.85}\text{Se}$  sample, ICP-AES analysis was performed. Table 6.1 shows that the atomic percentage of Ni: Se is 1.4:1 in pristine  $\text{Ni}_{0.85}\text{Se}$ . The amount of Ce dopant in the  $\text{Ce}_{0.1}\text{Ni}_{0.85}\text{Se}$  sample is 6.4%, which represents Ce: Ni is 1:14.3. The Ce: Ni ratio is almost similar to the experimental amount, Ce: Ni = 1:19.8 (0.105: 2.09 in mmol).



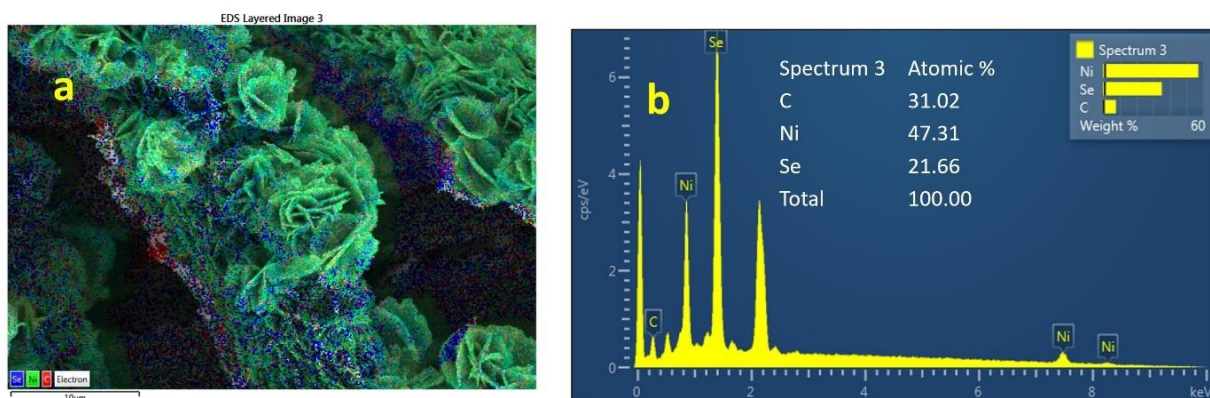


Figure 6.9: EDS analysis of  $\text{Ni}_{0.85}\text{Se}$ .

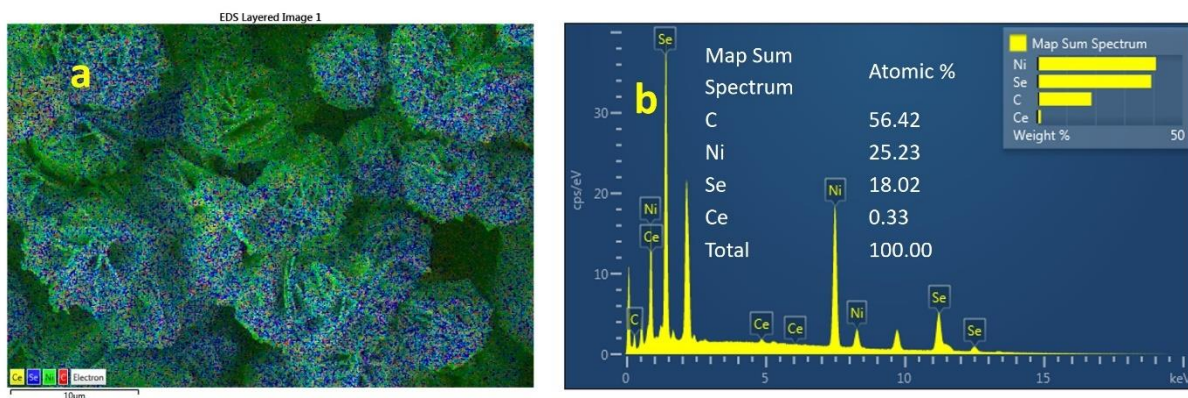


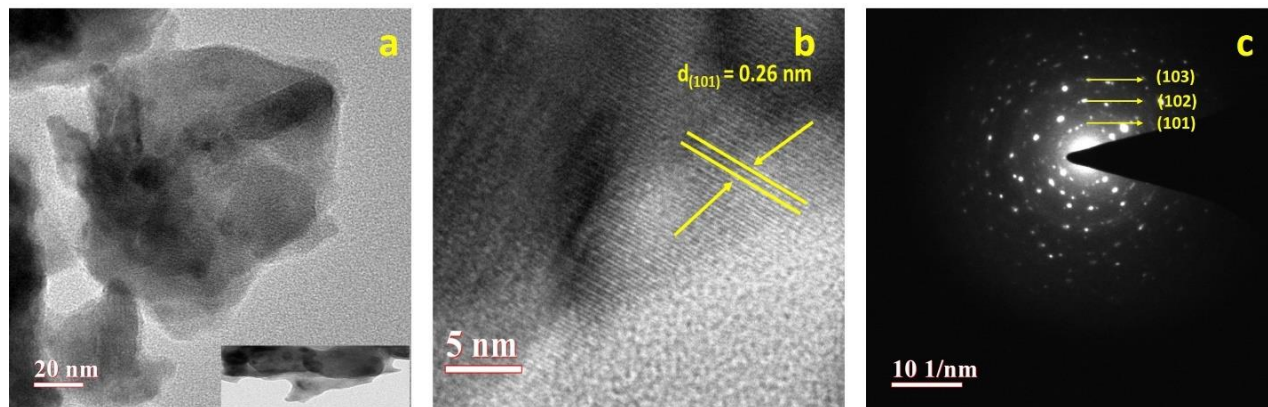
Figure 6.10: EDS analysis of  $\text{Ce}_{0.1}\text{Ni}_{0.85}\text{Se}$ .

Table 6.1: ICP-AES data of  $\text{Ni}_{0.85}\text{Se}$  and  $\text{Ce}_{0.1}\text{Ni}_{0.85}\text{Se}$ .

Sample	Ce	Ni	Se
$\text{Ni}_{0.85}\text{Se}$		72.3 %	48.67 %
$\text{Ce}_{0.1}\text{Ni}_{0.85}\text{Se}$	6.4 %	91.3 %	56.0 %

To further confirm the morphology, size, and lattice distortion, TEM, HRTEM, and SAED analysis were performed. The TEM image of  $\text{Ni}_{0.85}\text{Se}$  can be seen in Figure 6.11a, representing 2D nanosheet having contrast verifying the porous nature of  $\text{Ni}_{0.85}\text{Se}$  nanosheets. The 2D nanosheets of  $\text{Ni}_{0.85}\text{Se}$  are made up of hexagonal structures, as seen in Figure 6.11a, which is well corroborated to FESEM analysis. The HRTEM image in Figure 6.11b represents the d spacing of 0.26 nm, which is well indexed with the (101) plane of the  $\text{Ni}_{0.85}\text{Se}$  lattice.<sup>40</sup> The crystalline nature

of pristine  $\text{Ni}_{0.85}\text{Se}$  is confirmed through SAED analysis in Figure 6.11c; the bright spots are clearly visible due to the crystallinity and lattice planes of the  $\text{Ni}_{0.85}\text{Se}$ .



**Figure 6.11:** (a) TEM, (b) HRTEM (c) SAED analysis of  $\text{Ni}_{0.85}\text{Se}$ .

The introduction of Ce dopant reduces the thickness of 2D nanosheets of  $\text{Ni}_{0.85}\text{Se}$ , as shown in Figure 6.12a, which is well corroborated with FESEM. Figure 6.12a represents the 2D nanosheet morphology is maintained after doping. The 2D thinner, porous nanosheet of Ce doped  $\text{Ni}_{0.85}\text{Se}$  is well-matched with the FESEM and BET analysis. The lattice distortion is also confirmed with HRTEM analysis; Figure 6.12b represents the 0.29 nm lattice spacing with (101) plane. It is clearly observed that the lattice spacing of 0.26 nm increased to 0.29 nm after doping with Ce in  $\text{Ni}_{0.85}\text{Se}$ , which reflects the lattice expansion and distortion. The SAED pattern also confirms the crystallinity and the presence of (101), (102), and (103) lattice planes of the Ce doped  $\text{Ni}_{0.85}\text{Se}$  sample, shown in Figure 6.12 c.

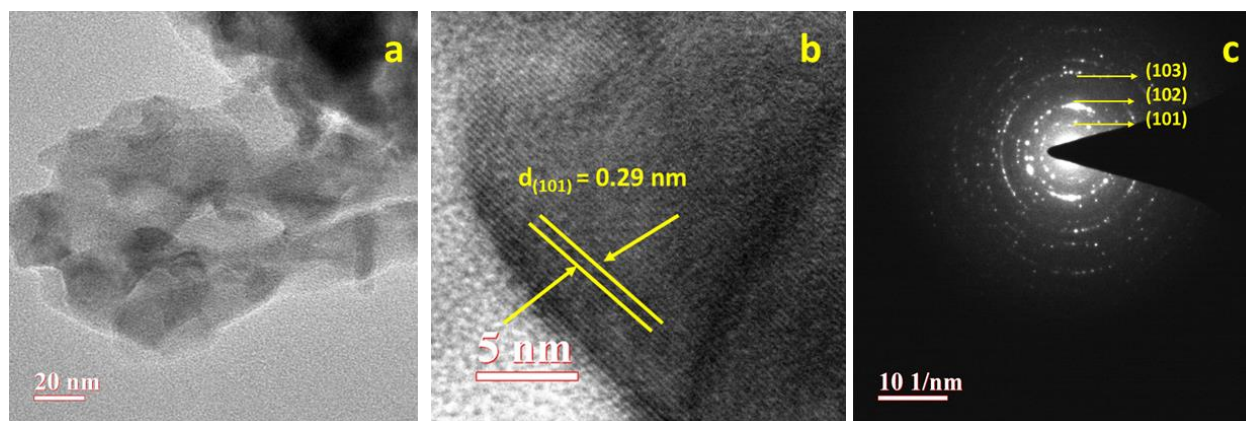


**Figure 6.12:** (a) TEM images, (b) HRTEM, (c) SAED analysis of  $\text{Ce}_{0.1}\text{Ni}_{0.85}\text{Se}$ .

Therefore, some critical points emerged from the discussions in the doped sample. First, Ce doping expands the lattice of  $\text{Ni}_{0.85}\text{Se}$ , which is confirmed with XRD and HRTEM analysis.

Second, morphology tuning generates a thinner 2D nanosheet of  $\text{Ni}_{0.85}\text{Se}$ . The thinner 2D nanosheets generate more active sites. Third, shifts in the binding energy values and synergistic effects between the metal ions ( $\text{Ce}^{3+}$ ,  $\text{Ce}^{4+}$ ,  $\text{Ni}^{2+}$ ,  $\text{Ni}^{3+}$ ) and  $\text{Se}^{2-}$  ion help to regulate the electronic environment. Fourth, BET analysis proves that the specific surface area increases with high porosity that accelerates gas adsorption and desorption during the electrochemical reaction. These points speed up the efficient electrocatalytic activity of the Ce doped  $\text{Ni}_{0.85}\text{Se}$  sample. Therefore, Ce doped  $\text{Ni}_{0.85}\text{Se}$  can be a potential candidate for the water-splitting reaction.

### 6.3.4 Electrocatalytic study (HER and OER)

A three-electrode system was utilized, in which the working electrode comprised of carbon cloth with a fixed area of  $0.16 \text{ cm}^2$ , a graphite electrode, and an Ag/AgCl electrode, all immersed in a 1 M KOH solution. The pristine  $\text{Ni}_{0.85}\text{Se}$ ,  $\text{Ce}_{0.2}\text{Ni}_{0.85}\text{Se}$ ,  $\text{Ce}_{0.1}\text{Ni}_{0.85}\text{Se}$ ,  $\text{Ce}_{0.05}\text{Ni}_{0.85}\text{Se}$ , 5% Pt-C, and bare CC is checked for HER study by applying negative potential window using linear sweep voltammetry. In Figure 6.13a, the LSV curve for HER is presented. The bare CC exhibits minimal current density within the applied potential range. Pristine  $\text{Ni}_{0.85}\text{Se}$  demonstrates an onset potential of  $-0.268 \text{ V vs. the RHE}$  to achieve a current density of  $20 \text{ mA/cm}^2$ . After introducing Ce in the  $\text{Ni}_{0.85}\text{Se}$  system, HER performance improved.  $\text{Ce}_{0.1}\text{Ni}_{0.85}\text{Se}$  catalyst shows the lowest onset potential of  $-0.238 \text{ V vs. RHE}$  to obtain  $20 \text{ mA/cm}^2$  current density. To compare the current density at  $-0.4 \text{ V vs. RHE}$ , the bar diagram plotted in Figure 6.13b shows the high current density of  $\text{Ce}_{0.1}\text{Ni}_{0.85}\text{Se}$  catalyst among all other catalysts. The anodic shift of 30 mV is observed due to the presence of Ce dopant. Other Ce-doped samples,  $\text{Ce}_{0.2}\text{Ni}_{0.85}\text{Se}$  and  $\text{Ce}_{0.05}\text{Ni}_{0.85}\text{Se}$ , have onset potential values of  $-0.242$  and  $-0.29 \text{ V vs. RHE}$ , respectively (Figure 6.13c). The 5 % Pt-C shows the best HER performance in 1 M KOH with an onset potential of  $-0.134 \text{ V vs. RHE}$  at  $20 \text{ mA/cm}^2$  current density.

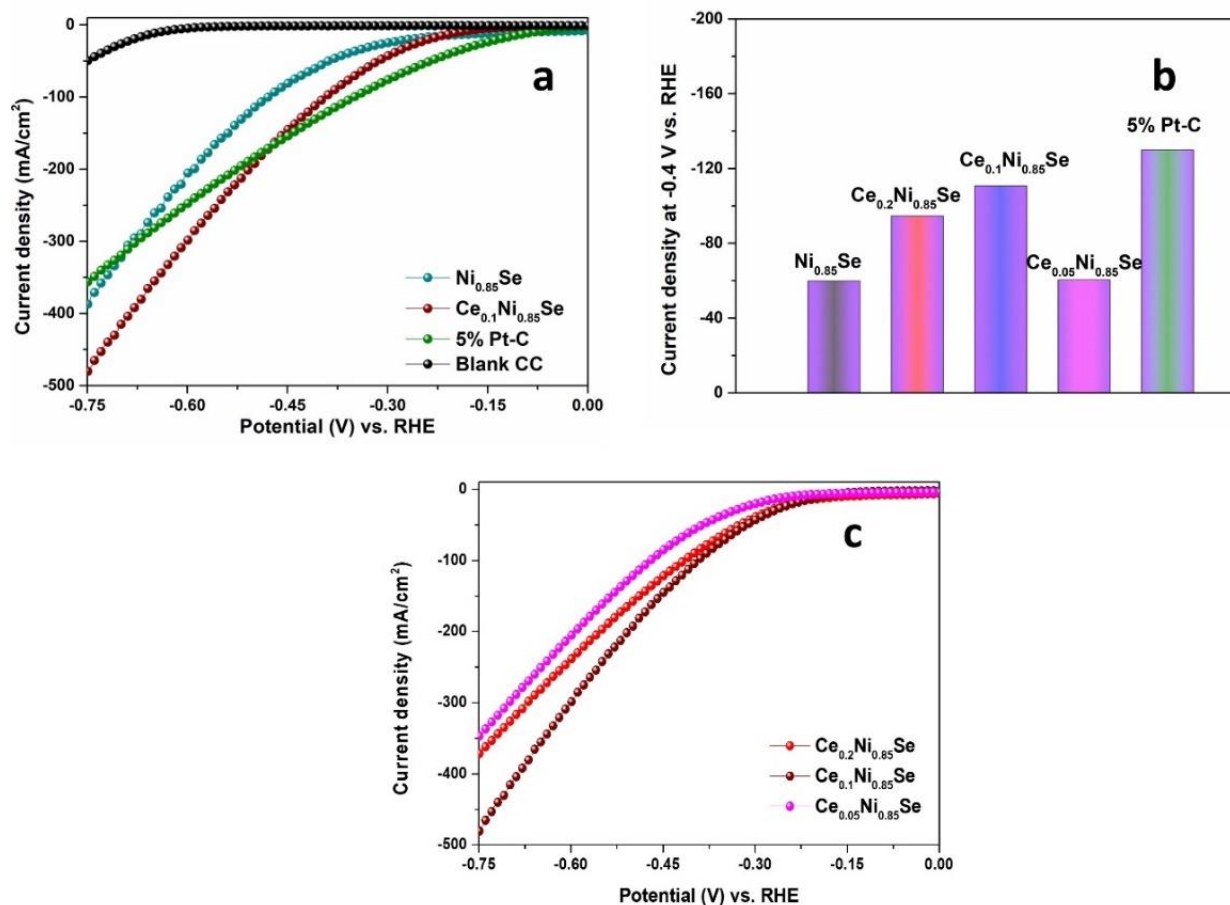


**Figure 6.13:** (a) Linear sweep voltammetry of blank CC, Ni<sub>0.85</sub>Se, Ce<sub>0.1</sub>Ni<sub>0.85</sub>Se, and 5% Pt/C for HER, (b) histogram plot at -0.4 V vs. RHE, (c) comparative HER of other doped samples.

The comparative table, which includes the relevant values reported in the literature for the HER, is provided in Table 6.2. The thinner 2D nanosheets and sharp edges (FESEM and TEM analysis) of the Ce<sub>0.1</sub>Ni<sub>0.85</sub>Se catalyst are beneficial to promote gas adsorption and evolution in the water-splitting reaction. The XPS study also proves the synergistic effect of Ce, Ni, and Se ions, which helps to regulate the active sites and electronic environment that promote HER performance.

**Table 6.2:** A comparative study of all the electrochemical parameters with the electrocatalyst.

S.N.	Electrocatalyst	Electrolyte	Reaction	Current density (mA/cm <sup>2</sup> )	Potential (mV vs. RHE)	Tafel slope	Ref.
1.	Co doped Ni <sub>0.85</sub> Se/GO	0.5 M H <sub>2</sub> SO <sub>4</sub>	HER	10	103 mV	43	19
2.	Fe doped Ni <sub>0.85</sub> Se	1 M KOH	HER and OER	10 and 100	120 mV and 1.54 V	34.1, and 73.4	16
3.	Ni <sub>0.85</sub> Se	1 M NaOH	HER and OER	10	200 and 302 mV	81 and 62	15
4.	NiSe-Ni <sub>0.85</sub> Se	1 M KOH	HER and OER	20 and 10	-131 mV and 1.53 V	74 and 98	40
5.	Ce <sub>0.1</sub> Ni <sub>0.85</sub> Se	1 M KOH	HER and OER	20 and 50	-238 mV and 1.56 V	144 and 58.8	This work

To further prove the better HER performance of the Ce<sub>0.1</sub>Ni<sub>0.85</sub>Se catalyst the mass activity is calculated at a specific potential of -0.4 V vs. RHE given in Table 6.3, the value of mass activity for bare Ni<sub>0.85</sub>Se, Ce<sub>0.2</sub>Ni<sub>0.85</sub>Se, Ce<sub>0.1</sub>Ni<sub>0.85</sub>Se, Ce<sub>0.05</sub>Ni<sub>0.85</sub>Se, and 5% Pt-C are 20.62 A/g, 32.6 A/g, 38.16 A/g, 20.84 A/g, and 44.7 A/g, respectively. The higher mass activity of optimized Ce<sub>0.1</sub>Ni<sub>0.85</sub>Se leads to more hydrogen production, enhancing the HER performance. The Tafel slope calculation is a crucial parameter to know the mechanistic insight of HER performance. To calculate the Tafel slope value, the graph in Figure 6.14a is plotted between the applied potential (V) vs. log|j|. From the SI equation, the slope value is calculated; the Pt-C catalyst has a Tafel slope value of 67.1 mV/dec, which is well-matched with the literature. The Bare Ni<sub>0.85</sub>Se has a Tafel slope value of 232 mV/dec., and after doping, the Ce<sub>0.1</sub>Ni<sub>0.85</sub>Se catalyst has a lower Tafel slope value of 118 mV/dec. The smaller Tafel slope signifies faster HER kinetics.



**Table 6.3:** All the electrochemical HER parameters for Ni<sub>0.85</sub>Se, Ce<sub>0.05</sub>Ni<sub>0.85</sub>Se, Ce<sub>0.1</sub>Ni<sub>0.85</sub>Se, Ce<sub>0.2</sub>Ni<sub>0.85</sub>Se, and 5% Pt-C deposited on carbon cloth.

Electrodes	Potential (V) vs. RHE ) required to generate 20 mA/cm <sup>2</sup>	Mass Activity (A/g) at -0.4 V vs. RHE	Tafel Slope (mV/decad e)	R <sub>s</sub> (Ω)	R <sub>CT</sub> (Ω)
Ni <sub>0.85</sub> Se	-0.268	20.62	232	4.35	24.32
Ce <sub>0.2</sub> Ni <sub>0.85</sub> Se	-0.242	32.60	-	-	-
Ce <sub>0.1</sub> Ni <sub>0.85</sub> Se	-0.238	38.16	144	5.08	10.5
Ce <sub>0.05</sub> Ni <sub>0.85</sub> Se	-0.29	20.84	-	-	-
5% Pt-C	-0.134	44.7	67.1	-	-

The HER mechanism follows two pathways, Volmer-Tafel and Volmer-Heyrovsky. In an alkaline medium, the first step of water dissociation is to adsorb the H intermediate. Adsorption of H occurs in the Volmer step, whereas desorption of the H<sub>2</sub> gas molecule occurs following the Heyrovsky or Tafel step. The Ce<sub>0.1</sub>Ni<sub>0.85</sub>Se catalyst has a 118 mV/dec Tafel slope value and follows the Volmer-Heyrovsky pathway during HER. The presence of different and variable oxidation states of metal ions (Ce<sup>4+</sup>, Ce<sup>3+</sup>, Ni<sup>2+</sup>, and Ni<sup>3+</sup>) and Se<sup>2-</sup> ions (refer to XPS analysis) are beneficial for the adsorption of intermediate and desorption of H<sub>2</sub> gas during electrocatalytic reactions in alkaline medium. In Ce<sub>0.1</sub>Ni<sub>0.85</sub>Se catalyst, the presence of Ni<sup>3+</sup> ion (d<sup>7</sup> system, more unfilled d orbital) is responsible for more adsorption of OH<sup>-</sup> intermediate during HER. The introduction of Ce<sup>4+</sup> dopant, which has an empty 4f orbital, is also beneficial for water dissociation and adsorption of intermediate species. The combined synergistic and thinner 2D nanosheet morphology helps in the better HER performance of doped samples. High porosity and small mesopores of the doped sample are also beneficial for higher electrocatalytic activity. In the Ce<sub>0.1</sub>Ni<sub>0.85</sub>Se catalyst, there is a decrement of charge in the Ni site, which signifies better adsorption of hydrogen intermediate and the change in electronic states and, therefore, improves the HER activity. In a similar context, Gao and co-workers<sup>38</sup> developed a doped CoP electrocatalyst for HER in acidic and basic mediums. They explained that Ce doping in CoP decreases the Bader charge on the Co site, which enhances the hydrogen adsorption and improves the electronic state.

The impedance plot is fitted as the Randle circuit given in the inset of Figure 6.14b; the impedance of pristine  $\text{Ni}_{0.85}\text{Se}$  and  $\text{Ce}_{0.1}\text{Ni}_{0.85}\text{Se}$  was exhibited at their respective onset potential. The  $R_{\text{CT}}$  values are listed in Table CC; the  $R_{\text{CT}}$  value for  $\text{Ce}_{0.1}\text{Ni}_{0.85}\text{Se}$  is  $10.5 \Omega$ , lower than bare  $\text{Ni}_{0.85}\text{Se}$  ( $24.32 \Omega$ ). The smaller value of charge transportation resistance indicates better electrocatalytic performance. The credible reason for the increment in the conductivity of the  $\text{Ni}_{0.85}\text{Se}$  system is due to the introduction of a higher-size Ce dopant, which also generates lattice distortion (refer to PXRD and HRTEM analysis). BET analysis also demonstrates a more porous nature and specific surface area in Ce doped  $\text{Ni}_{0.85}\text{Se}$  nanosheets, which produces more sites for gas adsorption and desorption during the reaction. The optimized  $\text{Ce}_{0.1}\text{Ni}_{0.85}\text{Se}$  catalyst was checked for 1000 consecutive cycles of LSV in an alkaline medium; in Figure 6.14c, no significant changes in current density or onset potential were observed, indicating the outstanding stability of the catalyst. The long-term stability is operated through chronoamperometric analysis at constant potential to generate  $135 \text{ mA/cm}^2$  current density. Figure 6.14d represents the 48-hour stability data for  $\text{Ce}_{0.1}\text{Ni}_{0.85}\text{Se}$  catalyst; there is no alter in current density, which shows the robustness of  $\text{Ce}_{0.1}\text{Ni}_{0.85}\text{Se}$  catalyst for HER in an alkaline medium.

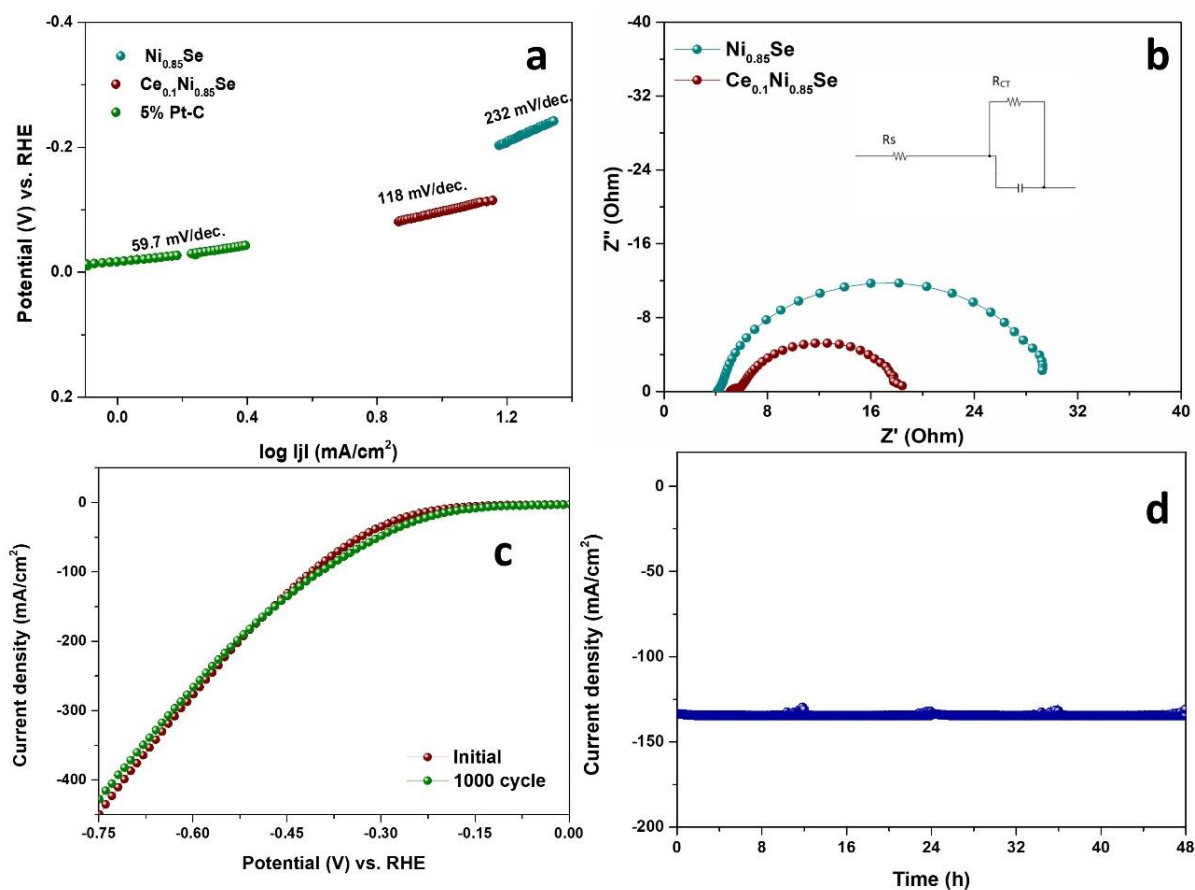


**Figure 6.14:** (a) Tafel slope, and (b) impedance of  $\text{Ni}_{0.85}\text{Se}$ ,  $\text{Ce}_{0.1}\text{Ni}_{0.85}\text{Se}$ , and 5% Pt/C. The inset of Figure b represents an equivalent circuit for impedance (c) 1000 cycle stability (d) chronoamperometric stability for 48 hours.

To prove better electrocatalytic activity, electrochemical active surface area (ECSA) is calculated for pristine and doped  $\text{Ni}_{0.85}\text{Se}$  catalyst. The CV analysis was done in non-Faradaic regions at different scan rates. The plot given in Figures 6.15a and b represents the CV graph of pristine  $\text{Ni}_{0.85}\text{Se}$  and  $\text{Ce}_{0.1}\text{Ni}_{0.85}\text{Se}$  samples. The graph is plotted at a fixed potential of 0.525 V vs. RHE between the current and scan rate (Figure 6.15c). The graph is fitted in a linear curve and gives the value of  $C_{dl}$  (double-layer capacitance). The ECSA value is calculated from  $C_{dl}$  values. The estimated ECSA value of pristine  $\text{Ni}_{0.85}\text{Se}$  is  $33.3 \text{ cm}^2$  and after doping the ECSA value improves to  $44.17 \text{ cm}^2$  after Ce doping. The roughness factor ( $R_f$ ) is also determined from ECSA values; pristine  $\text{Ni}_{0.85}\text{Se}$  has  $R_f$  value of 210, and after doping in  $\text{Ce}_{0.1}\text{Ni}_{0.85}\text{Se}$ , the  $R_f$  value is



276.06. Therefore, the number of active sites was increased after the dopant Ce introduction in  $\text{Ni}_{0.85}\text{Se}$ .

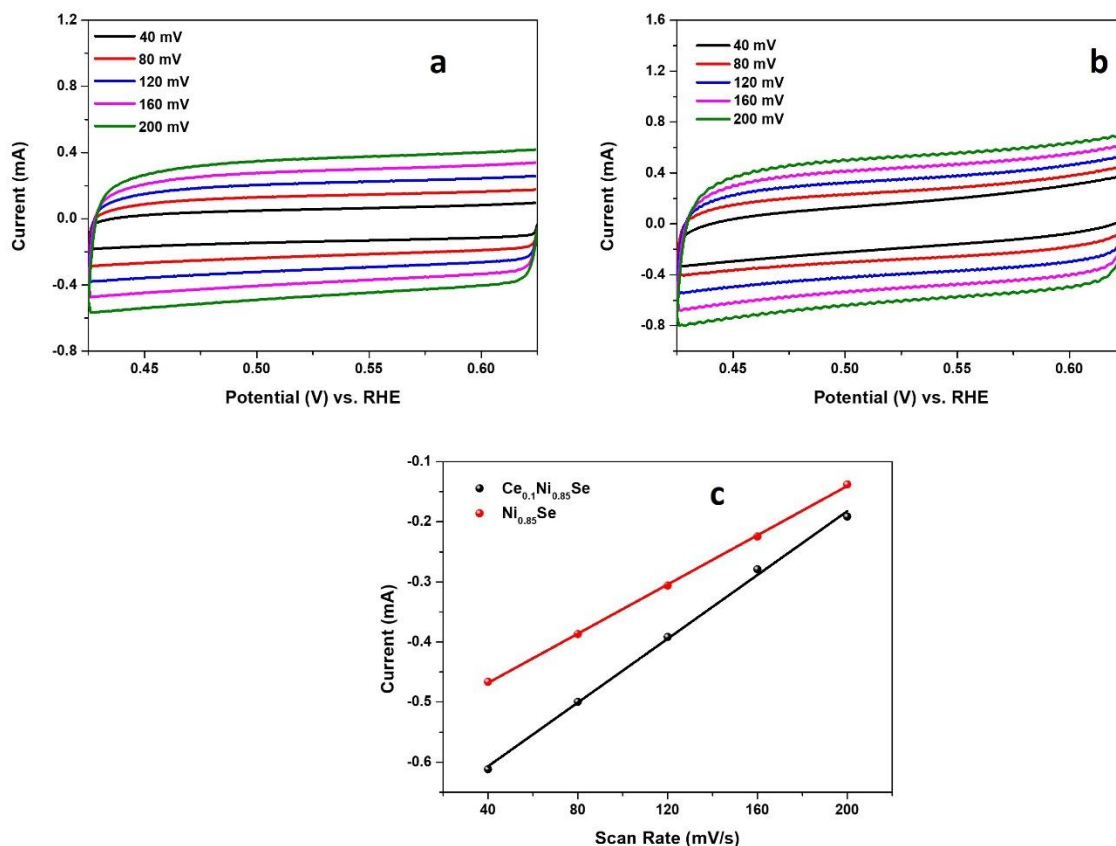


**Figure 6.15:** (a) CV analysis for  $\text{Ni}_{0.85}\text{Se}$  (b) CV analysis of Ce doped  $\text{Ni}_{0.85}\text{Se}$  (c) ECSA analysis of Bare and doped samples.

After examining HER activity, the OER activity was examined, including all samples, pristine  $\text{Ni}_{0.85}\text{Se}$ ,  $\text{Ce}_{0.2}\text{Ni}_{0.85}\text{Se}$ ,  $\text{Ce}_{0.1}\text{Ni}_{0.85}\text{Se}$ ,  $\text{Ce}_{0.05}\text{Ni}_{0.85}\text{Se}$ , commercial  $\text{RuO}_2$ , and bare CC using three-electrode system in alkaline medium. The onset potential is chosen to attain  $50 \text{ mA/cm}^2$  current density. In Figure 6.16a, the bare CC displays insignificant activity within the voltage range. The pristine  $\text{Ni}_{0.85}\text{Se}$  catalyst has the onset potential of  $1.60 \text{ V vs. RHE}$ . The optimized  $\text{Ce}_{0.1}\text{Ni}_{0.85}\text{Se}$  electrocatalyst shows maximum current density with a low onset potential value of  $1.56 \text{ V vs. RHE}$ , with a cathodic shift of  $40 \text{ mV}$ . The comparative plot to generate current density at  $1.65 \text{ V vs. RHE}$  is given in Figure 6.16b, which shows the maximum current density of the optimized catalyst. The  $\text{Ce}_{0.2}\text{Ni}_{0.85}\text{Se}$  and  $\text{Ce}_{0.05}\text{Ni}_{0.85}\text{Se}$  catalysts have an onset potential of  $1.583$  and  $1.57 \text{ V vs. RHE}$ , respectively (Figure 6.16c). The commercial  $\text{RuO}_2$  catalyst has an onset

potential of 1.654 V vs. RHE. The OER stability is checked, and  $\text{Ce}_{0.1}\text{Ni}_{0.85}\text{Se}$  is stable up to a consecutive 1000 cycle. There is no alteration in current density or onset potential after consecutive 1000 runs. Table 6.2 includes a comparative table with the reported electrocatalyst for OER. BET and FESEM analysis of the doped sample verify the porous nature and interconnected 2D thin nanosheets that are beneficial towards  $\text{O}_2$  adsorption and desorption, leading to faster OER reaction.

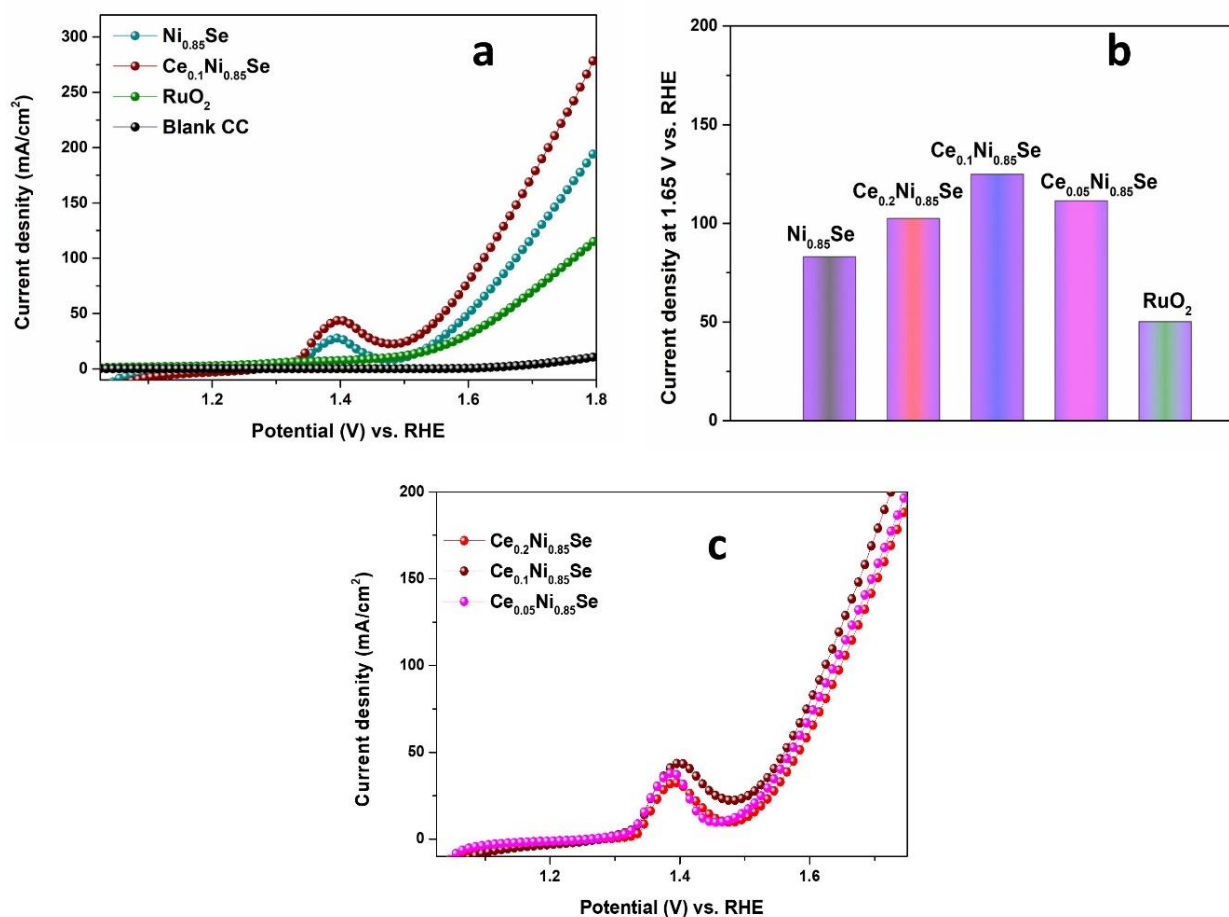


**Figure 6.16:** (a) Linear sweep voltammetry of blank CC,  $\text{Ni}_{0.85}\text{Se}$ ,  $\text{Ce}_{0.1}\text{Ni}_{0.85}\text{Se}$ , and  $\text{RuO}_2$  for OER, (b) histogram plot at 1.65 V vs. RHE, (c) comparative OER of other doped samples.

The analysis of mass activity is done at a potential of 1.65 V vs. RHE to know the better OER performance of the catalyst. The values for the mass activity are summarized in Table 6.4; the optimized catalyst  $\text{Ce}_{0.1}\text{Ni}_{0.85}\text{Se}$  exhibits a higher mass activity value of 42.71 A/g for OER,

which is better than the commercial RuO<sub>2</sub> (17.16 A/g). Moreover, to understand the kinetics of OER, Tafel slope calculation is done from LSV data (Figure 6.17a). Pristine Ni<sub>0.85</sub>Se displayed a Tafel slope of 151.2 mV/dec., and Ce<sub>0.1</sub>Ni<sub>0.85</sub>Se catalyst has 58.8 mV/dec. value. For comparison, the commercial RuO<sub>2</sub> showcased a Tafel slope of 82.3 mV/dec, aligning with the literature value. The lower Tafel slope value of the optimized Ce<sub>0.1</sub>Ni<sub>0.85</sub>Se catalyst shows the best OER performance after Ce doping. At the particular onset potential of the catalyst, the impedance analysis was done for Ni<sub>0.85</sub>Se and Ce<sub>0.1</sub>Ni<sub>0.85</sub>Se catalysts in 1 M KOH electrolyte. The smaller semicircle of the Ce<sub>0.1</sub>Ni<sub>0.85</sub>Se catalyst in Figure 6.17b represents the higher conductivity of the system. The values of R<sub>s</sub> and R<sub>CT</sub> are summarized in Table 6.4; the R<sub>CT</sub> value is 13.73Ω, and 7.7Ω for pristine Ni<sub>0.85</sub>Se and Ce<sub>0.1</sub>Ni<sub>0.85</sub>Se, respectively, which means the Ce<sup>4+</sup> doping lowers the charge transport resistance and improves the OER performance. The applied potential for CV analysis is 1.025 to 1.625 V vs. RHE at 10 mV/sec. scan rate in anodic direction as in in Figure 6.17c. In bare Ni<sub>0.85</sub>Se, the oxidation peak appears at 1.43 V vs. RHE, responsible for Ni<sup>2+</sup> to Ni<sup>3+</sup>; the reduction peak is evident at 1.24 V vs. RHE for the Ni<sup>3+</sup>/Ni<sup>2+</sup> redox couple. After doping with Ce in the Ni<sub>0.85</sub>Se sample, the redox oxidation peak shifted at 1.46 V vs. RHE. This positive shift indicates that the Ce<sup>4+</sup> dopant serves as an effective Lewis acid, contributing to a more active Ni<sup>3+</sup> ion in the system (refer to XPS analysis), which is beneficial for OER activity. Akbari and coworkers<sup>41</sup> developed a nickel/nickel oxide interface and introduced the Fe ion, where, they observed that the formation of Ni<sub>2</sub>O<sub>3</sub> (Ni<sup>3+</sup>) is more than Ni<sup>2+</sup>, which shows an increment in OER activity.

Electrodes	Potential (V) vs. RHE ) required to generate 50 mA/cm <sup>2</sup>	Mass Activity (A/g) at 1.65 V vs. RHE	Tafel Slope (mV/decad e)	R <sub>s</sub> (Ω)	R <sub>CT</sub> (Ω)
Ni <sub>0.85</sub> Se	1.60	28.4	151.2	5.51	13.73
Ce <sub>0.2</sub> Ni <sub>0.85</sub> Se	1.583	35.08	-	-	-
Ce <sub>0.1</sub> Ni <sub>0.85</sub> Se	1.56	42.71	58.8	5.33	7.7
Ce <sub>0.05</sub> Ni <sub>0.85</sub> Se	1.57	38.10	-	-	-
RuO <sub>2</sub>	1.654	17.16	82.3	-	-

**Table 6.4:** All the electrochemical OER parameters for Ni<sub>0.85</sub>Se, Ce<sub>0.05</sub>Ni<sub>0.85</sub>Se, Ce<sub>0.1</sub>Ni<sub>0.85</sub>Se, Ce<sub>0.2</sub>Ni<sub>0.85</sub>Se, and commercial RuO<sub>2</sub> deposited on carbon cloth.

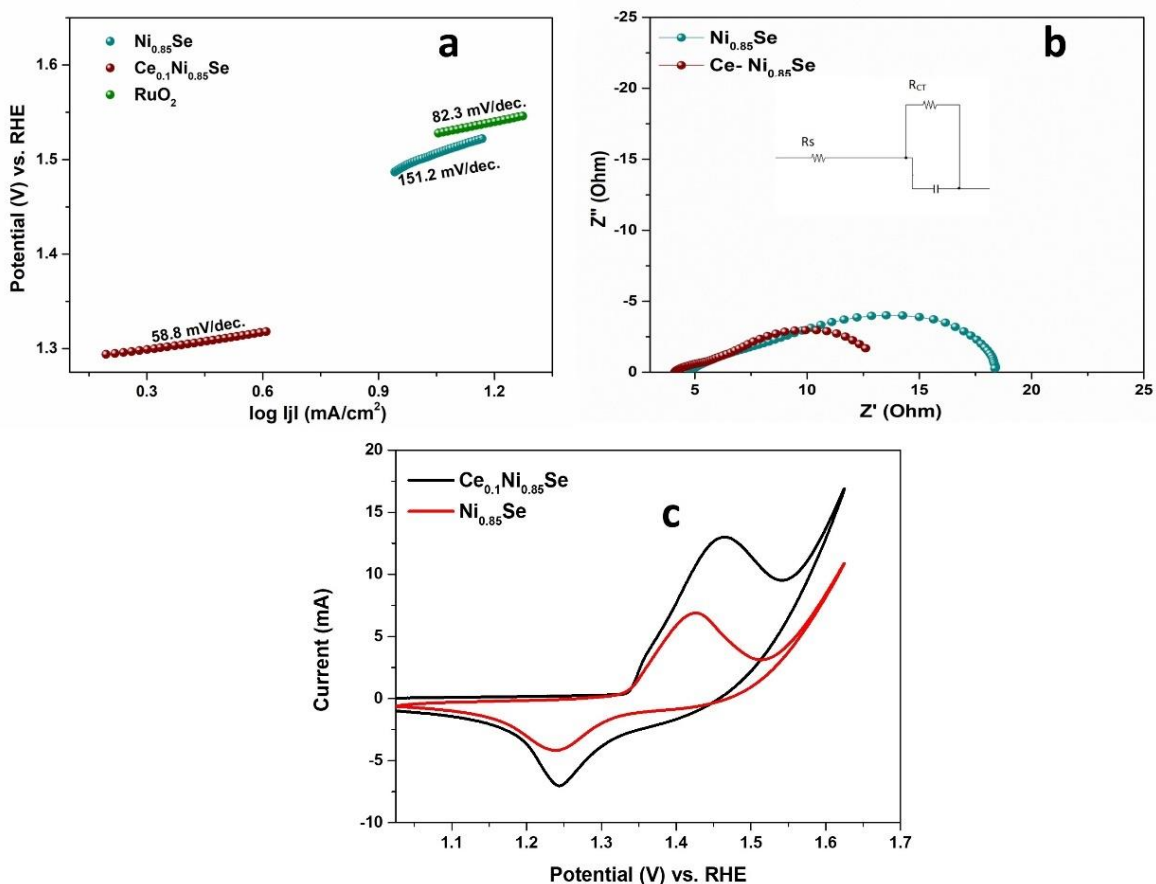


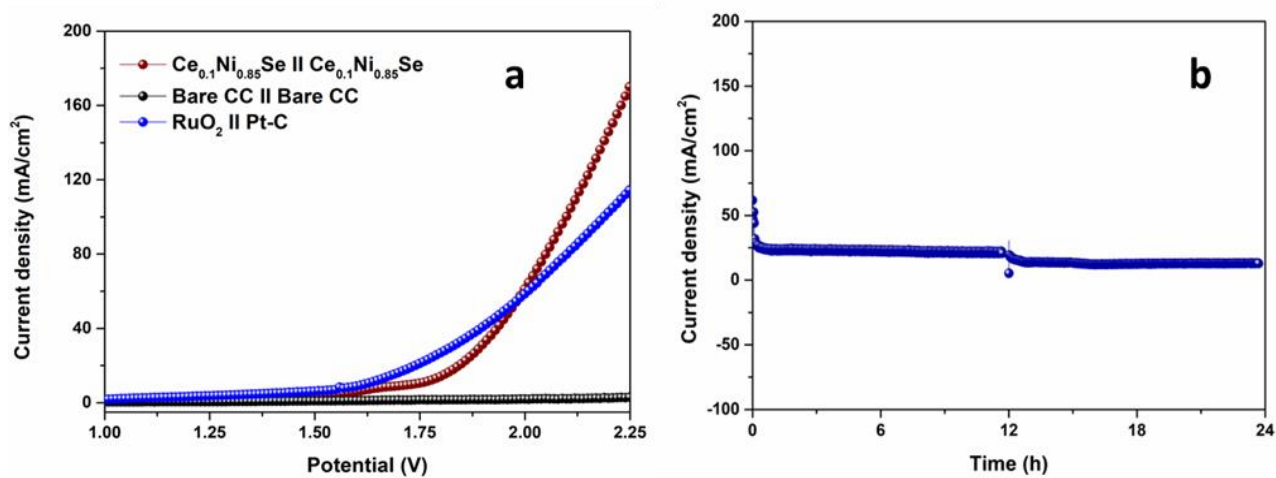
**Figure 6.17:** (a) Tafel slope, and (b) impedance of  $\text{Ni}_{0.85}\text{Se}$ ,  $\text{Ce}_{0.1}\text{Ni}_{0.85}\text{Se}$ , and  $\text{RuO}_2$ . The inset of Figure 6.14b represents an equivalent circuit for impedance (c) CV analysis for bare and doped samples.

### 6.3.5 Two electrode system

The optimized  $\text{Ce}_{0.1}\text{Ni}_{0.85}\text{Se}$  catalyst demonstrates impressive activity for both the HER and OER in 1.0 M KOH. Encouraged by these results, we embarked on evaluating the bifunctional activity of the  $\text{Ce}_{0.1}\text{Ni}_{0.85}\text{Se}$  catalyst both as an anode and cathode in water splitting. The  $\text{Ce}_{0.1}\text{Ni}_{0.85}\text{Se} \parallel \text{Ce}_{0.1}\text{Ni}_{0.85}\text{Se}$  cell works show good activity with an onset potential of 1.73 V to generate  $10 \text{ mA}/\text{cm}^2$  current density (Figure 6.18a). The  $\text{Ce}_{0.1}\text{Ni}_{0.85}\text{Se} \parallel \text{Ce}_{0.1}\text{Ni}_{0.85}\text{Se}$  cell necessitates 1.96 V and 2.09 V to attain current densities of 50 and  $100 \text{ mA}/\text{cm}^2$ , respectively. . The electrochemical activity of a commercial catalyst,  $\text{RuO}_2 \parallel \text{Pt-C}$  cell is checked in the same applied window. The  $\text{RuO}_2 \parallel \text{Pt-C}$  cell show an onset potential of 1.61 V to obtain  $10 \text{ mA}/\text{cm}^2$  current density. The  $\text{RuO}_2 \parallel \text{Pt-C}$  cell necessitates 1.95 V and 2.18 V to attain current densities of

50 and 100 mA/cm<sup>2</sup>, respectively, which is comparable to our developed electrocatalyst. To assess the endurance and stability of the Ce<sub>0.1</sub>Ni<sub>0.85</sub>Se || Ce<sub>0.1</sub>Ni<sub>0.85</sub>Se cell, a prolonged evaluation was conducted over a continuous 24 hour period at 1.85 V, producing a consistent current density of 20 mA/cm<sup>2</sup> (Figure 6.18b). Further, to check the post-electrocatalytic stability of the Ce<sub>0.1</sub>Ni<sub>0.85</sub>Se catalyst, the FESEM and XPS analysis were performed after 24 h of stability.

**Figure 6.18:** (a) LSV analysis of the two-electrode setup of Ce<sub>0.1</sub>Ni<sub>0.85</sub>Se || Ce<sub>0.1</sub>Ni<sub>0.85</sub>Se and blank



CC, (b) chronoamperometric data of Ce<sub>0.1</sub>Ni<sub>0.85</sub>Se || Ce<sub>0.1</sub>Ni<sub>0.85</sub>Se cell in 1.0 M KOH solution.

The FESEM image of the Ce<sub>0.1</sub>Ni<sub>0.85</sub>Se catalyst shows retention in the 2D nanosheet morphology (Figure 6.19). The EDS analysis shows a uniform elemental distribution of Ce, Ni, Se, and C throughout the CC. The XPS study of the Ce<sub>0.1</sub>Ni<sub>0.85</sub>Se sample was done after electrocatalysis; the deconvoluted Ni 2p spectra show two doublets with two satellite peaks in Figure 6.20a. The BE values at 855.7 eV and 857.1 eV correspond to Ni 2p<sub>3/2</sub>, and at 873.6 eV and 875.1 eV represent Ni 2p<sub>1/2</sub>, respectively. The BE values at 862.2 eV and 880.3 eV are indicative of satellite peaks. In Figure 6.20b, the 6.20d spectra peaks appear at 53.9 eV, with 54.9 eV corresponding to Se<sup>2-</sup> ions. Additionally, peaks at 57.9 eV and 60.5 eV are consistent with SeO<sub>x</sub>. In the Ce 3d deconvoluted spectra, the initial two peaks, with BE values of 873.8 eV and 878.1 eV, are attributed to Ni 2p<sub>1/2</sub>, indicating the presence of Ni within the system. As illustrated in Figure 6.20c, the spectra represent multiple peaks with BE range of 881-930 eV. These peaks signify the coexistence of both Ce<sup>4+</sup> and Ce<sup>3+</sup> oxidation states in the doped sample. Specifically, the peaks at 881.1 eV and 883.8 eV correspond to Ce 3d<sub>5/2</sub>, highlighting the mixed valence state of Ce<sup>4+</sup> and Ce<sup>3+</sup>. Additionally, peaks at 894.7 eV, 898.9 eV, 902.4 eV, 907.4 eV, and 914.6 eV

are attributed to Ce 3d<sub>3/2</sub>, reaffirming the presence of the valence state of Ce<sup>4+</sup> and Ce<sup>3+</sup>. Table 6.5 represents all the comparative BE values of Ni<sub>0.85</sub>Se, Ce<sub>0.1</sub>Ni<sub>0.85</sub>Se, and post electrocatalytic sample. The survey spectrum encompasses all the peaks corresponding to the elements Ni, Se, Ce, O, and C. Consequently, it can be inferred that the Ce<sub>0.1</sub>Ni<sub>0.85</sub>Se catalyst demonstrates noteworthy activity and stability, making it a promising candidate for use in alkaline electrolysis for water splitting.

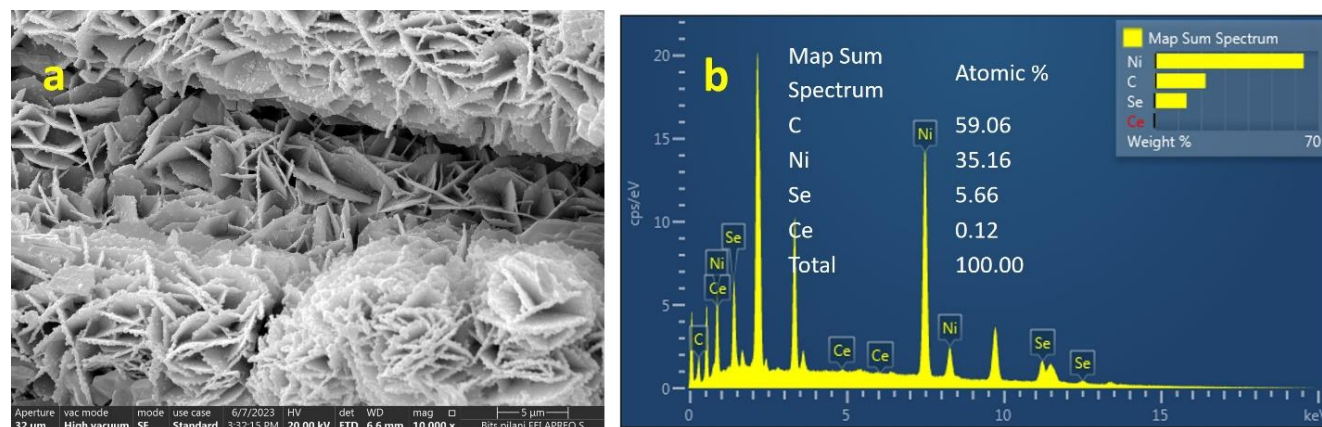


**Figure 6.19:** Post electrocatalysis (a) FESEM (b) EDS analysis of Ce<sub>0.1</sub>Ni<sub>0.85</sub>Se sample.

**Table 6.5:** Comparative table for XPS binding energy values.

Metal ions	Ni <sub>0.85</sub> Se	Ce <sub>0.1</sub> Ni <sub>0.85</sub> Se	Ce <sub>0.1</sub> Ni <sub>0.85</sub> Se Post electrolysis
Ni <sup>2+</sup> (2p <sub>3/2</sub> )	855.4 eV	856.01 eV	855.7 eV
Ni <sup>3+</sup> (2p <sub>3/2</sub> )	856.4 eV	857.2 eV	857.1 eV
Ni <sup>2+</sup> (2p <sub>1/2</sub> )	872.8 eV	873.7 eV	873.6 eV
Ni <sup>3+</sup> (2p <sub>1/2</sub> )	854.2 eV	875.0 eV	875.1 eV
Se <sup>2-</sup> (3d)	54.2 eV	53.9 eV	53.9 eV
Ce <sup>3+/4+</sup> (3d)	-	880 eV~ 930 eV	880 eV~ 930 eV



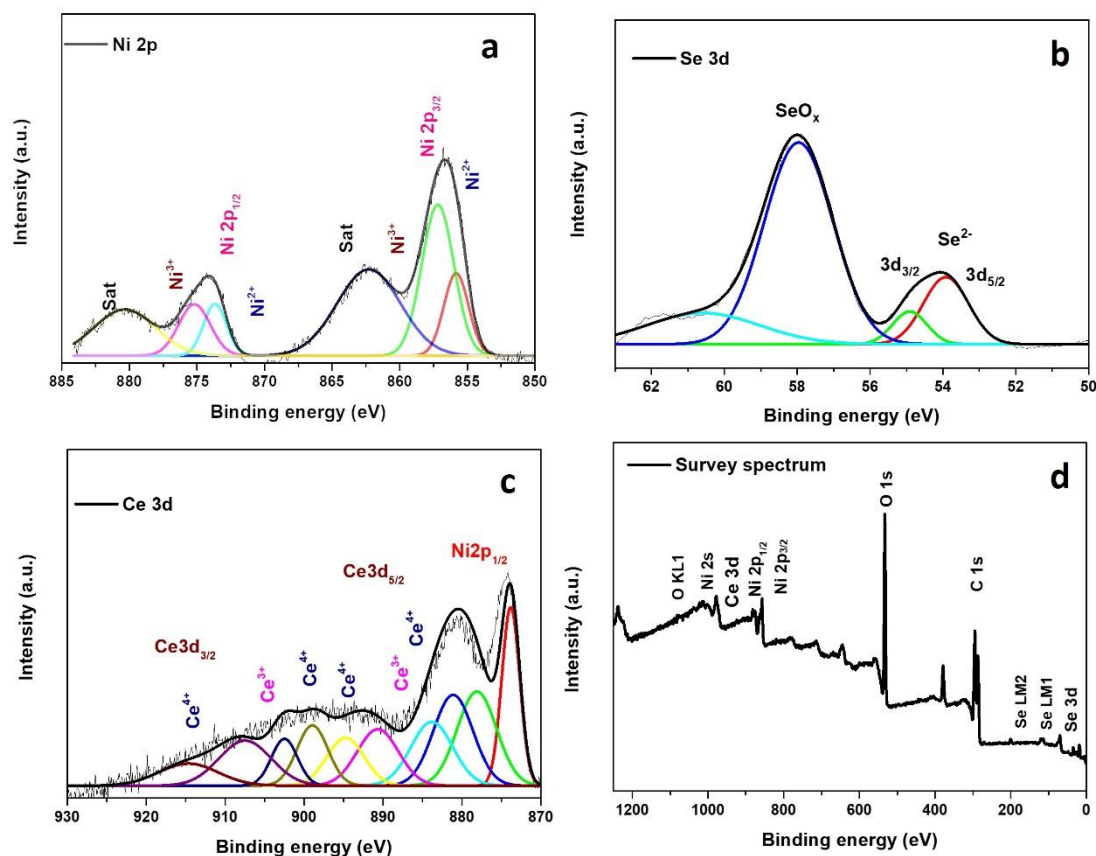


**Figure 6.20:** Post electrocatalysis XPS analysis of  $\text{Ce}_{0.1}\text{Ni}_{0.85}\text{Se}$  sample.

## 6.4 Conclusion

In summary, we have synthesized Ce-doped  $\text{Ni}_{0.85}\text{Se}$  electrocatalyst on CC by following a two-step hydrothermal method. The materials were characterized using various techniques. The XRD and TEM findings substantiate the lattice distortion and expansion after doping with Ce in  $\text{Ni}_{0.85}\text{Se}$  system. The BET and FESEM results prove the porous and interconnected 2D thinner nanosheets of Ce doped  $\text{Ni}_{0.85}\text{Se}$ , respectively. We have optimized the Ce dopant concentration in  $\text{Ni}_{0.85}\text{Se}$  with different molar ratios. The optimized  $\text{Ce}_{0.1}\text{Ni}_{0.85}\text{Se}$  electrocatalyst shows better efficiency for HER and OER. The lower Tafel slope values, 118 mV/dec for HER and 58.8 mV/dec for OER, indicate the swifter kinetics for the HER and OER. The bifunctional  $\text{Ce}_{0.1}\text{Ni}_{0.85}\text{Se}$  catalyst shows good stability at 24 h in an alkaline medium. The post electrocatalytic characterizations (XPS and FESEM) of  $\text{Ce}_{0.1}\text{Ni}_{0.85}\text{Se}$  catalyst confirm the composition and 2D

nanosheet morphology. The  $\text{Ce}^{4+}$  introduction in  $\text{Ni}_{0.85}\text{Se}$  expands the lattice distortion. The larger radii of Ce and available 4f orbital create the change in the  $\text{Ni}_{0.85}\text{Se}$  lattice. The thinner 2D nanosheets of Ce doped  $\text{Ni}_{0.85}\text{Se}$  on CC work as suitable sites for gas desorption. The synergistic effect of  $\text{Ni}^{2+}$ ,  $\text{Ni}^{3+}$ ,  $\text{Ce}^{3+}$ ,  $\text{Ce}^{4+}$ , and  $\text{Se}^{2-}$  ions can modulate the electronic transfer, which helps in HER and OER activity. This work not only exhibits a regulated morphology of Ce doped  $\text{Ni}_{0.85}\text{Se}$  material for better overall water splitting reaction but also opens new opportunities to explore rare earth metals doping in a nickel-based system.

### 6.5 References

1. Ifkovits, Z. P.; Evans, J. M.; Meier, M. C.; Papadantonakis, K. M.; Lewis, N. S., Decoupled electrochemical water-splitting systems: a review and perspective. *Energy Environ. Sci.* **2021**, *14* (9), 4740-4759.
2. Li, X.; Hao, X.; Abudula, A.; Guan, G., Nanostructured catalysts for electrochemical water splitting: current state and prospects. *J. Mater. Chem. A* **2016**, *4* (31), 11973-12000.
3. van der Zalm, J. M.; Quintal, J.; Hira, S. A.; Chen, S.; Chen, A., Recent trends in electrochemical catalyst design for hydrogen evolution, oxygen evolution, and overall water splitting. *Electrochim. Acta* **2023**, *439*, 141715.
4. Rathore, D.; Ghosh, S.; Chowdhury, J.; Pande, S., Fe-Doped  $\text{NiCo}_2\text{Se}_4$  Nanorod Arrays as Electrocatalysts for Overall Electrochemical Water Splitting. *ACS Appl. Nano Mater.* **2023**, *6* (4), 3095-3110.
5. Anantharaj, S., Ru-tweaking of non-precious materials: the tale of a strategy that ensures both cost and energy efficiency in electrocatalytic water splitting. *J. Mater. Chem. A* **2021**, *9* (11), 6710-6731.
6. Osgood, H.; Devaguptapu, S. V.; Xu, H.; Cho, J.; Wu, G., Transition metal (Fe, Co, Ni, and Mn) oxides for oxygen reduction and evolution bifunctional catalysts in alkaline media. *Nano Today* **2016**, *11* (5), 601-625.
7. Jin, S., Are metal chalcogenides, nitrides, and phosphides oxygen evolution catalysts or bifunctional catalysts? *ACS Energy Lett.* **2017**, *2*, 1937-1938.
8. Wu, T.; Sun, M.-Z.; Huang, B.-L., Non-noble metal-based bifunctional electrocatalysts for hydrogen production. *Rare Met.* **2022**, *41* (7), 2169-2183.



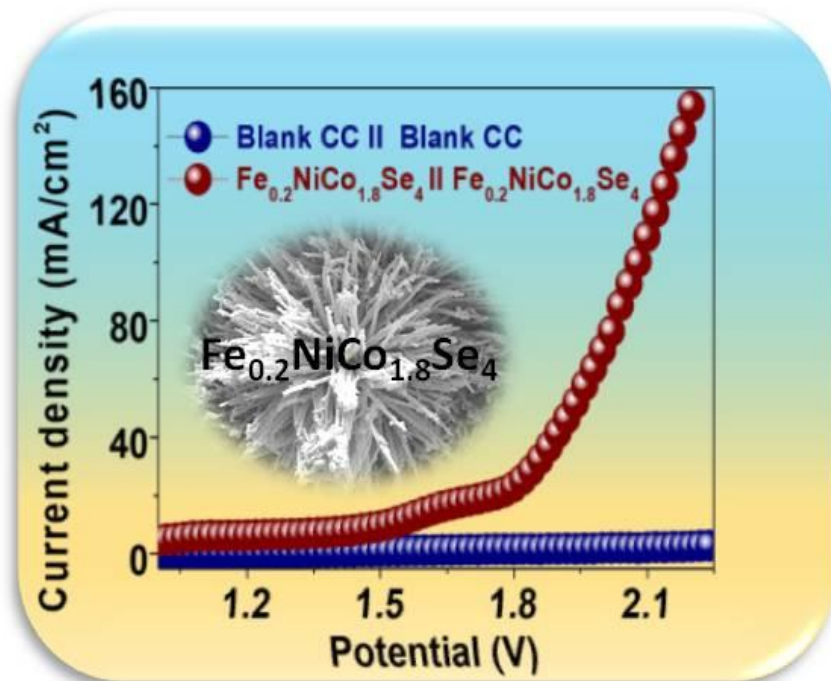
9. Wang, H.; Lee, H.-W.; Deng, Y.; Lu, Z.; Hsu, P.-C.; Liu, Y.; Lin, D.; Cui, Y., Bifunctional non-noble metal oxide nanoparticle electrocatalysts through lithium-induced conversion for overall water splitting. *Nat. Commun.* **2015**, *6* (1), 7261.
10. Wang, F.; Shifa, T. A.; Zhan, X.; Huang, Y.; Liu, K.; Cheng, Z.; Jiang, C.; He, J., Recent advances in transition-metal dichalcogenide based nanomaterials for water splitting. *Nanoscale* **2015**, *7* (47), 19764-19788.
11. Wang, X.; Li, F.; Li, W.; Gao, W.; Tang, Y.; Li, R., Hollow bimetallic cobalt-based selenide polyhedrons derived from metal–organic framework: an efficient bifunctional electrocatalyst for overall water splitting. *J. Mater. Chem. A* **2017**, *5* (34), 17982-17989.
12. Xia, X.; Wang, L.; Sui, N.; Colvin, V. L.; William, W. Y., Recent progress in transition metal selenide electrocatalysts for water splitting. *Nanoscale* **2020**, *12* (23), 12249-12262.
13. Zeng, C.; Dai, L.; Jin, Y.; Liu, J.; Zhang, Q.; Wang, H., Design strategies toward transition metal selenide-based catalysts for electrochemical water splitting. *Sustain. Energy Fuels* **2021**, *5* (5), 1347-1365.
14. Yang, C.; Lu, Y.; Duan, W.; Kong, Z.; Huang, Z.; Yang, T.; Zou, Y.; Chen, R.; Wang, S., Recent progress and prospective of nickel selenide-based electrocatalysts for water splitting. *Energy Fuels* **2021**, *35* (18), 14283-14303.
15. Wu, X.; He, D.; Zhang, H.; Li, H.; Li, Z.; Yang, B.; Lin, Z.; Lei, L.; Zhang, X., Ni<sub>0.85</sub>Se as an efficient non-noble bifunctional electrocatalyst for full water splitting. *Int. J. Hydrog. Energy* **2016**, *41* (25), 10688-10694.
16. Liu, Y.; Cao, J.; Chen, Y.; Wei, M.; Liu, X.; Li, X.; Wu, Q.; Feng, B.; Zhang, Y.; Yang, L., Regulation of the morphology and electrochemical properties of Ni<sub>0.85</sub>Se via Fe doping for overall water splitting and supercapacitors. *CrystEngComm* **2022**, *24* (9), 1704-1718.
17. Ibraheem, S.; Yasin, G.; Kumar, A.; Mushtaq, M. A.; Ibrahim, S.; Iqbal, R.; Tabish, M.; Ali, S.; Saad, A., Iron-cation-coordinated cobalt-bridged-selenides nanorods for highly efficient photo/electrochemical water splitting. *Appl. Catal. B: Environ.* **2022**, *304*, 120987-120997.
18. Sun, Y.; Xu, K.; Wei, Z.; Li, H.; Zhang, T.; Li, X.; Cai, W.; Ma, J.; Fan, H. J.; Li, Y., Strong electronic interaction in dual-cation-incorporated NiSe<sub>2</sub> nanosheets with lattice distortion for highly efficient overall water splitting. *Adv. Mater.* **2018**, *30* (35), 1802121.

19. Zhao, W.; Wang, S.; Feng, C.; Wu, H.; Zhang, L.; Zhang, J., Novel Cobalt-Doped Ni<sub>0.85</sub>Se Chalcogenides (Co<sub>x</sub>Ni<sub>0.85-x</sub>Se) as High Active and Stable Electrocatalysts for Hydrogen Evolution Reaction in Electrolysis Water Splitting. *ACS Appl. Mater. Interfaces* **2018**, *10* (47), 40491-40499.
20. Yang, C.; Wang, C.; Zhou, L.; Duan, W.; Song, Y.; Zhang, F.; Zhen, Y.; Zhang, J.; Bao, W.; Lu, Y.; Wang, D.; Fu, F., Refining d-band center in Ni<sub>0.85</sub>Se by Mo doping: A strategy for boosting hydrogen generation via coupling electrocatalytic oxidation 5-hydroxymethylfurfural. *J. Chem. Eng.* **2021**, *422*, 130125.
21. Rathore, D.; Banerjee, A.; Pande, S., Bifunctional Tungsten-Doped Ni(OH)<sub>2</sub>/NiOOH Nanosheets for Overall Water Splitting in an Alkaline Medium. *ACS Appl. Nano Mater.* **2022**.
22. Rathore, D.; Ghosh, S.; Chowdhury, J.; Pande, S., Co-Doped Ni<sub>9</sub>S<sub>8</sub> Nanostructures for Electrocatalytic Water Splitting over a Wide pH Range. *ACS Appl. Nano Mater.* **2022**.
23. Rong, M.; Zhong, H.; Wang, S.; Ma, X.; Cao, Z., La/Ce doped CoFe layered double hydroxides (LDH) highly enhanced oxygen evolution performance of water splitting. *Colloids Surf. A: Physicochem. Eng.* **2021**, *625*, 126896.
24. Li, J.; Zou, S.; Liu, X.; Lu, Y.; Dong, D., Electronically Modulated CoP by Ce Doping as a Highly Efficient Electrocatalyst for Water Splitting. *ACS Sustain. Chem. Eng.* **2020**, *8* (27), 10009-10016.
25. Tong, G.-X.; Liu, F.-T.; Wu, W.-H.; Shen, J.-P.; Hu, X.; Liang, Y., Polymorphous  $\alpha$ - and  $\beta$ -Ni(OH)<sub>2</sub> complex architectures: morphological and phasal evolution mechanisms and enhanced catalytic activity as non-enzymatic glucose sensors. *CrystEngComm* **2012**, *14* (18), 5963-5973.
26. Zhang, L.; Wang, H.; Ji, S.; Wang, X.; Wang, R., Porous-sheet-assembled Ni(OH)<sub>2</sub>/NiS arrays with vertical in-plane edge structure for supercapacitors with high stability. *Dalton Transactions* **2019**, *48* (46), 17364-17370.
27. Ahmadian, F.; Salarvand, V.; Saghafi, M.; Noghani, M. T.; Yousefifar, A., Production and characterization of high-performance cobalt–nickel selenide catalyst with excellent activity in HER. *Journal of Materials Research and Technology* **2021**, *15*, 3942-3950.

28. Gong, F.; Wang, H.; Xu, X.; Zhou, G.; Wang, Z.-S., In Situ Growth of  $\text{Co}_{0.85}\text{Se}$  and  $\text{Ni}_{0.85}\text{Se}$  on Conductive Substrates as High-Performance Counter Electrodes for Dye-Sensitized Solar Cells. *JACS* **2012**, *134* (26), 10953-10958.
29. Yu, B.; Hu, Y.; Qi, F.; Wang, X.; Zheng, B.; Liu, K.; Zhang, W.; Li, Y.; Chen, Y., Nanocrystalline  $\text{Ni}_{0.85}\text{Se}$  as Efficient Non-noble-metal Electrocatalyst for Hydrogen Evolution Reaction. *Electrochim. Acta* **2017**, *242*, 25-30.
30. Xu, P.; Zhang, J.; Ye, Z.; Liu, Y.; Cen, T.; Yuan, D., Co doped  $\text{Ni}_{0.85}\text{Se}$  nanoparticles on RGO as efficient electrocatalysts for hydrogen evolution reaction. *Applied Surface Science* **2019**, *494*, 749-755.
31. Zhao, W.; Li, M.; Wu, H.; Feng, C.; Zhang, G., Rod-like nonstoichiometric  $\text{Ni}_{0.85}\text{Se}$  as efficient electrocatalysts for hydrogen evolution reaction. *International Journal of Hydrogen Energy* **2018**, *43* (28), 12653-12660.
32. Liu, G.; Shuai, C.; Mo, Z.; Guo, R.; Liu, N.; Dong, Q.; Wang, J.; Pei, H.; Liu, W.; Guo, X., Fe-doped  $\text{Ni}_{0.85}\text{Se}$  nanospheres interspersed into carbon nanotubes as efficient and stable electrocatalyst for overall water splitting. *Electrochimica Acta* **2021**, *385*, 138452.
33. Xiong, S.; Weng, S.; Tang, Y.; Qian, L.; Xu, Y.; Li, X.; Lin, H.; Xu, Y.; Jiao, Y.; Chen, J., Mo-doped  $\text{Co}_3\text{O}_4$  ultrathin nanosheet arrays anchored on nickel foam as a bi-functional electrode for supercapacitor and overall water splitting. *J. Colloid Inter. Sci.* **2021**, *602*, 355-366.
34. Cao, L. M.; Hu, Y. W.; Tang, S. F.; Iljin, A.; Wang, J. W.; Zhang, Z. M.; Lu, T. B., Fe-CoP electrocatalyst derived from a bimetallic Prussian Blue analogue for large-current-density oxygen evolution and overall water splitting. *Adv. Sci.* **2018**, *5* (10), 1800949.
35. Chen, D.; Shen, J.; Li, X.; Cao, S.-a.; Li, T.; Luo, W.; Xu, F.,  $\text{Ni}_{0.85}\text{Se}$  hexagonal nanosheets as an advanced conversion cathode for Mg secondary batteries. *J. Energy Chem.* **2020**, *48*, 226-232.
36. Bai, Y.; Shen, W.; Song, K.; Zhang, S.; Wang, Y.; Xu, T.; Xu, J.; Dai, S.; Wang, X., Controlled synthesis of  $\text{NiSe-Ni}_{0.85}\text{Se}$  nanocomposites for high-performance hybrid supercapacitors. *J. Electroana. Chem.* **2021**, *880*, 114795.
37. Seo, J.; Gowda, A.; Babu, S., Almost Complete Removal of Ceria Particles Down to 10 nm Size from Silicon Dioxide Surfaces. *ECS J. Solid State Sci. Technol.* **2018**, *7*.

38. Gao, W.; Yan, M.; Cheung, H.-Y.; Xia, Z.; Zhou, X.; Qin, Y.; Wong, C.-Y.; Ho, J. C.; Chang, C.-R.; Qu, Y., Modulating electronic structure of CoP electrocatalysts towards enhanced hydrogen evolution by Ce chemical doping in both acidic and basic media. *Nano Energy* **2017**, *38*, 290-296.
39. Mahala, C.; Devi Sharma, M.; Basu, M., Fe-Doped Nickel Hydroxide/Nickel Oxyhydroxide Function as an Efficient Catalyst for the Oxygen Evolution Reaction. *ChemElectroChem* **2019**, *6* (13), 3488-3498.
40. Peng, L.-J.; Huang, J.-P.; Pan, Q.-R.; Liang, Y.; Yin, N.; Xu, H.-C.; Li, N., A simple method for the preparation of a nickel selenide and cobalt selenide mixed catalyst to enhance bifunctional oxygen activity for Zn–air batteries. *RSC Adv.* **2021**, *11* (32), 19406-19416.
41. Ali Akbari, M. S.; Bagheri, R.; Song, Z.; Najafpour, M. M., Oxygen-evolution reaction by nickel/nickel oxide interface in the presence of ferrate(VI). *Scientific Reports* **2020**, *10* (1), 8757.

### *Fe-Doped NiCo<sub>2</sub>Se<sub>4</sub> Nanorod Arrays as Electrocatalysts for Overall Electrochemical Water-Splitting*



- \* In this chapter, Fe doped NiCo<sub>2</sub>Se<sub>4</sub> nanorod was developed on carbon cloth.
- \* The Fe doped NiCo<sub>2</sub>Se<sub>4</sub> nanorod has good electrochemical activity with cell volatage of 1.51 V.

## *Abstract*

The development of efficient, affordable, and earth-abundant bifunctional electrocatalysts is vital for the water-splitting reaction. In this article, we have fabricated NiCo<sub>2</sub>Se<sub>4</sub> and Fe-doped NiCo<sub>2</sub>Se<sub>4</sub> through a simple hydrothermal route on the surface of carbon cloth with nanorod morphology. The developed electrocatalyst was thoroughly investigated by various techniques like PXRD, XPS, FESEM, ICP-AES, and TEM analysis. The optimized Fe<sub>0.2</sub>NiCo<sub>1.8</sub>Se<sub>4</sub> has worked finest for hydrogen and oxygen evolution in an alkaline medium; it entails a potential of 148 mV and 1.656 V vs. RHE, to obtain 50 and 100 mA/cm<sup>2</sup> current density for HER and OER, respectively. The Tafel slope values for HER and OER are 85.7 and 56.3 mV/dec, respectively. This catalyst is stable under an alkaline medium for 48 hours. The best HER and OER activity recommend the catalyst as a bifunctional in an alkaline medium, and the developed cell consisting of a doped sample requires 1.51 V to generate a 10 mA/cm<sup>2</sup> current density with 24 hours of stability. The Fe<sub>0.2</sub>NiCo<sub>1.8</sub>Se<sub>4</sub> catalyst has good Faradaic efficiency of 89.9 % for overall water splitting. The nanorod morphology has a specific role in enhancing the electron transportation and conductivity of Fe<sub>0.2</sub>NiCo<sub>1.8</sub>Se<sub>4</sub>. The doping with Fe in NiCo<sub>2</sub>Se<sub>4</sub> enhances the active sites and increases its electrocatalytic performance. The SCN<sup>-</sup> poisoning effect on metal ions in Fe<sub>0.2</sub>NiCo<sub>1.8</sub>Se<sub>4</sub> suggest that Fe, Co, and Ni metals have a prominent impact on the overall electrocatalytic activity. Additionally, DFT investigation indicates that after Fe doping in NiCo<sub>2</sub>Se<sub>4</sub> zero band gap, minimum Gibbs free energy, maximum hydrogen, and oxygen coverage calculation are accountable for the higher conductivity of the system. This research provides a simple approach for synthesizing a Fe-doped ternary NiCo<sub>2</sub>Se<sub>4</sub> nanorod array on the surface of carbon cloth, which is highly active and stable for water-splitting in an alkaline medium.

### 7.1 Introduction

The continuous consumption of fossil fuel resources requires an urgent substitute to produce energy as an alternate source, which will satisfy the vast energy crisis. One of the most effective ways to generate hydrogen and oxygen at a large scale is electrochemical water-splitting.<sup>1-2</sup> The theoretical potential to electrolyze water is 1.23 V vs. RHE, but this process requires a very high overpotential and splits water more than the thermodynamic potential. The two half-reactions have extra overpotential because of the sluggish kinetics of water splitting.<sup>3-4</sup> As a result, the energy needed for water-splitting is greater than the associated energy for hydrogen generation. In this context, there is an urgent need to develop an electrocatalyst that can reduce the overpotential value related to this hydrogen and oxygen evolution reaction (HER and OER).<sup>5-6</sup> The common electrocatalyst for HER and OER are Pt, and RuO<sub>2</sub>, IrO<sub>2</sub>, respectively. However, these electrocatalysts are higher costs and scarcity, making these precious metals and metal oxides incompetent for wide-scale application.<sup>7</sup> So, replacing these precious materials with transition metals like Ni, Co, Cu, and Fe, which are abundant on earth for HER and OER, is essential. Transition metal hydroxides, oxides, phosphides, sulphides, and selenides are better electrocatalysts studied to improve activity and durability for hydrogen energy production.<sup>8-10</sup>

In recent years, transition metal-based selenides have been attracted to water electrolysis because of their intrinsic metallic property and high electron density. Multi-metallic selenides are better electrocatalysts than single-metal selenides due to abundant redox active sites and synergistic effects between the metal ions.<sup>11</sup> Furthermore, adding multi-metal to the single metal catalyst is essential to tune the electronic environment and adsorption/desorption energy of the intermediate ions. However, multi-metal compounds have some limitations in synthesizing due to the unusual dispersal of metal ions.<sup>12-13</sup> So, it is significant to find a synthetic method through which uniformly distributed multi-metal selenides can be formed for water-splitting. Apart from synthesizing uniformly distributed multi-metal selenides, it is also essential to develop an electrocatalyst with bifunctional (HER and OER) electrocatalytic activity.<sup>14</sup> In the last couple of years, scientists have reported many materials, including doped material, transition metal alloy, metal-organic framework, spinel oxides, and perovskites, towards bifunctionality for HER and OER.<sup>15-17</sup> In this quest, the significant manifestation of transition metal selenides is multifold. First, higher covalency surrounding the transition metal center enhances electrocatalytic activity.

Second, transition metal selenides are better than sulphides and hydroxides due to their high electron density. Third, electrocatalytic activity can be increased by doping with another metal, which reduces the overpotential and change the electronic environment of the catalytically active center. The rate of electron transportation within the system can also be enhanced by doping which improvises the conductivity of the developed electrocatalyst.<sup>18-19</sup>

In view of this, metallic NiCo<sub>2</sub>Se<sub>4</sub> holey nanosheets for OER are developed by Fang and co-workers.<sup>20</sup> The theoretical and experimental evidence confirmed that metallic nature, holey nanostructure, and large electrochemical active sites are beneficial for OER. The developed catalyst efficiently works in overall water-splitting with the potential of 1.68 V to obtain a 10 mA/cm<sup>2</sup> current density. Sancho and co-workers<sup>21</sup> reported NiCo<sub>2</sub>Se<sub>4</sub> nanowires as a promising electrocatalyst for OER. The nanowire morphology increases the material's electrochemically active surface area and porosity, which leads to better activity. Recently, Wang and co-workers<sup>22</sup> reported a phosphorous-doped NiCo<sub>2</sub>Se<sub>4</sub> nanoneedle array for efficient HER activity in different pH mediums. P doped NiCo<sub>2</sub>Se<sub>4</sub> electrocatalyst fabricated on carbon fiber paper shows outstanding HER performance with low overpotentials of 33, 57, and 69 mV in acidic, alkaline, and neutral medium, respectively, to achieve 10 mA/cm<sup>2</sup> current density. They have done DFT studies also to know the atomic level modulation and prove that P doping can optimize the charge densities in metallic and non-metallic centers of NiCo<sub>2</sub>Se<sub>4</sub>, improving the electrocatalytic HER activity. Qi and co-workers<sup>12</sup> reported iron-doped nickel-cobalt phosphide (NiCoP) on Ni foam with hyperbranched hierarchical morphology for overall water splitting. Fe doping changes the electronic environment of NiCoP, enhancing the catalytic site and creating a larger electrolyte contact area which accelerates the electrocatalytic activity. The improved performance of the electrocatalyst is attributable to the interaction between the tailored hyperbranched morphology and the changed electronic structure brought about by Fe doping. Cao and co-workers<sup>23</sup> reported multi-transition metal selenides as highly efficient oxygen evolution electrocatalyst developed with electrodeposition technique. The developed mixed metal selenide composition of Ni-Co-Fe shows excellent performance with a small overpotential of 0.23 V vs. RHE for 10 mA/cm<sup>2</sup> current density generation and 8-hour stability in 0.3 M KOH medium. They observed that doping of Co and Fe in the NiSe matrix enhances the electrocatalytic efficiency, which is due to electron reorganization and d band overlapping. Moreover, the multi-metallic centre favours the adsorption of OH<sup>-</sup> ion, which facilitates faster OER kinetics. Therefore, efforts are made to develop bare and



doped transition metal chalcogenides for water-splitting reactions. Among them, ternary nickel cobalt-based material is much attracted because of its more redox-active sites ( $\text{Ni}^{+2}/\text{Ni}^{+3}$  and  $\text{Co}^{+2}/\text{Co}^{+3}$ ), synergistic effect, and spinel structure.

Inspired by the above studies, we developed a Fe-doped  $\text{NiCo}_2\text{Se}_4$  nanorod on a conducting substrate following a hydrothermal technique for application in an overall water-splitting reaction. The synthesized bare and doped catalysts are characterized through various methods such as Powder X-ray diffraction (PXRD), X-ray photoelectron spectroscopy (XPS), Field emission scanning electron microscopy (FESEM), Inductively coupled plasma atomic emission spectroscopy (ICP-AES) and Transmission electron microscopy (TEM), etc. The dopant amount is optimized with respect to Co to get efficient electrocatalysts in water-splitting.  $\text{Fe}_{0.2}\text{NiCo}_{1.8}\text{Se}_4$  electrocatalyst only requires an onset potential value of -0.148 and 1.656 V vs. RHE to obtain 50 and 100  $\text{mA}/\text{cm}^2$  current density HER and OER, respectively. The Tafel slope values are 85.7 and 56.3  $\text{mV}/\text{dec}$  for HER and OER in 1.0 M KOH, respectively. The long-term stability is performed for 48 hours for HER and OER, which reflects unaltered current density. The doped electrocatalyst ( $\text{Fe}_{0.2}\text{NiCo}_{1.8}\text{Se}_4$ ) shows excellent activity in the two-electrode cell, which requires 1.51 V to generate a 10  $\text{mA}/\text{cm}^2$  current density and 24 hours of stability in an alkaline medium. The advantage of this work can be folded as follows. First, a simple hydrothermal approach is used to synthesize Fe doped  $\text{NiCo}_2\text{Se}_4$ . Second, the doping of Fe enhances the electrocatalytic activity and stability of  $\text{NiCo}_2\text{Se}_4$ . Third, Fe-doped  $\text{NiCo}_2\text{Se}_4$  has roughened nanorod morphology that increases the electrochemically active surface area and maximizes the electrolyte penetration. This morphology also minimizes agglomeration, thus enhancing electrocatalytic performance and stability. Fourth, multi-transition metals (Fe, Ni, and Co) generate a synergistic effect and redox centers within the electrocatalyst environment and increase efficiency. Fifth, the thiocyanate ion poisoning effect on the metal center activity during electrocatalytic reaction confirms the importance of the multi-metallic center. Sixth, the doped electrocatalyst has a remarkable efficiency in two electrode systems with 89.9 % Faradaic efficiency. Seventh, DFT studies prove that the metallic behavior increases after Fe doping in  $\text{NiCo}_2\text{Se}_4$ , which helps in the electrocatalytic activity. The minimum Gibbs free energy values and highest oxygen and hydrogen coverage also make the doped  $\text{NiCo}_2\text{Se}_4$  catalyst a better candidate for water splitting.

### 7.2 Experimental Section

**7.2.1 Synthesis of bare NiCo<sub>2</sub>Se<sub>4</sub>:** The synthesis of NiCo<sub>2</sub>Se<sub>4</sub> on carbon cloth was performed with the two-step hydrothermal methods. The synthesis of the Ni-Co urea complex was developed in the primary step. 0.596 gm nickel chloride, 1.18 gm cobalt chloride, and 0.45 gm urea were mixed and sonicated for 10 minutes in 60 mL DI water. NiCl<sub>2</sub>·6H<sub>2</sub>O, CoCl<sub>2</sub>·6H<sub>2</sub>O, and urea were used in the molar ratio of 1:2:3, and the hydrothermal reaction was kept at 110 °C for 10 hours. CC with an area of 3×2 cm<sup>2</sup> was placed in the reaction mixture during the hydrothermal process. After the primary step, a light pink colored sample of the Ni-Co urea complex was developed and deposited on CC. The complex-deposited CC was thoroughly dried in a hot air oven after being cleaned with MilliQ and ethanol. In the second step, selenization of the as-developed Ni-Co urea complex was performed. For selenization, 4.6 mmol of Na<sub>2</sub>SeO<sub>3</sub> and 10 mL of 80% H<sub>2</sub>N-NH<sub>2</sub> were prepared and mixed well. After that, the reaction mixture (Na<sub>2</sub>SeO<sub>3</sub> and N<sub>2</sub>H<sub>4</sub>) along with the Ni-Co urea complex deposited CC was transferred into the Teflon-lined autoclave, and the hydrothermal reaction was performed at 180 °C for 10 hours. In this process, hydrazine hydrate was used as a reducing agent. At the end of the reaction, the black color NiCo<sub>2</sub>Se<sub>4</sub> was deposited on the surface of CC. The sample deposited CC was washed with DI water and ethanol.

**7.2.2 Synthesis of Fe-doped NiCo<sub>2</sub>Se<sub>4</sub>:** During the synthesis of Fe-doped NiCo<sub>2</sub>Se<sub>4</sub>, 0.5 mmol of FeCl<sub>3</sub>, 2.5 mmol nickel chloride, 4.5 mmol cobalt chloride, and 7.5 mmol urea were mixed and sonicated for 10 minutes in 60 mL DI water. The hydrothermal reaction was for 10 hours fixed at a temperature of 110 °C. During the hydrothermal setup, CC with an area of 3×2 cm<sup>2</sup> was placed inside the Teflon line autoclave. The light orange-colored Fe-doped Ni-Co urea complex was synthesized on CC and washed adequately with DI water and ethanol. The Fe-doped Ni-Co urea complex was characterized by PXRD (Figure 7.1a), FESEM, and EDS mapping analysis (Figure 7.1 b and c), which proves the formation of the Ni-Co carbonate hydroxide complex. Therefore, Fe doped Ni-Co urea complex was developed on CC in this process. In the next step, the Fe doped complex deposited CC was kept along with 4.6 mmol of sodium selenite, 10 mL hydrazine hydrate, and 20 mL DI water in a Teflon-lined autoclave, and the selenization process was carried out at 180 °C for 10 hours. Black-colored Fe-doped NiCo<sub>2</sub>Se<sub>4</sub> was deposited on the CC, washed well with pure water, and ethanol dried at 50 °C. As per the ratio of FeCl<sub>3</sub> and CoCl<sub>2</sub>·6H<sub>2</sub>O, the developed catalyst is represented as Fe<sub>0.2</sub>NiCo<sub>1.8</sub>Se<sub>4</sub>.

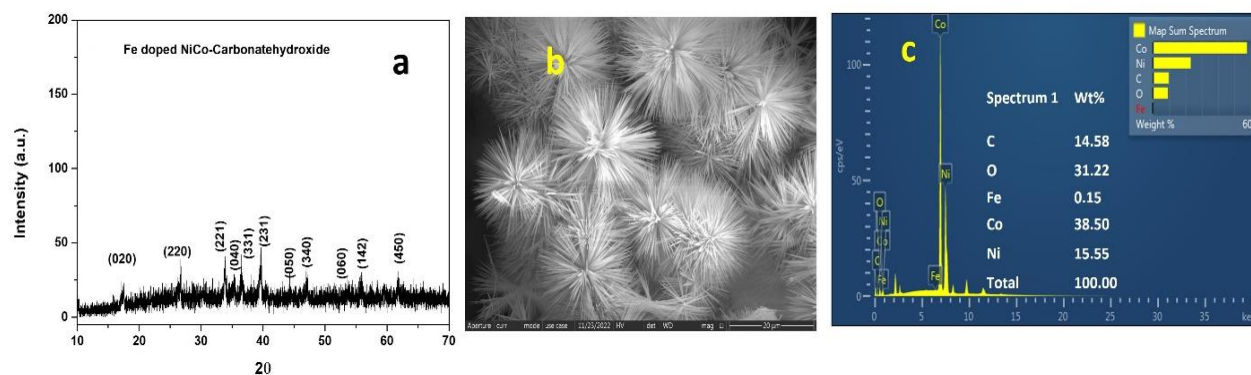
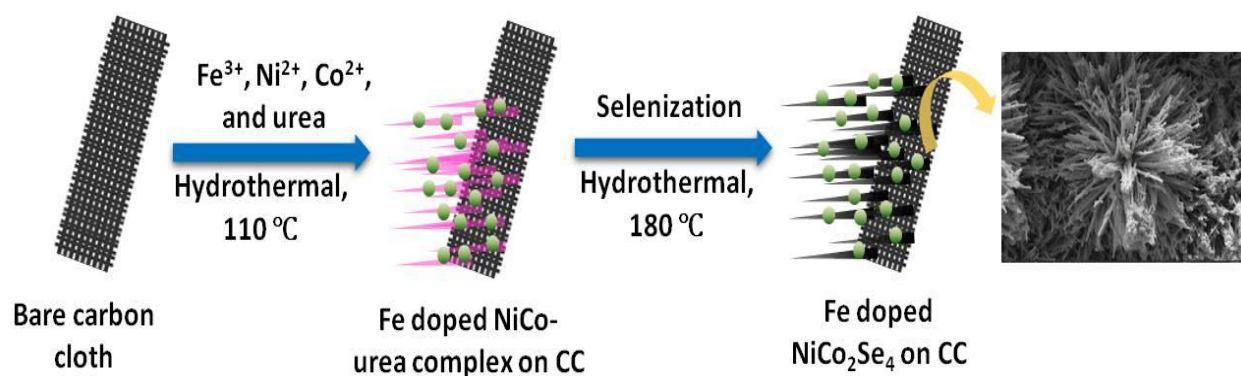


**Figure 7.1:** (a) PXRD pattern (b) FESEM (c) EDS analysis for Fe doped Ni-Co urea precursor complex.

Different amount of Fe doping in  $\text{NiCo}_2\text{Se}_4$  was developed using a similar protocol, except the amount of  $\text{FeCl}_3$  and  $\text{CoCl}_2 \cdot 6\text{H}_2\text{O}$  were varied. To lower the amount of dopant, 0.25 mmol of  $\text{FeCl}_3$  and 4.75 mmol of  $\text{CoCl}_2 \cdot 6\text{H}_2\text{O}$  were taken. To increase the amount of Fe dopant, 1 mmol of  $\text{FeCl}_3$  and 4 mmol of  $\text{CoCl}_2 \cdot 6\text{H}_2\text{O}$  were mixed. According to the molar ratio of  $\text{FeCl}_3$  and  $\text{CoCl}_2 \cdot 6\text{H}_2\text{O}$ , all the developed catalysts were named  $\text{Fe}_{0.1}\text{NiCo}_{1.9}\text{Se}_4$  and  $\text{Fe}_{0.4}\text{NiCo}_{1.6}\text{Se}_4$  throughout the MS. After the synthesis of bare and doped catalyst, and the product was used further for characterization and application. The overall synthetic procedure is represented schematically in Scheme 7.1.



**Scheme 7.1:** Schematic representation for the development of Fe doped  $\text{NiCo}_2\text{Se}_4$ .

#### 7.2.4 Electrochemical Study

The electrochemical study was done using the three-electrode systems, and the sample deposited CC as a working electrode, graphite as a counter electrode, and  $\text{Ag}/\text{AgCl}$  as a reference

electrode using the CHI604E working station. During the electrochemical reaction, the area of the working electrode was  $0.16 \text{ cm}^2$ , fixed with insulated epoxy paste and dried in normal air. The catalyst loading amount was calculated as  $4.16 \text{ mg/cm}^2$  for both doped and bare  $\text{NiCo}_2\text{Se}_4$ . 1.0 M KOH solution was used as an electrolyte for both HER and OER. Primarily linear sweep voltammetry (LSV) was carried out at an applied potential of  $-0.8$  to  $-1.8 \text{ V vs. Ag/AgCl}$  for HER and  $0$  to  $0.8 \text{ V vs. Ag/AgCl}$  for OER, respectively. The three-electrode system was used to record the Impedance of doped and bare  $\text{NiCo}_2\text{Se}_4$ . The onset potential was used as execution bias with the frequency range of  $75 \text{ kHz}$  to  $0.04 \text{ Hz}$  with a  $5 \text{ mV}$  of AC dither.

### 7.2.5 Computational methodology

The first-principle calculations have been accomplished within the density functional theory (DFT) framework using the Quantum ESPRESSO suite of software<sup>24-26</sup>. The crystal structure for the face-centered cubic (space group:  $Fd\bar{3}m$  and space group no. 227) phase of the  $\text{NiCo}_2\text{Se}_4$  compound has been primarily optimized using the Broyden-Fletcher-Goldfarb-Shanno scheme<sup>27-30</sup> in the variable cell relaxation method. The projector augmented wave (PAW) pseudopotential method<sup>31</sup> has been incorporated to consider the electron-ion interactions, and the exchange-correlation term of the pseudopotential has been estimated from the generalized gradient approximation (GGA) in conjunction with the modified Perdew-Burke-Ernzerhof (PBEsol) functional<sup>32</sup>. The plane wave kinetic energy cut-off of  $\sim 75 \text{ Ry}$  has been set for the valance electrons  $3d^84s^2$ ,  $3d^74s^2$ , and  $4s^24p^4$  for Ni, Co, and Se atoms, respectively, of the  $\text{NiCo}_2\text{Se}_4$  compound. The gamma-centered  $10 \times 10 \times 10$  Monkhorst-Pack grid points have been chosen in the Brillouin zone for the geometry optimization and self-consistent-field (SCF) calculations of the compound. After primary relaxation, the convergences of the Hellman-Feynman force and total electronic energy of the system are found to be  $\sim 10^{-3} \text{ Ry/Bohr}$  and  $10^{-9} \text{ Ry}$ , respectively under ambient pressure ( $P = 0 \text{ GPa}$ ).

To evaluate the defect formation energies ( $\Delta E_{\text{df}}$ ), electronic band structures (BS), and density of states (DOS) of the bare and Fe-doped  $\text{NiCo}_2\text{Se}_4$  compounds ( $\text{Fe}_{0.12}\text{NiCo}_{1.88}\text{Se}_4$ ,  $\text{Fe}_{0.2}\text{NiCo}_{1.8}\text{Se}_4$ , and  $\text{Fe}_{0.5}\text{NiCo}_{1.5}\text{Se}_4$ ), a  $2 \times 2 \times 2$  supercell consisting of 96 atoms of the pre-optimized bare  $\text{NiCo}_2\text{Se}_4$  system has been formed. The number of Co atoms has been substituted systematically from 2 to 8 by the Fe dopants to achieve the dopant concentration of Fe atoms between  $\sim 6\%$  and  $25\%$  in the optimized supercell of the  $\text{NiCo}_2\text{Se}_4$  compound. A denser k-point

mesh of  $20 \times 20 \times 20$  Monkhorst-Pack grid has been used for the non-self-consistent-field (nSCF) calculations (ca. BS and DOS). To understand the magnetic properties of bare and Fe-doped  $\text{NiCo}_2\text{Se}_4$  systems, the spin-spin interactions have been considered for all the magnetic atoms. To estimate precisely the electronic band gaps ( $E_g$ ) and magnetic properties of the aforementioned systems, the differences between the on-site Coulomb repulsion  $U_{dd}$  and exchange interaction  $J$  ( $U_{\text{eff}} = U_{dd} - J$ ) have been set to 6.60, 3.70, and 5.91 eV for the  $3d$  electrons of Ni, Co and Fe atoms respectively<sup>33-34</sup>. The Bader charges for pristine and Fe-doped  $\text{NiCo}_2\text{Se}_4$  systems have been estimated using the *BADER CHARGE ANALYSIS* code developed by Henkelman Group<sup>35-37</sup>. The Gibbs free energy and exchange current density in terms of hydrogen and oxygen coverages are calculated by adsorbing ‘n’ hydrogens followed by ‘n’ oxygens on the dopant atoms of the Fe-doped  $\text{NiCo}_2\text{Se}_4$  systems.

### 7.3 Result and discussion

#### 7.3.1 PXRD, and XPS analysis

To analyze the crystal structure, phase purity, and crystallinity PXRD is performed for  $\text{NiCo}_2\text{Se}_4$  and  $\text{Fe}_{0.2}\text{NiCo}_{1.8}\text{Se}_4$  samples, and the result is shown in Figure 7.2a. The PXRD pattern shows sharp and prominent peaks for the pure phase of both bare and doped samples. It can be noticed from Figure 7.2a that the  $2\theta$  values are at  $33.6^\circ$ ,  $45.2^\circ$ ,  $51.1^\circ$ ,  $60.3^\circ$ ,  $62.5^\circ$  and  $70.5^\circ$  for (111), (311), (-313), (511), (420), and (222) diffraction planes of bare  $\text{NiCo}_2\text{Se}_4$  (JCPDS 081-4821), respectively with cell parameters  $a = 12$ ,  $b = 3.59$  and  $c = 6.14 \text{ \AA}$ . All the peaks are well-matched with the monoclinic phase of  $\text{NiCo}_2\text{Se}_4$ , and no extra peak is present.<sup>22, 38-39</sup> In the doped sample of  $\text{NiCo}_2\text{Se}_4$ , all the peak positions, and patterns remain unchanged, except the highest intense peak located at  $2\theta$  of  $33.6^\circ$  shifted to a lower angle at  $33.3^\circ$  (Figure 7.1b). The peak shift in the PXRD pattern may be due to the larger covalent radius of  $\text{Fe}^{3+}$  (78.5 pm) than the  $\text{Co}^{3+}$  (75 pm) ion. The monoclinic crystal structure of  $\text{NiCo}_2\text{Se}_4$  remains the same in the  $\text{Fe}_{0.2}\text{NiCo}_{1.8}\text{Se}_4$  sample, as all the planes are well-matched after doping. The doping of  $\text{Fe}^{3+}$  ions in the system creates strain, which can be calculated from Williamson-Hall (W-H) method.<sup>40</sup> During W-H calculation, the diffraction angles at  $2\theta = 33.6^\circ$ ,  $45.2^\circ$ , and  $60.3^\circ$  for (111), (311), and (511) planes are selected. The W-H plot is drawn between  $4\epsilon \sin\theta$  vs.  $\beta \cos\theta$ , and the slope value ( $4\epsilon$ ) represents the strain

(Figure 7.1c). It can be observed from the plot that the resultant value of strain is 0.48 and 0.68 for  $\text{NiCo}_2\text{Se}_4$  and  $\text{Fe}_{0.2}\text{NiCo}_{1.8}\text{Se}_4$  samples, respectively. Therefore, the positive value of strain allocates to tensile strain in the doped system. In this context, our group also reported a positive strain value, i.e., tensile strain after doping with W doped  $\text{Ni}(\text{OH})_2/\text{NiOOH}$  sample.<sup>41</sup> The absence of any extra peak in the doped sample represents no formation of  $\text{FeSe}_x$  and other side products.

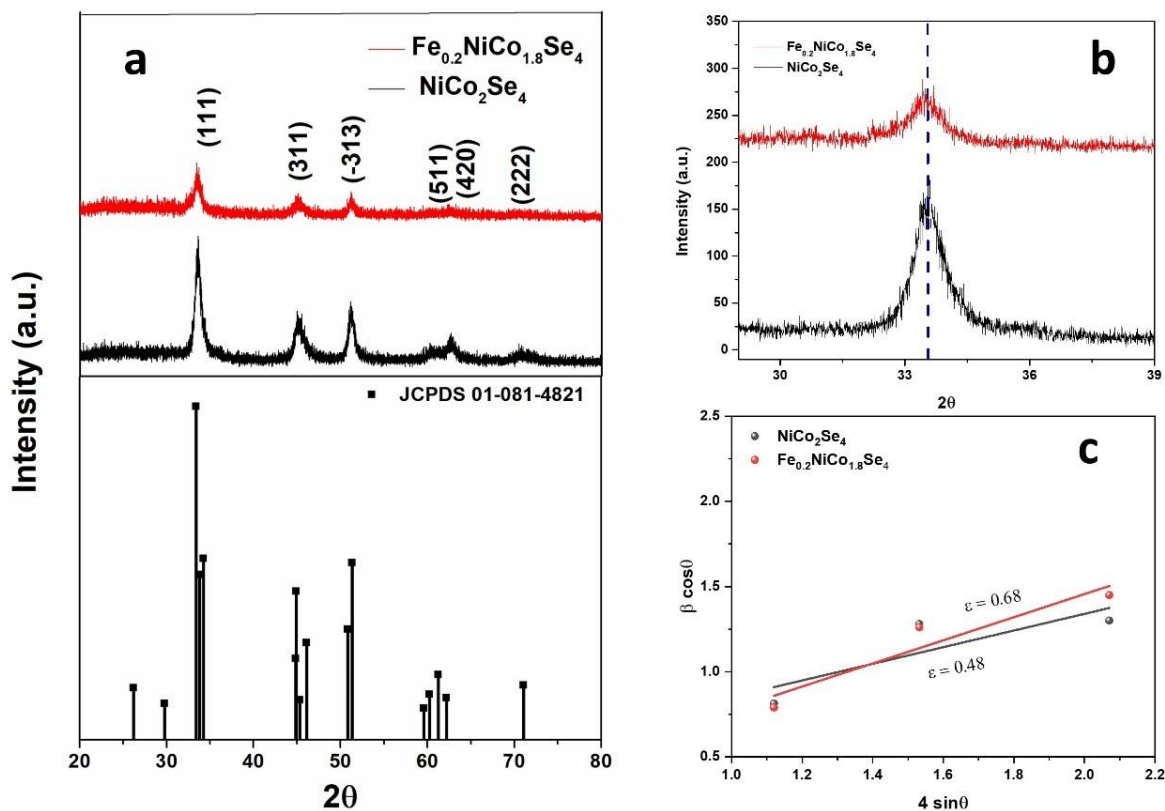


**Figure 7.2:** (a) PXRD analysis of  $\text{NiCo}_2\text{Se}_4$  and  $\text{Fe}_{0.2}\text{NiCo}_{1.8}\text{Se}_4$  with standard JCPDS card (b) Peak shift in XRD (c) Williamson-Hall plot of  $\text{NiCo}_2\text{Se}_4$  and  $\text{Fe}_{0.2}\text{NiCo}_{1.8}\text{Se}_4$ .

X-ray photoelectron spectroscopy is used to investigate the change in the electronic environment and binding energy values of  $\text{NiCo}_2\text{Se}_4$  before and after Fe doping. In Figure 7.3a, the deconvoluted Ni 2p spectra show six peaks. The peak with the binding energy (BE) values of 853.05 and 871.4 eV confirm the presence of  $\text{Ni}^{2+}$ ; other peaks at 855.5 and 873.1 eV are due to  $\text{Ni}^{3+}$  ions in the system. The binding energy values at 855.5, and 873.1 eV represents the formation

of the Ni-Se bond in the system. The first two spin-orbit coupling for Ni  $2p_{3/2}$  at 853.05 and 855.5 eV and Ni  $2p_{1/2}$  at 871.4 and 873.1 eV, respectively. The remaining peaks at 861.6 and 880.4 eV are satellite peaks of  $Ni^{2+}$  and  $Ni^{3+}$  ions. Similarly, deconvoluted spectra of Co 2p in Figure 7.3b exhibit binding energy at 778.2 and 780.1 eV for spin-orbit coupling of Co  $2p_{3/2}$  and 793.1 and 796.3 eV for spin-orbit coupling of Co  $2p_{1/2}$  of  $Co^{3+}$  and  $Co^{2+}$  ion, respectively. The existence of two shakeup satellite peaks at 784.2 and 801.8 eV corresponds to the presence of  $Co^{2+}$  and  $Co^{3+}$  ions. In Figure 7.3c, the BE value at 54.6 eV and 55.7 eV for  $3d_{5/2}$  and  $3d_{3/2}$ , respectively, confirm the presence of  $Se^{2-}$  ion in the multi-metallic selenide system. Another peak at 59.3 and 60.3 eV is attributed to  $SeO_x$ , which may be due to partial surface oxidation of the sample. Thus, XPS analysis confirms the presence of  $Ni^{2+}$ ,  $Ni^{3+}$ ,  $Co^{2+}$ ,  $Co^{3+}$ , and  $Se^{2-}$  ion in bare  $NiCo_2Se_4$ , which is well matched with the existing literature.<sup>42-43</sup> Liu and co-workers<sup>44</sup> reported similar binding energy values for  $Ni^{2+}$ ,  $Ni^{3+}$ ,  $Co^{2+}$ ,  $Co^{3+}$ , and  $Se^{2-}$  in  $NiCo_2Se_4$  with N doped carbon system. Sakthivel and co-workers<sup>11</sup> developed an ellipsoid-like structure of  $NiCoSe_2$  via hydrothermal and reported the presence of  $SeO_x$  at 58.61 eV binding energy due to partial surface oxidation. The survey spectrum in Figure 7.4d shows the presence of Ni, Co, Se, O, and C in the sample.

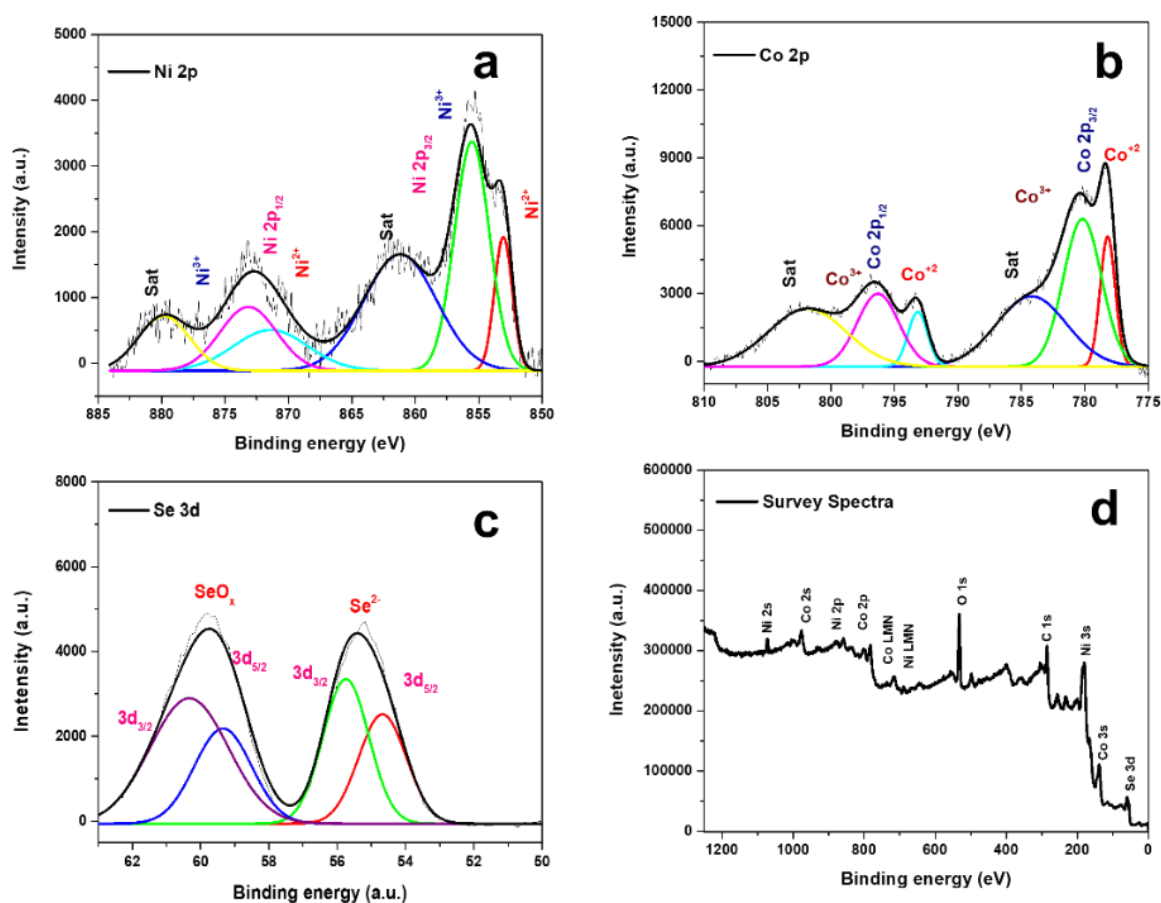


**Figure 7.3:** XPS analysis of  $\text{NiCo}_2\text{Se}_4$  (a) deconvoluted spectra of Ni 2p, (b) deconvoluted spectra of Co 2p, and (c) deconvoluted spectra of Se 3d and (d) survey spectrum.

Figure 7.4a represents the deconvoluted Ni 2p spectra in the  $\text{Fe}_{0.2}\text{NiCo}_{1.8}\text{Se}_4$  sample, which shows binding energy values at 855.7 and 857.1 eV for Ni  $2p_{3/2}$  state. The other values at 873.1 and 875.1 eV for spin-orbit coupling of Ni  $2p_{1/2}$ . The binding energy values at 855.7 and 873.1 eV are responsible for  $\text{Ni}^{2+}$  ion, with a difference is 17.5 eV. Furthermore, the binding energy values at 857.1 and 875.1 eV are related to the presence of  $\text{Ni}^{3+}$  ion in the Fe-doped  $\text{NiCo}_2\text{Se}_4$  sample. The satellite peak appears at 861.5 and 879.6 eV in Ni 2p spectra, denoting the presence of  $\text{Ni}^{2+}$  and  $\text{Ni}^{3+}$  ions. It is visualized from Figure 7.4b that the Co 2p spectra show spin-orbit coupling at different binding energy values. The binding energy values at 780.4 and 796.6 eV denoted the occurrence of  $2p_{3/2}$  and  $2p_{1/2}$  states, respectively, of  $\text{Co}^{3+}$  ion. The other two peaks at 782.4 and 798.2 eV for  $2p_{3/2}$  and  $2p_{1/2}$  states, respectively, of  $\text{Co}^{2+}$  ion. Furthermore, the presence of two



satellite peaks at 785.5 and 802.8 eV corresponds to the Co 2p state of  $\text{Co}^{2+}$  and  $\text{Co}^{3+}$  ions in the system. Therefore, the  $\text{Fe}_{0.2}\text{NiCo}_{1.8}\text{Se}_4$  sample consists of  $\text{Ni}^{2+}$ ,  $\text{Ni}^{3+}$ , and  $\text{Co}^{2+}$ ,  $\text{Co}^{3+}$  redox centers.<sup>45</sup> Figure 7.4c represents the deconvoluted XPS spectra of the Fe 2p system in the doped sample. It is envisaged that Figure 7.4c consists of four binding energy values. Out-of-all, the values at 711.5 and 720.7 eV corroborate the presence of Fe 2p<sub>3/2</sub> and 2p<sub>1/2</sub> states due to  $\text{Fe}^{3+}$  ions. The two shakeup satellite peaks of Fe 2p at 715.1 and 723.3 eV binding energy values represented 2p<sub>3/2</sub> and 2p<sub>1/2</sub> states of  $\text{Fe}^{3+}$  ion, respectively. There is no existence of other peaks for Fe-Se or another species in the XPS spectra of Fe 2p, which confirms the successful doping of the  $\text{Fe}^{3+}$  ion in the  $\text{NiCo}_2\text{Se}_4$  system and sample developed in the pure phase. In this regard, Lai and co-workers also reported the successful development of the Fe-doped  $\text{NiCo}_2\text{S}_4$  pure phase and the dopant to exist as  $\text{Fe}^{3+}$  ion.<sup>46</sup> However, XPS analysis confirms the presence of  $\text{Fe}^{3+}$  ions in the doped sample. To compare the binding energy values of Ni 2p and Co 2p states in bare and doped samples, it is observed that the values in the doped sample are shifted ( $\sim 1.6 - 2.6$  eV) in higher binding energy. The deconvoluted Se 3d spectra in Figure 7.4d show the first doublet with the BE values at 53.9 eV (3d<sub>5/2</sub>) and 54.8 eV (3d<sub>3/2</sub>), denoted as  $\text{Se}^{2-}$  ion in the doped sample. The other doublet is present at 58.9 and 60.13 eV due to partial oxidation of the surface of the  $\text{Se}^{2-}$  ion. However, it is observed that the BE values of  $\text{Se}^{2-}$  ion in  $\text{Fe}_{0.2}\text{NiCo}_{1.8}\text{Se}_4$  (53.9 and 54.8 eV) reduced to lower energy (1.2 and 1.4 eV) in comparison with bare  $\text{NiCo}_2\text{Se}_4$  (54.6 and 55.7 eV). The huge shifting in binding energy values correlates with the existence of electronic interactions and synergistic effects between Fe, Ni, and Co atoms in the doped sample. The survey spectrum in Figure 7.4e confirms the presence of Ni, Co, Fe, Se, O, and C in the composition.

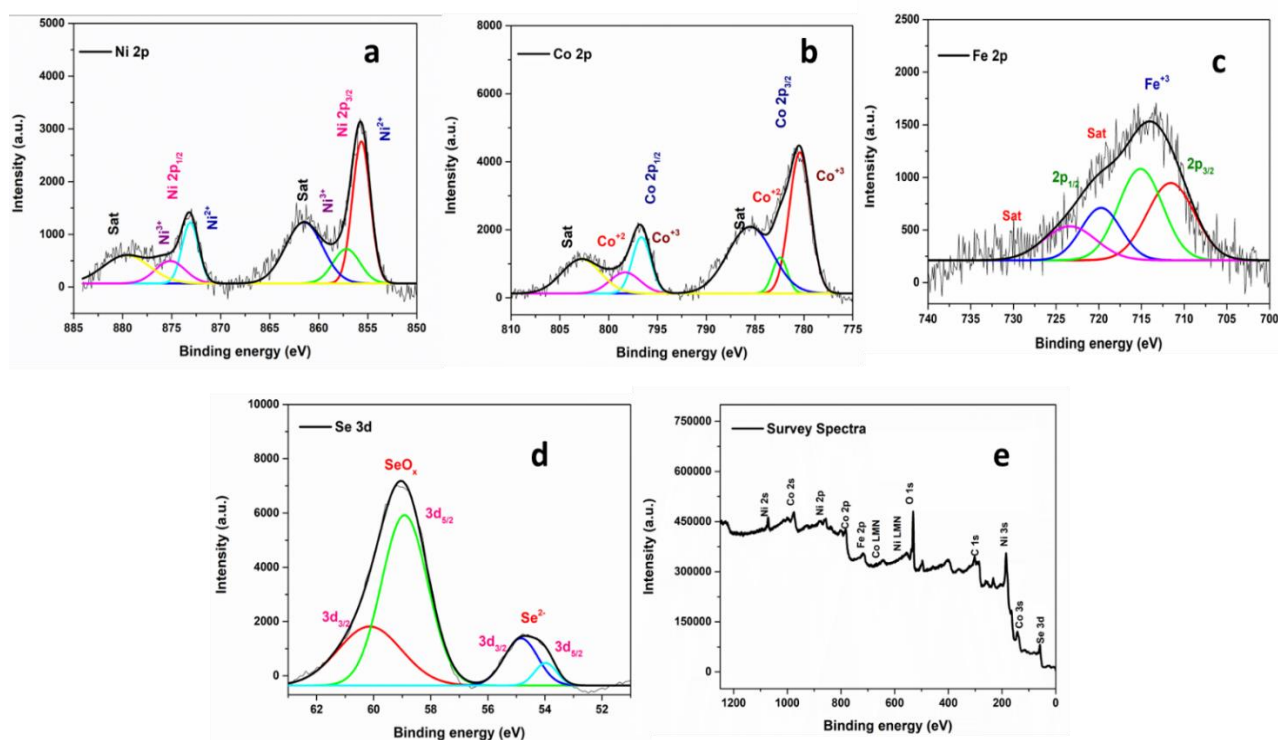


**Figure 7.4:** XPS analysis of  $\text{Fe}_{0.2}\text{NiCo}_{1.8}\text{Se}_4$  (a) Ni 2p, (b) Co 2p, (c) Fe 2p, (d) Se 3d deconvoluted spectra, and (e) survey spectrum.

The sample,  $\text{Fe}_{0.2}\text{NiCo}_{1.8}\text{Se}_4$ , consists of the dopant as  $\text{Fe}^{3+}$  ion, a  $d^5$  system (high-spin,  $t_{2g}^3e_g^2$ ), which can behave as a Lewis acid. So,  $\text{Fe}^{3+}$  can withdraw the electron, and  $\text{Co}^{2+}$  ( $d^7$  system) can be converted into  $\text{Co}^{3+}$  ( $d^6$  system) ion, which creates a more electrocatalytically active center during the water-splitting reaction. The electron pulling behaviour of  $\text{Fe}^{3+}$  ion can be explained based on the binding energy value shift of the Co 2p state in higher energy, which also changes the electronic environment after doping. The binding energy values of Co 2p<sub>3/2</sub> state before and after doping are 778.2, 780.1 eV, and 780.4, 782.4 eV, respectively. Therefore, the binding energy value difference is 2.2 to 2.3 eV. This huge variation in the binding energy value represents the electron-withdrawing nature of  $\text{Fe}^{3+}$  in the doped sample and the generation of more  $\text{Co}^{3+}$  ion in the system. This phenomenon of  $\text{Co}^{3+}$  ion formation after doping is well corroborated with the atomic percentage calculation of the  $\text{Co}^{2+}/\text{Co}^{3+}$  ratio before and after doping. In Co 2p<sub>3/2</sub> spectra, the ratio of  $\text{Co}^{2+}/\text{Co}^{3+}$  is 2.75 and 0.18 for bare  $\text{NiCo}_2\text{Se}_4$  and  $\text{Fe}_{0.2}\text{NiCo}_{1.8}\text{Se}_4$ , respectively. So, the decrease in atomic percentage ratio ( $\text{Co}^{2+}/\text{Co}^{3+} = 0.18$ ) confirms that the amount of  $\text{Co}^{3+}$  ion increases after doping in the system. All the binding energy values (Co, Fe, Ni, and Se) are

tabulated in Table 7.1. Basu and co-workers<sup>47</sup> reported the Lewis acidity nature of Fe<sup>3+</sup> in the Ni(OH)<sub>2</sub>/NiOOH system, where more Ni<sup>3+</sup> ion is generated after doping. Our group also reported similar nature of Lewis acidity of W<sup>6+</sup> in the Ni(OH)<sub>2</sub>/NiOOH system and Co<sup>2+</sup> ions in the Ni<sub>9</sub>S<sub>8</sub> system.<sup>41, 48</sup>

**Table 7.1:** XPS binding energy value for bare and doped NiCo<sub>2</sub>Se<sub>4</sub>.

Binding energy	Ni <sup>2+</sup> 2p <sub>3/2</sub>	Ni <sup>3+</sup> 2p <sub>3/2</sub>	Co <sup>2+</sup> 2p <sub>3/2</sub>	Co <sup>3+</sup> 2p <sub>3/2</sub>	Se 3d <sub>5/2</sub>	Fe 2p <sub>3/2</sub>
NiCo <sub>2</sub> Se <sub>4</sub>	853.05 eV	855.5 eV	780.1 eV	778.2 eV	54.6 eV	
Fe <sub>0.2</sub> NiCo <sub>1.8</sub> Se <sub>4</sub>	855.6 eV	857.1 eV	782.4 eV	780.4 eV	53.9 eV	711.2 eV

### 7.3.2 FESEM, EDS, ICP-AES and TEM analysis

The size, shape, and distribution of the bare and doped samples are confirmed by FESEM analysis. The FESEM image of bare NiCo<sub>2</sub>Se<sub>4</sub> in lower resolution shows that a vertically grown nanorod is present uniformly throughout the surface of CC (inset of Figure 7.5a). High-resolution FESEM images show that the nanorod surface is smooth and grown vertically. The 1D nanorod of NiCo<sub>2</sub>Se<sub>4</sub> has around 1-2 μm in length and 200-300 nm in diameter (Figures 7.5a). In Figures 7.5b, the morphology of Fe<sub>0.2</sub>NiCo<sub>1.8</sub>Se<sub>4</sub> represents a vertically grown nanorod array with a rough outer surface. The diameter of the nanorod array is reduced (100-200 nm) and rough after doping (Figure 7.5b). The generation of a rough surface and reduction of nanorod diameter in the doped sample is probably due to the addition of Fe<sup>3+</sup> ions. It is visualized from Figures 7.6a and 7.6b that the tiny nanosheets are stacked together and grown vertically for the formation of nanorods in bare and doped samples. FESEM analysis of Fe<sub>0.4</sub>NiCo<sub>1.6</sub>Se<sub>4</sub> and Fe<sub>0.1</sub>NiCo<sub>1.9</sub>Se<sub>4</sub> samples are also performed to check the effect of Fe doping on the surface roughness of nanorod array (Figure 7.5c and 7.5d). The increment of the dopant amount (Fe<sub>0.4</sub>NiCo<sub>1.6</sub>Se<sub>4</sub>) shows a rough outer surface with agglomerated particle deposition. By lowering the dopant amount (Fe<sub>0.1</sub>NiCo<sub>1.9</sub>Se<sub>4</sub>), the nanorod arrays are less rough and uniform. Jin and co-workers<sup>49</sup> developed Fe-doped nickel selenide on Ni foam, where they observed similar phenomena of size reduction and rougher surface of Ni-Se after Fe doping.

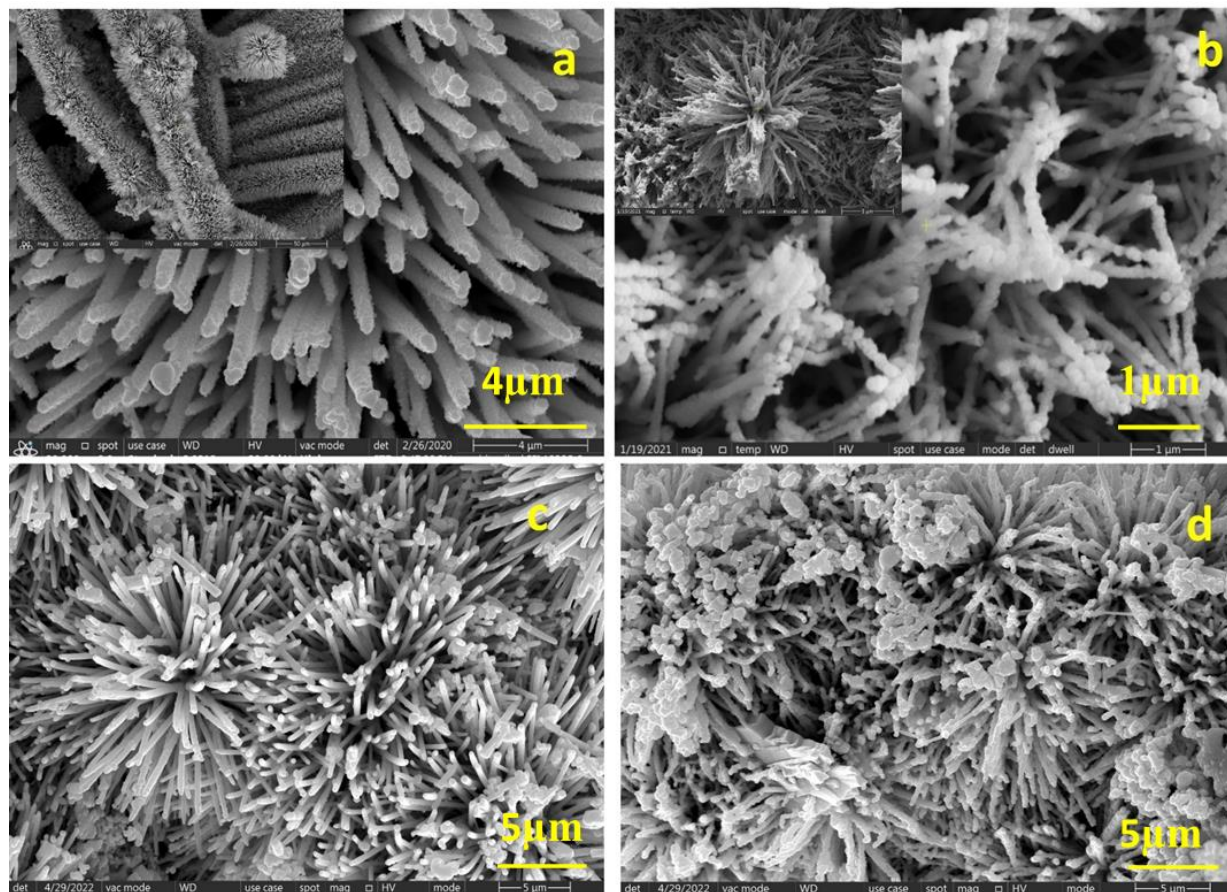


**Figure 7.5:** FESEM images of (a)  $\text{NiCo}_2\text{Se}_4$  (b)  $\text{Fe}_{0.2}\text{NiCo}_{1.8}\text{Se}_4$  (c)  $\text{Fe}_{0.1}\text{NiCo}_{1.9}\text{Se}_4$  and (d)  $\text{Fe}_{0.4}\text{NiCo}_{1.6}\text{Se}_4$ . Inset of Figure 7.5a and 7.5b show uniform distribution of sample.

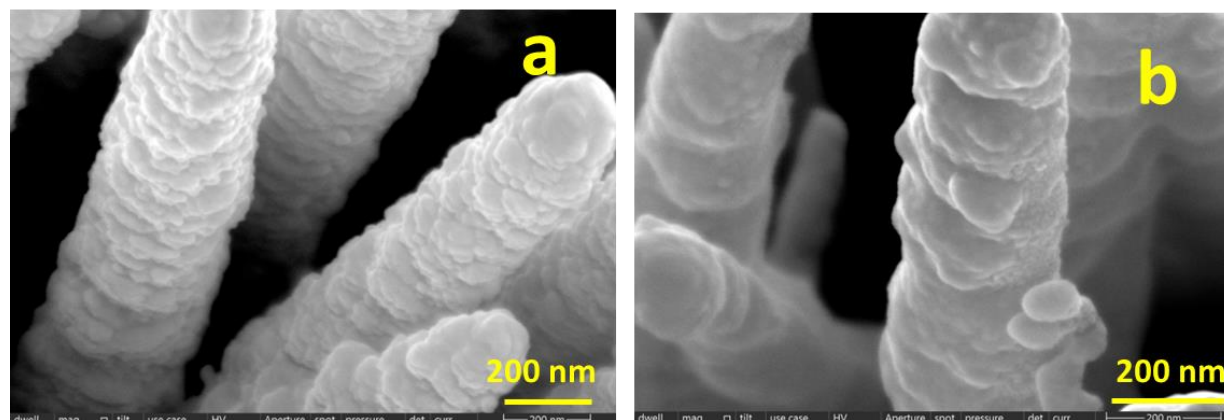


**Figure 7.6:** High magnification FESEM images (a)  $\text{NiCo}_2\text{Se}_4$  and (b)  $\text{Fe}_{0.2}\text{NiCo}_{1.8}\text{Se}_4$ .



EDS results of the bare sample ( $\text{NiCo}_2\text{Se}_4$ ) confirm the presence of Ni, Co, Se, and C on the surface of CC in Figure 7.7. Whereas, in Figure 7.8 EDS spectrum of the doped sample ( $\text{Fe}_{0.2}\text{NiCo}_{1.8}\text{Se}_4$ ) show the uniform presence of Fe, Ni, Co, Se, and C elements. From EDS analysis, the atomic percentage ratio of Fe:Co =  $\sim 1:10$ , which is well matched with the experimental ratio (Fe:Co = 1:9).

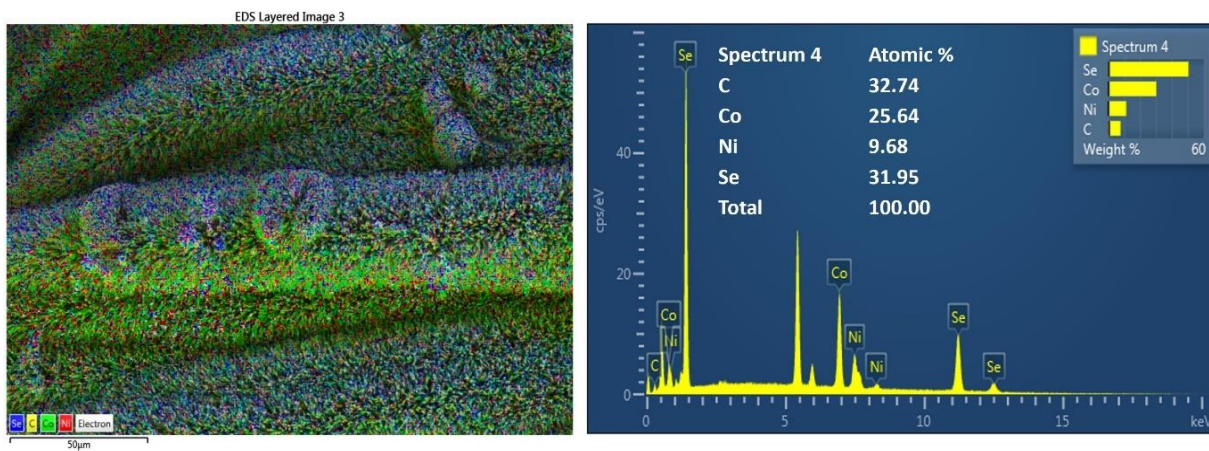


**Figure 7.7:** (a) EDS mapping and (b) elemental distribution of  $\text{NiCo}_2\text{Se}_4$  sample.

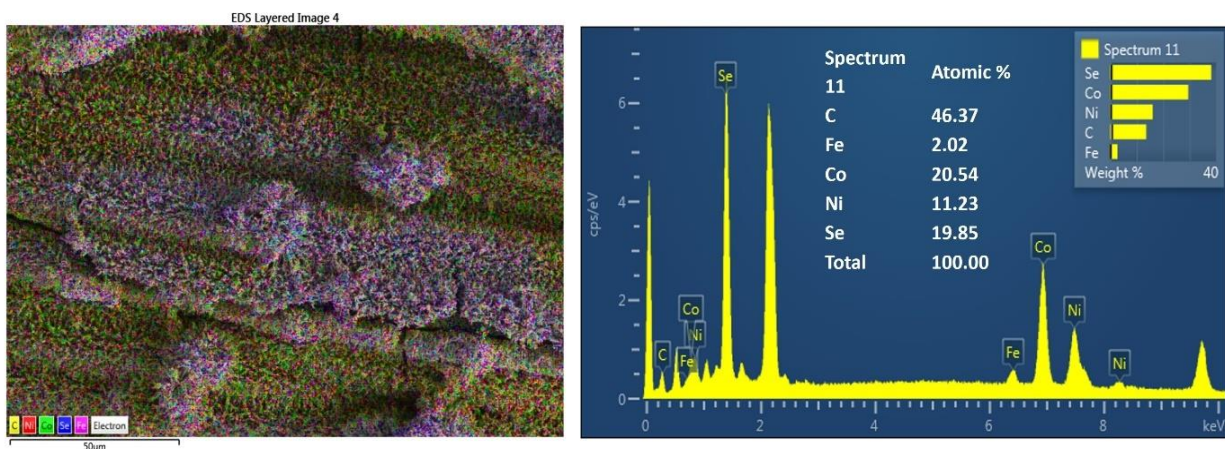


**Figure 7.8:** (a) EDS mapping and (b) elemental distribution of  $\text{Fe}_{0.2}\text{NiCo}_{1.8}\text{Se}_4$  sample.

The line mapping analysis also confirms the same (Fe, Ni, Co, Se, and C) elemental distribution (Figure 7.9). The metal ratio in the bare and doped samples is further verified with the help of ICP-AES analysis. ICP-AES analysis helps to get the quantitative composition of the sample. The bare  $\text{NiCo}_2\text{Se}_4$  sample gives the atomic percentage ratio of Ni:Co is 1:2.5. Whereas for  $\text{Fe}_{0.2}\text{NiCo}_{1.8}\text{Se}_4$ , the atomic percent ratio of Fe:Ni:Co is 1:2.07:6.5 (Table 7.2).

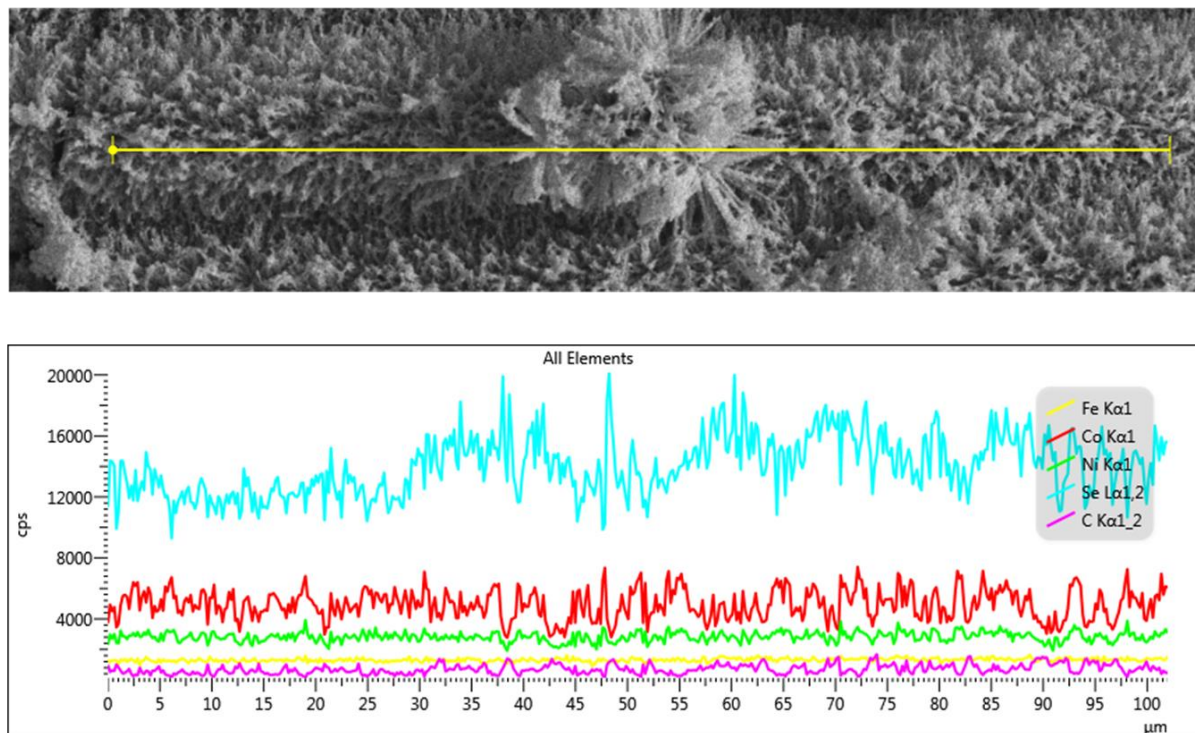


**Figure 7.9:** Line mapping analysis of  $\text{Fe}_{0.2}\text{NiCo}_{1.8}\text{Se}_4$  sample showing the uniform distribution of elements.

**Table 7.2:** ICP-AES data for undoped and doped  $\text{NiCo}_2\text{Se}_4$ .

	Ni (atomic%)	Co (atomic%)	Fe (atomic %)
$\text{NiCo}_2\text{Se}_4$	0.9 %	2.5 %	
$\text{Fe}_{0.2}\text{NiCo}_{1.8}\text{Se}_4$	1.87 %	3.93 %	0.6 %

TEM, HRTEM, and SAED analyses of  $\text{NiCo}_2\text{Se}_4$  and  $\text{Fe}_{0.2}\text{NiCo}_{1.8}\text{Se}_4$  are performed to confirm the size, morphology, and diffraction pattern. The diameter of  $\text{NiCo}_2\text{Se}_4$  nanorod is 200-300 nm, which is in good agreement with the FESEM result. Bare  $\text{NiCo}_2\text{Se}_4$  nanorod has a smooth outer surface seen in Figure 7.10a. It is envisaged that the d spacing value in the bare sample is 0.26 nm, matched well with the (111) plane of monoclinic  $\text{NiCo}_2\text{Se}_4$  (Figure 7.10b). The SAED

pattern of bare  $\text{NiCo}_2\text{Se}_4$  (Figure 7.10c) shows polycentric rings with the existence of (111), (311), (-313), and (511) planes, proving its polycrystalline nature.

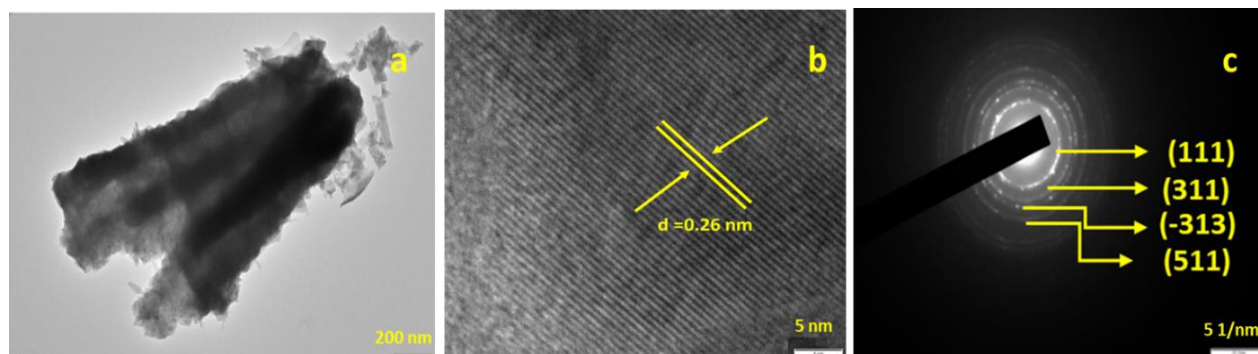


**Figure 7.10:** (a) TEM, (b) HRTEM image, and (c) SAED of bare  $\text{NiCo}_2\text{Se}_4$ .

$\text{Fe}_{0.2}\text{NiCo}_{1.8}\text{Se}_4$  has a rough outer surface with nanorod-shaped morphology, as seen in Figure 7.11a. The diameter of  $\text{Fe}_{0.2}\text{NiCo}_{1.8}\text{Se}_4$  is reduced to 100-200 nm, compatible with the FESEM analysis. The shrinkage of the diameter of the nanorod and rough outer surface after doping in  $\text{NiCo}_2\text{Se}_4$  is also confirmed by the TEM analysis. Figure 7.11b HRTEM of  $\text{Fe}_{0.2}\text{NiCo}_{1.8}\text{Se}_4$  shows the d-spacing value of 0.27 nm corresponding to the (111) plane. The SAED pattern of  $\text{Fe}_{0.2}\text{NiCo}_{1.8}\text{Se}_4$  exhibits polycentric rings with the same plane, similar to bare  $\text{NiCo}_2\text{Se}_4$  (Figure 7.11c). The increase in the d-spacing value after doping confirms the lattice expansion due to the higher covalent radius of  $\text{Fe}^{3+}$  than the  $\text{Co}^{3+}$  ion. The lattice distortion in the doped sample may generate more active sites for electrocatalytic reaction (Figure 7.11b). A similar result of lattice distortion and better electrocatalytic performance is also reported in Fe-doped  $\text{NiSe}_2$  by Shi and co-workers.<sup>50</sup>

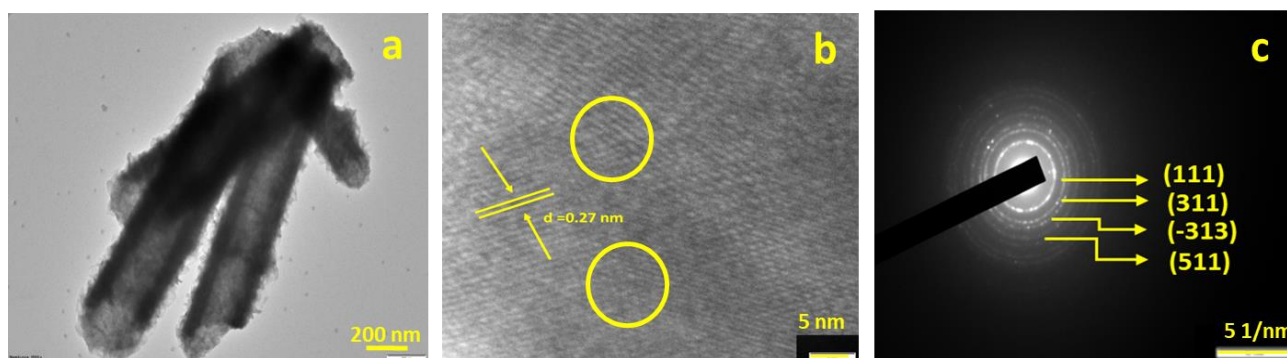


**Figure 7.11:** (a) TEM, (b) HRTEM (yellow circle shows lattice distortion), and (c) SAED analysis of  $\text{Fe}_{0.2}\text{NiCo}_{1.8}\text{Se}_4$ .

Therefore, a few conclusive points can emerge from the above characterization results of bare and Fe doped  $\text{NiCo}_2\text{Se}_4$ . First, XRD and HRTEM results confirm the lattice expansion of  $\text{NiCo}_2\text{Se}_4$  after Fe doping. Lattice distortion in the doped sample affects the electronic structure. Second, the roughness is increased in the nanorod of the  $\text{Fe}_{0.2}\text{NiCo}_{1.8}\text{Se}_4$  sample, verified from FESEM and TEM analysis. Third, the dopant  $\text{Fe}^{3+}$  ion behaves as a strong Lewis acid which modulates the electronic environment of ternary metal selenide, confirmed by XPS results. Fourth, the higher binding energy of the Co 2p and Ni 2p system ensures the generation of a synergistic effect between the Ni, Co, and Fe atoms in multi-metallic selenides. The above points demonstrated that Fe doped  $\text{NiCo}_2\text{Se}_4$  could be a potential candidate as an efficient electrocatalyst for overall water-splitting reactions.

### 7.3.3 Electrocatalytic study (HER and OER)

The electrocatalytic study of bare  $\text{NiCo}_2\text{Se}_4$ ,  $\text{Fe}_{0.1}\text{NiCo}_{1.9}\text{Se}_4$ ,  $\text{Fe}_{0.2}\text{NiCo}_{1.8}\text{Se}_4$ , and  $\text{Fe}_{0.4}\text{NiCo}_{1.6}\text{Se}_4$  is executed for both HER and OER in 1.0 M KOH solution. Three-electrode system is used to study the electrocatalysis of water, where sample deposited CC, graphite rod, and Ag/AgCl are utilized as working electrodes, counter rod, and reference electrode, respectively. Primarily linear sweep voltammetry (LSV) of bare CC, undoped  $\text{NiCo}_2\text{Se}_4$ ,  $\text{Fe}_{0.1}\text{NiCo}_{1.9}\text{Se}_4$ ,  $\text{Fe}_{0.2}\text{NiCo}_{1.8}\text{Se}_4$ ,  $\text{Fe}_{0.4}\text{NiCo}_{1.6}\text{Se}_4$ , and 5% Pt-C are recorded in the negative potential window for HER. LSV of all the electrocatalysts is represented in Figure 7.12a, where bare CC shows negligible current in the applied potential window. Undoped  $\text{NiCo}_2\text{Se}_4$  has a higher onset potential value of -0.289 V *vs.* RHE to generate a 50 mA/cm<sup>2</sup> current density. It is observed from Figure 7.12a that the existence of an anodic shift after Fe doping in the onset potential. All the Fe-doped  $\text{NiCo}_2\text{Se}_4$  samples exhibit better electrocatalytic response than the bare  $\text{NiCo}_2\text{Se}_4$  in the cathodic potential window.  $\text{Fe}_{0.1}\text{NiCo}_{1.9}\text{Se}_4$ ,  $\text{Fe}_{0.2}\text{NiCo}_{1.8}\text{Se}_4$ , and  $\text{Fe}_{0.4}\text{NiCo}_{1.6}\text{Se}_4$  have onset potentials of -0.17, -0.148, and -0.169 V *vs.* RHE, respectively to obtain 50 mA/cm<sup>2</sup> current density. The optimized  $\text{Fe}_{0.2}\text{NiCo}_{1.8}\text{Se}_4$  shows the best HER activity among other catalysts with -141 mV *vs.* RHE anodic shift compared to bare  $\text{NiCo}_2\text{Se}_4$ . The novel Pt/C catalyst requires -0.145 V *vs.* RHE to generate a 50 mA/cm<sup>2</sup> current density comparable with the best-optimized  $\text{Fe}_{0.2}\text{NiCo}_{1.8}\text{Se}_4$  sample. In Figure 7.12b histogram plot is given to compare the current density (mA/cm<sup>2</sup>) at -0.3 V *vs.* RHE potential. Fe doped  $\text{NiCo}_2\text{Se}_4$  shows improved efficiency towards HER compared to bare  $\text{NiCo}_2\text{Se}_4$ . The outer rough nanorod



surface of  $\text{Fe}_{0.2}\text{NiCo}_{1.8}\text{Se}_4$  is helpful for the adsorption of electrolyte ions and gas desorption during the water-splitting (FESEM and TEM analysis) reaction. The synergistic effect of all the metal ions  $\text{Fe}^{3+}$ ,  $\text{Ni}^{2+}$ ,  $\text{Ni}^{3+}$ ,  $\text{Co}^{2+}$ , and  $\text{Co}^{3+}$  (XPS analysis) promotes the HER activity

To have a better insight into the higher electrocatalytic performance of  $\text{Fe}_{0.2}\text{NiCo}_{1.8}\text{Se}_4$ , mass activity is calculated for all the electrocatalysts. The calculation is done at a fixed potential of  $-0.3$  V vs. RHE; the values are 13.65, 28.69, 39.66, 34.85, and 102.16 A/g for  $\text{NiCo}_2\text{Se}_4$ ,  $\text{Fe}_{0.1}\text{NiCo}_{1.9}\text{Se}_4$ ,  $\text{Fe}_{0.2}\text{NiCo}_{1.8}\text{Se}_4$ ,  $\text{Fe}_{0.4}\text{NiCo}_{1.6}\text{Se}_4$ , and 5% Pt-C, respectively (Table 7.3). The higher value of mass activity indicates higher HER performance. Furthermore, to know the kinetics of HER, the Tafel slope calculation is achieved with the help of LSV data. The Tafel slope values are calculated with the plot between applied potential (V) plotted versus  $\log|j|$  (Figure 7.12c). The observed Tafel slope value of  $\text{Fe}_{0.2}\text{NiCo}_{1.8}\text{Se}_4$  is 85.7 mV/dec, whereas bare  $\text{NiCo}_2\text{Se}_4$  shows 144.9 mV/dec. 5%-Pt/C shows a 61.5 mV/dec Tafel slope, which is well-matched with the previous reports.<sup>51</sup> Electron transportation and resistance play an important role in defining better electrocatalytic performance during electrocatalysis. Here, the electrochemical impedance study of bare  $\text{NiCo}_2\text{Se}_4$ ,  $\text{Fe}_{0.1}\text{NiCo}_{1.9}\text{Se}_4$ ,  $\text{Fe}_{0.2}\text{NiCo}_{1.8}\text{Se}_4$ , and  $\text{Fe}_{0.4}\text{NiCo}_{1.6}\text{Se}_4$  is checked in 1.0 M KOH at the bias of onset potential. Observed data is fitted with the equivalent circuit of Randle's, accordingly given in the inset of Figure 7.12d, and results in the value of solution resistance ( $R_s$ ), charge transfer resistance ( $R_{CT}$ ), and constant phase element (CPE). The value of  $R_s$  and  $R_{CT}$  is summarized in Table 7.3; the  $R_{CT}$  value of  $\text{Fe}_{0.2}\text{NiCo}_{1.8}\text{Se}_4$  is 26.7  $\Omega$ , which is lower than that of bare  $\text{NiCo}_2\text{Se}_4$  (84.39  $\Omega$ ). The lower value of  $R_{CT}$  signifies higher charge transportation on the electrode and electrolyte interface. Therefore, after doping in  $\text{NiCo}_2\text{Se}_4$ , charge transfer resistance is lower, showing faster electron transportation and better electrocatalytic performance.

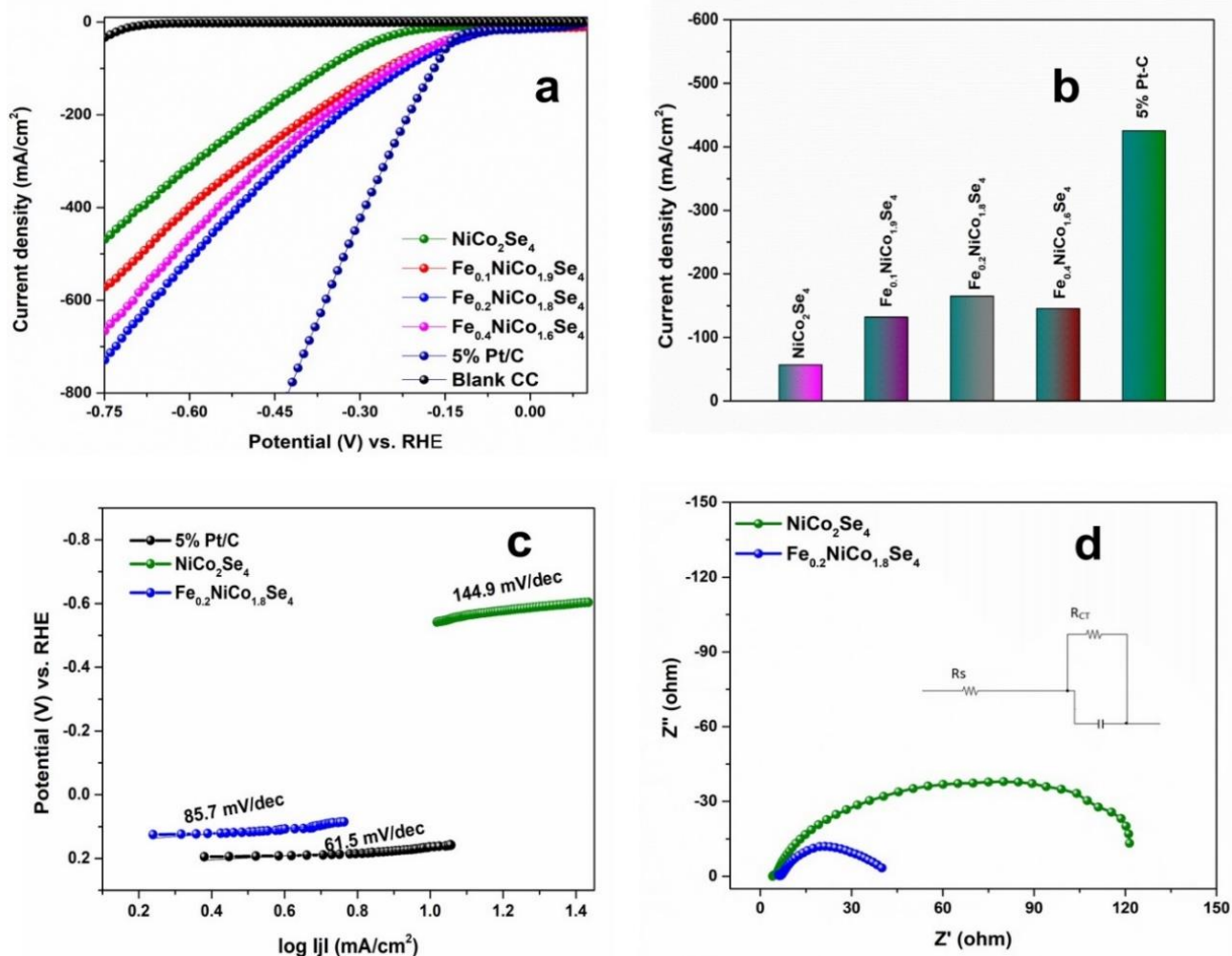


**Figure 7.12:** (a) Linear sweep voltammetry of blank CC, NiCo<sub>2</sub>Se<sub>4</sub>, Fe<sub>0.1</sub>NiCo<sub>1.9</sub>Se<sub>4</sub>, Fe<sub>0.2</sub>NiCo<sub>1.8</sub>Se<sub>4</sub>, Fe<sub>0.4</sub>NiCo<sub>1.6</sub>Se<sub>4</sub>, and Pt/C for HER, (b) histogram plot at -0.3 V vs. RHE, (c) Tafel slope, and (d) impedance of NiCo<sub>2</sub>Se<sub>4</sub> and Fe<sub>0.2</sub>NiCo<sub>1.8</sub>Se<sub>4</sub>. The inset of Figure 7.12d represents an equivalent circuit for impedance.

**Table 7.3:** All the electrochemical HER parameters for NiCo<sub>2</sub>Se<sub>4</sub>, Fe-doped NiCo<sub>2</sub>Se<sub>4</sub>, and 5% Pt-C were deposited on carbon cloth.

Electrodes	Potential (V) vs. RHE ) required to generate 50 mA/cm <sup>2</sup>	Mass Activity (A/g) at -0.3 V vs. RHE	Tafel Slope (mV/decade)	R <sub>s</sub> (Ω)	R <sub>CT</sub> (Ω)
NiCo <sub>2</sub> Se <sub>4</sub>	-0.289	13.65	144.9	4.87	84.39
Fe <sub>0.1</sub> NiCo <sub>1.9</sub> Se <sub>4</sub>	-0.17	28.69	-	-	-
Fe <sub>0.2</sub> NiCo <sub>1.8</sub> Se <sub>4</sub>	-0.148	39.66	85.7	5.8	26.7
Fe <sub>0.4</sub> NiCo <sub>1.6</sub> Se <sub>4</sub>	-0.169	34.85	-	-	-
Pt/C (5%)	-0.145	102.1	61.5	-	-

According to the literature for HER, the steps are either Volmer-Heyrovsky or Volmer-Tafel.<sup>48</sup> Based on the Tafel slope value of Fe<sub>0.2</sub>NiCo<sub>1.8</sub>Se<sub>4</sub> (85.7 mV/dec) Volmer step is the first step, where adsorption of H occurs on the surface of the catalyst. The second step is either electrochemical desorption or recombination of hydrogen, suggesting Heyrovsky and Tafel's mechanism, respectively. The Volmer-Heyrovsky mechanism is preferred for HER. The rate-determining step (RDS) of Fe<sub>0.2</sub>NiCo<sub>1.8</sub>Se<sub>4</sub> is hydrogen adsorption or discharge reaction. XPS result shows that the formation of higher oxidized states such as Fe<sup>3+</sup> (d<sup>5</sup> system) and Co<sup>3+</sup> (d<sup>6</sup> system) can attract OH<sup>-</sup> ion due to more unoccupied d-orbital and electropositive character. Additionally, the electron transfer kinetics increased after doping, which induced the hydrogen adsorption and desorption rate due to the rough outer surface and reduced diameter of the nanorod array. It is essential to observe that due to the synergistic and morphology effect of the doped sample, the rate of Volmer and Heyrovsky step subsequently improves the HER kinetics. The effect of metal ions during HER is further verified by the thiocyanate poisoning effect, which can selectively poison the active metal sites. Accordingly, 10 mM KSCN is introduced during the HER along with 1.0 M KOH solution. The electrocatalytic activity is tested using a Fe<sub>0.2</sub>NiCo<sub>1.8</sub>Se<sub>4</sub> catalyst. It is observed from Figure 7.13a (LSV) that the HER activity of the Fe<sub>0.2</sub>NiCo<sub>1.8</sub>Se<sub>4</sub> sample remarkably decreases in the presence of KSCN. Figure 7.13b also shows the decrease in current density from ~165 mA/cm<sup>2</sup> to ~16 mA/cm<sup>2</sup>, which is almost 90% activity loss during the HER in the presence of KSCN. So, SCN<sup>-</sup> ion poisons the metal sites by forming complexes,

drastically diminishing the HER activity.<sup>52</sup> Therefore, the role of metals in the  $\text{Fe}_{0.2}\text{NiCo}_{1.8}\text{Se}_4$  catalyst is vital and plays significant activity in enhancing HER efficiency.

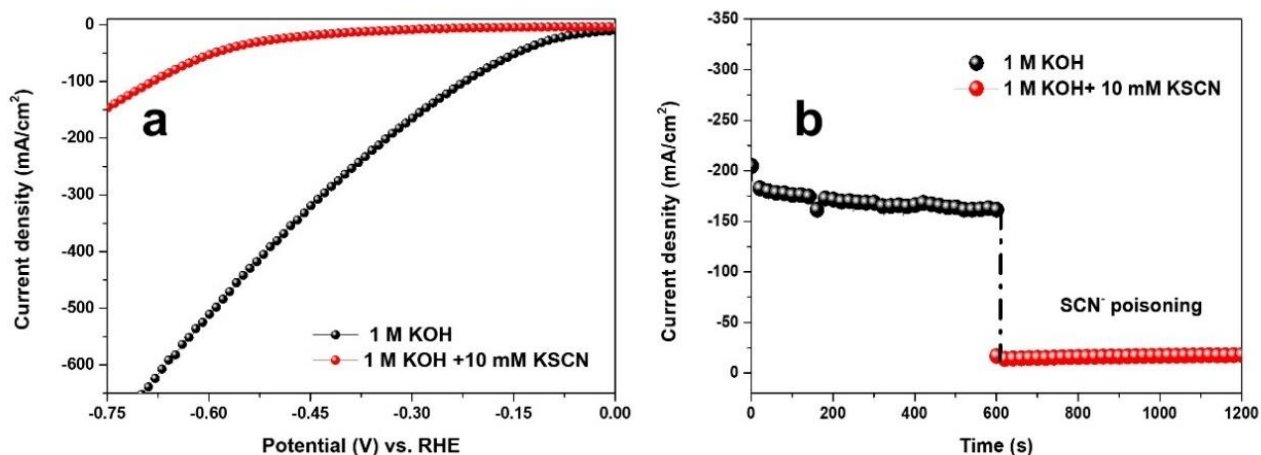


**Figure 7.13:** Effect of KSCN on the HER current of  $\text{Fe}_{0.2}\text{NiCo}_{1.8}\text{Se}_4$  sample (a) LSV (b) chronoamperometric data.

Electrochemical active surface area (ECSA) is an essential parameter of electrocatalysts in water-splitting reactions. To calculate ECSA for  $\text{NiCo}_2\text{Se}_4$  and  $\text{Fe}_{0.2}\text{NiCo}_{1.8}\text{Se}_4$ , cyclic voltammetry is executed in a non-faradaic region of 0.425 to 0.625 V vs. RHE and given in Figures 7.14a and 7.14b. The double-layer capacitance ( $C_{dl}$ ) value is determined at a fixed potential of 0.525 V vs. RHE by calculating the slope between the scan rate and current (Figure 7.14c). The ECSA values are calculated by dividing  $C_{dl}$  with specific capacitance ( $C_s$ ). Bare  $\text{NiCo}_2\text{Se}_4$  has an ECSA value of  $6.3 \text{ cm}^2$ ; after Fe doping, the ECSA value increases to  $33.2 \text{ cm}^2$ . The roughness factor ( $R_f$ ) is also calculated from ECSA. The  $R_f$  values are 39.37 and 207.5 for bare  $\text{NiCo}_2\text{Se}_4$  and  $\text{Fe}_{0.2}\text{NiCo}_{1.8}\text{Se}_4$ , respectively. Thus, after Fe doping, the ECSA and  $R_f$  increase 5.26 times in  $\text{Fe}_{0.2}\text{NiCo}_{1.8}\text{Se}_4$  which improves the active sites and facilitates HER. In the case of HER, the exchange current density values for  $\text{NiCo}_2\text{Se}_4$  and  $\text{Fe}_{0.2}\text{NiCo}_{1.8}\text{Se}_4$  are  $0.00169 \text{ mA/cm}^2$  and  $0.0147 \text{ mA/cm}^2$  respectively. From these values, we have calculated rate constant values ( $k$ ) for  $\text{NiCo}_2\text{Se}_4$  and  $\text{Fe}_{0.2}\text{NiCo}_{1.8}\text{Se}_4$  are  $8.79 \times 10^{-9} \text{ cm/S}$  and  $8.1 \times 10^{-8} \text{ cm/S}$ , respectively, which proves to be better for HER kinetics.

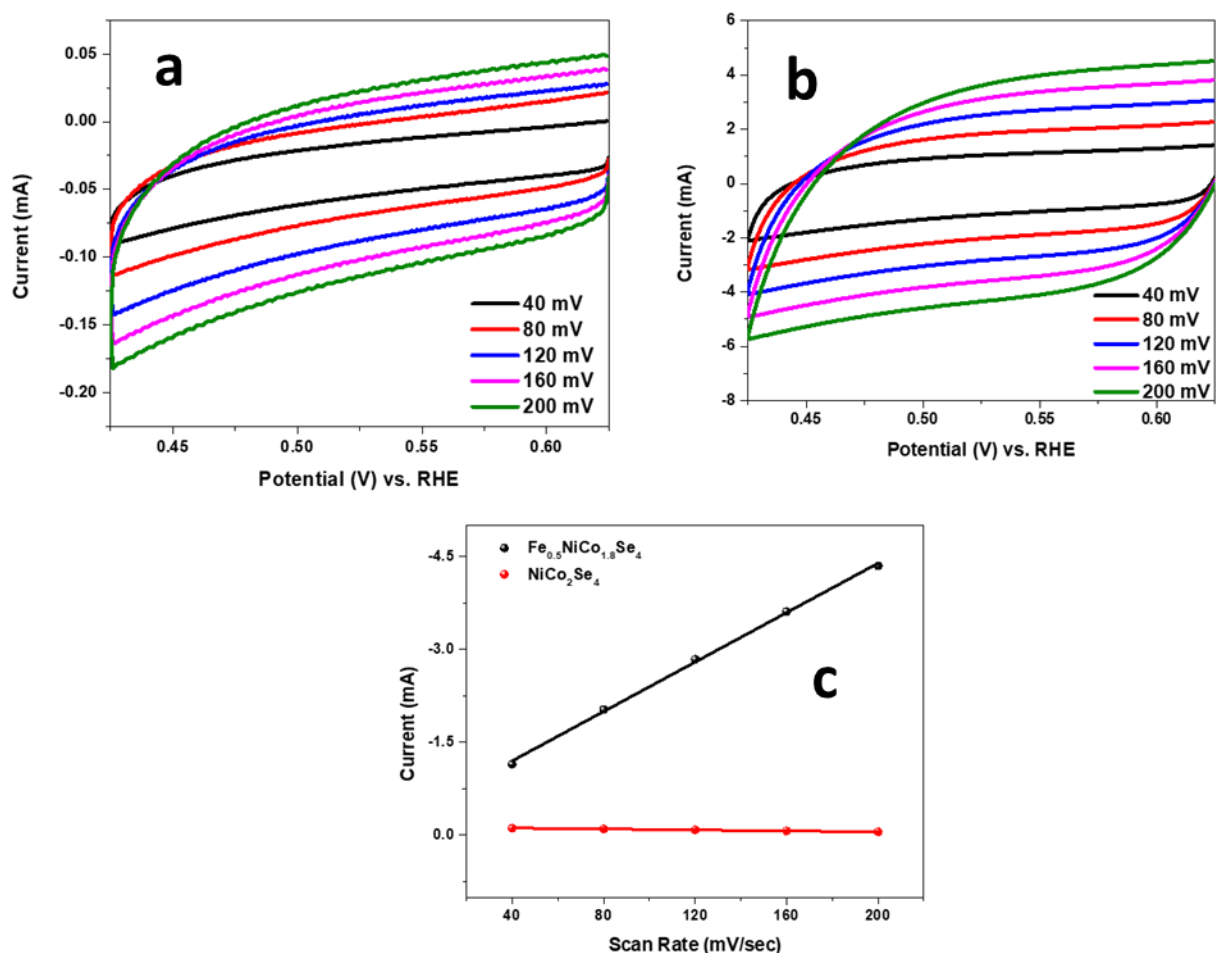


**Figure 7.14:** Cyclic voltammetry curves of  $\text{NiCo}_2\text{Se}_4$  and  $\text{Fe}_{0.2}\text{NiCo}_{1.8}\text{Se}_4$  at different scan rates (a) and (b) capacitive current at 0.525 (V vs. RHE) as a function of scan rate for ECSA calculation (c).

Electrocatalytic stability is an essential parameter for any electrocatalyst. Repetitive LSV and chronoamperometric analysis are done in 1.0 M KOH. Figure 7.15a shows 1000 continuous LSV cycles of  $\text{Fe}_{0.2}\text{NiCo}_{1.8}\text{Se}_4$ ; after 1000 cycles, there is no significant change in the onset potential and current density for HER in an alkaline medium. The long-term stability is checked at a fixed potential of -0.358 V vs. RHE to obtain a 220 mA/cm<sup>2</sup> current density for 48 hours (Figure 7.15b). There is no change in current density up to 48 hours for hydrogen evolution, which proves  $\text{Fe}_{0.2}\text{NiCo}_{1.8}\text{Se}_4$  is a robust and durable electrocatalyst for HER.

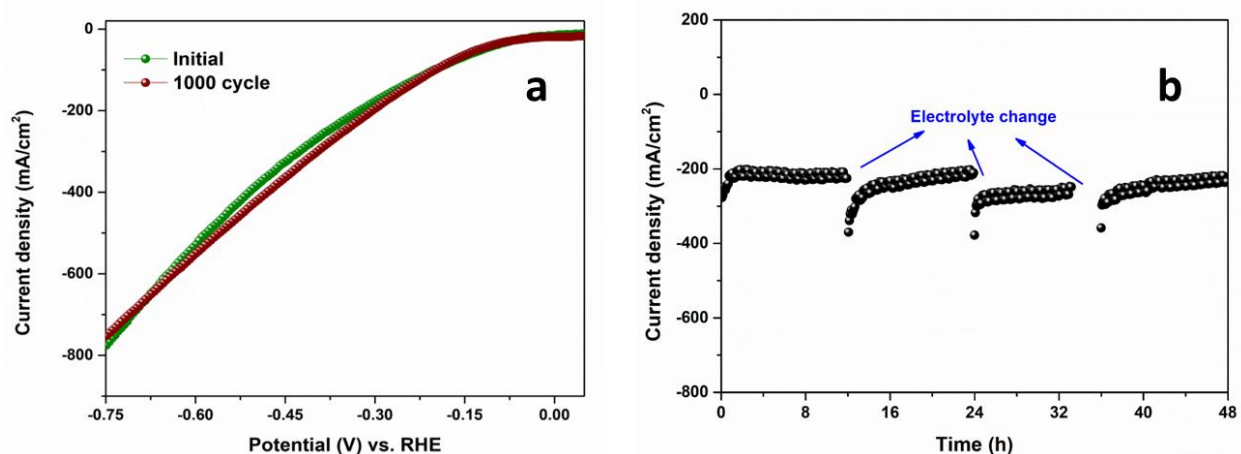


**Figure 7.15:** (a) Polarization curve of  $\text{Fe}_{0.2}\text{NiCo}_{1.8}\text{Se}_4$  initial and after 1000 cycles (b) 48 hours chronoamperometric data of  $\text{Fe}_{0.2}\text{NiCo}_{1.8}\text{Se}_4$  for HER.

The phase purity of the catalyst is checked through post-XRD analysis after the HER and found to have a very stable nature of  $\text{Fe}_{0.2}\text{NiCo}_{1.8}\text{Se}_4$ . There is no change in the peak position and crystal planes after the HER activity of the  $\text{Fe}_{0.2}\text{NiCo}_{1.8}\text{Se}_4$  sample (Figure 7.16a). FESEM and XPS analysis of the  $\text{Fe}_{0.2}\text{NiCo}_{1.8}\text{Se}_4$  sample after 48 hours of HER are also performed. FESEM (Figure 7.16b) result shows that the nanorod morphology of the  $\text{Fe}_{0.2}\text{NiCo}_{1.8}\text{Se}_4$  catalyst is well maintained. The nanorod is grown by combining nanosheets, which can be visualized in Figure 7.16b. Furthermore, XPS results (Figure 7.17) show similar binding energy values of all the ions.

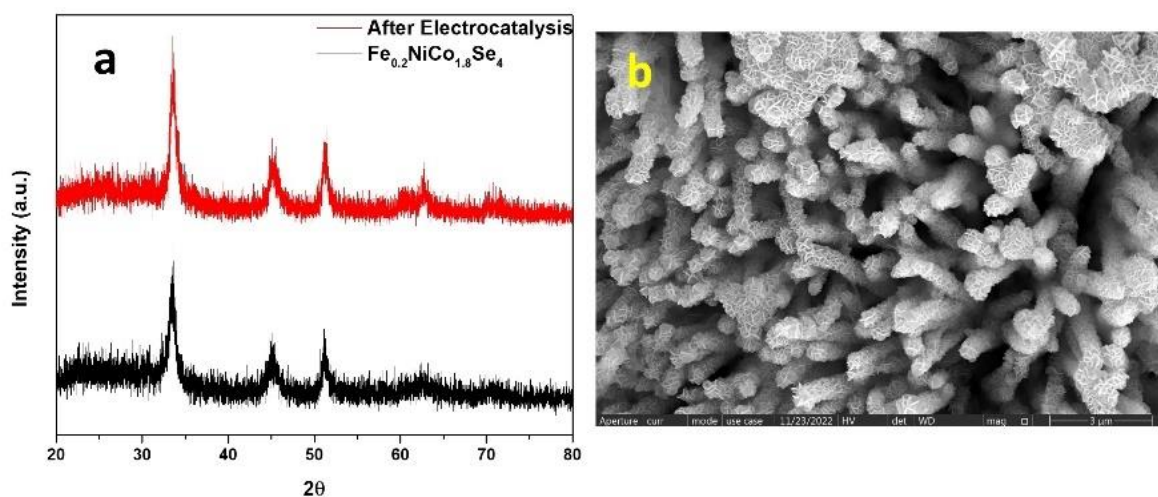


**Figure 7.16:** (a) PXRD pattern (b) FESEM of  $\text{Fe}_{0.2}\text{NiCo}_{1.8}\text{Se}_4$  sample after HER analysis.

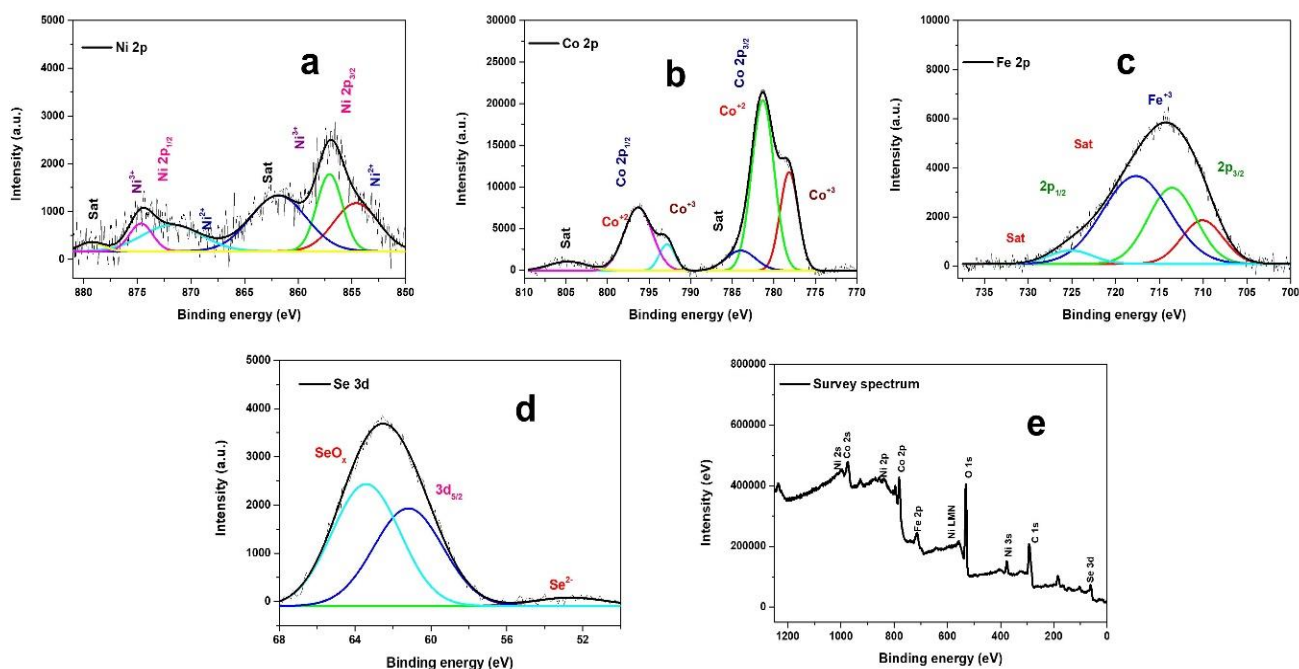


**Figure 7.17.** Post HER XPS analysis of  $\text{Fe}_{0.2}\text{NiCo}_{1.8}\text{Se}_4$  (a) deconvoluted spectra of Ni 2p, (b) deconvoluted spectra of Co 2p, and (c) deconvoluted spectra of Fe 2p (d) deconvoluted spectra of Se 3d, and (e) survey spectrum.

After checking HER activity, all the developed electrocatalysts are applied for oxygen evolution reaction (OER) in an alkaline medium. The comparative LSV plot of developed  $\text{NiCo}_2\text{Se}_4$ ,  $\text{Fe}_{0.1}\text{NiCo}_{1.9}\text{Se}_4$ ,  $\text{Fe}_{0.2}\text{NiCo}_{1.8}\text{Se}_4$ ,  $\text{Fe}_{0.4}\text{NiCo}_{1.6}\text{Se}_4$ , blank CC, and commercial  $\text{RuO}_2$  is given in Figure 7.18a. Blank CC shows significantly less activity for OER in the applied potential window. The OER performance of the  $\text{Fe}_{0.2}\text{NiCo}_{1.8}\text{Se}_4$  catalyst represents minimum onset potential and maximum current density compared with other doped samples. The onset potential was chosen to avoid the Ni and Co redox region at a current density of  $100 \text{ mA/cm}^2$ . Bare  $\text{NiCo}_2\text{Se}_4$  has the onset potential value of  $1.728 \text{ V vs. RHE}$ ; after  $\text{Fe}^{3+}$  doping, the value of onset potential noticeably shifts to the cathodic side.  $\text{Fe}_{0.1}\text{NiCo}_{1.9}\text{Se}_4$ ,  $\text{Fe}_{0.2}\text{NiCo}_{1.8}\text{Se}_4$ , and  $\text{Fe}_{0.4}\text{NiCo}_{1.6}\text{Se}_4$  have onset potential values of  $1.699$ ,  $1.656$ , and  $1.672 \text{ V vs. RHE}$ , respectively, to generate  $100 \text{ mA/cm}^2$  current density (Figure 7.18a).  $\text{Fe}_{0.2}\text{NiCo}_{1.8}\text{Se}_4$  exhibit the best OER activity with  $72 \text{ mV}$  cathodic shift in the onset potential. It requires only  $426 \text{ mV vs. RHE}$  overpotential to obtain a  $100 \text{ mA/cm}^2$  current density. Commercial  $\text{RuO}_2$  has less OER activity than Fe-doped  $\text{NiCo}_2\text{Se}_4$  catalyst, and it requires  $1.743 \text{ V vs. RHE}$ . The higher electrocatalytic OER performance is compared in the histogram plot in Figure 7.18b at  $1.65 \text{ V vs. RHE}$ ,  $\text{Fe}_{0.2}\text{NiCo}_{1.8}\text{Se}_4$  shows



maximum current density. The current response of  $\text{Fe}_{0.2}\text{NiCo}_{1.8}\text{Se}_4$  is 3.4 and 1.4 folds better than bare  $\text{NiCo}_2\text{Se}_4$  and commercial  $\text{RuO}_2$ , respectively. Fe doping in  $\text{NiCo}_2\text{Se}_4$  enhances the OER activity, the varying oxidation state in Ni, Co, and Fe might lower the onset of water oxidation and enhances the conductivity in the system. The vertically grown nanorod array, the rough surface of the nanorod, and the smaller diameter after doping in  $\text{Fe}_{0.2}\text{NiCo}_{1.8}\text{Se}_4$  could be beneficial for electrolyte penetration and transportation during the water-splitting reaction.

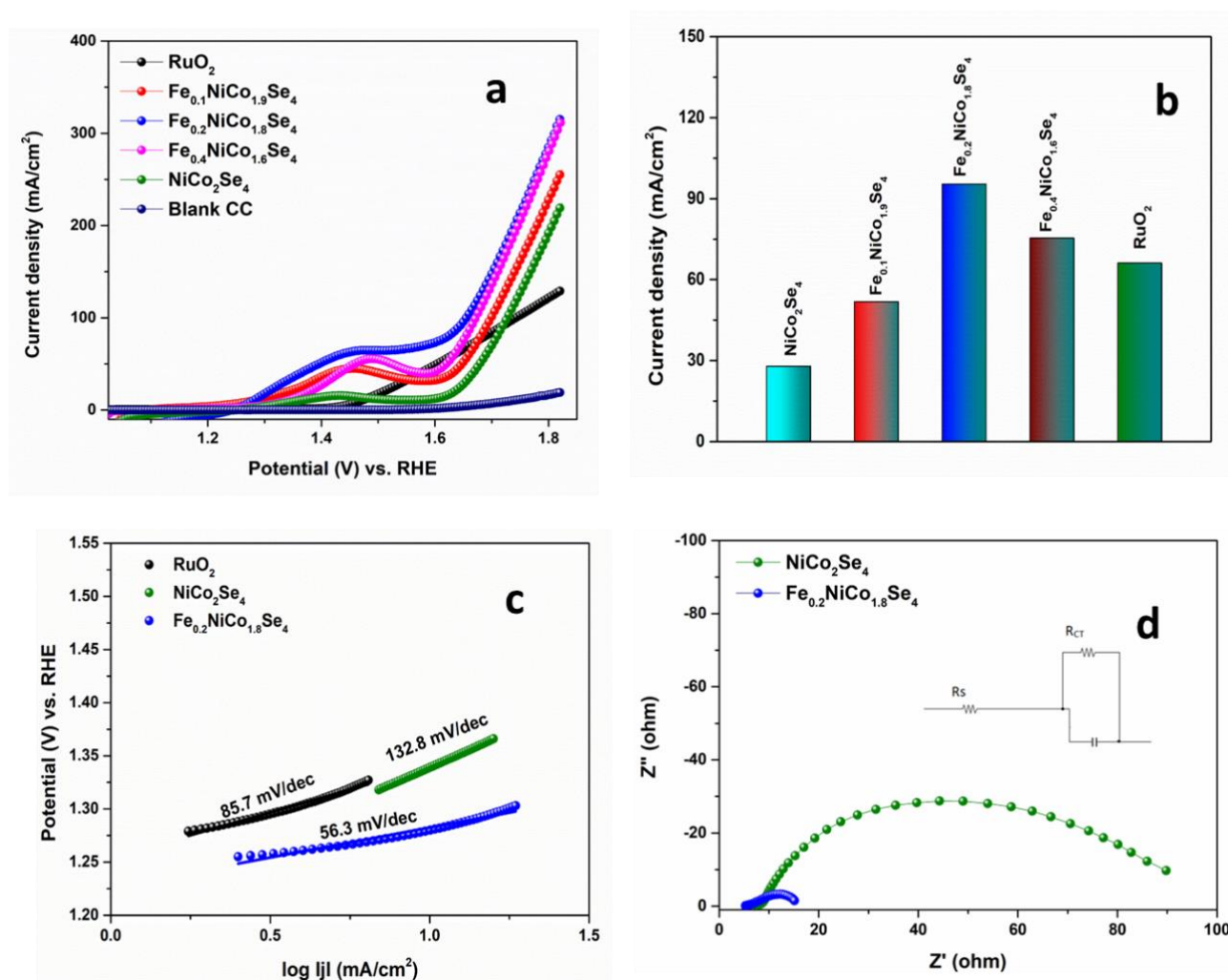


**Figure 7.18:** (a) Linear sweep voltammetry of blank CC,  $\text{NiCo}_2\text{Se}_4$ ,  $\text{Fe}_{0.1}\text{NiCo}_{1.9}\text{Se}_4$ ,  $\text{Fe}_{0.2}\text{NiCo}_{1.8}\text{Se}_4$ ,  $\text{Fe}_{0.4}\text{NiCo}_{1.6}\text{Se}_4$ , and  $\text{RuO}_2$  for OER, (b) histogram plot at 1.65 V vs. RHE, (c) Tafel slope, and (d) impedance of  $\text{NiCo}_2\text{Se}_4$  and  $\text{Fe}_{0.2}\text{NiCo}_{1.8}\text{Se}_4$ . The inset of Figure 7.18d shows an equivalent circuit for impedance.



Further, to judge the better OER performance of  $\text{Fe}_{0.2}\text{NiCo}_{1.8}\text{Se}_4$  in an alkaline medium, mass activity is checked at 1.65 V vs. RHE for all the developed electrocatalysts and given in Table 7.4.  $\text{Fe}_{0.2}\text{NiCo}_{1.8}\text{Se}_4$  has the highest value of 22.94 A/g compared to bare  $\text{NiCo}_2\text{Se}_4$ ,  $\text{Fe}_{0.1}\text{NiCo}_{1.9}\text{Se}_4$ ,  $\text{Fe}_{0.4}\text{NiCo}_{1.6}\text{Se}_4$ , and commercial  $\text{RuO}_2$ . The better electrocatalytic performance can be proved with a more charge transportation rate, which can be determined through the Tafel slope value (Figure 7.18c). The observed lower value of Tafel slope indicates excellent performance for OER in alkaline medium,  $\text{Fe}_{0.2}\text{NiCo}_{1.8}\text{Se}_4$  has 56.3 mV/dec Tafel slope value (Table 7.4), which is lower than bare  $\text{NiCo}_2\text{Se}_4$  and commercial  $\text{RuO}_2$ . Commercial  $\text{RuO}_2$  shows an 85.7 mV/dec Tafel slope value.<sup>53</sup> In the case of OER, the Tafel slope value of Fe doped NiCo-urea complex is 143.1 mV/dec, which shows less activity. At the respective onset potential of  $\text{NiCo}_2\text{Se}_4$  and  $\text{Fe}_{0.2}\text{NiCo}_{1.8}\text{Se}_4$ , the impedance study is executed in 1.0 M KOH (Figure 7.18d). In Figure 7.18d,  $\text{Fe}_{0.2}\text{NiCo}_{1.8}\text{Se}_4$  has a smaller diameter semicircle than  $\text{NiCo}_2\text{Se}_4$ , which means it is more conductive and electrocatalytically active than the bare sample. The values for  $R_S$  and  $R_{CT}$  are given in Table 7.4. The  $R_{CT}$  value of  $\text{Fe}_{0.2}\text{NiCo}_{1.8}\text{Se}_4$  is 7.32  $\Omega$ , which is much smaller than the  $R_{CT}$  value of bare  $\text{NiCo}_2\text{Se}_4$  (65.05  $\Omega$ ). The result confirms that Fe doping increases the conductivity of  $\text{NiCo}_2\text{Se}_4$ .

**Table 7.4:** All the Electrochemical Parameters for OER Using  $\text{NiCo}_2\text{Se}_4$ ,  $\text{Fe}_{0.1}\text{NiCo}_{1.9}\text{Se}_4$ ,  $\text{Fe}_{0.2}\text{NiCo}_{1.8}\text{Se}_4$ ,  $\text{Fe}_{0.4}\text{NiCo}_{1.6}\text{Se}_4$ , and  $\text{RuO}_2$  Electrocatalysts.

Electrodes	Potential (V) vs. RHE ) required to generate 100 mA/cm <sup>2</sup>	Mass Activity (A/g) at 1.65 V vs. RHE	Tafel Slope (mV/decade)	$R_S$ ( $\Omega$ )	$R_{CT}$ ( $\Omega$ )
$\text{NiCo}_2\text{Se}_4$	1.728	6.72	132.8	8.2	65.05
$\text{Fe}_{0.1}\text{NiCo}_{1.9}\text{Se}_4$	1.699	12.47	-	-	-
$\text{Fe}_{0.2}\text{NiCo}_{1.8}\text{Se}_4$	1.656	22.94	56.3	5.96	7.32
$\text{Fe}_{0.4}\text{NiCo}_{1.6}\text{Se}_4$	1.672	18.14	-	-	-
$\text{RuO}_2$	1.743	16.02	85.7	-	-

The developed  $\text{Fe}_{0.2}\text{NiCo}_{1.8}\text{Se}_4$  electrocatalyst is checked for 1000 consecutive LSV cycles, and there is an unaltered change in the current density and onset potential (Figure 7.19a).  $\text{Fe}_{0.2}\text{NiCo}_{1.8}\text{Se}_4$  can generate an alternate current density of 110 mA/cm<sup>2</sup> for up to 48 continuous hours

(Figure 7.19b). To further confirm the robustness and stability after the OER study, the electrocatalyst is checked with FESEM and XPS analyses. Fe-doped  $\text{NiCo}_2\text{Se}_4$  shows a rough surface of the nanorod array (Figure 7.20a) after electrocatalysis. All the elements (Fe, Ni, Co, Se, and C) present uniformly (Figure 7.20b), confirmed by EDS analysis.

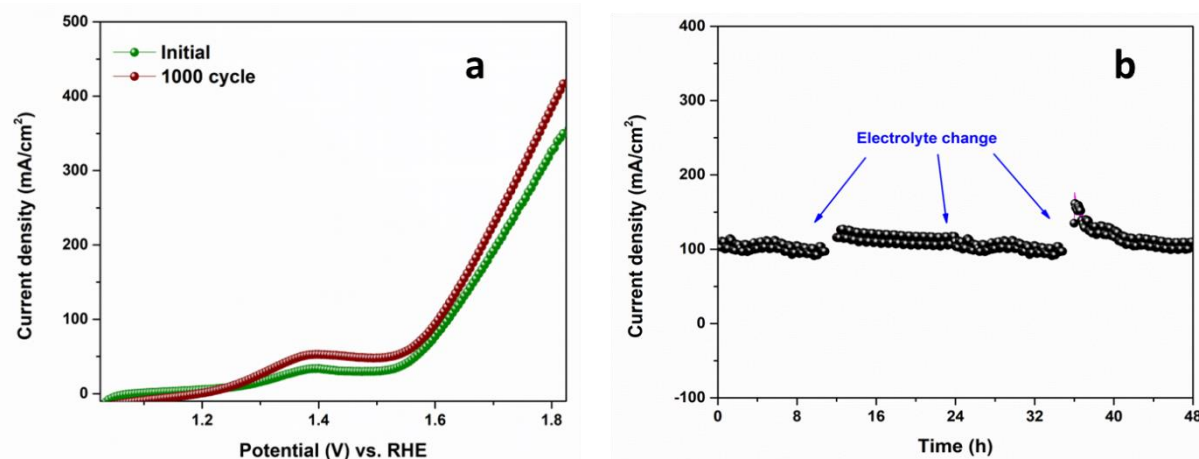


**Figure 7.19:** (a) Polarization curve of  $\text{Fe}_{0.2}\text{NiCo}_{1.8}\text{Se}_4$  initial and after 1000 cycles (b) 48 hours chronoamperometric data of  $\text{Fe}_{0.2}\text{NiCo}_{1.8}\text{Se}_4$  for OER.

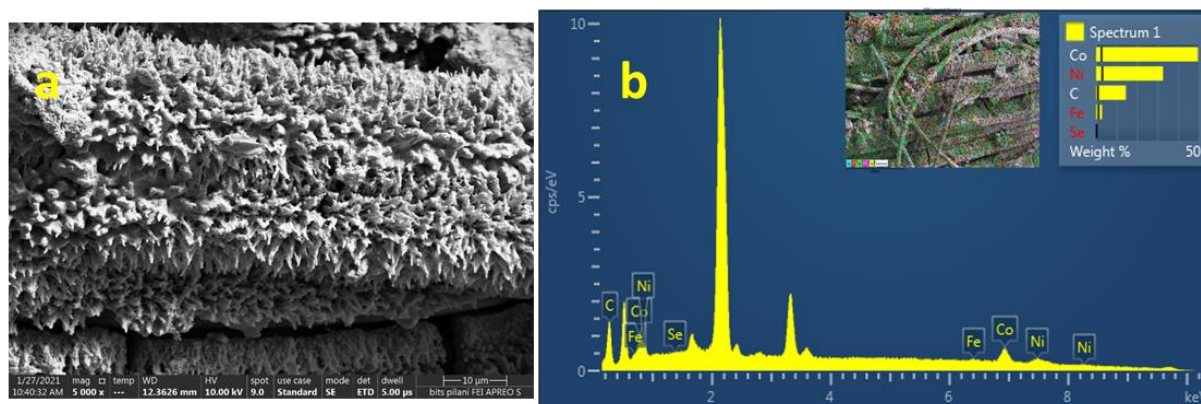


**Figure 7.20:** (a) FESEM image and (b) EDS mapping of  $\text{Fe}_{0.2}\text{NiCo}_{1.8}\text{Se}_4$  after electrocatalysis.

Furthermore, XPS analysis established the presence of  $\text{Ni}^{2+}$ ,  $\text{Ni}^{3+}$ ,  $\text{Co}^{2+}$ ,  $\text{Co}^{3+}$ ,  $\text{Fe}^{3+}$ , and  $\text{Se}^{2-}$  ions in the  $\text{Fe}_{0.2}\text{NiCo}_{1.8}\text{Se}_4$  sample (Figure 7.21). The post-XPS analysis suggests no change in the valence states of the  $\text{Fe}_{0.2}\text{NiCo}_{1.8}\text{Se}_4$  sample. Deconvoluted spectra of Ni 2p show the binding energy values of 855.7, 857.5, 871.08, and 874.5 eV. The first two doublet exhibit Ni 2p<sub>3/2</sub> and the other two represent Ni 2p<sub>1/2</sub>, respectively. The peaks at 861.6 and 880.1 eV are due to Ni 2p satellite. The Co

2p spectra represent peaks at 780.4 and 781.8 eV, corresponding to Co 2p<sub>3/2</sub>, and other peaks at 795.3 and 797.01 eV represent Co 2p<sub>1/2</sub>. The satellite peaks are present at 786.8 and 803.9 eV for Co 2p. The binding energy value at 710.7 eV represents the presence of Fe 2p<sub>3/2</sub> and the satellite peak at 713.6 eV. The binding energy at 718.7 eV corresponds to Fe 2p<sub>1/2</sub>, and the satellite peak at 724.1 eV. The Se<sup>2-</sup> ion binding energy values appear at 54.2 and 55.1 eV for Se 3d spectra. Therefore, the Fe<sub>0.2</sub>NiCo<sub>1.8</sub>Se<sub>4</sub> sample is robust and stable for OER in an alkaline medium. However, the intensity of Se<sup>2-</sup> ion decreases after the electrocatalytic reaction, which may be due to the formation of NiOOH and CoOOH during the electrocatalytic reaction, active species for water-splitting reaction. This result corroborates with the enhanced oxide peak (O 2p) in XPS analysis. The formation of NiOOH and CoOOH during the electrocatalytic reaction is reported in the literature.<sup>54-56</sup>

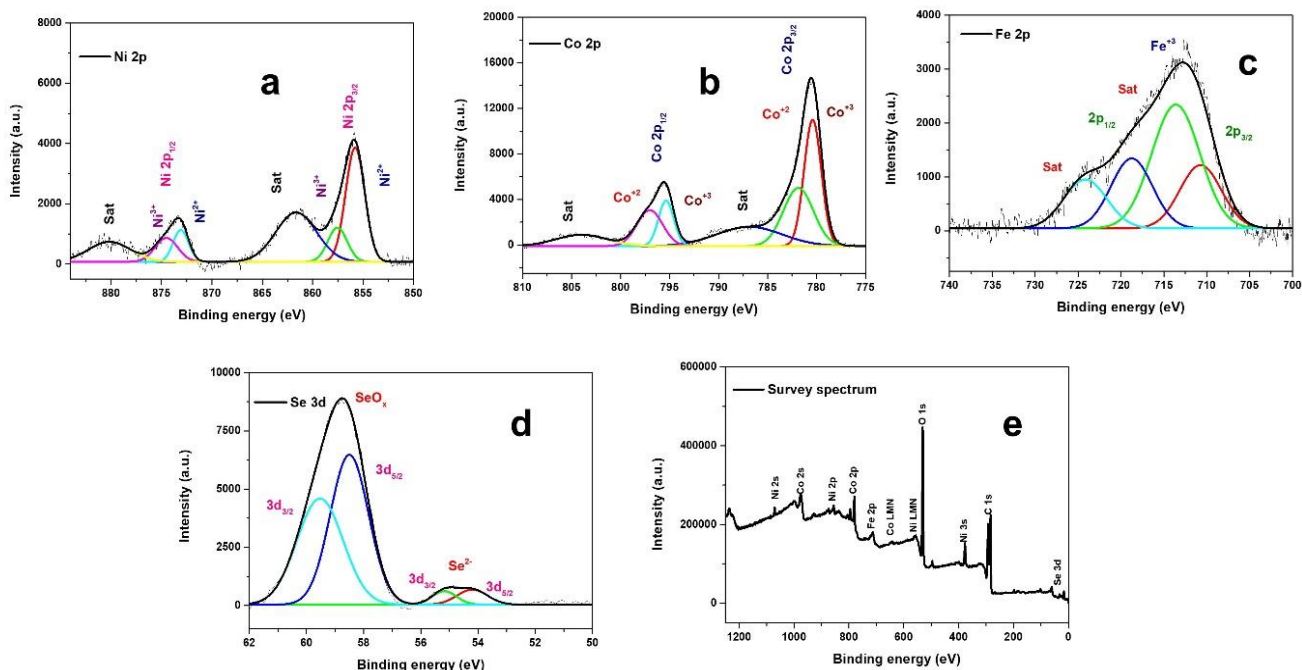


**Figure 7.21:** XPS of Fe<sub>0.2</sub>NiCo<sub>1.8</sub>Se<sub>4</sub> after OER electrocatalysis (a) deconvoluted spectra of Ni 2p (b) deconvoluted spectra of Co 2p (c) deconvoluted spectra of Fe 2p (d) deconvoluted spectra of Se 3d deconvoluted spectra, and (e) survey spectrum.

The better electrocatalytic OER results can be proved with the CV analysis, and Figure 7.22 represents the CV of bare and doped NiCo<sub>2</sub>Se<sub>4</sub>. The CV is recorded with the applied voltage of 1.025 to 1.65 V vs. RHE. The CV of NiCo<sub>2</sub>Se<sub>4</sub> and Fe<sub>0.2</sub>NiCo<sub>1.8</sub>Se<sub>4</sub> shows reversible peaks for the Ni and Co

redox processes. The broad oxidation peak between 1.2 to 1.6 V vs. RHE is responsible for  $\text{Co}^{2+}/\text{Co}^{3+}$ ,  $\text{Ni}^{2+}/\text{Ni}^{3+}$ , and  $\text{Co}^{3+}/\text{Co}^{4+}$  redox couples in the system. It is not easy to get separate oxidation peaks of Ni and Co due to similar redox behavior in the system. Among the broad peak,  $\text{Co}^{2+}/\text{Co}^{3+}$  and  $\text{Co}^{3+}/\text{Co}^{4+}$  redox couple appear at 1.2 and 1.54 V vs. RHE, respectively. The peak at 1.45 V vs. RHE and the reversible peak at 1.29 V vs. RHE in bare  $\text{NiCo}_2\text{Se}_4$  is due to  $\text{Ni}^{2+}/\text{Ni}^{3+}$ . After doping with Fe, the oxidation peak of  $\text{Ni}^{2+}/\text{Ni}^{3+}$  shifted to 1.50 V vs. RHE, and the reduction peak appeared at 1.28 V vs. RHE. This positive shift in the value of the oxidation peak and a negative shift in the reduction peak is due to doping with  $\text{Fe}^{3+}$ , which behaves as a Lewis acid, well corroborated with the XPS analysis result. During OER,  $\text{H}_2\text{O}$  and  $\text{OH}^-$  are adsorbed on the catalyst surface, which results in the evolution of  $\text{O}_2$  by following a cyclic process and regenerating the active sites.  $\text{Fe}_{0.2}\text{NiCo}_{1.8}\text{Se}_4$  consists of metal ions such as  $\text{Fe}^{3+}$ ,  $\text{Ni}^{2+}$ ,  $\text{Ni}^{3+}$ ,  $\text{Co}^{2+}$ , and  $\text{Co}^{3+}$ , which are considered active sites for OER. During LSV analysis, the broad electrooxidation peak between 1.2 to 1.6 V vs. RHE (Figure 7.18a) corresponds to the generation of  $\text{Co}^{3+}$ ,  $\text{Ni}^{3+}$ , and  $\text{Co}^{4+}$  species. Furthermore, the Lewis acid behavior of the  $\text{Fe}^{3+}$  ion pulls the electrons from  $\text{Co}^{2+}$  and generates more  $\text{Co}^{3+}$  species. Therefore,  $\text{NiCoO}/\text{NiCo-OOH}$  heterostructure formation is more in the doped sample, which is beneficial for OER.

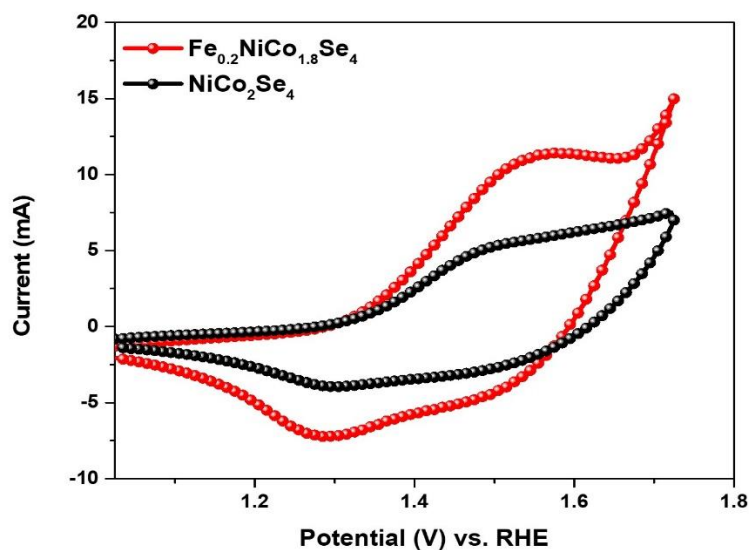


**Figure 7.22:** CV analysis of  $\text{NiCo}_2\text{Se}_4$  and  $\text{Fe}_{0.2}\text{NiCo}_{1.8}\text{Se}_4$  in a particular potential window.

In the case of OER, the exchange current density values for  $\text{NiCo}_2\text{Se}_4$  and  $\text{Fe}_{0.2}\text{NiCo}_{1.8}\text{Se}_4$  are  $0.592 \text{ mA/cm}^2$  and  $0.663 \text{ mA/cm}^2$ , respectively. From these values, we have calculated rate constant values ( $k$ ) for  $\text{NiCo}_2\text{Se}_4$  and  $\text{Fe}_{0.2}\text{NiCo}_{1.8}\text{Se}_4$  are  $1.53 \times 10^{-6} \text{ cm/S}$  and  $1.72 \times 10^{-6} \text{ cm/S}$ ,

respectively. From the above values, it is clearly proved that after doping with Fe in  $\text{NiCo}_2\text{Se}_4$ , the rate constant values increase, which proves the improved OER kinetics. The importance of metal ions during OER activity of  $\text{Fe}_{0.2}\text{NiCo}_{1.8}\text{Se}_4$  catalyst is also evaluated with  $\text{SCN}^-$  poisoning effect. The polarization curve (Figure 7.23a) confirms the decrease in OER activity after adding 10 mM KSCN to the electrolyte. Similar phenomena were also observed from the measurement of OER current density (Figure 7.23b) of the  $\text{Fe}_{0.2}\text{NiCo}_{1.8}\text{Se}_4$  sample, which reduced from  $\sim 220 \text{ mA/cm}^2$  to  $\sim 62 \text{ mA/cm}^2$ , nearly 71% OER activity loss after  $\text{SCN}^-$  poisoning. Therefore, the huge reduction of current density is due to the poison of metal ions in the presence of  $\text{SCN}^-$  ion, which confirms the role of active metal sites in the doped  $\text{NiCo}_2\text{Se}_4$  during OER. Janani and co-workers reported<sup>15</sup> the formation of NiCoO and NiCo-OOH heterostructure as active sites during OER.

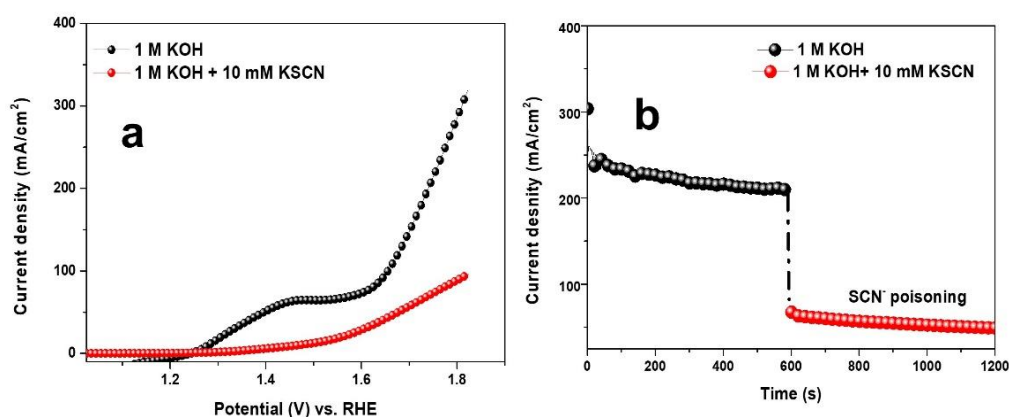


**Figure 7.23:** Effect of KSCN on the OER current of  $\text{Fe}_{0.2}\text{NiCo}_{1.8}\text{Se}_4$  sample (a) LSV and (b) chronoamperometric data.

The aforementioned findings show that Fe-doped  $\text{NiCo}_2\text{Se}_4$  is a good candidate for the water-splitting process in an alkaline medium. The optimization of the dopant concentration was completed; amongst all,  $\text{Fe}_{0.2}\text{NiCo}_{1.8}\text{Se}_4$  shows superior electrocatalytic activity both in HER and OER. The results can be summoned as follows. First, the XPS result proves that Fe is behaving as a Lewis acid which can significantly affect the electronic environment of  $\text{NiCo}_2\text{Se}_4$ . Second, Fe acts as a growth regulator for the rougher nanorod surface in  $\text{NiCo}_2\text{Se}_4$ , which is proven by FESEM and TEM results. The sharpening and reduced diameter of the nanorod array of  $\text{Fe}_{0.2}\text{NiCo}_{1.8}\text{Se}_4$  are helpful for electrolyte contact. Third, the lattice distortion can be seen after Fe doping in HRTEM analysis. Lattice distortion can increase the active site and electrocatalytic activity. Fourth, Fe doping creates lattice expansion, as evidenced in PXRD and HRTEM analysis. Fifth, the synergy of all the atoms (Fe, Ni, and Co) in  $\text{Fe}_{0.2}\text{NiCo}_{1.8}\text{Se}_4$



helps increase the electrochemically active sites. Sixth, DFT studies explain that changes in band structure after doping in NiCo<sub>2</sub>Se<sub>4</sub> make the metallic nature of Fe<sub>0.2</sub>NiCo<sub>1.8</sub>Se<sub>4</sub>, which helps in the bifunctional activity for water splitting. A detailed comparison of Fe<sub>0.2</sub>NiCo<sub>1.8</sub>Se<sub>4</sub> with the previously reported literature is given in Table 7.5.

**Table 7.5:** A comparative electrochemical study of all the electrochemical parameters with the electrocatalyst.

S.N.	Electrocatalyst	Electrode reaction	Electrolyte	Potential (mV vs. RHE) at 10 mA/cm <sup>2</sup> Current density	Tafel slope (mV/dec)	Substrate	Ref.
1.	Fe doped NiCo-phosphide	OER and HER	1 M KOH	269 and 122.5 mV	54.3 and 72.01	Nickel foam	12
2.	(Ni <sub>0.25</sub> Fe <sub>0.68</sub> Co <sub>0.07</sub> ) <sub>3</sub> Se <sub>4</sub>	OER	0.3 M KOH	230 mV	41.7	Au coated glass	23
3.	NiCo <sub>2</sub> Se <sub>4</sub>	OER	1 M KOH	1.68 V	53	Rotating disk electrode	20
4.	NiCo <sub>2</sub> Se <sub>4</sub> /NiCo <sub>2</sub> S <sub>4</sub>	OER and HER	1 M KOH	248 and 180 mV	98.5 and 107.4	Glassy carbon electrode	39
5.	Fe <sub>0.2</sub> NiCo <sub>1.8</sub> Se <sub>4</sub>	OER & HER	1 M KOH	1.656 V @100 mA/cm <sup>2</sup> & 148 mV @50 mA/cm <sup>2</sup>	56.3 & 85.7	Carbon cloth	This work

### 7.3.4 Two-electrode setup for overall water-splitting

Fe-doped NiCo<sub>2</sub>Se<sub>4</sub> electrocatalyst exhibits efficient activity for HER and OER in an alkaline medium. The bifunctional activity of Fe<sub>0.2</sub>NiCo<sub>1.8</sub>Se<sub>4</sub> for both HER and OER motivated us to construct a cell for overall water splitting. Figure 7.24a shows the LSV curve for Fe<sub>0.2</sub>NiCo<sub>1.8</sub>Se<sub>4</sub> || Fe<sub>0.2</sub>NiCo<sub>1.8</sub>Se<sub>4</sub> as cathode and anode in 1.0 M KOH solution. It requires 1.51 V to generate a 10 mA/cm<sup>2</sup> current density. The same cell, Fe<sub>0.2</sub>NiCo<sub>1.8</sub>Se<sub>4</sub> || Fe<sub>0.2</sub>NiCo<sub>1.8</sub>Se<sub>4</sub>, requires 1.93 and 2.07 V to generate 50 and 100 mA/cm<sup>2</sup> current density, respectively. The long-term stability of the Fe<sub>0.2</sub>NiCo<sub>1.8</sub>Se<sub>4</sub> || Fe<sub>0.2</sub>NiCo<sub>1.8</sub>Se<sub>4</sub> cell is checked for 24 hours at the voltage of 1.75 V, which exhibits unaltered current density (Figure 7.24b). To know the performance of Fe<sub>0.2</sub>NiCo<sub>1.8</sub>Se<sub>4</sub> || Fe<sub>0.2</sub>NiCo<sub>1.8</sub>Se<sub>4</sub> cell during electrocatalysis. Faradaic efficiency is calculated at 2 V, and the plot is given in Figure 7.24c. The experimental and theoretical amounts of H<sub>2</sub> and O<sub>2</sub> gases are calculated, which exhibits that the generated amount for H<sub>2</sub>:O<sub>2</sub> is nearly 2:1 (Figure 7.24c). The cell shows calculated Faradaic efficiency for OER and HER is 89.9 % and 91.3 %, respectively.

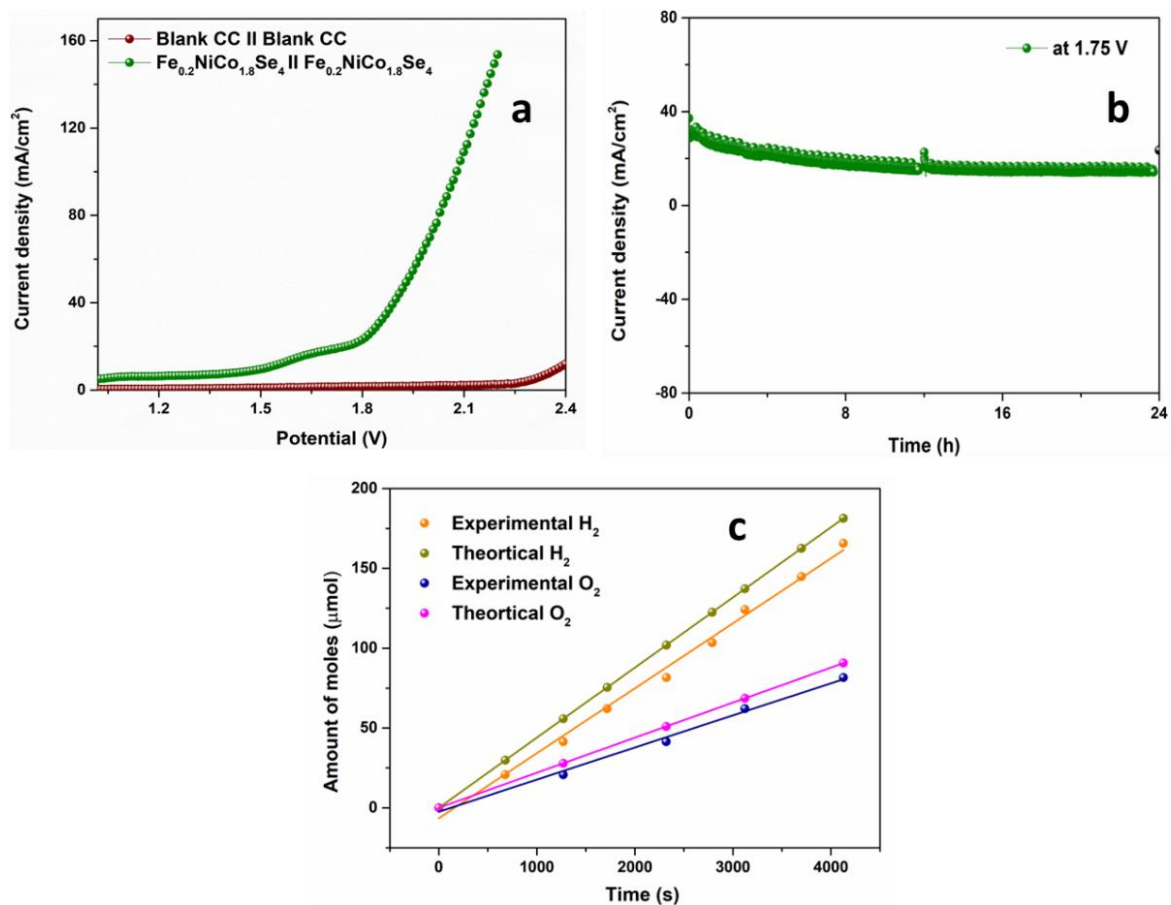


**Figure 7.24:** (a) Linear sweep voltammetry of the two electrode setup of  $\text{Fe}_{0.2}\text{NiCo}_{1.8}\text{Se}_4 \parallel \text{Fe}_{0.2}\text{NiCo}_{1.8}\text{Se}_4$  and blank CC, (b) 24 hours chronoamperometric data of  $\text{Fe}_{0.2}\text{NiCo}_{1.8}\text{Se}_4 \parallel \text{Fe}_{0.2}\text{NiCo}_{1.8}\text{Se}_4$  cell in 1.0 M KOH solution, and (c) theoretically calculated and experimentally measured  $\text{H}_2$  and  $\text{O}_2$  gas vs. time for overall water-splitting of  $\text{Fe}_{0.2}\text{NiCo}_{1.8}\text{Se}_4 \parallel \text{Fe}_{0.2}\text{NiCo}_{1.8}\text{Se}_4$  cell.

The role of metal centers in  $\text{Fe}_{0.2}\text{NiCo}_{1.8}\text{Se}_4$  samples is further checked while performing the two-electrode system using  $\text{Fe}_{0.2}\text{NiCo}_{1.8}\text{Se}_4 \parallel \text{Fe}_{0.2}\text{NiCo}_{1.8}\text{Se}_4$  cell. Figure 7.25a represents the overall decrease in the electrocatalytic activity in the presence of KSCN. The current density of  $\sim 60 \text{ mA/cm}^2$  reduces to  $\sim 20 \text{ mA/cm}^2$  after the addition of  $\text{SCN}^-$  ion poison, which proves the synergy of metal ions in  $\text{Fe}_{0.2}\text{NiCo}_{1.8}\text{Se}_4$  is important for overall water-splitting (Figure 7.25b).

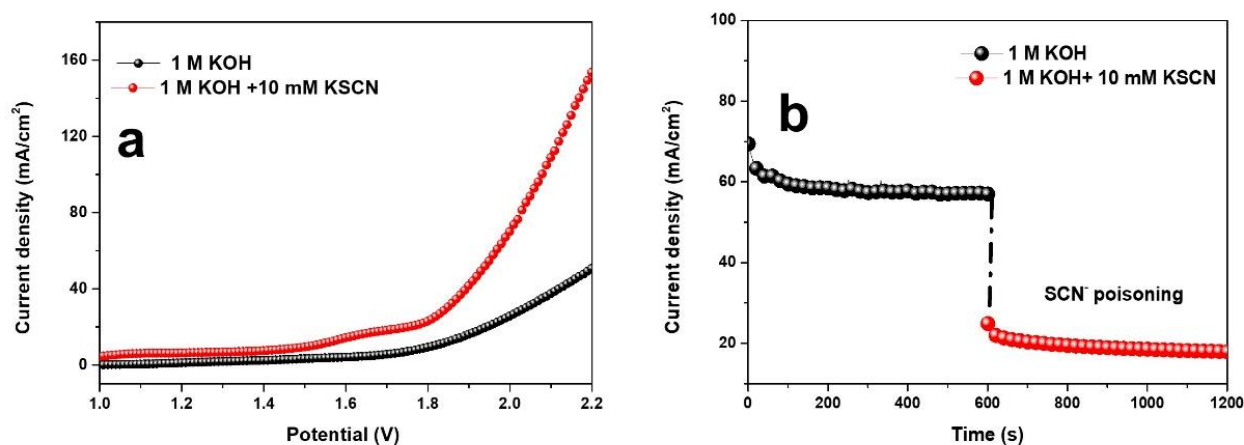


**Figure 7.25:** Effect of KSCN on the overall current (for two-electrode system) of  $\text{Fe}_{0.2}\text{NiCo}_{1.8}\text{Se}_4$  sample (a) LSV and (b) chronoamperometric data.

To check the robustness and stability of the  $\text{Fe}_{0.2}\text{NiCo}_{1.8}\text{Se}_4$  catalyst in the overall water-splitting reaction, the FESEM and XPS analysis are performed after 24 h, shown in Figures 7.26 and 7.27. It can be observed from Figure 7.26a that the nanorod morphology is retained. The EDS analysis (Figure 7.26b) confirms the uniform distribution of Fe, Ni, Co, Se, and C elements in the  $\text{Fe}_{0.2}\text{NiCo}_{1.8}\text{Se}_4$  sample. XPS analysis confirms the composition of the  $\text{Fe}_{0.2}\text{NiCo}_{1.8}\text{Se}_4$  sample, where the binding energy values are well matched with the pre-electrocatalysis result. All the binding energy values of  $\text{Fe}^{3+}$ ,  $\text{Ni}^{2+}$ ,  $\text{Ni}^{3+}$ ,  $\text{Co}^{2+}$ ,  $\text{Co}^{3+}$ ,  $\text{Se}^{2-}$  ions are well matched. Therefore, the electrocatalyst,  $\text{Fe}_{0.2}\text{NiCo}_{1.8}\text{Se}_4$ , represents remarkable efficiency and stability as an alkaline electrolyzer.



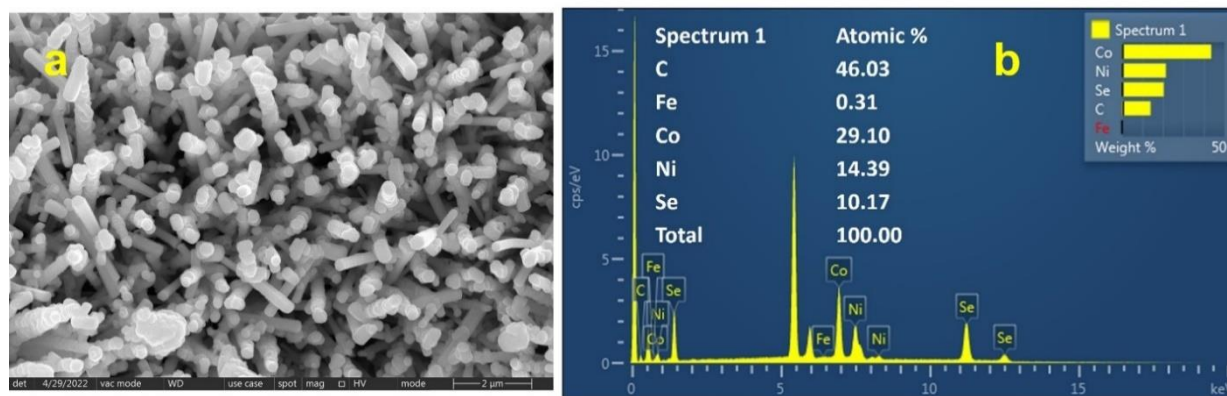


**Figure 7.26:** (a) FESEM image and (b) EDS mapping of  $\text{Fe}_{0.2}\text{NiCo}_{1.8}\text{Se}_4$  after two electrode electrocatalysis.

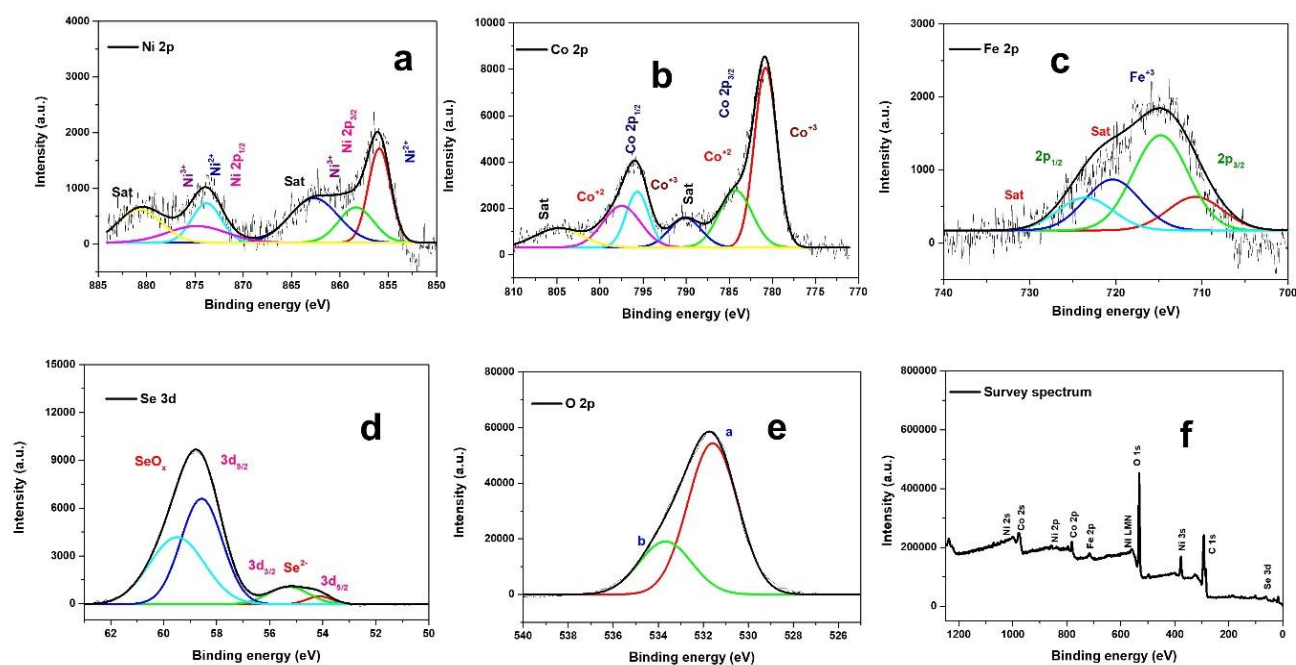


**Figure 7.27:** XPS of  $\text{Fe}_{0.2}\text{NiCo}_{1.8}\text{Se}_4$  (a) deconvoluted spectra of Ni 2p, (b) deconvoluted spectra of Co 2p, (c) deconvoluted spectra of Fe 2p, (d) deconvoluted spectra of Se 3d, (e) deconvoluted spectra of O 2p, and (f) survey spectrum after two electrode electrocatalysis.

### 7.3.5 Structural properties of bare and Fe-doped $\text{NiCo}_2\text{Se}_4$ compounds

Under ambient conditions, the  $\text{NiCo}_2\text{Se}_4$  compound crystallizes into a face-centered cubic phase and belongs to the  $Fd\bar{3}m$  space group symmetry (Space group no. 227). The crystal structure of  $\text{NiCo}_2\text{Se}_4$  is modeled to be identical to the structure of  $\text{NiCo}_2\text{O}_4$  or  $\text{NiCo}_2\text{S}_4$  compound<sup>34, 57-60</sup>.

The optimized geometry of the NiCo<sub>2</sub>Se<sub>4</sub> system, so obtained from the GGA-PBEsol level of theory, is depicted in the upper panel of Figure 7.28 NiCo<sub>2</sub>Se<sub>4</sub> represents a spinel structure with Ni atoms occupy at the corner of the edges of the supercell, and Se atoms are distributed in a cubic close-packed arrangement. While the Ni atoms are distributed over the octahedral sites, the Co atoms occupy the center of both octahedral and tetrahedral sites of the crystal lattice with corner-sharing Se atoms.

To comprehend the structural stabilities of the Fe-doped NiCo<sub>2</sub>Se<sub>4</sub> compounds, the defect formation energies per dopant ( $\Delta E_{df}$ ) have been estimated according to the following relation<sup>61</sup>:

$$\Delta E_{df} = \frac{1}{N_{Fe}} [E_{doped} - E_{bare} - N_{Fe}(\mu_{Fe} - \mu_{Co})] \quad (1)$$

where  $E_{doped}$  is the total energy of the Fe-doped NiCo<sub>2</sub>Se<sub>4</sub> system,  $E_{bare}$  is the total energy of bare NiCo<sub>2</sub>Se<sub>4</sub> supercell,  $N_{Fe}$  is the number of Fe dopants,  $\mu_{Fe}$  and  $\mu_{Co}$  are the chemical potentials of the individual Fe and Co atoms, respectively. The optimized crystal structures of Fe<sub>0.12</sub>NiCo<sub>1.88</sub>Se<sub>4</sub>, Fe<sub>0.2</sub>NiCo<sub>1.8</sub>Se<sub>4</sub>, and Fe<sub>0.5</sub>NiCo<sub>1.5</sub>Se<sub>4</sub> compounds and their respective defect formation energy values are shown in the lower panel of Figure 7.28 and Figure 7.29 respectively. The  $\Delta E_{df}$  values for Fe<sub>0.12</sub>NiCo<sub>1.88</sub>Se<sub>4</sub>, Fe<sub>0.2</sub>NiCo<sub>1.8</sub>Se<sub>4</sub>, and Fe<sub>0.5</sub>NiCo<sub>1.5</sub>Se<sub>4</sub> systems, as depicted in Figure 7.29, are found to be 1.00, 0.81 and 2.04 Ry respectively. From  $\Delta E_{df}$  values, it is clearly seen that the Fe-doped NiCo<sub>2</sub>Se<sub>4</sub> systems are not only endothermic in nature, but Fe<sub>0.2</sub>NiCo<sub>1.8</sub>Se<sub>4</sub> compound (10% Fe-doped NiCo<sub>2</sub>Se<sub>4</sub>) is energetically most feasible among the other Fe-doped NiCo<sub>2</sub>Se<sub>4</sub> systems under study.

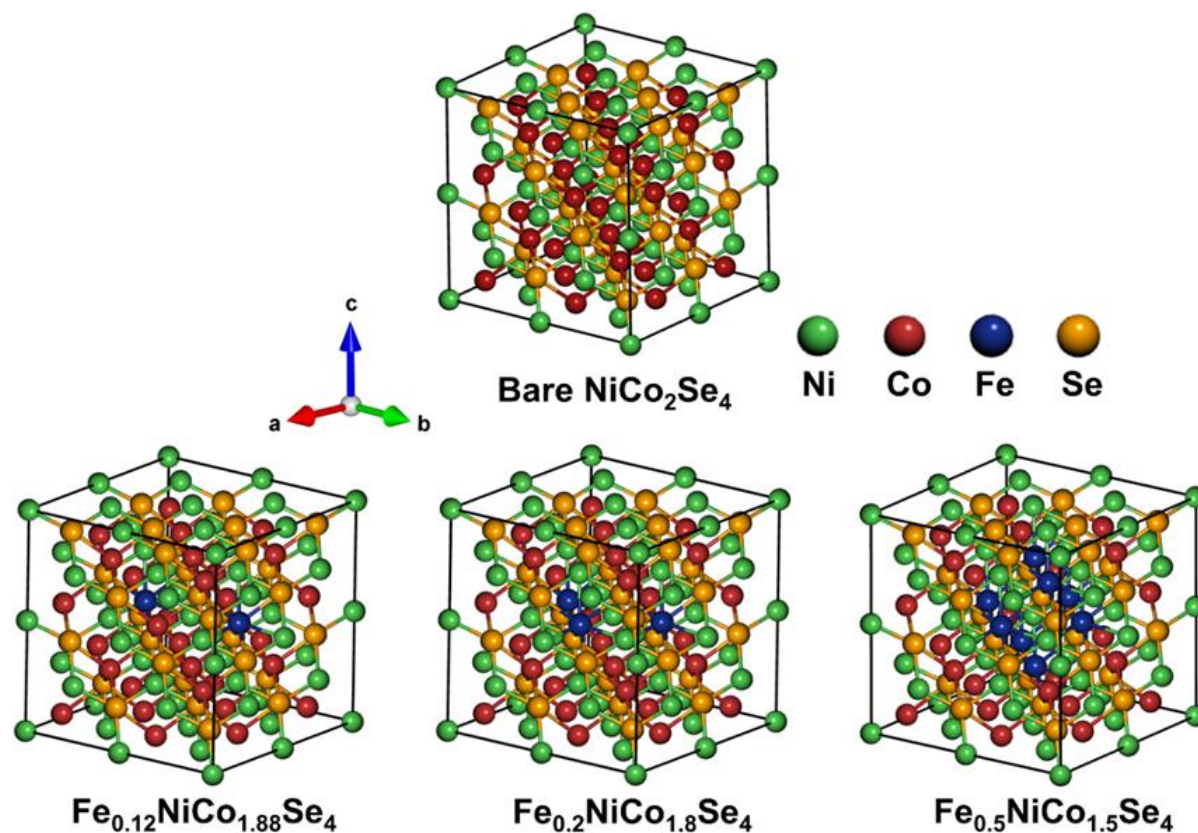


**Figure 7.28:** Upper and lower panels represent the optimized crystal structures of the bare and Fe-doped  $\text{NiCo}_2\text{Se}_4$  compounds ( $\text{Fe}_{0.12}\text{NiCo}_{1.88}\text{Se}_4$ ,  $\text{Fe}_{0.2}\text{NiCo}_{1.8}\text{Se}_4$ , and  $\text{Fe}_{0.5}\text{NiCo}_{1.5}\text{Se}_4$ ) respectively as estimated from the first-principle calculations.

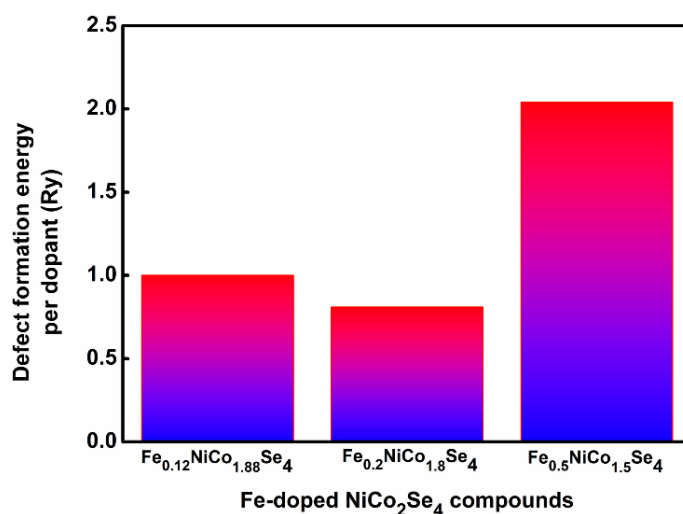


**Figure 7.29:** Defect formation energies per dopant ( $\Delta E_{df}$ ) for different Fe-doped  $\text{NiCo}_2\text{Se}_4$  systems as obtained from DFT+ $U_{dd}$  level of theory.

### 7.3.6 Electronic properties of bare and Fe-doped NiCo<sub>2</sub>Se<sub>4</sub> systems

To precisely understand the enhanced electrocatalytic activities of the Fe<sub>0.2</sub>NiCo<sub>1.8</sub>Se<sub>4</sub> compound among the bare and other Fe-doped NiCo<sub>2</sub>Se<sub>4</sub> systems, the electronic band structures have been estimated. The corresponding spin-polarized E-**k** diagrams of NiCo<sub>2</sub>Se<sub>4</sub> and Fe<sub>0.2</sub>NiCo<sub>1.8</sub>Se<sub>4</sub> crystal systems along the  $\Gamma \rightarrow R \rightarrow M \rightarrow \Gamma \rightarrow X \rightarrow R$  high-symmetry points in the Brillouin zone are depicted in Figure 7.30(a) and 7.30(b) respectively. Interestingly, from Figure 7.30(a), the asymmetries between the up and down spin configurations in the E-**k** diagrams have been observed. These asymmetries in the band structure plots primarily correspond to the non-zero magnetic moment of the compound. NiCo<sub>2</sub>Se<sub>4</sub> indeed shows ferrimagnetic behavior with magnetic moment  $\sim 5 \mu_B/\text{cell}$ , which closely matches the magnetic properties of the NiCo<sub>2</sub>O<sub>4</sub> compound that shows similar ferrimagnetic behavior of magnetic moment  $\sim 4 \mu_B/\text{cell}$ <sup>62-63</sup>. Figure 7.30(a) further reveals that the valance band maximum (VBM) and the conduction band minimum (CBM) of the bare compound are localized at X high-symmetry point around the Fermi energy ( $E_F$ ). No trace of dispersive energy levels is found on  $E_F$  in the E-**k** diagrams. This result suggests that the NiCo<sub>2</sub>Se<sub>4</sub> system is a direct band gap semiconductor with up and down spin energy band gap ( $E_g$ ) values of 1.32 and 0.60 eV, respectively.

Surprisingly, dramatic changes in the E-**k** diagrams [Figure 7.30(b)] for the up and down spin configurations of the 10% Fe-doped NiCo<sub>2</sub>Se<sub>4</sub> system (Fe<sub>0.2</sub>NiCo<sub>1.8</sub>Se<sub>4</sub>) have been noticed. From Figure 7.30(b), significant contributions of energy states generated from the conduction band edges have been found at  $E_F$ . This observation implies the zero-band gap or the conducting behavior of the Fe<sub>0.2</sub>NiCo<sub>1.8</sub>Se<sub>4</sub> compound. The metallic behavior of Fe<sub>0.2</sub>NiCo<sub>1.8</sub>Se<sub>4</sub> may induce enhanced HER and OER performance compared to the bare NiCo<sub>2</sub>Se<sub>4</sub> system. This observation also agrees with our experimental results, where Fe<sub>0.2</sub>NiCo<sub>1.8</sub>Se<sub>4</sub> is found to be the most favorable candidate for HER and OER activities among the bare and other Fe-doped NiCo<sub>2</sub>Se<sub>4</sub> systems. Besides, the large asymmetries between the up and down spin band profiles [Figure 7.30(b)] also suggest the ferrimagnetic nature of the Fe<sub>0.2</sub>NiCo<sub>1.8</sub>Se<sub>4</sub> compound with a magnetic moment of  $\sim 4.64 \mu_B/\text{cell}$ .

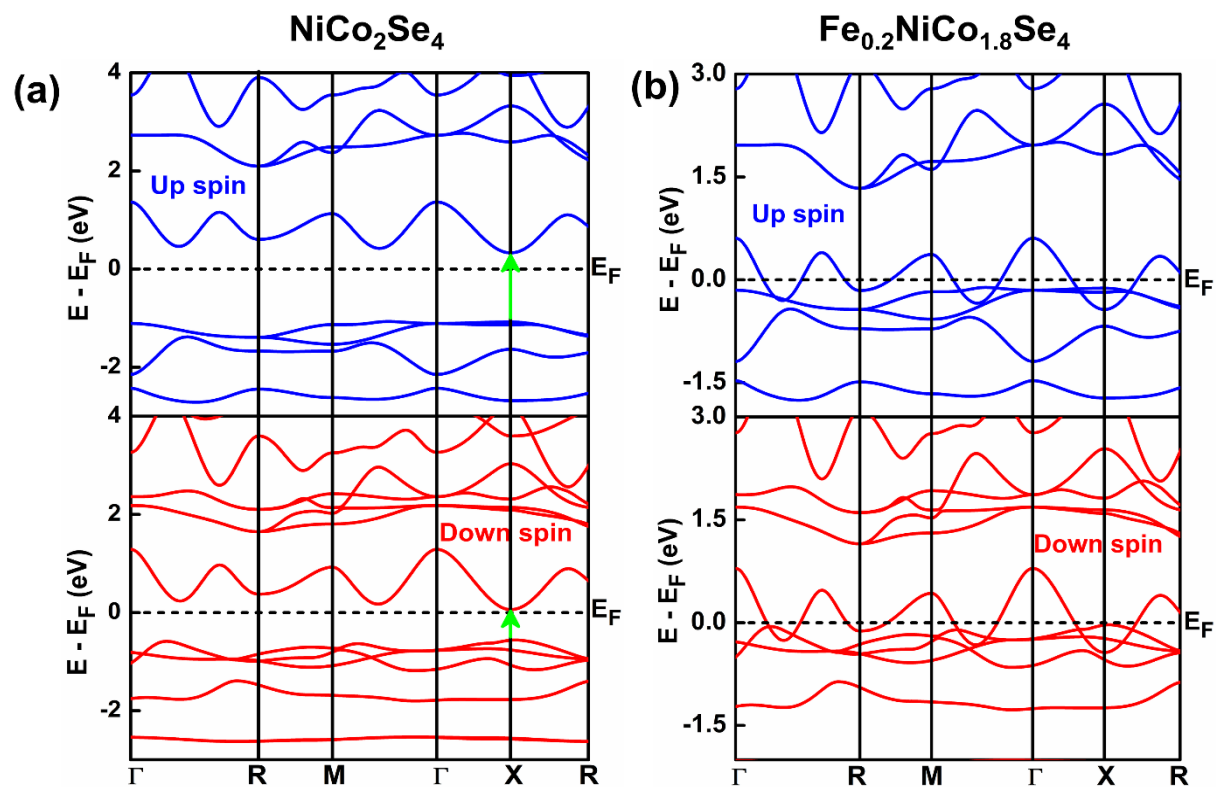


**Figure 7.30:** The electronic band structures along the  $\Gamma \rightarrow R \rightarrow M \rightarrow \Gamma \rightarrow X \rightarrow R$  high-symmetry points of (a)  $\text{NiCo}_2\text{Se}_4$  and (b)  $\text{Fe}_{0.2}\text{NiCo}_{1.8}\text{Se}_4$  systems as obtained from the DFT+ $U_{\text{dd}}$  level of calculations. [The band gaps in Figure (a) and the Fermi energies ( $E_{\text{F}}$ ) are marked with green arrows and horizontal dashed lines, respectively].

To further corroborate the performance of bare and other Fe-doped  $\text{NiCo}_2\text{Se}_4$  compounds in HER and OER activities, the total, orbital resolved partial atomic density of states (TDOS, PDOS) of  $\text{NiCo}_2\text{Se}_4$  and  $\text{Fe}_{0.2}\text{NiCo}_{1.8}\text{Se}_4$  systems have been calculated. The results are illustrated in Figures 7.31(a, b) and 7.31(c, d), respectively. Akin to E- $\mathbf{k}$  diagrams (*vide supra*), the asymmetries between the up and down spin channels in TDOS have been found. From Figure 7.31(a), narrow band gaps around  $E_{\text{F}}$  have also been observed in the TDOS plot for both up and down spin channels of the bare  $\text{NiCo}_2\text{Se}_4$  compound. The subsequent PDOS plot of  $\text{NiCo}_2\text{Se}_4$ , as shown in Figure 7.31(b), further reveals that the top of the valance bands, ranging between -2 and 0 eV, originated mainly from the Se-4p orbital, while small contributions from Ni-4s and Co-4s orbitals have also been found. Besides, the predominant contribution of Ni-3d orbital has been observed in the bottom of the conduction bands ranging from 0 to 2 eV, along with the weak

signature of Co-4s and Se-4p orbitals. However, the TDOS plot of the  $\text{Fe}_{0.2}\text{NiCo}_{1.8}\text{Se}_4$  compound, as depicted in Figure 7.31(c), shows noticeable changes in its spectral features compared to the bare  $\text{NiCo}_2\text{Se}_4$  system. The TDOS plot illustrates the dense nesting of energy states in the form of the van-Hove singularity at  $E_F$ . This observation also suggests the metallic nature of the  $\text{Fe}_{0.2}\text{NiCo}_{1.8}\text{Se}_4$  compound in accordance with our early conjecture (*vide supra*). The TDOS plots of other Fe-doped  $\text{NiCo}_2\text{Se}_4$  systems ( $\text{Fe}_{0.12}\text{NiCo}_{1.88}\text{Se}_4$  and  $\text{Fe}_{0.5}\text{NiCo}_{1.5}\text{Se}_4$ ) are shown in Figure 7.32. Interestingly, the PDOS plot of the  $\text{Fe}_{0.2}\text{NiCo}_{1.8}\text{Se}_4$  compound, as shown in Figure 7.31(d), reveals the significant contribution of the 3d orbital of the dopant Fe atom in the energy states at  $E_F$ . The prime contribution of the Fe-3d orbital at  $E_F$  is thus responsible for the conducting behavior of  $\text{Fe}_{0.2}\text{NiCo}_{1.8}\text{Se}_4$ , which is known to promote improved electrocatalytic activities among the bare and other Fe-doped  $\text{NiCo}_2\text{Se}_4$  compounds (*vide supra*).

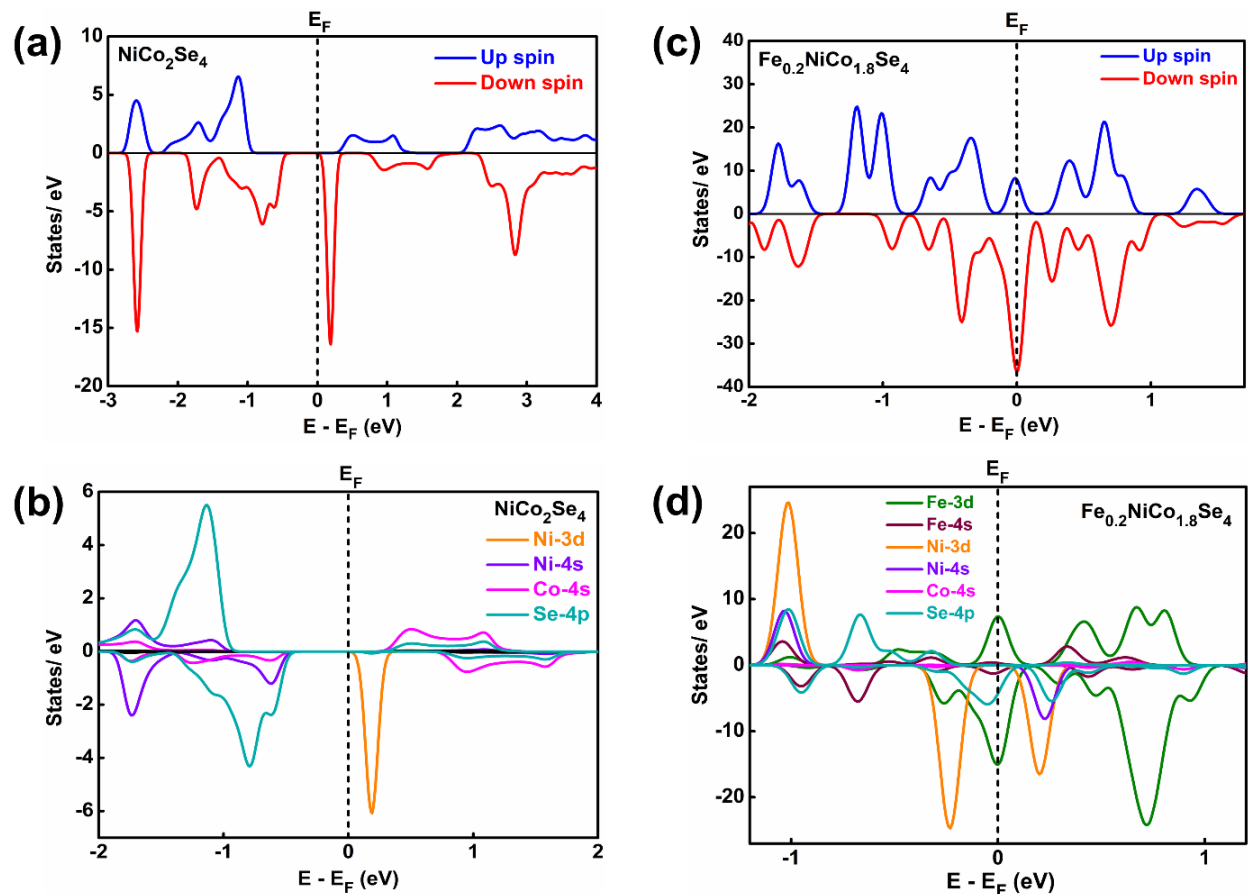


**Figure 7.31:** (a to d) Left and right panels depict the total, orbital resolved partial atomic density of states of  $\text{NiCo}_2\text{Se}_4$  and  $\text{Fe}_{0.2}\text{NiCo}_{1.8}\text{Se}_4$  compounds, respectively, as obtained from the DFT+ $U_{\text{dd}}$  level of theory. [The Fermi energies ( $E_F$ ) are marked with vertical dashed lines].

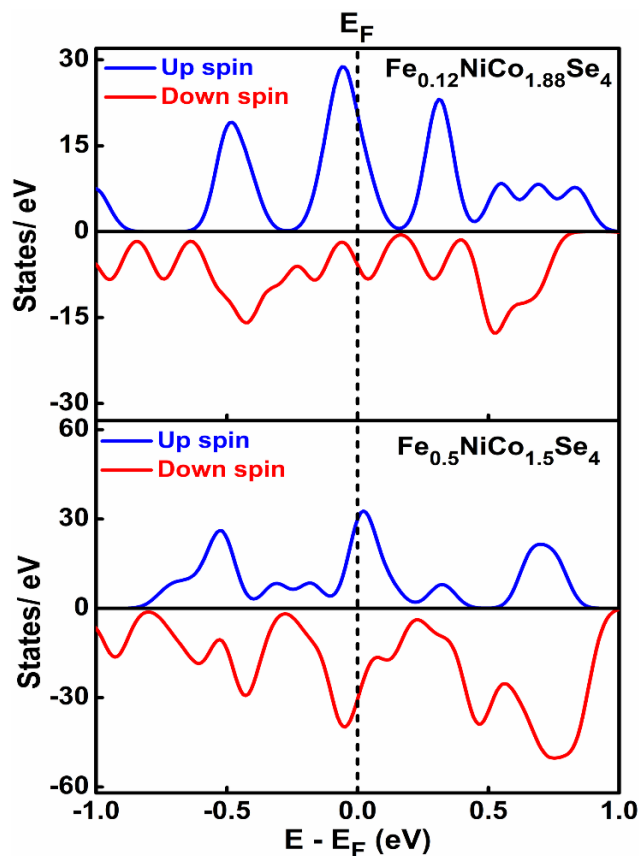


**Figure 7.32:** Total density of states of  $\text{Fe}_{0.12}\text{NiCo}_{1.88}\text{Se}_4$  and  $\text{Fe}_{0.5}\text{NiCo}_{1.5}\text{Se}_4$  compounds as estimated from DFT+ $U_{\text{dd}}$  level of theory.

To estimate the charge transfer or charge pulling effect between the Co and Fe atoms of the Fe-doped  $\text{NiCo}_2\text{Se}_4$  systems, the Mulliken and Bader charge analyses have been performed<sup>64-65</sup>. The Mulliken (Bader) charges for Ni, Co, and Se atoms of the pristine  $\text{NiCo}_2\text{Se}_4$  compound are found to be +0.05e (+0.06e), -0.49e (-0.50e) and -0.67e (-0.68e) respectively. However, the Mulliken (Bader) charges for the respective Fe, Ni, Co, and Se atoms of the Fe-doped  $\text{Fe}_{0.2}\text{NiCo}_{1.8}\text{Se}_4$  system are estimated to be -1.75e (-1.77e), +0.03e (+0.04e), -0.32e (-0.30e), -0.50e (-0.48e). The Mulliken and Bader charge analyses for pristine  $\text{NiCo}_2\text{Se}_4$  and  $\text{Fe}_{0.2}\text{NiCo}_{1.8}\text{Se}_4$  compounds collectively suggest that there is a significant decrease in Mulliken (Bader) charge of 0.17e (0.20 e) on the Co atom due to the presence of dopant Fe atom. Interestingly, alteration of Mulliken (Bader) charge on the Fe atom has also been estimated and shows a considerable increase of -1.75e (-1.77e) charge. This result not only indicates the charge-pulling nature of the Fe atom



but may also reflect the prevalence of synergistic effect between the Fe and Co atoms in the  $\text{Fe}_{0.2}\text{NiCo}_{1.8}\text{Se}_4$  compound, which in turn may promote higher electrocatalytic efficiency.

### 7.3.7 Gibbs free energy and current density for HER and OER

To understand the HER and OER activities of Fe-doped  $\text{NiCo}_2\text{Se}_4$  compounds for various dopant concentrations, the variations in Gibbs free energy ( $\Delta G$ ) as a function of hydrogen and oxygen coverages for  $\text{Fe}_{0.12}\text{NiCo}_{1.88}\text{Se}_4$ ,  $\text{Fe}_{0.2}\text{NiCo}_{1.8}\text{Se}_4$  and  $\text{Fe}_{0.5}\text{NiCo}_{1.5}\text{Se}_4$  compounds have been estimated under zero overpotential energy value. The results are shown in Figures 7.33(A) and 7.33(B). From Figure 7.33(A) and 7.33(B), the minimum values of  $\Delta G$  are found to be -7.44 and -11.29 eV for 37.5% of hydrogen and oxygen coverages, respectively, for the  $\text{Fe}_{0.2}\text{NiCo}_{1.8}\text{Se}_4$  system. However, for  $\text{Fe}_{0.12}\text{NiCo}_{1.88}\text{Se}_4$  and  $\text{Fe}_{0.5}\text{NiCo}_{1.5}\text{Se}_4$  compounds, the lowest estimated  $\Delta G$  values are -6.00 (-9.93) eV and -6.82 (-7.72) eV for 25% and 100% hydrogen (oxygen) coverage respectively. All these calculations indicate the minimum value of  $\Delta G$  to be -7.44 (-11.29) eV for 37.5% hydrogen (oxygen) coverage in doped  $\text{Fe}_{0.2}\text{NiCo}_{1.8}\text{Se}_4$  compound which may stand responsible for improved HER and OER activities of the Fe-doped  $\text{NiCo}_2\text{Se}_4$  systems.

To comprehend the HER and OER activities of the active sites of Fe-doped  $\text{NiCo}_2\text{Se}_4$  systems, the exchange current density (J) has also been estimated. The corresponding volcano plots, which represent the logarithm of J as a function of  $\Delta G^{66-69}$ , for HER and OER, are shown in Figure 7.33(a) and 7.33(b), respectively. From Figure 7.33(a) and 7.33(b), it is clearly seen that the maximum values of J are found at  $\Delta G = 0$  for  $\text{Fe}_{0.2}\text{NiCo}_{1.8}\text{Se}_4$  system, which in turn may represent the ideal candidate for the evolution of hydrogen and oxygen among its other Fe-doped counterparts. These results are also in agreement with our experimental observations where the  $\text{Fe}_{0.2}\text{NiCo}_{1.8}\text{Se}_4$  compound exhibits better HER and OER activities with the highest value of current density in comparison to its other Fe-doped complements (*vide supra*).



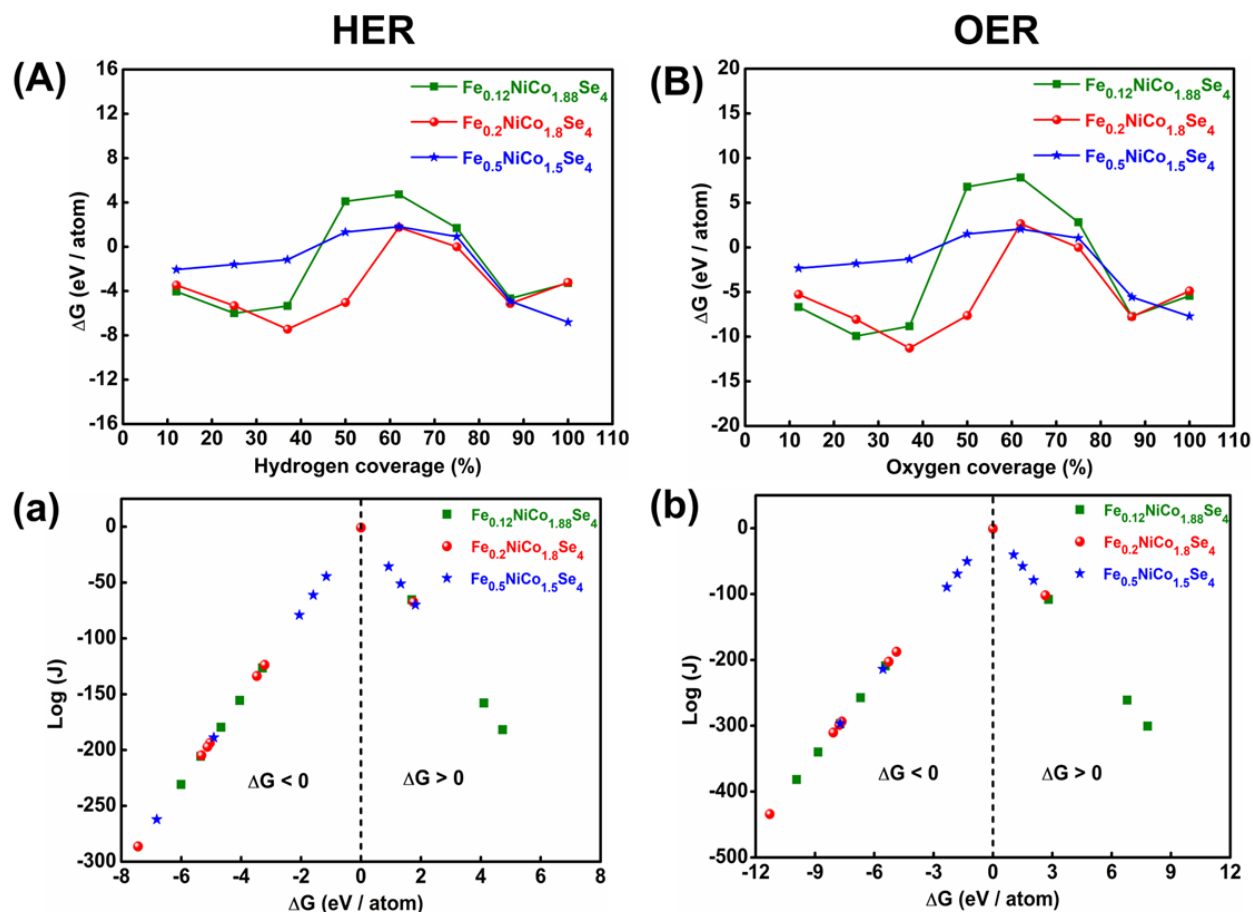


**Figure 7.33:** The Gibbs free energy ( $\Delta G$ ) vs. (A) hydrogen and (B) oxygen coverage and the exchange current density ( $J$ ) as a function of  $\Delta G$  for (a) HER and (b) OER activities of Fe-doped  $\text{NiCo}_2\text{Se}_4$  compounds.

## 7.4 Conclusion

In conclusion, Fe-doped  $\text{NiCo}_2\text{Se}_4$  material on CC is developed through a straightforward hydrothermal method. Various ratios of  $\text{Fe}_{0.1}\text{NiCo}_{1.9}\text{Se}_4$ ,  $\text{Fe}_{0.2}\text{NiCo}_{1.8}\text{Se}_4$ , and  $\text{Fe}_{0.4}\text{NiCo}_{1.6}\text{Se}_4$  are synthesized in which  $\text{Fe}_{0.2}\text{NiCo}_{1.8}\text{Se}_4$  is the best-optimized ratio for the electrocatalytic activity, which is also well validated with both experimental and theoretical evidence. The  $\text{Fe}^{3+}$  introduction in  $\text{NiCo}_2\text{Se}_4$  reduces the diameter of the nanorod, creating rougher morphology and lattice distortion, which synergizes the water-splitting reaction. The fast electron kinetics and higher electrochemical active surface area after Fe doping in  $\text{NiCo}_2\text{Se}_4$  favor the water-splitting reaction. XPS analysis confirms the Lewis acidity of the  $\text{Fe}^{3+}$  ion, which changes the electronic environment of  $\text{NiCo}_2\text{Se}_4$  and improves the electrocatalytic activity. The doped electrocatalyst,  $\text{Fe}_{0.2}\text{NiCo}_{1.8}\text{Se}_4$ , has

a higher value of ECSA than the bare NiCo<sub>2</sub>Se<sub>4</sub>. The optimized Fe<sub>0.2</sub>NiCo<sub>1.8</sub>Se<sub>4</sub> requires a lower Tafel slope value of 85.7 and 56.3 mV/dec for HER and OER, respectively. The improved electron conduction during water-splitting is ensured by the synthesis and growth of the electrocatalyst on the CC, a conducting substrate. The presence of a multimetallic center and synergistic effect of all the metal ions Fe<sup>3+</sup>, Ni<sup>2+</sup>, Ni<sup>3+</sup>, Co<sup>2+</sup>, and Co<sup>3+</sup> in Fe<sub>0.2</sub>NiCo<sub>1.8</sub>Se<sub>4</sub> plays an essential role in the development of efficient and durable electrocatalyst. The Mulliken and Bader charge analysis also supports that dopant Fe has charge pulling nature which turns into a synergistic effect. The role of metal sites in the overall water-splitting reaction is further evidenced by using KSCN because SCN<sup>-</sup> ion can selectively poison the metal sites during the electrocatalytic reactions. Finally, the same doped material is used as a cathode and anode for the generation of hydrogen and oxygen, respectively, with a cell voltage of 1.51 V to generate 10 mA/cm<sup>2</sup> current density in an alkaline medium. For the performance measurement of Fe<sub>0.2</sub>NiCo<sub>1.8</sub>Se<sub>4</sub> || Fe<sub>0.2</sub>NiCo<sub>1.8</sub>Se<sub>4</sub> cell, the Faradaic efficiency is also calculated and reported as 89.9 % and 91.3 % for OER and HER, respectively. The band gap and DOS calculation also prove that Fe<sub>0.2</sub>NiCo<sub>1.8</sub>Se<sub>4</sub> is more metallic and dopant Fe contributes an essential role in the system's conductivity. Moreover, the theoretical calculation also proves that the Fe<sub>0.2</sub>NiCo<sub>1.8</sub>Se<sub>4</sub> catalyst has optimum Gibbs free energy for HER and OER, high exchange current density with maximum hydrogen and oxygen coverage value. So, this work provides us with a simple route for the synthesis of Fe-doped NiCo<sub>2</sub>Se<sub>4</sub>, a nanorod array, for better electrocatalytic performance with clean energy generation.

## 7.5 References

1. Li, Y.; Sun, Y.; Qin, Y.; Zhang, W.; Wang, L.; Luo, M.; Yang, H.; Guo, S., Recent advances on water-splitting electrocatalysis mediated by noble metal based nanostructured materials. *Adv. Energy Mater.* **2020**, *10* (11), 1903120.
2. Yang, C.; Lu, Y.; Duan, W.; Kong, Z.; Huang, Z.; Yang, T.; Zou, Y.; Chen, R.; Wang, S., Recent Progress and Prospective of Nickel Selenide-Based Electrocatalysts for Water Splitting. *Energy Fuels* **2021**, *35* (18), 14283-14303.
3. Wang, X.; She, G.; Mu, L.; Shi, W., Amorphous Co–Mo–P–O Bifunctional Electrocatalyst via Facile Electrodeposition for Overall Water Splitting. *ACS Sustain. Chem. Eng.* **2020**, *8* (7), 2835-2842.

- Li, X.; Zhao, L.; Yu, J.; Liu, X.; Zhang, X.; Liu, H.; Zhou, W., Water Splitting: From Electrode to Green Energy System. *Nano-Micro Lett.* **2020**, *12* (1), 131.
- Boppella, R.; Tan, J.; Yun, J.; Manorama, S. V.; Moon, J., Anion-mediated transition metal electrocatalysts for efficient water electrolysis: Recent advances and future perspectives. *Coord. Chem. Rev.* **2021**, *427*, 213552.
- Li, X.; Zhang, L.; Huang, M.; Wang, S.; Li, X.; Zhu, H., Cobalt and nickel selenide nanowalls anchored on graphene as bifunctional electrocatalysts for overall water splitting. *J. Mater. Chem. A* **2016**, *4* (38), 14789-14795.
- Tang, C.; Cheng, N.; Pu, Z.; Xing, W.; Sun, X., NiSe Nanowire Film Supported on Nickel Foam: An Efficient and Stable 3D Bifunctional Electrode for Full Water Splitting. *Angew. Chem. Int. Ed.* **2015**, *54* (32), 9351-5.
- Yuan, C.-Z.; Zhong, S.-L.; Jiang, Y.-F.; Yang, Z. K.; Zhao, Z.-W.; Zhao, S.-J.; Jiang, N.; Xu, A.-W., Direct growth of cobalt-rich cobalt phosphide catalysts on cobalt foil: an efficient and self-supported bifunctional electrode for overall water splitting in alkaline media. *J. Mater. Chem. A* **2017**, *5* (21), 10561-10566
- Zahra, R.; Pervaiz, E.; Yang, M.; Rabi, O.; Saleem, Z.; Ali, M.; Farrukh, S., A review on nickel cobalt sulphide and their hybrids: Earth abundant, pH stable electro-catalyst for hydrogen evolution reaction. *Int. J. Hydrog. Energy* **2020**, *45* (46), 24518-24543.
- Wen, S.; Huang, J.; Li, T.; Chen, W.; Chen, G.; Zhang, Q.; Zhang, X.; Qian, Q.; Ostrikov, K., Multiphase nanosheet-nanowire cerium oxide and nickel-cobalt phosphide for highly-efficient electrocatalytic overall water splitting. *Appl. Catal. B* **2022**, *316*, 121678.
- Sakthivel, M.; Sukanya, R.; Chen, S.-M.; Pandi, K.; Ho, K.-C., Synthesis and characterization of bimetallic nickel-cobalt chalcogenides (NiCoSe<sub>2</sub>, NiCo<sub>2</sub>S<sub>4</sub>, and NiCo<sub>2</sub>O<sub>4</sub>) for non-enzymatic hydrogen peroxide sensor and energy storage: Electrochemical properties dependence on the metal-to-chalcogen composition. *Renew. Energy* **2019**, *138*, 139-151.
- Qi, Y.; Zhang, Q.; Meng, S.; Li, D.; Wei, W.; Jiang, D.; Chen, M., Iron-doped nickel cobalt ternary phosphide hyperbranched hierarchical arrays for efficient overall water splitting. *Electrochim. Acta* **2020**, *334*, 135633.

13. Chen, H.; Chen, S.; Fan, M.; Li, C.; Chen, D.; Tian, G.; Shu, K., Bimetallic nickel cobalt selenides: a new kind of electroactive material for high-power energy storage. *J. Mater. Chem. A* **2015**, *3* (47), 23653-23659.
14. Li, Y.; Bao, X.; Chen, D.; Wang, Z.; Dewangan, N.; Li, M.; Xu, Z.; Wang, J.; Kawi, S.; Zhong, Q., A Minireview on Nickel-Based Heterogeneous Electrocatalysts for Water Splitting. *ChemCatChem* **2019**, *11* (24), 5913-5928.
15. Janani, G.; Yuvaraj, S.; Surendran, S.; Chae, Y.; Sim, Y.; Song, S.-J.; Park, W.; Kim, M.-J.; Sim, U., Enhanced bifunctional electrocatalytic activity of Ni-Co bimetallic chalcogenides for efficient water-splitting application. *J. Alloys Compd.* **2020**, *846*, 156389.
16. Si, C.; Zhang, W.; Lu, Q.; Guo, E.; Yang, Z.; Chen, J.; He, X.; Luo, J., Recent Advances in Perovskite Catalysts for Efficient Overall Water Splitting. *Catalysts* **2022**, *12* (6), 601.
17. Nemiwal, M.; Gosu, V.; Zhang, T. C.; Kumar, D., Metal organic frameworks as electrocatalysts: Hydrogen evolution reactions and overall water splitting. *Int. J. Hydrog. Energy* **2021**, *46* (17), 10216-10238.
18. Min, K.; Yoo, R.; Kim, S.; Kim, H.; Shim, S. E.; Lim, D.; Baeck, S.-H., Facile synthesis of P-doped NiCo<sub>2</sub>S<sub>4</sub> nanoneedles supported on Ni foam as highly efficient electrocatalysts for alkaline oxygen evolution reaction. *Electrochim. Acta* **2021**, *396*, 139236.
19. He, W.; Zhang, R.; Zhang, J.; Wang, F.; Li, Y.; Zhao, J.; Chen, C.; Liu, H.; Xin, H. L., Promoting the water dissociation of nickel sulfide electrocatalyst through introducing cationic vacancies for accelerated hydrogen evolution kinetics in alkaline media. *J. Catal.* **2022**, *410*, 112-120.
20. Fang, Z.; Peng, L.; Lv, H.; Zhu, Y.; Yan, C.; Wang, S.; Kalyani, P.; Wu, X.; Yu, G., Metallic Transition Metal Selenide Holey Nanosheets for Efficient Oxygen Evolution Electrocatalysis. *ACS Nano* **2017**, *11* (9), 9550-9557.
21. Sancho, H.; Zhang, Y.; Liu, L.; Barevadia, V. G.; Wu, S.; Zhang, Y.; Huang, P.-W.; Zhang, Y.; Wu, T.-H.; You, W.; Liu, N., NiCo<sub>2</sub>Se<sub>4</sub> Nanowires as a High-Performance Bifunctional Oxygen Electrocatalyst. *J Electrochem. Soc.* **2020**, *167* (5), 056503.
22. Wang, G.; Sun, Y.; Zhao, Y.; Zhang, Y.; Li, X.; Fan, L.; Li, Y., Phosphorus-induced electronic structure reformation of hollow NiCo<sub>2</sub>Se<sub>4</sub> nanoneedle arrays enabling highly efficient and durable hydrogen evolution in all-pH media. *Nano Res.* **2022**, *15*, 8771-8782.

23. Cao, X.; Hong, Y.; Zhang, N.; Chen, Q.; Masud, J.; Zaeem, M. A.; Nath, M., Phase Exploration and Identification of Multinary Transition-Metal Selenides as High-Efficiency Oxygen Evolution Electrocatalysts through Combinatorial Electrodeposition. *ACS Catal.* **2018**, *8* (9), 8273-8289.
24. Giannozzi, P.; Baseggio, O.; Bonfà, P.; Brunato, D.; Car, R.; Carnimeo, I.; Cavazzoni, C.; de Gironcoli, S.; Delugas, P.; Ferrari Ruffino, F.; Ferretti, A.; Marzari, N.; Timrov, I.; Urru, A.; Baroni, S., Quantum ESPRESSO toward the exascale. *J. Chem. Phys.* **2020**, *152* (15), 154105.
25. Giannozzi, P.; Andreussi, O.; Brumme, T.; Bunau, O.; Buongiorno Nardelli, M.; Calandra, M.; Car, R.; Cavazzoni, C.; Ceresoli, D.; Cococcioni, M.; Colonna, N.; Carnimeo, I.; Dal Corso, A.; de Gironcoli, S.; Delugas, P.; DiStasio, R. A.; Ferretti, A.; Floris, A.; Fratesi, G.; Fugallo, G.; Gebauer, R.; Gerstmann, U.; Giustino, F.; Gorni, T.; Jia, J.; Kawamura, M.; Ko, H. Y.; Kokalj, A.; Küçükbenli, E.; Lazzeri, M.; Marsili, M.; Marzari, N.; Mauri, F.; Nguyen, N. L.; Nguyen, H. V.; Otero-de-la-Roza, A.; Paulatto, L.; Poncé, S.; Rocca, D.; Sabatini, R.; Santra, B.; Schlipf, M.; Seitsonen, A. P.; Smogunov, A.; Timrov, I.; Thonhauser, T.; Umari, P.; Vast, N.; Wu, X.; Baroni, S., Advanced capabilities for materials modelling with Quantum ESPRESSO. *J. Phys.: Condens. Matter* **2017**, *29* (46), 465901.
26. Giannozzi, P.; Baroni, S.; Bonini, N.; Calandra, M.; Car, R.; Cavazzoni, C.; Ceresoli, D.; Chiarotti, G. L.; Cococcioni, M.; Dabo, I.; Dal Corso, A.; de Gironcoli, S.; Fabris, S.; Fratesi, G.; Gebauer, R.; Gerstmann, U.; Gougoussis, C.; Kokalj, A.; Lazzeri, M.; Martin-Samos, L.; Marzari, N.; Mauri, F.; Mazzarello, R.; Paolini, S.; Pasquarello, A.; Paulatto, L.; Sbraccia, C.; Scandolo, S.; Sclauzero, G.; Seitsonen, A. P.; Smogunov, A.; Umari, P.; Wentzcovitch, R. M., QUANTUM ESPRESSO: a modular and open-source software project for quantum simulations of materials. *J. Phys.: Condens. Matter* **2009**, *21* (39), 395502.
27. Shanno, D. F., Conditioning of quasi-Newton methods for function minimization. *Math. Comp.* **1970**, *24*, 647-656.
28. Goldfarb, D., A family of variable-metric methods derived by variational means. *Math. Comp.* **1970**, *24*, 23-26.

29. Fletcher, R., A new approach to variable metric algorithms. *Comput. J.* **1970**, *13* (3), 317-322.
30. Broyden, C. G., The Convergence of a Class of Double-rank Minimization Algorithms 1. General Considerations. *IMA J. Appl. Math.* **1970**, *6* (1), 76-90.
31. Dal Corso, A., Pseudopotentials periodic table: From H to Pu. *Comput. Mater. Sci.* **2014**, *95*, 337-350.
32. Perdew, J. P.; Ruzsinszky, A.; Csonka, G. I.; Vydrov, O. A.; Scuseria, G. E.; Constantin, L. A.; Zhou, X.; Burke, K., Restoring the Density-Gradient Expansion for Exchange in Solids and Surfaces. *Phys. Rev. Lett.* **2008**, *100* (13), 136406-13410.
33. Anisimov, V. I.; Zaanen, J.; Andersen, O. K., Band theory and Mott insulators: Hubbard U instead of Stoner I. *Phys. Rev. B* **1991**, *44* (3), 943-954.
34. Chang, T.-C.; Lu, Y.-T.; Lee, C.-H.; Gupta, J. K.; Hardwick, L. J.; Hu, C.-C.; Chen, H.-Y. T., The Effect of Degrees of Inversion on the Electronic Structure of Spinel NiCo<sub>2</sub>O<sub>4</sub>: A Density Functional Theory Study. *ACS Omega* **2021**, *6* (14), 9692-9699.
35. Tang, W.; Sanville, E.; Henkelman, G., A grid-based Bader analysis algorithm without lattice bias. *J. Phys.: Condens. Matter* **2009**, *21* (8), 084204.
36. Henkelman, G.; Arnaldsson, A.; Jónsson, H., A fast and robust algorithm for Bader decomposition of charge density. *Comput. Mater. Sci.* **2006**, *36* (3), 354-360.
37. Sanville, E.; Kenny, S. D.; Smith, R.; Henkelman, G., Improved grid-based algorithm for Bader charge allocation. *J. Comput. Chem.* **2007**, *28* (5), 899-908.
38. Ganguli, S.; Ghosh, S.; Tudu, G.; Koppiseti, H. V. S. R. M.; Mahalingam, V., Design Principle of Monoclinic NiCo<sub>2</sub>Se<sub>4</sub> and Co<sub>3</sub>Se<sub>4</sub> Nanoparticles with Opposing Intrinsic and Geometric Electrocatalytic Activity toward the OER. *Inorg. Chemistry* **2021**, *60* (13), 9542-9551.
39. Wang, K.; Lin, Z.; Tang, Y.; Tang, Z.; Tao, C.-L.; Qin, D.-D.; Tian, Y., Selenide/sulfide heterostructured NiCo<sub>2</sub>Se<sub>4</sub>/NiCoS<sub>4</sub> for oxygen evolution reaction, hydrogen evolution reaction, water splitting and Zn-air batteries. *Electrochim. Acta* **2021**, *368*, 137584.
40. Li, C.; Tian, P.; Pang, H.; Gong, W.; Ye, J.; Ning, G., Trace tungsten and iron-doped nickel hydroxide nanosheets for an efficient oxygen evolution reaction. *Sustain. Energy Fuels* **2020**, *4* (6), 2792-2799.

41. Rathore, D.; Banerjee, A.; Pande, S., Bifunctional Tungsten-Doped Ni(OH)<sub>2</sub>/NiOOH Nanosheets for Overall Water Splitting in an Alkaline Medium. *ACS Appl. Nano Mater.* **2022**, *5* (2), 2664-2677.
42. Yin, X.; Han, L.; Fu, Y.; Lu, J.; Song, Q.; Li, H., (Ni,Co)Se<sub>2</sub> nanoparticles on vertical graphene nanosheets@carbon microtubes for high-performance solid-state asymmetric supercapacitors. *J. Energy Storage* **2022**, *53*, 105205.
43. Zhang, C.; Biendicho, J. J.; Zhang, T.; Du, R.; Li, J.; Yang, X.; Arbiol, J.; Zhou, Y.; Morante, J. R.; Cabot, A., Combined high catalytic activity and efficient polar tubular nanostructure in urchin like metallic NiCo<sub>2</sub>Se<sub>4</sub> for high performance lithium–sulfur batteries. *Adv. Funct. Mater.* **2019**, *29* (34), 1903842.
44. Liu, X.; Yang, L.; Xu, G.; Cao, J., Pomegranate-like porous NiCo<sub>2</sub>Se<sub>4</sub> spheres with N-doped carbon as advanced anode materials for Li/Na-ion batteries. *Green Energy Environ.* **2022**, *7* (3), 554-565.
45. Ma, S.; Huang, J.; Zhang, C.; Chen, G.; Chen, W.; Shao, T.; Li, T.; Zhang, X.; Gong, T.; Ostrikov, K. K., One-step in-situ sprouting high-performance NiCoS<sub>x</sub>Se<sub>y</sub> bifunctional catalysts for water electrolysis at low cell voltages and high current densities. *J. Chem. Eng.* **2022**, *435*, 134859.
46. Lai, F.; Feng, J.; Heil, T.; Tian, Z.; Schmidt, J.; Wang, G.-C.; Oschatz, M., Partially delocalized charge in Fe-doped NiCo<sub>2</sub>S<sub>4</sub> nanosheet–mesoporous carbon-composites for high-voltage supercapacitors. *J. Mater. Chem. A* **2019**, *7* (33), 19342-19347.
47. Mahala, C.; Devi Sharma, M.; Basu, M., Fe Doped Nickel Hydroxide/Nickel Oxyhydroxide Function as an Efficient Catalyst for the Oxygen Evolution Reaction. *ChemElectroChem* **2019**, *6* (13), 3488-3498.
48. Rathore, D.; Ghosh, S.; Chowdhury, J.; Pande, S., Co-Doped Ni<sub>9</sub>S<sub>8</sub> Nanostructures for Electrocatalytic Water Splitting over a Wide pH Range. *ACS Appl. Nano Mater.* **2022**, *5*, 11823–11838.
49. Jin, C.; Hou, M.; Li, X.; Liu, D.; Qu, D.; Dong, Y.; Xie, Z.; Zhang, C., Rapid electrodeposition of Fe-doped nickel selenides on Ni foam as a bi-functional electrocatalyst for water splitting in alkaline solution. *J. Electroanal. Chem.* **2022**, *906*, 116014.

50. Shi, L.; Fang, H.; Yang, X.; Xue, J.; Li, C.; Hou, S.; Hu, C., Fe-cation Doping in NiSe<sub>2</sub> as an Effective Method of Electronic Structure Modulation towards High-Performance Lithium-Sulfur Batteries. *ChemSusChem* **2021**, *14* (7), 1710-1719.
51. Wang, X.; Li, W.; Xiong, D.; Petrovykh, D. Y.; Liu, L., Bifunctional Nickel Phosphide Nanocatalysts Supported on Carbon Fiber Paper for Highly Efficient and Stable Overall Water Splitting. *Adv. Funct. Mater.* **2016**, *26* (23), 4067-4077.
52. Zhang, G.; Feng, Y.-S.; Lu, W.-T.; He, D.; Wang, C.-Y.; Li, Y.-K.; Wang, X.-Y.; Cao, F.-F., Enhanced Catalysis of Electrochemical Overall Water Splitting in Alkaline Media by Fe Doping in Ni<sub>3</sub>S<sub>2</sub> Nanosheet Arrays. *ACS Catal.* **2018**, *8* (6), 5431-5441.
53. Mahala, C.; Sharma, R.; Sharma, M. D.; Pande, S., Development of copper cobalt sulfide with Cu: Co ratio variation on carbon cloth as an efficient electrode material for the oxygen evolution reaction. *ChemElectroChem* **2019**, *6* (20), 5301-5312.
54. Ren, H.; Yu, L.; Yang, L.; Huang, Z.-H.; Kang, F.; Lv, R., Efficient electrocatalytic overall water splitting and structural evolution of cobalt iron selenide by one-step electrodeposition. *J Energy Chem.* **2021**, *60*, 194-201.
55. Su, H.; Du, X.; Zhang, X., NiCoP coated on NiCo<sub>2</sub>S<sub>4</sub> nanoarrays as electrode materials for hydrogen evolution reaction. *Int. J. Hydrog. Energy* **2019**, *44* (59), 30910-30916.
56. Sivanantham, A.; Ganesan, P.; Shanmugam, S., Hierarchical NiCo<sub>2</sub>S<sub>4</sub> Nanowire Arrays Supported on Ni Foam: An Efficient and Durable Bifunctional Electrocatalyst for Oxygen and Hydrogen Evolution Reactions. *Adv. Funct. Mater.* **2016**, *26* (26), 4661-4672.
57. Zaki, N. H. M.; Ali, A. M. M.; Yaakob, M. K.; Taib, M. F. M.; Hassan, O. H.; Lepit, A.; Yahya, M. Z. A., Structural and electronic properties of nickel doped cobalt oxide electrode for supercapacitors: A first principle study. *IOP Conf. Ser.: Earth Environ. Sci.* **2021**, *685* (1), 012029.
58. Yin, J.; Zhang, H.; Luo, J.; Yao, M.; Hu, W., High-boiling-point solvent synthesis of mesoporous NiCo<sub>2</sub>S<sub>4</sub> with high specific surface area as supercapacitor electrode material. *J Mater Sci: Mater Electron* **2017**, *28* (2), 2093-2099.
59. Kong, W.; Lu, C.; Zhang, W.; Pu, J.; Wang, Z., Homogeneous core-shell NiCo<sub>2</sub>S<sub>4</sub> nanostructures supported on nickel foam for supercapacitors. *J. Mater. Chem. A* **2015**, *3* (23), 12452-12460.



60. Wang, Q.; Liu, B.; Wang, X.; Ran, S.; Wang, L.; Chen, D.; Shen, G., Morphology evolution of urchin-like  $\text{NiCo}_2\text{O}_4$  nanostructures and their applications as pseudocapacitors and photoelectrochemical cells. *J. Mater. Chem.* **2012**, *22* (40), 21647-21653.
61. M. Dieb, T.; Hou, Z.; Tsuda, K., Structure prediction of boron-doped graphene by machine learning. *J. Chem. Phys.* **2018**, *148* (24), 241716.
62. Pandey, P.; Bitla, Y.; Zschornak, M.; Wang, M.; Xu, C.; Grenzer, J.; Meyer, D.-C.; Chin, Y.-Y.; Lin, H.-J.; Chen, C.-T.; Gemming, S.; Helm, M.; Chu, Y.-H.; Zhou, S., Enhancing the magnetic moment of ferrimagnetic  $\text{NiCo}_2\text{O}_4$  via ion irradiation driven oxygen vacancies. *APL Mater.* **2018**, *6* (6), 066109.
63. Battle, P. D.; Cheetham, A. K.; Goodenough, J. B., A neutron diffraction study of the ferrimagnetic spinel  $\text{NiCo}_2\text{O}_4$ . *Mater. Res. Bull.* **1979**, *14* (8), 1013-1024.
64. Richardson, R. C. D., The wear of metals by hard abrasives. *Wear* **1967**, *10* (4), 291-309.
65. Ghosh, S.; Sarkar, S.; Chowdhury, J., Structural and electronic properties of wide band gap charge transfer insulator  $\text{Hg}_2\text{Cl}_2$ : Insights from the first-principle calculations. *Mater. Chem. Phys.* **2022**, *276*, 125379.
66. Nørskov, J. K.; Rossmeisl, J.; Logadottir, A.; Lindqvist, L.; Kitchin, J. R.; Bligaard, T.; Jónsson, H., Origin of the Overpotential for Oxygen Reduction at a Fuel-Cell Cathode. *J. Phys. Chem. B* **2004**, *108* (46), 17886-17892.
67. Parsons, R., The rate of electrolytic hydrogen evolution and the heat of adsorption of hydrogen. *Trans. Faraday Soc.* **1958**, *54* (0), 1053-1063.
68. Behera, S. K.; Deb, P.; Ghosh, A., Driving electrocatalytic activity by interface electronic structure control in a metalloprotein hybrid catalyst for efficient hydrogen evolution. *Phys. Chem. Chem. Phys.* **2016**, *18* (33), 23220-23230.
69. Würger, T.; Feiler, C.; Vonbun-Feldbauer, G. B.; Zheludkevich, M. L.; Meißner, R. H., A first-principles analysis of the charge transfer in magnesium corrosion. *Sci Rep* **2020**, *10* (1), 15006.

**Summary, conclusion, and future scope**

- \* *The work completed for this thesis is summarized in this chapter by emphasizing its salient features.*
- \* *Future fields of research that can be carried out using this thesis are also established.*

**Chapter 1:** A review of the literature and a brief summary of nanoparticles in electrochemistry are given at the beginning of this thesis. In the area of electrocatalytic water splitting, the production and use of transition metal chalcogenides are explored as sustainable energy options. For the nickel-based electrocatalyst, all electrochemical parameters and practical approaches are provided in detail. A detailed description of the doping technique is given, including instances of doping with cations and anions in transition metal-based chalcogenides. The difficulties and shortcomings of the research are explicitly stated.

**Chapter 2:** This chapter covers all the substances, reagents, instruments, calculation techniques, and methods used in the thesis work from the perspective of analytical chemistry.

**Chapter 3:** In this chapter, Ni/Ni(OH)<sub>2</sub>/NiOOH heterostructure has been carried out through a single electrodeposition step. The mechanism of synthesis of Ni/Ni(OH)<sub>2</sub>/NiOOH on carbon cloth is reported. The developed Ni/Ni(OH)<sub>2</sub>/NiOOH heterostructure sample is utilized in an electrochemical HER reaction with 200 h of stability. The role of Ni, Ni(OH)<sub>2</sub>, and NiOOH have been discussed for the enhancement of HER activity.

**Chapter 4:** In this chapter, the synthesis of Ni(OH)<sub>2</sub>/NiOOH and W-doped Ni(OH)<sub>2</sub>/NiOOH nanosheets is reported. The optimization of the W dopant has been done through various ratios. Vertically grown nanosheet morphology of W<sub>0.1</sub>Ni(OH)<sub>2</sub>/NiOOH is highly active towards HER and OER in an alkaline medium. The synergistic effect between W<sup>6+</sup> and Ni<sup>2+</sup> ions play a vital role in enhancing the active surface area and electrocatalytic activities. The theoretical result also proves that the enhanced electrocatalytic activity of Ni(OH)<sub>2</sub>/NiOOH through W doping.

**Chapter 5:** In this chapter, the synthesis of Ni<sub>9</sub>S<sub>8</sub> and Co doped Ni<sub>9</sub>S<sub>8</sub> on CC through the hydrothermal method. Different ratios of Co:Ni, Co<sub>0.1</sub>Ni<sub>8.9</sub>S<sub>8</sub>, Co<sub>0.05</sub>Ni<sub>8.95</sub>S<sub>8</sub>, and Co<sub>0.03</sub>Ni<sub>8.97</sub>S<sub>8</sub> are developed, but Co<sub>0.05</sub>Ni<sub>8.95</sub>S<sub>8</sub> exhibits superior electrocatalytic activity. The Co-doped Ni<sub>9</sub>S<sub>8</sub> electrocatalyst was applied as a bifunctional catalyst in an alkaline medium. The water-splitting reaction is studied in a wide pH region for the Co<sub>0.05</sub>Ni<sub>8.95</sub>S<sub>8</sub> sample. The strain engineering and change in the electronic environment with Co doping in Ni<sub>9</sub>S<sub>8</sub> is investigated with experimental and theoretical results.

**Chapter 6:** In this chapter, we have investigated the Ce doping in Ni<sub>0.85</sub>Se hexagonal nanosheets with experimental and theoretical results. The Ce dopant concentration is optimized in Ni<sub>0.85</sub>Se

nanosheets with various ratios. The optimized  $\text{Ce}_{0.1}\text{Ni}_{0.85}\text{Se}$  electrocatalyst shows better efficiency for HER and OER. The DFT results prove the zero-band gap after doping with Ce in  $\text{Ni}_{0.85}\text{Se}$  catalyst; the charge-pulling nature of Ce benefits the change in an electronic environment.

**Chapter 7:** In this chapter, Fe-doped  $\text{NiCo}_2\text{Se}_4$  material on CC is developed through a straightforward hydrothermal method. The as-developed multi-metallic selenides have been utilized for HER, OER, and bifunctional activity. The role of multi-metal centers in electrochemical activity has been explained through thiocyanate study. The band gap and DOS calculation also prove that  $\text{Fe}_{0.2}\text{NiCo}_{1.8}\text{Se}_4$  is more metallic, and dopant Fe contributes an essential role in the system's conductivity.

The summary of the present thesis work is given in Table 8.1. In the context of electrocatalytic stability, the  $\text{W}_{0.1}\text{Ni}(\text{OH})_2/\text{NiOOH}$  electrode shows maximum stability of 120 h of HER and OER reactions. The  $\text{Fe}_{0.2}\text{NiCo}_{1.8}\text{Se}_4$  material shows a lower cell potential of 1.51 V to obtain  $10 \text{ mA/cm}^2$  current density. (as given in Table 8.1)

**Table 8.1:** Comparative table for HER, OER data and cell potential, and stability for all the developed electrodes.

Electrocatalyst	Catalyst loading ( $\text{mg/cm}^2$ )	HER onset potential (V) vs. RHE	OER onset potential (V) vs. RHE	Cell potential	Stability (HER and OER)	Stability (2 electrode)
$\text{Ni}/\text{Ni}(\text{OH})_2/\text{NiOOH}$	3.8	-0.045 ( $10 \text{ mA/cm}^2$ )	1.588 ( $50 \text{ mA/cm}^2$ )	-	200 h	-
$\text{W}_{0.1}\text{Ni}(\text{OH})_2/\text{NiOOH}$	3.9	-0.084 ( $20 \text{ mA/cm}^2$ )	1.523 ( $50 \text{ mA/cm}^2$ )	1.62 V	120 h	12 h
$\text{Co}_{0.05}\text{Ni}_{8.95}\text{S}_8$	1.62	-0.147 ( $50 \text{ mA/cm}^2$ )	1.557 ( $50 \text{ mA/cm}^2$ )	1.89 V	60 h and 80 h	24 h
$\text{Ce}_{0.1}\text{Ni}_{0.85}\text{Se}$	2.87	-0.238 ( $50 \text{ mA/cm}^2$ )	1.56 ( $50 \text{ mA/cm}^2$ )	1.73 V	48 h	24 h
$\text{Fe}_{0.2}\text{NiCo}_{1.8}\text{Se}_4$	4.16	-0.148 ( $50 \text{ mA/cm}^2$ )	1.656 ( $100 \text{ mA/cm}^2$ )	1.51 V	48 h	24 h

### Future research scope

1. To address practical catalyst requirements, innovations that provide scalable methodologies for simultaneously engineering elementary reactions, charge diffusion, gas control, and morphological and electronic structures are desirable. To design chemically and physically robust electrocatalysts fit for industrial use, new electrolyzers are required. E-waste typically contains metals such as copper, aluminum, and rare earth elements, which are crucial components in electrode materials. By recycling and reusing these materials, valuable resources can be recovered, reducing the need for virgin materials and minimizing the environmental impact associated with mining and extraction.
2. Effective electrocatalysts for the evolution of hydrogen and oxygen have been created. By combining with a photoanode or photocathode for PEC water-splitting, the generated electrocatalyst can be employed as a co-catalyst to speed up the kinetics of the reaction and improve photostability.
3. Nickel-based electrocatalysts show good electrical conductivity, low cost, and better electrochemical stability. Further, through doping strategy, the HER and OER performance can be improved. Considering the broad perspective, it is important to develop new and modified nickel-based electrocatalysts for industrial-level application.
4. We have used various characterization techniques such as PXRD, XPS, FESEM, TEM, and BET to study the surface structure and composition of desired electrocatalysts. Some advanced techniques such as XAS (X-ray absorption spectroscopy) and HAADF-STEM (high-angle-annular-dark-field scanning transmission electron microscopy) are required to examine the surface characteristics of catalysts, as well as the changes in surface electronic structure that occur during the catalytic process. It can also be utilized to look at the characteristics of chemical bonds between macromolecules and the coordination structure of atoms.
5. By combining experimental with DFT calculation, time and resources can be saved for the designing of the electrocatalyst. Combining theoretical computations allowed for the determination of the catalyst's electrical structure and characteristics. It simultaneously advances the understanding of electrocatalyst systems and has guiding implications for the design of highly efficient electrocatalysts.

# *Appendices*

## List of Publications [A-1]

---

1. **\*\*Rathore D.**; Sharma M. D.; Sharma, A.; Basu, M.; Pande S. Aggregates of Ni/Ni(OH)<sub>2</sub>/NiOOH Nanoworms on Carbon Cloth for Electrocatalytic Hydrogen Evolution. *Langmuir* 2020, 36, 14019-14030.
2. **\*\*Rathore, D.**; Banerjee, A.; Pande, S., Bifunctional Tungsten-Doped Ni(OH)<sub>2</sub>/NiOOH Nanosheets for Overall Water Splitting in an Alkaline Medium. *ACS Appl. Nano Mater.* 2022, 5 (2), 2664-2677.
3. **\*\*Rathore, D.**; Ghosh, S.; Chowdhury, J.; Pande, S., Co-Doped Ni<sub>9</sub>S<sub>8</sub> Nanostructures for Electrocatalytic Water Splitting over a Wide pH Range. *ACS Appl. Nano Mater.* 2022, 5 (8), 11823-11838.
4. **\*\*Rathore, D.**; Ghosh, S.; Chowdhury, J.; Pande, S., Fe-Doped NiCo<sub>2</sub>Se<sub>4</sub> Nanorod Arrays as Electrocatalysts for Overall Electrochemical Water Splitting. *ACS Appl. Nano Mater.* 2023, 6 (4), 3095-3110.
5. **\*\*Rathore, D.**; Ghosh, S.; Gupta, A.; Chowdhury, J.; Pande, S., Ce-Doped Ni<sub>0.85</sub>Se 2D Nanosheets Developed on Carbon Cloth for Electrochemical Water-Splitting. *ACS Appl. Nano Mater.* 2024, 7, 9730–9744.
6. **Rathore, D.**; Pande, S., Unveiling the effect of Doping in Nickel-Based Electrocatalysts for Electrochemical Water Splitting reaction. (*Review Article, Under preparation*)
7. Mishra, D.; **Rathore, D.**; Bansal, P.; Pande, S.; Chatterjee, S.; Iron-doped titanium dioxide-based metal-organic framework for electrocatalytic water-splitting applications. (*Communicated MS*).

**\*\*Incorporated in the Thesis**

## List of Poster Presented in Conferences [A-2]

---

1. **Rathore D.**, “Symposium on Carbon Nanomaterial Electronics” (SCNE), 8-9 November 2019, BITS-Pilani, Pilani Campus.
2. **Rathore D.**, International workshop on “Supporting Chemistry Research with modern DFT (Density Functional Theory): Software, Techniques, and Applications, 5-16 February 2019, S. S. Patel Science and Commerce college, Gujarat.
3. **Rathore D.**, 4<sup>th</sup> National Conference in Chemistry, 6-7 August 2021, Indian Institute of Technology, Gandhinagar, held virtually (**One of the best flash talks awarded**).
4. **Rathore D.**, Presented paper entitled as “Aggregates of Ni/Ni(OH)<sub>2</sub>/NiOOH Nanoworms on Carbon Cloth for Electrocatalytic Hydrogen Evolution”, 31 August 2021, Dr. K V Rao Research Award.
5. **Rathore D.**, ICON-NSLE 2022 INTERNATIONAL CONFERENCE ON Nanotechnology for Sustainable Living & Environment, 14-16 April 2022, BITS-Pilani, Pilani Campus.



## Brief Biography of the Candidate [A-3]

---



**Name:** Divya Rathore

**Born at** Jhunjhunu, Rajasthan, India

**Bachelor of Science** in Chemistry, Zoology, and Botany from University of Rajasthan, Rajasthan, India in 2015 (Gold Medalist).

**Master's in science** from University of Rajasthan, Rajasthan (India) in 2017 with the specialization in Physical Chemistry.

***Permanent Address:***

Divya Rathore

Village-Mandawara

Teh. –Udaipurwati

District-Jhunjhunu

Pin-333302

Rajasthan, India

Email: [divyarathorechem@gmail.com](mailto:divyarathorechem@gmail.com)

## Brief Biography of the Supervisor [A-4]

---



**Dr. SUROJIT PANDE**

Professor, Department of  
Chemistry, BITS Pilani, Pilani  
Campus, Rajasthan, 333031

**Email:**

spande@pilani.bitspilani.ac.in,  
surojitpande@gmail.com,

Dr. Pande earned his M.Sc. in Inorganic Chemistry from Kalyani University, Kalyani, West Bengal, and obtained his Ph.D. from the Indian Institute of Technology, Kharagpur. Throughout his doctoral studies, he focused on metal and metal oxide nanoparticles, exploring their applications in catalysis and surface-enhanced Raman spectroscopy. His research encompassed various areas, including catalysis, analytical and environmental chemistry, and surface-enhanced Raman scattering (SERS).

Before joining BITS in March 2012, Dr. Pande was a postdoctoral fellow in the Richard M. Crooks research group at The University of Texas at Austin, Texas (USA). During this time, his research interests extended to homogeneous catalysis utilizing dendrimer-encapsulated nanoparticles. He specialized in the spectroscopic study of the sixth and fourth generations of hydroxy-terminated poly(amidoamine) (PAMAM) dendrimers.

Upon joining BITS Pilani as an Assistant Professor in March 2012, Dr. Pande continued to make significant contributions to the field of catalysis and electrocatalysis. His work involved the development of various mono- and bi-metallic, oxide, sulfide, and heterostructure nanomaterials for catalysis, photocatalysis, and electrocatalysis reactions. Dr. Pande successfully managed projects from DST, UGC, CSIR, NAMPET, Private funded, and BITS agencies. Furthermore, five of his students defended their theses successfully as PI and Co-PI in catalysis, electrocatalysis, photocatalysis, and photoelectrochemical water-splitting.